

FEDERAL UNIVERSITY OF SANTA CATARINA
SCHOOL OF TECHNOLOGY
GRADUATE PROGRAM IN MECHANICAL ENGINEERING

Guilherme Fidelis Peixer

OPTIMIZATION OF THE PERFORMANCE OF MAGNETIC REFRIGERATION SYSTEMS USING ARTIFICIAL INTELLIGENCE

Florianópolis
2026

Guilherme Fidelis Peixer

OTIMIZAÇÃO DO DESEMPENHO DE SISTEMAS DE REFRIGERAÇÃO MAGNÉTICA COM O USO DE INTELIGÊNCIA ARTIFICIAL

Tese de doutorado apresentada ao Programa de Pós-Graduação em Engenharia Mecânica da Universidade Federal de Santa Catarina para obtenção do Grau de Doutor em Engenharia Mecânica.

Orientador: Prof. Jader Riso Barbosa Jr., Ph.D.

Coorientador: Prof. Jaime A. Lozano Cadena, Dr.Eng.

Florianópolis

2026

Ficha catalográfica gerada por meio de sistema automatizado gerenciado pela BU/UFSC.
Dados inseridos pelo próprio autor.

Fidelis Peixer, Guilherme
Otimização do Desempenho de Sistemas de Refrigeração Magnética com o Uso de Inteligência Artificial / Guilherme Fidelis Peixer ; orientador, Jader Riso Barbosa Jr., coorientador, Jaime Andrés Lozano Cadena, 2026.
356 p.

Tese (doutorado) - Universidade Federal de Santa Catarina, Centro Tecnológico, Programa de Pós-Graduação em Engenharia Mecânica, Florianópolis, 2026.

Inclui referências.

1. Engenharia Mecânica. 2. Refrigeração Magnética. 3. Transição Energética. 4. Inteligência Artificial. 5. Aprendizado de Máquina. I. Barbosa Jr., Jader Riso. II. Lozano Cadena, Jaime Andrés. III. Universidade Federal de Santa Catarina. Programa de Pós-Graduação em Engenharia Mecânica. IV. Título.

Guilherme Fidelis Peixer

OTIMIZAÇÃO DO DESEMPENHO DE SISTEMAS DE REFRIGERAÇÃO MAGNÉTICA COM O USO DE INTELIGÊNCIA ARTIFICIAL

O presente trabalho em nível de doutorado foi avaliado e aprovado em 18 de Dezembro de 2025 por banca examinadora composta pelos seguintes membros:

Prof. Angelo Maiorino, Ph.D.
Universidade de Salerno, Itália

Prof. Andrej Kitanovski, Ph.D.
Universidade de Liubliana, Eslovênia

Prof. Alexandre Kupka da Silva, Ph.D.
Universidade Federal de Santa Catarina

Prof. Amir Antônio Martins de Oliveira Jr., Ph.D.
Universidade Federal de Santa Catarina

Certificamos que esta é a versão original e final do trabalho de conclusão, que foi julgado adequado para a obtenção do título de Doutor em Engenharia Mecânica.

Documento assinado digitalmente
Jader Riso Barbosa Junior
Data: 08/01/2026 16:21:32-0300
CPF: ***.026.207-**
Verifique as assinaturas em https://v.ufsc.br

Prof. Jader Riso Barbosa Jr., Ph.D.
Orientador

Documento assinado digitalmente
Jaime Andres Lozano Cadena
Data: 06/01/2026 15:37:05-0300
CPF: ***.171.599-**
Verifique as assinaturas em https://v.ufsc.br

Prof. Jaime A. Lozano Cadena, Dr.Eng.
Coorientador

Documento assinado digitalmente
Armando Albertazzi Goncalves Junior
Data: 08/01/2026 20:46:42-0300
CPF: ***.495.015-**
Verifique as assinaturas em https://v.ufsc.br

Prof. Armando Albertazzi Gonçalves Jr., Dr. Eng.
Coordenador em Exercício do Programa de Pós-Graduação

Florianópolis, 2026.

Aos meus pais, Izaias e Rozania, e a minha irmã, Teresa

ACKNOWLEDGEMENTS

First and foremost, I express my deepest gratitude to my advisors, Prof. Jader Riso Barbosa Jr. and Prof. Jaime Lozano. I was welcomed to Polo in the second year of my undergraduate studies, and ever since, it has been a cornerstone of my professional, academic, and personal growth. I am profoundly thankful for your teachings, guidance, and support throughout these years. Thank you for believing in my potential, encouraging me to take on challenges even when I doubted myself, and trusting that I could achieve excellence in performance and results. You remain true role models of dedication, integrity, and academic rigor, and your influence continues to shape my development in countless ways.

I would also like to thank the members of my examination committee: Prof. Angelo Maiorino, Prof. Andrej Kitanovski, Prof. Alexandre Kupka, and Prof. Amir Antônio Oliveira Martins, for accepting my invitation to participate in this defense and for evaluating this thesis. Your insights and recommendations were invaluable to improving this work.

Among the many opportunities I was fortunate to experience during this journey, I am especially grateful to the institutions and people who welcomed me. My sincere thanks to Dr. Urban Tomc and Prof. Andrej Kitanovski for hosting me at the University of Ljubljana; to Prof. Angelo Maiorino for opening the doors of his laboratory and classroom at the University of Salerno; and to Prof. Daniel Tartakovsky for welcoming me at Stanford University. These experiences were essential for my academic and professional development.

I am deeply thankful to the entire team at Polo and our partner laboratories. This work is the result of the collective effort of many talented individuals from diverse backgrounds. Each contribution, no matter its nature or duration, was fundamental to the outcomes presented here. I am especially grateful to Alan Nakashima for his long-standing partnership and essential support both in the laboratory and on the basketball court, and to Anderson Lorenzoni, whose skill and dedication were crucial in transforming our ideas into tangible results. I also express my gratitude to the students I had the privilege to advise: Sergio Luiz Dutra, Diego dos Santos, Luis Felipe Cattelan, Maria Cláudia Régio e Silva, Elias Pagnan, Pedro Miola da Silva, Marco Antônio Cerutti, Gabriel Nandi, Yan Azeredo, Jhonatta Casagrande Bordignon, Tamayo Dias, Rogério Sawaya Sucaria, Kevin Costa, Rodrigo Vilamil, Julia Sebold May, Ana Laura Lima Vieira, Yogan Sganzerla and Júlio Michels Jeremias. Regardless of the time we worked together, each of you provided me with invaluable learning experiences, and it has been a joy to witness your achievements and growth.

A major part of this thesis revolves around magnetocaloric technology, which encompasses several fields of knowledge. For this reason, I relied on the expertise of many specialists whose support was essential for developing the models and prototype. I am sincerely grateful to Bernardo Vieira, Higor Teza, Paulo de Faria, and Dr. Henrique Neves Bez (in memoriam) for their contributions to the active magnetic regenerator models; to Dr. Fábio Fortkamp and Prof. Maurício da Luz for their support with the magnetic circuit model; to Gislaine Hoffmann, Gabriel do Rosário, and Prof. Rodolfo Flesch for their work on the hydraulic and control systems; to Allan Doring, Marcelo Rosa, Diego Reif, Prof. Paulo Wendhausen, and Prof. Cristiano da Silva Teixeira for the characterization of magnetocaloric materials; to Marcelo Ribeiro, Rafael Valdir Lima, Matheus Capovilla, and Pedro Cardoso for their contributions to the mechanical design and commissioning of the system; to Dr. Mayara Silvestre de Oliveira, Laryssa Antunes, and Prof. Fernando Forcelini for supporting the project management; to Eduardo Marese, Luis Eduardo Castro Anaya, and Prof. Sergio Yesid Gómez for their participation in magnetocaloric material discovery; and to Natália Maleski de Sá and Vitor dos Santos for their work on the magnetic wine cooler.

This research also allowed me to explore applications in other areas in which I initially had only superficial knowledge. The contribution of specialists in each of these fields was essential to advancing this work. I gratefully acknowledge Eduardo Alves, Mariah Pereira, Dr. Fábio Fortkamp, and Dr. Júlio César Alves Ferreira for their guidance in oil and gas applications; Dr. Marcus Vinícius Pedron Carneiro, Dr. Lucas Militão, and Dr. Luis Gustavo Medeiro de Luca for supporting the cabon capture, utilization and storage applications; Andre Vicente, Enzo Remlinger, Prof. Joel Boeng, and Prof. Amir Antônio Oliveira Martins for their contributions to hydrogen fuel cells; Thomas Lex for the development of the heat transformer models; and Ricardo Vargas for his support with the 3W dataset.

My appreciation also extends to all staff and friends at Polo, particularly Tiago Melo, Nara Santos, Luiza de Nóbrega, João Luís Gomes, Alexandre dos Santos, Jorge Lubas, Fernando Knabben, Rodolfo Espíndola, Pedro Magalhães, and, with special thanks, to Márcio Demétrio and Fernando Czubinski. I am also grateful for Polo's current and previous faculty: Prof. Claúdio Melo (in memorian), Prof. Álvaro Toubes Prata, Prof. Rogério Tadeu Ferreira, Prof. César José Deschamps and Prof. Cristian Hermes, that together with Prof. Jader Barbosa Jr. and Prof. Jaime Andrés Lozano Cadena, have built and maintained a center of excellence in science, engineering and technology, shaping generations of world-class engineers. I am proud to count myself among them.

I gratefully acknowledge the financial support provided by CNPq (Conselho Nacional de Desenvolvimento Científico e Tecnológico), FAPESC (Fundação de Amparo à Pesquisa e Inovação do Estado de Santa Catarina), CODEMGE (Companhia de Desenvolvimento de Minas Gerais), Petrobras (Petróleo Brasileiro), and EMBRAPII (Empresa Brasileira

de Pesquisa e Inovação Industrial). I also acknowledge the funding and opportunities provided by DWIH (Centro Alemão de Ciência e Inovação São Paulo), Academia Brasileira de Ciência, MCTI (Ministério de Ciência, Tecnologia e Inovação), and Erasmus+ Programme, and the support provided by SINOVA (Deparamento de Inovação) and SINTER (Secretaria de Relações Internacionais) of the Federal University of Santa Catarina, FEESC (Fundação de Ensino e Engenharia de Santa Catarina) and Fundo Catarina.

I acknowledge the Federal University of Santa Catarina, the Department of Mechanical Engineering, the Graduate Program in Mechanical Engineering, and Polo – Research Laboratories for Emerging Technologies in Cooling and Thermophysics for providing the education, infrastructure, and environment necessary for the development of this work. Presenting my research in many places around the world has only reinforced my appreciation for the world-class education offered by these institutions.

Por fim, e mais importante, agradeço e dedico este trabalho à minha família. Ao meu pai, Izaías, que me ensinou, acima de tudo, a importância de ser uma pessoa boa e me mostrou como me tornar uma. À minha mãe, Rozania, que me ensinou o que é o amor incondicional e o que ele nos torna capazes de fazer pelos outros. E à minha irmã, Teresa, que me ensinou o que significa ter alguém a quem você pode sempre contar, mesmo para os menores e mais insignificantes percalços da vida. Independentemente do caminho que eu siga, estou tranquilo, pois sei que com vocês nunca estarei sozinho e sempre terei um lar.

"Simplicity is the ultimate sophistication."

Leonardo da Vinci

RESUMO

A refrigeração tem transformado significativamente a sociedade moderna, com sistemas que desempenham um papel vital na vida cotidiana e nos processos industriais. No entanto, esses sistemas contribuem significativamente para o consumo global de energia e para a degradação ambiental, representando 20% do consumo global de eletricidade e 10% das emissões de gases de efeito estufa. Tal cenário tende a se tornar cada vez mais crítico, uma vez que a Agência Internacional de Energia projeta que as instalações de aparelhos de ar-condicionado em todo o mundo triplicarão até 2050. Além disso, a Emenda de Kigali, uma extensão do Protocolo de Montreal, estabelece a redução e a eliminação dos refrigerantes comumente utilizados em sistemas convencionais de aquecimento, ventilação e refrigeração. Esses desafios posicionam a demanda por tecnologias de refrigeração energeticamente eficientes e ambientalmente amigáveis como uma questão crítica no debate global sobre energia. A refrigeração magnetocalórica surgiu como uma das alternativas mais promissoras, aproveitando o efeito magnetocalórico para proporcionar um resfriamento eficiente e sustentável. Esta tecnologia utiliza refrigerantes sólidos, eliminando o vazamento de substâncias prejudiciais e minimizando o consumo de energia durante a operação. Apesar de seu potencial, a refrigeração magnetocalórica ainda não atingiu viabilidade comercial, com mais de 40 institutos de pesquisa em todo o mundo trabalhando no desenvolvimento de protótipos e dispositivos experimentais. Nos últimos anos, aplicações de inteligência artificial têm ganhado cada vez mais destaque, podendo ser utilizadas em sistemas de engenharia para otimizar esses sistemas. Esta tese explora a integração de inteligência artificial para otimizar o desenvolvimento e o desempenho de sistemas de refrigeração magnetocalórica. Um protótipo em larga escala para aplicações de ar-condicionado foi avaliado experimentalmente e utilizado como fonte de dados para o desenvolvimento de modelos. O estudo incorpora dados experimentais e literários para construir uma Rede Neural Artificial capaz de prever o desempenho do sistema em diferentes condições operacionais. Além disso, modelos transientes foram desenvolvidos para simular comportamentos dinâmicos e melhorar a eficiência do sistema. Técnicas de inteligência artificial também foram aplicadas à análise de incerteza, fornecendo insights sobre os principais parâmetros de projeto que afetam o desempenho do sistema. Os métodos aplicados à otimização de sistemas magnetocalóricos também foram explorados em outras áreas da engenharia, como as energias renováveis e os sistemas de óleo e gás. A integração de inteligência artificial não apenas melhora a precisão dos modelos do sistema, mas também abre caminho para novas aplicações na engenharia, particularmente na otimização do consumo de energia, da confiabilidade do sistema e do desempenho. Os resultados apresentados nesta tese demonstram que a inteligência artificial pode desempenhar um papel fundamental no avanço da comercialização da refrigeração magnetocalórica, melhorando a eficiência do design e da operação do sistema. Este trabalho

contribui para o desenvolvimento contínuo de soluções de refrigeração mais sustentáveis e energeticamente eficientes, oferecendo valiosos insights para pesquisas futuras e aplicações em setores críticos, como o de ar-condicionado e o de refrigeração, entre outros.

Palavras-chave: refrigeração magnética, eficiência energética, inteligência artificial, aprendizado de máquina, redes neurais artificiais.

ABSTRACT

Refrigeration has significantly transformed modern society, with systems that play a vital role in daily life and industrial processes. However, these systems contribute substantially to global energy consumption and environmental degradation, accounting for 20% of global electricity use and 10% of greenhouse gas emissions. This scenario tends to become increasingly critical, as the International Energy Agency projects that air-conditioning installations worldwide will triple by 2050. In addition, the Kigali Amendment, an extension of the Montreal Protocol, mandates the reduction and phase-out of refrigerants commonly used in conventional heating, ventilation, and cooling systems. These challenges position the demand for energy-efficient and environmentally friendly refrigeration technologies as a critical issue in the global energy debate. Magnetocaloric refrigeration has emerged as one of the most promising alternatives, harnessing the magnetocaloric effect to provide efficient and sustainable cooling. This technology uses solid refrigerants, eliminating the leakage of harmful substances and minimizing energy consumption during operation. Despite its potential, magnetocaloric refrigeration has not yet reached commercial viability, with more than 40 research institutes worldwide working on the development of prototypes and experimental devices. In recent years, artificial intelligence applications have gained increasing prominence and can be used in engineering systems for optimization. This thesis explores the integration of artificial intelligence to optimize the development and performance of magnetocaloric refrigeration systems. A large-scale prototype for air-conditioning applications was experimentally evaluated and used as a data source for model development. The study incorporates experimental and literature data to build an Artificial Neural Network capable of predicting system performance under different operating conditions. Furthermore, transient models were developed to simulate dynamic behaviors and improve system efficiency. Artificial intelligence techniques were also applied to uncertainty analysis, providing insights into the key design parameters that affect system performance. The methods applied to the optimization of magnetocaloric systems were also explored in other engineering fields, such as renewable energy and oil and gas systems. The integration of artificial intelligence not only improves the accuracy of system models but also paves the way for new AI applications in engineering, particularly in optimizing energy consumption, system reliability, and performance. The results presented in this thesis demonstrate that artificial intelligence can play a fundamental role in advancing the commercialization of magnetocaloric refrigeration by improving system design and operation efficiency. This work contributes to the ongoing development of more sustainable and energy-efficient refrigeration solutions, offering valuable insights for future research and applications in critical sectors such as air conditioning and refrigeration, among others.

Keywords: magnetic refrigeration, energy efficiency, artificial intelligence, machine learning, artificial neural networks.

RESUMO EXPANDIDO

Introdução

A tecnologia de refrigeração é essencial na sociedade moderna, impactando a vida cotidiana e os processos industriais. Apesar disso, os sistemas convencionais consomem quantidades consideráveis de energia e geram emissões significativas de CO_2, o que representa cerca de 20% do consumo global de eletricidade e 10% das emissões de gases de efeito estufa. Com a previsão de triplicação das instalações de ar-condicionado até 2050, há uma demanda crescente por alternativas mais sustentáveis e eficientes.

A Emenda de Kigali reforça o compromisso global de reduzir o uso de refrigerantes, que, apesar de eficazes, causam danos ao meio ambiente devido ao alto potencial de aquecimento global equivalente. A refrigeração magnetocalórica, que utiliza o efeito magnetocalórico para operar refrigeradores sem fluidos refrigerantes, surge como uma alternativa promissora. Porém, ainda enfrenta desafios técnicos e econômicos, como baixa eficiência em altas temperaturas e custos elevados. Mais de 40 centros de pesquisa estão trabalhando em protótipos, e a implementação dessa tecnologia poderia transformar a indústria de refrigeração e reduzir significativamente o impacto ambiental.

A Inteligência Artificial (IA) tem grande potencial para otimizar sistemas de engenharia, melhorando a eficiência e reduzindo custos. No contexto da refrigeração magnetocalórica, a IA pode acelerar a modelagem, a simulação e a otimização de componentes e sistemas. Com técnicas como redes neurais artificiais, a IA identifica padrões complexos e pode prever o comportamento dos sistemas, aprimorando continuamente os modelos em tempo real. Dessa forma, a IA não só impulsiona a inovação, mas também oferece soluções sustentáveis para os desafios globais de energia e de meio ambiente.

Objetivos

Esta tese faz parte de um projeto de pesquisa realizado no Polo/UFSC, com o objetivo de:

> *"Projetar e implementar um protótipo de ar-condicionado TRL-6 com capacidade de refrigeração de 9000 BTU/h (2637 W), operado por uma Unidade de Refrigeração Magnetocalórica (MRU) composta por ímãs permanentes e refrigerantes sólidos à base de elementos de terras raras"*.

O objetivo deste protótipo é conectar avanços teóricos na tecnologia de refrigeração magnetocalórica a aplicações reais. Alcançar o TRL-6 permitirá validar o projeto em condições práticas, garantindo que o sistema atenda a padrões críticos de desempenho, eficiência e confiabilidade. Além disso, trata-se de um dos protótipos pioneiros capazes de refrigerar um ambiente inteiro. Esta tese consiste na montagem, operacionalização e análise detalhada do desempenho termodinâmico do protótipo, oferecendo insights sobre sua eficiência operacional e efetividade em condições reais.

Além de realizar avaliações experimentais do desempenho termodinâmico, esta pesquisa visa investigar o potencial da IA para otimizar o desempenho do sistema e de aplicações relacionadas à refrigeração magnetocalórica. Utilizando dados derivados do protótipo, juntamente com amostras da literatura relevante e simulações numéricas, o objetivo é desenvolver modelos capazes de prever o comportamento do sistema em diversas condições operacionais, com alta precisão e baixo custo computacional. Ademais, as aplicações dos métodos desenvolvidos, com foco em sistemas de refrigeração magnetocalórica, serão exploradas em outras áreas da engenharia, como as energias renováveis e o setor de petróleo e gás.

Esta tese busca superar a lacuna entre a operação prática e a modelagem teórica, oferecendo uma avaliação do sistema de refrigeração enquanto explora o potencial da aplicação de IA nas tecnologias. Espera-se que os resultados desta pesquisa não apenas validem o desempenho do protótipo atual, mas também abram caminho para inovações futuras na refrigeração magnetocalórica e em outras aplicações de engenharia. Assim, dada a oportunidade proporcionada pelo projeto de pesquisa, o objetivo principal proposto para esta tese é:

> *"Projetar, montar e avaliar o desempenho termodinâmico da unidade de refrigeração magnetocalórica e investigar o potencial das técnicas de IA para otimizar seu desempenho e aplicá-las em sistemas de engenharia"*.

Métodos

Este trabalho seguiu uma abordagem integrada e multidisciplinar para o desenvolvimento e otimização do sistema de refrigeração magnetocalórica projetado para aplicações de climatização, com uma capacidade de refrigeração de 9.000 BTU/h, operando entre 22°C e 35°C. A metodologia envolveu modelagem teórica e experimental, bem como a aplicação de técnicas avançadas de IA para otimizar o desempenho. Inicialmente, foram desenvolvidos modelos dos componentes do sistema, tais como o regenerador magnético ativo, o circuito magnético, os trocadores de calor e o sistema hidráulico. A IA foi aplicada aos regeneradores e ao circuito magnético, enquanto os trocadores de calor e o sistema hidráulico foram modelados analiticamente. Esses modelos foram integrados a uma simulação de nível de sistema, com foco em minimizar o consumo de energia e os custos operacionais, maximizando a eficiência. A otimização foi realizada com o Algoritmo Genético NSGA-II, que ajudou a identificar as principais trocas de desempenho, e o design final foi escolhido a partir da fronteira de Pareto, com um critério global ponderado. Modelos substitutos baseados em redes neurais artificiais foram utilizados para explorar de forma eficiente o espaço de design e facilitar a otimização multiobjetivo.

A avaliação experimental foi realizada no protótipo, com a caracterização dos componentes individuais, incluindo o circuito magnético, os materiais magnetocalóricos e os regeneradores magnético-ativos. A avaliação seguiu normas internacionais e a análise de três gerações de protótipos permitiu compreender o comportamento real dos componentes, destacando as

principais fontes de consumo de energia e de degradação do desempenho.

A IA foi aplicada para otimizar o desempenho do sistema de diversas maneiras. Desenvolveu-se um modelo para prever o desempenho de sistemas de refrigeração a temperatura ambiente, treinado com dados experimentais e da literatura. Também foi desenvolvido um modelo especializado para prever o comportamento dinâmico do sistema, com base em dados experimentais transientes. A IA foi ainda usada na análise de incertezas, como a temperatura de Curie dos materiais magnetocalóricos, por meio de análise de Monte Carlo, para destacar o impacto das incertezas materiais no desempenho do sistema.

As metodologias de otimização foram expandidas para outras tecnologias, como a liquefação de hidrogênio, otimizando refrigerantes multicomponentes e avaliando sistemas de óleo e gás, bem como fenômenos termoestruturais dos poços. Técnicas de detecção de anomalias com IA também foram aplicadas ao monitoramento de poços, evidenciando a viabilidade industrial dessas abordagens.

Resultados e Discussão

A avaliação experimental do protótipo da Unidade de Refrigeração Magnetocalórica foi realizada com base em requisitos de climatização de 9.000 BTU/h, operando entre 22°C e 35°C. Embora o protótipo tenha enfrentado limitações devido à quantidade insuficiente de materiais magnetocalóricos, ele alcançou algumas das maiores capacidades de refrigeração e de diferença de temperatura já reportadas para sistemas dessa tecnologia. O protótipo foi capaz de refrigerar um ambiente relevante, o que representa um avanço significativo, já que a refrigeração magnetocalórica tradicionalmente apresenta dificuldades de demonstração. A avaliação de três gerações de protótipos permitiu identificar fontes de perdas de desempenho e irreversibilidades, destacando as perdas térmicas no regenerador magnético ativo e o comportamento não ideal dos materiais magnetocalóricos como os principais desafios.

A integração de IA mostrou-se eficaz na otimização do sistema. O modelo preditivo desenvolvido para o desempenho à temperatura ambiente mostrou boa concordância com os dados experimentais, embora tenha apresentado limitações ao ser extrapolado para condições fora do intervalo caracterizado. Isso enfatiza a importância da personalização dos modelos para garantir previsões precisas. A modelagem do comportamento transiente com uma rede neural artificial especializada foi bem-sucedida, permitindo prever com precisão o desempenho dinâmico do sistema e demonstrando o potencial da IA para otimização em tempo real por meio de técnicas como o controle preditivo.

A análise de incertezas, por meio da abordagem de Monte Carlo, revelou que a temperatura de Curie dos materiais magnetocalóricos é uma das principais fontes de incerteza no desempenho do sistema. A variação material, influenciada por processos de fabricação e condições ambientais, foi identificada como um desafio significativo. Embora o superdimensionamento dos componentes possa mitigar essas incertezas, a redução da variabilidade no processo de

fabricação dos materiais foi considerada a solução mais eficaz.

As metodologias de otimização desenvolvidas foram aplicadas a outras áreas de engenharia, como a liquefação de hidrogênio, onde a utilização de modelos substitutos otimizou o desempenho de refrigerantes multicomponentes, superando o de sistemas convencionais. Essas metodologias também foram estendidas ao setor de petróleo e gás, com a análise do impacto das condições de contorno na cabeça do poço, das propriedades termofísicas dos fluidos e da geometria dos poços sobre os fenômenos termoestruturais do sistema. Técnicas de detecção de anomalias, aplicadas ao monitoramento de poços offshore, mostraram grande potencial para identificar comportamentos anômalos precocemente.

Considerações Finais

Esta pesquisa contribuiu para o avanço da tecnologia de refrigeração magnetocalórica, explorando seu potencial para aplicações em climatização e otimizando seu desempenho por meio de técnicas avançadas de IA. O estudo demonstrou que, apesar dos desafios associados à disponibilidade de materiais magnetocalóricos e às limitações operacionais dos protótipos, o sistema desenvolvido foi capaz de obter resultados notáveis, como a refrigeração de um ambiente relevante. Além disso, a aplicação de IA, especialmente por meio de modelos substitutos baseados em redes neurais artificiais, revelou-se uma ferramenta eficaz para acelerar o processo de design e de otimização, permitindo a exploração de configurações de alto desempenho que, de outra forma, seriam computacionalmente inviáveis.

A análise experimental detalhada e a modelagem por IA proporcionaram uma compreensão mais profunda das limitações termodinâmicas dos sistemas de refrigeração magnetocalórica e de suas possíveis soluções. A investigação das incertezas nos materiais magnetocalóricos e sua influência no desempenho do sistema destacou a necessidade de aprimoramento contínuo na fabricação e no controle da qualidade dos componentes. A implementação de técnicas de aprendizado de máquina para modelagem transiente e controle preditivo também demonstrou grande potencial para melhorar a eficiência operacional em tempo real, uma vez que essas abordagens permitem ajustes dinâmicos nas condições de operação.

Além disso, as metodologias de otimização desenvolvidas para sistemas de refrigeração magnetocalórica foram aplicadas com sucesso em outras áreas da engenharia, como na liquefação de hidrogênio e na exploração de petróleo e gás, evidenciando o impacto transformador da IA em diversas indústrias. O trabalho realizado nesta tese não só avança o campo da refrigeração magnetocalórica, mas também amplia as possibilidades de uso de IA na engenharia, com potencial para influenciar a otimização de sistemas em setores críticos de energia e de recursos naturais.

Palavras-chaves: refrigeração magnética, eficiência energética, inteligência artificial, aprendizado de máquina, redes neurais artificiais.

LIST OF FIGURES

Figure 1.1 – Schematic representation of an MR system and its main components. . . . 48

Figure 1.2 – Comparison between the frameworks of traditional programming and ML. 49

Figure 2.1 – Demonstration of the MCE through the adiabatic temperature change and isothermal entropy change by an increase in the applied magnetic field in a temperature versus entropy chart. Adapted from Smith *et al.* (2012). . . . 54

Figure 2.2 – Experimental data for the adiabatic temperature change in commercial-grade Gd for a magnetic field change of 1 T. Adapted from Smith *et al.* (2012). . . . 55

Figure 2.3 – Experimental data for isothermal entropy change for different MCM samples for an applied magnetic field change between 0 and 2 T. Adapted from Brück (2005). . . . 56

Figure 2.4 – Schematic representation of an idealized thermo-magnetic regenerative Brayton cycle. Adapted from Trevizoli (2015). . . . 57

Figure 2.5 – MR prototypes developed by Astronautics Corporation of America. Figure (a) presents the rotary regenerator prototype developed by Zimm *et al.* (2006) and (b) the rotary magnet prototype developed by Jacobs *et al.* (2014). | 60

Figure 2.6 – Second generation of the prototypes developed by the University of Victoria (Arnold *et al.*, 2014). . . . 61

Figure 2.7 – MR prototypes developed by the Technical University of Denmark. Figure (a) presents the rotary regenerator prototype developed by Bahl *et al.* (2011) and (b) the Rotary magnet prototype developed by Dall'Olio *et al.* (2021). 63

Figure 2.8 – Prototype developed at the Technical University of Delft (Huang *et al.*, 2019). 64

Figure 2.9 – Prototype developed at the University of Ljubljana (Tušek *et al.*, 2013). . . 65

Figure 2.10–Prototype developed at the University of Salerno (Aprea *et al.*, 2014). . . . 66

Figure 2.11–Prototype developed by Magnoric (Lionte *et al.*, 2020). . . . 66

Figure 2.12–Prototype developed by the University of Genoa (Bocanegra *et al.*, 2024). . 67

Figure 2.13–Prototype developed by the University of Science and Technology of China (Hai *et al.*, 2024). . . . 68

Figure 2.14–Prototype developed by Magnotherm (Liang *et al.*, 2025). . . . 68

Figure 2.15–MR prototypes developed by Polo/UFSC. Pictures of the prototypes developed by (a) Trevizoli *et al.* (2011), (b) Trevizoli *et al.* (2016b), (c) Rotary magnet prototype developed by Lozano *et al.* (2016), and (d) Rotary magnet prototype developed by Nakashima *et al.* (2021). 70

Figure 2.16–Example of the hierarchical structure of a Decision Tree (Kingsford & Salzberg, 2008). 81

Figure 2.17–Illustrative example of the trade-off between overfitting and underfitting. 84

Figure 2.18–Validation error as a function of the allocated resources for different configurations according to the Hyperband algorithm (Li *et al.*, 2018). 86

Figure 2.19–Schematic diagram of (a) a perceptron and (b) a DNN. 89

Figure 2.20–Schematic representation of an Autoencoder (Pratella *et al.*, 2021). 94

Figure 2.21–Schematic Representation of PINN (Trahan *et al.*, 2024). 97

Figure 3.1 – Strategy for the integrated design of the System (Oliveira *et al.*, 2018). . . . 105

Figure 3.2 – Comparison between the numerical cooling capacity and the predicted outcomes. 109

Figure 3.3 – Cross-section area (first quadrant) of the MC-AMR assembly. Black regions: soft magnetic material; white regions: air; light gray regions: hard magnetic material; Dark gray region at the bottom left: stator/shaft; gray regions: AMRs; arrows: remanence directions. 111

Figure 3.4 – Comparison between the numerical and the predicted outcomes of the AMR magnetization power. 113

Figure 3.5 – Training of the MC models. Results for (a) the average two-dimensional magnetic flux density and (b) three-dimensional magnetic flux density. . . 116

Figure 3.6 – Flowchart of the optimization process. Yellow stars indicate the application of ANN in the process. 123

Figure 3.7 – Resulting Pareto front of the MOO problem. 125

Figure 3.8 – Breakdown of the contributions of (a) cost, (b) power consumption, and (c) mass of the system. Attained values of (d) mass of MCM, (e) COP, and (f) second-law efficiency for the system and for the AMR, associated with the designs that make up the Pareto front. 126

Figure 3.9 – Behavior of the AMR parameters of the optimal systems making up the Pareto front as a function of the power consumption of the system: (a) mass flow rate, (b) magnetic flux density of the AMR, (c) frequency, (d) height, (e) width, (f) length of the AMR, (g) inlet temperature of the cold blow and (h) inlet temperature f the hot blow. 128

Figure 3.10–Behavior of the MC geometric parameters of the optimal systems making up the Pareto front as a function of power consumption of the system: (a) inner and outer radius of the rotor and stator, (b) length of the MC, (c) angle of the magnets, and (d) thickness of the flux concentrator tube. . . . 130
Figure 3.11–Behavior of the CHEx and HHEx parameters of the optimal systems making up the Pareto front as a function of $\dot{W}_{\text{sys}}$: (a) $(\varepsilon C^*)_{\text{HEx}}$, (b) height, (c) width, (d) length, (e) fin density and (f) diameter of the tube for CHEx and HHEx. . . . 132
Figure 3.12–Component breakdown for (a) power consumption, (b) cost, and (c) mass of the system for the optimum configuration. . . . 134
Figure 4.1 – The MRU and its main components. . . . 137
Figure 4.2 – Photograph of the MRU. . . . 137
Figure 4.3 – Photograph of the full prototype. . . . 138
Figure 4.4 – Cross-section view (first quadrant) of the MC-AMR assembly. Black regions: soft magnetic material; white regions: air; light gray regions: hard magnetic material; Dark gray region at the bottom left: stator/shaft; arrows: remanence directions. . . . 139
Figure 4.5 – Stator of the MC. . . . 140
Figure 4.6 – Exploded representation of the rotor. (1) Screws, (2) Protective Magnetic Layer, (3) Supporting Lid, (4) External Protective Tube, (5) Internal Protective Tube, (6) Magnetic Assembly. . . . 141
Figure 4.7 – Assembly of the Rotor. . . . 142
Figure 4.8 – AMR assembled in the radial gap between the rotor and stator. . . . 142
Figure 4.9 – Assembling process of the AMR. Pictures of (a) the inner section of the AMR casing during the allocation of MCM and (b) the arrangement of the metallic frames and separating meshes on the last MCM layer of the AMR. 143
Figure 4.10–MCM employed in the MRU. Darker and smaller samples are Gd particles. Lighter and bigger samples are $La(Fe,Mn,Si)_{13}H_z$ particles. . . . 144
Figure 4.11–Hydraulic diagram of the MRU. . . . 146
Figure 4.12–Heat Exchangers used in the MRU. Pictures of (a) HEx without the coupling of the fans and (b) with the fans coupled. . . . 147
Figure 4.13–Schematic representation of the MRU and the calorimeter. . . . 149
Figure 4.14–Calibrated calorimeter developed to evaluate the performance of the MRU. (a) Indoor (b) outdoor chamber, and (c) external view. The vapor compression evaporator and condensing unit shown in (a) and (b) were evaluated for the validation of the calorimeter. . . . 151
Figure 4.15–Reconditioning equipment of the calibrated calorimeter. Picture of (a) axial fans placed in the cold chamber and (b) heaters of the cold chamber. . . . 152

Figure 4.16–Cross-section view for the configurations of the AMR-MC arranged for each version of the MRU. Black regions: soft magnetic material; white regions: air; light gray regions: hard magnetic material; gray regions: AMRs; Dark gray region at the bottom left: stator/shaft; arrows: remanence directions. The numbering of AMR beds is according to that in Fig. 4.11. Representations of the (a) first, (b) second, and (c) third configurations of the system. 154
Figure 5.1 – Comparison between experimental data and numerical results for the modulus of the magnetic flux density at the center of the magnetic gap for the first configuration of the MC. 164
Figure 5.2 – Comparison between experimental data and numerical results for the modulus of the magnetic flux density at the center of the magnetic gap for the second configuration of the MC. 165
Figure 5.3 – Comparison between the experimental measurements from the first and second configurations of the MC. 166
Figure 5.4 – SEM-SE (left), SEM-BSE (middle), and OM (right) images of microparticles of T_{C2} before and after immersion testing over a year (Döring *et al.*, 2024a). 167
Figure 5.5 – Evolution of the Curie temperature of the three samples during the immersion testing (Döring *et al.*, 2024a). 168
Figure 5.6 – Comparison between the mean experimental pressure drop values and the ones obtained via the corrected correlation. 170
Figure 5.7 – Schematic diagram of the simplified HMS. 171
Figure 5.8 – Comparison between the electric actuation signal of the solenoid and the transient fluid flow response for a mass flow rate of 700 kg h^{-1}, a frequency of 0.75, and a blow fraction of 40%. 173
Figure 5.9 – Evaluation of the effect of the mass flow rate for a fixed frequency of 0.75 Hz and blow fraction of 40%. The figures depict a mass flow rate of (a) 350 kg h^{-1}, (b) 525 kg h^{-1}, and (c) 700 kg h^{-1}. 174
Figure 5.10–Evaluation of the effect of the frequency for a fixed mass flow rate of 525 kg h^{-1} and blow fraction of 25%. The figures depict a frequency of (a) 0.75 Hz, (b) 1 Hz, and (c) 1.5 Hz. 176
Figure 5.11–Evaluation of the effect of the blow fraction for a fixed frequency of 0.75 Hz and mass flow rate of 700 kg h^{-1}. The figures depict a mass flow rate of (a) 25% and (b) 40%. 177
Figure 5.12–Evaluation of the cooling capacity for each version of the MRU as a function of (a) mass flow rate and (b) AMR temperature difference. 180
Figure 5.13–Evaluation of the AMR temperature spans of the system, displaying the correlation between (a) the mass flow rate, and (b) system temperature span. 181

Figure 5.14–Evaluation of the COP of the (a) AMR and (b) system, for each version of the MRU as a function of the mass flow rate. 183
Figure 5.15–Evaluation of the second-law efficiency (a) of the AMR and (b) of the system, for each version of the MRU as a function of the mass flow rate. . 184
Figure 5.16–Comparison between the performance of the three versions of the MRU and selected prototypes presented in the literature. References in the Figure are according to [1]: Engelbrecht *et al.* (2012), [2]: Lozano *et al.* (2013), [3]: Eriksen *et al.* (2015), [4]: Fortkamp *et al.* (2018), [5]: Dall'Olio *et al.* (2021), [6]: Masche *et al.* (2021), [7]: Masche *et al.* (2022), [8]: Tura & Rowe (2011), [9]: Jacobs *et al.* (2014), [10]: Huang *et al.* (2019), [11]: Aprea *et al.* (2016), [12]: Lionte *et al.* (2020), [13]: Hai *et al.* (2024), [14]: Liang *et al.* (2025), [15]: Trevizoli *et al.* (2016b),[16]: Trevizoli *et al.* (2017), [17]: Nakashima *et al.* (2018), [18]: Lozano *et al.* (2016), [19]: Nakashima *et al.* (2021). The values of the coefficient of performance from an AMR standpoint are presented in parentheses. * Represents prototypes where ΔT_{sys} and COP_{sys} are depicted. 186
Figure 5.17–Comparison between the temperature span from the AMR and system points of view. 187
Figure 5.18–Breakdown of the contributions of the torque in the system. 188
Figure 5.19–Breakdown of the contributions of the pressure drop in the system. 189
Figure 5.20–Breakdown of the contributions of the mechanical transmission power in the system. 190
Figure 5.21–Breakdown of the contributions of the pumping power in the system. . . . 191
Figure 5.22–Breakdown of the contributions to the overall power consumption in the system. 192
Figure 5.23–Assessment of the cooling capacity of the system through different standpoints. 193
Figure 5.24–Assessment of the coefficient of performance of the system through different standpoints. 194
Figure 5.25–Assessment of the second law efficiency of the system through different standpoints. 195
Figure 6.1 – Distribution of the mass flow rate of the system in the dataset. 201
Figure 6.2 – Distribution of the operating frequency of the system in the dataset. . . . 202
Figure 6.3 – Distribution of the temperature span in the dataset. 203
Figure 6.4 – Distribution of the utilization factor of the system in the dataset. 204
Figure 6.5 – Distribution of the cooling capacity of the system in the dataset. 205
Figure 6.6 – Correlation Matrix of selected numeric parameters of the dataset. 206
Figure 6.7 – General Representation of the Architecture of the ANN. 210

Figure 6.8 – Comparison between the experimental results for the cooling capacity and predictions by the ANN for the training, validation, and test sets. Black Dashed lines represent $\pm$ 10% deviations. The red dotted line represents the ground truth. 214
Figure 6.9 – Comparison between the experimental results for the AMR cooling capacity below 50 W and predictions by the ANN for the training, validation, and test sets. Black Dashed lines represent $\pm$ 7 W deviations. The red dotted line represents the ground truth. 215
Figure 6.10–Comparison between the experimental results for the AMR cooling capacity above 50 W and predictions by the ANN for the training, validation, and test sets. Black Dashed lines represent $\pm$ 10% deviations. The red dotted line represents the ground truth. 216
Figure 6.11–Histogram between the deviations between the model and the experimental data for the (a) training, (b) validation, and (c) test sets. 217
Figure 6.12–Distribution of the five excitation signals generated by the LHC sampling strategy. 220
Figure 6.13–Projections of the LHC excitation signals considering different pairs of variables. 221
Figure 6.14–Amplitudes of the excitation signals according to the pseudo-random binary approach. 222
Figure 6.15–NARX ANN comprised with m delayed inputs and n delayed outputs. z^{-1} represents a unit time delay. 223
Figure 6.16–Comparison between the experimental temperature and predictions of the model for 1- and 90-step ahead in the training set. 225
Figure 6.17–Comparison between the experimental temperature and predictions of the model for 1- and 90-step ahead in the validation set. 226
Figure 6.18–Comparison between the experimental temperature and predictions of the model for 1- and 90-step ahead in the test set. 226
Figure 6.19–Histogram of the deviation between the experimental temperature and predictions of the model for 1- and 90-step ahead in the training set. . . . 227
Figure 6.20–Histogram of the deviation between the experimental temperature and predictions of the model for 1- and 90-step ahead in the validation set. . . 227
Figure 6.21–Histogram of the deviation between the experimental temperature and predictions of the model for 1- and 90-step ahead in the test set. 228
Figure 6.22–Comparison between the experimental temperature and predictions of the model for 1- and 90-step ahead in the training set. 228
Figure 6.23–Comparison between the experimental temperature and predictions of the model for 1- and 90-step ahead in the validation set. 229

Figure 6.24–Comparison between the experimental temperature and predictions of the model for 1- and 90-step ahead in the test set. 229
Figure 6.25–Histogram of the deviation between the experimental temperature and predictions of the model for 1- and 90-step ahead in the training set. . . . 230
Figure 6.26–Histogram of the deviation between the experimental temperature and predictions of the model for 1- and 90-step ahead in the validation set. . . 230
Figure 6.27–Histogram of the deviation between the experimental temperature and predictions of the model for 1- and 90-step ahead in the test set. 231
Figure 6.28–Schematic representation of a multilayer AMR. 233
Figure 6.29–Schematic representation of the Curie temperature deviation. Solid lines represent the original curves and dashed lines represent the ones achieved by the manufacturing process. 233
Figure 6.30–Comparison between the cooling capacity calculated by the numerical model and predicted by the ANN for the AMR with (a) 5, (b) 10, and (c) 15 layers. 237
Figure 6.31–Schematic representation of the proposed method. 240
Figure 6.32–Effect of the uncertainty of the Curie Temperature on the performance of an AMR with (a) 5, (b) 10, and (c) 15 layers. 241
Figure 6.33–Cumulative Distribution Function for the AMR with (a) 5, (b) 10, and (c) 15 layers. 243
Figure 6.34–Cooling capacity achieved with a 95% confidence for an AMR with 5, 10, and 15 layers. 244
Figure 6.35–Effect of the certainty level on the achieved performance of the AMR operating with (a) 5, (b) 10, and (c) 15 layers. 245
Figure 7.1 – Schematic representation of the Claude cycle. LN2 stands for liquid nitrogen, GN2 stands for gaseous nitrogen, LH2 stands for liquid Hydrogen, GH2 stands for gaseous Hydrogen, $\dot{Q}$ stands for the heat dissipated by the compressor, and $\dot{W}$ stands for the turbine power. Adapted from (Bordignon *et al.*, 2023). 248
Figure 7.2 – Simplified schematic diagram of the precooling cycle. 249
Figure 7.3 – Comparison between the numerical and ANN prediction for (a) temperature after the Joule-Thomson expansion, (b) specific heat absorption, (c) specific power. 251
Figure 7.4 – Pareto front of the optimization problem. 253
Figure 7.5 – Composition of each one of the mixtures that make up the Pareto front. . 254
Figure 7.6 – Pressure of each one of the precooling systems that make up the Pareto front. 254

Figure 7.7 – Comparison between the predictions of the ANN and the simulations with the E-PPR78. 258
Figure 7.8 – Effect of the contaminants on the cricondenbar. 259
Figure 7.9 – Compositions that result in the largest cricondenbar. 261
Figure 7.10–Schematic representation of the well geometry and lithology (Veiga *et al.*, 2022). 264
Figure 7.11–Input variables and output parameters of the Simulation 267
Figure 7.12–Comparison between the numerical and ANN prediction evaluating (a) well head boundary conditions, (b) fluid thermophysical properties of the fluids, (c) well geometry. 270
Figure 7.13–Total Sobol coefficients for the operational boundary conditions. 271
Figure 7.14–Total Sobol coefficients for the thermophysical properties of the fluids. . . 271
Figure 7.15–Total Sobol coefficients for the geometric parameters of the well. 272
Figure 7.16–Distribution of maximum pressure difference at a given well depth under uncertain boundary conditions using Monte Carlo simulations. 273
Figure 7.17–Distribution of maximum pressure difference at a given well depth under uncertain boundary conditions using Monte Carlo simulations. 274
Figure 7.18–Distribution of maximum pressure difference at a given well depth under different sources of uncertainty using Monte Carlo simulations: (a) mud, (b) nitrogen, (c) brine, and (d) production oil. 275
Figure 7.19–Distribution of maximum pressure difference at a given well depth under uncertain boundary conditions using Monte Carlo simulations. 276
Figure 7.20–Distribution of maximum pressure difference at a given well depth under geometric parameter uncertainty using Monte Carlo simulations: (a) hole size and (b) outer diameter. 276
Figure 7.21–Schematic representation of a naturally flowing offshore well (Vargas *et al.*, 2019). 278
Figure 7.22–Temporal evolution of selected variables during a spurious DHSV closure. Blue: normal; green: transient; red: anomalous state. 280
Figure 7.23–Correlation matrix between input variables and anomaly classes. 281
Figure 7.24–Confusion matrix of the developed model on the test set. 282
Figure A.1 – Schematic diagram of the procedure performed by the NSGA-II algorithm. Adapted from Deb *et al.* (2002) 335
Figure A.2 – Schematic representation of the crowding-distance calculation. Filled circles represent the solutions of the same nondominated front. Adapted from Deb *et al.* (2002) 336

Figure B.1 – Schematic representation of a multi-circuit tube-fin HEx and its main geometric parameters. The figure presents the side view (left) and the front view (right). 338
Figure B.2 – Schematic diagram of the corrugated fin on a tube array and its main geometric parameters. Adapted from Shah & Sekulic (2003) 343
Figure B.3 – Schematic representation of a unit cell of a staggered tube arrangement and the parameters used to define the minimum free-flow area. Adapted from Shah & Sekulic (2003) 344
Figure C.1 – Comparison between the experimental results, training and test sets, and the fitted equation for the performance curve of the model S4E350-AN19-43 fan. 353
Figure C.2 – Comparison between the experimental results and the fitted equation for the efficiency curve of the model S4E350-AN19-43 fan. 354
Figure C.3 – Product drawings for the model S4E350-AN19-43 fan 355
Figure C.4 – Performance curve provided by the catalogue for the S4E350-AN19-43 fan 356

LIST OF TABLES

Table 2.1 – Overview of magnetocaloric cooling and heat pumping prototypes. 72
Table 2.2 – Categorization of learning approaches. 75
Table 2.3 – Example of a One-hot encoding 78
Table 3.1 – Range of the design variables utilized as features for the ML models. 107
Table 3.2 – Coefficient of Determination for the developed models. 109
Table 3.3 – Summary of the Architecture of the ANN 113
Table 3.4 – Summary of the Architecture of the ANN 116
Table 3.5 – Design variables and their ranges in the system optimization problem. . . . 123
Table 3.6 – Design parameters and operating conditions of the optimal system configuration. 135
Table 4.1 – Curie temperatures of the available MCMs. 145
Table 4.2 – Experimental uncertainties of the measuring instruments installed in the MRU. 148
Table 4.3 – Dimensions of the calorimeter. 149
Table 4.4 – Reconditioning equipment employed in the calorimeter. 150
Table 4.5 – Experimental uncertainties of the measuring instruments installed in the calorimeter. 152
Table 4.6 – Results of experimental overall heat transfer coefficient 153
Table 4.7 – Mass and Curie Temperature for the layers that compose the AMR beds for each version of the MRU. 155
Table 4.8 – Summary of the main distinct design characteristics for each version of the MRU. 157
Table 5.1 – Parameters for the solenoid valves tests. 172
Table 5.2 – Operation conditions of the tests for each version of the prototype. 178
Table 5.3 – Overview of the optimal performance conditions observed across the three prototype versions. 182
Table 6.1 – Summary of the data collected from the main MR prototypes reported in the literature. 198
Table 6.2 – Summary of the Hyperparameters optimized in the ANN 211
Table 6.3 – Summary of the Hyperparameters for the evaluation of the Physics-Guided ANN 211
Table 6.4 – Results of the physics embedding on the performance of the model 212

Table 6.5 – Optimal Hyperparameters for the Physics-Guided ANN 212
Table 6.6 – Performance metrics of the AI Models 213
Table 6.7 – Hyperparameter space for the random search. 224
Table 6.8 – Hyperparameters of the final NARX ANN for the predictions of temperature and power consumption. 224
Table 6.9 – Performance metrics of the models for the evaluated datasets 231
Table 6.10–Fixed parameters of the numerical simulation 235
Table 6.11–Dataset samples for each case. 236
Table 6.12–Number of Neurons in the ANN. 237
Table 6.13–Performance metrics of the models for the AMRs with 5, 10, and 15 layers. 238
Table 7.1 – R^2 and MSE of the test set for each variable. 252
Table 7.2 – Admissible concentration range for the components of the mixtures. 256
Table 7.3 – Geometric characteristics of the tubular diameters. 265
Table 7.4 – Geometric characteristics of the hole sizes. 265
Table 7.5 – Uncertainty ranges adopted for each fluid property. 268
Table 7.6 – Summary of event types and their number of instances in the 3W dataset. . 279
Table 7.7 – Performance metrics of the model on the test set. 283
Table C.1 – Main characteristics of the model S4E350-AN19-43 fan 352
Table C.2 – Operation points provided in the catalogue by the supplier for the model S4E350-AN19-43 fan 352

LIST OF SYMBOLS AND ABBREVIATIONS

Roman

A	Area	m^2
B	Magnetic flux density	T
BS	Batch size	-
c	Specific heat	$J\,kg^{-1}\,K^{-1}$
$\dot{C}$	Heat capacity rate	$W\,K^{-1}$
COP	Coefficient of Performance	-
D	Diameter	m
$\mathbb{E}$	Expected value	-
f	Frequency	Hz
$\mathcal{F}$	Mapping function	-
Fo	Fourier number	-
G	Mass flux	$kg\,m^{-2}\,s^{-1}$
H	Height	m
$\hbar$	Convective heat transfer coefficient	$W\,m^{-2}\,K^{-1}$
h	Specific enthalpy	$J\,kg^{-1}$
j	Colburn factor	-
K	Porous media permeability	m^2
k	Thermal conductivity	$W\,m^{-1}\,K^{-1}$
L	Length	m
$\mathcal{L}$	Loss function	-
m	Mass	kg

$\dot{m}$	Mass flow rate	kg s^{-1}
N	Number	-
NTU	Number of transfer units	-
Nu	Nusselt number	-
P	Pressure	Pa
Pr	Prandtl number	-
q	Specific heat trasfer	J kg^{-1}
$\dot{Q}$	Heat transfer rate	W
Re	Reynolds number	-
s	Specific entropy	J kg^{-1} K^{-1}
T	Temperature	K
t	Time	s
U	Overall heat transfer coefficient	W m^{-2} K^{-1}
u	Specific internal energy	J kg^{-1}
$\mathcal{U}$	Uniform distribution	-
UA	Overall thermal conductance	W K^{-1}
V	Variance	-
$\forall$	Volume	m^3
W	Width	m
w	Specific work	J kg^{-1}
$\dot{W}$	Power Consumption	W
X	Composition	-
x	Input parameters	-
Y	Neuron output	-
y	Output variables	-
$\hat{y}$	Predictions	-

Z	Pre-activation neuron output	-

Greek

α	Learning rate	-
β	Surface area density	$\mathrm{m^2\ m^{-3}}$
β_{fin}	Fin density	$\mathrm{m^{-1}}$
Δ	Variation	-
δ	Error	-
δ_{fin}	Thickness of the fin	m
δ_{hp}	Thickness of the header plate	m
δ_{h}	Horizontal spacing between the air gap and the casing	m
δ_{w}	Radial spacing between the each regenerator	m
η	Efficiency	-
η_{o}	Extended surface efficiency	-
Λ	Mean value	-
λ	Regularization coefficient	-
μ_{f}	Dynamic viscosity	Pa s
Ω	Activation function	-
ω	Frequency	Hz
Φ	Time constant	s
Π_{B}	Nondimensional magnetic field	-
Π_{Tc}	Nondimensional Curie temperature	-
Π_{T}	Nondimensional temperature span	-
ρ	Density	$\mathrm{kg\ m^{-3}}$
σ	Standard deviation	-
σ_{e}	Ratio of the minimum free-flow and frontal areas	-
σ_{o}	Contraction and expansion area ratio	-

τ	Torque	N m
Θ	Parameters	-
θ	Angular position	rad
Υ	Specific magnetization	A m^2 kg^{-1}
ε	Effectivness	-
φ	Utilization factor	-
φ_{f}	Porosity	-
Ξ	Hyperparameters	-
p_{cri}	Cricondenbar	Pa
Ar	Argon	-
C_2H_6	Ethane	-
C_3H_8	Propane	-
CH_4	Methane	-
CO	Carbon Monoxide	-
CO_2	Carbon Dioxide	-
H_2	Hydrogen	-
N_2	Nitrogen	-

Composed and constants

A_{R}	Aspect Ratio	-
$A_{\mathrm{fr,o}}$	External frontal area	m^2
A_{f}	Secondary surface area	m^2
A_{p}	Primary surface area	m^2
A_{s}	Surface area	m^2
B_{f}	Final magnetic flux density	T
B_{i}	Initial magnetic flux density	T
B^*_{Prof}	Profile of the magnetic field	-

B_{rem}	Remanence magnetic flux density	T
C^{*}	Heat capacity rate ratio	-
c_{B}	Specific heat at constant magnetic flux density	J kg^{-1} K^{-1}
c_{p}	Specific heat at constant pressure	J kg^{-1} K^{-1}
c_{E}	Ergun constant	-
D_{h}	Hydraulic diameter	m
$D_{\mid\mid}$	Longitudinal thermal dispersion	m^{2} s^{-1}
d_{h}	Porous medium characteristic diameter	m
d_{p}	Particle diameter	m
F°	Utopia point	-
F_{1}	F1 score	-
$F_{\%}$	Blow fraction	-
f_{D}	Friction factor	-
f_{i}	Internal flow Fanning friction factor	-
f_{o}	External flow Fanning friction factor	-
G^{*}_{AMR}	Geometry of the AMR	-
h_{fc}	Thickness of the flux concentrator tube	m
K_{bend}	Equivalent length of the bends	50
k_{ef}	Effective thermal conduction	W m^{-2} K^{-1}
K_{v}	Flow coefficient	m^{3} h^{-1} Pa$^{-0.5}$
L_{T}	Length of the tubes	m
L_{xt}	Additional length factor	-
l_{x}	Input lags	-
l_{y}	Output lags	-
$\dot{m}_{\mathrm{f}}$	Mass flow rate of fluid	kg s^{-1}
$m_{\$}$	Cost weighted mass	kg

M^*_{MCM}	Type of Magnetocaloric Material Alloy	-
$M_{\%}$	Magnetization fraction	-
N_{bed}	Demagnetization factor for a prismatic solid	-
N_{circ}	Number of circuits	-
N_{D}	Demagnetization factor	-
N_{l}	Longitudinal number of tube rows	-
$N_{\mathrm{t,circ}}$	Transversal number of tube rows per circuit	-
N_{t}	Transversal number of tube rows	-
N_{B}	Number of regenerators operating simultaneously	-
O_{c}	Overall criterion of the optimization	-
$\mathbf{P}_{\mathrm{HEx}}$	Optimization problem of the HEx	-
$\mathbf{P}_{\mathrm{Sys}}$	Optimization problem of the system	-
p_{d}	Fin pattern peak to valley distance	m
p_{fin}	Fin pitch	m
p_{pc}	precooling pressure	Pa
$\dot{q}_{\mathrm{C}}$	Cooling capacity per mass of MCM	W kg^{-1}
$\dot{Q}_{\mathrm{C,net}}$	Net cooling capacity	W
$\dot{Q}_{\mathrm{C}}$	Cooling capacity	W
$\dot{Q}_{\mathrm{H}}$	Heat rejection rate in the hot thermal reservoir	W
R^2	Coefficient of Determination	-
r_{xy}	Pearson correlation coefficient	m
R_{a}	Thermal resistance of the external flow of the HEx	K W^{-1}
R_{c}	Outer radius of the rotor	m
R_{g}	Inner radius of the rotor	m
R_{i}	Inner radius of the stator	m
R_{l}	Thermal resistance of the internal flow of the HEx	K W^{-1}

R_{o}	Outer radius of the stator	m
R_{s}	Outer radius of the magnet segments of the rotor	m
R_{T}	Thermal resistance of the tubes of the HEx	$\mathrm{K\,W^{-1}}$
Δs_{iso}	Isothermal entropy change	$\mathrm{J\,kg^{-1}\,K^{-1}}$
S^{*}_{AMR}	Shape of the AMR	-
S_{T}	Total Sobol coefficient	-
ΔT_{ad}	Adiabatic temperature change	K
ΔT_{AMR}	Temperature span of the AMR	K
$\Delta T_{\mathrm{C,AMR}}$	Temperature difference of the cold end of the AMR	K
ΔT_{sys}	Temperature span of the system	K
T_{CE}	Temperature of the cold end of the AMR	K
T_{Curie}	Temperature of Curie	K
T_{C}	Temperature of the cold thermal reservoir	K
T_{HE}	Temperature of the hot end of the AMR	K
T_{H}	Temperature of the hot thermal reservoir	K
u_{max}	Maximum velocity	$\mathrm{m\,s^{-1}}$
$\dot{V}$	Volumetric flow rate	$\mathrm{m^3\,s^{-1}}$
$\dot{V}_{\mathrm{a}}$	Volumetric air flow rate	$\mathrm{m^3\,s^{-1}}$
v_{s}	Surface Velocity	$\mathrm{m\,s^{-1}}$
$\mathbf{x}_{\mathrm{HEx}}$	Design variables of the HEx	-
$\mathbf{x}_{\mathrm{Sys}}$	Design variables of the system	-
x_{fin}	Fin project way length	m
X_{l}	Longitudinal tube pitch	m
X_{t}	Transversal tube pitch	m

Subscript and Superscript

$\overline{}$	Average value

2nd Second law

2D Two-dimensional

3D Three-dimensional

AMR Active magnetic regenerator

aux Auxiliary components

bend Tube bends

C Cold

CHEx Cold heat exchanger

circ Circuits

cnt Carnot

csg Casing

Curie Temperature of Curie

CV Check valve

Dummy Dummy regenerators

ext External

f Fluid

fan Fan

fc Flux concentrator tube

fil Filters

Gd Gd-based alloys

Gen General

geo Geometry

H Hot

HB Hot blow

heat Heaters

HEx Heat exchanger

HHEx Hot heat exchanger

high High

HT Heat transfer

l Liquid

L1 Lasso regularization

L2 Ridge regularization

La La-based alloys

lay Layers

loss Losses

low Low

mag Magnetization

magnet Magnet

max Maximum

MCM Magnetocaloric Material

min Minimum

ML Multilayer

mt Motor

neu Neurons

Nom Nominal

out Out

par Parasitic

Phy Physics-Guided

pp Pumping

pump Pumping

rt Rotor

s Solid

st Stator

SV Solenoid valve

sys System

trans Transmission system

tub Tubing

void Void

wall Calorimeter Walls

Abbreviation

Adam Adaptive Momentum Estimation

AEM Abnormal Event Management

AI Artificial Intelligence

AMR Active Magnetic Regenerator

ANN Artificial Neural Network

B Boron

CCDF Complementary Cumulative Distribution Function

CDF Cumulative Distribution Function

CH-H Calorivac-H

CH-HS Calorivac-HS

CHEx Cold Heat Exchanger

CNN Convolutional Neural Network

Co Cobalt

CS Cold Side

DL Deep Learning

DNN Deep Neural Network

ELU Exponential Linear Unit

Er Erbium

FC Fully Connected

Fe Iron

FN False negative

FOPT First-Order Phase Transition

FP False positive

Gd Gadolinium

GPU Graphic Processing Unit

H Hydrogen

HEx Heat Exchanger

HHEx Hot Heat Exchanger

HMS Hydraulic Management System

HS Hot Side

IoT internet of Things

KNN K-Nearest Neighbors

La Lanthanum

LHC Latin Hypercube

MAE Mean Absolute Error

MC Magnetic Circuit

MCE Magnetocaloric Effect

MCM Magnetocaloric Material

ML Machine Learning

MLP Multilayer Perceptron

Mn Manganese

MOO Multi Objective Optimization

MR Magnetocaloric Refrigeration

MRU Magnetic Refrigeration Unit

MSE Mean Squared Error

NARX Nonlinear Autoregressive with Exogenous Inputs

ND Neodymium

OS Outside

PBE Point-base engineering

PINN Physics-Informed Neural Network

PM Permanent Magnet

ReLU Rectified Linear Unit

RF Random Forest

RMSE Root Mean Square Error

RMSProp Root Mean Square Propagation

RNN Recurrent Neural Network

SBCE Set-based concurrent engineering

SELU Standard Exponential Linear Unit

SGD Stochastic Gradient Descent

Si Silicon

Sig Sigmoid

SOO Single Objective Optimization

SOPT Second-Order Phase Transition

SVM Support Vector Machine

SVR Support Vector Regression

Tanh Hyperbolic Tangent

TN True negative

TP True positive

TRL Technology Readiness Level

XGBoost Extreme Gradient Boosting

Y Yttrium

CONTENTS

Page

1 INTRODUCTION 46
1.1 Magnetic Refrigeration Systems 47
1.2 Artificial Intelligence and Machine Learning 49
1.3 Motivation and Main Objective 51
1.4 Outline of this Document 52

2 FUNDAMENTALS AND STATE-OF-THE-ART 53
2.1 Fundamentals of Magnetic Refrigeration 53
2.1.1 The Magnetocaloric Effect 53
2.1.1.1 Thermodynamics of the Magnetocaloric Effect 53
2.1.1.2 Magnetocaloric Materials 55
2.1.1.3 Thermo-magnetic Refrigeration Cycles 55
2.1.2 State-of-the-art Magnetic Refrigerators 58
2.1.2.1 Astronautics Corporation of America (United States of America) 59
2.1.2.2 University of Victoria (Canada) 61
2.1.2.3 Technical University of Denmark (Denmark) 62
2.1.2.4 Technical University of Delft (Netherlands) 63
2.1.2.5 University of Ljubljana (Slovenia) 64
2.1.2.6 University of Salerno (Italy) 65
2.1.2.7 Magnoric (France) 65
2.1.2.8 University of Genoa (Italy) 66
2.1.2.9 University of Science and Technology of China (China) 67
2.1.2.10 Magnotherm (Germany) 67
2.1.2.11 Federal University of Santa Catarina (Brazil) 69
2.1.3 Modelling Strategies used in Magnetic Refrigerators 71
2.2 Fundamentals of Artificial Intelligence and Machine Learning 74
2.2.1 Types of Learning Algorithms and Problems 75
2.2.2 Pipeline for the Development of a Machine Learning Model 76
2.2.2.1 Problem Definition 76
2.2.2.2 Data Collection and Preparation 77
2.2.2.3 Model Selection 78

2.2.2.4 Model Training . . . 81
2.2.2.5 Model Optimization . . . 83
2.2.2.6 Model Evaluation . . . 87
2.2.2.7 Model Deployment and Applications . . . 88
2.2.3 Deep Learning . . . 88
2.2.3.1 Artificial Neural Network . . . 88
2.2.3.2 The Backpropagation Algorithm . . . 90
2.2.3.3 Activation Functions . . . 90
2.2.3.4 Artificial Neural Network Architectures . . . 92
2.2.3.5 Advanced Techniques and Enhancements in Artificial Neural Networks 95
2.2.4 Applications of Artificial Intelligence in Engineering Systems . . . 97
2.2.4.1 Modeling of Systems, Components, and Phenomena . . . 98
2.2.4.2 Optimization . . . 99
2.2.4.3 Sensitivity and Uncertainty Analysis . . . 100
2.2.4.4 Anomaly Detection . . . 101
2.3 Summary and Specific Objectives . . . 102

3 INTEGRATED DESIGN OF THE SYSTEM . . . 104
3.1 Design Strategy . . . 104
3.2 Development of the AMR Model . . . 106
3.2.1 Problem Formulation . . . 106
3.2.2 Data Collection and Preparation . . . 107
3.2.3 Model Selection . . . 108
3.2.4 Model Training and Optimization . . . 108
3.2.5 Model Evaluation . . . 108
3.3 Modeling of the System . . . 110
3.3.1 Configurations of the Components . . . 110
3.3.2 AMR Modeling . . . 111
3.3.2.1 Development of the Artificial Neural Network . . . 112
3.3.3 Magnetic Circuit . . . 113
3.3.3.1 Development of the Artificial Neural Network . . . 115
3.3.4 Heat Exchangers . . . 116
3.3.5 Hydraulic Management System . . . 118
3.3.6 Integrating the Components . . . 118
3.3.6.1 Active Magnetic Regenerator and Magnetic Circuit . . . 119
3.3.6.2 Active Magnetic Regenerator and Heat Exchangers . . . 119
3.3.7 System Performance Metrics . . . 120
3.4 System-level Integrated Optimization . . . 121

3.4.1 Solution of the Optimization Problem . . . 122
3.4.2 Evaluation of the Optimal Solution . . . 124
3.4.2.1 Performance Metrics of the System . . . 124
3.4.2.2 Design Parameters . . . 127
3.4.3 Selection of the Final Design . . . 133
3.5 Outline of the Chapter . . . 135

4 EXPERIMENTAL APPARATUS . . . 136
4.1 Magnetic Refrigeration Unit . . . 136
4.1.1 Magnetic Circuit . . . 138
4.1.2 Active Magnetic Regenerators . . . 142
4.1.3 Magnetocaloric Materials . . . 144
4.1.4 Hydraulic Management System . . . 145
4.1.5 Heat Exchangers . . . 147
4.1.6 Data Acquisition and Instrumentation . . . 148
4.2 Calibrated Calorimeter . . . 148
4.2.1 Design of the Calorimeter . . . 149
4.2.2 Calibration of the Calorimeter . . . 153
4.3 Design Evolution of the Prototype . . . 153
4.4 Performance Metrics of the System . . . 158
4.5 Outline of the Chapter . . . 162

5 EXPERIMENTAL PERFORMANCE EVALUATION OF THE SYSTEM . . . 163
5.1 Component Characterization . . . 163
5.1.1 Magnetic Circuit . . . 163
5.1.2 Magnetocaloric Materials . . . 165
5.1.3 Active Magnetic Regenerator . . . 169
5.1.4 Hydraulic Management System . . . 170
5.2 Magnetic Refrigeration Unit . . . 178
5.2.1 Performance Evolution of the System . . . 178
5.2.2 Advanced Thermodynamic Evaluation . . . 185
5.3 Outline of the Chapter . . . 196

6 APPLICATION OF ARTIFICIAL INTELLIGENCE IN MAGNETIC REFRIGERATION . . . 197
6.1 Steady-State Model . . . 197
6.1.1 Problem Formulation . . . 197
6.1.2 Data Collection and Preparation . . . 198
6.1.2.1 Exploratory Data Analysis . . . 200

6.1.3 Model Selection . . . 206
6.1.3.1 Physics-Guided Neural Network . . . 207
6.1.4 Model Training and Optimization . . . 209
6.1.5 Model Evaluation . . . 211
6.2 Transient Model . . . 216
6.2.1 Problem Formulation . . . 218
6.2.2 Data Collection and Preparation . . . 219
6.2.3 Model Selection . . . 222
6.2.4 Model Training and Optimization . . . 223
6.2.5 Model Evaluation . . . 224
6.3 Uncertainty Analysis of the Curie Temperature of Magnetocaloric Materials . . 232
6.3.1 Problem Formulation . . . 232
6.3.2 Data Collection and Preparation . . . 234
6.3.3 Model Selection . . . 236
6.3.4 Model Training and Optimization . . . 236
6.3.5 Model Evaluation . . . 236
6.3.6 Model Application . . . 238
6.3.6.1 Monte Carlo Uncertainty Analysis . . . 240
6.4 Outline of the Chapter . . . 246

7 APPLICATION OF ARTIFICIAL INTELLIGENCE IN ENGINEERING SYSTEMS 247
7.1 Applications in Energy Transition . . . 247
7.1.1 Optimization of Hydrogen Liquefaction Systems . . . 248
7.1.1.1 Problem definition . . . 249
7.1.1.2 Data Collection and Preprocessing . . . 250
7.1.1.3 Model Selection. Training and Optimization . . . 250
7.1.1.4 Model Evaluation . . . 251
7.1.1.5 Model Application . . . 252
7.1.2 Uncertainty Analysis for Carbon Capture, Storage and Utilization Applications 255
7.1.2.1 Problem Definition . . . 256
7.1.2.2 Data Collection and Preprocessing . . . 256
7.1.2.3 Model Selection, Training and Optimization . . . 257
7.1.2.4 Model Evaluation . . . 257
7.1.2.5 Model Application . . . 258
7.2 Application in Oil and Gas Systems . . . 262
7.2.1 Sensitivity and Uncertainty Analysis of Thermostructural Phenomena in Oil Wells . . . 262
7.2.1.1 Problem definition . . . 263

7.2.1.2 Data Collection and Preprocessing . . . 263
7.2.1.3 Model Selection Training and Optimization . . . 269
7.2.1.4 Model Evaluation . . . 269
7.2.1.5 Model Application . . . 271
7.2.2 Anomaly Detection in Offshore Oil Wells . . . 276
7.2.2.1 Problem Definition . . . 277
7.2.2.2 Data Collection and Preprocessing . . . 277
7.2.2.3 Model Selection, Training and Optimization . . . 280
7.2.2.4 Model Evaluation . . . 282
7.3 Outline of the Chapter . . . 283

8 FINAL REMARKS . . . 284
8.1 Future Work . . . 286
8.2 Closing Remarks . . . 288

BIBLIOGRAPHY . . . 290

LIST OF PUBLICATIONS . . . 322
Papers Published in Peer Reviewed Journals . . . 322
Papers Published in Conference Proceedings . . . 324
Papers Submitted for Publication or in Preparation . . . 330
Intellectual Property Registered . . . 332
Awards and Grants . . . 333

A NUMERICAL METHODS . . . 334
A.1 Nondominated Sorting Genetic Algorithm II (NSGA-II) . . . 334

B MATHEMATICAL MODEL OF THE HEAT EXCHANGERS . . . 337
B.1 Design and Modeling of the Heat Exchanger . . . 337
B.2 Basic Geometric Definitions . . . 338
B.3 Thermal-Hydraulic Model . . . 340
B.3.1 Conduction Through the Tubes . . . 340
B.3.2 Internal Convection . . . 340
B.3.3 External Convection . . . 342
B.4 The εNTU Method . . . 348

C CHARACTERISTICS OF THE FAN . . . 351
C.1 Selection of the Fan . . . 351
C.2 Characteristics of the Fan . . . 352
C.3 Catalogue Figures . . . 354

Chapter 1

INTRODUCTION

Refrigeration and air conditioning systems play a crucial role in modern society, significantly impacting daily activities, health, and comfort. Their importance and influence on contemporary life are often overlooked. These systems control indoor environments, providing comfort regardless of external weather, and are vital to preserving food and pharmaceuticals, which are essential to health and safety. As urbanization increases and climate challenges emerge, effective heating and cooling systems are critical to energy efficiency and environmental sustainability.

A formal definition of refrigeration states that it is concerned with the cooling of bodies or fluids to temperatures lower than those available in the surroundings at a particular time and place (Gosney, 1982). From a practical standpoint, a refrigeration system is a device that removes heat from a cold reservoir at a specified temperature, T_{C}. It transfers it to a hot reservoir at a higher temperature, T_{H}. The rate of heat absorption from the cold reservoir is called the cooling capacity, $\dot{Q}_{\mathrm{C}}$. In contrast, the temperature difference between the hot and cold reservoirs is called the temperature span of the system, ΔT_{sys}. In refrigeration systems, these two last parameters usually signify the main operational requirements of such devices. Moreover, according to the second law of thermodynamics, work must be done on the system to allow heat transfer from the cold to the hot heat reservoirs. The work rate performed on the system is known as the system power consumption, $\dot{W}_{\mathrm{sys}}$.

Contemporary refrigeration predominantly uses a combination of mechanical vapor compression and expansion, along with phase-change heat transfer. Over a century of advancement has made vapor compression a well-established and widely used technology for most refrigeration needs (Bansal *et al.*, 2012). However, the significant role of these systems in global warming has led society and regulatory authorities to increase their focus on their efficiency and carbon footprint. According to estimates, approximately 20% of global electricity consumption (IIR, 2025) and 10% of greenhouse gas emissions (Dong *et al.*, 2021) are attributed to these systems. Only air conditioning accounts for more than 12% of electricity consumption and 5% of greenhouse gas emissions (IIR, 2024). Not only is the current impact of these systems considerable, but their demand is expected to increase over the coming decades, with an estimated threefold increase in the worldwide number of air conditioning units by 2050 (IEA, 2018). Moreover, the use of volatile refrigerants in these systems has been restricted by international agreements over the last decade, with particular emphasis on the Kigali amendment to the Montreal Protocol (Heath, 2017). Ratified by 160 countries and

the European Union, the agreement schedules the phase-down and phase-out of hydrofluorocarbons, currently used in many cooling systems, particularly those used in developing countries (Gauß *et al.*, 2017). Research on alternative fluids is constantly ongoing. However, the main concerns regarding these novel fluids are related to their efficiency in systems, as their thermophysical and transport properties may not be as effective as those of current refrigeration solutions; safety, since many of them are flammable and toxic (Abas *et al.*, 2018); and environmental impact.

Hence, the refrigeration community has been stimulated to develop innovative solutions to overcome these challenges. In addition to improving the efficiency of current vapor compression systems and developing new refrigerant fluids, many researchers seek to reduce the carbon footprint of cooling systems by developing technologies that do not rely on volatile fluids. Among various alternatives, caloric technologies emerge as viable solutions for this challenge. These technologies depend on inducing a thermal effect in a solid-state refrigerant via a physical stimulus or driving force. The solid nature of the refrigerant eliminates the risk of leakage during operation. Several caloric technologies have been assessed at the laboratory scale, including barocaloric, electrocaloric, and elastocaloric cooling. However, magnetocaloric refrigeration (MR) is the most advanced caloric technology, with potential for long-term commercial application (Kitanovski *et al.*, 2015; Qian *et al.*, 2016; Klinar *et al.*, 2024).

To date, more than 40 research groups have conducted numerous studies worldwide, resulting in the creation of more than 70 prototypes (Kitanovski, 2020; Klinar *et al.*, 2024). Despite extensive research and development across the components of the system, MR has not yet reached commercial viability, with few institutes and companies worldwide able to demonstrate or commercialize the technology (Liang *et al.*, 2025), and prototypes that do not meet the expected performance (Kamran *et al.*, 2020; Klinar *et al.*, 2024). Despite that, interest in technology remains mainly for two factors: (i) elimination of harmful gases typically used in conventional vapor compression systems, which is increasingly critical given the phase-out scenario for such refrigerants (Gottschall *et al.*, 2019); and (ii) potential to achieve high efficiencies through a combination of factors, such as the reversibility of the magnetocaloric effect (MCE) and the recuperation of part of the energy expended to magnetize the solid refrigerant, when magnetic circuits based on permanent magnets are utilized.

1.1 Magnetic Refrigeration Systems

The main components of an MR are (i) the active magnetic regenerator (AMR), (ii) the magnetic circuit (MC), (iii) the cold and hot heat exchangers (CHEx and HHEx), and (iv) the hydraulic management system (HMS) (Trevizoli *et al.*, 2016). Other components are also crucial for the operation of MR devices, such as transmission and control systems. A

schematic representation of an MR and its components is shown in Fig. 1.1.

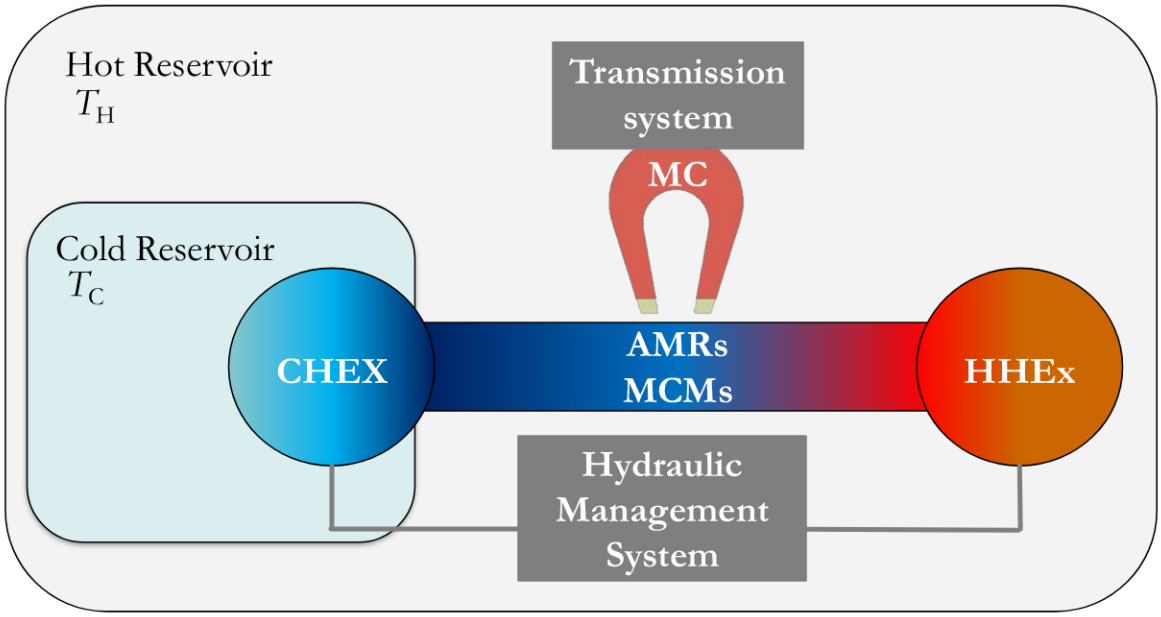


Figure 1.1 – Schematic representation of an MR system and its main components.

The AMRs are made of magnetocaloric materials (MCMs), which exhibit MCE upon the application and removal of a magnetic field. The MC generates the magnetic field, and its variation can be achieved by moving either the MC or the AMR. The HMS is tasked with delivering a controlled flow of a heat transfer fluid to the AMR at precise timings and rates. This heat transfer fluid exchanges heat with the solid refrigerant within the AMR, transporting it to and from the HHEx and CHEx. These exchangers serve as the thermal interfaces between the cooling system and the respective hot and cold heat reservoirs.

Several challenges still prevent the large-scale adoption and commercialization of MR. The primary requirement for a cooling system is to provide the necessary cooling capacity for a specified temperature range, as dictated by the application. Due to the low magnitude of the MCE, achieving high temperatures in MR devices requires regenerative cycles, which, in turn, result in complex systems with substantial losses. From the perspective of power consumption, MRs have the theoretical potential to operate at very high efficiencies, attributable to the reversible nature of the MCE and the ability to recover power during demagnetization. However, in practical applications, while the power consumption intrinsic to MCE is low, the necessity for liquid pumping through porous beds, complex hydraulic management, and the rotation of heavy parts cumulatively increases the overall power consumption of the system.

Another essential consideration is the cost of the systems. MR has been investigated for room-temperature applications for approximately 20 years; however, the lack of a structured supply chain and specialized suppliers significantly increases component costs, particularly those associated with MC and MCM. Many of the solutions adopted for developing MR prototypes were not specifically tailored to the application but instead adapted from

other products. Also, given the low number and wide variability of prototypes that use the technology, many solutions designed specifically for the systems do not meet the required reliability standards. Additional factors, such as noise and size (mass and volume), which can influence assembly, transportation, and installation, are critical to understanding the current challenges in MR commercialization. Also, the mining and processing of rare earth elements continues to present environmental challenges, which could increase the life-cycle carbon footprint of MR (Monfared *et al.*, 2014; Benke *et al.*, 2020). In addition, modeling of MR systems involves fundamental and applied concepts in thermodynamics, heat transfer, fluid mechanics, hydraulics, magnetism, and mechanical design. That, coupled with the dozens of design parameters that characterize the performance of an MR and interconnections between its components, gives rise to numerous trade-offs, turning the modeling and design of these systems into a onerous and complex task.

1.2 Artificial Intelligence and Machine Learning

Artificial Intelligence (AI) and Machine Learning (ML) represent successive domains of computer science. A fundamental way to highlight this evolution is by comparing traditional programming with the ML paradigm, as illustrated in Fig. 1.2.

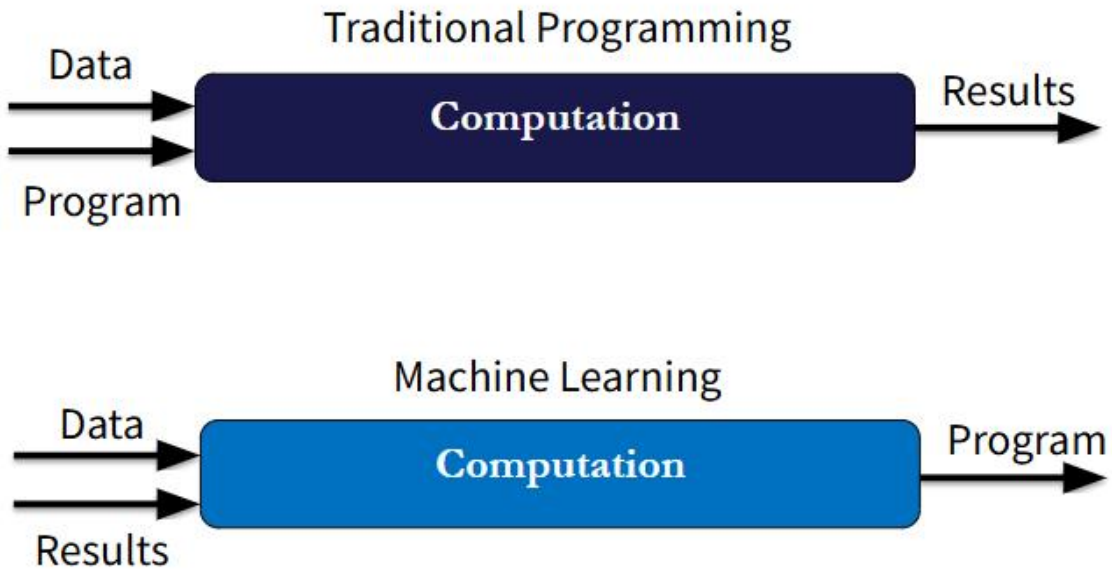


Figure 1.2 – Comparison between the frameworks of traditional programming and ML.

In traditional programming, data and a predefined set of rules (the program) are combined through computation to generate results. In contrast, ML reverses this logic: both data and the desired results are provided to the algorithm, which, through computation, learns and produces a program (the model). This shift emphasizes that, while traditional approaches

depend on human-made rules, ML relies on the ability of the system to automatically infer patterns from data, generating adaptable models capable of generalization.

In recent years, these technologies have attracted the attention of both experts and the general public because of their powerful applications. Despite their modern success, these fields have been in development for decades. McCulloch & Pitts (1943) proposed a mathematical model for neurons in 1943. In 1955, the term "Artificial Intelligence" was coined at the Dartmouth Conference to describe the science aimed at developing machines that simulate human behavior (Assen *et al.*, 2022). In 1958, Frank Rosenblatt proposed the perceptron structure (Rosenblatt, 2021), which serves as the basis for modern Artificial Neural Networks (ANNs) and Deep Learning (DL) algorithms. For years, slow progress, limitations, and unmet expectations regarding these technologies have kept the general public skeptical about their applications.

However, over the past few decades, significant advances have been made in these technologies. In the 1990s, a shift toward ML occurred, with algorithms that learned from data gaining preference over traditional rule-based systems. This shift was exemplified by IBM's Deep Blue, which defeated world chess champion Garry Kasparov in 1997 (Hsu, 1999), demonstrating the potential of AI systems. More recently, a new revolution has been driven by DL algorithms. In 2012, Geoffrey Hinton and his team achieved a breakthrough by winning the ImageNet competition with convolutional neural networks (Krizhevsky *et al.*, 2012), marking a significant leap in image recognition capabilities. In 2016, Google's AlphaGo defeated the top Go player (Chang *et al.*, 2016), demonstrating the ability of DL algorithms to handle complex systems. In recent years, the rise of Generative AI, particularly the transformer architecture (Vaswani, 2017) and large language models such as GPT-3, Bard, and Llama, has further accelerated the development of the field and the widespread adoption of these technologies.

These achievements have been made possible by several key factors. First, there has been a significant increase in computational power, notably with the advent of Graphics Processing Units (GPUs) and the rise of cloud computing, which have enabled more efficient model training and the management of large datasets. Furthermore, the exponential growth in data generation from various sources has provided the raw material needed to develop robust algorithms. The versatility of these applications is another crucial factor, as models developed in one domain can often be adapted and applied to others. Moreover, the accessibility of models and frameworks has dramatically improved, with open-source platforms providing easy access and enabling widespread application of these technologies. Lastly, the success of these algorithms fuels further development as novel applications are explored, more powerful hardware is developed, and new data streams are utilized to create even more advanced models, creating a positive feedback for the exponential development of those technologies.

As a result, these models can become powerful tools across different domains, including engineering applications, opening new frontiers in system development and addressing complex challenges.

1.3 Motivation and Main Objective

The present thesis is part of a research project being carried out at Polo, the Research Laboratories for Cooling and Thermophysics of the Federal University of Santa Catarina (UFSC), with the aim of:

> *"Design and commission a TRL-6 air-conditioner with a cooling capacity of 9000 BTU/h (2637 W) operated by a Magnetic Refrigeration Unit (MRU) composed of permanent magnets and solid refrigerants based on rare-earth elements".*

the abbreviation TRL stands for Technology Readiness Level, where a level 6 is associated with a prototype demonstration in a relevant environment (Frerking, 2016). The requirements for an air conditioning system for that application and its relevant environment were established in accordance with Brazilian (ABNT/NBR-15372, 2006) and international standards (ISO-5151, 2017).

This prototype seeks to connect theoretical breakthroughs in MR with real-world applications. Achieving TRL-6 will allow design validation under practical conditions, ensuring that the system meets critical performance, efficiency, and reliability standards. In addition, it will be one of the pioneering prototypes capable of refrigerating an entire room. This thesis will conduct an extensive analysis of the thermodynamic performance of the prototype, offering insights into its operational efficiency and effectiveness under actual conditions.

In addition to conducting experimental thermodynamic evaluations, this research aims to investigate the potential of AI to enhance the performance of MRU and related MR applications. Using data from the prototype, along with samples from the relevant literature and numerical simulations, the goal is to develop models that accurately predict the behavior of the system under various operating conditions at low computational cost. Moreover, the methods developed for magnetic refrigeration systems will be applied in other engineering areas, such as renewable energy and oil and gas systems.

This thesis aims to bridge the gap between practical operation and theoretical modeling, offering an evaluation of the MRU while exploring the potential application of AI in the technologies. The findings of this research are expected not only to validate the performance of the current prototype but also to pave the way for future innovations in MR and other engineering applications. Hence, given the opportunity presented by the research project, the main objective proposed for this thesis is

"To design, commission and evaluate the thermodynamic performance of the magnetic refrigeration unit and investigate the potential of artificial intelligence techniques to optimize its performance and to be applied in engineering systems".

1.4 Outline of this Document

Chapter 2 presents the fundamentals of MR, going from the thermodynamics of the MCE to the state-of-the-art prototypes. A review of the fundamentals of AI and ML is also provided, with a special focus on DL. Chapter 3 presents the methodology and optimization procedure for designing the MRU. Chapter 4 presents the main design characteristics of the MRU and its components. Chapter 5 presents the experimental results for each element of the MRU, as well as the performance of the system across three iterations. Chapter 6 presents an exploration of AI, ML, and DL models for their application in MR, for the development of steady-state and transient models of the systems, and for the evaluation of uncertainties in the MCM. Chapter 7 presents an exploration of AI and ML methods developed for MR applications in renewable energy and oil and gas systems. Chapter 8 presents the final remarks and recommendations for future work. After that, the bibliography is provided, along with a list of papers published in reviewed journals and conference proceedings. Lastly, three appendices are presented in this thesis. The first one details the numerical methods employed for the development of the work, mainly focusing on genetic algorithms. The second details the mathematical models of the heat exchangers. Lastly, the characteristics of the fans are presented.

Chapter 2

FUNDAMENTALS AND STATE-OF-THE-ART

This chapter aims to establish the foundation for the present research by exploring the two central themes of this work: the MCE and its applications in refrigeration technologies, followed by the fundamentals of AI and ML. The first section of this chapter will provide an exploration of the MCE, a review of the principal MR prototypes reported in the literature, and an analysis of the modeling strategies developed to simulate them. In the second section, the fundamentals of AI will be presented, beginning with a discussion of the different types of learning paradigms and tasks. The typical pipeline for developing ML models will be outlined to provide a comprehensive understanding of the AI model development process. This section will conclude with an examination of DL, emphasizing its architectures, applications, and potential to enhance predictive modeling in the context of MR and engineering.

2.1 Fundamentals of Magnetic Refrigeration

2.1.1 The Magnetocaloric Effect

The MCE is the fundamental phenomenon that governs the development and functioning of an MR. It is characterized by the thermal response that particular magnetic materials exhibit when exposed to variations in the applied magnetic field (Pecharsky & Gschneidner Jr., 1999).

2.1.1.1 Thermodynamics of the Magnetocaloric Effect

Two fundamental metrics are employed to characterize the magnitude of the MCE, given a variation of the magnetic flux density from an initial value, B_{i}, to a final value, B_{f}. The first one assumes an adiabatic variation of the magnetic flux density applied to the MCM. In this scenario, the thermal response of the material is given by a temperature change, which is called the adiabatic temperature change, ΔT_{ad}, and is calculated by:

$$\Delta T_{\mathrm{ad}} = -\int_{\mathrm{B_i}}^{\mathrm{B_f}} \frac{T}{c_{\mathrm{B}}} \left(\frac{\partial \Upsilon}{\partial T}\right)_{\mathrm{B}} dB \tag{2.1}$$

The second case to be evaluated considers that the magnetic flux density variation is performed at a constant temperature. In this case, the thermodynamic response of the material will occur by a change in the entropy called isothermal entropy change, Δs_{iso}, given

by:

$$\Delta s_{\mathrm{iso}} = \int_{\mathrm{B_i}}^{\mathrm{B_f}} \left(\frac{\partial \Upsilon}{\partial T} \right)_{\mathrm{B}} dB \tag{2.2}$$

For materials of interest in MR, the derivative of the specific magnetization (Υ) with respect to the temperature at a constant magnetic field is lower than zero. Therefore, ΔT_{ad} has the same sign as the magnetic field change, and Δs_{iso} has opposite signs. Both parameters described previously are used to characterize the MCE and are depicted in Fig. 2.1.

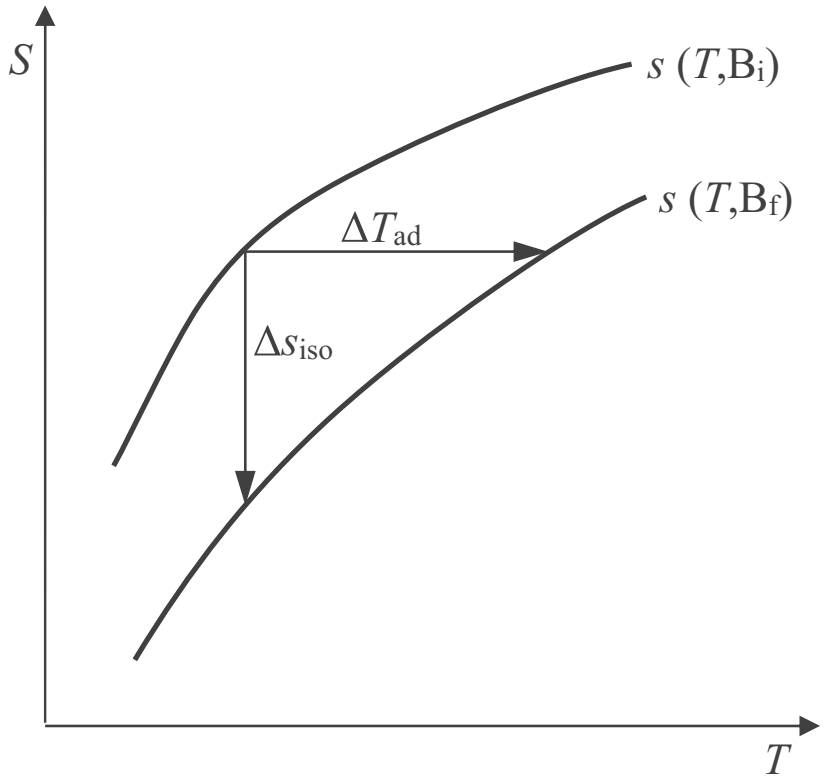


Figure 2.1 – Demonstration of the MCE through the adiabatic temperature change and isothermal entropy change by an increase in the applied magnetic field in a temperature versus entropy chart. Adapted from Smith *et al.* (2012).

MCMs exhibit higher MCE when the derivatives of specific magnetization with respect to temperature at a constant magnetic field, as shown in Eq. (2.1) and Eq. (2.2), are large (Tishin & Spichkin, 2003; Bez, 2016). This phenomenon occurs at the temperature at which the transition from ferromagnetic to paramagnetic phase occurs, known as the Curie temperature, T_{Curie}. Figure 2.2 illustrates the behavior of the adiabatic temperature change with respect to the temperature of commercial grade Gadolinium (Gd) for a magnetic field variation of 1 T.

One of the main appeals of MR is the reversibility of the MCE, which is observed in MCMs with a continuous magnetic phase transition at the Curie Temperature (Nielsen *et al.*, 2010). This reversibility has been demonstrated by measuring the adiabatic temperature change by Bahl & Nielsen (2009) and Trevizoli *et al.* (2012).

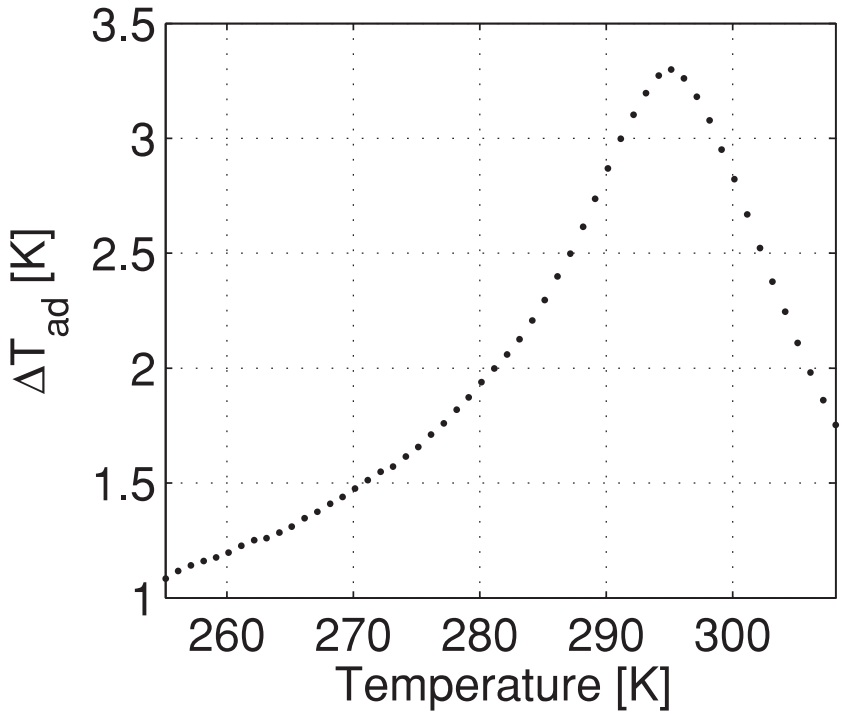


Figure 2.2 – Experimental data for the adiabatic temperature change in commercial-grade Gd for a magnetic field change of 1 T. Adapted from Smith *et al.* (2012).

2.1.1.2 Magnetocaloric Materials

MCMs are categorized into two types based on the nature of the magnetic phase transition (Smith *et al.*, 2012). Second-order phase transition (SOPT) materials exhibit a gradual phase transformation related to magnetization. In contrast, first-order phase transition (FOPT) materials undergo a sudden change at a specific temperature, often accompanied by structural deformation (Kitanovski *et al.*, 2015). Although SOPT materials have moderate values of isothermal entropy change and adiabatic temperature change, FOPT materials have a much higher peak of the former and equivalent magnitude for the latter, as can be observed in Fig. (2.3), where Lanthanum-based alloys are FOPT MCM and Gd is a SOPT MCM.

Gd is the benchmark material for MR at near room temperature. It has been used in most of the prototypes developed so far for this target operation (Yu *et al.*, 2010; Kitanovski, 2020). However, several other MCMs have been developed in recent decades, such as alloys based on Lanthanum, Iron, and Silicon (La-Fe-Si) (Shen *et al.*, 2009) and Manganese-Iron (Mn-Fe) (Brück *et al.*, 2008), which have demonstrated promising results in terms of MCE and cost (Gutfleisch *et al.*, 2011).

2.1.1.3 Thermo-magnetic Refrigeration Cycles

To transform the MCE into applicable refrigeration devices, thermodynamic cycles must be employed. As in vapor-compression refrigerators, several cycles can be applied in

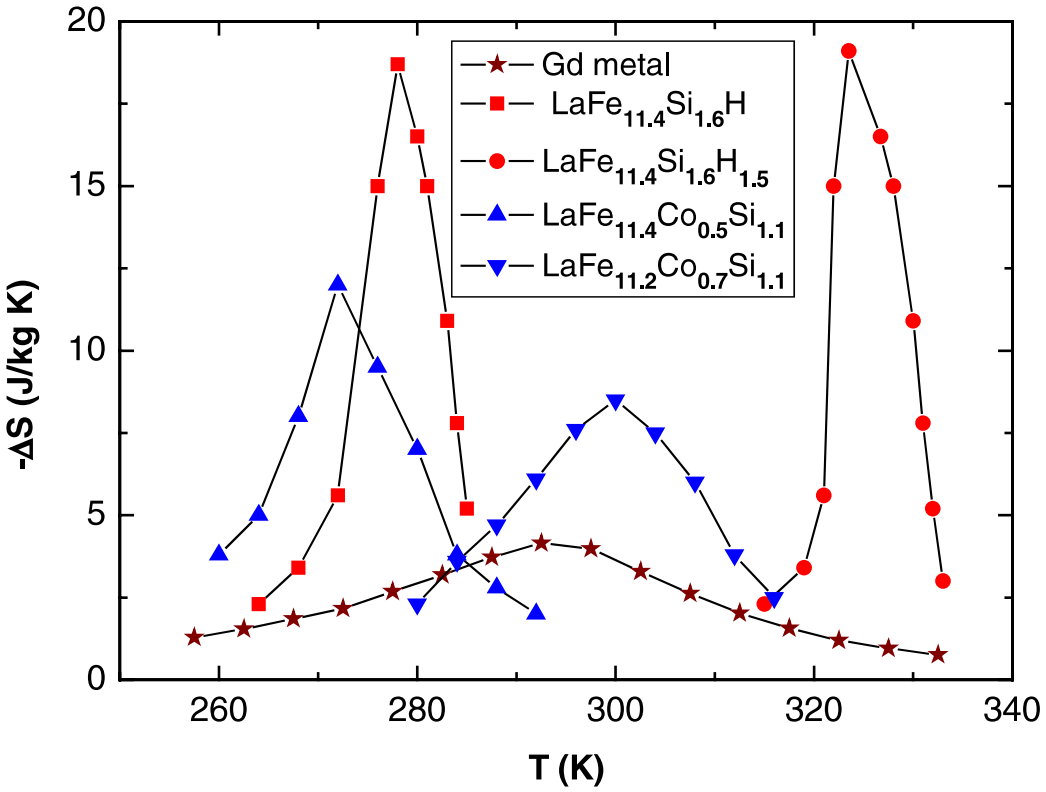


Figure 2.3 – Experimental data for isothermal entropy change for different MCM samples for an applied magnetic field change between 0 and 2 T. Adapted from Brück (2005).

MR, such as the Brayton, Ericsson, and Carnot cycles (Kitanovski *et al.*, 2014). However, as illustrated in Figs. 2.1 and 2.2, the small temperature change achieved with magnetic field variations around 1 T restricts the utilization of the cycles mentioned above. To extend the temperature range of MR, Barclay & Steyert (1982) introduced the AMR cycle. Within this cycle, MCM is used as a porous medium that serves as both a refrigerant and a regenerative matrix. A working fluid oscillates through the solid matrix, enabling heat transfer between the solid refrigerant and the thermal reservoirs via the HEx. This regeneration process increases the temperature change within the cycle, making its use in refrigeration devices viable.

The AMR cycle is performed by the following steps, which are illustrated in Fig. 2.4.

- *Adiabatic Magnetization*: During this phase, the magnetic field applied on the AMR is raised, leading to a rise in the temperature of the MCM, as described by Eq. (2.1);

- *Cold blow*: The solid matrix remains magnetized as the cold fluid from the CHEx flows through the AMR and absorbs heat from the solid medium. The now warmer fluid, at a temperature above that of the high temperature reservoir, rejects heat at the HHEx;

- *Adiabatic demagnetization*: Subsequently, the magnetic field is removed. Consequently, the temperature of the MCM, which had already been lowered by the working fluid in the preceding step, decreases further as described by Eq. (2.1);

- *Hot blow*: Finally, in the absence of a magnetic field on the MCM, the fluid from the HHEx passes through the AMR and rejects heat to the material. As a result of this heat transfer, the working fluid is cooled and then absorbs heat from the cold reservoir via the CHEx.

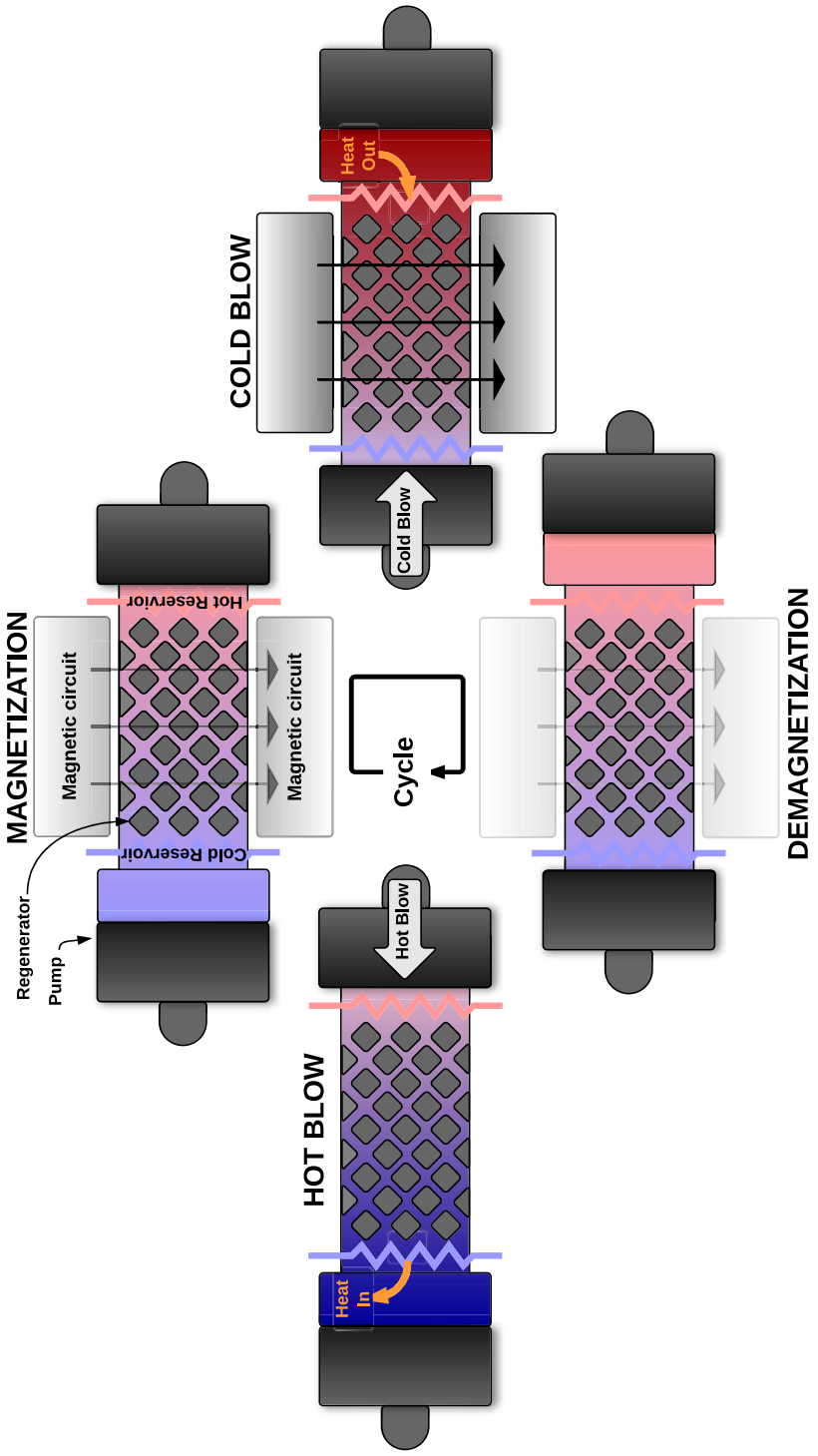


Figure 2.4 – Schematic representation of an idealized thermo-magnetic regenerative Brayton cycle. Adapted from Trevizoli (2015).

In actual devices and experimental prototypes that use permanent magnets, main-

taining a constant magnetic field during the hot- and cold-blow phases is difficult. This is mainly due to the non-uniform spatial distribution of the magnetic field in permanent magnets, as well as constraints in the fluid dynamics or HMS. For that, the actual thermodynamic cycle carried out by the AMR is determined by the interaction of the magnetic and hydraulic profiles (Kitanovski *et al.*, 2014; Teyber *et al.*, 2017b; Nakashima *et al.*, 2018; Vieira *et al.*, 2023).

2.1.2 State-of-the-art Magnetic Refrigerators

As shown in Fig. 1.1, the primary elements of an MR include: (i) an AMR, composed of a porous matrix of MCM serving both as the refrigerant and the regenerative matrix; (ii) a MC, responsible for providing the necessary magnetic field; (iii) an HMS, which generates the oscillating flow of thermal fluid through the AMR and HEX; (iv) a transmission system, that delivers the varying magnetic field; and (v) CHEx and HHEx, which allow thermal exchange between the working fluid and the heat reservoirs. Each component has multiple configurations, resulting in numerous possible combinations for MR prototypes (Trevizoli *et al.*, 2016), making the design of these devices challenging.

MR can be categorized by the method used to move the MC relative to the AMR. Four basic configurations are possible, namely the reciprocating magnet (Trevizoli *et al.*, 2011), the reciprocating AMR (Bahl *et al.*, 2008), the rotating magnet (Lozano *et al.*, 2016), or the rotating AMR (Engelbrecht *et al.*, 2012). Reciprocating systems, whether with a stationary AMR or MC, are typically employed in small-scale setups and experimental apparatus, working with one or two regenerators at frequencies under 1 Hz. (Trevizoli *et al.*, 2016). In contrast, rotary mechanisms are usually implemented in larger setups. Although rotating AMR setups can operate at higher frequencies, they require a complex fluid distribution network and are more prone to leakage. On the other hand, rotating magnet setups not only have simpler flow distribution requirements but also face fewer leakage issues and can operate at mid-range frequencies. (Tura & Rowe, 2011).

In addition, many other design decisions define the configuration of a magnetic refrigerator. Depending on the MCM processing characteristics, they can be assembled into distinct geometries such as spheres, particles, plates, pins, or microchannels (Lei *et al.*, 2015; Trevizoli *et al.*, 2017; Vieira *et al.*, 2021). Regarding HMS, most devices in the literature use double-displacement pumps (Trevizoli *et al.*, 2016b) or a pump-and-valve system. Rotary valves can mechanically activate these valve systems (Lozano *et al.*, 2016; Nakashima *et al.*, 2018) or poppet valves (Eriksen *et al.*, 2015), usually coupled to the MC transmission system, or electronically by solenoid valves (Nakashima *et al.*, 2021; Dall'Olio *et al.*, 2021). In terms of HEx, although they have been poorly explored in the MR prototypes developed so far, numerous validated configuration options exist in the industry and the literature (Shah & Sekulic, 2003). However, tube-fin configurations are the standard options for these prototypes

(Nakashima *et al.*, 2021).

Regardless of the working principle, the coefficient of performance (COP) is the standard metric for evaluating the performance of cooling systems. It is defined as the ratio between $\dot{Q}_{\mathrm{C}}$ and $\dot{W}_{\mathrm{sys}}$, which is given by the following:

$$COP = \frac{\dot{Q}_{\mathrm{C}}}{\dot{W}_{\mathrm{sys}}} \tag{2.3}$$

Another metric commonly used to evaluate the performance of refrigeration systems is the second-law efficiency, η_{2nd}. This parameter is defined by the ratio between the COP of the real system and the ideal system, COP_{cnt}, *i.e.* the Carnot COP, when subjected to the same system temperature span.

$$\eta_{\mathrm{2nd}} = \frac{COP}{COP_{\mathrm{cnt}}} = COP\left(\frac{T_{\mathrm{H}} - T_{\mathrm{C}}}{T_{\mathrm{C}}}\right) \tag{2.4}$$

As will be seen, most of the MR prototypes developed to this date do not use actual HEx to perform thermal interaction with thermal reservoirs; therefore, the temperature difference achieved (and reported by such studies) is the temperature span of the regenerator, ΔT_{AMR}, rather than ΔT_{sys}, the former always being higher than the latter.

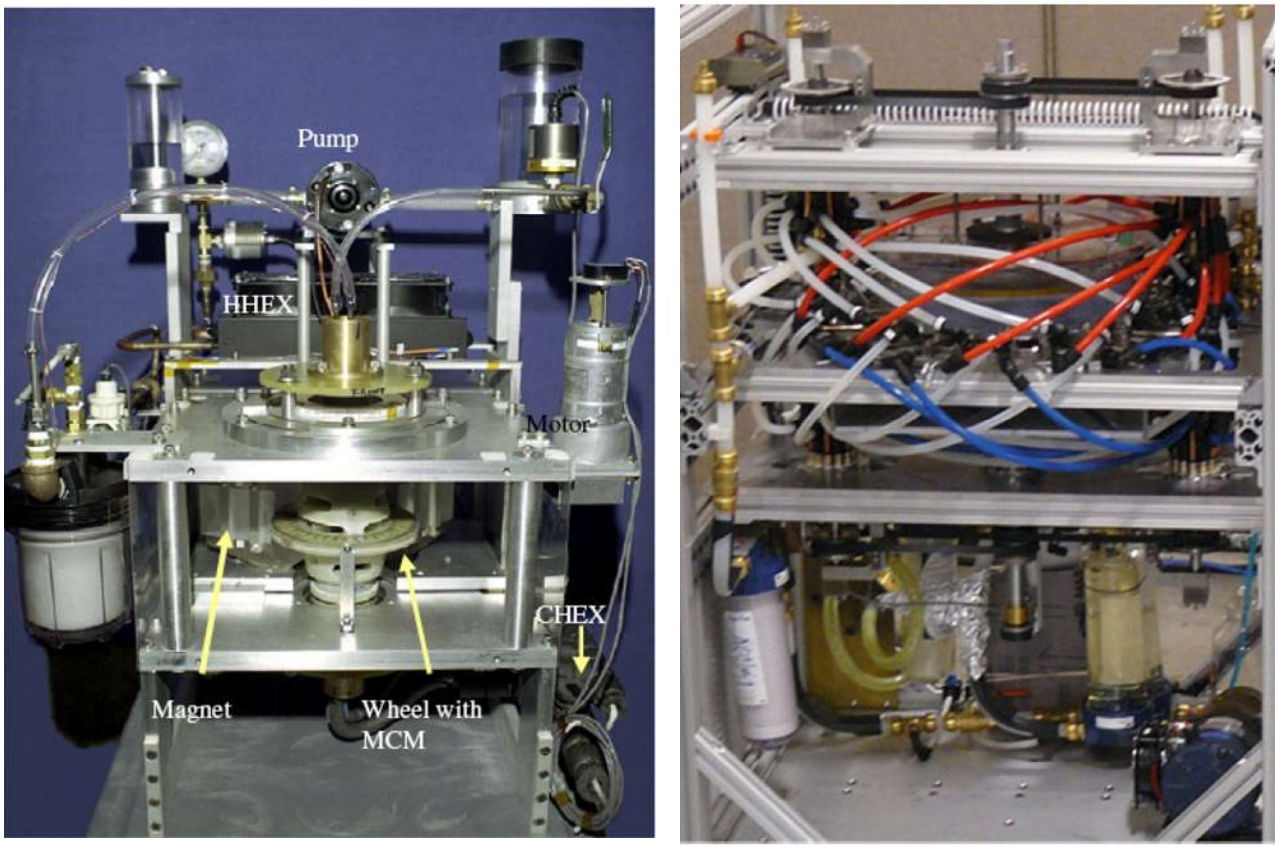
More than 70 prototypes have been designed and commissioned worldwide in recent years (Yu *et al.*, 2010; Kitanovski *et al.*, 2015; Greco *et al.*, 2019; Kamran *et al.*, 2020; Kitanovski, 2020; Klinar *et al.*, 2024). An overview of their main design configurations and performance metrics is presented below. Although some small-scale test benches are given, the review focuses on large-scale prototypes. The description will be based on the historical evolution of the prototypes developed by the following eleven institutions: Astronautics Corporation of America (United States of America), University of Victoria (Canada), Technical University of Denmark (Denmark), Technical University of Delft (Netherlands), University of Ljubljana (Slovenia), University of Salerno (Italy), Magnoric (France), University of Genoa (Italy), University of Science and Technology of China (China), Magnotherm (Germany) and Federal University of Santa Catarina (Brazil). Among the prototypes not included in this review, one can highlight the ones recently presented by Zhang *et al.* (2022) from the South China University of Technology (China) and Lei *et al.* (2023) from the Baotou Research Institute of Rare Earth (China).

2.1.2.1 Astronautics Corporation of America (United States of America)

The prototype developed by Astronautics Corporation of America examined in this review is the one described by Zimm *et al.* (2006). The researchers designed a compact MR that employs a rotary AMR to test three different alloys and MCM configurations: (i) Gd-packed spheres (with particles diameters raging from 425-500 μm), (ii) Gadolinium and Erbium (Gd-Er) packed spheres (250-325 μm), and (iii) irregular particles of $La(Fe_{0.88}Si_{0.12})_{13}H_{1.0}$

(250-500 μm). The system achieved a maximum cooling capacity of 50 W at a frequency, f, of 1 Hz and a mass flow rate, $\dot{m}_{\mathrm{f}}$, of 40 kg h^{-1}. A maximum AMR temperature span of 25 K was reached at 4 Hz and 40 kg h^{-1}. An image of this system is shown in Fig. 2.5 (a).

More recently, Jacobs *et al.* (2014) created a large-scale rotating magnet MR utilizing the MC developed by Chell & Zimm (2006) and a six-layer AMR made of a La(Fe,Mn,Si)$_{13}$H$_{\mathrm{y}}$, with the Curie Temperature arrangement selected to enhance the performance of the system at an AM temperature span of 12 K. The total mass of MCM, m_{MCM}, is 1.52 kg, used in spherical particles with diameters, d_{p} ranging from 177 μm to 246 μm. Epoxy was used to bond the layers, assuming an average porosity of 37%. The HMS featured four rotating disk valves mechanically connected to the MC. At any given time, four AMR beds were in the hot-blow phase, four in the cold-blow phase, and four in transition. On the cold side, an electric heater simulated the thermal load, while on the hot side, HHEx was linked to a thermal bath to control the hot end inlet temperature of the AMR. At 1272 kg h^{-1} and 4 Hz, a cooling capacity output of 2090 W was achieved at an AMR temperature span of 12 K, corresponding to a COP of 1.6. A photograph of this system is shown in Fig. 2.5 (b).



(a) (b)

Figure 2.5 – MR prototypes developed by Astronautics Corporation of America. Figure (a) presents the rotary regenerator prototype developed by Zimm *et al.* (2006) and (b) the rotary magnet prototype developed by Jacobs *et al.* (2014). |

2.1.2.2 University of Victoria (Canada)

The initial prototype constructed by the University of Victoria that will be examined is the one developed by Tura & Rowe (2011). The system consists of dual Halbach cylindrical magnets, operating between 0.1 and 1.47 T, with two fixed AMR beds, each filled with 55 g of 0.3-mm-diameter Gd spheres. A double-acting piston pump performs hydraulic management. The maximum AMR temperature span achieved was 29 K. The system operated with a cooling capacity of 50 W and a COP of 1.03 at an AMR temperature span of 10 K and 4 Hz; and with a cooling capacity of 40 W and a COP of 1.28 at an AMR temperature span of 10 K and 2 Hz.

A second-generation room-temperature permanent magnet AMR test apparatus was developed by Arnold *et al.* (2014). The basic configuration remains the same as the first-generation prototype, *i.e.*, rotary concentric Halbach arrays and stationary cylindrical AMRs. The main changes concern the MC, which consists of three nested Halbach cylinders, and the larger regenerator volume. Using 650 g of 0.5 mm Gd spheres, the prototype was able to achieve a maximum AMR temperature span of 33 K and operate with a cooling capacity of 50 W at 15 K. The rendering of the 3D model and a picture of this prototype are presented in Fig. 2.6.

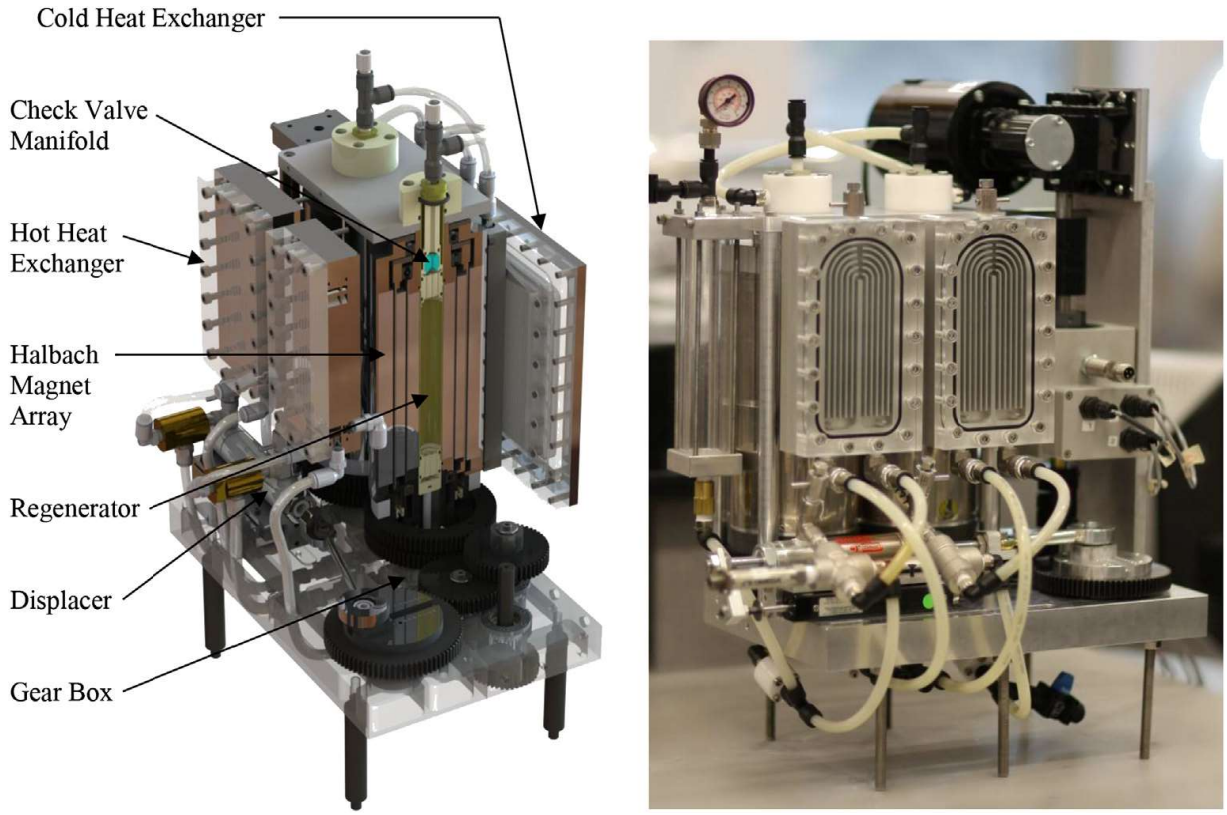


Figure 2.6 – Second generation of the prototypes developed by the University of Victoria (Arnold *et al.*, 2014).

2.1.2.3 Technical University of Denmark (Denmark)

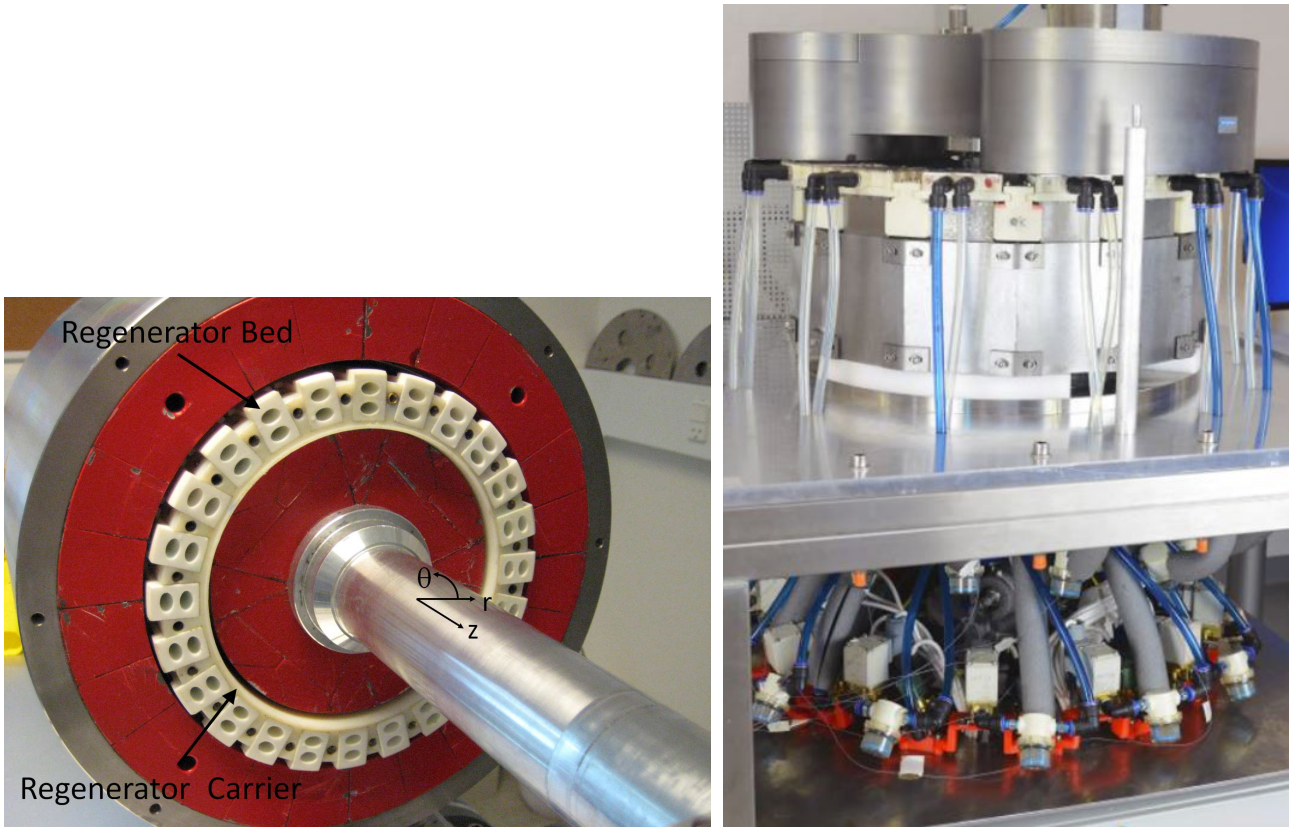
Over the years, the MR team at the Technical University of Denmark has developed multiple large-scale prototypes. Bahl *et al.* (2011) have designed a prototype of a 24-bed rotating regenerator, which was mounted around and within two Halbach-type stationary concentric four-pole MCs with a peak magnetic field of 1.24 T (Bjørk *et al.*, 2010). Engelbrecht *et al.* (2012) tested that prototype with 2.8 kg of Gd spheres. A resistance heater emulated the thermal load, and the temperature of the hot side of the AMR was controlled by a counterflow HEx connected to a thermal bath. The prototype operated at a maximum cooling capacity of 1010 W at 0 K and at an AMR temperature span of 25.4 K under no-load conditions (Engelbrecht *et al.*, 2012; Bahl *et al.*, 2014). The prototype operated at frequencies up to 10 Hz (Lozano *et al.*, 2014), the highest achieved by any MR. Through an evaluation of the performance of the device, Lozano *et al.* (2013) encountered a maximum second law efficiency of 5.6% at a cooling capacity of 400 W and a temperature span of 12.9 K. A photograph of the arrangement between the MC and the AMRs of this system is presented in Fig. 2.7 (a).

A new generation prototype was developed by Eriksen *et al.* (2015). The regenerators were composed of 1.7 kg of 1 layer of Gd and three layers of $Gd_{100-x}Y_x$ in the format of spheres and arranged in 11 fixed beds housed in two concentrated stainless steel cylinders. The MC consists of an outer rotary cylinder composed of N50-grade permanent magnet blocks and an inner static cylinder core composed of laminated iron plates and glass fiber-reinforced epoxy, with a peak magnetic field of 1.13 T. Hydraulic management was performed using poppet valves actuated by cam rings. The prototype achieved a maximum second-law efficiency of 18% at a cooling capacity of 82.5 W at 15.5 K, with a COP of 3.1. The authors concluded that considerable power consumption was caused by auxiliary components (21% from external pumping components and 7% from friction and gear and bearing losses), which could be significantly reduced by optimizing their design and selection. By optimizing the hydraulic profile of the prototype, Fortkamp *et al.* (2018) achieved, at 80 W of cooling capacity and 10.5 K of AMR temperature span, a COP of 5.1 and a second law efficiency of 19.1%.

More recently, Dall'Olio *et al.* (2021) developed a large-scale MR system with 13 fixed AMR beds composed of 10 layered $La(Fe,Mn,Si)_{13}H_z$ particles. The MCM mass used in the prototype was approximately 3.4 kg. Tapered-shaped AMRs were used to optimize system performance. The rotary MC assembly produced an axial magnetic field with mean and peak magnitudes of 1.44 T and 1.6 T, respectively. Twenty-six solenoid valves and check valves performed hydraulic management. The system reached a maximum cooling capacity of 950 W and a maximum AMR temperature span of 15.8 K. Operating at a cooling capacity of 340 W and an AMR temperature span of 10.3 K, the system achieved a COP of 6.7 and a second-law efficiency of 20.6%. Adjusting the blow fraction through the solenoid valves, Masche *et al.* (2021) achieved a maximum cooling capacity of 815 W at 5.6 K, and operated

with a COP of 6 and second-law efficiency of 11.6%.

Furthermore, Masche *et al.* (2022) substituted the MCM for 3.83 kg of Gd in a single layer. Using SOPT MCM, the authors reached a maximum cooling capacity of 1000 W and a maximum AMR temperature span of 20.8 K. Operating at a cooling capacity of 444 W at an AMR temperature span of 7.3 K, the system achieved a COP of 15.9. The results demonstrate that the system performed better when a single-layered Gd was used, rather than a 10-layered $La(FeMnSi)_{13}H_z$. A picture of this system is presented in Fig. 2.7 (b).



(a) (b)

Figure 2.7 – MR prototypes developed by the Technical University of Denmark. Figure (a) presents the rotary regenerator prototype developed by Bahl *et al.* (2011) and (b) the Rotary magnet prototype developed by Dall'Olio *et al.* (2021).

2.1.2.4 Technical University of Delft (Netherlands)

Huang *et al.* (2019) designed and commissioned a rotary magnet prototype at the Technical University of Delft. The AMR arrangement consisted of 7 beds, each mounted with 1.18 kg of epoxy-bonded Gd spheres with particle diameters ranging from 400 to 800 μm. A custom-shaped MC generated an average magnetic field of 0.875 T, and hydraulic control was achieved using solenoid valves. The system operated at frequencies from 0.5 to 1.7 Hz and mass flow rates from 70 to 260 kg h^{-1}. The prototype achieved a maximum AMR temperature span of 11.6 K and a maximum cooling capacity of 162.4 W. A picture of the prototype is presented in Fig. 2.8.

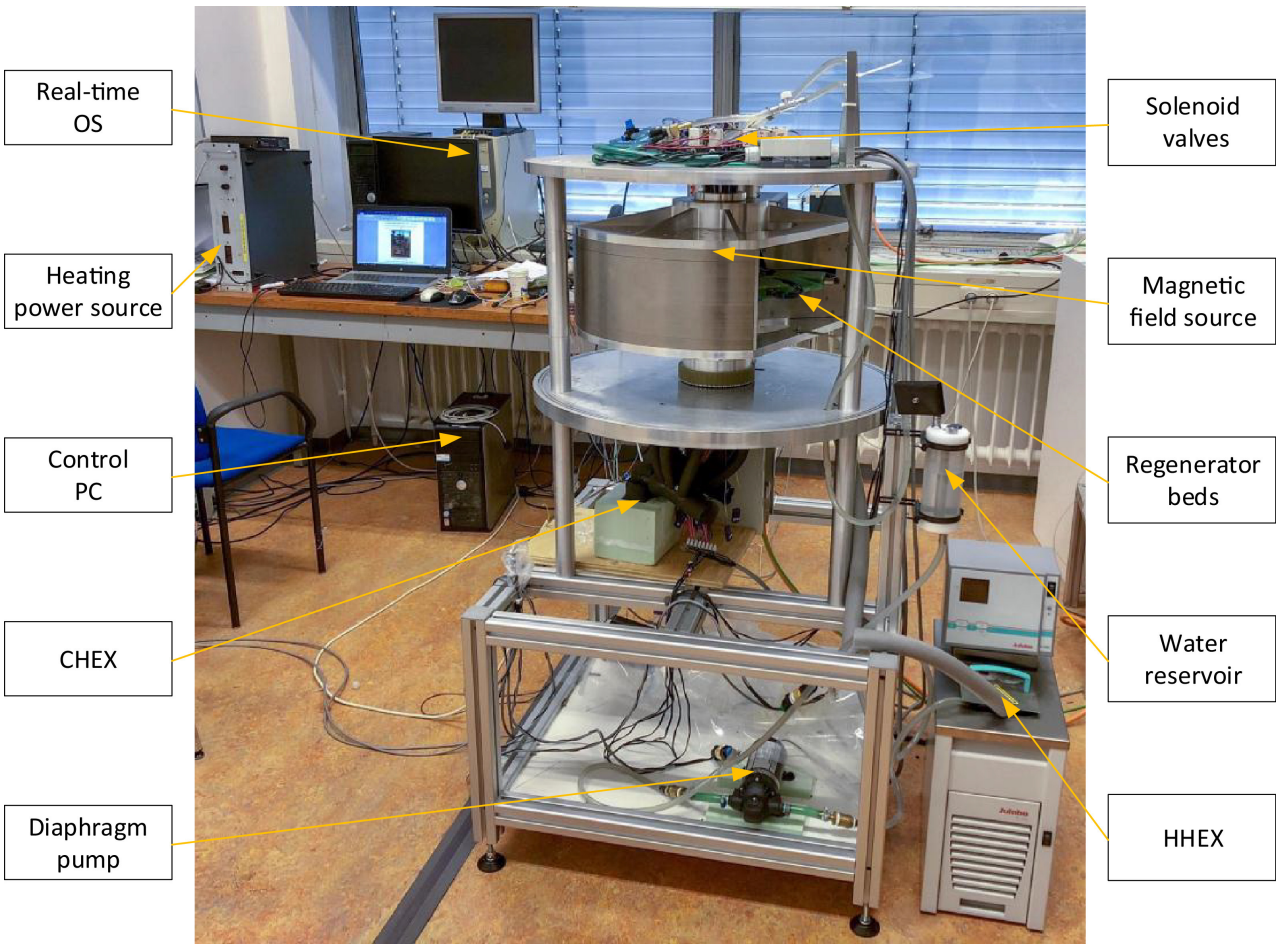


Figure 2.8 – Prototype developed at the Technical University of Delft (Huang *et al.*, 2019).

2.1.2.5 University of Ljubljana (Slovenia)

Tušek *et al.* (2010) developed a rotary magnet MR. The prototype employed approximately 600 g of Gd plates. A rotor-stator MC could achieve magnetic flux densities of 0.05-0.98 T in the air gap. No performance data were presented for the prototype.

More recently, Tušek *et al.* (2014) developed a test bench for the evaluation of AMRs. A custom-shaped MC was used and moved by a pneumatic cylinder. Hydraulic management was performed using piston pumps. The authors used Gd as the MCM and evaluated four porous medium geometries: parallel plates, spheres, powders, and cylinders. Only no-load tests were performed, and the maximum AMR temperature span achieved was 19.8 K. Tušek *et al.* (2014) compared the no-load performance of a single-layered Gd AMR with multilayered $LaFe_{13-x-y}Co_xSi_y$. The best results were achieved by Gd, reaching an AMR temperature span of approximately 23 K. In recent years, the team has focused on developing high-frequency systems with electromagnets (Klinar *et al.*, 2019; Tomc *et al.*, 2023), but no results have been published yet. A picture of the prototype developed at the University of Ljubljana is presented in Fig. 2.9.

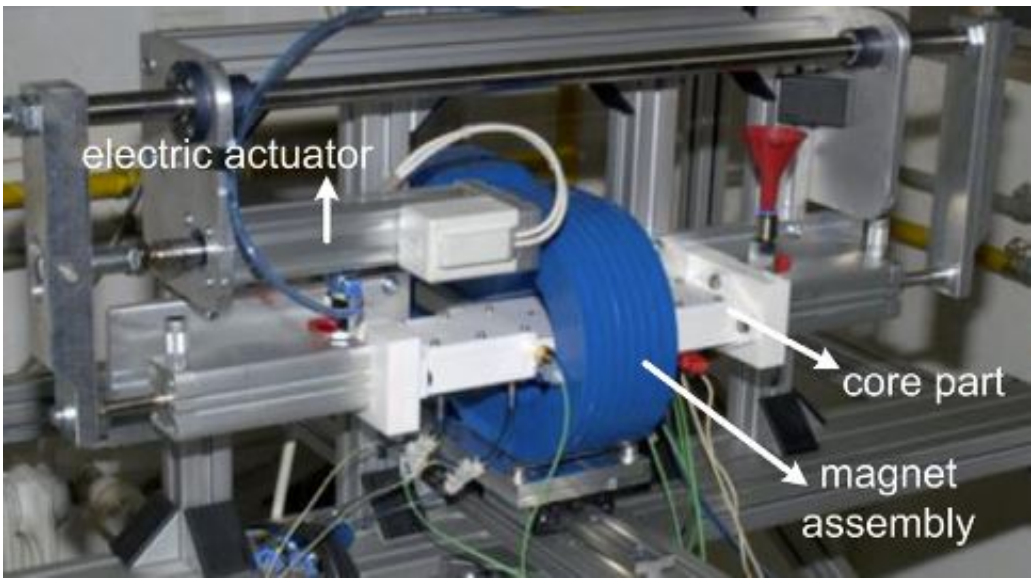


Figure 2.9 – Prototype developed at the University of Ljubljana (Tušek *et al.*, 2013).

2.1.2.6 University of Salerno (Italy)

At the University of Salerno, Aprea *et al.* (2014) devised a prototype with a two-pole rotary MC with a peak magnetic field of 1.25 T, eight AMR beds, and 1.2 kg of Gd spheres. A rotary valve coupled with the magnetic circuit was used as the hydraulic management system, and the system operated at frequencies between 0.36 and 1.79 Hz and a fixed mass flow rate of 420 kg h^{-1}. The system reached a maximum AMR temperature span of 13.5 K under no-load conditions. Through an experimental performance evaluation, Aprea *et al.* (2016) mapped several operating conditions of the device, ranging from frequencies between 0.26 and 1.38 Hz and mass flow rates from 300 to 420 kg h^{-1}. The system achieved a maximum cooling capacity of 200 W and a maximum COP of 2.5. A picture of the prototype developed by the University of Salerno is presented in Fig. 2.10.

2.1.2.7 Magnoric (France)

Magnoric is a French company (formerly Cooltech and Ubiblue) that has been developing MR systems since 2003. Among the company's prototypes, one can highlight the 15 kW proof-of-concept presented by Lionte *et al.* (2020). The system operates with a custom-shaped 4-pole MC, with a peak magnetic flux density of 1.34 T. The AMRs are composed of Gd and Gd-Er parallel plates. The system is designed to hold 32 AMR beds, each with 2.75 kg of MCM, but is currently operating with only two as a proof-of-concept experiment. Custom mechanical valves are used as the HMS. The system used a fan-assisted air-liquid heat exchanger installed in a refrigerated cabinet on the cold side and a thermostatic bath to control the temperature on the hot side. Operating at 388 kg h^{-1} and 0.26 Hz, the system achieved a cooling capacity of 900 W at an AMR temperature span of 18.35 K and a COP of 9.7. A picture of the prototype developed by Magnoric is presented in Fig. 2.11.



Figure 2.10 – Prototype developed at the University of Salerno (Aprea *et al.*, 2014).

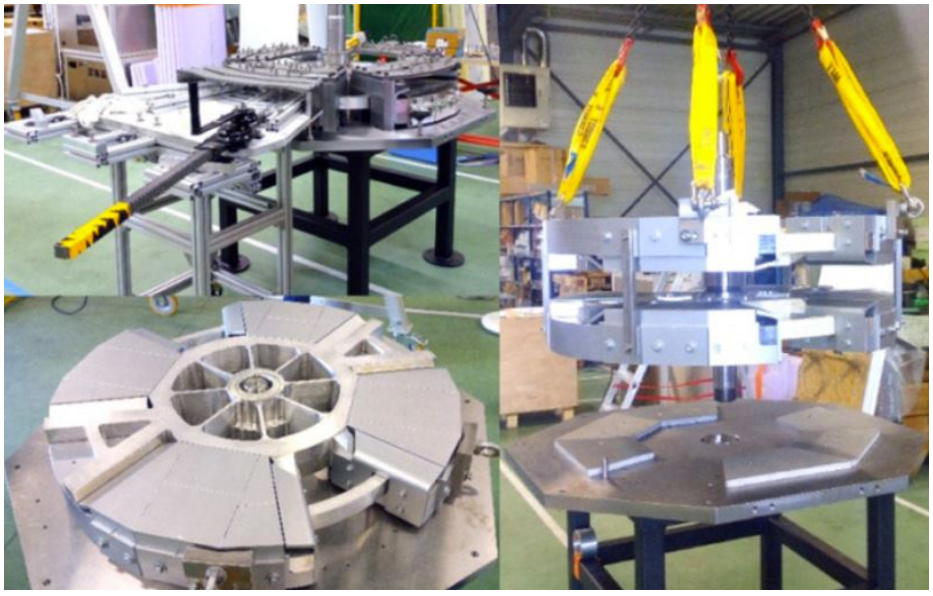


Figure 2.11 – Prototype developed by Magnoric (Lionte *et al.*, 2020).

2.1.2.8 University of Genoa (Italy)

Recently, Bocanegra *et al.* (2024) presented the design and experimental evaluation of a novel MR prototype. The authors used a rotary AMR configuration comprising 2.41 kg of Gd in the form of parallel plates, housed in 3D-printed cylindrical cartridges. A custom shape MC was used, composed of two concentric cylinders, with permanent magnets applied only

to the inner one. Both cylinders remained static and produced a peak magnetic flux density of approximately 0.945 T. Only numerical simulation results were presented. No experimental results from the prototype have been reported to date. A picture of the prototype is presented in Fig. 2.12

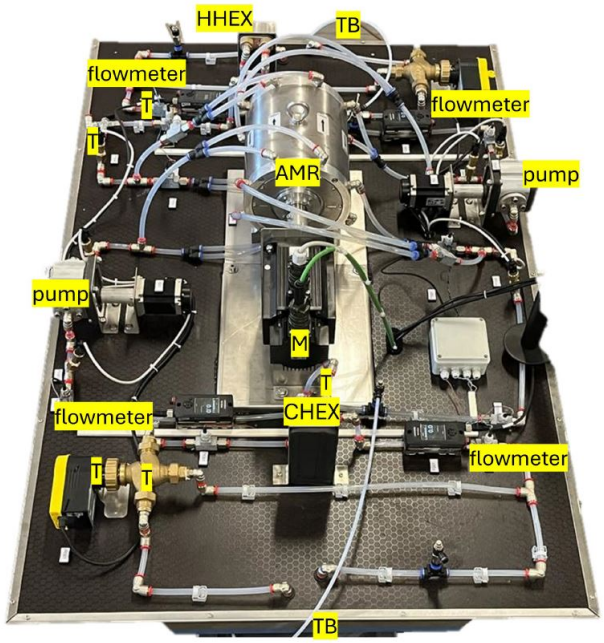


Figure 2.12 – Prototype developed by the University of Genoa (Bocanegra *et al.*, 2024).

2.1.2.9 University of Science and Technology of China (China)

Hai *et al.* (2024) has also recently presented the design and results of a prototype. The authors designed a rotary rotor-stator MC, composed of two concentric cylinders, with the inner one static. A maximum magnetic flux induction of 1.23 T was achieved in the air gap. A total of 8 AMR beds, each housing 1.35 kg of Gd particles, were used. An arrangement of solenoid valves, check valves, and manifolds was used to manage the hydraulics. The authors experimentally evaluated the operation at frequencies of 0.25, 0.33, and 0.5 Hz and mass flow rates of 45, 69, 93, and 117 kg h^{-1}. The prototype achieved a maximum cooling capacity of 126 W at 0.5 Hz, 117 kg h^{-1} and 0 K, and a maximum no-load AMR temperature span of 17.5 at 0.5 Hz and 69 kg h^{-1}. The maximum COP was roughly 15, achieved at 0.25 Hz, 69 kg h^{-1}, and 3 K, with a cooling capacity of approximately 70 W. A picture of the prototype is presented in Fig. 2.13.

2.1.2.10 Magnotherm (Germany)

Magnotherm is a German company founded in 2017 as a spin-off from the research group at the Technical University of Darmstadt. The company has worked for several years on prototype development, and so far, its main product, and the one reported in the literature, is

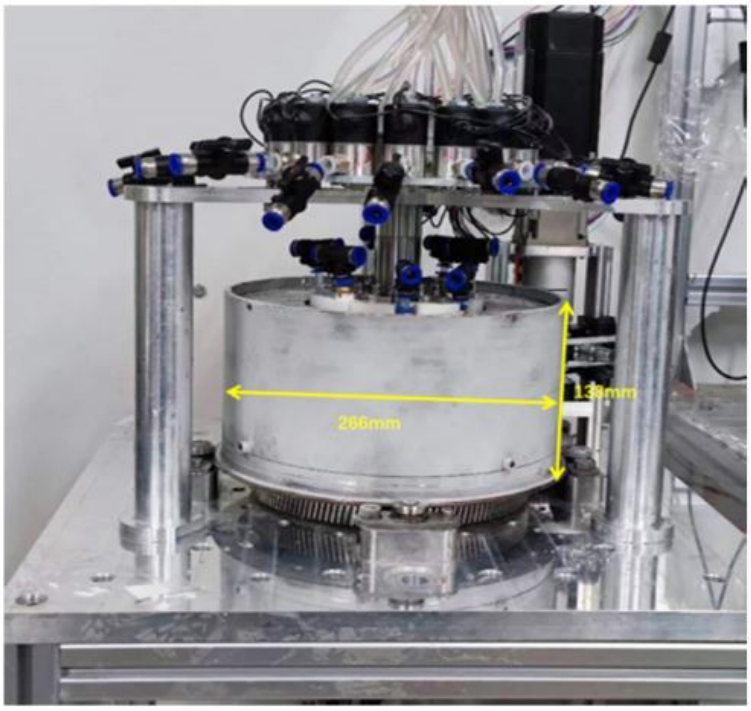


Figure 2.13 – Prototype developed by the University of Science and Technology of China (Hai *et al.*, 2024).

the beverage cooler named Polaris. Liang *et al.* (2025) reported the results from the prototype, the first certified commercial magnetic beverage cooler. The prototype employs 4 AMR beds, with 260 g of Gd and GdEr alloys as MCMs, a two-pole Neodymium-Iron-Boron (Nd-Fe-B) MC, and solenoid valves coupled with check valves as HMS. The optimized configuration achieved a specific cooling capacity, $\dot{q}_C$ of 131 W/kg (of MCM), operating with a COP of 1 and a second-law efficiency of 5.4%. A picture of Polaris is presented in Fig. 2.14.



Figure 2.14 – Prototype developed by Magnotherm (Liang *et al.*, 2025).

2.1.2.11 Federal University of Santa Catarina (Brazil)

Over the past decade, the MR research group at Polo, Federal University of Santa Catarina (UFSC), has distinguished itself as a preeminent team on the global stage. Trevizoli *et al.* (2011) designed the first prototype at Polo/UFSC, a reciprocating magnet AMR test apparatus. The regenerator was composed of 28 parallel Gd plates, each 0.85 mm thick, forming parallel channels 0.1 mm thick. A Halbach array generated the magnetic field. The system achieved a maximum AMR temperature span of 4.45 K and a maximum cooling capacity of 3.9 W. A picture of the prototype is presented in Fig. 2.15 (a).

Subsequently, Trevizoli *et al.* (2016b) developed and built an experimental setup to assess the performance of AMRs. The test bench featured a rotating MC and a single-bed AMR filled with Gd spheres with diameters between 500 μm and 600 μm. The MC consisted of a two-concentric cylinder Halbach array with a rectified sinusoidal waveform, achieving a maximum magnetic flux density of 1.69 T (Trevizoli *et al.*, 2015). A double-effect pump performed fluid pumping and hydraulic management. At the same time, thermal contact with the cold and hot heat reservoirs was simulated using HEx and thermal baths, allowing control of the inlet temperatures for the cold and hot blow. The system achieved a maximum AMR temperature span of approximately 30 K, and a peak cooling capacity of 54 W. Since this study, the apparatus has been used to evaluate the performance of passive regenerators (Trevizoli *et al.*, 2016), compare porous medium geometries for AMRs (Trevizoli *et al.*, 2017; Vieira *et al.*, 2021; Teza *et al.*, 2021; Faria *et al.*, 2022), investigate the impact of the void volume (Trevizoli *et al.*, 2018) and magnetic-hydraulic profile coupling (Nakashima *et al.*, 2018), compare different HMSs (Nakashima *et al.*, 2018), analyze multilayer AMR (Bez *et al.*, 2020; Vieira *et al.*, 2021; Teza *et al.*, 2024), and develop a control strategy for MR (Hoffmann *et al.*, 2021; Hoffmann *et al.*, 2024). A picture of the prototype is presented in Fig. 2.15 (b).

Lozano *et al.* (2016) designed a prototype featuring a rotary MC and a stationary regenerator setup. In the device, 1.7 kg of Gd spherical particles were allocated across 16 regenerators with particle diameters ranging from 425 μm to 600 μm. The magnetic field was produced by a two-pole rotor-stator MC, showing average high and low magnetic flux densities of 0.892 T and 0.011 T, respectively. Hydraulic management was performed using two rotary valves. At the hot side of the regenerator, the fluid temperature was controlled by a brazed plate heat exchanger linked to a thermal bath. Meanwhile, on the cold side, the heat load was replicated using an electrical resistance heater. The device achieved a cooling capacity of 80.4 W at AMR temperature span of 7.1 K, resulting in a COP of 0.54 and a second-law efficiency of 1.16%. Analyzing the power consumption of the system, Capovilla *et al.* (2016) demonstrated that the rotary valves were the primary power consumers within the transmission system, with total transmission power consistently exceeding pumping power in the experiments. An image of this system is shown in Fig. 2.15 (c).

In addition to the MR prototype discussed later in this document, the innovative cooling technologies team at Polo is also working on a magnetic wine cooler (Nakashima *et al.*, 2021). This apparatus features a rotary MC setup (Fortkamp *et al.*, 2023) and includes eight stationary regenerator beds, each holding about 2.2 kg of Gd spheres (one layer) and Gd-Y spheres (two layers) (Bez *et al.*, 2020). Its HMS functions through solenoid valves (Nakashima *et al.*, 2018) and uses fan-assisted herringbone wave tube fin HEx (Peixer *et al.*, 2022) coupled with a commercial wine cooler cabinet (Calomeno *et al.*, 2022). The system was able to refrigerate the cabinet, being one of the first reported in the literature to demonstrate the technology in a relevant environment, achieving a system temperature span of 14 K and a cooling capacity of 28 W. Despite that, the system achieved a COP of 0.38, still short of commercial application (Sá *et al.*, 2023). Figure 2.15 (d) displays an image of the system.

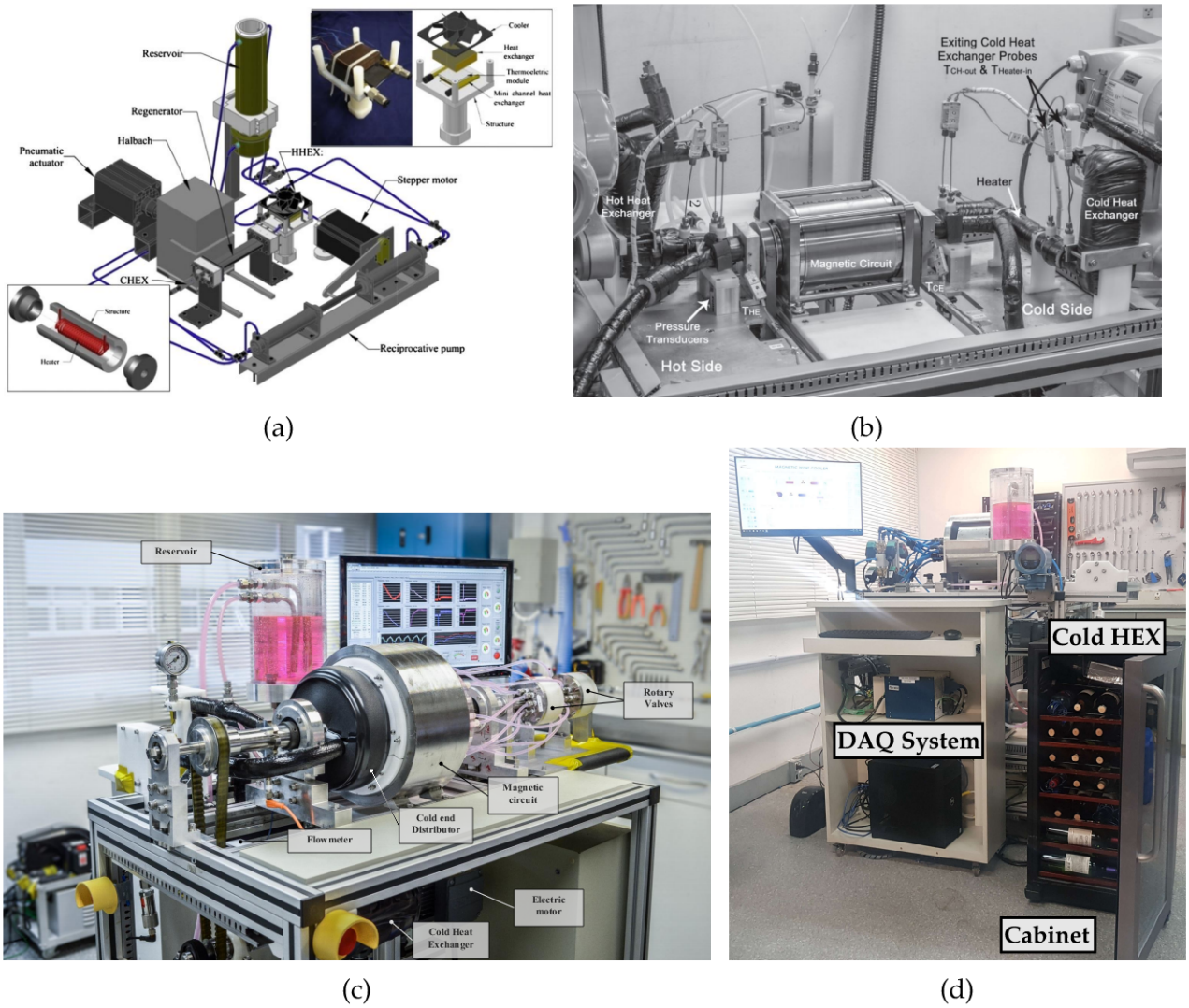


Figure 2.15 – MR prototypes developed by Polo/UFSC. Pictures of the prototypes developed by (a) Trevizoli *et al.* (2011), (b) Trevizoli *et al.* (2016b), (c) Rotary magnet prototype developed by Lozano *et al.* (2016), and (d) Rotary magnet prototype developed by Nakashima *et al.* (2021).

A summary of the subsystem configurations, the main design parameters, and the performance metrics of the previously described prototypes is presented in Table 2.1. Some

quantities were retrieved from data plots, so minor discrepancies are expected. Except for the heat pump of Dall'Olio *et al.* (2021), all systems operate as refrigerators. Only the prototype of Nakashima *et al.* (2021) and Liang *et al.* (2025) use actual HEx in both heat reservoirs; the others use electric heaters and thermal baths to emulate the heat load and the thermal reservoir temperatures. Thus, except for Nakashima *et al.* (2021), the values of cooling capacity and ΔT_{span} refer to the AMR. $\dot{Q}_{\mathrm{C,max}}$ and ΔT_{max} are the maximum values reported by the authors, not necessarily the no-load and zero-span values. The last column of Table 2.1 displays COP at a specified operating point, not necessarily the highest COP.

2.1.3 Modelling Strategies used in Magnetic Refrigerators

In general terms, modeling strategies can be classified into two major categories: physics-based and data-driven (Solomatine & Ostfeld, 2008; Goldstein & Coco, 2015; Chang & Dinh, 2019; Jia *et al.*, 2021; Oliveira *et al.*, 2023). Physics-driven models, also known as deductive or white-box models, rely on the description of the phenomena or processes via physical first-order principles, governing equations, conservation laws, and closure relations. Data-driven models, also known as inductive, empirical, or black-box models, rely on statistical and mathematical correlations to incorporate unknown relations between inputs and outputs, including methods such as ML and DL.

The main modeling challenge in MR concerns AMRs. Modeling an AMR is a multi-disciplinary task that integrates fields such as thermodynamics, heat transfer, and magnetism. Beyond the complexity of the implementation and computational expense, the accuracy of the performance predictions remains a critical criterion for evaluating existing methodologies. Most of the models developed over the last few years for predicting the performance of MR systems are physics-driven. They are based on the numerical solution of the governing equations of AMRs (Nielsen *et al.*, 2011; Trevizoli *et al.*, 2016a; Vieira *et al.*, 2021), namely the conservation of momentum and energy in the fluid phase and energy in the solid phase, which are given respectively by Eqs. (2.5)-(2.7).

$$\frac{\rho_{\mathrm{f}}}{\varphi_{\mathrm{f}}}\left(\frac{\partial v_{\mathrm{s}}}{\partial t}\right) = -\frac{\partial P}{\partial x} - \frac{\mu_{\mathrm{f}}}{K} v_{\mathrm{s}} - \frac{c_{\mathrm{E}}\rho_{\mathrm{f}}}{K^{1/2}}|v_{\mathrm{s}}|v_{\mathrm{s}} \tag{2.5}$$

where ρ_{f} stands for the density of the fluid, φ_{f} the porosity of the medium, v_{s} the superficial (Darcy) velocity, t the time, P the pressure, x the length in the flow direction, μ_{f} the dynamic viscosity of the fluid, K the permeability of the porous medium and c_{E} the Ergun constant. The term on the left side of the equation represents the inertial force of the fluid flow, while the ones on the right represent the pressure gradient, microscopic shear stress (Darcy term), and microscopic inertial force (Ergun inertial term)

$$\rho_{\mathrm{f}} c_{\mathrm{p,f}}\left(\varphi_{\mathrm{f}}\frac{\partial T_{\mathrm{f}}}{\partial t} + v_{\mathrm{s}}\frac{\partial T_{\mathrm{f}}}{\partial x}\right) = (\hbar\beta)_{\mathrm{AMR}}\left(T_{\mathrm{s}} - T_{\mathrm{f}}\right) + \left|v_{\mathrm{s}}\frac{\partial P}{\partial x}\right| + \varphi_{\mathrm{f}}\left[k_{\mathrm{f}}^{\mathrm{eff}} + \rho_{\mathrm{f}} c_{\mathrm{p,f}} D_{\parallel}\right]\frac{\partial^2 T_{\mathrm{f}}}{\partial x^2} \tag{2.6}$$

Table 2.1 – Overview of magnetocaloric cooling and heat pumping prototypes.

	Configuration				Design Parameter				Performance Metric		
Author	MC (poles)	MCM	HMS	HEx	m_{MCM} [g]	B [T]	f [Hz]	$\dot{m}_{\mathrm{f}}$ [kg h^{-1}]	$\dot{Q}_{\mathrm{C,max}}$ [W] (ΔT_{span} [K])	ΔT_{max} [K] ($\dot{Q}_{\mathrm{C}}$ [W])	COP[-] ($\dot{Q}_{\mathrm{C}}$ [W] / ΔT_{span} [K])
Zimm *et al.* (2006)	DU (2)	0.250 -0.500 mm Gd and Gd-Er spheres $La(Fe_{0.88}Si_{0.12})_{13}H_{1.0}$ particles	MV	-	-	1.5 (peak)	0.5 - 4	20 - 40	50 (0)	25 (0)	-
Jacobs *et al.* (2014)	RS (2)	0.177 -0.246 mm $La(Fe,Mn,Si)_{13}H_y$ particles	MV	-	1520	1.44 (peak)	4	750 - 1290	3042 (0)	18 (0)	1.6 (2000 / 12)
Tura & Rowe (2011)	HB (2)	0.3 mm Gd spheres	PP	-	110	1.47 (peak)	2 - 4	22 - 96	50 (10)	29 (0)	1.28 (40/1.28)
Arnold *et al.* (2014)	HB (2)	0.5 mm Gd spheres	PP	-	650	1.25 (mean)	0.5 - 0.8	25 - 118	96 (0)	33 (0)	-
Bahl *et al.* (2011)	HB (4)	-	MV	-	-	1.24 (peak)	-	-	-	-	-
Engelbrecht *et al.* (2012)	HB (4)	0.25 - 0.8 mm Gd spheres	MV	-	2800	1.24 (peak)	1 - 2	200 - 700	1010 (0)	25.4 (0)	1.8 (400 / 8.9)
Lozano *et al.* (2013)	HB (4)	0.25 - 0.8 mm Gd spheres	MV	-	2800	1.24 (peak)	1.5	200 - 600	400 (10)	16 (200)	1.51 (400 / 7.1)
Lozano *et al.* (2014)	HB (4)	0.25 - 0.8 mm Gd spheres	MV	-	2800	1.24 (peak)	2-10	500	630 (0)	18.9 (100)	-
Bahl *et al.* (2014)	HB (4)	0.25 - 0.8 mm Gd spheres	MV	-	2800	1.24 (peak)	1.5 -2.25	200 - 600	1010 (0)	25.4 (0)	-
Eriksen *et al.* (2015)	RS (2)	0.3 - 0.6 mm Gd and $Gd_{100-x}Y_x$ spheres	MV	-	1700	1.13 (peak)	0.75	180	360 (2)	25 (0)	3.1 (82.5 / 15.5)
Fortkamp *et al.* (2018)	RS (2)	0.3 - 0.6 mm Gd and $Gd_{100-x}Y_x$ spheres	MV	-	1700	1.13 (peak)	1	80 - 185	110 (12)	19 (50)	5.1 (80 / 10.5)
Dall'Olio *et al.* (2021)	RS (2)	0.4 -0.63 mm $La(Fe,Mn,Si)_{13}H_y$ particles	SV	-	3400	1.44 (mean)	0.5 - 1.2	500 - 1280	950 (5.6)	15.8 (90)	6.7 (340 / 10.3)
Masche *et al.* (2021)	RS (2)	0.4 -0.63 mm $La(Fe,Mn,Si)_{13}H_y$ particles	SV	-	3400	1.44 (mean)	0.5 - 1.2	400 - 1300	815 (5.6)	15.8 (20)	5.7 (288 / 10.3)
Masche *et al.* (2022)	RS (2)	0.35 - 0.71 mm Gd spheres	SV	-	3830	1.44 (mean)	0.5 - 1.7	420 - 1650	1000 (8)	20.8 (0)	15.9 (444 / 7.3)
Huang *et al.* (2019)	CS (2)	0.4 - 0.8 mm Gd spheres	SV	-	1180	0.875 (mean)	0.5 - 1.7	70 - 260	162.4 (0)	11.6 (0)	1.85 (102.4 / 0)
Tušek *et al.* (2010)	RS (4)	0.3 mm Gd plates	MV	-	600	0.98 (mean)	0.25 - 4	-	-	-	-
Tušek *et al.* (2013)	CC (2)	Gd plates, spheres, powders and cylinders	PP	-	-	1.15 (mean)	0.15 - 0.33	2.88 - 14.4	-	19.8	-
Tušek *et al.* (2014)	CC (2)	Gd and $LaFe_{13-x-y}Co_xSi_y$ plates	PP	-	-	1.15 (mean)	0.15 - 0.45	2.16 - 72	-	23	-
Aprea *et al.* (2014)	DU (2)	0.4 - 0.5 mm Gd spheres	MV	-	1200	1.25 (peak)	0.36 - 1.79	420	-	13.5 (0)	-
Aprea *et al.* (2016)	DU (2)	0.4 - 0.5 mm Gd spheres	MV	-	1200	1.25 (peak)	0.26- 1.38	300 - 420	200 (1.2)	11.9 (0)	2.5 (200 / 5.9)
Lionte *et al.* (2020)	RS (4)	0.4 mm Gd and Gd-Er plates	MV	-	5500	1.34 (peak)	0.26	388	900 (18.35)	21.4 (768)	9.7 (900 / 18.35)
Bocanegra *et al.* (2024)	CC (4)	Gd plates	MV	-	2410	0.945 (peak)	-	-	-	-	-
Hai *et al.* (2024)	RS (4)	0.45 - 0.6 mm Gd spheres	SV	-	1350	1.23 (mean)	0.25 - 0.5	45 - 117	126 (0)	17.5 (0)	15 (70 /3)
Liang *et al.* (2025)	RS (2)	Gd and GdEr spheres	SV	-	260	0.68 (mean)	2.0 - 2.5	48 - 120	57 (5)	22 (5)	1 (34 /15)
Trevizoli *et al.* (2016b)	HB (2)	0.55 mm Gd spheres	PP	-	195	1.69 (peak)	0.25 - 1	5 - 103	53.7 (0)	30 (0)	4.6 (11 / 5)
Trevizoli *et al.* (2017)	HB (2)	0.8 mm Gd spheres, plates and pins	PP	-	195	1.69 (peak)	0.25 - 1	5 - 103	33 (0)	31 (0)	3.1 (6.6 / 3)
Nakashima *et al.* (2018)	HB (2)	0.55 mm Gd spheres	MV	-	195	1.69 (peak)	0.25 - 0.5	10 - 100	32 (0)	10 (22)	2.3 (25 / 5)
Lozano *et al.* (2016)	RS (2)	0.425 - 0.6 mm Gd spheres	MV	-	1700	0.892 (mean)	0.4 - 1.4	150 - 200	150 (0)	12 (0)	0.54 (80.4 / 7.1)
Capovilla *et al.* (2016)	RS (2)	0.425 - 0.6 mm Gd spheres	MV	-	1700	0.892 (mean)	0.4 - 0.8	100 - 200	104 (4)	8 (48)	2.46 (72 / 4)
Nakashima *et al.* (2021)	RS (2)	0.4 mm Gd and $Gd_{100-x}Y_x$ Spheres	SV	Tube-fin	2240	0.98 (mean)	0.5 - 1	125 - 225	28 (14.2)	14.2 (28)	0.37 (24 / 12.5)
Vieira *et al.* (2021)	HB (2)	0.4 - 0.65 mm $La(Fe,Mn,Si)_{13}H_y$ particles	SV	-	75	1.69 (peak)	0.5	30 - 60	22 (0)	12 (0)	-

Legend: HB: Halbach array, RT: Rotor-stator, CC: Custom Shaped magnet, DU: Double-U magnet, MV: Mechanical valves, SV: Solenoid valves, PP: Piston pump.

where $c_{\mathrm{p,f}}$ stands for the specific heat at constants pressure of the fluid phase, T_{f} the temperature of the fluid, h_{AMR} the interstitial heat transfer coefficient between the solid and fluid phases, β_{AMR} the surface area density of the porous medium, T_{s} the temperature of the solid phase, $k_{\mathrm{f}}^{\mathrm{eff}}$ the effective thermal conductivity of the fluid phase, $D_{\parallel}$ the longitudinal thermal dispersion. The terms on the left side of the equation correspond to thermal inertia effects and advection, while the ones on the right side are for the interstitial heat transfer between solid and fluid phases, heat generation through viscous dissipation, and axial conduction.

$$\rho_{\mathrm{s}}\varphi_{\mathrm{s}}\frac{\partial u_{\mathrm{s}}}{\partial t} = (\hbar\beta)_{\mathrm{AMR}}\left(T_{\mathrm{f}} - T_{\mathrm{s}}\right) + \varphi_{\mathrm{s}}k_{\mathrm{s}}^{\mathrm{eff}}\frac{\partial^2 T_{\mathrm{s}}}{\partial x^2} + \rho_{\mathrm{s}}\varphi_{\mathrm{s}}B\frac{\partial \Upsilon}{\partial t} \tag{2.7}$$

where φ_{s} stands for the volumetric fraction of MCM, u_{s} for the internal energy of the solid phase, $k_{\mathrm{s}}^{\mathrm{eff}}$ for the equivalent thermal conductivity of the solid phase. The term on the left side of the equation accounts for the energy storage in the solid, whereas the ones on the right account for the interstitial heat transfer between the solid and the fluid, axial conduction in the solid phase, and magnetic work transfer.

For the solution of Eqs. (2.5)-(2.7), several information are required, among which one can highlight the measurements of thermomagnetic properties of the MCM (Vieira *et al.*, 2021; Franco, 2021), characterization of the magnetic field (Bjørk *et al.*, 2014; Trevizoli *et al.*, 2015; Teyber *et al.*, 2017a; Fortkamp *et al.*, 2023) and thermohydraulic behavior of the porous medium geometry (Trevizoli *et al.*, 2016; Trevizoli *et al.*, 2016b; Trevizoli *et al.*, 2017; Lei *et al.*, 2018; Liang *et al.*, 2020; Liang *et al.*, 2021) and quantification of losses (Niknia *et al.*, 2016; Trevizoli *et al.*, 2017). Despite their complexity, the agreement between the models and the experimental results is generally good only for the prototypes with which they were calibrated, failing especially in some design ranges such as high frequencies and temperature spans. Some examples of 1D AMR models are the ones developed by Engelbrecht (2008), Tušek *et al.* (2011), Lei *et al.* (2015), Trevizoli *et al.* (2016a), Niknia *et al.* (2016) and Vieira *et al.* (2021).

The need for fine discretization and detailed temporal and spatial solutions of temperature and velocity fields often results in high computational costs for the numerical solution of the AMR model. This makes rapid performance evaluation challenging, hindering their use in optimization, sensitivity and uncertainty analysis, and transient modeling tasks. To address this issue, alternative approaches such as semi-analytical (Burdyny *et al.*, 2014) and

lumped (Nakashima *et al.*, 2022a) methodologies have been adopted. These methods provide quick performance forecasts for magnetic refrigerators by integrating empirical data to adjust coefficients in physics-driven models, avoiding reliance on numerical solutions but remaining valid only for individual prototypes.

In contrast to physics-based models, data-driven methodologies rely on statistical correlations between input parameters and performance metrics (Brunton & Kutz, 2022). These models can provide fast, accurate predictions within their validity range, but usually require a large amount of data for training and lack generalization when extrapolated. ML and ANNs are included in this category of models. Their use has soared in recent years due to the availability of large amounts of data, increased hardware processing power, and the development of more efficient models.

Given their capabilities, data-driven models can fill the gaps left by physics-based approaches in magnetic refrigeration and other engineering applications, providing fast, accurate predictions without the need for in-depth characterization of the underlying phenomena. For that, several works have used data-driven models in engineering, thermal, and refrigeration systems (Mohanraj *et al.*, 2012; Maiorino *et al.*, 2022; Izanloo *et al.*, 2022; Tschora *et al.*, 2022), as ANNs are one of the most popular choices given their flexibility and prowess in regression tasks. In MR, neural networks have been employed to model material properties (Maiorino *et al.*, 2019) and components (Aprea *et al.*, 2018; Maiorino *et al.*, 2022; Peixer *et al.*, 2023). To better understand the capabilities and limitations of these types of models, the following section provides a fundamental basis for AI, ML, and ANNs.

2.2 Fundamentals of Artificial Intelligence and Machine Learning

In this section, the core principles of AI and ML are discussed. In the rapidly evolving landscape of technology, understanding the distinctions between them is essential. AI is a domain within computer science dedicated to the development of systems capable of performing tasks that traditionally require human cognitive functions. AI integrates a diverse array of methodologies and strategies, ranging from conventional rule-based frameworks and expert systems to contemporary data-centric approaches. On the other hand, ML is a subfield of AI that uses data and algorithms to enable systems to learn and make predictions or decisions without being explicitly programmed for specific tasks. ML involves training models on datasets to discern patterns and generate predictions. Techniques such as regression, classification, and clustering are included in this domain. Lastly, DL is a specialized subdivision of ML, focusing on algorithms inspired by the architecture and functionality of the human brain, commonly known as artificial neural networks (ANNs).

2.2.1 Types of Learning Algorithms and Problems

Understanding the different types of learning is crucial to understanding how AI systems learn and apply knowledge. ML can be categorized into several types, each with its own techniques, objectives, and benefits (Brunton & Kutz, 2022). The ones described in this review are supervised and unsupervised learning. Supervised learning is the process of training a model using labeled data, where each training instance is associated with a corresponding output label. The primary objective of this methodology is to establish a mapping function from input to output, which allows the model to predict labels for unseen data (Brunton & Kutz, 2022). Throughout the training process, the model is provided with a dataset comprising input features and corresponding target values or labels, allowing it to learn patterns and relationships that can be applied to new data. This involves minimization of a loss function to quantify the discrepancy between predicted outputs and true labels (Wang *et al.*, 2020).

There are two main types of tasks in supervised learning: regression and classification. Regression problems involve predicting a continuous numeric variable, such as temperature (Paniagua-Tineo *et al.*, 2011), sales forecasting (Lu, 2014), or stock prices (Cakra & Trisedya, 2015). On the other hand, classification tasks involve assigning data to distinct, discrete categories, such as spam (Mansoor *et al.*, 2021) or images (Lu & Weng, 2007).

In contrast, unsupervised learning addresses data that lacks labeled outputs (Brunton & Kutz, 2022). The primary objective is to uncover latent patterns, structures, or relationships within the data. These algorithms discern patterns and clusters without predefined labels, organizing the data in a meaningful way (Ghahramani, 2003). In the absence of labels to guide the learning process, evaluating model performance poses greater challenges and often requires qualitative assessment. Unsupervised learning techniques encompass clustering (Xu & Wunsch, 2008) and dimensionality reduction (Maaten *et al.*, 2009). Clustering algorithms group data into distinct clusters based on similarities and can be used in applications such as customer segmentation (Kansal *et al.*, 2018), anomaly detection (Münz *et al.*, 2007), and recommendation systems (Gong, 2010). Dimensionality reduction techniques aim to reduce the number of features while preserving the fundamental structure of the data. They can be used in applications such as noise removal (Sheybani, 2011), image compression (Jaradat *et al.*, 2021), and as preprocessing for ML (Yan *et al.*, 2006). A categorization by learning approach is presented in Tab. 2.2. There are other categories of learning, such as semi-supervised learning,

Table 2.2 – Categorization of learning approaches.

Learning Type	Continuous Data	Discrete Data
Supervised Learning	Regression	Classification
Unsupervised Learning	Dimensionality reduction	Clustering

which combines elements of both supervised and unsupervised learning to improve model performance with a limited amount of labeled data (Zhu, 2005); or reinforcement learning, which involves training models to make a sequence of decisions by interacting with an environment (Kaelbling *et al.*, 1996); but they are not going to be explored here.

2.2.2 Pipeline for the Development of a Machine Learning Model

The construction of an ML model involves a sequence of structured phases, each critical to building a strong and efficient model (Brunton & Kutz, 2022). This systematic approach not only tackles the complexities of ML but also maximizes the chances that the model is well prepared to execute the designated task with high accuracy and generalization. Given the challenges outlined in this thesis, the pipeline will focus on developing regression tasks. The following subsections offer a brief analysis of every stage, elaborating on the processes of problem definition, data collection and preparation, model selection, training, optimization, and evaluation.

2.2.2.1 Problem Definition

In the initial stage of developing an ML model, it is essential to define the problem the model aims to solve clearly. This step is fundamental yet often overlooked. Various structured frameworks exist to aid this process (Watanabe *et al.*, 2017), including the ML formalism, which describes ML as: "*A computer program is said to learn from experience E with respect to some class of tasks T and performance measure P, if its performance in tasks in T, as measured by P, improves with experience E*" (Mitchell & Mitchell, 1997). Identifying tasks, experience, and performance can serve as the basis for defining the problem.

The key aspect of the step is to determine the nature of the problem, the need to solve it, and the justification for using ML as a solution. Then, it is essential to identify the specific ML task (e.g., classification, regression, clustering, or anomaly detection) and the domain-specific requirements. It is also vital to outline any limitations, including data availability, performance benchmarks, and computational restrictions, which could affect the model development process.

In ML, the goal is to develop models that generalize well to new data, ensuring accurate performance not only on the training set but also on previously unseen inputs. Essentially, a regression model is a mapping function ($\mathcal{F}$) that generates predictions ($\hat{y}$) for given input data (x), parameters (Θ) and hyperparameters (Ξ) as described by:

$$\hat{y} = \mathcal{F}(x, \Theta, \Xi) \tag{2.8}$$

where the parameters are the variables which are updated according to the learning algorithm of the model, and the hyperparameters are configuration variables set before the training

starts. This difference will be discussed further in this chapter.

The problems proposed to be tackled in this thesis will be determined according to Eq. (2.8). For the sake of brevity, in many cases the variables Θ and Ξ will be omitted, although it is considered implicit that all models are comprised of both.

2.2.2.2 Data Collection and Preparation

The data collection and preparation phase seeks to ensure the quality and reliability of the data provided to develop an ML model. It begins with gathering data, which may include structured databases, experimental results, numerical simulations, literature reviews, web scraping, or real-time sensor data. The goal is to compile detailed, relevant data that effectively captures the features and complexities necessary to address the given problem within the design space in which the model is intended to make predictions.

Raw datasets often contain noise and inconsistencies, making data cleaning a critical process (Ilyas & Chu, 2019). This stage involves removing inaccuracies, such as outliers and duplicate records, to ensure that the data are free of distortions that could affect model performance. One major challenge in this phase is handling missing data (Allison, 2009), which can seriously impact many ML algorithms. It can be solved by discarding incomplete features or samples or by imputing missing values using statistical methods such as mean, median, or mode substitution (Zhang, 2016). For more complex situations, advanced imputation techniques, such as K-Nearest Neighbors (KNN) imputation, may be used (Jadhav *et al.*, 2019). Furthermore, applying noise reduction techniques can significantly enhance data quality (Kaur, 2015). Techniques such as moving averages (Guiñón *et al.*, 2007) or low-pass (Mahmoud *et al.*, 2013) filters can be effective in mitigating random noise.

Once the data are cleaned, transformation processes are applied to enhance their usability. It may involve different tasks, but the main one of interest in the present work is the transformation of categorical variables into numerical representations. Among the most widely used techniques, one can highlight one-hot encoding (Kim, 2024). In this technique, each discrete category is represented as a new binary vector, creating as many new binary features as distinct categories in the categorical variable. To illustrate this, Tab. 2.3 presents an example of the application of the technique. The original vector comprises three colors and is transformed into three distinct binary features, each representing a color (or category) in the original vector.

Data scaling and normalization can improve the learning of algorithms (Ali *et al.*, 2014). The features are typically scaled using Min-Max normalization, given by Eq. (2.9), where the minimum and maximum values of each feature are used to transform them. In addition, a popular strategy is z-score standardization, given by Eq. (2.10), which uses the mean ($\Lambda(x)$ and standard deviation (σ). Data scaling and normalization ensure consistency

Table 2.3 – Example of a One-hot encoding

Original Vector	Encoded Vector		
Color	Red	Green	Blue
Red	1	0	0
Green	0	1	0
Blue	0	0	1

across the data set and prevent any single feature from disproportionately influencing the model.

$$x' = \frac{x - \min(x)}{\max(x) - \min(x)} \tag{2.9}$$

$$x' = \frac{x - \Lambda(x)}{\sigma(x)} \tag{2.10}$$

In addition, feature engineering can be a powerful technique in data preparation. It involves creating new features or modifying existing ones to highlight significant patterns in the data. This practice often requires domain knowledge and can significantly improve model performance by revealing relationships hidden in raw data. This stage might involve the imputation of physical knowledge on the model, which can substantially increase its performance (Bikmukhametov & Jäschke, 2020).

Finally, to ensure the quality, accuracy, and generalization of the model, the data should be divided into distinct sets: training, validation, and testing, each with a different objective. This ensures that the performance of the model can be rigorously evaluated. The training set is used to fit the model and adjust its parameter values, namely its weights and biases. The validation set helps fine-tune hyperparameters and select the best-performing model. The test set is reserved for the final evaluation, ensuring that the performance of the model is assessed on unseen data. Properly splitting the data helps prevent overfitting and provides an unbiased estimate of the ability of the model to generalize to unseen situations.

2.2.2.3 Model Selection

One of the main challenges in ML is selecting a model, or, according to Eq. (2.8), a mapping function $\mathcal{F}$, that accurately captures the inherent patterns in the data. For that, model selection is a crucial step in the pipeline, significantly affecting its performance and its ability to generalize to phenomena, processes, components, or systems of interest. Choosing the right model involves balancing complexity, interpretability, and computational efficiency while considering the problem domain and data characteristics (Brunton & Kutz, 2022). A well-suited model captures essential patterns in the data without overfitting, leading to better predictions on new data. On the other hand, a poorly chosen model can result in poorer performance, longer training times, and incorrect inferences.

Understanding the trade-offs of different models and tailoring them to specific use cases is critical to developing robust, accurate, and efficient ML solutions. The following section will describe several popular ML models, explaining their key features and the trade-offs they entail in terms of complexity, accuracy, and computational cost. This overview will provide a foundation for selecting the most appropriate model based on the specific needs of the tasks at hand.

Linear regression models are among the most basic and understandable techniques in ML (Su *et al.*, 2012). They assume a linear correlation between the input and output variables. The model generates predictions by fitting a line (or a hyperplane in higher dimensions) that minimizes the difference between the predicted and actual values. This fitting is done using an optimization process that reduces the cost function to find the best coefficients for each predictor. Despite their straightforward structure, linear regression models are highly effective when the relationship among variables is roughly linear. These models offer clarity by showing how each input feature affects the output via its coefficient. However, they fall short in representing complex, non-linear interactions or outliers in the dataset. The general formula for a linear regression model, according to the format given by Eq. (2.8), is provided by:

$$\hat{y} = \mathcal{F}(x, \Theta) = \Theta_0 + \Theta_1 x_1 + \Theta_2 x_2 + \cdots + \Theta_{\mathrm{n}} x_{\mathrm{n}} \tag{2.11}$$

Many real-world phenomena exhibit nonlinear behavior that a simple linear model cannot adequately capture. Polynomial regression extends linear regression by adding polynomial features, enabling the model to fit a more flexible curve to the data. It consists of converting the input features into polynomial terms to identify non-linear relationships (Ostertagová, 2012). These transformations significantly improve the ability of the model to capture complex patterns in the data. Although polynomial regression can increase the capacity of the model to capture complexity, it also introduces several challenges. Higher-degree polynomials might lead to overfitting, where the model captures even the noise in the training data rather than the core pattern. To address this, choosing an appropriate polynomial degree and using regularization methods are crucial for balancing model complexity and generalization (Brunton & Kutz, 2022). The general formula for a polynomial regression model, according to the format given by Eq. (2.8), is provided by:

$$\hat{y} = \mathcal{F}(x, \Theta) = \Theta_0 + \sum_{\mathrm{i}=1}^{\mathrm{n}} \left(\sum_{\mathrm{j}=1}^{\mathrm{p_i}} \Theta_{\mathrm{ij}} x_{\mathrm{i}}^{\mathrm{j}} \right) \tag{2.12}$$

Support Vector Regression (SVR) is an algorithm for regression, extending the Support Vector Machine (SVM) approach to continuous outcomes (Suthaharan & Suthaharan, 2016). The core idea of SVR is to establish a function that closely approximates the target values of the training data within a certain tolerance. The aim is to reduce the complexity of the function while keeping deviations from the observed values within the specified margin.

The function mapping is numerically defined as:

$$\hat{y} = \mathcal{F}(x, \Theta) = \Theta\phi(x) + \Theta_0 \tag{2.13}$$

where $\phi(x)$ is a feature transformation function (often a kernel function). The formulation of SVR includes an optimization problem with a loss function, $\mathcal{L}$, that penalizes deviations outside the margin, ϵ, often using the epsilon-insensitive loss function:

$$\mathcal{L}(y, \mathcal{F}(x, \Theta)) = \begin{cases} 0 & \text{if } |y - \mathcal{F}(x, \Theta)| \leq \epsilon \\ |y - \mathcal{F}(x, \Theta)| - \epsilon & \text{otherwise} \end{cases} \tag{2.14}$$

By using different kernel functions (linear or polynomial), SVR can model complex, non-linear relationships between features and targets.

Another popular ML model is the Decision Tree, which represents a suitable framework for both classification and regression tasks (Kingsford & Salzberg, 2008). This model determines decisions and their possible consequences within a tree-shaped hierarchical structure, where each internal node represents a feature, each branch specifies a decision rule, and each leaf (terminal node) indicates an outcome or class label (Rokach & Maimon, 2005). Building the tree involves recursively splitting the data at each node by selecting features that either maximize information gain or minimize impurity in classification tasks, or reduce variance in regression tasks. Trees offer several advantages, such as being easy to interpret, handling both numerical and categorical data, and requiring minimal preprocessing. However, they can overfit, especially with deeper trees that capture noise from the training data.

Building on the advantages of Decision Trees, Random Forests (RF) are an ensemble learning technique that combines multiple Decision Trees to improve predictive accuracy and generalization (Breiman, 2001). This method leverages the strength of decision trees by combining their outputs to produce a final prediction. In an RF, each tree is trained on a randomly selected subset of training data obtained through bootstrapping (Abney, 2002). This randomness helps reduce overfitting and enhances the generalization ability of the model to new data. The final prediction from the RF is usually determined by averaging the output of all trees (in regression) or by majority voting (in classification).

Extreme Gradient Boosting (XGBoost) is an advanced ML technique that improves predictive accuracy by combining decision trees. In contrast to RF, which generates trees independently, XGBoost sequentially constructs trees, addressing errors from earlier trees (Chen, 2015). Each new tree focuses on the residual errors of the preceding ensemble. XGBoost is a powerful tool that includes features such as regularization to prevent overfitting, handling of missing values, and efficient parallel computation.

In addition to the models previously discussed, several other ML techniques offer unique benefits for different tasks. KNN is a learning approach that classifies new data points

Gene Pair	Interact?	Expression correlation	Shared localization?	Shared function?	Genomic distance
A-B	Yes	0.77	Yes	No	1 kb
A-C	Yes	0.91	Yes	Yes	10 kb
C-D	No	0.1	No	No	1 Mb
⋮					

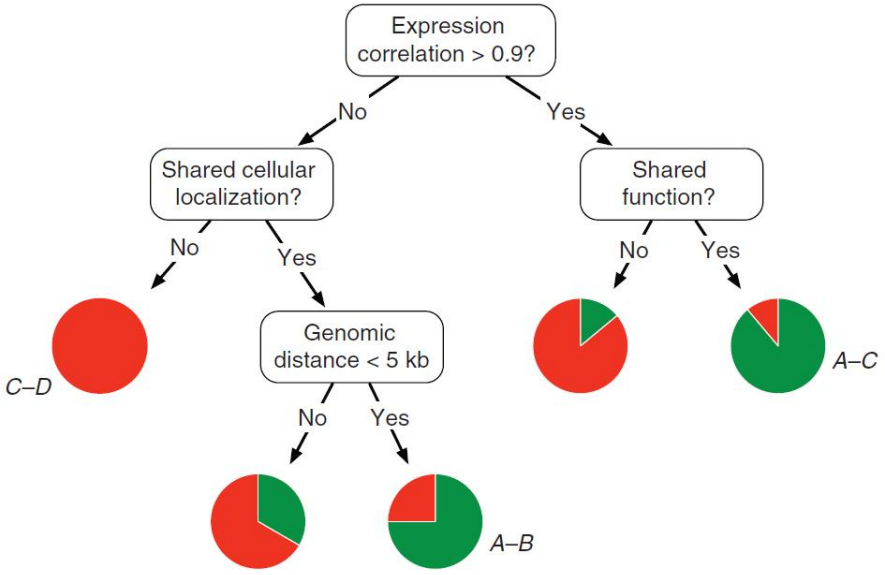


Figure 2.16 – Example of the hierarchical structure of a Decision Tree (Kingsford & Salzberg, 2008).

based on the majority class of their K nearest neighbors. Likewise, SVMs are utilized for classification by identifying the optimal hyperplane that maximizes the separation between classes. Moreover, ANN has emerged as a flexible and powerful class of models capable of identifying intricate patterns within datasets. To that end, a dedicated section on ANNs, exploring their structures, architectures, and applications in more detail, will be provided in this document.

2.2.2.4 Model Training

In ML, the training process has the primary objective of adjusting the parameters of the model to make accurate predictions on new data, *i.e.*, the learning process. Optimization algorithms are used to find parameter values that minimize the error between predicted and actual values, as measured by a loss metric. For that, optimization is one of the cornerstones of ML (Brunton & Kutz, 2022).

The training process is guided by the loss function ($\mathcal{L}$). It quantifies the difference between the prediction of the models, given by Eq. (2.8), and the actual outcomes (Wang *et al.*, 2020). For regression tasks, two commonly used loss functions are the mean squared error (MSE) and the mean absolute error (MAE), given by Eqs. (2.15) and (2.16), respectively. MSE penalizes larger errors more severely, making it sensitive to outliers, while MAE does

not square the errors, providing a more straightforward interpretation of the predictions.

$$\mathcal{L}_{\mathrm{MSE}} = \frac{1}{n}\sum_{i=1}^{n}(y_{\mathrm{i}} - \hat{y}_{\mathrm{i}})^2 \tag{2.15}$$

$$\mathcal{L}_{\mathrm{MAE}} = \frac{1}{n}\sum_{i=1}^{n}|y_{\mathrm{i}} - \hat{y}_{\mathrm{i}}| \tag{2.16}$$

Additionally, other loss functions are more appropriate for different tasks, such as cross-entropy loss for classification or Huber loss, which combines MSE and MAE.

The foundational optimization algorithm for ML is the gradient descent (Ketkar & Ketkar, 2017). It aims to find the minimum of an objective function by iteratively moving in the direction of the steepest descent, given by the negative gradient of the function. The update rule is given by:

$$\Theta \leftarrow \Theta - \alpha\nabla_{\Theta}\mathcal{L}(\Theta) \tag{2.17}$$

where the term α is called the learning rate and is a hyperparameter of the model to be adjusted.

Despite its effectiveness, several variants have been developed to address the limitations of gradient descent (Ruder, 2016). The first is based on the sample size used to calculate the gradient. Using the entire training dataset to compute gradients can yield reliable estimates, but it can be computationally expensive and slow for large datasets. To address this, techniques have been devised that use only a subset of training data. Stochastic Gradient Descent (SGD) updates the parameters using just one sample at a time (Ketkar & Ketkar, 2017). Although computationally efficient, SGD can lead to unstable learning and significant noise. Mini-Batch Gradient Descent, which uses small subsets of random data, combines the advantages of full-batch and stochastic methods (Khirirat *et al.*, 2017). This approach aims to improve both the efficiency and stability of training and is usually the choice when developing ML models.

Moreover, to improve the convergence of the gradient descent, momentum techniques have been introduced, leading to the momentum gradient descent (Qian, 1999). This technique integrates information from previous gradient updates into the current one, helping reduce gradient oscillations, accelerate convergence, and avoid or escape local minima. The momentum method accomplishes this by including a term that considers the impact of previous gradients on the current update, represented by:

$$\begin{aligned} v_{\mathrm{t}} &= \xi v_{\mathrm{t}-1} + (1-\xi)\nabla_{\Theta}\mathcal{L}(\Theta) \\ \Theta &\leftarrow \Theta - \alpha v_t \end{aligned} \tag{2.18}$$

In addition, to address the issue of varying learning rates, adaptive learning rates have been introduced (Zaheer & Shaziya, 2019). The Root Mean Square Propagation (RMSProp) optimizer normalizes the learning rate by using the moving average of squared

gradients. This method improves the stability of the learning process by adjusting the learning rate based on the magnitude of previous gradients. The RMSProp algorithm is expressed as follows:

$$\begin{aligned} s_{\mathrm{t}} &= \psi s_{\mathrm{t}-1} + (1-\psi)(\nabla_{\Theta}\mathcal{L}(\Theta))^2 \\ \Theta &\leftarrow \Theta - \frac{\alpha}{\sqrt{s_{\mathrm{t}}+\epsilon}}\nabla_{\Theta}\mathcal{L}(\Theta) \end{aligned} \tag{2.19}$$

Using both momentum and adaptive learning rates, the Adam optimization algorithm (Adaptive Momentum Estimation) has become popular in recent years (Kingma, 2014). Adam integrates the benefits of both momentum and adaptive learning rates by combining them into a single update rule. It also incorporates bias correction to counteract the initialization bias of estimates, which are initialized to zero and can thus be biased towards zero, especially during the initial training steps. The update rules for Adam, including the bias correction terms, are given by:

$$\begin{aligned} \hat{v}_{\mathrm{t}} &= \frac{v_{\mathrm{t}}}{1-\xi} \\ \hat{s}_{\mathrm{t}} &= \frac{s_{\mathrm{t}}}{1-\psi} \\ \Theta &\leftarrow \Theta - \frac{\alpha}{\sqrt{\hat{s}_t+\epsilon}}\hat{v}_t \end{aligned} \tag{2.20}$$

According to Eqs. (2.17)-(2.20), determining the learning rate is an essential task for the proper optimization of ML models. This hyperparameter controls the size of the steps taken during the minimization of the loss function process. If its value is too high, the training might achieve a suboptimal solution or even diverge. On the other hand, a value that is too low can lead to slow convergence or to a potential crash in local minima.

To address such issues, several strategies have been proposed. The adaptive learning rate described earlier is one of them. Data normalization can also accelerate and enhance the stability of the training process. In addition, a common approach is the so-called learning rate scheduler, where the learning rate decays according to predefined schemes, such as exponential or polynomial decay. This allows the model to take larger steps at the beginning of the training process, when it is far from the optimal solution, and smaller ones as it approaches convergence.

2.2.2.5 Model Optimization

Model optimization is a step aimed at enhancing the performance of the ML model being developed. It involves not only increasing its predictive accuracy but also making better generalizations on unseen data and improving computational efficiency, making it well-suited for deployment and practical use across various applications.

Among the main challenges in ML, which can be addressed with model optimization, one can highlight the trade-off between overfitting and underfitting (Jabbar & Khan, 2015).

Overfitting occurs when the model learns not only the underlying patterns in the data but also the noise present in the training set. That usually occurs when a model is too complex with respect to the amount of training data, for instance, a high-degree polynomial regression. An overfitted model performs well on the training set but poorly on the validation and test sets. On the other hand, underfitting occurs when a model is too simplistic to capture the structure of the data, often due to overly simple models or insufficient training. An underfitted model performs poorly even on the training set. An illustrative example of the underfitting, overfitting, and adequate fitting of models into a given dataset is presented in Fig. 2.17

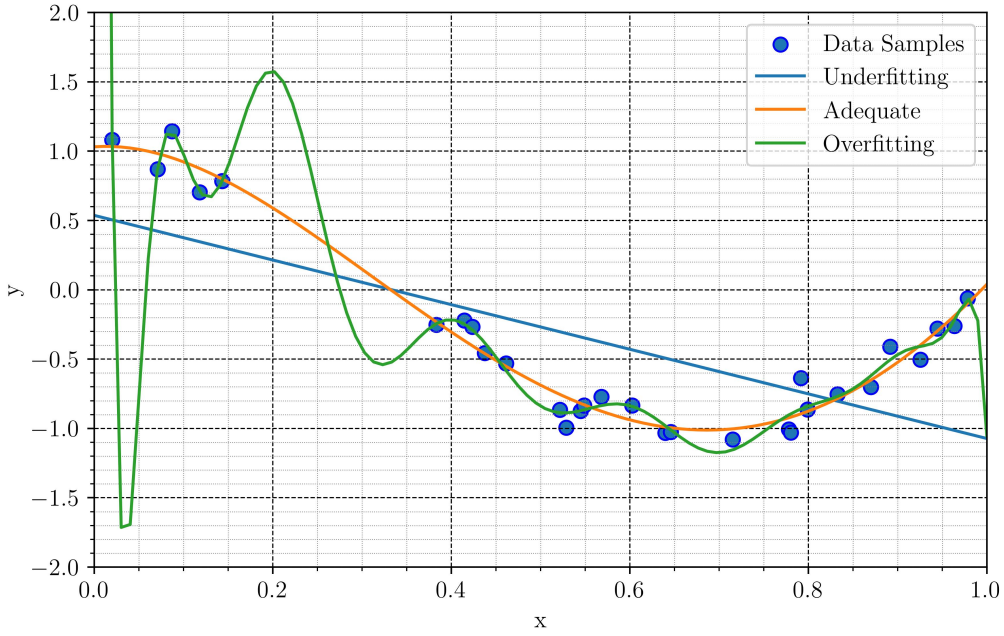


Figure 2.17 – Illustrative example of the trade-off between overfitting and underfitting.

Although underfitting can usually be addressed by increasing the complexity of the model or training time, dealing with overfitting can be more complex. For that, a whole class of techniques called regularization was developed (Jabbar & Khan, 2015). They rely on constraints or penalties that control the complexity of the model and prevent it from learning the structure of the data relative to the noise.

Some of the most widely used regularization techniques involve incorporating penalties into the loss functions, which are proportional to the magnitude of the coefficients of the model (Moore & DeNero, 2011). The Lasso regularization, or L1 regularization, introduces a penalty equal to the absolute value of the magnitude of the coefficients, which encourages sparsity and aids in feature selection. Ridge regression, or L2 regularization, applies a penalty proportional to the square of the magnitudes of the coefficients, penalizing large coefficients and making the model less sensitive to minor variations in the training data. Mathematically,

the L1 and L2 regularization can be coupled to the MSE loss by (Brunton & Kutz, 2022):

$$\mathcal{L}_{\mathrm{L1}} = \frac{1}{2n}\sum_{i=1}^{n}(y_{\mathrm{i}} - \hat{y}_{\mathrm{i}})^2 + \lambda_{\mathrm{L1}}\sum_{j=1}^{m}|\Theta_j| \tag{2.21}$$

$$\mathcal{L}_{\mathrm{L2}} = \frac{1}{2n}\sum_{i=1}^{n}(y_{\mathrm{i}} - \hat{y}_{\mathrm{i}})^2 + \frac{\lambda_{\mathrm{L2}}}{2}\sum_{j=1}^{m}\Theta_j^2 \tag{2.22}$$

Another effective method to prevent overfitting is called Early Stopping (Yao *et al.*, 2007). It involves monitoring the performance of the model on the validation set during training and stopping training when performance no longer improves or starts to degrade. By stopping the training process, this technique prevents the model from learning noise and overfitting the training data. Early stopping is implemented by setting a patience parameter, which determines how many epochs to wait after the last improvement before stopping.

A popular method for minimizing overfitting is cross-validation, a technique that evaluates the performance of the model by partitioning the data into subsets (Berrar *et al.*, 2019). This procedure involves training the model on a subset of the data while validating it on a different segment. By systematically splitting the data into training and validation sets, cross-validation enables the identification of models that perform robustly on unseen data, reducing the risk of overfitting to the noise in the training dataset. One of the most popular cross-validation techniques is k-fold cross-validation (Zhang & Liu, 2023), where the training data is divided into k subsets, and the model is trained and validated k times, with each iteration using a distinct subset as the validation set.

Regarding the overall performance of the model, hyperparameter optimization is a popular approach for improving ML model development (Feurer & Hutter, 2019; Yang & Shami, 2020). It involves selecting the hyperparameters that will perform best according to a given metric on the validation set. In this context, hyperparameters are configuration parameters that control the structure of the model and the training process, such as learning rates, regularization parameters, and the number of layers in a neural network. The difference between parameters and hyperparameters is that the former are learned with the data, while the latter are set before the training process begins. Hyperparameter optimization can considerably improve the predictive power, computational speed, and general performance of the model.

Several methods have been proposed for hyperparameter optimization of ML models (Liashchynskyi & Liashchynskyi, 2019). One of the most basic and famous searches is called grid search (Alibrahim & Ludwig, 2021). It relies on specifying a grid of values for the different hyperparameters and actively evaluating the performance of the model on each of them. Although comprehensive, grid search can be computationally intensive and time-prohibitive, particularly when handling a substantial number of hyperparameters or a wide range of their values. To overcome this, the Random Search technique evaluates the performance

of the model on a randomly sampled subset of the full hyperparameter grid (Bergstra & Bengio, 2012). This approach can be more efficient than grid search as it does not require an exhaustive evaluation and can often find adequate hyperparameter combinations with fewer evaluations.

More sophisticated techniques have been developed over the years to avoid exhaustive search for the best hyperparameter configuration. Among them, a popular one is the Hyperband algorithm (Li *et al.*, 2018). It is a technique for effectively allocating computational resources during hyperparameter tuning by combining random search with adaptive resource allocation. In its initial stages, the algorithm allocates a fixed amount of computational resources, such as training epochs, to a large number of random hyperparameter sets. As training progresses, it evaluates performance for each configuration and discards the poorly performing ones, focusing computational resources on the most promising configurations. The efficiency of the algorithm comes from its ability to balance exploration (trying a wide range of hyperparameter values) with exploitation (focusing on the best-performing configurations). By adjusting resource allocation and using early stopping, hyperband reduces the computational cost compared to exhaustive search methods and provides a practical solution for hyperparameter optimization in complex models.

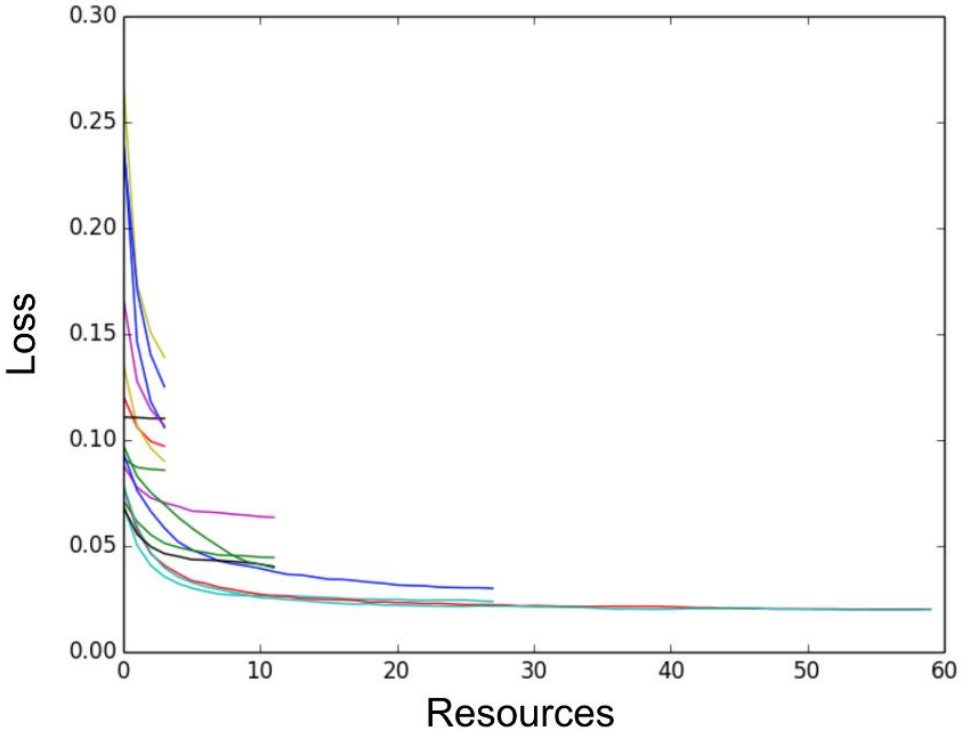


Figure 2.18 – Validation error as a function of the allocated resources for different configurations according to the Hyperband algorithm (Li *et al.*, 2018).

Other advanced techniques include Bayesian optimization (Wu *et al.*, 2019), which uses probabilistic models to assess the performance of various sets of hyperparameters and iteratively chooses the most promising ones based on previous evaluations; gradient-based

optimizations (Franceschi *et al.*, 2017), which can speed up convergence but usually require computing gradients with respect to hyperparameters, a task that can be both complex and computationally heavy, and evolutionary algorithms (Vincent & Jidesh, 2023), which evolve a population of hyperparameter configurations by selecting and recombining the most successful ones.

2.2.2.6 Model Evaluation

The performance of the prediction of the ML model must be assessed against actual outcomes to evaluate its ability to generalize. Among the main performance metrics in regression techniques, previously defined MSE and MAE are popular choices. In addition, a popular metric used in regression tasks is the Coefficient of Determination (R^2). It provides a measure of how well the model explains the variability in the target variable. It determines the proportion of variance captured by the model, and comparing models within the same dataset provides a standardized measure of fit (Nagelkerke *et al.*, 1991). The metric can be calculated as follows:

$$R^2 = 1 - \frac{\sum_{i=1}^{n}(y_\mathrm{i} - \hat{y}_\mathrm{i})^2}{\sum_{i=1}^{n}(y_\mathrm{i} - \bar{y})^2} \tag{2.23}$$

To evaluate the performance of classification models and to compare them with alternative solutions reported in the literature, four commonly adopted metrics are employed: accuracy, precision, recall, and the F1 score ($F1$). Accuracy provides a global measure of the proportion of correctly classified instances, while precision indicates the fraction of correctly identified positive cases among all predicted positive cases. Recall measures the ability of the model to correctly identify actual positive cases, which is particularly important in anomaly detection tasks where missing an anomaly can be costly. Finally, the F1 score combines precision and recall into a single metric, providing a balanced evaluation when class distributions are uneven. These metrics are computed as:

$$\mathrm{Accuracy} = \frac{TP + TN}{TP + FP + TN + FN} \tag{2.24}$$

$$\mathrm{Precision} = \frac{TP}{TP + FP} \tag{2.25}$$

$$\mathrm{Recall} = \frac{TP}{TP + FN} \tag{2.26}$$

$$F1 = 2\frac{\mathrm{Precision} \cdot \mathrm{Recall}}{\mathrm{Precision} + \mathrm{Recall}} \tag{2.27}$$

where TP is the number of true positives, TN is the number of true negatives, FP is the number of false positives, and FN is the number of false negatives (Elmrabit *et al.*, 2020).

2.2.2.7 Model Deployment and Applications

Because of their predictive accuracy and computational efficiency, ML models can be deployed to support a variety of tasks, extending their utility in engineering and scientific analyses. A key advantage of these models is their ability to drastically reduce simulation time, enabling the exploration of large-scale studies that would otherwise be computationally prohibitive. For instance, surrogate models can be integrated into optimization frameworks, replacing high-fidelity simulations and encouraging the efficient exploration of extensive design spaces. Similarly, they can be used to support sensitivity and uncertainty analyses, enabling the quantification of parameter influence on system behavior and the assessment of robustness under varying operating conditions. Another important application lies in anomaly detection, where trained models can identify deviations from expected patterns in system operation. This capability is particularly valuable in safety-critical environments, where early recognition of irregularities can prevent failures and mitigate risks. These examples demonstrate that machine learning models are not limited to accurate predictions but also serve as enablers for higher-level analyses that support optimization, resilience assessment, and system monitoring. Their versatility in deployment makes them powerful tools for engineering design and operation. This topic will be further discussed in this chapter, in a dedicated section focusing on applications in engineering systems.

2.2.3 Deep Learning

Deep learning, a specialized subset of ML, uses ANNs to capture intricate features and perform tasks that conventional models often struggle with. The following section will clarify the core principles, ANN architectures, applications, and intricacies of DL algorithms.

2.2.3.1 Artificial Neural Network

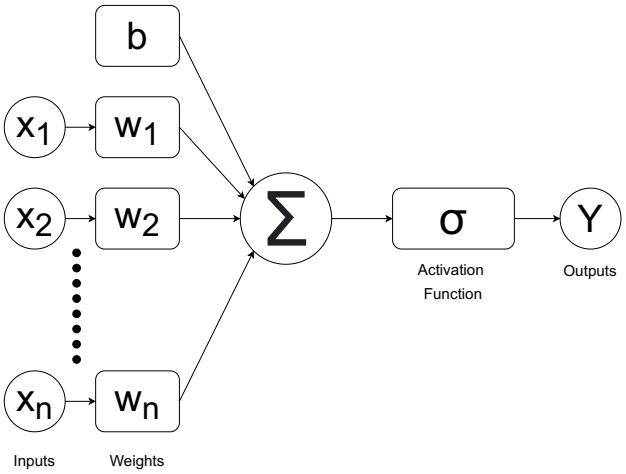
ANNs emulate the functionality of neurons in the brain by establishing statistical correlations between input and output variables. Figure 2.19 (a) presents a schematic diagram of a perceptron, or neuron, the fundamental unit of an ANN. The perceptron processes a finite set of n inputs, x_{i}, which are subsequently multiplied by their respective weights, w_{i}. The products of each input and its associated weight are then summed and combined with the bias term, b. This resultant value serves as the input to the activation function, Ω, which produces the perceptron output, Y:

$$Y = \Omega(b + \Sigma_{i=1}^{n} w_{\mathrm{i}} x_{\mathrm{i}}) \tag{2.28}$$

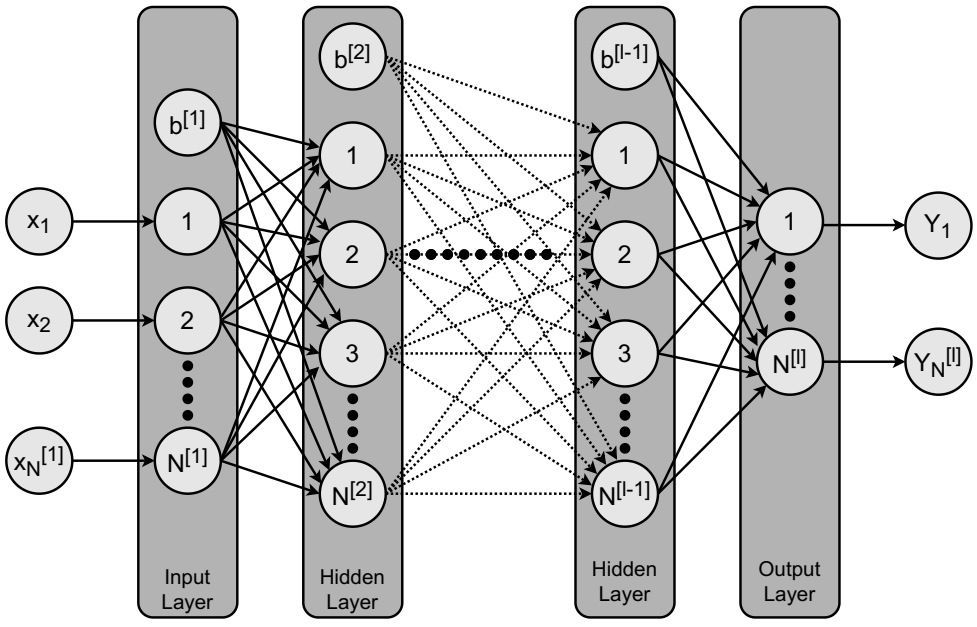
In a multilayer perceptron (MLP), a finite ensemble of perceptrons is interconnected as processing elements organized into layers. Each layer comprises a collection of perceptrons,

with each perceptron having associated biases, inputs, weights, and outputs. Deep Neural Networks (DNNs) are a subset of ANNs characterized by having more than two layers. Consequently, the l-layer DNN depicted in Fig. 2.19 (b) includes $(l-2)$ intermediate (hidden) layers positioned between the input and output layers. This DNN consists of $N^{[1]}$ input variables and $N^{[l]}$ output variables. Given that the input layer serves as the initial interface for the DNN, a general formulation for the outputs of each layer, $\mathbf{Y}^{[l]}$, is articulated by (Schweidtmann & Mitsos, 2019):

$$\begin{aligned} \mathbf{Y}^{[1]} &= \Omega_1\left(\mathbf{Z}^{[1]}\right) \\ \mathbf{Y}^{[l]} &= \Omega_l\left(\mathbf{W}^{[l-1]}\mathbf{Y}^{[l-1]} + \mathbf{b}^{[l-1]}\right) \end{aligned} \tag{2.29}$$



(a)



(b)

Figure 2.19 – Schematic diagram of (a) a perceptron and (b) a DNN.

2.2.3.2 The Backpropagation Algorithm

The learning process involves modifying the parameters of the ANN, namely its weights **W**, and biases **b**, to reduce the deviation between the ANN outputs and the actual values. Backpropagation combined with an optimization scheme, such as those given by Eqs. (2.17) - (2.20), is the learning strategy adopted in ANNs (Johansson *et al.*, 2011).

The backpropagation algorithm computes the gradient of the loss function with respect to each parameter in the network, using the chain rule. For a given layer l, the loss gradient with respect to the weights $\mathbf{W}^{[l]}$ and the biases $\mathbf{b}^{[l]}$ is calculated as follows (Rojas & Rojas, 1996):

$$\begin{aligned} \frac{\partial \mathcal{L}}{\partial \mathbf{W}^{[l]}} &= \delta^{[l+1]} \cdot (\mathbf{Y}^{[l]})^{\top} \\ \frac{\partial \mathcal{L}}{\partial \mathbf{b}^{[l]}} &= \delta^{[l+1]} \end{aligned} \tag{2.30}$$

where $\delta^{[l+1]}$ represents the error term propagated back from layer $l+1$, and $\mathbf{Y}^{[l]}$ is the output of layer l. The error term $\delta^{[l+1]}$ is updated using:

$$\delta^{[l+1]} = (\mathbf{W}^{[l+1]})^{\top} \delta^{[l+2]} \odot \Omega'(\mathbf{Z}^{[l+1]}) \tag{2.31}$$

where $\Omega'(\mathbf{Z}^{[l+1]})$ denotes the derivative of the activation function applied to the pre-activation values $\mathbf{Z}^{[l+1]}$, and $\odot$ represents the elementwise multiplication.

This process is repeated recursively for each layer, ensuring that gradients are calculated for the entire network and allowing weight and bias updates that minimize overall loss according to the updating rules given by Eqs. (2.17) - (2.20).

2.2.3.3 Activation Functions

Activation functions are critical in ANNs as they introduce non-linearity into the model, enabling the network to learn and approximate complex functions (Rasamoelina *et al.*, 2020). In the absence of activation functions, an ANN would function simply as a linear model, regardless of the number of layers, thus significantly limiting its capacity to identify intricate patterns in data.

Additionally, activation functions are integral to the backpropagation process, in which the network updates its weights based on the error. The derivative of the activation function is utilized to compute the gradients for each neuron, according to Eq. (2.31). Although any function can, in theory, serve as an activation function, only a select few are commonly employed due to their effectiveness and computational efficiency (Apicella *et al.*, 2021; Dubey *et al.*, 2022). An adequate activation function ensures that gradients do not vanish or explode and has an easily computable derivative, reducing computational time during training. Some of the most widely used activation functions include:

- Sigmoid (Sig): Maps the input values to a range between 0 and 1, according to:

$$\text{Sig}(x) = \frac{1}{1 + e^{-x}} \tag{2.32}$$

Its derivative is:

$$\text{Sig}'(x) = \text{Sig}(x) \cdot (1 - \text{Sig}(x)) \tag{2.33}$$

- Hyperbolic Tangent (Tanh): Maps the input values to a range between -1 and 1, according to:

$$\text{Tanh}(x) = \frac{e^{x} - e^{-x}}{e^{x} + e^{-x}} \tag{2.34}$$

Its derivative is:

$$\text{Tanh}'(x) = 1 - \text{Tanh}^2(x) \tag{2.35}$$

- Rectified Linear Unit (ReLU): Outputs the input directly if it is positive; otherwise, it outputs zero:

$$\text{ReLU}(x) = \max(0, x) \tag{2.36}$$

Its derivative is:

$$\text{ReLU}'(x) = \begin{cases} 1 & \text{if } x > 0 \\ 0 & \text{if } x \leq 0 \end{cases} \tag{2.37}$$

- Leaky ReLU: Allows a small, nonzero gradient when the input is negative:

$$\text{Leaky ReLU}(x) = \begin{cases} x & \text{if } x > 0 \\ \zeta x & \text{if } x \leq 0 \end{cases} \tag{2.38}$$

Its derivative is:

$$\text{Leaky ReLU}'(x) = \begin{cases} 1 & \text{if } x > 0 \\ \zeta & \text{if } x \leq 0 \end{cases} \tag{2.39}$$

where ζ is a small positive constant.

- Exponential Linear Unit (ELU): Introduces non-linearity and smooths the output for negative inputs:

$$\text{ELU}(x) = \begin{cases} x & \text{if } x > 0 \\ \zeta(e^{x} - 1) & \text{if } x \leq 0 \end{cases} \tag{2.40}$$

Its derivative is:

$$\text{ELU}'(x) = \begin{cases} 1 & \text{if } x > 0 \\ \text{ELU}(x) + \zeta & \text{if } x \leq 0 \end{cases} \tag{2.41}$$

where ζ is a positive constant.

- SELU: The Scaled Exponential Linear Unit introduces self-normalizing properties and is defined as:

$$\text{SELU}(x) = \lambda \begin{cases} x & \text{if } x > 0 \\ \alpha(e^x - 1) & \text{if } x \leq 0 \end{cases} \tag{2.42}$$

  Its derivative is:

$$\text{SELU}'(x) = \lambda \begin{cases} 1 & \text{if } x > 0 \\ \alpha e^x & \text{if } x \leq 0 \end{cases} \tag{2.43}$$

  where λ and α are positive constants.

- Swish: The Swish function introduces smooth non-linearity and is defined as:

$$\text{Swish}(x) = x \cdot \text{Sig}(x) \tag{2.44}$$

  Its derivative is:

$$\text{Swish}'(x) = \text{Swish}(x) + \text{Sig}(x) \cdot (1 - \text{Swish}(x)) \tag{2.45}$$

- GELU: The Gaussian Error Linear Unit introduces smooth, probabilistic non-linearity and is defined as:

$$\text{GELU}(x) = x \cdot \Phi(x) \tag{2.46}$$

  where $\Phi(x)$ is the cumulative distribution function of a standard normal distribution. Its derivative is:

$$\text{GELU}'(x) = \Phi(x) + x \cdot \Phi(x) \tag{2.47}$$

  where $\phi(x)$ is the standard normal probability density function.

The selection of activation functions profoundly influences the dynamics of training, the convergence rate, and the performance of the network. The appropriate selection of these functions can substantially enhance the generalization of the ANN capabilities on novel data, making them a pivotal component in the design and optimization of neural network architectures.

2.2.3.4 Artificial Neural Network Architectures

DL and ANN have become the cornerstone of modern AI algorithms, especially given their ability to capture complex patterns in data, their flexibility in tackling different challenges, and their capacity to harness the power of modern hardware, especially GPUs. ANNs can handle a wide range of tasks, including prediction, classification, clustering, dimensionality reduction, and anomaly detection, and are used in applications such as image processing, large language models, and time series classification. Depending on the nature of the data and the task at hand, different neural network architectures are more suitable.

The MLP is one of the most basic ANN architectures. It consists of a fully connected network (Popescu *et al.*, 2009). Each layer is composed of a finite number of neurons, according to Fig. 2.19 (b), and is connected to the previous and subsequent layers. The first layer, which receives the input vector, is known as the input layer. The final layer that produces the output predictions is known as the output layer. The layers between the input and output layers are known as hidden layers. In the MLP, information flows only in one direction: from the input to the hidden layers and then to the output layers, making it a feedforward network. MLPs are versatile ANNs and can be applied to a wide range of applications (Popescu *et al.*, 2009). Despite that, their fully connected structure makes them less efficient at handling high-dimensional data, such as images or sequences. For that, more specialized architectures have been developed (Mühlenbein, 1990).

To enable ANNs to deal with unsupervised learning tasks, the Autoencoder architecture was developed (Bank *et al.*, 2023). It excels particularly at dimensionality reduction, data compression, and feature extraction. It works by learning an efficient, compressed representation of the input data in a lower-dimensional latent space and later reconstructing it in the original input space from the compressed representation. It consists of two main components: the encoder and the decoder. A schematic representation of an autoencoder is presented in Fig. 2.20. The encoder corresponds to the first layers of the autoencoder network, which are typically fully connected. It maps the high-dimensional input space to a lower-dimensional representation, often called the latent space. The latent space is a compressed representation of the input data that captures the key features needed to reconstruct the original data. The decoder reconstructs the original input data from the latent space to minimize the difference between the input vector and the reconstructed space. Among many applications, autoencoders are usually applied for dimensionality reduction, anomaly detection, and data denoising.

In addition, to address the efficiency challenges posed by grid-structured data, such as images, on the MLP architecture, convolutional neural networks (CNNs) were developed (Li *et al.*, 2021). The primary operation of a CNN is the convolutional filter (or kernel). This involves a matrix operation that slides the input space, computing the dot products between the filter and the local regions of the input. Usually, numerous filters are employed in parallel in the CNN layers to capture distinct features. This operation enables CNNs to capture spatial hierarchies through local connections. Furthermore, the kernel weights are shared across the entire input, significantly decreasing the number of parameters estimated by a CNN, and enhancing computational efficiency (Wu, 2017). CNNs typically employ convolutional layers as the initial layers of the ANN. The output of the CNN layers is generally connected to pooling layers, which aggregate the mean or maximum value over a subgrid of the data to represent it, thereby reducing the dimensionality of the feature subspace.

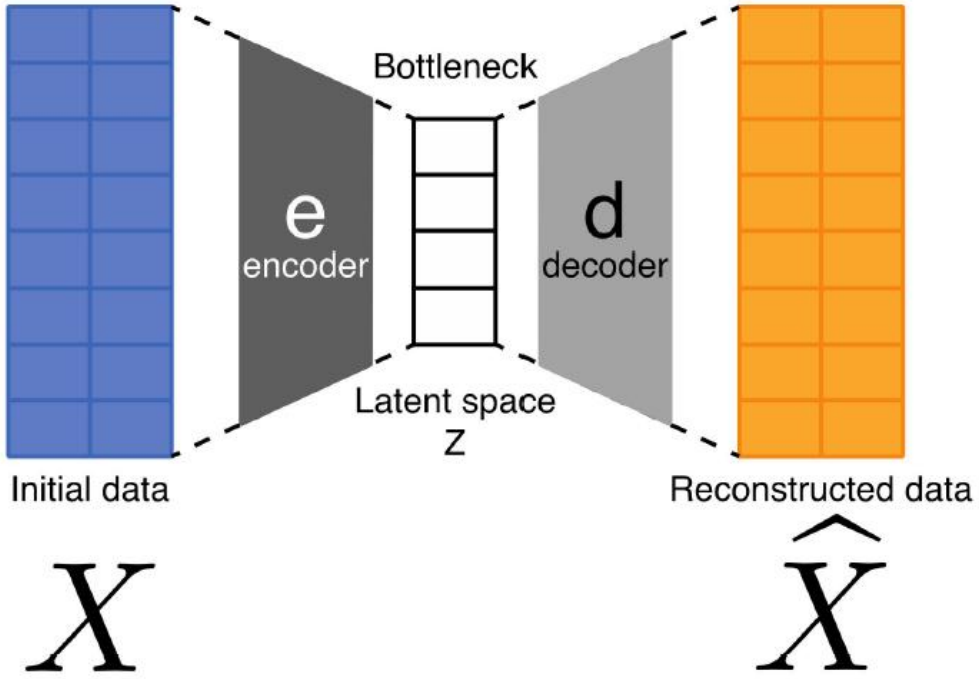


Figure 2.20 – Schematic representation of an Autoencoder (Pratella *et al.*, 2021).

Convolutional and pooling layers can be coupled multiple times, and the resulting feature maps are generally flattened and followed by fully connected layers to produce a prediction. CNNs are particularly well-suited for image-based tasks such as image classification, object detection, and segmentation (Krizhevsky *et al.*, 2012; Chauhan *et al.*, 2018).

Similarly, given the limitations of MLP in handling sequential data, recurrent neural networks (RNNs) were developed (Medsker *et al.*, 2001). A primary characteristic of these networks is their ability to retain information from previous inputs. They can handle variable-length sequences by applying the same set of weights to each time step. However, vanilla RNNs are highly susceptible to the vanishing gradient problem, as the propagation of gradients through a large number of sequence steps causes the gradient to decrease exponentially (Medsker *et al.*, 2001). To address this issue, advanced gradient architectures such as the Gated Recurrent Unit (Chung *et al.*, 2014) and the Long Short-Term Memory (Graves & Graves, 2012) were developed. These networks introduced a gating mechanism that allowed the network to retain or forget information over extended sequence intervals selectively. RNNs and their variants have been extensively used in applications that involve sequential data, including language translation (Auli *et al.*, 2013), speech recognition (Miao *et al.*, 2015), and time series forecasting (Hewamalage *et al.*, 2021). However, the introduction of the Transformer architecture (Vaswani, 2017) has significantly revolutionized deep learning, particularly in Natural Language Processing.

The Transformer architecture is characterized by its encoder-decoder structure. In contrast to traditional RNNs, transformers do not rely on sequential processing, thereby enhancing efficiency and suitability for parallelization. The principal innovation of the

Transformer lies in its self-attention mechanism, which allows the model to attend to multiple segments of the input sequence concurrently (Vaswani, 2017). This capability enables effective capture of long-range dependencies, surpassing those of RNNs and LSTMs. The self-attention mechanism allows the model to evaluate the significance of different parts of the input sequence for each token. To capture a variety of dependencies, multiple attention mechanisms (or "heads") function in parallel. The outputs of these heads are concatenated and then transformed to produce the final output of the attention layer. Transformers have emerged as the preeminent architecture for numerous tasks, especially in natural language processing. Transformer-based models such as BERT (Devlin, 2018), GPT (Brown *et al.*, 2020), and Llama (Touvron *et al.*, 2023) have achieved state-of-the-art results across applications, including machine translation, text generation, question answering, and sentiment analysis.

2.2.3.5 Advanced Techniques and Enhancements in Artificial Neural Networks

To harness the full potential of ANNs and mitigate the challenges encountered during both training and deployment, it is fundamental to investigate advanced methodologies and enhancements. Such approaches not only improve model performance but also make ANNs more robust, efficient, and versatile across various applications. This section delves into several advanced topics that build upon the core concepts of neural networks.

As with any ML model, ANNs are also prone to overfitting. For that, several methodologies can be applied, including L1 and L2 regularization and early stopping, as discussed earlier in this chapter. In addition, a popular and efficient regularization technique for ANNs is called dropout (Srivastava *et al.*, 2014). It works by randomly deactivating a subset of neurons with a specified probability at each training iteration. That technique prevents the ANN from relying too heavily on a single neuron, promotes a more even distribution among all neurons, and forces the ANN to learn more redundant operators. Dropout is usually applied only during training and is turned off during inference.

Another effective method previously discussed that addresses overfitting while simultaneously enhancing training efficiency in ANNs is batch normalization (Ioffe & Szegedy, 2015a). In the context of ANNs, batch normalization normalizes the inputs to each layer rather than only the dataset input. By preserving a more stable distribution of activation, batch normalization allows the use of higher learning rates, accelerates convergence, and can also function as a form of regularization by introducing a minor degree of noise into the network during training (Bjorck *et al.*, 2018). Unlike dropout, batch normalization is applied during both training and inference, making it a versatile tool for improving ANN performance.

As previously presented, the training process of ANNs can also be improved with the use of learning rate schedulers (Li & Arora, 2019). The learning rate is a crucial hyperpa-

rameter that determines the step size in the optimization process, directly influencing the convergence speed and model performance. Static learning rates may lead to suboptimal training: large values can cause divergence, while minimal values can slow convergence. Learning rate schedulers dynamically adjust the learning rate during training, typically by decreasing it as the optimization progresses. This adaptive behavior allows for rapid exploration of the parameter space in the early stages while enabling fine-tuning convergence in the later stages.

In addition to regularization methods and normalization techniques, weight initialization plays a vital role in practical ANN training (Kumar, 2017). Appropriate initialization ensures that gradients during backpropagation are neither excessively small nor excessively large, thereby influencing the convergence speed and overall performance of the network. Inadequate initialization can lead to vanishing or exploding gradients, hindering effective learning. Popular initialization strategies include Xavier initialization (Glorot & Bengio, 2010), given by Eq. (2.48). It allows the model to begin training from a stable state, enabling more effective learning and avoiding the issues associated with suboptimal initial conditions.

$$\Theta \sim \mathcal{U}\left(-\frac{\sqrt{6}}{\sqrt{n_{\text{in}}+n_{\text{out}}}}, \frac{\sqrt{6}}{\sqrt{n_{\text{in}}+n_{\text{out}}}}\right) \tag{2.48}$$

$\mathcal{U}(a,b)$ represents a uniform distribution between a and b, and n_{in} and n_{out} are the number of input and output units, respectively.

Another widely used initialization strategy is LeCun initialization (LeCun *et al.*, 2002), specifically designed to maintain activation variance across layers when using activation functions such as SELU. It samples weights from a distribution with variance inversely proportional to the number of input units:

$$\Theta \sim \mathcal{U}\left(-\frac{\sqrt{3}}{\sqrt{n_{\text{in}}}}, \frac{\sqrt{3}}{\sqrt{n_{\text{in}}}}\right) \tag{2.49}$$

This initialization ensures that the signal variance is preserved as it propagates through the network, helping to prevent vanishing or exploding gradients.

Furthermore, quantization is an interesting technique for addressing challenges in the deployment of ANNs (Jacob *et al.*, 2017). By employing quantization, the precision of weights and activation is lowered, typically converting 32-bit floating-point values to 8-bit integers. This reduction substantially reduces computational and memory requirements, facilitating much faster inference while maintaining satisfactory accuracy.

Another emerging and powerful approach in the realm of ANNs, especially for engineering applications, is the incorporation of physical knowledge into ANNs to enhance their performance and mitigate their shortcomings. Among many works, one can highlight the groundbreaking Physics-Informed Neural Networks (PINNs) proposed by Raissi *et al.* (2019), which have been used for different applications (Karniadakis *et al.*, 2021; Gokhale *et al.*, 2022).

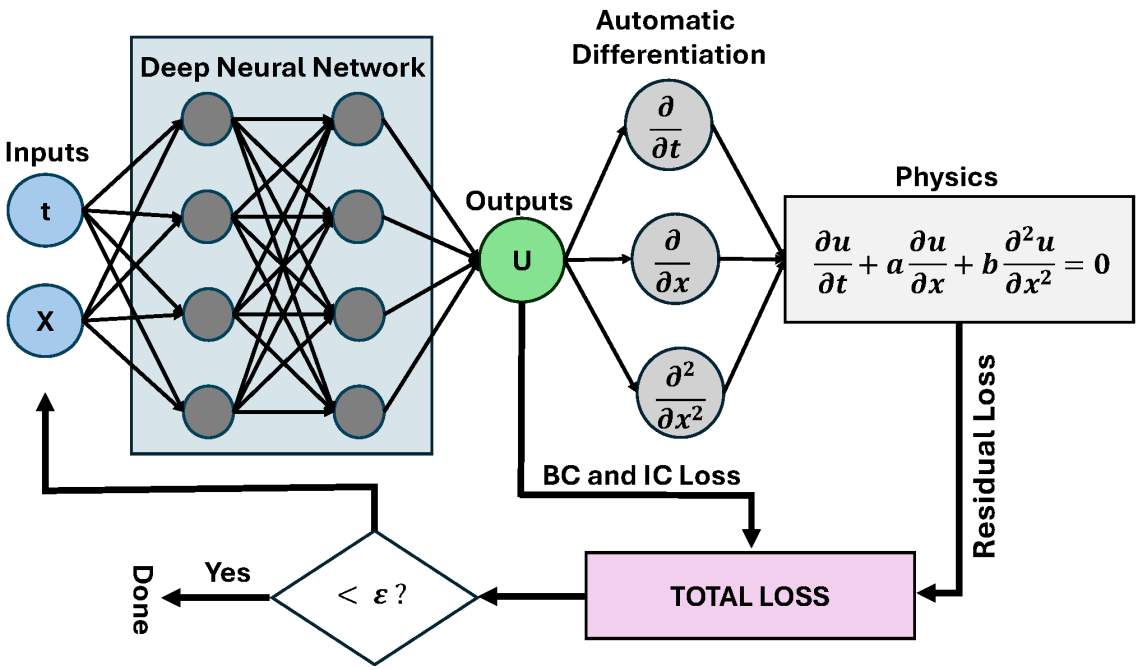


Figure 2.21 – Schematic Representation of PINN (Trahan *et al.*, 2024).

Unlike traditional ANNs that rely solely on data for training, PINNs incorporate physical laws, expressed as partial differential equations or other constraints, directly into the training process. By embedding these physical principles into the loss function, PINNs can efficiently learn and predict solutions to complex scientific and engineering problems. This integration of domain knowledge allows PINNs to achieve more accurate and generalizable results, even with limited data. Furthermore, they can offer significant computational savings compared to traditional numerical methods for solving physical systems. A schematic representation of PINN is presented in Fig. 2.21 (Trahan *et al.*, 2024).

Incorporating prior knowledge into the network structure not only improves accuracy but also ensures physically consistent predictions, adding an extra layer of reliability to the model output. Following their work, several authors have proposed different methodologies to incorporate physical knowledge to improve neural network performance. Among them is the application of physical knowledge to create latent spaces (Chandra *et al.*, 2025) or to perform feature engineering of input parameters. This last technique has been used for goals such as improving model performance (Montanez-Barrera *et al.*, 2022) and reducing dimensionality (Ngo *et al.*, 2024; Chandra *et al.*, 2024).

2.2.4 Applications of Artificial Intelligence in Engineering Systems

AI technologies are driving transformative change across sectors such as medicine, finance, retail, and engineering. Their integration into engineering has become increasingly significant, fundamentally altering how complex systems are designed, analyzed, and optimized. The application of AI methodologies in engineering has led to important advances in multiple domains (Patel *et al.*, 2021; Fischer *et al.*, 2020), including thermal engineering (Yang,

2007; Olabi *et al.*, 2023; Devasenan & Madhavan, 2024). As interest in AI continues to grow, it is essential to evaluate both the benefits and limitations of these technologies rigorously. This evaluation is crucial to accurately identify scenarios and applications in which AI can effectively address engineering challenges, rather than being applied indiscriminately. To ensure effective use of AI, several key considerations must be addressed.

First, data are fundamental for the development of AI models, both in terms of quantity and quality (Liang *et al.*, 2022; Zha *et al.*, 2023; Kumar *et al.*, 2024). With the widespread use of sensors and the Internet of Things (IoT), data availability has been increasing significantly. When real-world data are not available, data from well-validated numerical simulations can be used to train AI models. However, it is essential to acknowledge that numerical models have inherent errors, and whenever possible, experimental data should be preferred for training. When properly trained, AI models can generate highly accurate predictions within their established validity range. However, extrapolating beyond this range can be risky and yield unreliable results (Yousefzadeh & Cao, 2022). Therefore, it is preferable to use AI models within the parameter range for which they were trained. Staying within this range helps ensure the predictions of the model remain accurate and reliable. If predictions outside the training range are necessary, it is crucial to validate the performance of the model using additional data or testing to assess its reliability under new conditions.

Lastly, predictions of AI models can be extremely fast compared to traditional numerical simulations, as they do not require iterative processes or the solving of differential equations. This speed is particularly advantageous for applications that involve making many predictions or require results within a short timeframe. As a result, AI models are well-suited for scenarios where rapid decision-making or real-time analysis is essential. Hence, engineering applications that fall within one of those demands can be suitable for AI tools.

2.2.4.1 Modeling of Systems, Components, and Phenomena

Engineering activities require dealing with complex, multidisciplinary, and intricate systems, components, and phenomena, and their modeling is a fundamental step. It involves creating mathematical representations of interactions and behaviors that often involve high-dimensional, nonlinear, and interdependent correlations. Traditional methods, such as physics-based models, frequently struggle to capture the full complexity of the process.

For that, AI has emerged as a powerful tool to overcome these challenges (Brunton & Kutz, 2022). The potential of AI models has been demonstrated in the inference of thermophysical properties (Maiorino *et al.*, 2021; Jamei & Said, 2022), prediction of empirical correlations such as friction factors (Plascencia *et al.*, 2020; Montanez-Barrera *et al.*, 2022) and the Nusselt number (Kang & Kwon, 2022), and components, such as AMRs (Aprea *et al.*, 2017) and turbines (Chatterjee & Dethlefs, 2021).

In system modeling, steady-state modeling focuses on representing systems in a state in which the interactions and behaviors of components are analyzed under constant conditions. Transient modeling, on the other hand, involves studying systems that change over time, accounting for the temporal evolution of the state and interactions of the system, which requires modeling equations that describe how system variables evolve. Transient models are essential for understanding how systems respond to varying inputs or conditions over time. However, the complexity of these models can increase significantly due to the need to solve differential equations and simulate time-dependent behaviors. AI methods can handle the intricate behavior of complex systems, providing fast predictions of steady-state performance and operation (Pérez-Gomariz *et al.*, 2023), and allowing transient predictions of system performance (Elmaz & Yücel, 2020; Asgari *et al.*, 2021).

2.2.4.2 Optimization

Optimization is the process of determining one or more solutions that achieve the minimization or maximization of one or more objectives while adhering to any constraints that may or may not be imposed on a specific problem (Branke *et al.*, 2008). A critical step in this process is defining objectives, as the optimal solution depends on the precise formulation of the goals of the problem (Arora, 2004).

The number of objective functions may classify optimization problems. Single-objective optimization (SOO) problems involve a single objective function and, in most cases, yield a unique optimal solution. Multi-objective optimization (MOO) involves the systematic, simultaneous optimization of a collection of functions with conflicting objectives (Arora, 2004), resulting in a set of alternatives with different trade-offs, known as the Pareto Front. Formally, an MOO problem **P** can be defined as (Arora, 2004):

$$\mathbf{P}_{\mathrm{MOO}} = \left\{ \begin{array}{ll} \text{Minimize} & \mathrm{F}(\mathbf{x}) = [f_1(\mathbf{x}), f_2(\mathbf{x}), \ldots, f_k(\mathbf{x})]^{\mathrm{T}} \\ \text{subject to} & g_i(\mathbf{x}) \leq 0, \text{ for: } j = 1, 2, \ldots, I \\ & h_e(\mathbf{x}) = 0, \text{ for: } l = 1, 2, \ldots, E \end{array} \right\} \tag{2.50}$$

AI has advanced the field of optimization by providing robust methodologies capable of addressing complex, high-dimensional, and nonlinear problems. AI methodologies excel at managing large, intricate search spaces, which often pose challenges for conventional optimization techniques. Furthermore, AI takes advantage of parallel and distributed computing to enhance the efficiency of the optimization process (Schryen, 2020). By performing multiple evaluations or iterations simultaneously, AI techniques can substantially reduce computation time, making them appropriate for large-scale, computationally demanding problems. AI also demonstrates high efficacy in multi-objective optimization scenarios, where multiple conflicting objectives must be balanced, often requiring millions of simulations of systems (Qu *et al.*, 2021; Liu *et al.*, 2022). Furthermore, AI enables real-time optimization,

which is critical for rapid decision-making. AI models can adapt to dynamic environments and evolving conditions, allowing real-time adjustments and optimizations (Elsheikh, 2023).

2.2.4.3 Sensitivity and Uncertainty Analysis

Sensitivity and uncertainty analysis are robust methodologies for comprehending the behavior and reliability of engineering models (Ionescu-Bujor & Cacuci, 2004; Cacuci & Ionescu-Bujor, 2004; Loucks *et al.*, 2017). Sensitivity analysis involves determining the extent to which variations in input parameters affect model output. This analysis is used to determine which parameters are most impactful on model predictions and to evaluate the consequences of altering these parameters (Taylor, 2009). This analysis helps to prioritize focus on critical parameters and directs refinement of model inputs to enhance accuracy. Sensitivity analysis is crucial for assessing the robustness of a model and for making informed decisions about allocating resources for further research or data collection.

The Sobol method represents a popular global sensitivity analysis technique that quantifies the contribution of each input parameter to the variance of the model output (Iooss & Lemaître, 2015). It relies on decomposing the output variance into components attributable to individual parameters and their interactions. Let the model be represented as:

$$y = \mathcal{F}(x_1, x_2, ..., x_{\mathrm{k}}) \tag{2.51}$$

where y is the output variable of interest and $(x_1, x_2, ..., x_{\mathrm{k}})$ are the k independent input variables, which in the present case assumes the form given by Eq. (2.8). The total variance of the model output can be decomposed into contributions from each input and their interactions:

$$V(y) = \sum_{i=1}^{k} V_{\mathrm{i}} + \sum_{i<j} V_{ij} + \sum_{i<j<l} V_{\mathrm{ijl}} + \cdots + V_{12\ldots k} \tag{2.52}$$

where, V_{i} represents the variance contribution from input x_{i} and $V_{\mathrm{i,j}}$ represents the interaction between x_{i} and x_{j}, and so on. The total effect Sobol index ($S_{\mathrm{T_i}}$) measures the total contribution of input X_{i}, including all its interactions with other variables:

$$S_{\mathrm{T_i}} = 1 - \frac{\mathrm{V}_{\sim X_i}\left[\mathbb{E}_{X_i}(Y|\sim X_i)\right]}{\mathrm{V}(Y)} \tag{2.53}$$

The Sobol offers a comprehensive understanding of how various factors influence the model, allowing for the identification of key parameters that drive output variability. However, the Sobol method requires a large number of model simulations to estimate the sensitivity indices accurately (Razavi *et al.*, 2021). This computational demand can be substantial, particularly for complex models with numerous input parameters or high-dimensional parameter spaces. Each simulation generates data points used to compute variance and interactions, making the process time-intensive and resource-intensive. To

address the high computational demands of the Sobol method, ML techniques have proven to be highly beneficial (Scholbeck *et al.*, 2024). ML can significantly reduce computational costs by creating surrogate models that approximate the behavior of the complex system with much lower computational costs (Shahane *et al.*, 2022; Pham *et al.*, 2022; Kim *et al.*, 2023). These surrogate models, trained on data from a smaller set of high-fidelity simulations, can provide rapid predictions and estimates of sensitivity indices.

In addition, uncertainty analysis quantifies the uncertainty inherent in model predictions arising from variability in input parameters, model assumptions, and other sources (Macdonald & Strachan, 2001). It offers a metric for assessing the model's confidence in its output by accounting for potential errors and variability. Uncertainty analysis enables understanding of the spectrum of possible outcomes and evaluation of the reliability of model predictions across varying scenarios. This analysis is essential for assessing potential risks and formulating decisions that remain robust under uncertainty.

Monte Carlo simulations are a commonly used method for uncertainty quantification (Zhang, 2021). The Monte Carlo method consists of drawing N independent samples from the joint input distribution:

$$\left(x_1^{(i)}, x_2^{(i)}, ..., x_k^{(i)}\right)_{i=1}^{N} \tag{2.54}$$

And evaluating the model for each sample, according to the framework given by Eq. (2.8):

$$y^{(i)} = \mathcal{F}\left(x_1^{(i)}, x_2^{(i)}, ..., x_k^{(i)}\right), \quad i = 1, 2, ..., N \tag{2.55}$$

Once the output samples ${y^{(i)}}_{i=1}^{N}$ are obtained, statistical quantities such as the mean (Λ_Y) and variance ($V(y)$) of the output can be estimated as:

$$\Lambda_Y \approx \frac{1}{N}\sum_{i=1}^{N} y^{(i)}, \quad V(Y) \approx \frac{1}{N-1}\sum_{i=1}^{N}\left(y^{(i)} - \Lambda_Y\right)^2 \tag{2.56}$$

The empirical distribution of the output can also be used to construct cumulative distribution functions (CDFs), or complementary CDFs (CCDFs), enabling the estimation of risk-related quantities such as the probability of exceeding critical thresholds. However, when the simulation time ranges from minutes to hours, this method can become impractical (Sudret *et al.*, 2017). To address this challenge, recent advances have incorporated ML-based surrogate models (Wang *et al.*, 2022). These methods combine the rapid, accurate predictions of ML techniques with Monte Carlo methods to efficiently run a sufficient number of simulations.

2.2.4.4 Anomaly Detection

Various undesirable events can occur during the operation of engineering systems, leading to financial strains and potential environmental or operational challenges. This

highlights the critical need for preventive measures to mitigate risks and enhance system reliability (Mahmood *et al.*, 2023). To address these challenges, both industry professionals and academic researchers have developed advanced forecasting techniques and models. These tools are designed to anticipate potential issues, enabling proactive measures to prevent disasters and reduce the frequency and cost of maintenance procedures (Jambol *et al.*, 2024).

Abnormal Event Management (AEM) involves detecting and handling unexpected or irregular events within a system. ML plays a pivotal role in AEM by enabling the identification of abnormal events through data pattern analysis. By applying ML algorithms to the output data from the system, it is possible to detect defects and analyze abnormal events, thus enhancing anomaly detection capabilities (Ha, 2022). In various engineering sectors, ML can significantly improve operational efficiency, safety, and risk management practices. For example, ML can be used to predict abnormal events such as equipment failures, system leaks, or safety hazards, allowing proactive maintenance and mitigation strategies (Lin *et al.*, 2022). Implementing ML-based anomaly detection systems can enhance asset monitoring, prevent costly downtime, and ensure regulatory compliance by identifying and addressing abnormal events in real time (Canizo *et al.*, 2019).

Furthermore, AEM contributes to optimizing production processes, reducing environmental risks, and improving overall operational resilience. By detecting anomalies in operational parameters such as pressure, temperature, and flow rates, ML algorithms can enable early intervention to prevent accidents and optimize resource utilization (Xue *et al.*, 2021). Additionally, ML-based AEM systems support decision-making by providing timely information on potential risks and deviations from normal operating conditions. This capability improves overall operational performance and safety standards in diverse engineering applications.

2.3 Summary and Specific Objectives

In this chapter, the phenomena and state-of-the-art components and prototypes of MR were reviewed and discussed. The fundamentals of AI, ML, and DL were detailed, emphasizing best practices and advanced techniques for developing reliable models, along with potential applications in MR and engineering systems.

Hence, given the objectives of the present work and the opportunities outlined in this chapter, the following specific objectives are proposed:

- Develop models for the components and for the Magnetic Refrigeration Unit and design the system, minimizing the cost and maximizing the performance of the system;
- Assemble and carry out a structured set of experiments on the Magnetic Refrigeration Unit, which allows the detailed characterization of the performance of the system;

- Develop an advanced thermodynamic evaluation on the performance of the Magnetic Refrigeration Unit, which focuses on determining the main contributions to the losses and irreversibilities in the system;
- Collect samples from the operation of the Magnetic Refrigeration Unit and from the most relevant Magnetic Refrigeration prototypes reported in the literature, to create datasets for the development of Artificial Intelligence models;
- Develop steady-state and transient Artificial Intelligence models for the operation of the Magnetic Refrigeration Unit and other Magnetic Refrigerators, able to predict the performance of these systems with accuracy and low computational cost;
- Implement advanced Deep Learning techniques such as hyperparameter optimization, physics embedding, and regularization, and evaluate their effect on the improvement of performance of the models;
- Explore the use of Artificial Intelligence on Magnetic Refrigeration and other areas such as renewable energies and oil and gas, focusing on applications such as sensitivity and uncertainty analysis and anomaly detection, highlighting their potential impacts, advantages, and limitations.

Chapter 3

INTEGRATED DESIGN OF THE SYSTEM

This chapter presents a description of the procedure used to design the MRU. First, the strategy employed to design the system is detailed, outlining the characteristics and requirements of the models developed. Then, the development of the AMR model is described using the pipeline for ML model development presented in Chapter 2, where different models are evaluated. Then, a detailed description of the models and techniques employed for the design of the remaining components, namely the MC, the HMS, and the HExs, as well as their integration and coupling into a complete system, is presented. Following this, the optimization procedure is explained, including the definition of objectives, decision variables, and constraints. The strategy for exploring the design space, the computational tools employed, and the convergence criteria are discussed. Finally, the optimal solution is selected, and the performance of the final system design is evaluated against the required specifications.

3.1 Design Strategy

The prototype was designed by a multidisciplinary team comprising experts in thermal, hydraulic, and magnetic systems, as well as specialists in instrumentation, controls, and materials science. A Set-Based Concurrent Engineering (SBCE) convergence strategy was adopted to design the prototype in a Lean Product Development environment (Oliveira *et al.*, 2022; Oliveira *et al.*, 2023; Oliveira *et al.*, 2025). SBCE was chosen over traditional Point-Based Engineering (PBE) because it enables development teams to explore multiple design alternatives in parallel before making final commitments (Oliveira *et al.*, 2018). Unlike PBE, where a single solution is selected early and iteratively refined, often leading to costly rework if late-stage incompatibilities emerge, SBCE allows teams to maintain flexibility throughout the development process by mapping out sets of feasible solutions and gradually narrowing down options based on new information and evolving requirements. This methodology reduces the risk of premature convergence and rework, promotes organizational learning, and supports innovation by retaining broader solution spaces for more extended periods (Oliveira *et al.*, 2018). In complex multidisciplinary projects such as this, SBCE offers improved integration between subsystems, decreases the likelihood of incompatibilities, and provides a more efficient pathway to optimized system-level performance than the linear, commitment-driven approach of PBE.

In the design process, four main subsystems were considered: (i) AMR, (ii) MC, (iii) HEx and Calorimeter, and (iv) HMS. The integration approach, as illustrated in Figure 3.1, ensured that each subsystem was developed not in isolation but with continuous cross-disciplinary collaboration and system-level considerations. Since a segregated subsystem design does not guarantee optimal performance, a system-level integrated multi-objective optimization was adopted, using low-computational-cost models for each subsystem. The results provided design guidelines for all four subsystems in *integration events*. Next, each subsystem was optimized individually, and the guidelines were updated. The design cycle was repeated until the final system configuration was achieved.

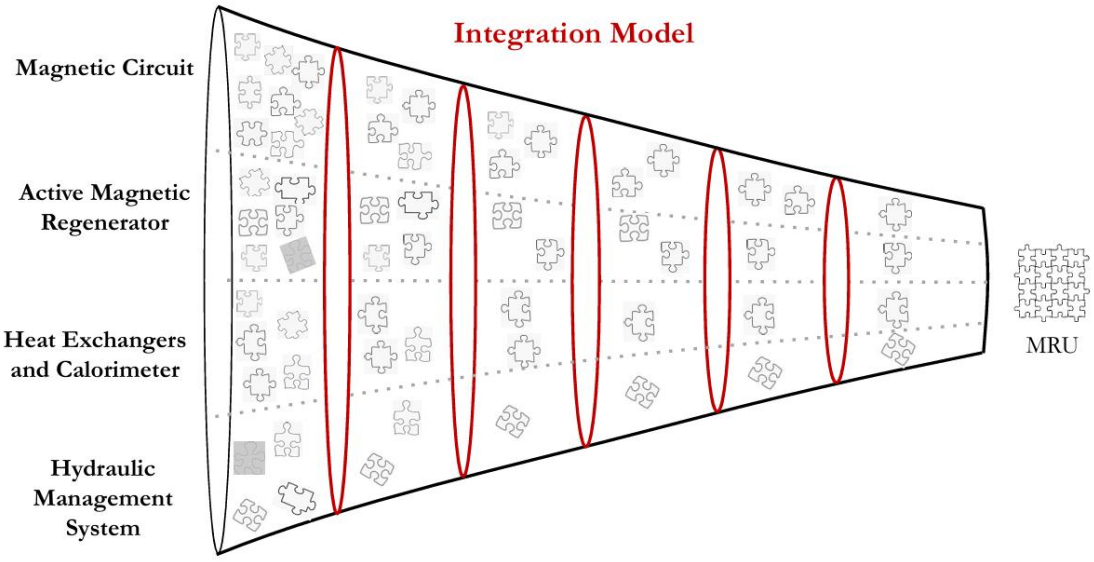


Figure 3.1 – Strategy for the integrated design of the System (Oliveira *et al.*, 2018).

Each subsystem (AMR, MC, HEx, and HMS) was addressed by dedicated teams that developed numerical models and experiments focused exclusively on their respective domains. However, despite their accuracy, such detailed models, especially those for the AMR and MC, are computationally demanding and unsuitable for rapid design-space exploration across all interacting subsystems. To overcome this challenge, an integration model was developed to couple the behaviors and performance constraints of all four subsystems. This model acts as a system-level mockup, incorporating key features and interdependencies of each domain. The integrated model then became the cornerstone of multi-objective optimization: these global optimizations defined the direction each subsystem design team should follow to achieve cohesive, optimal system performance. For example, the HMS was required to enable higher operating frequencies to reduce the size and cost of the MC.

Given the vast design space and the need to iterate rapidly, the integration model required low-computational-cost representations for each subsystem. Rapid and accurate model responses were essential for efficiently navigating the coupled optimizations. This

necessity, especially for AMR and MC, which are traditionally modeled using complex numerical solvers, highlighted the potential of AI and ML. Once trained, ML models serve as effective surrogate models, providing the required speed and sufficient accuracy for integrated system optimization. It is worth noting that surrogate modes must be sufficiently accurate to capture the Behavior of the subsystem. Still, deviations in the surrogate model results are expected due to their lower computational cost. However, they can be overcome through the design strategy. The next step is to deliver the results from the high-level models into the integration model for evaluation by the detailed models of the subsystem team.

Hence, one of the objectives of the present work is to develop fast-executing, accurate models for AMR and MC, and to couple them with existing analytical models for HEx and HMS. These were integrated into the overall system model to enable large-scale, system-level optimization, supporting a robust, iterative design approach that converges on high-performance configurations within the budget of the research project.

3.2 Development of the AMR Model

The development of a reliable and efficient AMR model is a critical step toward enabling rapid system-level optimization in MR. Given the complexity of the underlying physics, traditional numerical methods are computationally expensive and challenging to deploy within large-scale design studies. To address this limitation, the present work investigates the application of various machine learning techniques, assessing their ability to emulate AMR cooling capacity with high fidelity at a fraction of the computational cost. By systematically comparing model types and their predictive performance, this study aims to identify surrogate approaches that provide the optimal balance between simulation speed and accuracy, thereby enabling integrated system optimization to be both feasible and scalable within typical research constraints.

3.2.1 Problem Formulation

As discussed previously, one of the main challenges in MR lies in the detailed modeling of its components, particularly AMRs. This process requires solving momentum and energy conservation equations, often using computationally intensive numerical methods, along with complex thermohydraulic characterization and proper coupling of the hydraulic and magnetic fields. To address these difficulties, ML techniques were selected. Although the training of such models may require significant computational effort, once developed, they provide rapid and accurate predictions, making them attractive surrogates for high-fidelity simulations. In this context, the present study aims to perform a preliminary evaluation of the capability of different ML approaches to predict the cooling capacity of AMRs (which will be denoted in the chapter simply as $\dot{Q}_{\mathrm{C}}$), according to the framework given by Eq. (2.8),

which is expressed expressed by the following relation:

$$\dot{Q}_{\mathrm{C}} = \mathcal{F}(x) \tag{3.1}$$

where the input vector x is composed of the parameters that determine the operation of the AMR.

3.2.2 Data Collection and Preparation

A reliable database of experimental results for large-scale AMRs is not available, which limits the direct development of data-driven models from measurements. Therefore, the AMR dataset consists of 533 samples that originate from the numerical solution of the governing equations (Vieira *et al.*, 2021). The dataset was previously used to develop empirical models (Peixer, 2020). The input parameters of the simulations were the mass flow rate ($\dot{m}_{\mathrm{f}}$), operating frequency (f_{AMR}), applied magnetic field (B_{AMR}), height of the AMR bed (H_{AMR}), width of the AMR bed (W_{AMR}), and length of the AMR bed (L_{AMR}), and inlet temperatures during the hot ($T^{\mathrm{in}}_{\mathrm{HB}}$), and cold($T^{\mathrm{in}}_{\mathrm{CB}}$) blows. With that, the model being developed, according to Eq. (3.1), is given by:

$$\dot{Q}_{\mathrm{C}} = \mathcal{F}(W_{\mathrm{AMR}}, H_{\mathrm{AMR}}, L_{\mathrm{AMR}}, B_{\mathrm{AMR}}, \dot{m}_{\mathrm{f}}, f, T^{\mathrm{in}}_{\mathrm{HB}}, T^{\mathrm{in}}_{\mathrm{CB}}) \tag{3.2}$$

Due to manufacturing restrictions, the simulations were carried out with a fixed particle diameter of 650 μm, porosity of 0.465, and hydraulic porosity, φ_{hyd}, used to correct the presence of epoxy-binder, of 0.3 (Vieira *et al.*, 2021). The range of design parameters is presented in Tab. 3.1 and was determined according to the specifics of the original application. Preliminary simulations showed that the heat gain from the environment never exceeded 5 W. Given the considerable extra computational cost of calculating this parameter and its limited influence on AMR performance, this effect was neglected in the simulations (Peixer *et al.*, 2017a). In addition to that, the blow fraction, $F_{\%}$, was kept fixed at 37.5%, given its favorable hydraulic operation and maximization of the cooling capacity, and the magnetization fraction,$M_{\%}$, at 25%, and a void volume of 5800 mm^2 was considered.

Table 3.1 – Range of the design variables utilized as features for the ML models.

Parameter [unit]	**Minimum**	**Maximum**
W_{AMR} [mm]	45	70
H_{AMR} [mm]	28	55
L_{AMR} [mm]	120	160
B_{AMR} [T]	0.8	1.5
$\dot{m}_{\mathrm{f}}$ [kg h^{-1}]	350	850
f_{AMR} [Hz]	0.5	4
$T^{\mathrm{in}}_{\mathrm{CB}}$ [°C]	14	19
$T^{\mathrm{in}}_{\mathrm{HB}}$ [°C]	39	44

The dataset is assumed to contain no outliers, duplicates, missing values, or noise, so no preprocessing techniques are applied to address these issues. Additionally, the dataset lacks categorical features, making encoding processes unnecessary. The data are standardized using the z-score method. The dataset is partitioned into 64%, 16%, and 20% for the training, validation, and test sets, respectively.

3.2.3 Model Selection

To evaluate the feasibility of ML techniques for AMR simulations, four distinct ML models were examined: RF, SVR, XGBoost, and ANN. Most of the models were developed using the Scikit-Learn open source library (Pedregosa *et al.*, 2011), except for the ANN, which was constructed using the Keras (Chollet *et al.*, 2015) framework in conjunction with a TensorFlow backend (Abadi *et al.*, 2015).

3.2.4 Model Training and Optimization

The training process for the RF, SVR, and XGBoost models used gradient descent with MSE as the loss function. A 5-fold cross-validation, coupled with hyperparameter optimization via a grid search, was conducted on these models due to their comparatively lower computational costs during training. For the RF model, the hyperparameters examined included the number of estimators (25, 50, 100) and the maximum tree depth (5, 10). For the SVR model, the hyperparameters included kernel functions (linear, radial basis, or sigmoid), regularization factors (0.1, 1, 10), and error margins (0.1 and 0.2). Regarding the XGBoost model, the hyperparameters assessed were the learning rates (0.01 and 0.02), the maximum tree depths (5 and 10), and the number of estimators (50 and 100).

The ANN was trained with the Adam Optimizer, a batch size of 32 samples, and MSE as the loss function. Only hyperparameter optimization was conducted via the hyperband algorithm, as integrating cross-validation would be computationally prohibitive given the demands of training ANNs. The optimized hyperparameters included the number of layers (N_{lay}): 1 and 2; the number of neurons in each layer (N_{neu}): 10, 20, and 30; the L2-regularization factor (λ_{L2}): 10^{-4}, 10^{-7}, and 0; and the learning rate (α): 0.1, 0.01, and 0.001.

3.2.5 Model Evaluation

The results of the trained models are depicted in Tab. 3.2, by the R^2 values for the training and test sets, and by graphical representations, as depicted in Figs. 3.2, where the predicted values are presented against the actual values. For enhanced visualization, error bars representing a margin of plus and minus 10% are included in each plot, except for the plot for ANNs in Fig. 3.2 (d), where the error bars represent a margin of plus and minus 5%. The results cover both the training (which also accounts for the validation) and test sets.

Table 3.2 – Coefficient of Determination for the developed models.

Model	R^2	
	Training	**Test**
RF	0.9760	0.8465
SVR	0.6070	0.6377
XGBoost	0.9994	0.9630
ANN	0.9962	0.9950

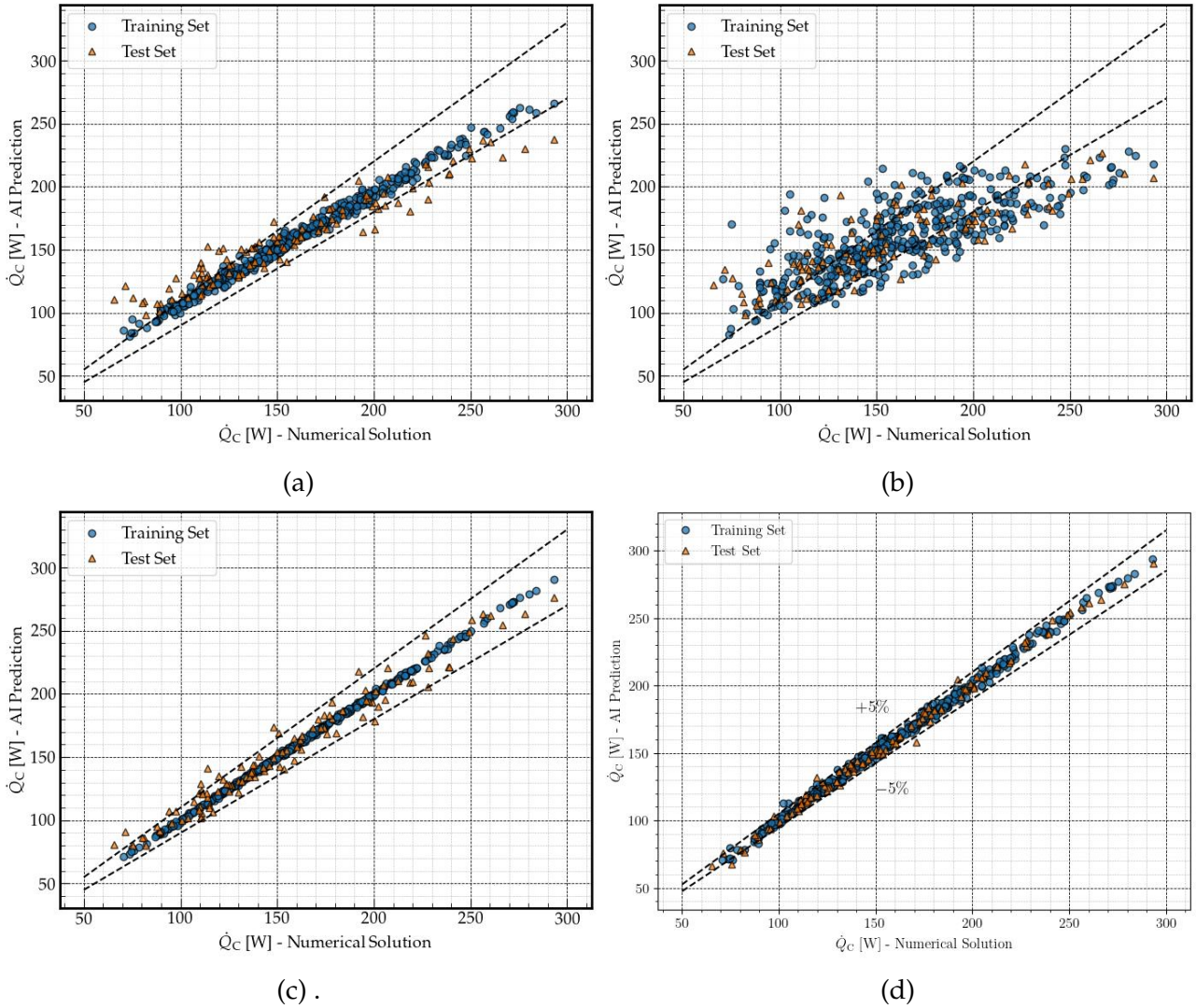


Figure 3.2 – Comparison between the numerical cooling capacity and the predicted outcomes. Results for (a) RF, (b) SVR, (c) XGBoost, and (d) ANN models.

Table 3.2 and Fig. 3.2 demonstrate the effect of model selection on the performance of ML algorithms. According to Fig. 3.2 (a), the predictions provided by the RF model are not linearly aligned with the numerical values, showing what is assumed to be an overfitting tendency, as the values of R^2 are considerably higher in the training set than those in the test set. In contrast, Figure 3.2 (b) shows that the SVR was unable to capture the complexities of the dataset, and an underfitting behavior is attributed, as given by the values of R^2. Furthermore, the results for the XGBoost model shown in Fig. 3.2 (c) demonstrate that the model achieved extreme accuracy on the training set but did not do so on the test sets. Figure 3.2 (d) shows

that the ANN was able to predict with high accuracy the performance of AMRs, with R^2 values that surpassed 0.99 in both the training and the test sets. That was expected, since the model was the most complex and required the highest computational power for training.

Based on these results, ANNs were selected as the modeling strategy for the remaining system parameters. Their superior generalization capability makes them better suited to capturing the nonlinearities and interactions inherent to the coupled components of the MRU. In addition, their flexibility in approximating complex functions ensures consistency in model representation across different subsystems, a key aspect when integrating component models into a global system-level optimization framework.

3.3 Modeling of the System

Magnetic refrigeration systems allow multiple configurations for each subsystem, each with specific advantages and limitations (Trevizoli *et al.*, 2016). Before introducing the models developed to provide fast, accurate predictions of component performance, the main design choices adopted in developing the prototype are outlined. It is worth noting that the design configurations presented here were determined after several iterations of the development cycle shown in Fig. 3.1, when the development of the system was at more advanced stages. In addition, the component description provided in this section is preliminary, simplified, and limited to the characteristics necessary for modelling. Detailed and advanced descriptions of the final versions of each are provided in Chapter 3.

3.3.1 Configurations of the Components

The MC consists of two concentric cylinders separated by an intermediate air gap. The inner cylinder (stator) is manufactured from soft ferromagnetic material in the form of laminated sheets of electrical steel, and it remains static during system operation. The outer cylinder (rotor) combines both soft and hard ferromagnetic materials and is enclosed by an external iron ring entirely composed of soft ferromagnetic material. The hard ferromagnetic component adopted in this study is a sintered Nd-Fe-B permanent magnet, grade N50M, with a minimum remanent flux density B_{rem} of 1.41 T.

Sixteen regenerator beds are distributed circumferentially and housed within a stainless steel casing located between the rotor and the stator. The regenerators are composed of $La(FeMnSi)_{13}H_z$ materials (commercialized as *Calorivac-HS*), supplied by Vacuumschmelze GmbH & Co. KG. This FOPT alloy represents a state-of-the-art solid-state refrigerant for room-temperature magnetic refrigeration. The configuration of the MC–AMR assembly was selected because it has been successfully employed in several previous prototypes (Jacobs *et al.*, 2014; Eriksen *et al.*, 2015; Lozano *et al.*, 2016; Nakashima *et al.*, 2021), and it has consistently

demonstrated the highest cooling capacities reported in the literature (Trevizoli *et al.*, 2016). A schematic representation of the AMR-MC arrangement is presented in Fig. 3.3.

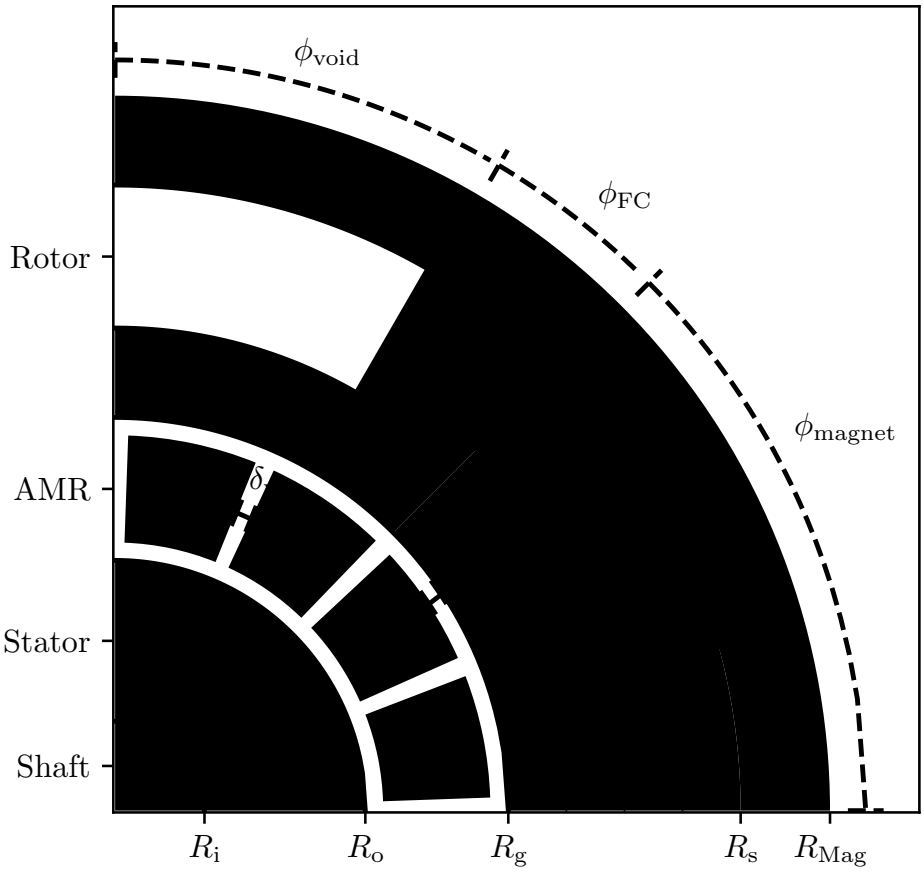


Figure 3.3 – Cross-section area (first quadrant) of the MC-AMR assembly. Black regions: soft magnetic material; white regions: air; light gray regions: hard magnetic material; Dark gray region at the bottom left: stator/shaft; gray regions: AMRs; arrows: remanence directions.

To provide efficient heat transfer between the working fluid and the hot and cold reservoirs, fan-supplied multi-circuited herringbone-wave tube-fin HExs are employed, due to their favorable thermal–hydraulic characteristics. The HMS is driven by a gear pump and assisted by solenoid valves (SVs) and check valves (CVs) for flow control. This solution was selected because of its robustness, low power consumption, and reliable performance under continuous operation (Santos *et al.*, 2021).

3.3.2 AMR Modeling

The present AMR modeling methodology focuses on evaluating the key performance metrics of the component, namely the cooling capacity, the AMR pumping power, $\dot{W}_{\text{AMR,pump}}$, the heat rejection rate, $\dot{Q}_{\text{H}}$, and the AMR magnetization power, $\dot{W}_{\text{AMR,mag}}$. To capture the nonlinear and multivariate nature of the system behavior, ANNs were employed to model the most critical parameters, *i.e.*, the cooling power, according to Eq. (3.2), and the AMR magnetization power, according to the Equation:

$$\dot{W}_{\text{AMR,mag}} = \mathcal{F}(W_{\text{AMR}}, H_{\text{AMR}}, L_{\text{AMR}}, B_{\text{AMR}}, \dot{m}_{\text{f}}, f, T_{\text{CB}}^{\text{in}}, T_{\text{CB}}^{\text{in}}) \tag{3.3}$$

Given the accuracy and simplicity of analytical expressions, the AMR pumping power can be calculated as:

$$\dot{W}_{\mathrm{AMR,pump}} = \left(\frac{\Delta P_{\mathrm{AMR}} \dot{m}_{\mathrm{f}}}{\rho_{\mathrm{f}}} \right) 2F_{\%} \tag{3.4}$$

where the pressure drop in the AMR bed, ΔP_{AMR}, is calculated by Ergun's Equation (Ergun, 1952):

$$\Delta P_{\mathrm{AMR}} = \left[150 \frac{\mu_{\mathrm{f}} (1-\varphi_{\mathrm{eff}})^2 v_{\mathrm{s}}}{d_{\mathrm{p}}^2 \varphi_{\mathrm{eff}}^3} + 1.75 \frac{\rho_f (1-\varphi_{\mathrm{eff}}) v_{\mathrm{s}}^2}{d_{\mathrm{p}} \varphi_{\mathrm{eff}}^3} \right] L_{\mathrm{AMR}} \tag{3.5}$$

where the empirically corrected (effective) porosity, $\varphi_{\mathrm{eff}} = 0.3$, was obtained from the experimental data of Vieira *et al.* (2021) for an epoxy-bonded porous structure, assuming a mean particle diameter of 650 μm.

From an energy balance in the AMR, the rate of heat rejection in the hot temperature source, $\dot{Q}_{\mathrm{H}}$, can be calculated as follows:

$$\dot{Q}_{\mathrm{H}} = \dot{Q}_{\mathrm{C}} + \dot{W}_{\mathrm{AMR,pump}} + \dot{W}_{\mathrm{AMR,mag}} \tag{3.6}$$

In addition to the energy transfer shares in the AMR, a fundamental quantity to be considered is the mass of magnetocaloric material, m_{MCM}, which is given by:

$$m_{\mathrm{MCM}} = N_{\mathrm{AMR}} (1-\varphi_{\mathrm{f}}) A_{\mathrm{cs}} L_{\mathrm{AMR}} \rho_{\mathrm{s}} \tag{3.7}$$

where A_{cs} is the cross sectional area of the AMR and ρ_{s} the density of the solid phase, *i.e.*, the MCM.

3.3.2.1 Development of the Artificial Neural Network

For the models given by Eqs. (3.2)-(3.3), the ANN architecture was optimized (Mohanraj *et al.*, 2012) by allowing a minimum of 0 hidden layers and a maximum of 2, with each layer containing 1 to 200 neurons. After each hidden layer, a batch normalization layer was added to improve performance further (Ioffe & Szegedy, 2015b). The batch size (Smith, 2018) and the activation functions (Bingham *et al.*, 2020) of each hidden layer were also optimized by evaluating ReLU, Sigmoid, and SELU functions. The Hyperband Algorithm (Li *et al.*, 2018) was used to tune the hyperparameters. The Adam optimizer (Kingma, 2014) was employed, and the ANNs were implemented using the Keras framework (Chollet *et al.*, 2015) with a TensorFlow backend (Abadi *et al.*, 2015). The data previously used in this chapter to evaluate the performance of different models in predicting AMR was used again.

The results for the cooling capacity were already presented in Fig. 3.2 and Tab. 3.2. A comparison between the numerical results and the ANN models is shown in Fig. 3.4 for the AMR magnetization power. The R^2 values for the Training and Test sets are respectively 0.9990 and 0.9991. Once again, the capability of ANNs in regression tasks can be visualized:

the system excels at capturing the intricate trade-offs in AMR operation, providing fast and accurate predictions of AMR magnetization power.

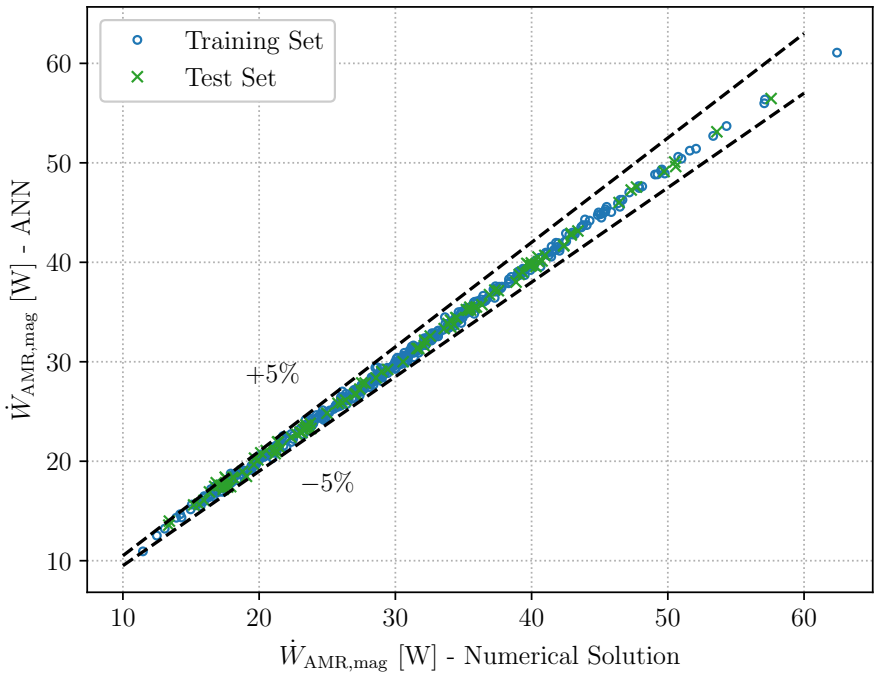


Figure 3.4 – Comparison between the numerical and the predicted outcomes of the AMR magnetization power.

The summary of the architectures of the ANNs after the hyperparameter optimization is provided in Tab. 3.3

Table 3.3 – Summary of the Architecture of the ANN

	Hidden Layer 1		Hidden Layer 2	
	Number of Neurons	Activation Function	Number of Neurons	Activation Function
$\dot{Q}_{\mathrm{C}}$	69	Sigmoid	81	SELU
$\dot{W}_{\mathrm{AMR,mag}}$	149	Sigmoid	-	-

3.3.3 Magnetic Circuit

To derive an MC model capable of reproducing a magnetic profile adequate for MR systems, it was assumed that (i) the value of the magnetic flux intensity during the low field period of the cycle,B_{low}, has a magnetic equal to 0 T, which can be achieved with soft magnetic materials that direct the magnetic field lines out of the gap in the low field regions (Eriksen *et al.*, 2015; Nakashima *et al.*, 2021), and (ii) the performance of the AMR can be predicted using a mean value in the high magnetic field region, B_{AMR}.

For a given MC geometry, it is further assumed that the magnetic flux density within the air gap, B, is radially uniform, being defined by the product of two terms: a two-dimensional, $B_{\mathrm{2D}}(\theta)$, and a tri-dimensional, $B_{\mathrm{3D}}(x_{\mathrm{MC}})$, components that account, respectively,

for the dependence on the angular position, θ, and axial distance, x_{MC}:

$$B(\theta, x_{\mathrm{MC}}) = B_{\mathrm{2D}}(\theta) B_{\mathrm{3D}}(x_{\mathrm{MC}}) \tag{3.8}$$

Furthermore, the average value of the two-dimensional magnetic flux density over the region of interest, $\overline{B}_{\mathrm{2D}}$, is defined as:

$$\overline{B}_{\mathrm{2D}} = \frac{1}{(\theta_{\mathrm{f}} - \theta_{\mathrm{i}})} \int_{\theta_{\mathrm{i}}}^{\theta_{\mathrm{f}}} B_{\mathrm{2D}}(\theta) d\theta = f(R_{\mathrm{i}}, R_{\mathrm{o}}, R_{\mathrm{g}}, R_{\mathrm{s}}, h_{\mathrm{FC}}, L_{\mathrm{MC}}, \phi_{\mathrm{magnet}}) \tag{3.9}$$

where h_{FC} = R_{Mag} - R_{s}, according to Fig. 3.3.

Due to a lack of sufficiently fast analytical tools to solve the MC design problem, an alternative strategy has been used to develop an ANN, as done for the cooling capacity and magnetization power of the AMR, to model the average value of the two-dimensional magnetic flux density over the region of interest. Hence, the general Equation is given by:

$$\overline{B}_{\mathrm{2D}} = \mathcal{F}(R_{\mathrm{i}}, R_{\mathrm{o}}, R_{\mathrm{g}}, R_{\mathrm{s}}, h_{\mathrm{FC}}, L_{\mathrm{MC}}, \phi_{\mathrm{magnet}}) \tag{3.10}$$

Considering that the tri-dimensional component functions as a scaling factor for the profile at the center of the MC, *i.e.* $x_{\mathrm{MC}} = 0$, a third-degree polynomial was used to calibrate the numerical results, for it provides good agreement between the datasets and reduces the computational time. Thus:

$$B_{\mathrm{3D}} = 1 + e_1 \left(\frac{x_{\mathrm{MC}}}{L_{\mathrm{MC}}}\right) + e_2 \left(\frac{x_{\mathrm{MC}}}{L_{\mathrm{MC}}}\right)^2 + e_3 \left(\frac{x_{\mathrm{MC}}}{L_{\mathrm{MC}}}\right)^3 \tag{3.11}$$

In addition, it is crucial to calculate the mass of both the stator and rotor. The stator is made of laminated sheets of E145 electrical steel and has a density, ρ_{st}, of 7750 kg m^{-3}. Hence, its mass, m_{st}, is given by:

$$m_{\mathrm{st}} = \pi \left(R_{\mathrm{o}}^2 - R_{\mathrm{i}}^2\right) L_{\mathrm{MC}} \rho_{\mathrm{st}} \tag{3.12}$$

The rotor is made of N50M sintered Nd-Fe-B, which has a density $\rho_{\mathrm{Nd}} = 7500$ kg/m^3, and of S235JR carbon steel, which has a density $\rho_{\mathrm{FC}} = 7850$ kg/m^3. Hence, the rotor mass, m_{rt}, is made up of a contribution due to the permanent magnet (PM) mass, m_{magnet}, and another due to the soft magnetic material, m_{FC}:

$$m_{\mathrm{rt}} = m_{\mathrm{magnet}} + m_{\mathrm{FC}} \tag{3.13}$$

After defining the MC geometry, m_{magnet} can be further reduced by decreasing the radii of the external segments while keeping the magnetic flux density constant (Cattelan *et al.*, 2024). Since generating sufficient data to develop analytical or ML relationships is computationally expensive, it was not applied to the previous equations. Nevertheless, an average 20% reduction in magnet mass is empirically estimated using a heuristic approach across different MC geometries. Therefore, the magnet mass can be calculated by:

$$m_{\mathrm{magnet}} = V_{\mathrm{magnet}} \rho_{\mathrm{Nd}} = 0.8\pi \left(R_{\mathrm{s}}^2 - R_{\mathrm{g}}^2\right) L_{\mathrm{MC}} \left(\frac{2\phi_{\mathrm{magnet}}}{\pi}\right) \rho_{\mathrm{Nd}} \tag{3.14}$$

For the soft-magnetic material portion of the rotor, the PM mass removed during the magnets optimization is replaced with carbon steel, and must be considered. Therefore, its mass can be calculated by:

$$m_{\mathrm{FC}} = \left\{ \pi \left[\left(R_{\mathrm{Mag}}^2 - R_{\mathrm{g}}^2 \right) - \left(R_{\mathrm{s}}^2 - \left(R_{\mathrm{g}} + h_{\mathrm{FC}} \right)^2 \right) \left(\frac{2\phi_{\mathrm{void}}}{\pi} \right) \right] L_{\mathrm{MC}} - V_{\mathrm{magnet}} \right\} \rho_{\mathrm{FC}} \tag{3.15}$$

3.3.3.1 Development of the Artificial Neural Network

The dataset used to fit Eq. (3.10) consisted of 3310 numerical samples (Fortkamp *et al.*, 2023), where the inner radius of the stator was fixed at 30 mm and its outer radius ranged from 100 to 180 mm. The inner radius of the rotor varied from 150 to 230 mm, and its outer radius from 300 to 450 mm. The thickness of the soft magnetic material, h_{FC}, ranged from 30 to 50 mm, the length of the magnetic circuit from 140 to 210 mm, and the angles of magnets, ϕ_{magnet}, from 0.6108 radians (35°) to 1.1345 radians (65°). Accordingly, the dataset used to calibrate Eq. (3.11) consisted of 8400 points, where the outer radius of the stator ranged from 100 to 180 mm, the inner radius of the rotor from 150 to 230 mm, the outer radius of the rotor from 300 to 450 mm, and the lenght of the MC from 140 to 190 mm, while R_{i}, h_{FC}, ϕ_{magnet} were kept fixed at 30 mm, 20 mm and 0.7854 radians (45 degrees), respectively.

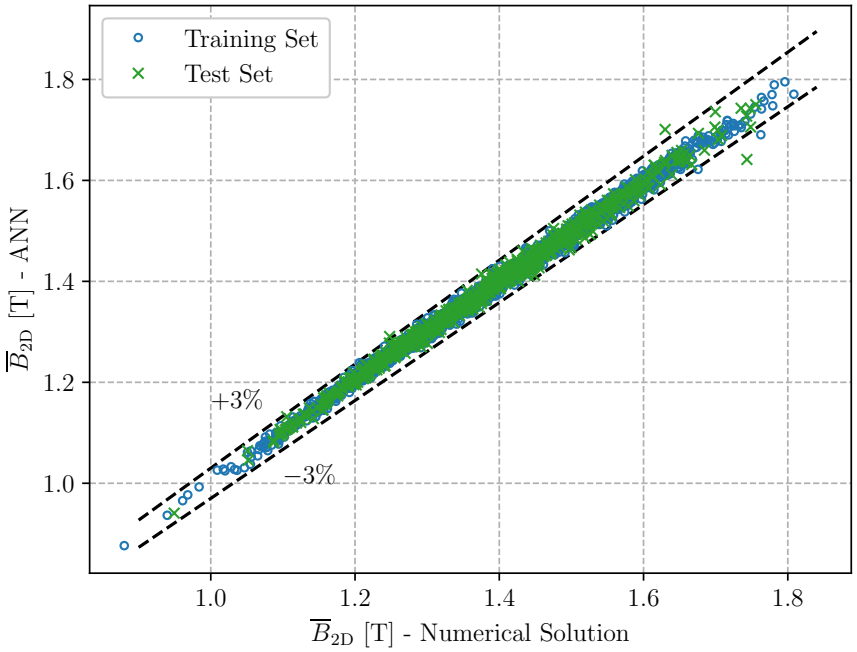
Since the dataset comprised conditions in which demagnetization of the PMs and saturation of the soft ferromagnetic materials were confined to small areas of the MC, these issues were neglected. Moreover, because the magnetic flux density profiles were calculated at an intermediate position within the air gap, minor radial variations in the magnetic field are not accounted for. As such, the magnetic profile depends on the angular position and the axial distance. From both datasets, 80% of the points were used for training and 20% for testing the correlations. For the ANN, 20% of the training set was used for validation during hyperparameter tuning.

A strategy similar to that developed for the ANNs was adopted for the MC, using the same architectures, optimizers, and hyperparameter optimization techniques. A comparison between the numerical results and the ANN model for $\overline{B}_{2\mathrm{D}}$ and $B_{3\mathrm{D}}$ is displayed in Fig. 3.5. The coefficient of determination of the training and test sets obtained with Eq. (3.10) are, respectively, 0.9947 and 0.9921, whereas the ones obtained with Eq. (3.16) are 0.9805 and 0.9802, respectively. Once again, the results demonstrate the high accuracy of the model in capturing the intricate trade-offs involved in the operation of MC.

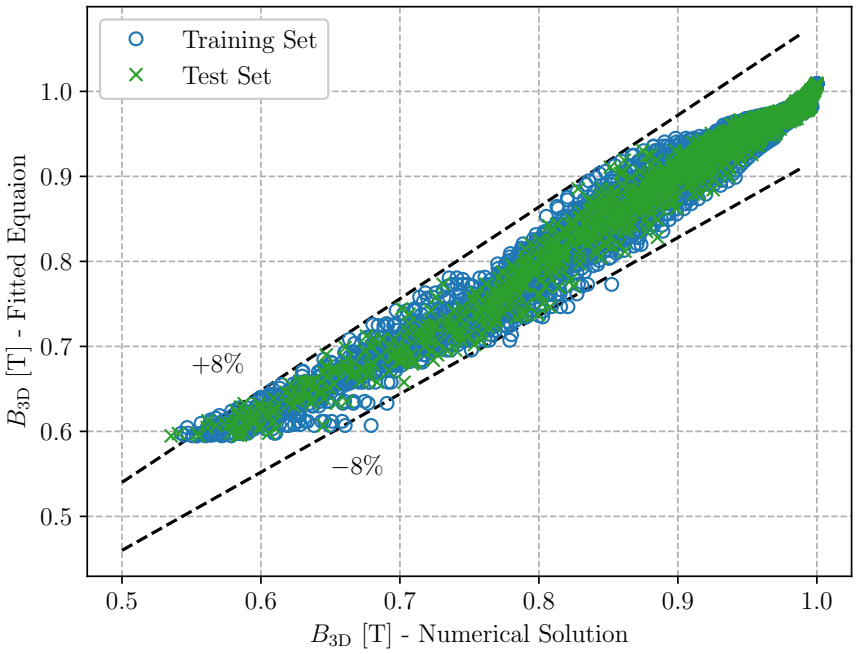
The expression proposed to calculate $B_{3\mathrm{D}}$ in the present work is given by:

$$B_{3\mathrm{D}} = 1 - 0.3761 \left(\frac{x_{\mathrm{MC}}}{L_{\mathrm{MC}}} \right) + 2.1388 \left(\frac{x_{\mathrm{MC}}}{L_{\mathrm{MC}}} \right)^2 - 6.0146 \left(\frac{x_{\mathrm{MC}}}{L_{\mathrm{MC}}} \right)^3 . \tag{3.16}$$

A summary of the resulting hyperparameters for the ANN is presented in Table 3.4.



(a)



(b)

Figure 3.5 – Training of the MC models. Results for (a) the average two-dimensional magnetic flux density and (b) three-dimensional magnetic flux density.

Table 3.4 – Summary of the Architecture of the ANN

	Hidden Layer 1		Hidden Layer 2	
	Number of Neurons	Activation Function	Number of Neurons	Activation Function
$\overline{B}_{2D}$	189	SELU	191	ReLU

3.3.4 Heat Exchangers

The multi-circuit HExs were modeled with the tube-by-tube technique (Domanski & Didion, 1983). Internally (on the liquid side), each circuit is treated as a control volume, and

the thermal-hydraulic calculations are performed independently. Externally (air-side), the coupling between the axial fan head curve and the system pressure drop curve considers the HEx as a lumped element to determine the operating point. The resulting air-side flow rate is used to compute the outer thermal resistance associated with each circuit. Correlations from the literature were used to calculate the HEx geometric, friction, and thermal-conductance parameters (Shah & Sekulic, 2003). A complete description of the HEx model is presented in Appendix B.

The liquid-side pumping power, $\dot{W}_{\mathrm{HEx,pump}}$, considers all parallel circuits as follows:

$$\dot{W}_{\mathrm{HEx,pump}} = N_{\mathrm{circ}} \left(\frac{\dot{m}_{\mathrm{circ}} \Delta P_{\mathrm{HEx,i}}}{\rho_{\mathrm{f}} \eta_{\mathrm{pump}}} \right) \tag{3.17}$$

where the liquid-side pressure drop, $\Delta P_{\mathrm{HEx,i}}$, was calculated using the Fanning friction coefficient for single-phase flow (Churchill, 1977). The pump efficiency, η_{pump}, was taken as 70% (Lozano *et al.*, 2013), even though lower values are expected given the operation condition and type of pump.

The air-side pumping power is calculated as:

$$\dot{W}_{\mathrm{HEx,fan}} = \frac{\dot{m}_{\mathrm{a}} \Delta P_{\mathrm{Hex,o}}}{\rho_{\mathrm{a}} \eta_{\mathrm{fan}}} \tag{3.18}$$

where the air-side pressure drop, $\Delta P_{\mathrm{HEx,o}}$, was calculated with the Fanning friction coefficient for herringbone wavy fins (Wang *et al.*, 2000). The fan efficiency, η_{fan}, was obtained from a curve provided by the manufacturer as a function of the flow rate, which is supplied in Appendix C.

The $\varepsilon - NTU$ method (Kays & London, 1984; ESDU, 1998) was used to compute the heat transfer rates in the CHEx and HHEx as follows:

$$\dot{Q}_{\mathrm{CHEx}} = N_{\mathrm{circ}} \dot{m}_{\mathrm{circ}} c_{\mathrm{p,l}} (\varepsilon C^*)_{\mathrm{CHEx}} \left(T^{\mathrm{in}}_{\mathrm{CHEx,a}} - T^{\mathrm{in}}_{\mathrm{CHEx,l}} \right) \tag{3.19}$$

$$\dot{Q}_{\mathrm{HHEx}} = N_{\mathrm{circ}} \dot{m}_{\mathrm{circ}} c_{\mathrm{p,l}} (\varepsilon C^*)_{\mathrm{HHEx}} \left(T^{\mathrm{in}}_{\mathrm{HHEx,a}} - T^{\mathrm{in}}_{\mathrm{HHEx,l}} \right) \tag{3.20}$$

Note that the so-called liquid-side effectiveness, $(\varepsilon C^*)_{\mathrm{HEx}}$, represents the dimensionless liquid-side temperature change in each HEx. It is equal to the product of the HEx effectiveness and the heat capacity ratio, which is defined as:

$$C^* = \frac{\dot{m}_{\mathrm{a}} c_{\mathrm{p,a}}}{N_{\mathrm{circ}} \dot{m}_{\mathrm{circ}} c_{\mathrm{p,l}}} \tag{3.21}$$

The HEx-fan assembly optimization can be time-consuming due to the large number of design variables involved ($\mathbf{x}_{\mathrm{HEx}} = [D_{\mathrm{i,HEx}}$, W_{HEx}, H_{HEx}, L_{HEx}, X_{l}, X_{t}, p_{fin}, N_{circ} and $N_{\mathrm{T}}]$) and the strong nonlinearity of the equations. Therefore, a component-level HEx analysis was performed before the system-level optimization to reduce the simulation time. Firstly, the HEx design space is reduced by including manufacturing and operating conditions as

constraints on the design variables. Next, the optimization problem given by Eq. (3.22) is solved for several target mass flow rates, $\dot{m}_{\mathrm{tgt}}$.

$$\mathbf{P}_{\mathrm{HEx}} = \left\{ \begin{array}{ll} \text{Minimize} & \mathrm{F}(\mathbf{x}_{\mathrm{HEx}}) = \left[\dot{W}_{\mathrm{HEx}}(\mathbf{x}_{\mathrm{HEx}}), -(\varepsilon C^*)_{\mathrm{HEx}}(\mathbf{x}_{\mathrm{HEx}})\right]^{\mathrm{T}} \\ \text{subjected to} & \dot{m}_{\mathrm{HEx,l}} = \dot{m}_{\mathrm{tgt}} \\ & W_{\mathrm{HEx}} \leq 550 \text{ mm} \\ & H_{\mathrm{HEx}} \leq 550 \text{ mm} \\ & N_{\mathrm{Circ}} \leq 8 \end{array} \right\} \tag{3.22}$$

The Pareto front for each liquid mass flow rate, determined by the maximum $(\varepsilon C^*)_{\mathrm{HEx}}$ and minimum overall HEx power consumption, $\dot{W}_{\mathrm{HEx}} = \dot{W}_{\mathrm{HEx,pump}} + \dot{W}_{\mathrm{HEx,fan}}$, is encountered, generating a data bank of optimal HEx. Then, the HEx optimization sub-routine in the system-level optimization is performed by selecting in the previously generated data bank the geometry that, for a given liquid mass flow rate and $(\varepsilon C^*)_{\mathrm{HEx}}$, yields the minimum HEx power consumption.

3.3.5 Hydraulic Management System

The HMS modeling is restricted to evaluating the power consumption of the fluid pump, SVs, and CVs. Again, a pump efficiency of 70% is assumed (Lozano *et al.*, 2016). An experimental study was developed to evaluate five commercially available SV alternatives (Santos *et al.*, 2021). The best results were obtained with the ASCO SC8210-112 model.

The following expression gives the total valve power consumption:

$$\dot{W}_{\mathrm{val}} = N_{\mathrm{SV}} F_{\%} \left(\dot{W}_{\mathrm{nom}} + \frac{\dot{V}_{\mathrm{SV}}^3}{\eta_{\mathrm{pump}} K_{\mathrm{v,SV}}^2} \right) + N_{\mathrm{CV}} F_{\%} \left(\frac{\dot{V}_{\mathrm{CV}}^3}{\eta_{\mathrm{pump}} K_{\mathrm{v,CV}}^2} \right) \tag{3.23}$$

where N_{SV} and N_{CV} are the total number of SVs and CVs. The first term in the first parenthesis is the power required to actuate one SV (Fortkamp *et al.*, 2020a), where $\dot{W}_{\mathrm{nom}}$ is the nominal power consumption of the selected SV, i.e., 6 W. The second term in the first parenthesis is the power required to pump fluid through an SV calculated in terms of the valve flow coefficient for water, $K_{\mathrm{v,SV}}$, defined as the ratio of the valve volumetric flow rate and the square root of the valve pressure drop (Santos *et al.*, 2021). The term in the second parenthesis is the CV pumping power calculated in the same way. Note that the values of the flow coefficient for the SV and CV are equal to 2.8 and 3, respectively (Santos *et al.*, 2021). The values of the volumetric flow rate for the SV are twice those of one AMR bed, while the ones for the CV correspond to one AMR bed.

3.3.6 Integrating the Components

In the previous section, the development of low-computational-cost standalone models for each component was presented. The next step towards a system-level integrated

optimization is the coupling of those models into a higher-level hierarchical system model, where the interaction between components is accounted for and performance metrics are determined to characterize the system.

3.3.6.1 Active Magnetic Regenerator and Magnetic Circuit

The interaction between the magnetic flux density generated by the MC and the magnetocaloric material in the AMRs positioned in the gap, as presented in Fig. 3.3, establishes an important system design trade-off (Fortkamp *et al.*, 2020a). The AMR cross-sectional area, A_{cs}, is given by:

$$A_{\mathrm{cs}} = \frac{\pi}{N_{\mathrm{AMR}}}\left[\left(R_{\mathrm{g}} - \delta_{\mathrm{h}}\right)^2 - \left(R_{\mathrm{o}} + \delta_{\mathrm{h}}\right)^2\right] - 3\delta_{\mathrm{w}}\left(R_{\mathrm{g}} - R_{\mathrm{o}} - 2\delta_{\mathrm{h}}\right) \tag{3.24}$$

where δ_{h} is the radial gap between AMRs and δ_{w} is the azimuthal gap between the AMR and the MC (see Fig. 3.3). In the present analysis, δ_{h} and δ_{w} are fixed at 2.5 mm and 2 mm, respectively. For a specified value of A_{cs}, the height of the AMR, H_{AMR} is given by:

$$H_{\mathrm{AMR}} = \left(R_{\mathrm{g}} - \delta_{\mathrm{h}}\right) - \left(R_{\mathrm{o}} + \delta_{\mathrm{h}}\right) \tag{3.25}$$

Even though the AMR beds are shaped as circular sectors, for simplicity, they are assumed to be rectangular for cross-sectional area calculations. Therefore, the mean width, W_{AMR}, of the AMR beds is defined as:

$$W_{\mathrm{AMR}} = \frac{A_{\mathrm{cs}}}{H_{\mathrm{AMR}}} \tag{3.26}$$

To minimize the influence of MC edge effects, its length, L_{MC}, is made larger than the length of the AMR, L_{AMR}. Therefore, the additional length factor of the MC to the AMR, L_{xt}, is defined as:

$$L_{\mathrm{xt}} = \frac{L_{\mathrm{AMR}}}{L_{\mathrm{MC}}} \tag{3.27}$$

The magnetic flux density in the AMR region, B_{AMR}, which depends on both the magnetic profile provided by the MC and the geometry of the AMR, is calculated as:

$$B_{\mathrm{AMR}} = \frac{2}{L_{\mathrm{AMR}}}\int_0^{L_{\mathrm{AMR}}/2} B(\theta, x_{\mathrm{MC}})dx_{\mathrm{MC}} = \overline{B}_{\mathrm{2D}}\left[1 + e_1\frac{L_{\mathrm{xt}}}{4} + e_2\frac{L_{\mathrm{xt}}^2}{12} + e_3\frac{L_{\mathrm{xt}}^3}{32}\right] \tag{3.28}$$

3.3.6.2 Active Magnetic Regenerator and Heat Exchangers

The AMR-HEx integration is implemented via mass and energy continuity relationships at the inlet and outlet of each component. As a result, the HEx inlet fluid flow rate is calculated as:

$$\dot{m}_{\mathrm{HEx,l}} = \dot{m}_{\mathrm{f}} N_{\mathrm{B}} \tag{3.29}$$

where N_{B} is the number of AMRs operating simultaneously during one blow.

At the hot and cold ends of the AMR, the energy continuity is such that the system cooling capacity, $\dot{Q}_{\mathrm{C,sys}}$, and heat rejection rate $\dot{Q}_{\mathrm{H,sys}}$, are given by:

$$\dot{Q}_{\mathrm{C,sys}} = \dot{Q}_{\mathrm{CHEx}} = N_{\mathrm{AMR}}\dot{Q}_{\mathrm{C}} = \dot{m}_{\mathrm{CHEx,l}}c_{\mathrm{p,l}}(\varepsilon C^{*})_{\mathrm{CHEx}}(\mathrm{T_C} - T^{\mathrm{in}}_{\mathrm{CHEx,l}}) \tag{3.30}$$

and

$$\dot{Q}_{\mathrm{H,sys}} = \dot{Q}_{\mathrm{HHEx}} = N_{\mathrm{AMR}}\dot{Q}_{\mathrm{H}} = \dot{m}_{\mathrm{HHEx,l}}c_{\mathrm{p,l}}(\varepsilon C^{*})_{\mathrm{HHEx}}(T^{\mathrm{in}}_{\mathrm{HHEx,l}} - \mathrm{T_H}) \tag{3.31}$$

3.3.7 System Performance Metrics

In addition to the heat transfer rates, $\dot{Q}_{\mathrm{C,sys}}$ and $\dot{Q}_{\mathrm{H,sys}}$, the total power consumption of the system, $\dot{W}_{\mathrm{sys}}$, is calculated as follows:

$$\dot{W}_{\mathrm{sys}} = N_{\mathrm{AMR}}\left(\dot{W}_{\mathrm{AMR,mag}} + \frac{\dot{W}_{\mathrm{AMR,pump}}}{\eta_{\mathrm{pump}}}\right) + \dot{W}_{\mathrm{val}} + \dot{W}_{\mathrm{CHEx,pump}} + \\ + \dot{W}_{\mathrm{HHEx,pump}} + \dot{W}_{\mathrm{CHEx,fan}} + \dot{W}_{\mathrm{HHEx,fan}} \tag{3.32}$$

The coefficient of performance, COP, and second-law efficiency, η_{2nd}, of the *system* are defined by:

$$COP_{\mathrm{sys}} = \frac{\dot{Q}_{\mathrm{C,sys}}}{\dot{W}_{\mathrm{sys}}} \tag{3.33}$$

$$\eta_{\mathrm{2nd,sys}} = COP_{\mathrm{sys}}\left(\frac{T_{\mathrm{H}} - T_{\mathrm{C}}}{T_{\mathrm{C}}}\right) = COP_{\mathrm{sys}}\left(\frac{\Delta T_{\mathrm{sys}}}{T_{\mathrm{C}}}\right) \tag{3.34}$$

Conversely, the AMR coefficient of performance and AMR second-law efficiency, COP_{AMR} and $\eta_{\mathrm{2nd,AMR}}$, are given by:

$$COP_{\mathrm{AMR}} = \frac{\dot{Q}_{\mathrm{C,sys}}}{N_{\mathrm{AMR}}(\dot{W}_{\mathrm{AMR,mag}} + \dot{W}_{\mathrm{AMR,pump}})} \tag{3.35}$$

$$\eta_{\mathrm{2nd,AMR}} = COP_{\mathrm{AMR}}\left(\frac{T^{\mathrm{in}}_{\mathrm{CB}} - T^{\mathrm{in}}_{\mathrm{CB}}}{T^{\mathrm{in}}_{\mathrm{CB}}}\right) \tag{3.36}$$

The total mass of the system, m_{sys}, is computed as:

$$m_{\mathrm{sys}} = m_{\mathrm{MCM}} + m_{\mathrm{st}} + m_{\mathrm{magnet}} + m_{\mathrm{FC}} \tag{3.37}$$

The masses of the SV, CV, CHEx, and HHEx were omitted because they have a negligible influence on the overall mass of the system.

Even though the mass and volume of the system are valuable indicators for operational and logistics (i.e., transport and installation) requirements, they represent another factor more relevant to the present analysis: the cost of the system and its components, especially the MCM and PMs. Therefore, to evaluate the economic aspects of the design, a

cost-weighted mass, $m^{\$}_{\text{sys}}$, is proposed based on an estimate of the cost associated with the mass of each component, C$\$_{\text{i}}$:

$$\begin{aligned} m^{\$}_{\text{sys}} =& \frac{\text{C}\$_{\text{MCM}} N_{\text{AMR}} m_{\text{MCM}} + \text{C}\$_{\text{magnet}} m_{\text{magnet}} + \text{C}\$_{\text{FC}} m_{\text{FC}} + \text{C}\$_{\text{st}} m_{\text{st}}}{\text{C}\$_{\text{MCM}} + \text{C}\$_{\text{magnet}} + \text{C}\$_{\text{FC}} + \text{C}\$_{\text{st}}} \\ =& m^{\$}_{\text{MCM}} + m^{\$}_{\text{magnet}} + m^{\$}_{\text{FC}} + m^{\$}_{\text{st}} \end{aligned} \tag{3.38}$$

where $m^{\$}_{\text{MCM}}$, $m^{\$}_{\text{magnet}}$, $m^{\$}_{\text{FC}}$, $m^{\$}_{\text{st}}$, are the cost weighted masses of the MCM, PM, FC and stator, respectively, and C$\$_{\text{MCM}}$, C$\$_{\text{magnet}}$, C$\$_{\text{FC}}$ and C$\$_{\text{st}}$ are normalized costs of the MCM, PM, FC and stator, respectively, estimated as 60, 35, 5 and 3 based on raw material prices and quotations provided by suppliers.

3.4 System-level Integrated Optimization

Given the development of individual models for the components of the system, integration of their couplings and interactions, and the determination of system-level performance metrics, a system-level integrated optimization can be carried out. The goal of the prototype being developed in the current study is to operate between indoor and outdoor ambient temperatures of 22°C and 35°C, respectively, generating a system cooling capacity, $\dot{Q}_{\text{C,sys}}$, of 9000 Btu/h (2638 W). In the actual calculations, the ambient temperatures were not modified, but the system cooling capacity was set to 2950 W, providing a safety margin to account for deviations inherent to the numerical models and to consider the heat dissipated by the CHEx fan. Hence, as the system cooling capacity and temperature span are fixed constraints rather than objective functions, the optimization algorithm seeks to minimize the power consumption and cost of the system, i.e., parameters directly related to operational and capital expenditures, respectively. Therefore, the design variables of the MR optimization are given by:

$$\begin{aligned} \mathbf{x}_{\text{sys}} = [&\dot{m}_{\text{f}}, f, N_{\text{AMR}}, F_{\%}, M_{\%}, \mathbf{T}_{\text{Curie}}, d_{\text{p}}, L_{\text{AMR}}, H_{\text{AMR}}, W_{\text{AMR}}, B_{\text{AMR}}, \\ &T^{\text{in}}_{\text{CB}}, T^{\text{in}}_{\text{CB}}, L_{\text{xt}}, h_{\text{FC}}, \phi_{\text{magnet}}, \phi_{\text{FC}}, H_{\text{CHEx}}, W_{\text{CHEx}}, L_{\text{CHEx}}, D_{\text{CHEx}}, \\ &N_{\text{f,CHEx}}, H_{\text{HHEx}}, W_{\text{HHEx}}, L_{\text{HHEx}}, D_{\text{HHEx}}, N_{\text{f,HHEx}}]^{\text{T}} \end{aligned} \tag{3.39}$$

where $\mathbf{T}_{\text{Curie}}$ is a vector specifying the Curie temperature of each AMR layer.

Important design constraints were applied, taking into account manufacturing limitations, component coupling, and supplier feedback. The MCM particles have a fixed diameter of 650 μm, the porosity is fixed at 0.465, and the effective porosity is set at 0.3. The number of layers of the AMR, N_{layer}, is fixed at 15. In addition, the arrangement of Curie temperatures varies linearly along the AMR bed from 2°C below the inlet temperature of the cold blow up to 2°C below the inlet temperature during the hot blow, as there has been evidence that such a profile improves the system cooling capacity (Vieira *et al.*, 2021; Lei *et al.*, 2015; Vieira *et al.*,

2023). The AMR comprises sixteen packed beds, and the fluid flow fraction is fixed at 37.5% (Nakashima *et al.*, 2018).

Due to manufacturing limitations of the MC, the maximum lengths of the magnetic circuit and its radius were set at 190 mm and 465 mm, respectively. Additionally, the inner radius of the stator was fixed at 30 mm. To avoid magnetic saturation, the minimum value of the thickness of the flux concentrator tube was set at 30 mm, and a constant value of 15° was assigned to ϕ_{FC}. Also, to prevent degradation of the magnetic profile, the value of ϕ_{magnet} was constrained between 0.6108 radians (35°) and 0.7854 radians (60°). Lastly, based on experience on the design of MC for MR, the magnetization fraction was fixed at 25% (Fortkamp *et al.*, 2018). As for the HEx, the maximum width and height were set at 550 mm.

The updated system optimization problem, i.e., fixed constraints and objective function, can be stated according to Eq. (2.50) as:

$$\mathbf{P}_{\mathrm{sys}} = \left\{ \begin{array}{ll} \text{Minimize} & \mathrm{F}(\mathbf{x}_{\mathrm{sys}}) = \left[\dot{W}_{\mathrm{sys}}(\mathbf{x}_{\mathrm{sys}}), m^{\$}_{\mathrm{sys}}(\mathbf{x}_{\mathrm{sys}})\right]^{\mathrm{T}} \\ \text{subjected to} & \dot{Q}_{\mathrm{C,sys}} = 2950 \text{ W} \\ & T_{\mathrm{C}} = 22°\mathrm{C} \\ & T_{\mathrm{H}} = 35°\mathrm{C} \\ & N_{\mathrm{AMR}} = 16 \\ & N_{\mathrm{layer}} = 15 \\ & F_{\%} = 37.5\% \\ & d_{\mathrm{p}} = 650\ \mu\mathrm{m} \\ & \varphi_{\mathrm{f}} = 0.465 \\ & \varphi_{\mathrm{eff}} = 0.3 \\ & \phi_{\mathrm{FC}} = 15\ ^{\circ} \\ & R_{\mathrm{c}} \leq 465 \text{ mm} \\ & R_{\mathrm{i}} = 30 \text{ mm} \end{array} \right\} \tag{3.40}$$

where the ranges of the design variables are presented in Table 3.5. Notice that such ranges were determined from previous experience in the assembly, operation, performance assessment, and component manufacturing for MRs. Also, the subscript HEx is valid for both the CHEx and HHEx.

3.4.1 Solution of the Optimization Problem

The Pareto front was obtained using the NSGA-II evolutionary algorithm (Deb *et al.*, 2002). The solution method relies on biologically inspired operators such as mutation, crossover, and selection to determine the optimal solution. During the optimization process, millions of possible systems can be evaluated thanks to the low computational cost of the complete system routine. The optimization flowchart, including the system and subsystem modules, is presented in Fig. 3.6.

Table 3.5 – Design variables and their ranges in the system optimization problem.

Design Variable					
Parameter	Minimum	Maximum	Parameter	Minimum	Maximum
$\dot{m}_{\mathrm{f}}$	350 kg/h	900 kg/h	f	0.5 Hz	4.5 Hz
L_{AMR}	120 mm	160 mm	H_{AMR}	28 mm	50 mm
W_{AMR}	45 mm	60 mm	$B_{\mathrm{AMR,eff}}$	0.8 T	1.25 T
$T_{\mathrm{HB}}^{\mathrm{in}}$	39 °C	44 °C	$T_{\mathrm{CB}}^{\mathrm{in}}$	14 °C	19 °C
h_{FC}	30 mm	50 mm	ϕ_{magnet}	35 °	60 °
L_{MC}	L_{AMR}	190 mm	W_{HEx}	350 mm	550 mm
L_{HEx}	132 mm	267 mm	H_{HEx}	350 mm	550 mm
$D_{\mathrm{i,HEx}}$	11.7 mm	14.1 mm	$N_{\mathrm{f,HEx}}$	4	9

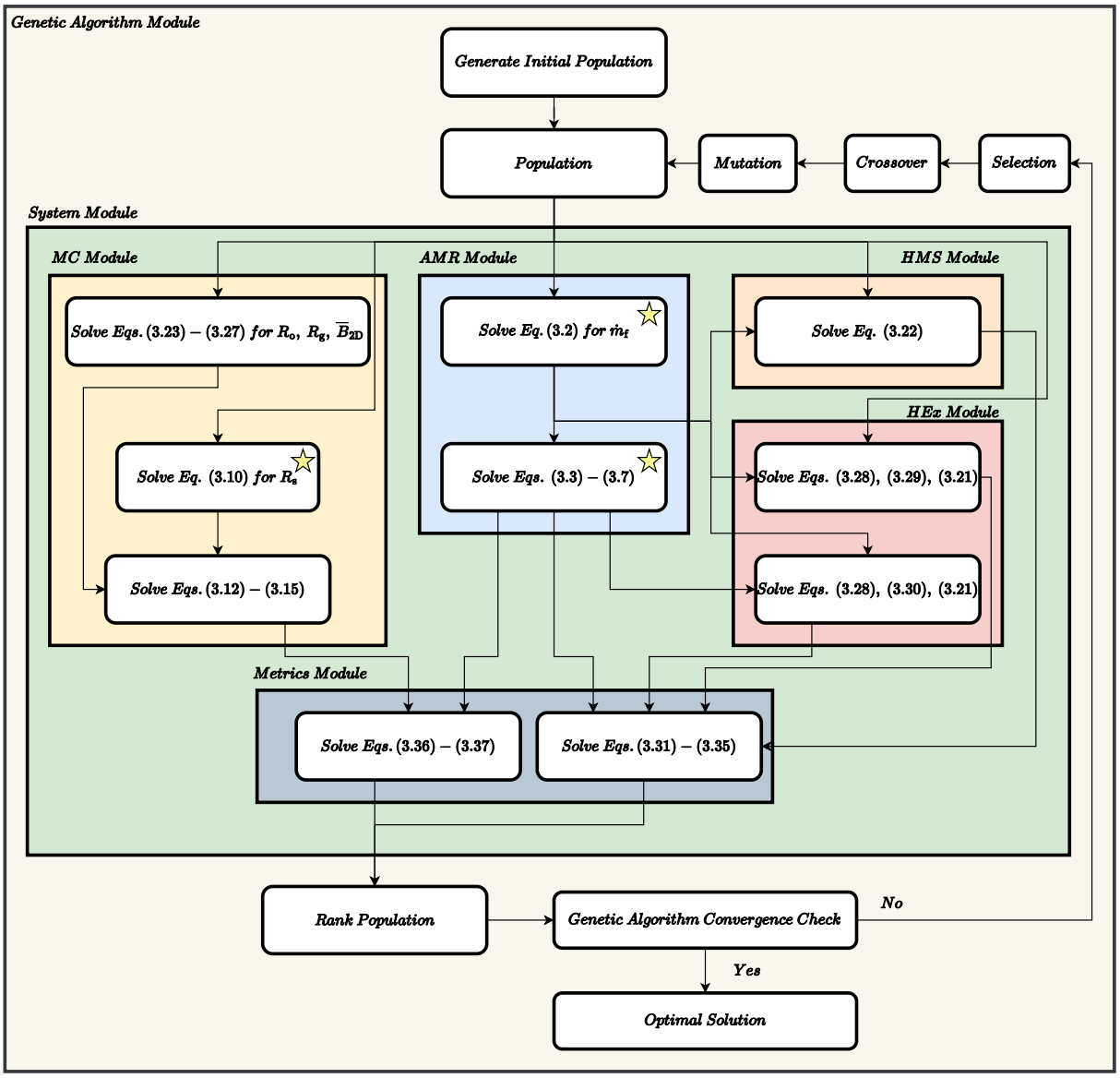


Figure 3.6 – Flowchart of the optimization process. Yellow stars indicate the application of ANN in the process.

The solution starts by generating an initial population of a predetermined size, where each individual has a gene representing one of the input parameters of the system. The input variables are divided into five categories: (i) System requirements: $\dot{Q}_{\mathrm{C,sys}}$, T_{C} and T_{H}; (ii) AMR

geometric parameters: N_{AMR}, L_{AMR}, H_{AMR}, W_{AMR}, d_{p}, φ_{s} and φ_{eff}; (iii) Operating conditions: f_{AMR}, $F_{\%}$, $T_{\mathrm{CB}}^{\mathrm{in}}$ and $T_{\mathrm{HB}}^{\mathrm{in}}$; (iv) MC geometric and operating parameters: B_{AMR}, L_{xt}, h_{FC}, ϕ_{magnet} and $M_{\%}$; (v) MCM properties: ρ_{s}. Fluid properties are calculated using the CoolProp package (Bell *et al.*, 2014), considering the working fluid as water and at the mean temperatures of the component at which they would be calculated: AMR, CHEx or HHEx. Then, in the AMR Module by solving Eq. (3.2) for $\dot{m}_{\mathrm{f}}$. With this value, the remaining performance metrics of the AMR, namely ΔP_{AMR}, $\dot{W}_{\mathrm{AMR,mag}}$, $\dot{W}_{\mathrm{AMR,pump}}$, $\dot{Q}_{\mathrm{H}}$ and m_{MCM} can be calculated from Eqs. (3.3)-(3.7). Moreover, in the MC module, the MC dimensions can be calculated solely from the input variables. Firstly, R_{o} and R_{g} can be calculated from Eqs. (3.24)-(3.26). Additionally, $\overline{B}_{\mathrm{2D}}$ can be calculated by Eqs. (3.27) and (3.28). Then, R_{s} can be calculated from Eq. (3.10), and the MC metrics can be obtained with Eqs. (3.12)-(3.15). The HMS module consists of calculating Eq. (3.23). The HEx module solves Eq. (3.29) and either Eq. (3.30) for the CHEx or Eq. (3.31) for the HHEx. Next, it searches for the solution to Eq. (3.22) in the HEx database. Lastly, the performance metrics of the MR system are calculated from Eqs. (3.32)–(3.38).

The system module outputs overall performance metrics for each individual in the population. The results are ranked based on the NSGA-II algorithm. Upon meeting the convergence criteria, the routine stops, and the resulting solution is deemed optimal. Otherwise, the algorithm enters its offspring generation phase. The selection step begins with choosing individuals for the parent population. Then, to create a new offspring, genetic information (features) from both parents are combined in the crossover step. Next, in the mutation phase, random mutations are assigned to the genetic material of the offspring population to generate diversity. Then, the offspring population is processed in the system module, and the resulting solutions are ranked. Finally, the algorithm is repeated until the GA converges. Further details on the NSGA-II method are presented in Appendix A.

3.4.2 Evaluation of the Optimal Solution

The solution of the optimization problem defined by Eq. (3.40) is obtained in the form of a set of optimal solutions, referred to as the Pareto front, since the problem involves MOO. Mathematically, all points on the Pareto front represent optimal trade-offs between the objectives. However, a single solution must be selected as the final design of the system. In this section, the characteristics of the solutions along the Pareto front are analyzed, and the most appropriate design is chosen based on the desired performance criteria.

3.4.2.1 Performance Metrics of the System

Figure 3.7 presents the solution of the MOO problem as a Pareto front. Thus, each of the 200 points consists of a combination of AMR-CM-HEX-HMS geometries and operating conditions that define an MR, which are the optimal solutions to the problem stated

in Eq. (3.40). The Pareto front illustrates the trade-off between system cost and power consumption, revealing that in the set of optimal solutions, decreasing the power consumption inevitably results in a heavier system, and vice versa, a behavior expected for the Pareto set. Each point on the curve represents a feasible design configuration balancing these competing objectives. The convex shape of the front highlights diminishing returns in cooling performance with increasing mass, allowing decision-makers to select an optimal compromise based on design priorities, as detailed further in this section.

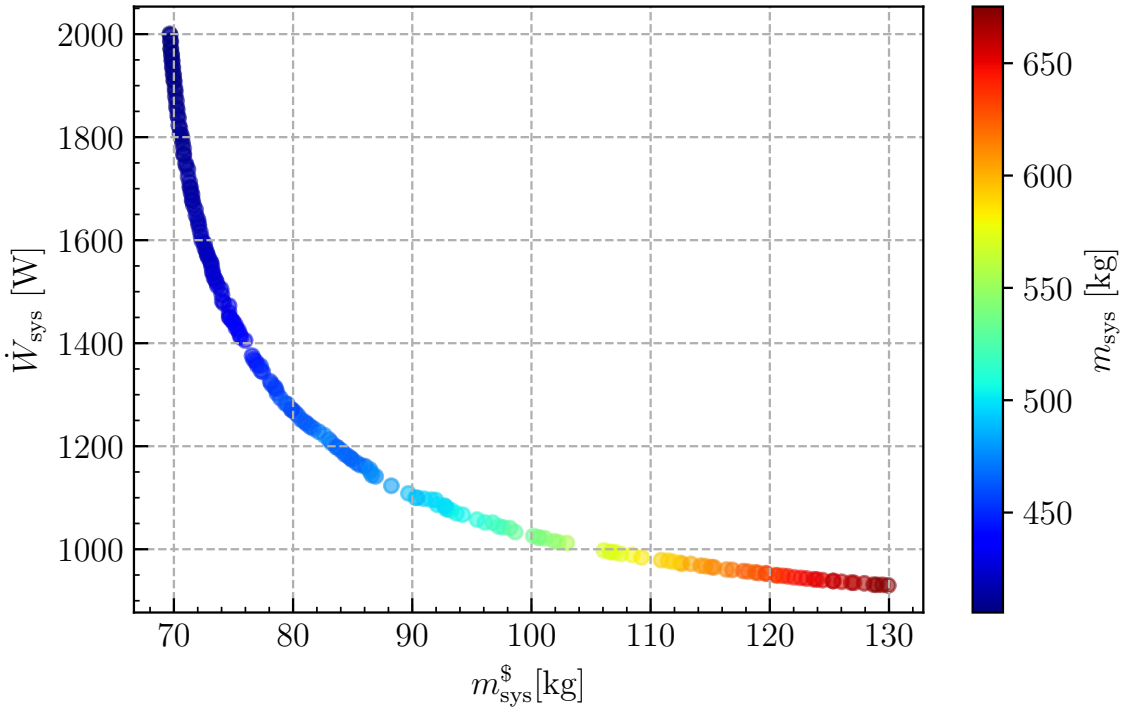


Figure 3.7 – Resulting Pareto front of the MOO problem.

Component breakdowns for the power consumption, cost, and mass of the system are exhibited in Fig. 3.8, along with the results for the mass of magnetocaloric material, m_{MCM}, COP_{sys}, and $\eta_{\text{2nd,sys}}$ for each system on the Pareto front. The contribution of each term in Eq. (3.38) is presented in Fig. 3.8(a). For all Pareto-optimal systems, the magnet represents the highest individual cost, and the most significant observed cost reduction results from a decrease in that share. The other components remain at a somewhat constant value compared to it. The MCM, due to its high cost, and the FC, due to its large mass, are the third- and second-most significant contributions.

According to Fig. 3.8(b), for the entire Pareto optimal set, power consumption is dominated by the contributions associated with the AMR, namely magnetization and fluid pumping. Moving along the Pareto set toward lower power consumptions reveals significant reductions in both those shares. The reasons for that are discussed later in the design parameters assessment. On the other hand, the power consumption of the HExs remains relatively constant throughout the Pareto set due to the constraints imposed during the

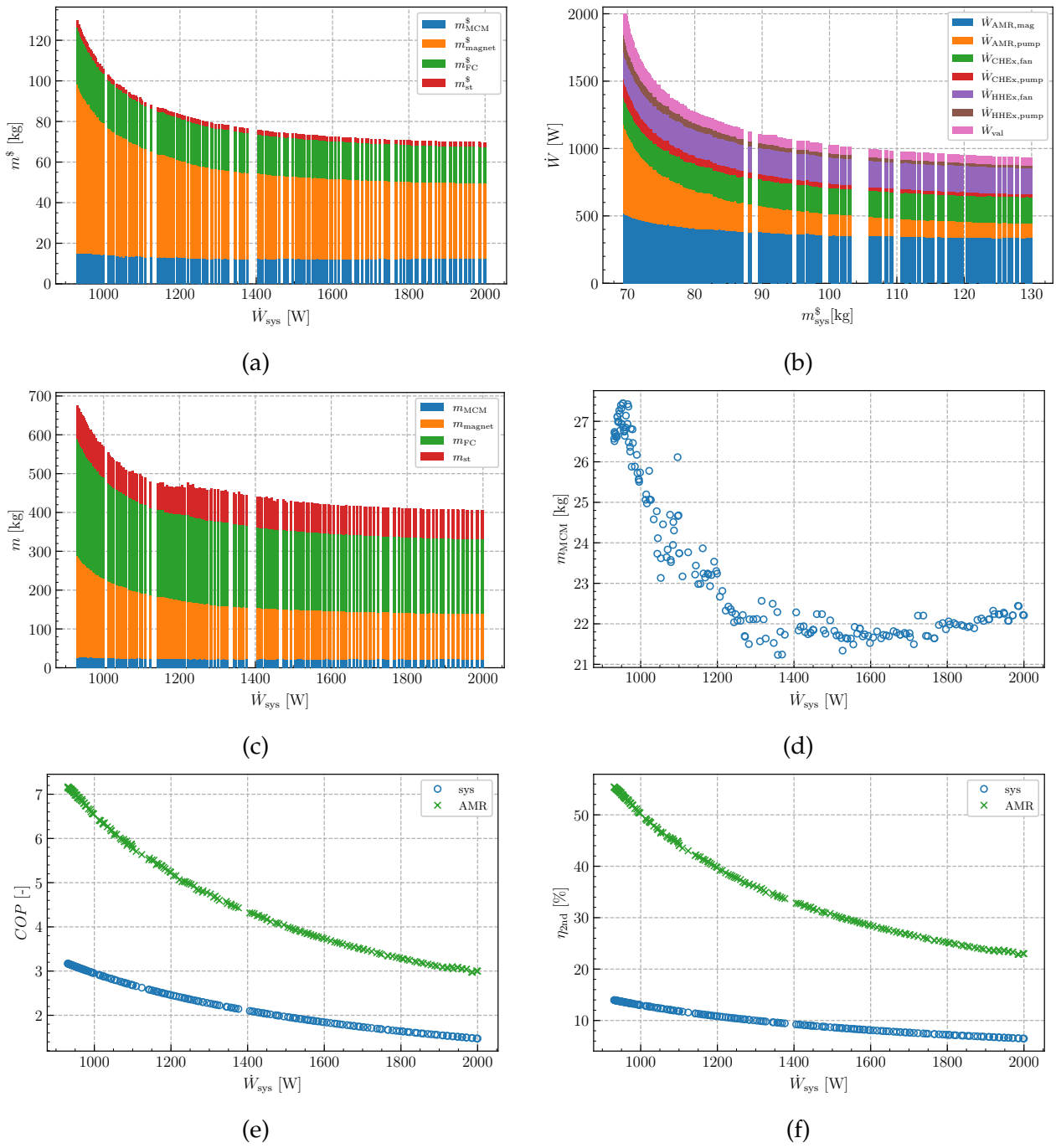


Figure 3.8 – Breakdown of the contributions of (a) cost, (b) power consumption, and (c) mass of the system. Attained values of (d) mass of MCM, (e) COP, and (f) second-law efficiency for the system and for the AMR, associated with the designs that make up the Pareto front.

component optimization process. Nevertheless, the internal pumping power in both HExs shows considerable variation, primarily due to changes in the mass flow rate, which are not readily perceptible given their low magnitude. The relatively small contributions of the heat exchanger liquid-side pumping power demonstrate the effectiveness of the multi-circuit strategy adopted. The Behavior of the power consumption of the HMS follows the same pattern as that of the HExs, given the increase in the pumping power due to the rise in the liquid mass flow rate.

The heat exchangers account for 25% to 45% of total power consumption, under-

scoring their significance in the design of any MR system (Peixer *et al.*, 2022). Even though AMR magnetization power can reach values around 1.2 times the Carnot power (considering the AMR temperature span instead of the system), which reflects the high thermodynamic efficiency of the MCE, irreversibilities associated with the fluid pumping through the AMR and heat transfer through the HEx, as well as the power consumption of the HMS, prevent the system from achieving the expected high efficiencies.

The contribution of each term in Eq. (3.37) is presented in Fig. 3.8(c). The differences between the mass and cost of each component can be compared from Figs. 3.8(a) and (c). The MCM accounts for a considerable share of the cost, whereas its total mass is almost negligible compared with the rest of the system. That is due to the high per-unit cost of this component. The steep price reduction is due to the decrease in the mass of the magnet. Lastly, the most significant contribution to the system mass is from the FC, which is explained by the MC geometry (since the FC is placed at the outer diameters).

Although not visually perceptible in Fig. 3.8(c), according to Fig. 3.8(d), a drop in the mass of MCM is associated with an increase in $\dot{W}_{\mathrm{sys}}$. That trend is related to the intricate coupling among the phenomena involved in modifying the envelope dimensions of the AMR. For that, a detailed evaluation of the resulting values of height, width, and length of the AMR is going to be carried out later in this section.

In addition to the COP_{sys} and COP_{AMR} presented in Fig. 3.8(e), $\eta_{\mathrm{2nd,sys}}$ and $\eta_{\mathrm{2nd,AMR}}$ are displayed in Fig. 3.8(f). It is worth highlighting that a vapor-compression refrigeration system has been tested in a certified calorimeter and used as a benchmark for the system design (Silva *et al.*, 2021). The conventional system produced a COP_{sys} of 2.48 and a $\eta_{\mathrm{2nd,sys}}$ of 10.91%. Fig. 3.8(e) and (f) reveal many available system configurations which can operate more efficiently than the conventional vapor-compression system, as long as the design allows an increase in the cost and mass of the system. Lastly, it is evident that the power consumption shares of the HMS, especially the HExs, are highly detrimental to the performance, significantly reducing both COP_{sys} and $\eta_{\mathrm{2nd,sys}}$.

3.4.2.2 Design Parameters

This section analyzes the Behavior of the design parameters associated with each optimal system configuration composing the Pareto front as a function of the system power consumption. Notice from Fig. 3.7 that the optimal systems with the lowest cost-weighted mass are those with the highest power consumption and vice-versa. The AMR parameters that compose the Pareto front are presented in Fig. 3.9.

Since the MC makes the most significant contribution to the system weight, the optimal systems with a low cost are associated with a relatively lower applied magnetic field strength. As the cooling capacity is fixed, the lower specific refrigerating capacity of these

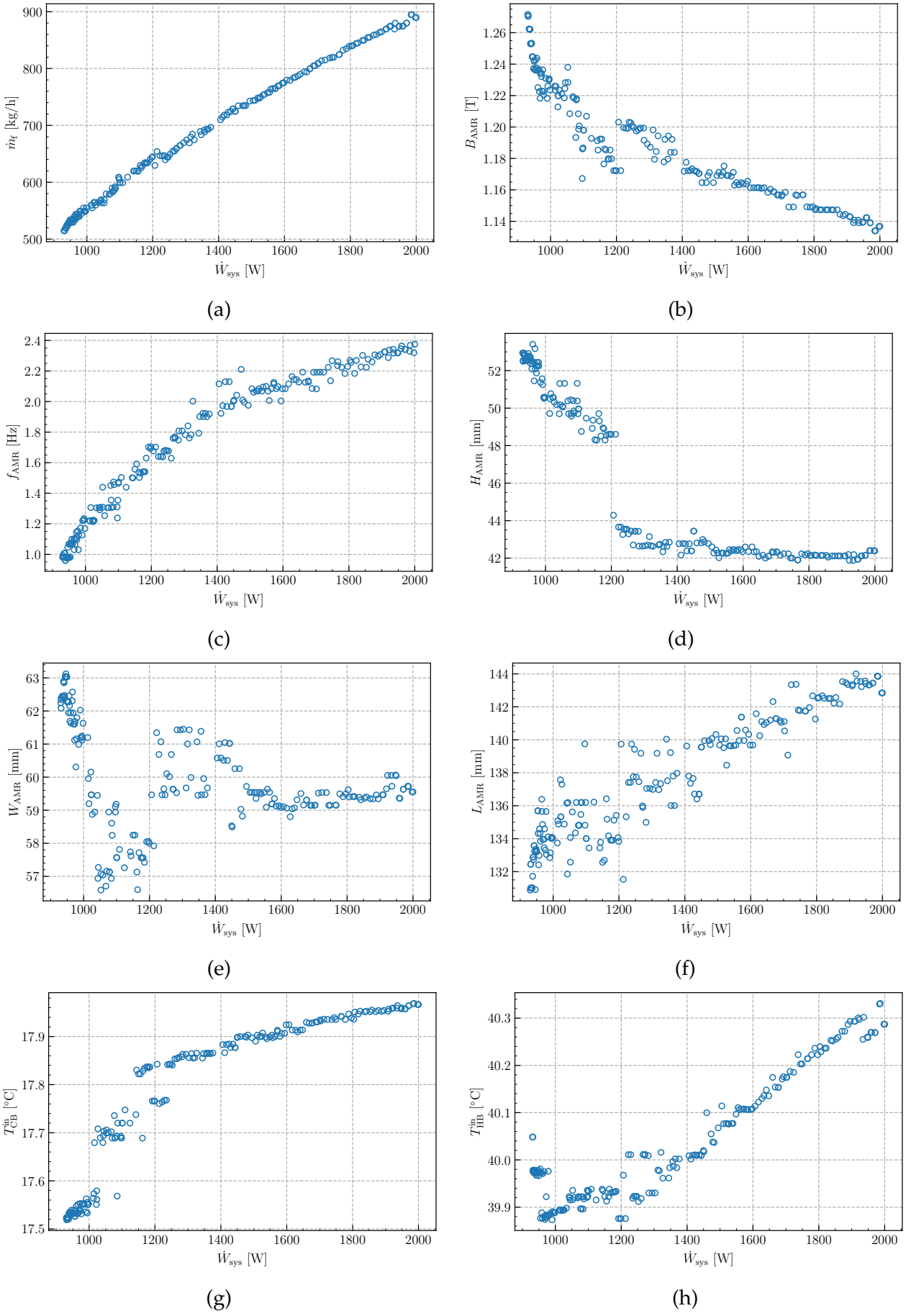


Figure 3.9 – Behavior of the AMR parameters of the optimal systems making up the Pareto front as a function of the power consumption of the system: (a) mass flow rate, (b) magnetic flux density of the AMR, (c) frequency, (d) height, (e) width, (f) length of the AMR, (g) inlet temperature of the cold blow and (h) inlet temperature f the hot blow.

lighter systems is compensated by an increase in the mass flow rate, as seen in Fig. 3.9(a). Conversely, as shown in Fig. 3.9(b), the trend in magnetic flux density is the opposite: the bulkiest optimal systems do not require a high fluid pumping power through the AMR to reach the target cooling capacity. In other words, the reduction in the magnetic flux density (and consequently the rise in the mass flow rate) is the least penalizing way encountered by the optimization process when a minimization of the cost of the magnet is sought. One may also notice from Fig. 3.9(b) that the resultant (or effective) magnetic flux density is considerably lower than the one generated by the MC (and actually applied on the AMR). Such a loss is directly linked to the geometric features of the AMR (bed shape, aspect ratio, and particle size) via demagnetizing effects.

Although not directly related, the frequency tracks the trend in the fluid flow rate, as shown in Fig. 3.9(c). A possible explanation for this Behavior is the deterioration of the effectiveness of the porous medium with increasing mass flow rate. Thus, for lighter system configurations, the system increases the frequency to perform more cycles per unit time and satisfy the cooling capacity constraint.

As for the AMR dimensions, the most evident trend is that of height, which decreases with the power consumption as seen in Fig. 3.9(d). As the MC dimensions are reduced and the mass flow rate is increased to maintain cooling capacity, the optimal configurations reduce the height to compensate for the loss of specific magnetization power due to the smaller magnet volume. Although the net effect is a reduction in magnetic flux density for the lighter systems, reducing the air gap height in the MC slows this reduction, despite a slight increase in demagnetizing effects. Nevertheless, the lower AMR height, coupled with the rise in the mass flow rate, increases the superficial fluid velocity, the AMR pressure drop, and, ultimately, the power consumption.

In Fig. 3.9(e), the width of the AMR does not exhibit a clear trend as it fluctuates between 62 and 57 mm for the most significant portion of the Pareto dataset. Nevertheless, such a slight variation does not imply a lack of influence of this variable on the MR performance. Instead, several alternative ways exist to reach optimal configurations amid complex trade-offs involving multiple objectives. Despite the scatter, the AMR length is clearly higher for the lighter optimal system configurations. The reduction in regenerator effectiveness with increased fluid flow rate can explain this Behavior. Moreover, in the high-power-consumption region, the AMR length has greater flexibility to increase due to the lower penalty for regenerator pressure drop.

The results for the inlet temperature during the cold blow, presented in Fig. 3.9(g), are directly related to those for $\varepsilon C^*_{\mathrm{CHEx}}$ presented later in this section. As will be seen, for all the cases under analysis, the optimal systems operate very close to the maximum $(\varepsilon C^*)_{\mathrm{CHEx}}$ allowed by the geometric constraints. Hence, as the mass flow rate increases, $(\varepsilon C^*)_{\mathrm{CHEx}}$

decreases. The results demonstrate that the minimum temperature difference in the CHEx is attained at the highest mass flow rates.

The results for the inlet temperature during the hot blow, Fig. 3.9(h), display an opposite trend to the ones exhibited in Fig. 3.9(g), *i.e.*, the systems operating at higher mass flow rates are attaining higher values of temperature difference. Although counterintuitive, this Behavior is due to the increase in the heat rejection rate to the hot reservoir for the lighter optimal systems; higher mass flow rates raise both the magnetization and fluid pumping shares of the AMR, increasing the heat rejection rate at the HHEx. Therefore, even though the HHEx operating at higher mass flow rates performs at higher $\varepsilon_{\mathrm{HHEx}}$, it is not enough to compensate for the extra heat transfer rate. Thus, even optimal systems must increase the temperature difference, thereby raising the inlet temperature.

Figure 3.10 shows the MC geometric parameters as a function of the system power consumption for the optimal configurations along the Pareto front. Notice that the values of such optimal parameters, which ultimately define the Behavior of B_{AMR}, are determined by the overall performance objective of providing the required $\dot{m}_{\mathrm{f}}$ through the MC gap utilizing the least amount of PM.

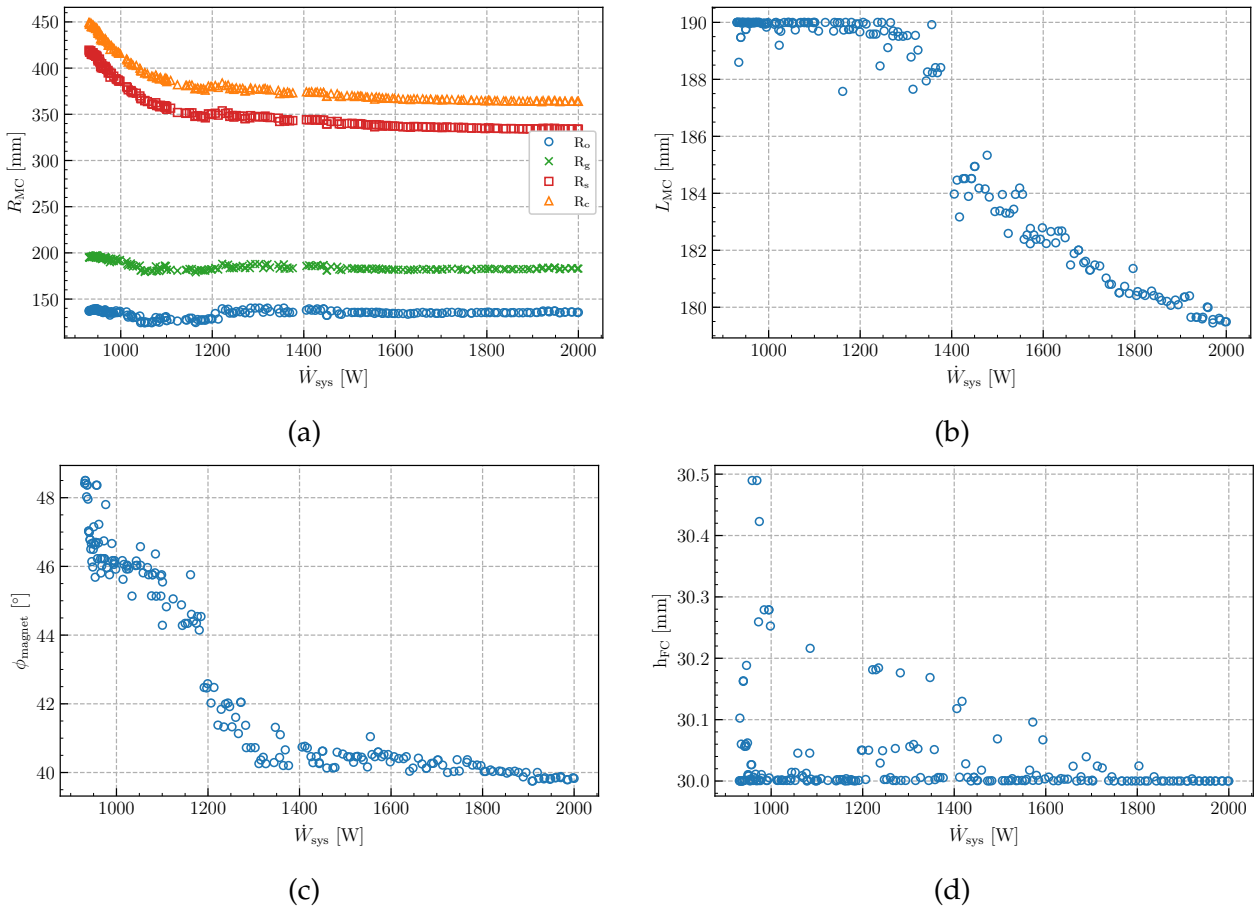


Figure 3.10 – Behavior of the MC geometric parameters of the optimal systems making up the Pareto front as a function of power consumption of the system: (a) inner and outer radius of the rotor and stator, (b) length of the MC, (c) angle of the magnets, and (d) thickness of the flux concentrator tube.

The results presented in Fig. 3.10(a) corroborate those already discussed in Figs. 3.8(a) and 3.8(c). While the outer radius of the stator and inner radius of the rotor exhibit a slight decrease along the Pareto set, the drops in the outer radii of the stator are sharper, given the steeper reduction observed in the mass of magnets in the same system power consumption range. This Behavior can be explained by the weight imposed by the optimization process on the mass reduction of the PM. Regarding the length of the MC, the Behavior reported in Fig. 3.10(b): the bulkier systems are constrained by the 190-mm upper limit, while the MC length decreases slightly as power consumption increases.

As can be seen in Fig. 3.10(c), the value of the angle of PM is maximum at the lowest values of power consumption, where there is room for the mass of magnets to increase and produce a high magnetic flux density. As that requirement is reduced and a minimization of the cost is needed, the values of the angle of PM start to drop to reduce the mass of magnets.

As for the thickness of the FC, Fig. 3.10(d) shows that along the entire Pareto set, their values remained within 2 mm from its minimum of 30 mm. This Behavior can be attributed to the constraints imposed on the outer radius of the rotor and the thickness of the FC itself. Since the effect of hard magnetic material on the magnetic field is much greater than that of the soft magnetic material, the optimizations tend to allocate as much PM as possible in the radial direction, forcing R_{c} to remain near the minimum value.

The Behavior of the design parameters of the CHEx and HHEx as a function of the power consumption of the system is presented in Fig. 3.11. Figure 3.11(a) reveals that all optimal systems along the Pareto front tend to operate near the limit of the imposed constraint, *i.e.*, at the lowest possible AMR temperature span. This Behavior is explained by the detrimental effect of that variable on the regenerator cooling capacity, which is avoided by increasing (εC^*) for both heat exchangers and achieved by expanding the envelope of the HEx, which assumes a maximum value of 550 mm in most optimal configurations.

Figure 3.11 also shows that the design parameters are almost the same for the CHEx and HHEx, which is due to the necessity of the system to operate at the highest possible values of εC^* in both components. The marginal difference observed between $(\varepsilon C^*)_{\mathrm{CHEx}}$ and $(\varepsilon C^*)_{\mathrm{HHEx}}$ in Fig. 3.11(a) is explained by the temperature-dependent properties of both fluid streams. Nevertheless, with a few exceptions, the geometric parameters remained practically constant, again, due to the need of the system for large heat transfer areas and low flow resistance, and, of course, the enforcement of discrete, rather than continuous, values for some design parameters. More specifically, the combination of low flow resistance and enhanced heat transfer requirements is validated by the large values of height, width, and length of the HEx, which either attain the maximum allowed values or remain close to them throughout the entire Pareto set, thereby maximizing the volume envelope of both HEx. Coupled with that, D_{HEx} is kept at its minimum value through all the Pareto set, as displayed in Fig.3.11(f).

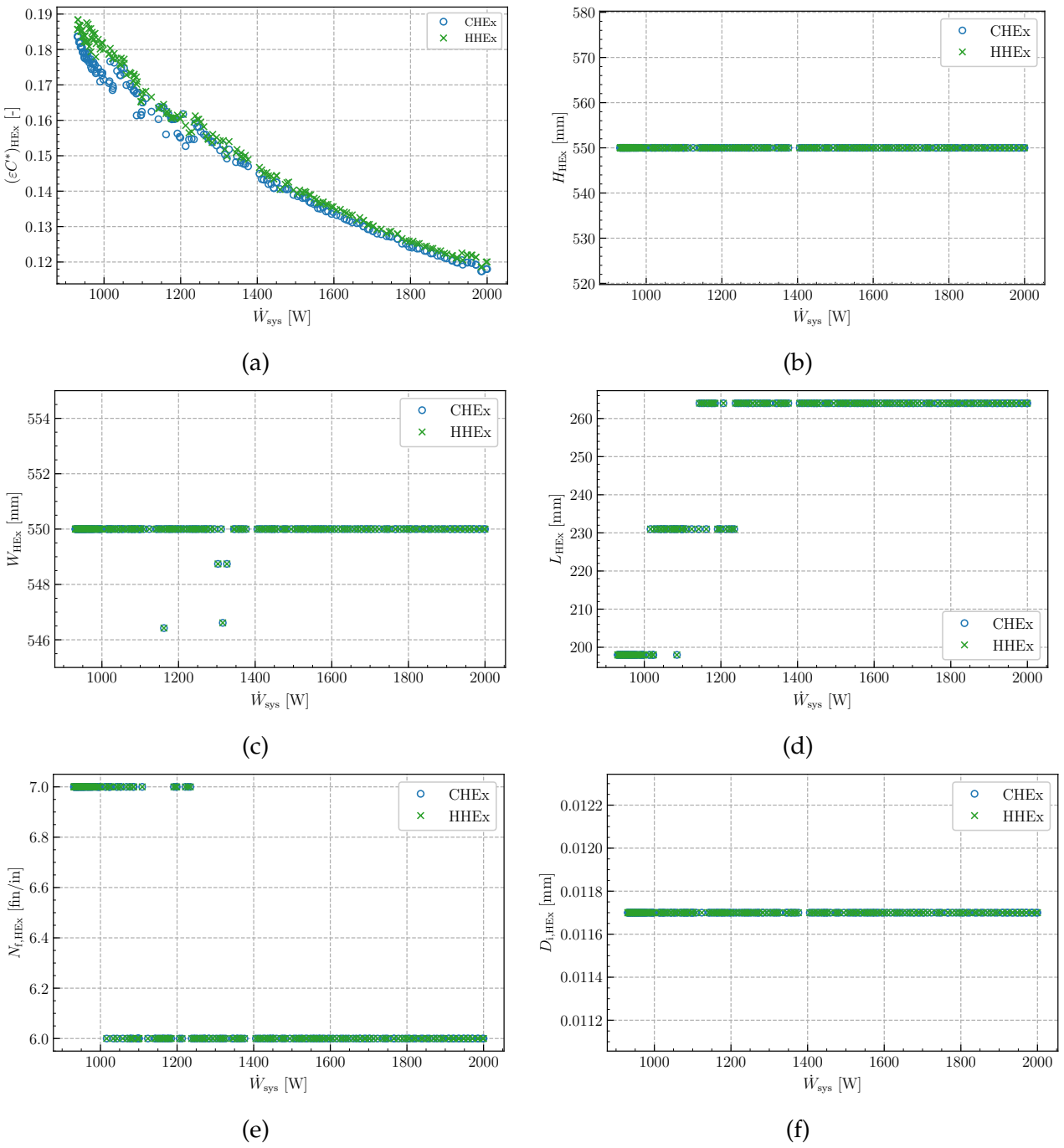


Figure 3.11 – Behavior of the CHEx and HHEx parameters of the optimal systems making up the Pareto front as a function of $\dot{W}_{\mathrm{sys}}$: (a) $(\varepsilon C^*)_{\mathrm{HEx}}$, (b) height, (c) width, (d) length, (e) fin density and (f) diameter of the tube for CHEx and HHEx.

Although counterintuitive, this is explained by the low pressure drops in the internal flow resulting from the multi-circuit strategy, and by the increase in the external free-flow area associated with the lower tube diameters. Additionally, the fin density remained at 6 or 7 fins per inch due to a trade-off between increased heat transfer area and higher flow resistance and power consumption.

3.4.3 Selection of the Final Design

Each point on the Pareto front represents an optimal trade-off between the competing objectives. Nevertheless, a single solution must be chosen to define the final system design. This selection is performed using the Weighted Global Criterion Method (Marler & Arora, 2004), based on the following utility function:

$$O_{\mathrm{c}} = \left\{ \sum_{i=1}^{k} w_{\mathrm{i}} \left[F_{\mathrm{i}}(\mathbf{x}) - F^{\circ} \right]^{p} \right\}^{\frac{1}{p}} \tag{3.41}$$

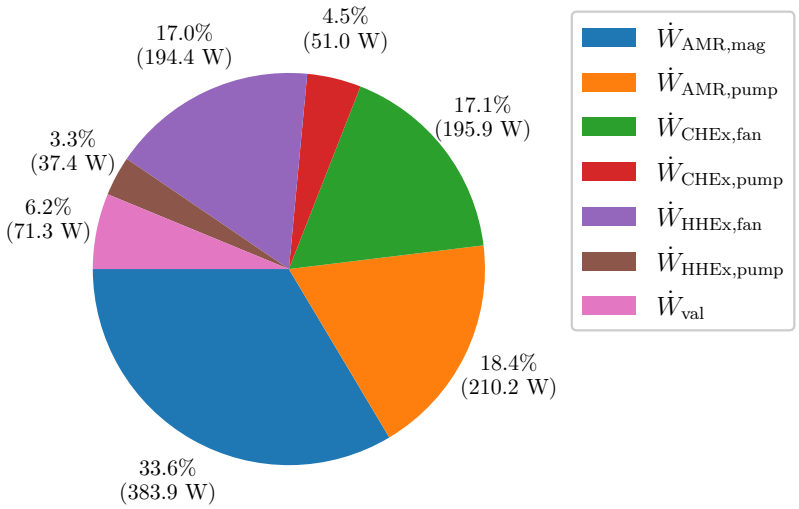
where O_{c} is the global criterion, w_{i} a vector of weights for each objective function, p is a coefficient to emphasize the minimization of one of the objectives, **F** represents the Pareto optimal systems and F° is the utopia point defined as:

$$F^{\circ} = [\min(m^{\$}_{\mathrm{sys}}), \min(\dot{W}_{\mathrm{sys}})] \tag{3.42}$$

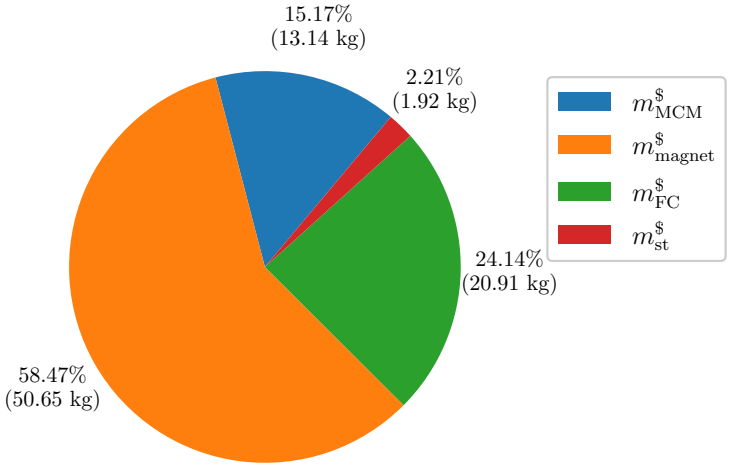
the objective functions were written in dimensionless form, and the weights employed for the cost and power consumption were 0.5 and 0.5, respectively. p was set equal to unity.

The system configuration selected as the optimum has the following operational and capital characteristics: $\dot{W}_{\mathrm{sys}}$ = 1169 W, $m^{\$}_{\mathrm{sys}}$ = 86.6 kg and m_{sys} = 474 kg, resulting in a COP_{sys} of 2.57 and $\eta_{\mathrm{2nd,sys}}$ of 11.4%. Figures 3.12(a)-3.12(c) display the component breakdowns for the power consumption, cost-weighted mass, and mass, respectively, for the optimum. Once again, given their low contribution (0.6%), $\dot{W}_{\mathrm{CV,pump}}$ is not depicted in Fig. 3.12(a).

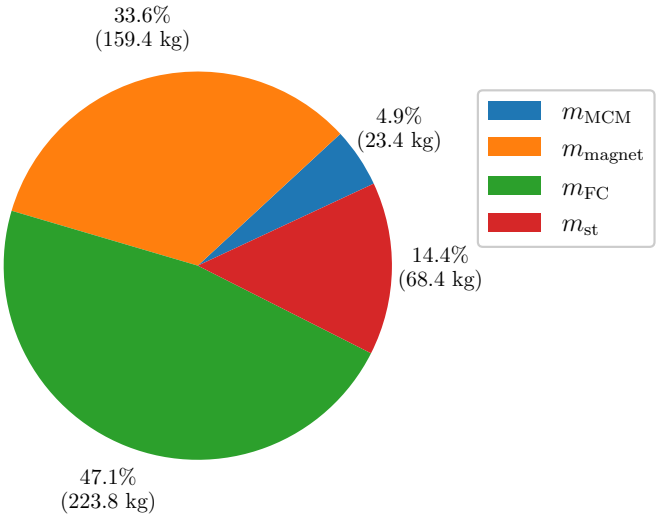
For all systems in the Pareto set, the AMR magnetization and pumping power have the most significant influence on total power consumption. Roughly one-third of the total system power consumption is due to magnetization of the AMR, the highest share, followed by fluid pumping in the AMR, which accounts for 18.5%. Outside the AMR, the most significant contributors to power consumption are the CHEx and HHEx fans. Also, the cost of the system is dominated by magnet share, which accounts for 58.47%. The second-highest cost is associated with the flux concentrator tube of the rotor. The remaining shares of the cost-weighted mass are related to the MCM and the stator. From this analysis, it is clear that the rotor is the most expensive component of the system, accounting for over 82% of the total cost. As expected, the mass of the system is dominated by the MC rotor contributions, *i.e.*, the flux concentrator tube and magnets, which correspond to 47.1% and 33.6%, respectively. The other MC component, the stator, is responsible for 14.4%. In contrast with the cost of the system, the MCM has a minor influence on nominal mass. The performance metrics and design parameters are presented in Table 3.6.



(a)



(b)



(c)

Figure 3.12 – Component breakdown for (a) power consumption, (b) cost, and (c) mass of the system for the optimum configuration.

Table 3.6 – Design parameters and operating conditions of the optimal system configuration.

Design Variables					
Parameter	Value	Parameter	Value	Parameter	Value
$\dot{m}_{\mathrm{f}}$	620 kg/h	f_{AMR}	1.5 Hz	L_{AMR}	133 mm
H_{AMR}	49 mm	W_{AMR}	57 mm	B_{AMR}	1.18 T
$T_{\mathrm{CB}}^{\mathrm{in}}$	17.8 °C	$T_{\mathrm{HB}}^{\mathrm{in}}$	39.9 °C	R_{o}	127 mm
R_{g}	181 mm	R_{s}	351 mm	L_{MC}	187 mm
h_{FC}	30 mm	ϕ_{magnet}	44 °	W_{CHEx}	550 mm
H_{CHEx}	550 mm	L_{CHEx}	264 mm	$D_{\mathrm{i,CHEx}}$	11.7 mm
$N_{\mathrm{f,CHEx}}$	6	W_{HHEx}	550 mm	H_{HHEx}	550 mm
L_{HHEx}	264 mm	$D_{\mathrm{i,HHEx}}$	mm	$N_{\mathrm{f,HHEx}}$	6

3.5 Outline of the Chapter

The chapter begins with a description of the strategy used to design the MRU, highlighting the requirements and demands for the models to be developed to enable system-level integrated optimization. Then, the AMR model is developed, structured according to the ML modeling framework introduced earlier. It then describes the models and methodologies used to design the other system components, highlighting their integration into a complete MRU. Next, the assumptions, boundary conditions, and simplifications made during modeling are examined, as they play a crucial role in shaping the optimization results. The optimization procedure is then detailed, covering the definition of objectives, decision variables, and constraints; the strategies used to explore the design space; the computational tools applied; and the convergence criteria adopted. The chapter concludes with the selection of the optimal design and its performance evaluation against the required specifications.

Chapter 4

EXPERIMENTAL APPARATUS

This chapter presents a detailed description of the final version of the MRU. The configuration and main geometric parameters for each component are described in more detail in comparison with the previous chapter. Due to unforeseen events during system operation, three distinct versions of the prototype were assembled and tested experimentally. The alterations and their justifications across the different generations of the prototype evaluated are thoroughly detailed. Details about the design and operation of the calibrated calorimeter are provided. Lastly, the performance metrics used to characterize the systems are defined.

4.1 Magnetic Refrigeration Unit

As previously described, the MRU consists of four main components: the AMR, MC, HMS, and HEx. The prototype is characterized in a calibrated calorimeter custom-built for its evaluation. All components of the MRU, except the CHEx, are placed in the warm (outside) chamber of the calorimeter. The CHEx is placed inside the cold (inside) chamber of the calorimeter. Further details on each component and the calorimeter are provided in this chapter.

A rendered image of the MRU, encompassing the components placed inside the warm chamber of the calorimeter, excluding the cold heat exchanger, is shown in Fig. 4.1. A photograph of the prototype inside the calorimeter is shown in Fig. 4.2, and a picture of the complete prototype is presented in Fig. 4.3. An explanatory video of the MRU and the calorimeter can be found at: https://youtu.be/5lVMstvAjgk. The innovations developed throughout the project culminated in a patent application (Lozano *et al.*, 2021) and three software registers (Peixer *et al.*, 2024; Cerutti *et al.*, 2024; Silva *et al.*, 2024) within the Brazilian National Institute of Industrial Property.

In the previous chapter, a preliminary description of the components was provided with enough detail to allow their modelling. In this chapter, a detailed description of the configurations and final designs of the components, along with their coupling, is provided. It is worth noting that several dimensions of the final version of the prototype were altered compared to those provided by the optimization procedure developed in Chapter 4. That has two main justifications. The first is that the components still went through a final round of individual optimization after the last integration step. The other is that alterations were re-

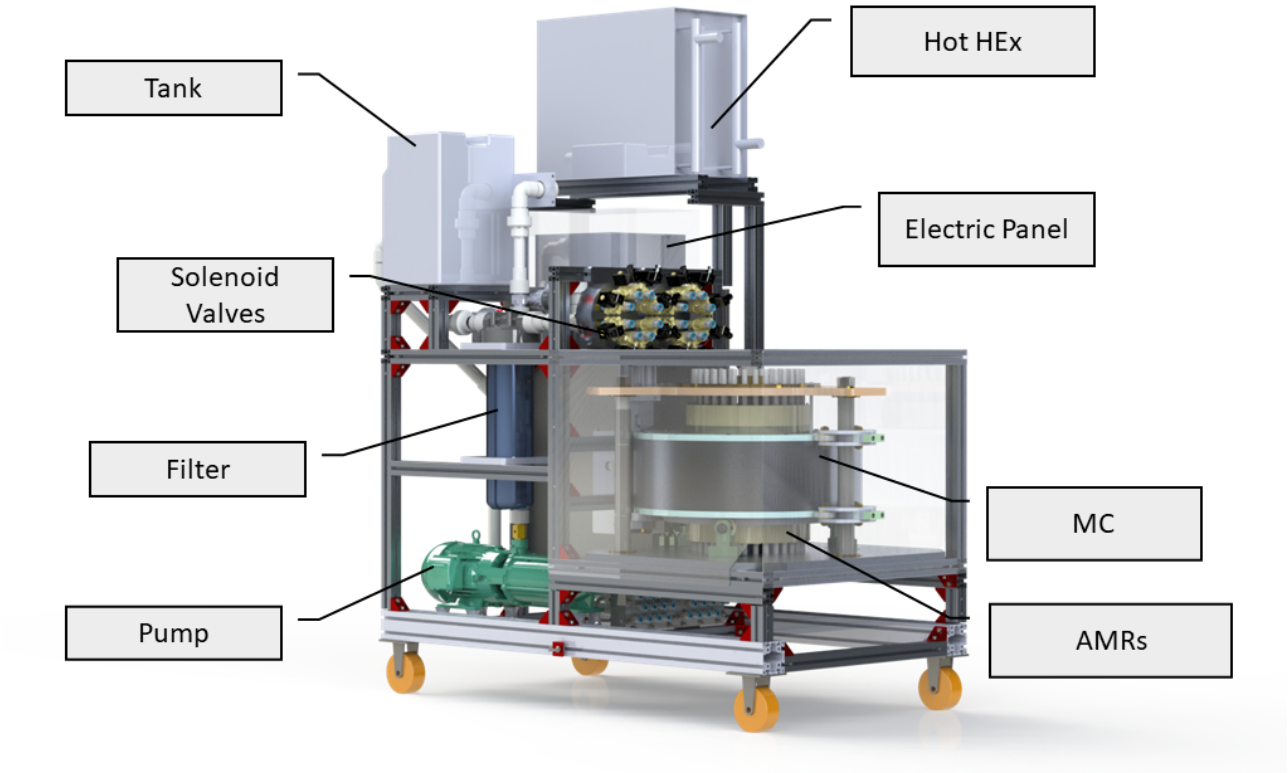


Figure 4.1 – The MRU and its main components.

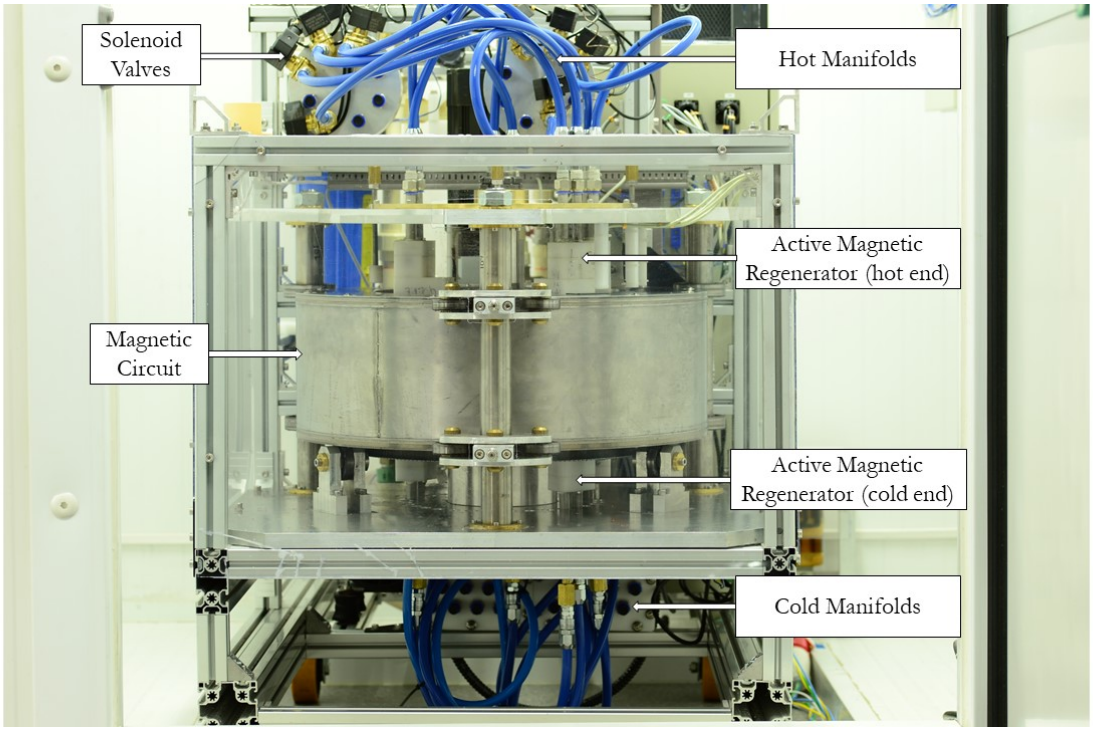


Figure 4.2 – Photograph of the MRU.

quired for manufacturing and coupling reasons, which could not be modeled in the previous steps of the design process. Both factors were regarded as learning to improve the design procedure proposed in the present work.

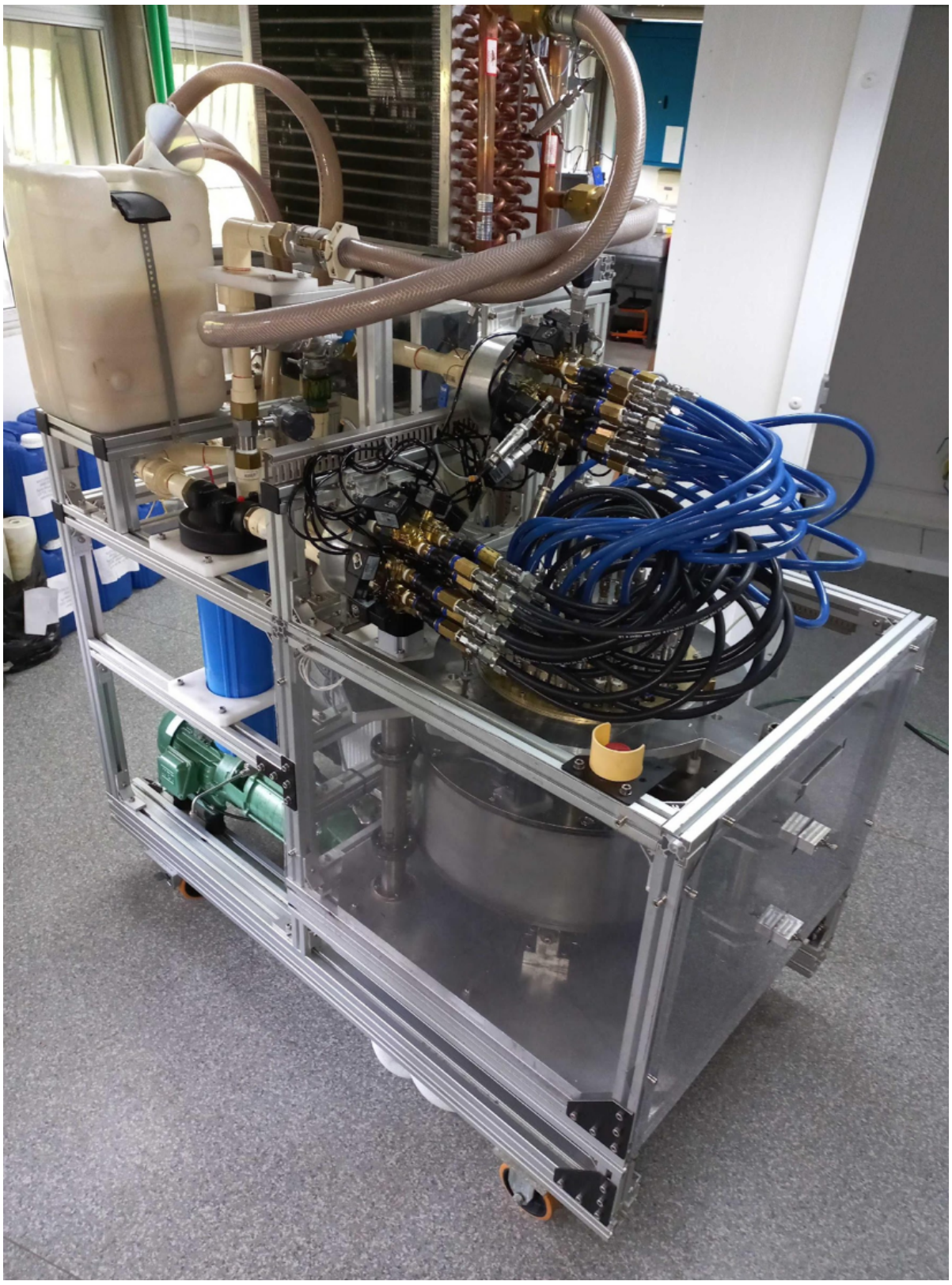


Figure 4.3 – Photograph of the full prototype.

4.1.1 Magnetic Circuit

The MC of the MRU consists of a rotor-stator configuration, known to achieve the highest cooling capacities in the available literature (Trevizoli *et al.*, 2016). In this configuration, two concentric cylinders are separated by the AMR (air) gap. The cross-sectional area of the first quadrant of the assembly is presented in Fig. 4.4, where the segmentation of the PMs

and remanence directions is merely illustrative.

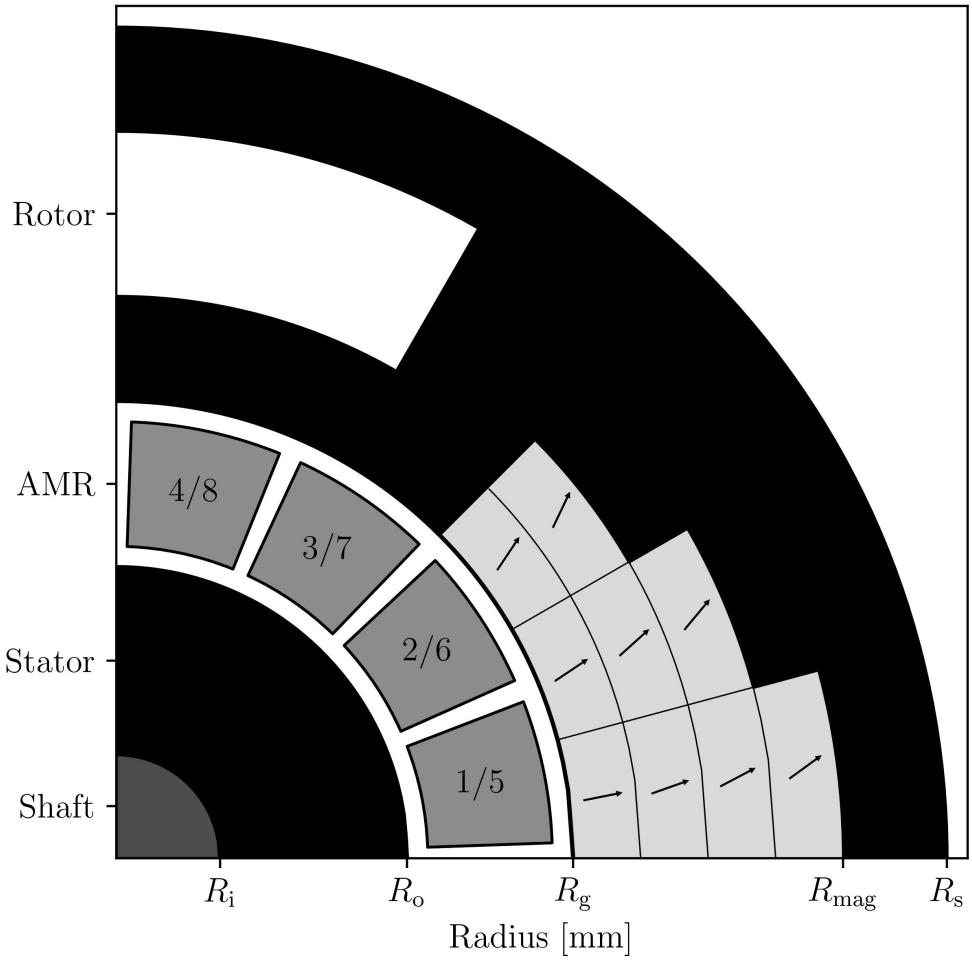


Figure 4.4 – Cross-section view (first quadrant) of the MC-AMR assembly. Black regions: soft magnetic material; white regions: air; light gray regions: hard magnetic material; Dark gray region at the bottom left: stator/shaft; arrows: remanence directions.

The inner cylinder (stator) is made from 0.5 mm-thick, circular, laminated sheets of E-145 electrical steel. This design reduces eddy current losses, which would otherwise appear due to the time-dependent nature of the magnetic field and the electrical conductivity of the stator material (Lozano *et al.*, 2016; Nakashima *et al.*, 2021; Dall'Olio *et al.*, 2021). These losses would not only increase torque and power consumption but also reduce the cooling capacity, as they are dissipated as heat in the stator adjacent to the AMRs. The laminated sheets are stacked around a fixed shaft and tied together by two flanges. The stator length is 190 mm, and its original inner and outer radii, R_i and R_o, are 34 and 134 mm, respectively. A picture of the stator of the MC is presented in Fig.4.5. Throughout the operation of the system, the dimensions of the stator had to be altered, mainly to accommodate the allocation of refrigerant in the AMRs, which will be discussed later in this chapter.

The rotor is composed of soft ferromagnetic material and PM segments. It is rotated at a specified frequency by a servo motor (WEG-SWA 56-4-8, driver WEG-SCA06), coupled with a pulley and belt system. Given that the MC has two magnetic poles, the AMR operation

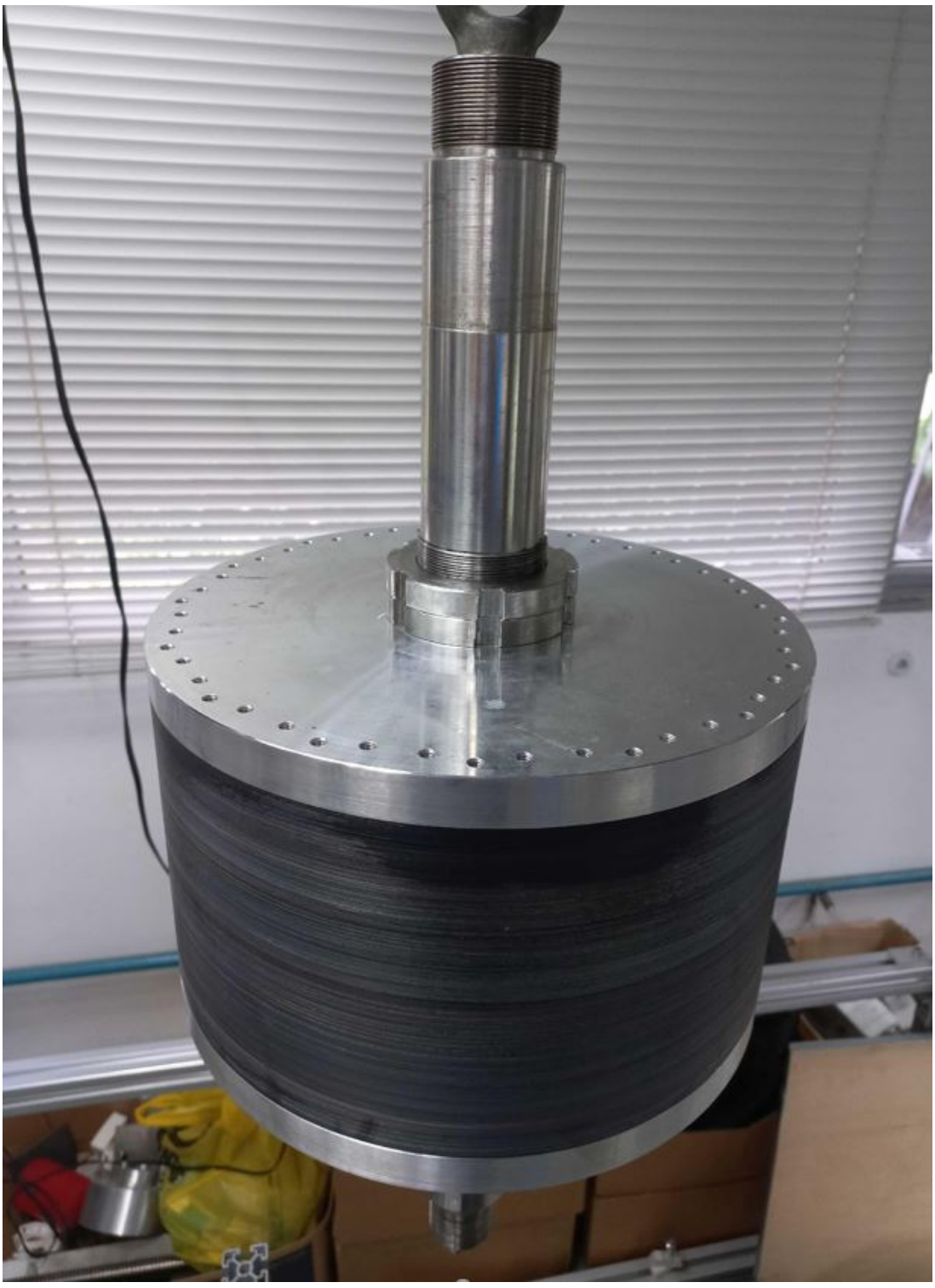


Figure 4.5 – Stator of the MC.

frequency is twice that of the rotor. The PMs used are N50M-sintered Nd-Fe-B grade, with a minimum remanence of 1.41 T. Each pole consists of 32 epoxy-glued PM segments assembled from eight distinct segment geometries. To reduce the overall PM mass, the number of segments in each PM layer progressively decreases as one moves away from the center of the magnetic pole (see Fig. 4.4). Approximately 12.5 liters of PM material are utilized in the MC. The soft ferromagnetic portion of the rotor, known as the flux concentrator, is constructed from laminated sheets of 1 mm and 5 mm thick S235JR. Unlike the stator, these laminations

are primarily intended to simplify manufacturing rather than to mitigate eddy currents. The flux concentrator features two void regions: one for positioning the PM segments (light gray areas) and another for reducing the overall mass of the system (white area). The inner and outer rotor radii, R_{g} and R_{Mag}, measure 185 mm and 338 mm, respectively. The outer radius of the PM segments, R_{s}, is 315 mm, and the rotor length is 190 mm. Given the cost of rotor changes, its dimensions remained constant across all versions of the MRU. An exploded representation of the rotor is presented in Fig. 4.6 and a picture of the assembly process of the component is presented in Fig. 4.7.

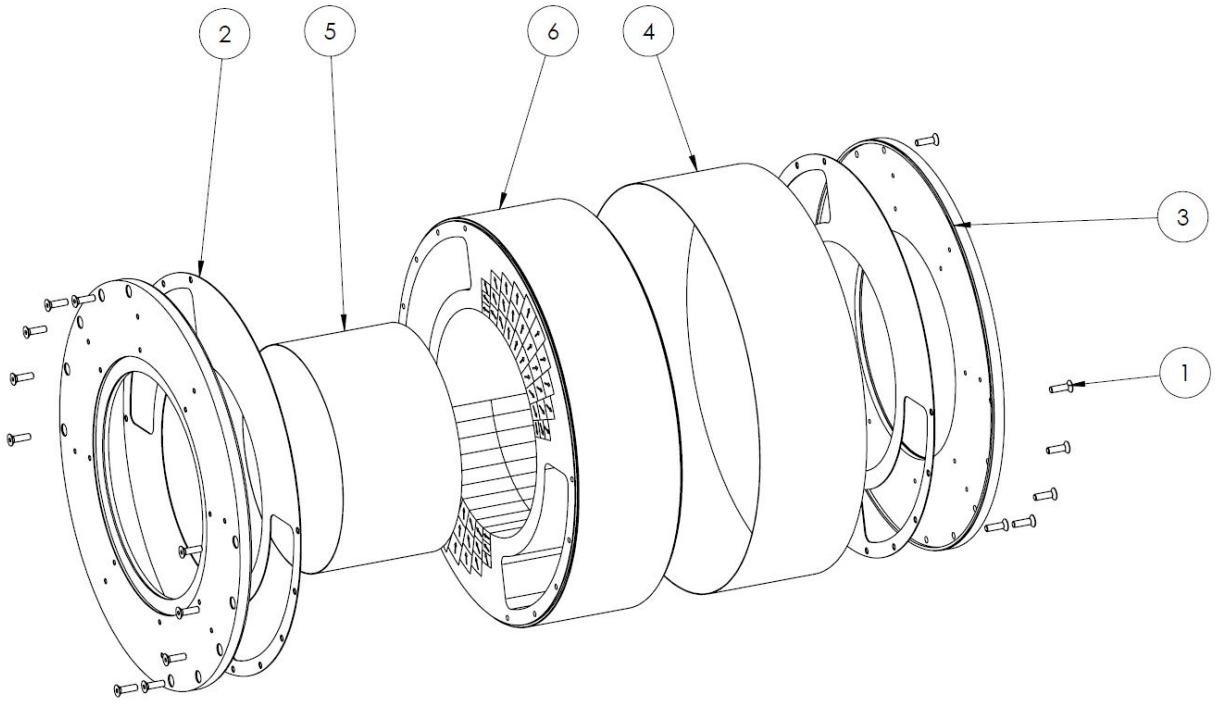


Figure 4.6 – Exploded representation of the rotor. (1) Screws, (2) Protective Magnetic Layer, (3) Supporting Lid, (4) External Protective Tube, (5) Internal Protective Tube, (6) Magnetic Assembly.

According to the description in Chapter 3, the MC dimensions were determined through a combination of subsystem- and system-level optimization procedures. At the subsystem level, the design was guided by the numerical method and optimization strategy proposed by Fortkamp *et al.* (2023). This approach minimizes the deviation between a target trapezoidal magnetic waveform and a numerical profile by adjusting the remanence directions of the PM segments. To reduce the mass of hard magnetic material, the external radii of the PM segment layers were independently reduced until the calculated magnetic field strength reached 99% of its original value (Cattelan *et al.*, 2024). Similarly, the size of the void segment in the flux concentrator was gradually increased until either the soft magnetic material reached saturation or the magnetic flux density in the low magnetic field region exceeded predetermined threshold values. At the system-level, the optimization followed the procedure described in Chapter 3.

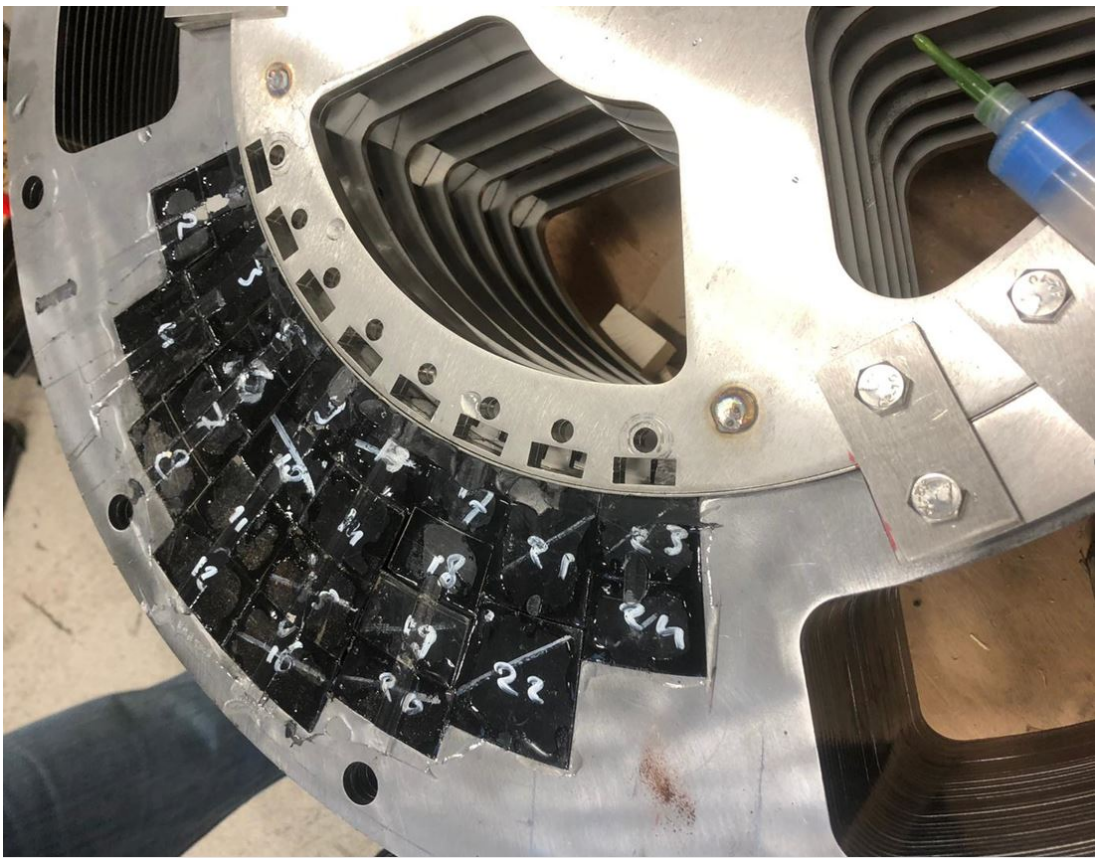


Figure 4.7 – Assembly of the Rotor.

4.1.2 Active Magnetic Regenerators

The AMRs comprise porous beds of MCM enclosed in stainless steel housings situated in the air gap between the rotor and the stator, as depicted in Figs. 4.4 and 4.8. These housings, which are shaped like segments of a cylindrical shell, are fixed to the stator and remain stationary during operation.

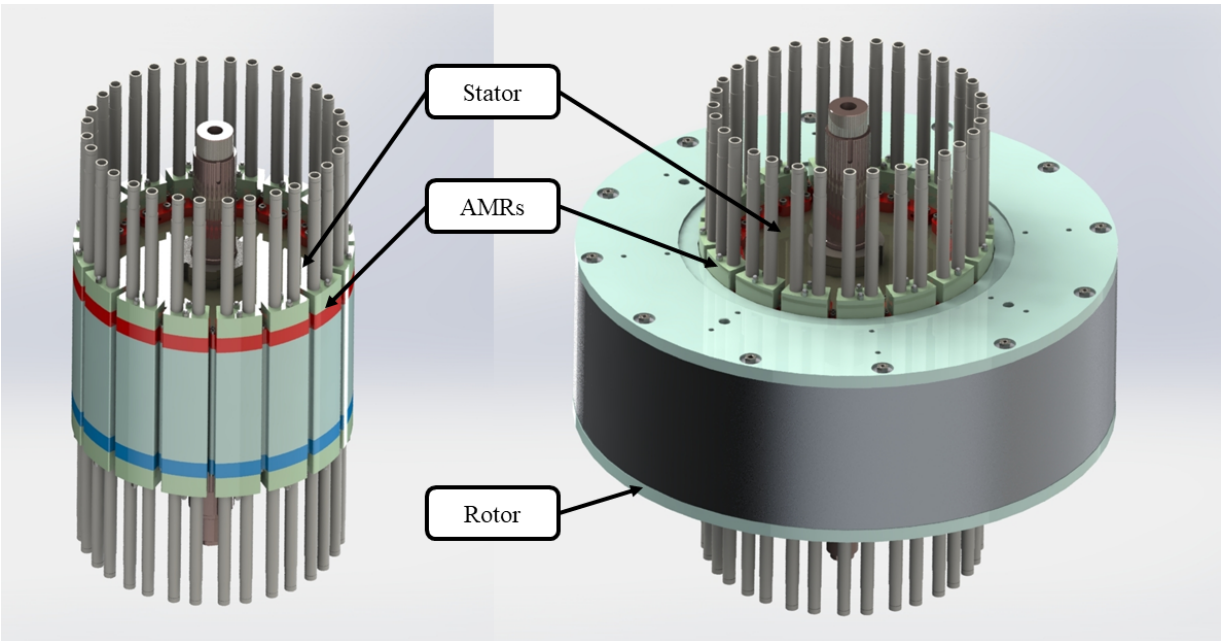


Figure 4.8 – AMR assembled in the radial gap between the rotor and stator.

The casings were designed to support cyclical mechanical loads with minimal thickness to maximize the internal volume allocated to MCM (Peixer *et al.*, 2017b). Each housing features two ends, one hot and one cold, each equipped with two fluid ports, an inlet and an outlet, which alternate in operation to direct the fluid flow through the porous bed according to the phase of the AMR cycle. The AMR casing, made of stainless steel, featured a central column to provide structural support. In addition, a set of metallic frames and individual meshes was used to separate adjacent MCM layers and allowed material reuse. These arrangements decrease the available magnetized volume, limiting the space for MCM allocation within the AMRs. Fig. 4.9 illustrates the inner part of the AMR casing, showing the arrangement of metallic frames and separate meshes during assembly.



(a) (b)

Figure 4.9 – Assembling process of the AMR. Pictures of (a) the inner section of the AMR casing during the allocation of MCM and (b) the arrangement of the metallic frames and separating meshes on the last MCM layer of the AMR.

The AMR was also designed by combining system and subsystem-level procedures. At the subsystem level, experimental tests (Teza *et al.*, 2024) were performed to validate numerical models (Vieira *et al.*, 2021). At the system level, ML models (Cerutti *et al.*, 2022) were integrated into the optimization scheme, enabling faster, more accurate performance predictions, as detailed in Chapter 3.

4.1.3 Magnetocaloric Materials

The porous structures within the AMRs consisted of packed layers of Gd and $La(Fe,Mn,Si)_{13}H_z$ arranged according to varying magnetic transition temperatures. Although Gd particles (provided by the Baotou Research Institute of Rare Earths, China) are mostly spherical, the $La(Fe,Mn,Si)_{13}H_z$ particles (marketed as *Calorivac-HS2* by Vacuumschmelze GmbH & Co) are slightly elongated cylinders (Vieira *et al.*, 2021), as presented in Fig. 4.10.

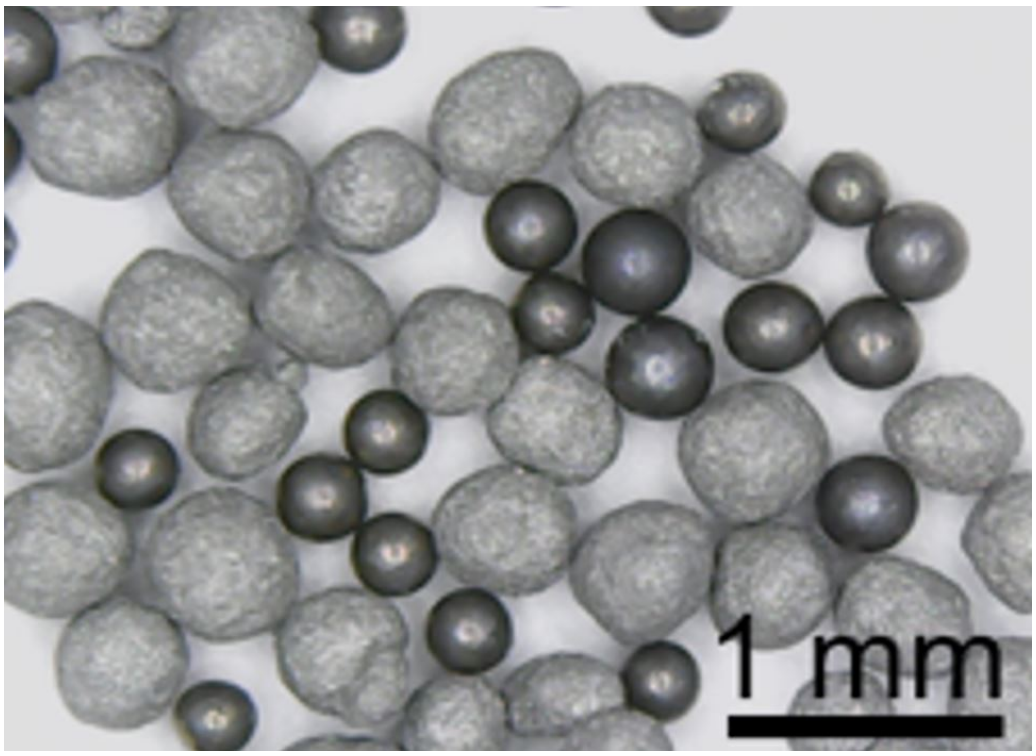


Figure 4.10 – MCM employed in the MRU. Darker and smaller samples are Gd particles. Lighter and bigger samples are $La(Fe,Mn,Si)_{13}H_z$ particles.

The number of AMR layers and their respective transition temperatures on each version of the MRU were determined by the availability of (limited) solid refrigerants (particularly the La-based alloys) and the system temperature requirements. The availability of La-based alloys was the main driving force behind the need to implement changes not only in the AMR but also in the MC and HMS. Thus, a single Gd layer and a determined number of $La(Fe,Mn,Si)_{13}H_z$ layers were used according to material availability in each design iteration. The original arrangement of Curie temperatures and the mass fraction of each layer of the optimal AMR configuration were defined by numerical simulation (Vieira, 2020) and coupling with the heat exchangers, as described in Chapter 3. Table 4.1 shows the values of the Curie temperatures that were ordered from the Gd and $La(Fe,Mn,Si)_{13}H_z$ alloys. Details about the multilayer composition of MCM, both in terms of the Curie temperature and in terms of mass fractions, will be discussed later in this chapter.

Table 4.1 – Curie temperatures of the available MCMs.

Layer	Material	T_{curie} [°C]
1	$La(Fe,Mn,Si)_{13}H_y$	15
2	$La(Fe,Mn,Si)_{13}H_y$	16.8
3	Gd	17.0
4	$La(Fe,Mn,Si)_{13}H_y$	19.3
5	$La(Fe,Mn,Si)_{13}H_y$	22.2
6	$La(Fe,Mn,Si)_{13}H_y$	24.6
7	$La(Fe,Mn,Si)_{13}H_y$	27.9
8	$La(Fe,Mn,Si)_{13}H_y$	30.0
9	$La(Fe,Mn,Si)_{13}H_y$	32.6
10	$La(Fe,Mn,Si)_{13}H_y$	34.6
11	$La(Fe,Mn,Si)_{13}H_y$	36.4
12	$La(Fe,Mn,Si)_{13}H_y$	39.0
13	$La(Fe,Mn,Si)_{13}H_y$	41.3

4.1.4 Hydraulic Management System

The hydraulic management system consists of a gear pump, a solenoid, and check valves. The arrangement provides versatility in controlling fluid profiles, rapid response, and robustness, similar to commercial solutions (Santos *et al.*, 2021). The design team also evaluated mechanically driven valves (Santos *et al.*, 2020), but electronic ones were chosen primarily for their efficiency and flexibility. Figure 4.11 presents the MRU hydraulic diagram. A gear pump (Thebe P11 7br) moves the fluid through the circuit. The oscillatory hydraulic profile of the AMR is set by sixteen solenoid valves (one pair of solenoid valves for each pair of AMRs), thirty-two check valves (two for each AMR bed), and four fluid manifolds. Two HEx, one hot and one cold, two filters, and a liquid tank are the remaining components of the liquid line.

The gear pump is positioned upstream of the HHEx to allow the HHEx to dissipate the heat generated by the gear pump. The fluid then flows to the high-pressure hot manifold and is distributed to the solenoid valves and AMR beds. The fluid is collected in the high-pressure cold manifold and pumped directly to the CHEx. The fluid is then once again distributed to the AMRs via the low-pressure cold manifold, flows through the beds, and is collected by the low-pressure hot manifold, then directed to the liquid tank and pump. Each AMR bed has one inlet and one outlet port on each side (hot and cold).

Magnetic and hydraulic profiles are synchronized via a control logic that uses the encoder signal coupled to the rotor. Additionally, the signals from eight Hall-effect sensors placed between the AMR beds are used to fine-tune the actuation of the solenoid valves. According to Figs. 4.4 and 4.11, the AMR beds are divided into eight sets (1, 2, 3, 4, 5, 6, 7 and 8) and two other sets (A and B), which are controlled by the same pair of solenoid valves and

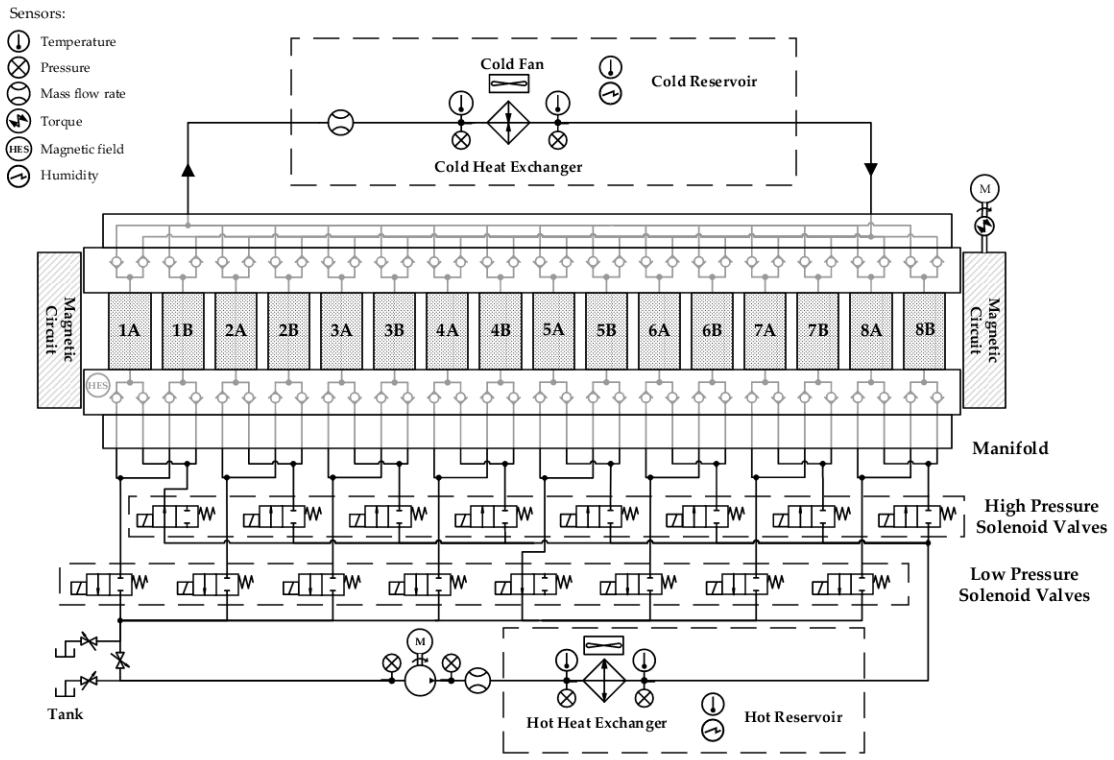


Figure 4.11 – Hydraulic diagram of the MRU.

are arranged in diametrically opposite positions in the air gap. To ensure continuous fluid flow through the HEx, AMR set 1 operates simultaneously with set 5, set 2 with set 6, set 3 with set 7, and set 4 with set 8.

The working fluid is composed of an anticorrosive additive, either 2% volume of ENTEK FNE or 5% volume of ME-1, applied to deionized water to prevent corrosion of the MCM. The first was used in the initial sets of experiments, and the second in subsequent versions of the tests, due to the chemical stability of the MCM, which will be explored later in this chapter.

At the subsystem level, the HMS was designed to achieve an adequate hydraulic profile while minimizing power consumption. Commercially available solenoid valves (Asco SC8210-112/220V-NC) were chosen to control the flow through the AMR beds. Not only do solenoid valves present similar transient responses, but they are also much more flexible regarding changes in operating conditions, robustness, simplicity, and low power consumption (6 W of nominal power consumption per valve) (Santos *et al.*, 2021). The design team also evaluated mechanically actuated valves (Santos *et al.*, 2020), although they proved not to be a superior solution to solenoid valves due to their high power consumption and limited flexibility. At the system level, the HMS design was guided primarily by its operational limitations, particularly in frequency and mass flow rate, as their power consumption and

costs were marginal compared to those of the remaining components.

4.1.5 Heat Exchangers

Due to their favorable thermal-hydraulic characteristics, fan-supplied multicircuited herringbone-wave tube-fin HEx were used to connect the system to the indoor and outdoor chambers. The coupling between the AMR, HEx, and thermal reservoirs creates two characteristic temperature spans: the AMR temperature span, ΔT_{AMR}, and the system temperature span, ΔT_{sys}. Due to the finite sizes of the HEx, the former is always larger than the latter. However, most MR prototypes did not employ actual HEx. Instead, Joule effect heaters were used to generate thermal loads (Kitanovski *et al.*, 2015). As a result, external losses are rarely quantified in the MR literature.

Figures 4.12 (a) and (b) present a picture of the cold and hot heat exchangers, without and with the coupling of the fans, respectively. The HEx dimensions were as follows: 515 mm (height), 550 mm (width), and 245 mm (length), with an eight fins per inch density and tube internal diameter and wall thickness of 11.9 mm and 0.4 mm, respectively. EBM-Papst S4E350-AN19-43 axial fans provided forced air flow through the fin tube arrays.



(a) (b)

Figure 4.12 – Heat Exchangers used in the MRU. Pictures of (a) HEx without the coupling of the fans and (b) with the fans coupled.

At the subsystem level, the $\varepsilon - NTU$ (Kays & London, 1984) method was used to design the HEx using empirical Colburn-j and friction factor relationships (Shah & Sekulic, 2003). At the system level, the contributions of the liquid and air pumping power to HHEx and CHEx were included in the overall system power consumption (Peixer *et al.*, 2022). Moreover, the thermal coupling between the heat transfer fluid and the air in the indoor and outdoor chambers was realized via energy balances in both HEx.

4.1.6 Data Acquisition and Instrumentation

Figure 4.11 indicates the temperature and pressure measurements along the hydraulic circuit. The mass flow rate is measured at the inlets of CHEx and HHEx. The rotor is equipped with torque and power meters, which are also used to measure fan power on the CHEx and HHEx, and pumping power at the hydraulic pump. An encoder and eight Hall-effect sensors measure the angular position of the rotor and magnetic flux density. Data acquisition and control were implemented in LabVIEW using National Instruments hardware (My-Rio 19000 and cDAQ-9179). The expanded uncertainties are presented in Table 4.2.

Table 4.2 – Experimental uncertainties of the measuring instruments installed in the MRU.

Measurement	**Uncertainty**
Fluid temperature	$\pm$ 0.11°C
Air temperature	$\pm$ 0.11°C
Fluid pressure	$\pm$ 0.01 bar
Torque	$\pm$ 0.25 Nm
Power consumption	$\pm$ 3.5 W
Mass flow rate (CHEx)	$\pm$ 6.8 kg h^{-1}
Mass flow rate (HHEx)	$\pm$ 1 %

4.2 Calibrated Calorimeter

The validation and characterization of air conditioning systems are often an expensive and onerous stage in the development of this equipment. Among several options established by the ruling standards, calorimetric methods are widely used in both academic and industrial environments. In general, a calorimeter used to evaluate the performance of an air conditioner is a chamber divided into two independent environments: one for the AC evaporator unit and the other for the condenser unit, both with temperature and humidity control (Ribeiro, 2015). A calibrated calorimeter was developed to test the MRU in accordance with international (ISO-5151, 2017) and Brazilian (Inmetro, 2011; Inmetro, 2012; Inmetro, 2013) standards. Although some specifications were not fully met due to laboratory space limitations, most parameters were within the margins deemed adequate for characterizing the system in a relevant environment.

4.2.1 Design of the Calorimeter

The calibrated calorimeter consists of two chambers separated by an insulated wall to emulate outdoor (warm) and indoor (cold) conditions. Table 4.3 shows the external dimensions of the calorimeter and the internal dimensions of the indoor and outdoor chambers. The walls are insulated with polyisocyanurate, which has a thermal conductivity of 0.02-0.03 W m^{-1} K^{-1}. The wall separating the indoor and outdoor chambers is 150 mm thick, whereas the remaining walls are 70 mm thick. The MRU and the calorimeter are schematically represented in Fig. 4.13.

Table 4.3 – Dimensions of the calorimeter.

Dimensions	**Width [mm]**	**Length [mm]**	**Height [mm]**
External - calorimeter	2200	4860	2640
Internal - indoor chamber	2060	2380	2490
Internal - outdoor chamber	2060	2190	2500

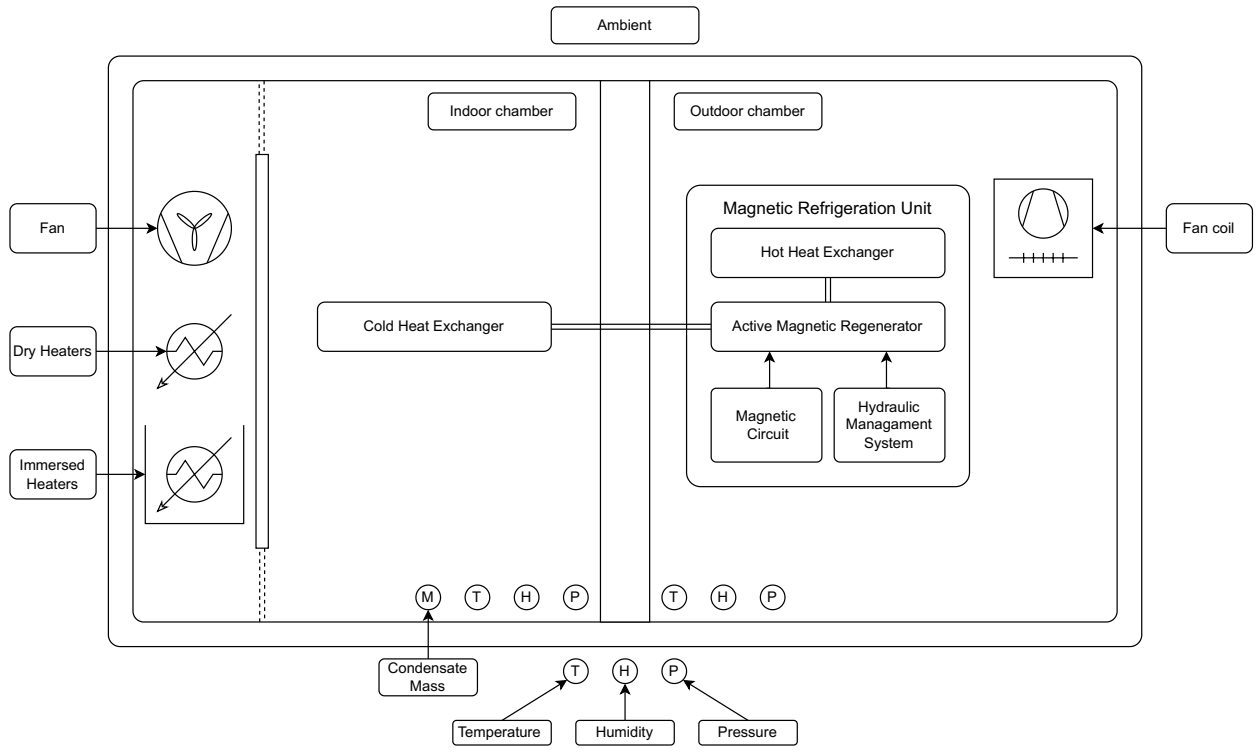


Figure 4.13 – Schematic representation of the MRU and the calorimeter.

The 10.7 m^2 calorimeter, pictured in Fig. 4.14, is divided into two thermally isolated chambers: the cold side (CS) and the hot side (HS). The area surrounding the calorimeter is called outside (OS) and refers to the room where it is located. The walls of the apparatus are made with polyisocyanurate to enhance thermal insulation. Unlike the recommendation in the standards, this calorimeter is closer than 460 mm to the ground and the ceiling of the room due to physical space restrictions. In addition, the HS base is in direct contact with the

floor to better accommodate the MRU. There is no pressure-equalizing device between CS and HS. Instead, three pressure transducers measure the pressure in each environment.

The indoor chamber is equipped with temperature and humidity reconditioning systems, whereas only the temperature is reconditioned in the outdoor chamber. In the indoor chamber reconditioning system, dry electric heaters and electric heaters immersed in water tanks control the temperature and humidity, respectively. The axial fans homogenize the air in the chamber, as shown in Fig. 4.15. The outdoor chamber reconditioning system consists of a fan coil unit coupled with a chiller and tangential fans. The reconditioning equipment for both chambers is summarized in Table 4.4.

The CS is equipped with four pairs of air resistances with a total supply capacity of 3500 W, combined with four fans, providing adequate airflow to the chamber. In addition, there are two reservoirs, each with two water resistances, to control the relative humidity inside the chamber. The CS acquisition system consists of nine thermocouples measuring ambient temperature, one thermocouple in the evaporator discharge, one thermocouple measuring water reservoir temperature, eight relative humidity transducers, and a pressure transducer. In addition, there is a balance that measures the mass of water condensed at the heat exchangers of the evaporator unit. The power of the set of fans, of each water resistance, and of air resistance pairs is measured by power transducers with a range of 1000 W.

The HS is equipped with a fan coil coupled to a chiller for chamber temperature control and a single fan to increase airflow. There is no humidity control inside the HS. Hence, this parameter is only monitored there. Measurements are made with nine thermocouples, eight relative humidity transducers, and a pressure transducer. The power supply for the fan coil and the air conditioning device is measured by a 1000 W and a 2000 W power transducer, respectively.

Lastly, the OS temperature is controlled by ambient air conditioners and measured by seven thermocouples. In the OS, there are also a pressure transducer and a thermo-hygrometer, which provide temperature and humidity measurements. The list of reconditioning equipment used in the three ambients, along with their specifications, is presented in Tab. 4.4.

Table 4.4 – Reconditioning equipment employed in the calorimeter.

Equipment	**Quantity**	**Specifications**
Electric heaters	8	1750 W heating power (each)
Immersion heaters	4	1000 W heating power (each)
Water reservoir	2	30 L stainless steel tanks
Axial fans	4	EBM-Papst S4E350-AN19-43
Fan coil unit	1	30000 Btu h^{-1} cooling capacity
Chiller	1	Connected to the fan coil unit



(a)



(b)



(c)

Figure 4.14 – Calibrated calorimeter developed to evaluate the performance of the MRU. (a) Indoor (b) outdoor chamber, and (c) external view. The vapor compression evaporator and condensing unit shown in (a) and (b) were evaluated for the validation of the calorimeter.



(a) (b)

Figure 4.15 – Reconditioning equipment of the calibrated calorimeter. Picture of (a) axial fans placed in the cold chamber and (b) heaters of the cold chamber.

Nine thermocouples, eight humidity transducers, and one pressure transducer, installed in each chamber, provide data for calculating their respective wet-bulb temperatures. Seven thermocouples and one thermo-hygrometer measure the temperature and humidity of the air surrounding the calorimeter. Electric power is measured by two power transducers with full 1000- and 2000-W scales. The condensate mass is calculated using a calibrated scale. Temperatures are also monitored in the immersion heater and condensate reservoir. The expanded uncertainties of the calorimeter instrumentation are shown in Table 4.5.

Table 4.5 – Experimental uncertainties of the measuring instruments installed in the calorimeter.

Measurement	**Equipment**	**Uncertainty**
Water temperature	Thermocouple	± 0.25°C
Air dry bulb temperature	Thermocouple	± 0.25°C
Air dry bulb temperature	Thermo-hygrometer	± 0.12°C
Air relative humidity	Humidity transducers	± 2.8 %
Air relative humidity	Thermo-hygrometer	± 2 %
Electric Power	Power transducers (1000 W)	± 3.6 W
Electric Power	Power transducers (2000 W)	± 3.6 W
Pressure	Pressure Transducers	± 2 kPa
Mass	Scale	± 0.1 g

4.2.2 Calibration of the Calorimeter

The calibration involved using electric heaters to produce a steady-state thermal load inside the chambers, with a temperature difference of at least 11°C relative to the outside. The overall thermal conductance of the calorimeter walls, UA, is calculated from the wall heat transfer rate and the temperature difference across the walls. Since the heat transfer area is known, the overall heat transfer coefficient, U, can also be calculated. This procedure is repeated three times: first, heating the indoor chamber only; then, heating the outdoor chamber only; and finally, heating both chambers simultaneously. The results are shown in Table 4.6.

Table 4.6 – Results of experimental overall heat transfer coefficient

Wall	UA [W K^{-1}]	U [W m^{-2} K^{-1}]
Partition wall	2.0 ± 0.1	0.358 ± 0.016
CS outer walls	16.4 ± 0.1	0.568 ± 0.005
HS outer walls	19.2 ± 0.1	0.843 ± 0.005

4.3 Design Evolution of the Prototype

The MRU underwent significant alterations during its experimental characterization. Researchers not only gained operational insights from results unattainable solely through mathematical or theoretical models, but also encountered several limitations and challenges that had to be overcome for successful system operation. Despite these deviations from the original design, the team successfully operationalized three versions of the MRU.

Regarding the original MRU design, the primary deviation concerned the availability and configuration of the MCM. The MC, HEx, HMS, pump, motor, AMR casings, and all remaining components that operated the first version of the prototype were the ones specified according to the original design. The main restriction was the lack of MCM available to fill all sixteen AMR beds, due to the limitation of manufacturer. Only half of the original mass intended for the system was provided, so only eight AMRs were used in the first version of the prototype.

The AMR configuration adopted odd-numbered beds, as shown in Fig. 4.11, where every other bed, according to the original design, was an AMR (Fig. 4.16 (a). Specifically, 7.858 kg of La(Fe,Mn,Si)$_{13}$H$_z$ alloys arranged in ten layers and 2.490 kg of Gd mounted in a single layer formed the eight AMR. Table 4.7 provides a breakdown of the total mass and Curie temperature of each MCM layer used in all versions of the MRU. Also, as the HMS requires two electro-valves to operate a pair of AMRs, only eight electro-valves were needed to operate the system.

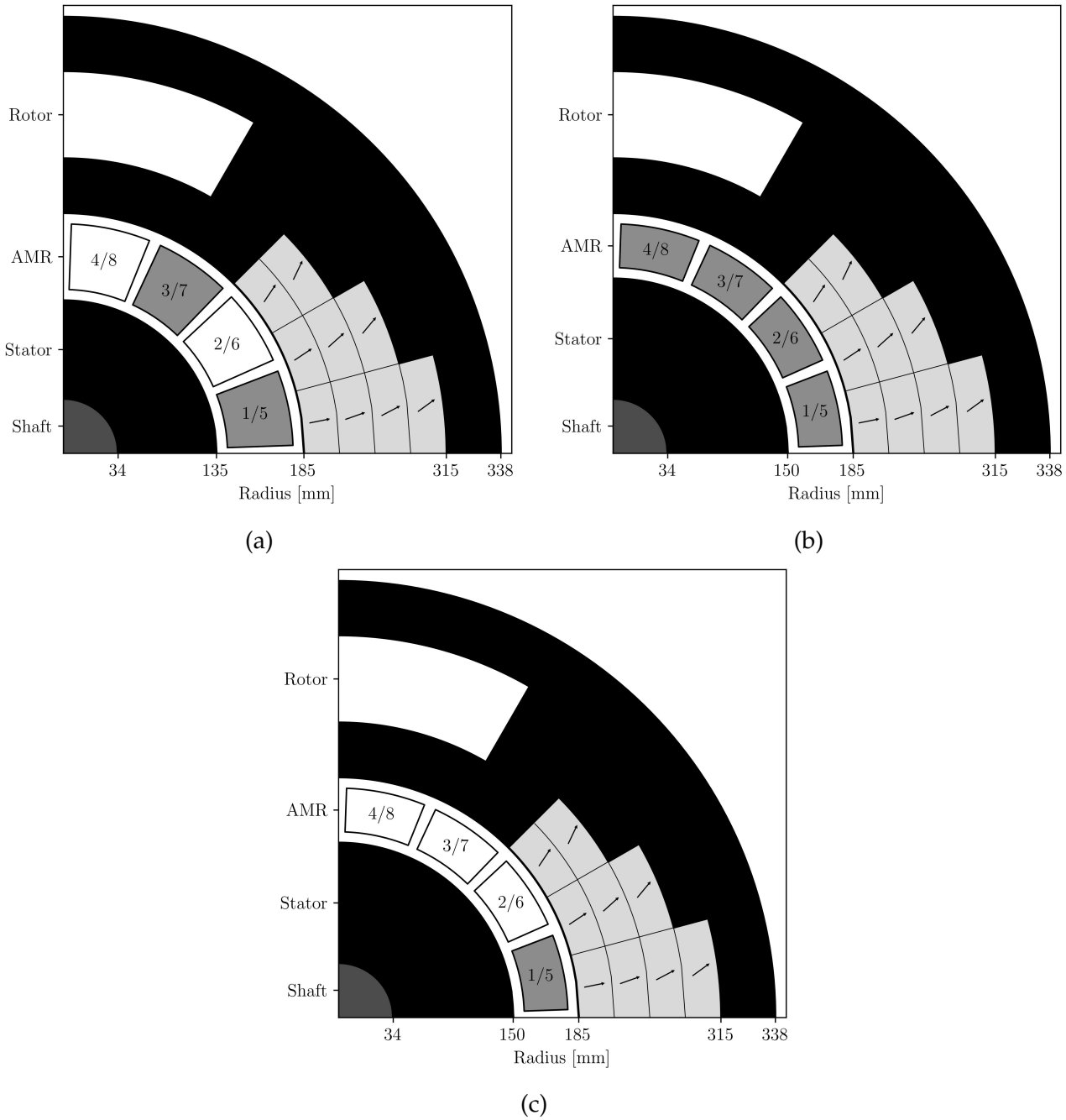


Figure 4.16 – Cross-section view for the configurations of the AMR-MC arranged for each version of the MRU. Black regions: soft magnetic material; white regions: air; light gray regions: hard magnetic material; gray regions: AMRs; Dark gray region at the bottom left: stator/shaft; arrows: remanence directions. The numbering of AMR beds is according to that in Fig. 4.11. Representations of the (a) first, (b) second, and (c) third configurations of the system.

These adaptations enabled the operation, but had significant implications for its performance. Operating with only half the original refrigerant load inevitably reduced the cooling capacity of the system. Furthermore, a critical limitation revealed during system operation was the emergence of preferential magnetic positions during rotor rotation. These positions, unexpected in a continuous array of AMRs, substantially increased the torque to rotate the rotor. Consequently, the frequency of the system was restricted to 0.6 Hz (Pagnan *et al.*, 2022), despite the HMS and mechanical transmission system supporting frequencies up

Table 4.7 – Mass and Curie Temperature for the layers that compose the AMR beds for each version of the MRU.

Material			**Mass [g]**		
Layer	**Material**	T_{curie} **[°C]**	**Version 1**	**Version 2**	**Version 3**
1	$La(Fe,Mn,Si)_{13}H_z$	15.0	0	483	425
2	$La(Fe,Mn,Si)_{13}H_z$	16.8	0	570	700
3	Gd	17.0	2490	4070	2150
4	$La(Fe,Mn,Si)_{13}H_y$	19.3	786	758	0
5	$La(Fe,Mn,Si)_{13}H_y$	22.2	786	810	0
6	$La(Fe,Mn,Si)_{13}H_y$	24.6	786	814	0
7	$La(Fe,Mn,Si)_{13}H_y$	27.9	786	781	0
8	$La(Fe,Mn,Si)_{13}H_y$	30.0	786	816	0
9	$La(Fe,Mn,Si)_{13}H_y$	32.6	786	819	0
10	$La(Fe,Mn,Si)_{13}H_y$	34.6	786	880	0
11	$La(Fe,Mn,Si)_{13}H_y$	36.4	786	864	0
12	$La(Fe,Mn,Si)_{13}H_y$	39.0	786	0	0
13	$La(Fe,Mn,Si)_{13}H_y$	41.3	786	0	0
$\mathbf{m_{La}}$ **[g](%)**			7858 (76%)	7595 (65%)	1125 (34%)
$\mathbf{m_{Gd}}$ **[g](%)**			2490 (24%)	4070 (35%)	2150 (66%)
$\mathbf{m_{mcm}}$ **[g]**			10348	11665	3275

to 1.5 Hz (Santos *et al.*, 2021). Furthermore, the mass flow rate was limited to 1600 kg h^{-1} due to the reduced number of beds available for fluid flow, and the blow fraction was fixed at 30%. Lastly, the system operated at a hot reservoir temperature of 35°C, in accordance with international standards (ISO-5151, 2017).

Despite the limitations encountered in the first version, significant advances have been made in its characterization. During the course of the project, the design team formulated strategies to address the MCM mass constraint, focusing on redesigning AMR and MC geometries. By narrowing the air gap, it became feasible to reduce the mass and volume of MCM per regenerator, enabling the use of all sixteen beds while also increasing peak magnetic flux densities. Given the impracticality of modifying the rotor due to the required investment, the team concentrated on redesigning the stator, specifically adjusting its outer radius (R_o). This adjustment required the manufacture of novel electrical steel sheets, flanges, and AMR casings.

However, upon opening the AMR beds after the characterization of the first version ended, degradation was observed on some of the $La(Fe,Mn,Si)_{13}H_z$ alloys. It was characterized as a visible reddish power and was discussed in detail by Döring *et al.* (2024b). It was particularly severe at the last two Curie temperatures on the hot side (39.0 and 41.3° C), making them unsuitable for future testing. The primary hypothesis for this deterioration was the inadequacy of the working fluid, a volumetric solution of 2% ENTEK FNE, which later proved ineffective in inhibiting corrosion in $La(Fe,Mn,Si)_{13}H_z$ alloys (Döring *et al.*, 2024b). In

response, a new strategy was devised, involving the use of a 5% volumetric solution of the commercial corrosion inhibitor ME-1.

The remaining mass of La(Fe,Mn,Si)$_{13}$H$_z$ alloys and Gd available in the laboratory was pooled and used to fill the new beds in the second version of the prototype. The outer radius of the stator was increased from 135 to 150 mm, while the dimensions of the regenerator (height, width, and length) were reduced from 45, 57, and 130 to 25, 52, and 129 mm, respectively. This enabled the integration of sixteen AMR beds into the system, as shown in Fig. 4.11 and Fig. 4.16 (b). The AMR beds comprised 7.595 kg of La(Fe,Mn,Si)$_{13}$H$_z$ alloys arranged in 10 layers and 4.070 kg of Gd in a single layer, as detailed in Table 4.7. Consequently, sixteen electro-valves were necessary to operate the system effectively.

The continuous arrangement of AMR beds allowed the system to operate at higher frequencies, achieving up to 1.3 Hz. This enhancement, coupled with the increase in MCM mass, allowed for mass flow rates of up to 2250 kg h^{-1}, the highest reported in MR prototypes. Moreover, by reducing the magnetized gap, the peak magnetic flux density was increased from 1.17 to 1.47 T, while a blow fraction of 35% was implemented. Furthermore, to account for the alteration in the MCM arrangement, the temperature of the hot heat reservoir during the experiments was set to 32°C, thereby optimizing the operational conditions.

The characterization of the prototype was carried out in accordance with the planned experiments. However, when disassembling the AMR beds after experimentation, there was further deterioration of the La(Fe,Mn,Si)$_{13}$H$_z$ alloys on the hot side of the regenerator. The affected layers exhibited varying degrees of degradation, ranging from Curie temperatures of 19.3 to 36.4° C, making them unsuitable for continued use. Unlike the previous version, where visible deterioration signals were the formation of reddish powders representative of chemical degradation (Döring *et al.*, 2024b), those encountered in the second version were related to particle atomization into smaller diameters, characteristic of mechanical degradation. The central hypothesis is that the high transient hydraulic pressures on the hot side of the regenerator caused by the water hammers, due to the increased mass flow rates and operating frequencies, contributed to the deterioration of La(Fe,Mn,Si)$_{13}$H$_z$ alloys. The unnoticeable chemical deterioration of the alloys in the previous version might have contributed to the mechanical degradation. Both likely caused the atomization of the La(Fe,Mn,Si)$_{13}$H$_z$ layers, whereas Gd, with its higher ductility and chemical stability, remained stable. As a result, a decision was made to design a third version of the MRU that exclusively utilized Gd and La(Fe,Mn,Si)$_{13}$H$_z$ alloys with lower Curie temperatures of 15.0 and 16.8°C.

In the third version, AMR and MC remained unchanged, but due to material constraints, only four AMR beds could be assembled, as illustrated in Fig. 4.16 (c). This configuration used a total of 1.125 kg of La(Fe,Mn,Si)$_{13}$H$_z$ alloys and 2.150 kg of Gd, as detailed in Table 4.7. It should be noted that during the operation of the second version, there was some

mixing between Gd and the $La(Fe,Mn,Si)_{13}H_z$ alloy with Curie temperature of 16.8°C, as evidenced by the comparison of masses in Table 4.7 between versions two and three. Despite this mixing, given the proximity of the Curie temperatures, it was determined to utilize both materials in the third version.

With only four AMR beds installed, the system required four electro-valves for operation. The exact working fluid solution, proven effective as a long-term corrosion inhibitor for $La(Fe,Mn,Si)_{13}H_z$ alloys, was retained (Döring *et al.*, 2024b). Given the key learning from the second version regarding the chemical and mechanical stability of $La(Fe,Mn,Si)_{13}H_z$, Gd was strategically placed on the layer most exposed to high hydraulic stresses on the hot side of the system.

To mitigate the high torque generated by operating with a discontinuous AMR arrangement, a novel solution called dummy generators was developed (Pagnan *et al.*, 2022). This involved filling the AMR bed casings with soft-magnetic material spheres and positioning them at the locations around the stator where no AMRs were installed (spots 2/6, 3/7, and 4/8 in Fig. 4.16 (c). This approach significantly reduced the torque required to rotate the rotor, allowing operation at frequencies up to 1 Hz and achieving mass flow rates of up to 800 kg h^{-1}, with blow fractions set at 35% and 40%. Furthermore, considering the reduction in the maximum Curie temperature of the materials, the temperature of the hot reservoir was adjusted to 18° C. A summary comparing the key design characteristics of the three versions of the MRU is provided in Table 4.8.

Table 4.8 – Summary of the main distinct design characteristics for each version of the MRU.

Parameter	**Version 1**	**Version 2**	**Version 3**
N_{amr} [-]	8	16	4
N_{dummy} [-]	0	0	12
m_{La} [g]	7858	7595	1125
m_{Gd} [g]	2490	4070	2150
m_{mcm} [g]	10348	11665	3275
N_{sv} [-]	8	16	4
N_{Curie} [-]	11	11	3
$T_{\mathrm{Curie}}^{\mathrm{max}}$ [°C]	41.3	36.4	17
$T_{\mathrm{Curie}}^{\mathrm{min}}$ [°C]	17	15	15
R_{o} [mm]	135	150	150
B_{max} [T]	1.17	1.47	1.47
H_{amr} [mm]	45	25	25
W_{amr} [mm]	57	52	52
L_{amr} [mm]	130	129	129
Anti-corrosive fluid (vol. %)	ENTEK (2%)	ME-1 (5%)	ME-1 (5%)

4.4 Performance Metrics of the System

Several methodologies and metrics are used to evaluate the thermodynamic performance of magnetic refrigerators. For that, this work seeks to conduct a thorough analysis of the primary sources of irreversibility. This can be accomplished through the extensive instrumentation at the MRU, which enables characterization of temperature differences, heat transfer rates, pressure drops, torques, and power consumption.

The first metric to be evaluated is the temperature span. In refrigeration systems, more specifically magnetic ones, the interaction between AMR, HEx, and thermal reservoirs leads to two distinct temperature spans: the AMR temperature span, ΔT_{amr}, and the system temperature span, ΔT_{sys}, as follows:

$$\Delta T_{\mathrm{amr}} = T_{\mathrm{CB}}^{\mathrm{out}} - T_{\mathrm{HB}}^{\mathrm{out}} \tag{4.1}$$

$$\Delta T_{\mathrm{sys}} = T_{\mathrm{H}} - T_{\mathrm{C}} \tag{4.2}$$

where $T_{\mathrm{HB}}^{\mathrm{out}}$ is taken as the temperature of the fluid in the outlet manifold of the hot side, and $T_{\mathrm{CB}}^{\mathrm{out}}$ is measured at the same spot on the cold side. On the other hand, T_{H} is determined from an average of the temperature measurements in the outdoor chamber, and an average of the temperature measurements in the indoor calorimeter chamber also gives T_{C}. In conventional refrigeration systems, the temperature span typically dictates the entire system design. However, because HEx is absent in most magnetic refrigeration prototypes, the AMR temperature span is used as a performance metric.

For a complete assessment of the power consumption of the system, it is essential to obtain information from a breakdown of its components. The total torque of the system, denoted as τ_{sys}, can be computed as follows:

$$\tau_{\mathrm{sys}} = \tau_{\mathrm{mag}} + \tau_{\mathrm{trans}} + \tau_{\mathrm{par}} \tag{4.3}$$

where the torque components in Eq. (4.3) were obtained from measurements at three different stages of the system assembly. First, the torque required to rotate only the rotor was measured, representing the mechanical transmission losses (τ_{trans}). Second, the stator and casings were installed, and the torque was measured again, capturing both mechanical transmission and parasitic losses ($\tau_{\mathrm{trans}} + \tau_{\mathrm{par}}$). Finally, the torque during regular operation was measured (τ_{sys}), which includes all previous contributions plus the torque required to magnetize the MCM (τ_{mag}), which is the share responsible for generating the magnetocaloric effect on the material and the refrigerating effect in the system.

The total pressure drop of the system, ΔP_{sys}, can be calculated by:

$$\Delta P_{\mathrm{sys}} = \Delta P_{\mathrm{amr}} + \Delta P_{\mathrm{tub}} + \Delta P_{\mathrm{aux}} + \Delta P_{\mathrm{HHEx}} + \Delta P_{\mathrm{CHEx}} \tag{4.4}$$

where ΔP_{amr} encompasses the pressure drop of the AMR during hot and cold blows; ΔP_{tub} the pressure drop of tubing and connections along all fluid lines; ΔP_{aux} the pressure drop of the auxiliary components of the AMR, *i.e.*, the casings, manifolds, end parts, check valves, and solenoid valves; ΔP_{HHEx} and ΔP_{CHEx} the pressure drop of HHEx and CHEx, respectively. Each pressure drop term was calculated as the difference between the pressure transducer measurements. The pressure drop of the AMR, ΔP_{amr}, was obtained as the difference between the measured pressure drop across the manifolds with the MCM in place and the corresponding pressure drop measured at the same locations without the MCM installed (the latter corresponding to ΔP_{aux}). In this work, ΔP_{amr} refers to the pressure drop of a pair of AMRs, one going through the hot and the other through the cold blow. The value of ΔP_{amr} was calculated by the difference between the pressure measurement in the manifolds with and without MCM in the casing, the latter being ΔP_{aux}. The value of ΔP_{tub} was given by the difference between ΔP_{sys}, taken at the inlet and outlet ports of the hydraulic pump, and the remaining contributions of the pressure drop. The pressure drop of the AMR was estimated through the correlation developed by (Ergun, 1952), which can be calculated as:

$$\Delta P_{\mathrm{amr}} = 150\frac{\mu_{\mathrm{f}}(1-\varphi)^2 v_{\mathrm{s}}}{d_{\mathrm{p}}^2\varphi^3}L_{\mathrm{amr}} + 1.75\frac{\rho_f(1-\varphi)v_{\mathrm{s}}^2}{d_{\mathrm{p}}\varphi^3}L_{\mathrm{amr}} \tag{4.5}$$

where fluid properties are taken as those of pure water at the mean temperature of the AMR. Given that the particles of the porous medium present considerable variation in morphology and particle diameter, it is expected that the porous medium is not homogeneously structured (Vieira *et al.*, 2021; Masche *et al.*, 2021). For that, Eq. (4.5) is calibrated with experimental data and a correction in porosity is applied (Vieira *et al.*, 2021), as previously presented in this dissertation.

The power of the mechanical transmission system, $\dot{W}_{\mathrm{mt}}$, is measured by a power transducer and is determined by the following:

$$\begin{aligned}\dot{W}_{\mathrm{mt}} &= \dot{W}_{\mathrm{mt,mag}} + \dot{W}_{\mathrm{mt,trans}} + \dot{W}_{\mathrm{mt,par}} + \dot{W}_{\mathrm{mt,loss}} \\ &= \omega\left(\tau_{\mathrm{mag}} + \tau_{\mathrm{trans}} + \tau_{\mathrm{par}}\right) + \dot{W}_{\mathrm{mt,loss}}\end{aligned} \tag{4.6}$$

where $\dot{W}_{\mathrm{mt,mag}}$ is the share associated with the magnetic interaction between the MCM and the MC; $\dot{W}_{\mathrm{mt,trans}}$ the share related to the transmission system, *i.e.*, bearings; and $\dot{W}_{\mathrm{mt,par}}$ the share associated with the parasitic torque generated by eddy currents in the stator and casings of the AMRs; and $\dot{W}_{\mathrm{mt,loss}}$, the share associated with the power dissipated due to irreversibilities in the motor. Each of the terms on the right side of Eq. (4.6) can be calculated by the product between the torque, given by Eq. (4.3), and the angular velocity, except for $\dot{W}_{\mathrm{mt,loss}}$. This share is calculated by the difference between the power input for the motor $\dot{W}_{\mathrm{mt}}$, and the useful power provided for the system $\dot{W}_{\mathrm{mt,mag}} + \dot{W}_{\mathrm{mt,trans}} + \dot{W}_{\mathrm{mt,par}}$.

The pumping power of the system, $\dot{W}_{\mathrm{pp}}$, is measured by a power transducer connected to the hydraulic pump and is given by the following:

$$\begin{aligned}\dot{W}_{\mathrm{pp}} &= \dot{W}_{\mathrm{pp,amr}} + \dot{W}_{\mathrm{pp,aux}} + \dot{W}_{\mathrm{pp,tub}} + \dot{W}_{\mathrm{pp,HHEx}} + \dot{W}_{\mathrm{pp,CHEx}} + \dot{W}_{\mathrm{pp,loss}} \\ &= \frac{\dot{m}_{\mathrm{f}}}{\rho_{\mathrm{l}}} \left(\Delta P_{\mathrm{amr}} + \Delta P_{\mathrm{aux}} + \Delta P_{\mathrm{tub}} + \Delta P_{\mathrm{HHEx}} + \Delta P_{\mathrm{CHEx}}\right) + \dot{W}_{\mathrm{pp,loss}}\end{aligned} \tag{4.7}$$

where $\dot{W}_{\mathrm{pp,amr}}$ is the pumping power of the AMR during hot and cold blows; $\dot{W}_{\mathrm{pp,aux}}$ is the pumping power of the auxiliary components of the AMR, *i.e.*, the casings, manifolds, end parts, check valves and solenoid valves; $\dot{W}_{\mathrm{pp,tub}}$ is the pumping power of the tubing and connections along the entire fluid line, $\dot{W}_{\mathrm{pp,CHEx}}$ and $\dot{W}_{\mathrm{pp,HHEx}}$ the pumping power of liquid in HHEx and CHEx, respectively; and $\dot{W}_{\mathrm{pp,loss}}$ the power dissipated in the pump due to irreversibilities. Each of the terms in Eq. (4.7) can be calculated by the product between the pressure drop, given by the terms in Eq. (4.4) and the mass flow rate (measured by the mass flow rate meters) divided by the density of the liquid, except for $\dot{W}_{\mathrm{pp,loss}}$. This contribution is calculated by means of the difference between the input power to the pump, measured by a power transducer, and the product of the volumetric flow rate and pressure drop of the system, ΔP_{sys}.

The total power consumption of the system, $\dot{W}_{\mathrm{sys}}$, is calculated as follows:

$$\dot{W}_{\mathrm{sys}} = \dot{W}_{\mathrm{pp}} + \dot{W}_{\mathrm{mt}} + \dot{W}_{\mathrm{HHEx,fan}} + \dot{W}_{\mathrm{CHEx,fan}} + \dot{W}_{\mathrm{SV}} \tag{4.8}$$

As highlighted previously, many studies consider only the power consumption shares related to the AMR in their performance evaluation. Therefore, the idealized (internal) power consumption of the AMR, $\dot{W}_{\mathrm{amr}}$, can be calculated as:

$$\dot{W}_{\mathrm{amr}} = \Delta P_{\mathrm{amr}} \dot{V}_{\mathrm{amr}} + \tau_{\mathrm{mag}} \omega \tag{4.9}$$

Given that the prototype is tested in a calibrated calorimeter, distinct methodologies can be used to evaluate the cooling capacity. The first is based on the energy balance in the AMR, resulting in $\dot{Q}_{\mathrm{C,amr}}$. In contrast, the second is based on the energy balance on the indoor (cold) chamber of the calorimeter, resulting in $\dot{Q}_{\mathrm{C,sys}}$, These metrics can be calculated, respectively, by:

$$\dot{Q}_{\mathrm{C,amr}} = \dot{m}_{\mathrm{f}} c_{\mathrm{p}} \Delta T_{\mathrm{C,amr}} \tag{4.10}$$

$$\dot{Q}_{\mathrm{C,sys}} = \dot{W}_{\mathrm{fan}} + \dot{W}_{\mathrm{heat}} + \dot{Q}_{\mathrm{wall}} \tag{4.11}$$

where in Eq. (4.10) $\Delta T_{\mathrm{C,amr}}$ is the temperature difference between the fluid entering and exiting the cold end of the AMR, measured in the manifolds on the cold side. In Eq. (4.11), $\dot{W}_{\mathrm{fan}}$ represents the power supplied to the fans, $\dot{W}_{\mathrm{heat}}$ is the power to the heaters and $\dot{Q}_{\mathrm{wall}}$ is the heat gain through the walls of the inner chamber. Since the liquid did not reach the air's dew point, no condensation or latent heat contribution was involved.

In addition, it is fundamental to consider that the power supplied to the CHEx fan is dissipated in the cold environment and cannot be accounted for as useful cooling capacity. Therefore, although the refrigeration system removes heat at a rate given by $\dot{Q}_{\mathrm{C,sys}}$, a fraction of it is consumed to absorb the heat generated by a component of the system itself. For this, the net cooling capacity, $\dot{Q}_{\mathrm{C,net}}$, is defined as the useful cooling capacity of the system and can be calculated by the heat transfer rate absorbed by the CHEx minus the work dissipated as heat by the fan, $\dot{W}_{\mathrm{CHEx,fan}}$, which is calculated by the following:

$$\dot{Q}_{\mathrm{C,net}} = \dot{Q}_{\mathrm{C,sys}} - \dot{W}_{\mathrm{CHEx,fan}} \tag{4.12}$$

Hence, given the definitions of the different cooling capacities, temperature spans, and power consumption, the performance of the system can be assessed via the COP and second-law efficiency. The COP from the AMR and system perspectives, COP_{amr} and COP_{sys}, respectively, can be calculated by:

$$COP_{\mathrm{amr}} = \frac{\dot{Q}_{\mathrm{C,amr}}}{\dot{W}_{\mathrm{amr}}} \tag{4.13}$$

$$COP_{\mathrm{sys}} = \frac{\dot{Q}_{\mathrm{C,net}}}{\dot{W}_{\mathrm{sys}}} \tag{4.14}$$

To evaluate the irreversibility sources of the system in more depth, a second-law analysis of its performance is conducted. For that, the COP of Carnot of the AMR and of the MRU, $COP_{\mathrm{cnt,amr}}$ and $COP_{\mathrm{cnt,sys}}$, respectively, are calculated by:

$$COP_{\mathrm{cnt,amr}} = \frac{T_{\mathrm{HB}}^{\mathrm{out}}}{T_{\mathrm{CB}}^{\mathrm{out}} - T_{\mathrm{HB}}^{\mathrm{out}}} \tag{4.15}$$

$$COP_{\mathrm{cnt,sys}} = \frac{T_{\mathrm{C}}}{T_{\mathrm{H}} - T_{\mathrm{C}}} \tag{4.16}$$

Lastly, a second-law efficiency analysis of the system is performed to understand its irreversibilities better. For this, different parameters are determined, seeking to evaluate the losses associated with various domains of the system (de SÁ *et al.*, 2023). The external second law efficiency, η_{ext}, which accounts for the irreversibilities due to the increase in the temperature span on the HEx, is defined as:

$$\eta_{\mathrm{ext}} = \frac{COP_{\mathrm{cnt,amr}}}{COP_{\mathrm{cnt,sys}}} \tag{4.17}$$

The second law efficiency of the AMR, η_{amr}, which accounts for the irreversibilities associated with the operation of the AMR, also known as internal (de SÁ *et al.*, 2023), is defined as:

$$\eta_{\mathrm{amr}} = \frac{COP_{\mathrm{amr}}}{COP_{\mathrm{cnt,amr}}} \tag{4.18}$$

The auxiliary second law efficiency, η_{aux}, which accounts for the irreversibilities of the auxiliary components of the MRU, that is, the components other than the AMR, is defined as:

$$\eta_{\text{aux}} = \frac{COP_{\text{sys}}}{COP_{\text{amr}}} \tag{4.19}$$

Finally, the second-law efficiency of the MRU, η_{sys}, which accounts for the total irreversibilities of the system, is defined as:

$$\eta_{\text{sys}} = \frac{COP_{\text{sys}}}{COP_{\text{cnt,sys}}} = \eta_{\text{ext}}\eta_{\text{amr}}\eta_{\text{aux}} \tag{4.20}$$

4.5 Outline of the Chapter

This chapter presents the experimental apparatus developed for evaluating the magnetic refrigeration prototype. The description encompassed the main subsystems of the magnetic refrigeration unit, namely, the MC, the AMRs, the HMS, and the HEx. The integration of these components within a calibrated calorimeter was detailed, ensuring that the thermal loads and cooling capacity of the prototype could be measured under controlled conditions. The instrumentation and data acquisition system were also introduced. In addition, the chapter highlighted the evolution of the prototype design, with refinements aimed at reducing losses and improving reliability over the successive iterations. Finally, the performance metrics adopted for the system were defined, such as cooling capacity, temperature range, coefficient of performance, and second-law efficiency. These metrics establish the foundation for the systematic analysis of the experimental results, which will be discussed in the following chapter.

Chapter 5

EXPERIMENTAL PERFORMANCE EVALUATION OF THE SYSTEM

This chapter presents the experimental evaluation of the MRU. It begins with the individual characterization of key components specific to MR, including MC, MCM, AMR, and HMS. Following this, the overall performance of three prototype generations is analyzed and compared using the performance metrics described in the previous chapters, and compared with the results attained by the most relevant prototypes reported in the literature. Finally, a detailed thermodynamic evaluation is conducted on the prototype version that demonstrated the best operating conditions for air conditioning applications.

5.1 Component Characterization

To better understand the performance of the MRU, the components that make up the system were individually characterized before the overall evaluation of the system. This section presents results for the standalone assessment of key performance metrics and operational results of the MC, MCM, AMR, and HMS.

5.1.1 Magnetic Circuit

According to the description provided in Section 4.3, the MC has gone through two different geometries, based on variations that were mainly characterized by alterations in the external radius of the stator. This approach was chosen because of the high financial cost associated with modifying the rotor, which prevented alterations to its geometry or configuration. In the first configuration, which corresponds to the original design, the stator features a smaller external radius of 134 mm, according to Fig. 4.16 (a), resulting in a larger air gap between the rotor and the stator.

Figure 5.1 presents a comparison between the experimental and numerical results for the magnetic flux density modulus B, measured in the center of the AMR gap as a function of the angular position Θ for this initial configuration. The experimental data were obtained with a Gaussmeter (LakeShore 425) and a transverse probe (MMT-6J04-VF).

Good agreement is observed between the experimental and simulated results, particularly in low-field regions and areas with sharp variations in magnetic flux density, characteristic features of MC studies (Trevizoli *et al.*, 2015; Fortkamp *et al.*, 2023). The maximum

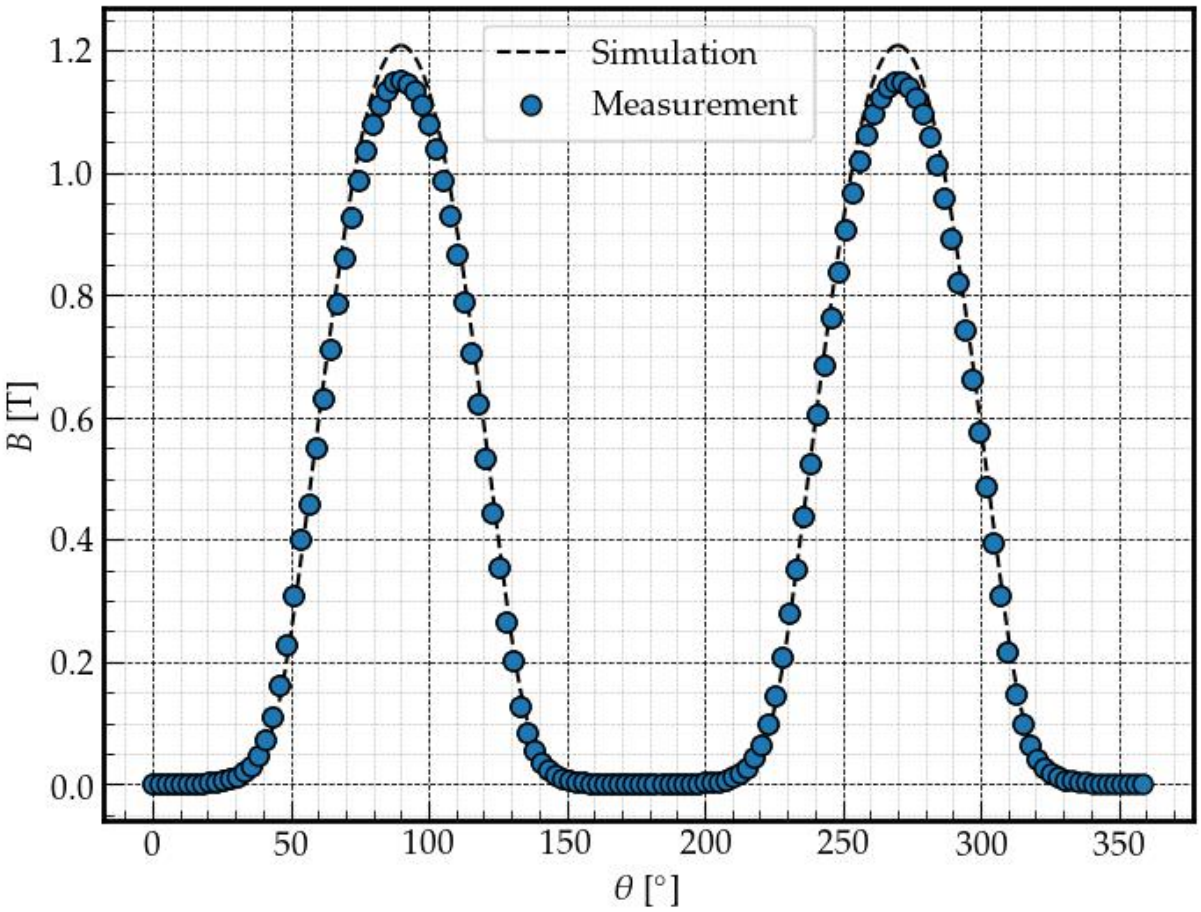


Figure 5.1 – Comparison between experimental data and numerical results for the modulus of the magnetic flux density at the center of the magnetic gap for the first configuration of the MC.

deviation, which remains below 5%, occurs near the peak of the magnetic field. Additionally, the low-field region spans a wide portion of the magnetized volume and approaches 0 T, which is a critical requirement for AMR operation. Although the high-field region does not exhibit as broad a plateau as observed in other systems (Lozano *et al.*, 2016), high magnetic flux density values were achieved, with a peak reaching 1.17 T.

The updated MRU design increased the outer radius of the stator from 135 mm in the original version to 150 mm, resulting in a significant increase in the peak magnetic flux density at the center of the radial magnetic gap from 1.17 T to 1.47 T. To evaluate this improvement, the modulus of the magnetic flux density as a function of the angular position in the air gap, θ, was compared for the complete updated MC. Figure 5.3 presents this Comparison, including results from the original MRU configuration.

As shown in Fig. 5.2, excellent agreement was again observed between the numerical simulations and the experimental measurements. The deviation at the peak magnetic flux density remained below 8%, demonstrating the reliability of the simulation model. The low-field region continues to span a significant portion of the magnetized volume and remains consistent with the requirements for AMR operation. Overall, the peak magnetic flux

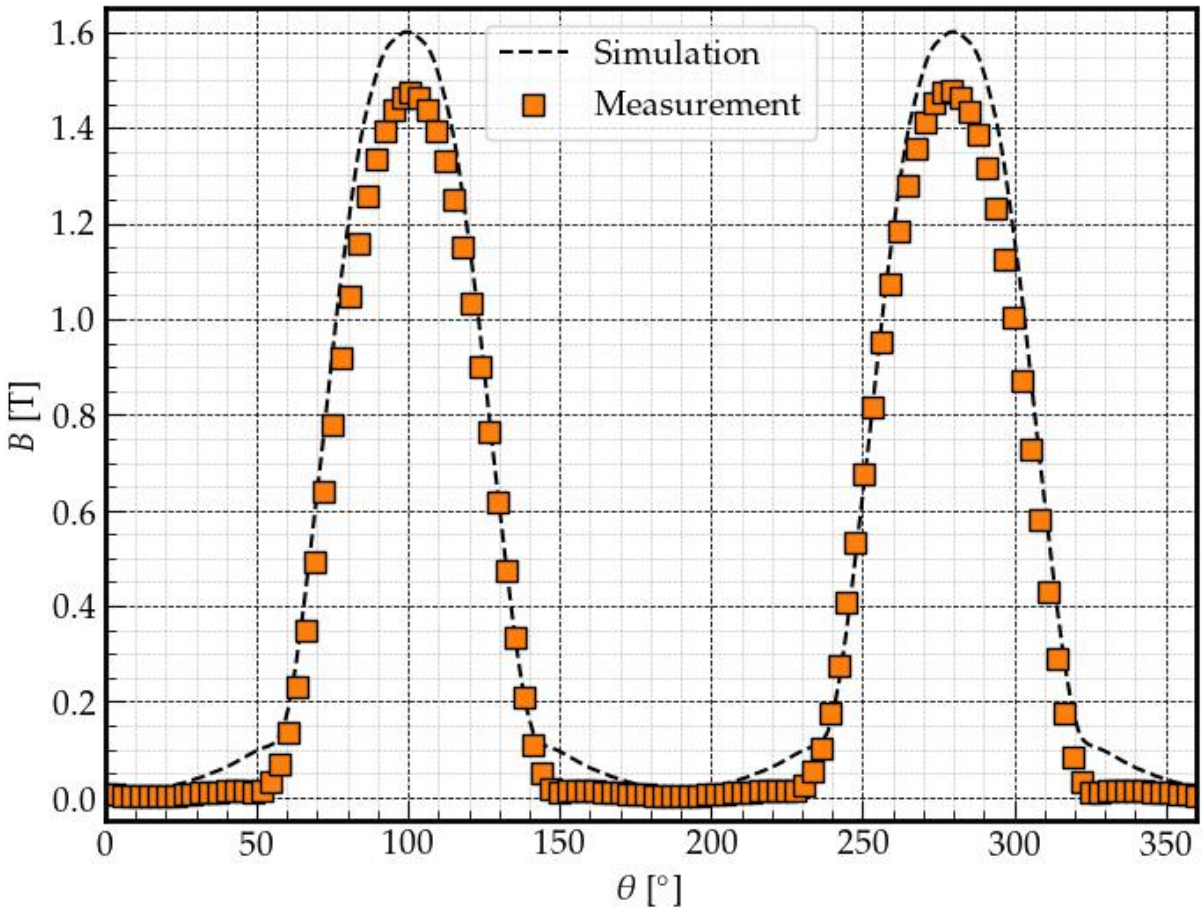


Figure 5.2 – Comparison between experimental data and numerical results for the modulus of the magnetic flux density at the center of the magnetic gap for the second configuration of the MC.

density increased by approximately 25%, from 1.17 T to 1.47 T. This enhancement is primarily attributed to a reduction of roughly 44% in magnetized volume, as the outer radius of the stator increased from 134 mm to 150 mm. The updated design preserves the characteristic low and high-field regions, while introducing a sharper transition between them, an improvement that offers performance advantages for AMR systems (Fortkamp *et al.*, 2020b).

To better understand the increase in magnetic flux density, Fig. 5.3 compares the experimental measurements for the first and second configurations of the MC. The increase in peak values between the two versions is clearly noticeable. Additionally, configuration 2 exhibits steeper transitions between the high- and low-field regions, which are more clearly observed when both profiles are visualized in the same figure and can be advantageous for MR operation. The durations of the low- and high-magnetic field plateaus were similar in both versions, due to the exact PM positioning, as the rotor remained unchanged.

5.1.2 Magnetocaloric Materials

As discussed in Section 4.3, the availability of MCM was the primary driving factor behind the modifications that led to the three generations of the MRU. Beyond the lim-

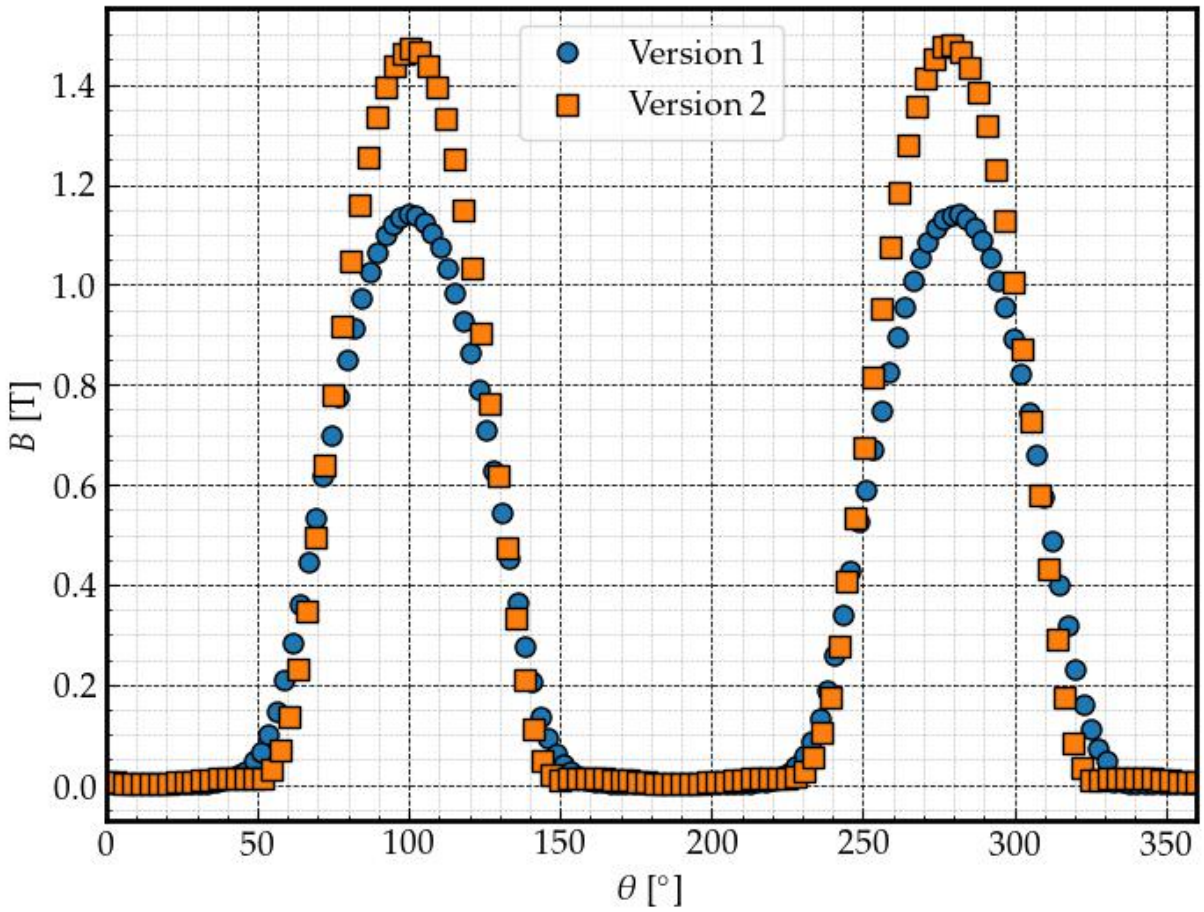


Figure 5.3 – Comparison between the experimental measurements from the first and second configurations of the MC.

ited supply from the manufacturer, the material also underwent chemical and mechanical degradation during system operation, further constraining options for assembling the AMR. Among the challenges faced by the design team, the lack of chemical stability of the materials was a critical issue that needed to be addressed during system operation.

The problem first emerged in the initial iteration of the MRU, when, after disassembling the AMRs, corrosion was visually detected in the alloys with the two hottest Curie temperatures of the system. The anticorrosive fluid was hypothesized not to provide adequate protection to the MCMs. To investigate this, an individual study on the effect of anticorrosive fluids in CV-HS2 was conducted by Döring *et al.* (2024a). The authors presented the first long-term aging study on lanthanum-based alloys reported in the literature, in which particles of three different Curie temperatures values (T_{C1}, T_{C2}, and T_{C3}) were immersed in pure water, in a solution of Entek FNE (2% vol) as recommended by the manufacturer, and in ME-1 (5% vol) and ME-3 (5% vol), two commercial anticorrosive additives. After the experiments, the particles were evaluated through visual inspection and thermomagnetic characterization.

Figure 5.4 presents the results of scanning electron microscopy (SEM) performed with a Jeol JSM-6390LV, where surface changes were examined using backscattered-electron (BSE)

and secondary-electron (SE) modes, together with optical microscopy (OM) observations obtained with a USB-type microscope during immersion.

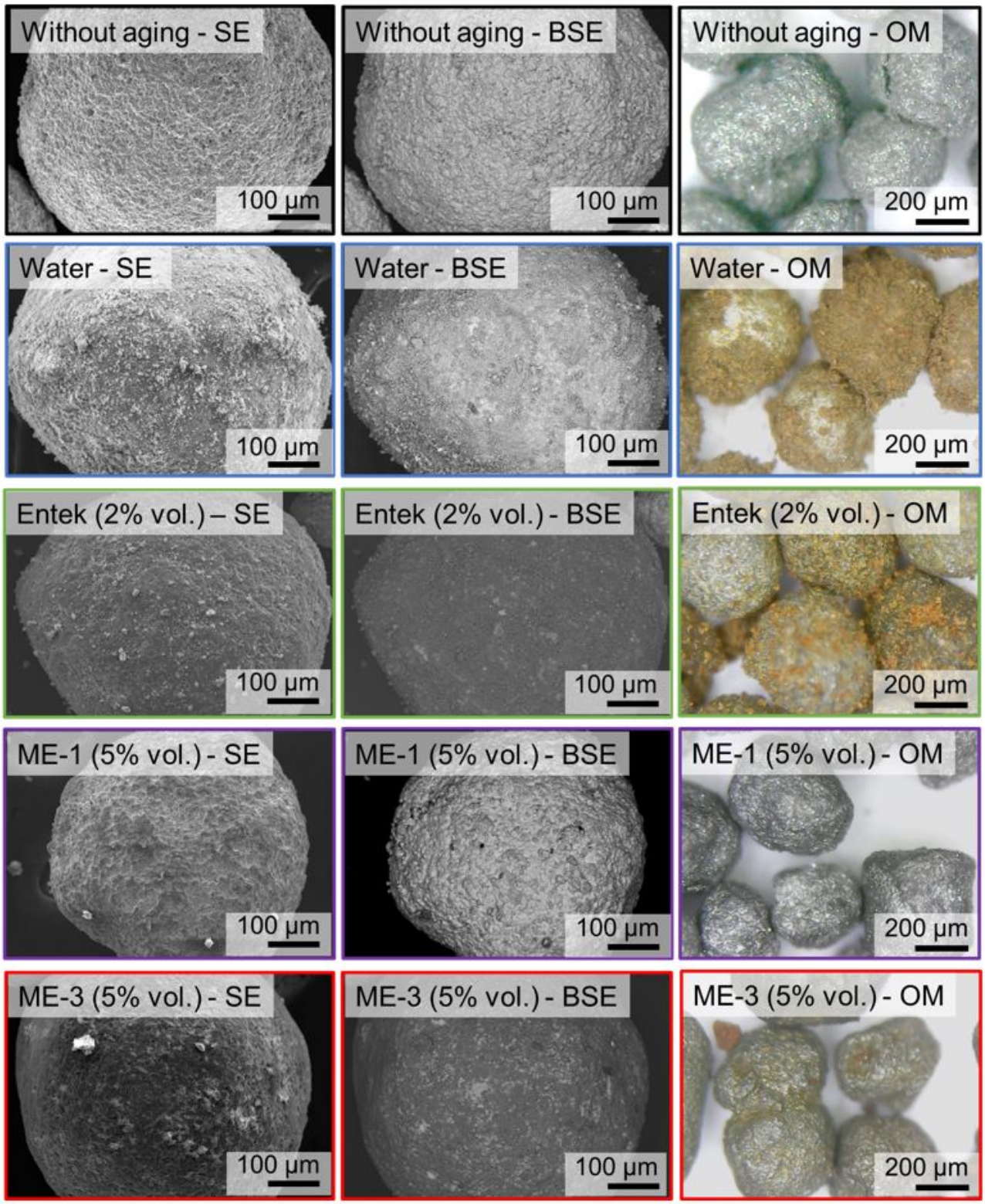


Figure 5.4 – SEM-SE (left), SEM-BSE (middle), and OM (right) images of microparticles of T_{C2} before and after immersion testing over a year (Döring *et al.*, 2024a).

According to Fig. 5.4, the microparticles immersed in water developed a brittle. These surface products were loosely bound and could be removed by rolling the microspheres on filter paper. The materials immersed in the ME-3 mixture exhibited a similar formation in

the OM analysis, but the product was less abundant and less loosely attached than in the water-immersed samples. This suggests that ME-3 may have provided partial protection, or at least delayed the onset of corrosion for a short period. This finding is consistent with the smaller amount of reddish products observed after immersion in ME-3 compared to water and Entek FNE (2% vol.). In contrast, ME-1 (5% vol.) appeared to effectively protect the magnetocaloric material, as no surface alterations were detected in the OM analysis for any of the three samples.

To further assess this effect, the evolution of T_{Curie} as a function of immersion time, determined from the minimum peaks of the differential scanning calorimetry (DSC) curves, is presented in Fig. 5.5. The results show that all materials immersed in water exhibited significant changes in T_{Curie} within the first weeks of testing. The T_{Curie} decreased rapidly during the initial immersion period, with further variations continuing to develop over longer aging times.

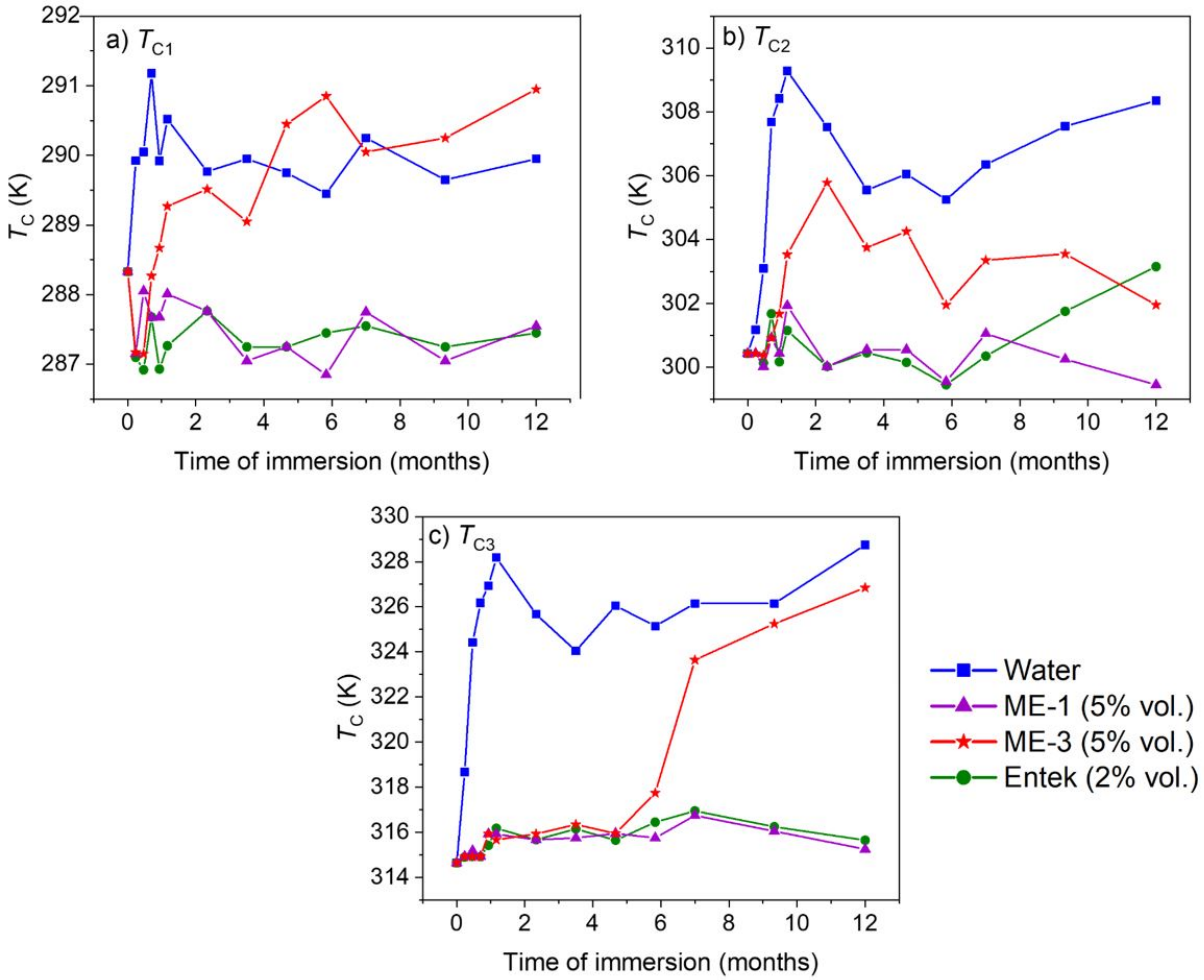


Figure 5.5 – Evolution of the Curie temperature of the three samples during the immersion testing (Döring *et al.*, 2024a).

Similar to the behavior observed during water immersion, all the Curie temperature batches showed changes upon immersion in ME-3 (5% vol.). In contrast, the variations detected in both ME-1 (5% vol.) and Entek FNE (2% vol.) were not significant for the T_{C1}

and T_{C3} groups. The apparent fluctuations in the Curie temperature values of materials immersed in these fluids, as shown in Fig. 5.5, may be attributed to the non-homogeneity of the chemical composition of the microparticles in their non-immersed state. This indicates that slight differences in the Curie temperature (up to 1 K) existed among microparticles within the same batch and remained stable throughout the immersion tests. Since approximately 15 mg of randomly selected microparticles (corresponding to about 20 individual particles) were used in each DSC analysis, sample inhomogeneities could explain the observed fluctuations in the Curie temperature. A significant variation, however, was observed in microparticles immersed in Entek FNE (2% vol.) within the T_{C2} group (approximately room temperature), which became evident only after nine months of testing. This result highlights potential limitations in using this fluid for long-term applications.

Consequently, Döring *et al.* (2024a) demonstrated that a mixture of water and ME-1 (5% vol.) is a promising alternative as a heat transfer fluid for magnetic refrigeration systems. This outcome not only provided valuable experimental evidence but also directly influenced the design choices of the present work, as the mixture was later incorporated into the second and third generations of the prototype to improve durability and performance. The results presented in Fig. 5.5 are also fundamental, as later in this document, an evaluation of the variation in the Curie temperature on the performance of MR systems will be carried out.

5.1.3 Active Magnetic Regenerator

To enhance the evaluation of the AMR, the pressure drop on the AMR beds was measured before the first-generation experimental assessment. It is important to note that this parameter depends solely on the flow resistance of the porous medium, calculated as the pressure drop difference across the bed with and without the MCM, following the standard practice in MR. While the metallic frames and separating meshes used to divide the multilayer MCM arrangement also have some impact, their influence is considered relatively low compared to that of the porous medium.

Equation (4.5) was calibrated using experimental data points, incorporating a corrected porosity to account for the nonhomogeneous characteristics of the La-Fe-Si porous medium. Using this approach, the effective porosity, calibrated against experimental data, was determined to be 0.325, which is significantly lower than the actual porosity of 0.423. The pressure drop results obtained through experimental means and the correlation provided by Eq. (4.5) for both the actual porosity (0.423) and the corrected porosity (0.325) are presented in Fig. 5.6.

Figure 5.6 shows that the correction applied to the porosity of the porous medium is capable of predicting the resulting pressure drop with good agreement. However, the actual pressure drop in the regenerator bed is significantly higher than that obtained with the actual

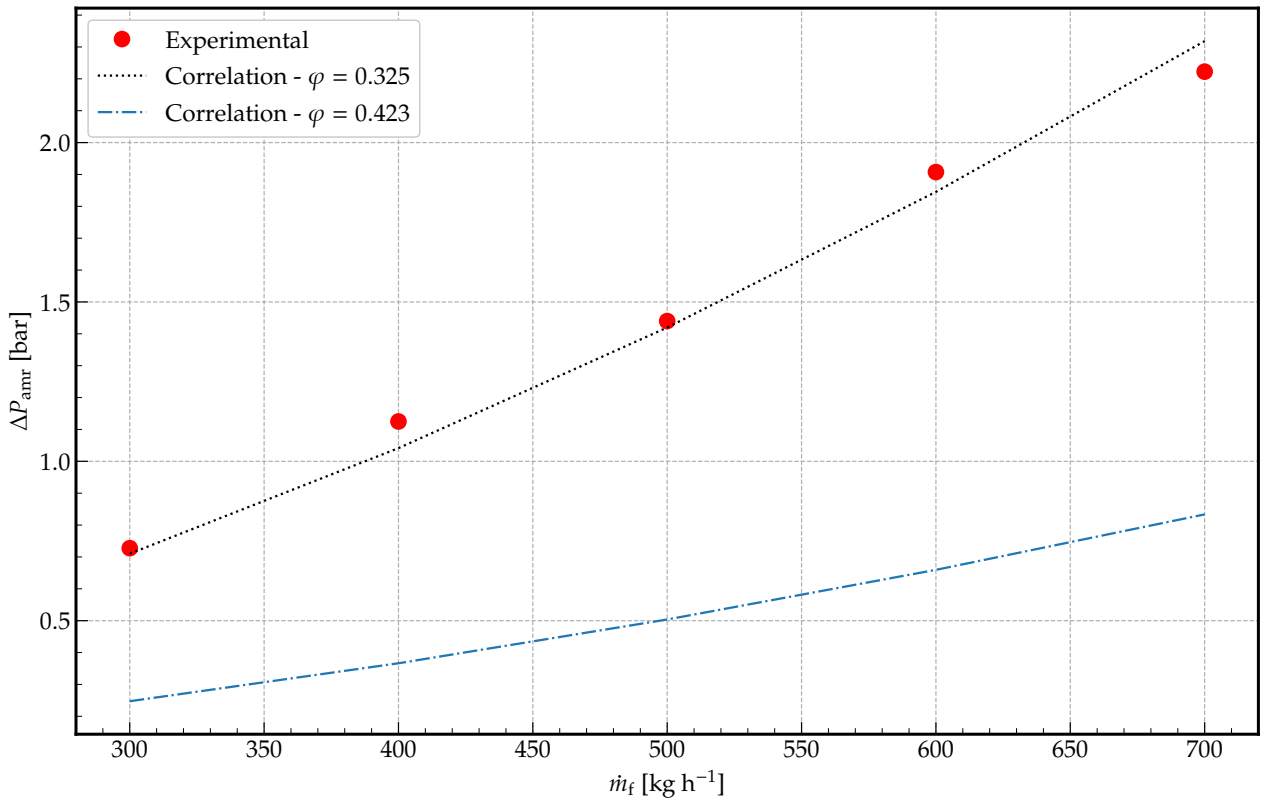


Figure 5.6 – Comparison between the mean experimental pressure drop values and the ones obtained via the corrected correlation.

parameters of the porous medium. This can be attributed to the variation in the diameter and morphology of the $La(FeMnSi)_{13}H_z$ particles, which resemble elongated cylinders more than spheres (Vieira *et al.*, 2021). As a result, the porous medium exhibits much greater resistance to fluid flow, leading to pressure drops approximately 180% higher than expected. Furthermore, it is worth noting that the Gd particles have a smaller diameter and morphology variations and show good agreement when compared to Eq. (4.5) (Trevizoli *et al.*, 2016b). Therefore, the Gd regenerator beds exhibit higher permeability compared to those composed of the current $La(FeMnSi)_{13}H_z$ alloys, which is highly advantageous for the operation of AMRs.

5.1.4 Hydraulic Management System

Given the limited availability of materials and to focus on the experimental evaluation and understanding of the HMS, a simplified hydraulic version of the magnetic air-conditioning apparatus was built. This configuration employs only two regenerator beds, operating in the opposite direction to the AMR cycle, and four solenoid valves, two in the high-pressure manifold and two in the low-pressure manifold. In this configuration, one valve in the high-pressure manifold and one in the low-pressure manifold manage the hydraulic flow to one regenerator bed. The pressure measurements are taken at eight spots along the fluid line: the inlet and outlet of the pump, the inlet of the high solenoid valve manifold, the outlet of each high-pressure solenoid valve, the outlet of the cold side high-

pressure manifold, the inlet of the cold side low-pressure manifold, and the outlet of the hot side low-pressure manifold. The schematic diagram of the simplified HMS is depicted in Fig.5.7.

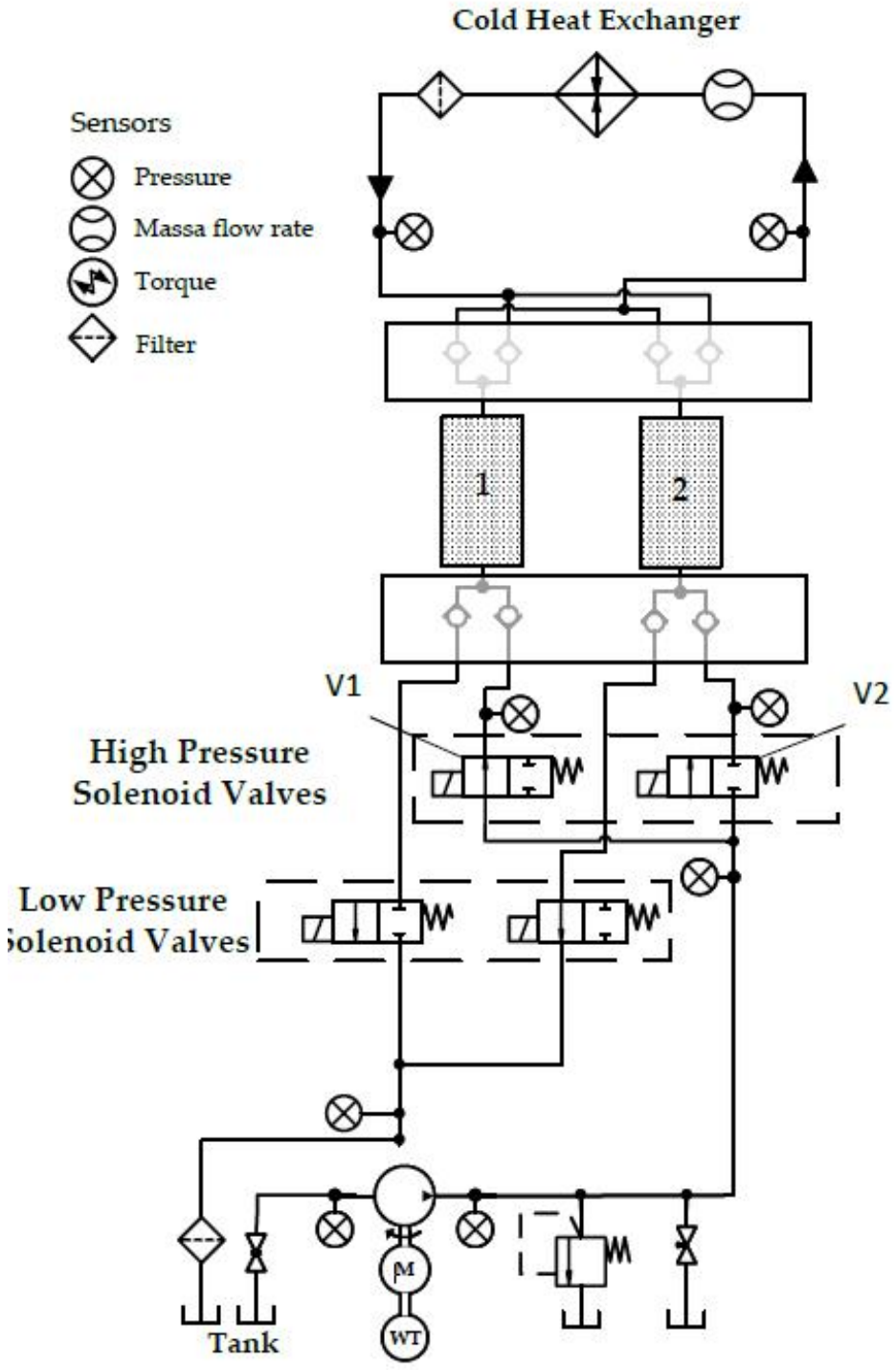


Figure 5.7 – Schematic diagram of the simplified HMS.

The hydraulic performance was evaluated to assess the operation of the candidate under each test condition, focusing on maintaining synchronization between blows in accordance with the AMR cycle requirements. For that, it was utilized pressure measurements at the outlet of each high pressure solenoid valve to characterize the transient response of the

fluid flow and the ones at the inlet of the high solenoid valve manifold, the outlet of the cold side high-pressure manifold, the inlet of the cold side low pressure manifold and the outlet of the hot side low pressure manifold to characterize the continuous response of the system.

Using these metrics to evaluate performance, the tests were defined to cover a zone around the previously determined working point for the operation requirements of the MR system. Tab. 5.1 presents a set of points for AMR frequency, mass flow rate, and blow fraction, which combined represent the 18 tests. The process for setting these conditions was performed directly in the MRU software interface to better validate the performance in real conditions.

Table 5.1 – Parameters for the solenoid valves tests.

AMR frequency [Hz]	Mass flow rate [kg h^{-1}]	Blow fraction [%]
0.75	350	25
1	525	40
1.5	700	

The main goal was to verify the ability of the selected solenoid valve to operate the entire apparatus and the conditions required to assemble the HMS in the MRU. Also, it is interesting to confirm whether the chosen valve has the shortest transition time, aiming to obtain an experimental profile that better approximates the instant profile. In addition to validating performance, the objective is to determine the optimal synchronization point between the AMR cycle and the HMS to achieve a higher COP for the refrigeration apparatus.

The performance of the HMS is evaluated based on pressure measurements taken at the inlet of the high solenoid valve manifold, the outlet of each high-pressure solenoid valve, the outlet of the cold-side high-pressure manifold, the inlet of the cold-side low-pressure manifold, and the outlet of the hot-side low-pressure manifold. These pressure points are referred to in the Figures depicted in this section as HB in, V1 out, V2 out, HB out, CB in, and CB out, respectively.

The results for 10 cycles are recorded at an acquisition frequency of 500 measurement points per cycle. The full data set is divided into five subsets, and the average of the two consecutive periods across the five subsets is calculated. After that, a filter is applied to remove signals with frequencies above 60 Hz. The first result to be displayed is regarding a comparison between the electric actuation signal of the solenoid and the transient fluid flow response, which are shown in Fig. 5.8. According to the schematic diagram presented in Fig. 5.7, when valve V1 is open and valve V2 is closed, there is a rise in the pressure at the outlet port of the first one and a drop in the same parameter on the last one. Such conditions result in AMR 1 and 2 undergoing the hot and cold blow, respectively. Conversely, when V1 is closed and V2 is open, there is a drop in the outlet port pressure of the first valve and a rise in the same parameter of the second valve. This condition results in AMR 1 and 2 undergoing

the cold and hot blows, respectively.

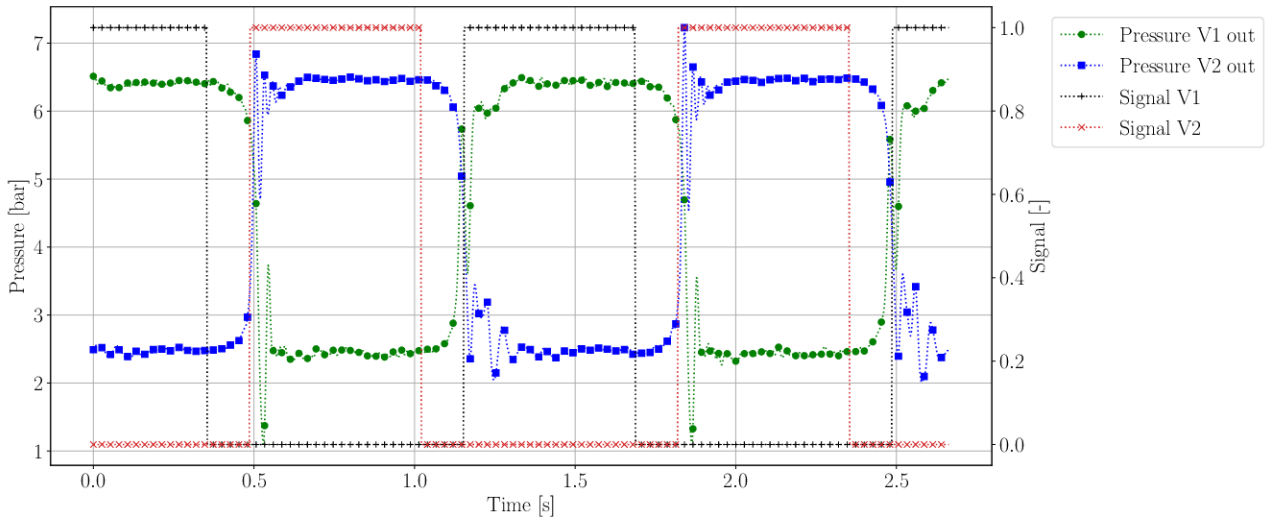


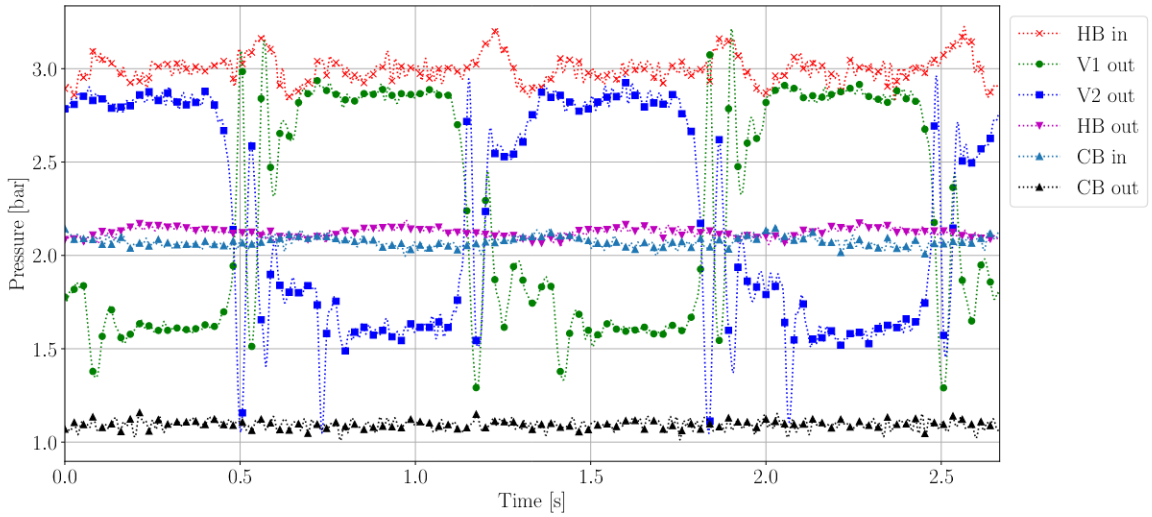
Figure 5.8 – Comparison between the electric actuation signal of the solenoid and the transient fluid flow response for a mass flow rate of 700 kg h^{-1}, a frequency of 0.75, and a blow fraction of 40%.

It is worth highlighting the coupling between the actuation signals of the solenoid valves and the resulting pressure profiles. The time response for opening the valves is faster than for their closing. As soon as the actuation signal occurs, there is a response in the pressure at the outlet ports of both valves. After the opening, a noisy behavior can be observed in the pressure signals, which is characteristic of the operation of solenoid valves. Later, there is a plateau in the pressure signal, where it remains virtually constant while the fluid flows. At some point, according to the blow fraction specification, the actuation signal to the solenoid valve is removed. Still, the flow response is relatively slow, taking up to 0.2 seconds for the pressure to reach the low plateau values. That slow closing behavior is also characteristic of solenoid valve operation, used to avoid water hammer effects that can damage the valve.

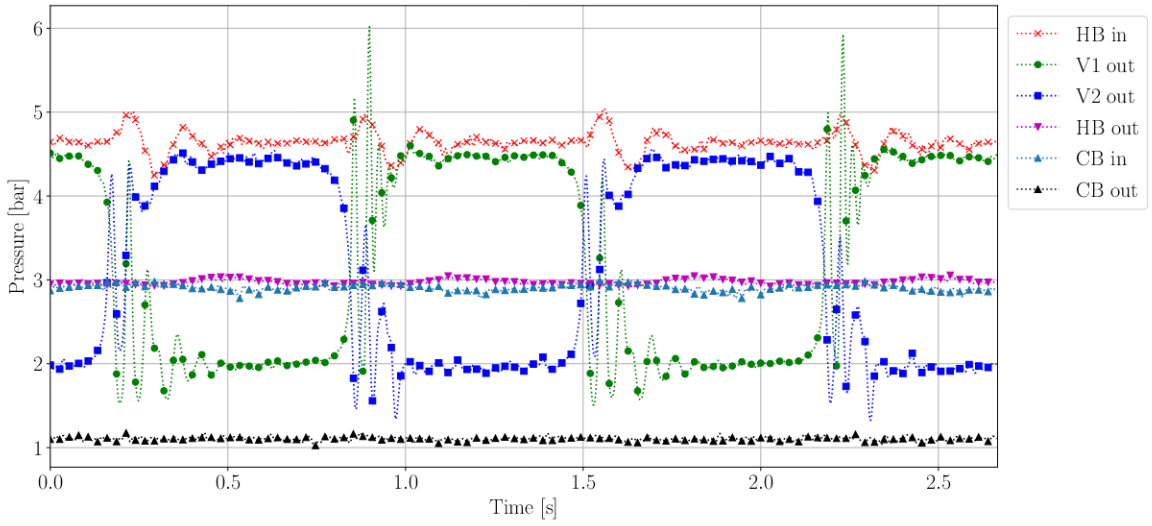
For the operation in caloric systems, the slow closing behavior of the solenoid must be considered, since it results in an increase of the cold and hot blow fractions in Comparison with the control blow fraction, *i. e.*, the valve actuation fraction. That deviation can be corrected by evaluating the time response of the valve closing and correcting such period by advancing the removal of the actuation signal in the solenoid valves. Hence, a preliminary assessment of the pressure signals indicates that the proposed HMS configuration can perform alternate hot and cold blows in a pair of regenerators operating in opposite directions. To better understand the results, the hydraulic profiles were evaluated across several operating conditions.

It is valuable to understand the effects of mass flow rate, operating frequency, and blow fraction on the hydraulic profiles generated by the proposed HMS. Hence, each parameter will be evaluated separately among the values presented in Tab. 5.1. The first parameter to be assessed is the mass flow rate. Results for a system operating at a frequency of 0.75 Hz

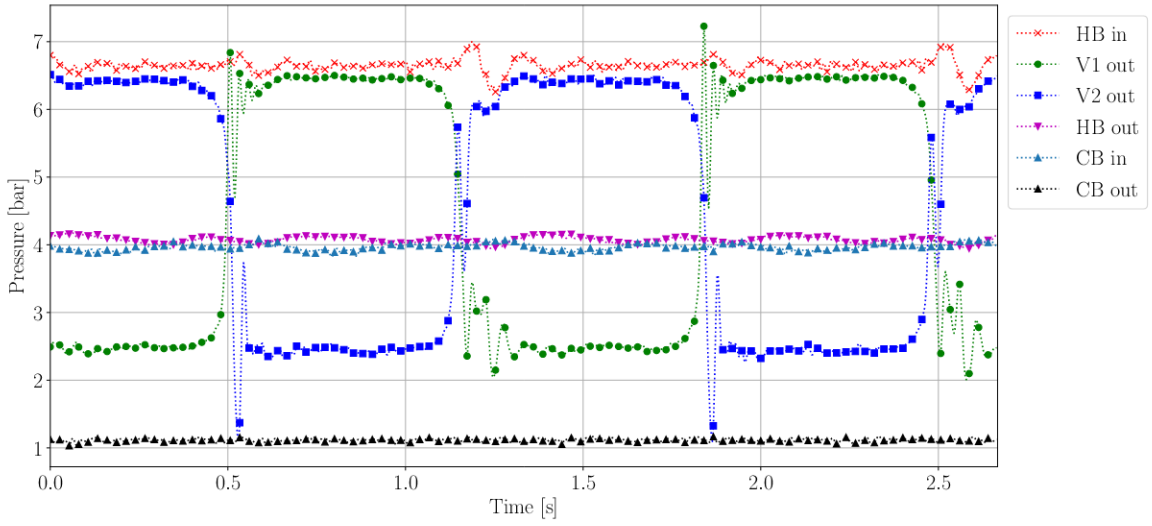
and a blow fraction of 40% for three distinct mass flow rate values are displayed in Fig. 5.9.



(a)



(b)



(c)

Figure 5.9 – Evaluation of the effect of the mass flow rate for a fixed frequency of 0.75 Hz and blow fraction of 40%. The figures depict a mass flow rate of (a) 350 kg h^{-1}, (b) 525 kg h^{-1}, and (c) 700 kg h^{-1}.

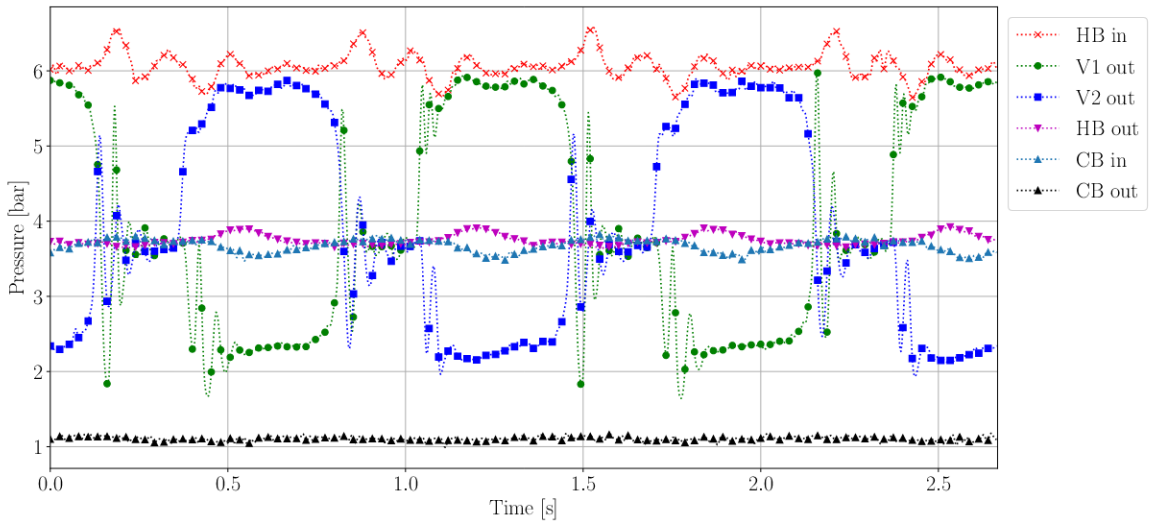
The results displayed in Fig. 5.9 (a), (b), and (c) demonstrate that the hydraulic profile improves with the rise in the mass flow rate. As one goes from the results to a mass flow rate of 350 kg h^{-1}, Fig. 5.9 (a), to 525 kg h^{-1}, Fig. 5.9 (b), and lastly 700 kg h^{-1}, Fig. 5.9 (c), it is noticeable that most characteristics of the hydraulic profile improves. The noisy behavior during solenoid valve opening and closing is attenuated at higher mass flow rates. Besides that, for such conditions, the attained profiles in the outlet of the solenoid valves during the blow periods are much more stable and restrained within a lower value range, and so is the profile for the inlet of the high-pressure hot side manifold, both characteristic of a more stable operation. That can be attributed to the high flow-driving force, provided by the higher pressure at the inlet of the hot-side high-pressure manifold, which overcomes the inertial forces required to attain oscillatory flow more easily. Also, as the mass flow rate is reduced, the valve closing period decreases, and the noisy behavior of the fluid pressure is enhanced, given the shorter time for the fluid to decelerate.

It is worth noting the considerable increase in the pressure drop in the system as the mass flow rate increases, with maximum pressures rising from 3 to 7 bar. Given that the full set of regenerator beds will operate in parallel according to the arrangement under evaluation, the pressure drop of the AMRs and HMS in the system is expected to be on the same order of magnitude as for the individual HMS test. The main difference expected to increase that value is that the current tests use passive stainless steel spheres, which have higher permeability than the MCMs.

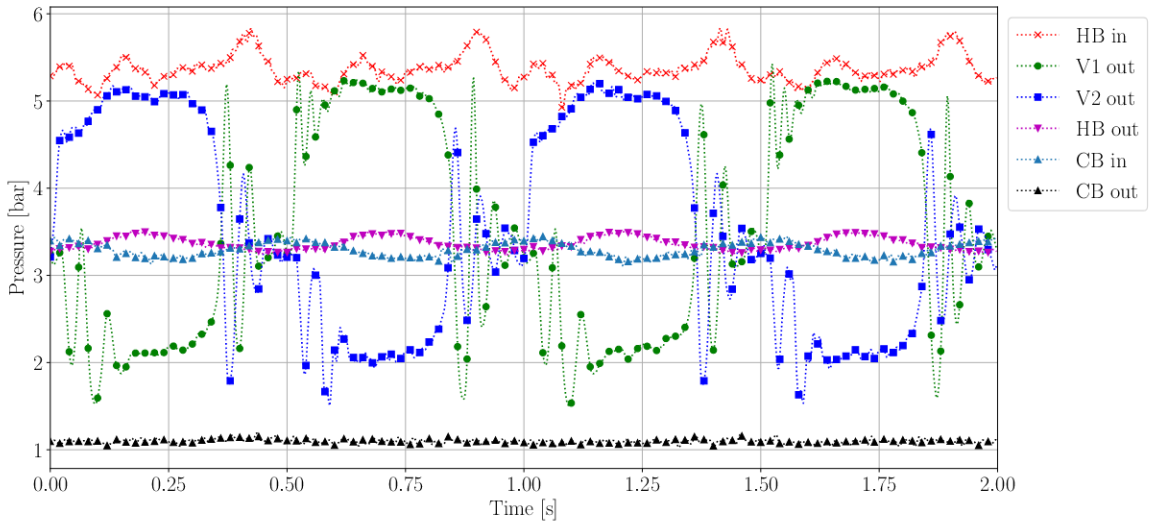
Following that, the results for a system operating at a mass flow rate of 525 kg h^{-1} and a blow fraction of 25% for three distinct frequency values are displayed in Fig. 5.10. The results shown in Fig. 5.10 (a), (b), and (c) demonstrate that the hydraulic profile improves with the reduction in the frequency of the oscillatory flow. As one evaluates the rise of frequency following the results of Fig. 5.10 (a), (b) and (c), it can be noticed that the noisy behavior of the opening and closing periods is enhanced, especially at 1 and 1.5 Hz, and that the hydraulic profile at the outlet of the solenoid valves and at the inlet of the hot side high pressure manifold is progressively deteriorated. These behaviors result from the faster requirements for the valve and fluid flow as the frequency increases. Hence, at lower frequencies, the valve has more time to open and close, and the fluid flow can develop and reach plateaus of constant pressure, generating more stable hydraulic profiles.

The maximum pressure drop across the different cases remains relatively constant, at around 6 bar, indicating that the influence of the mass flow rate on this parameter is much greater. Despite noisy behavior and unstable closure at higher frequencies, the valves were deemed adequate for operation up to 1.5 Hz, which was the primary limitation on the maximum rotation speed of the system.

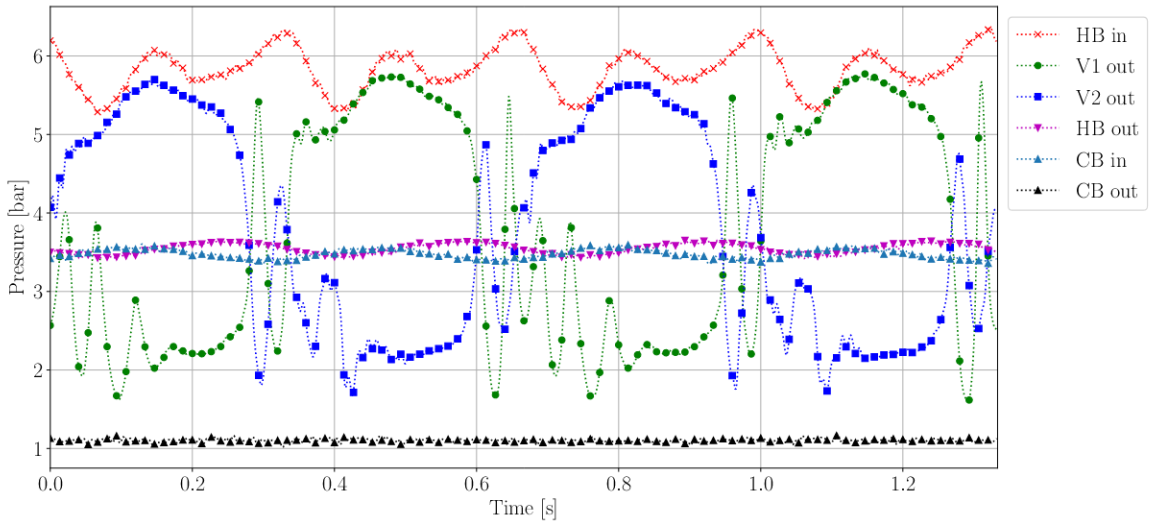
Lastly, the results for a system operating at a mass flow rate of 525 kg h^{-1} and a



(a)



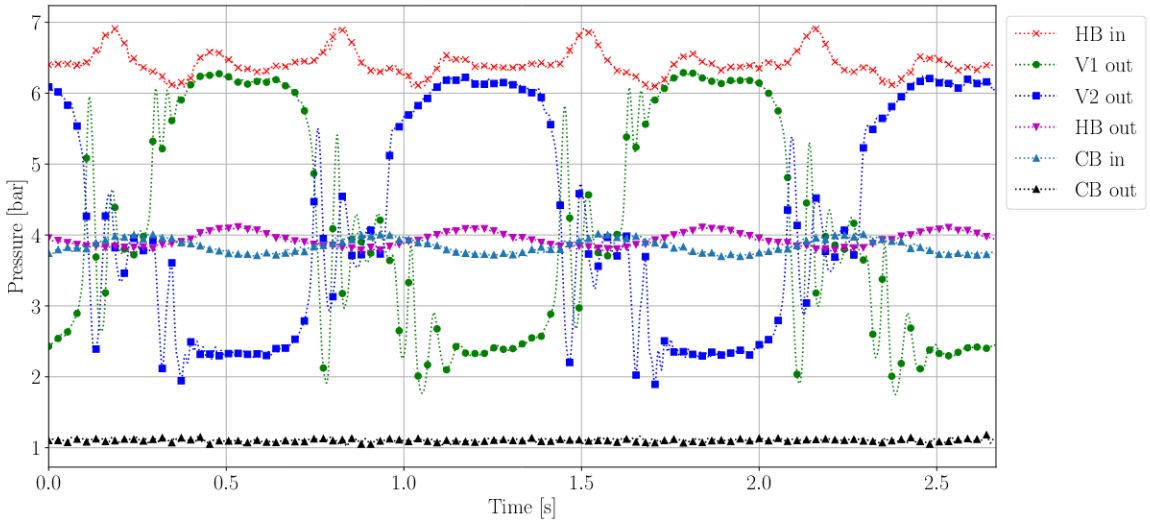
(b)



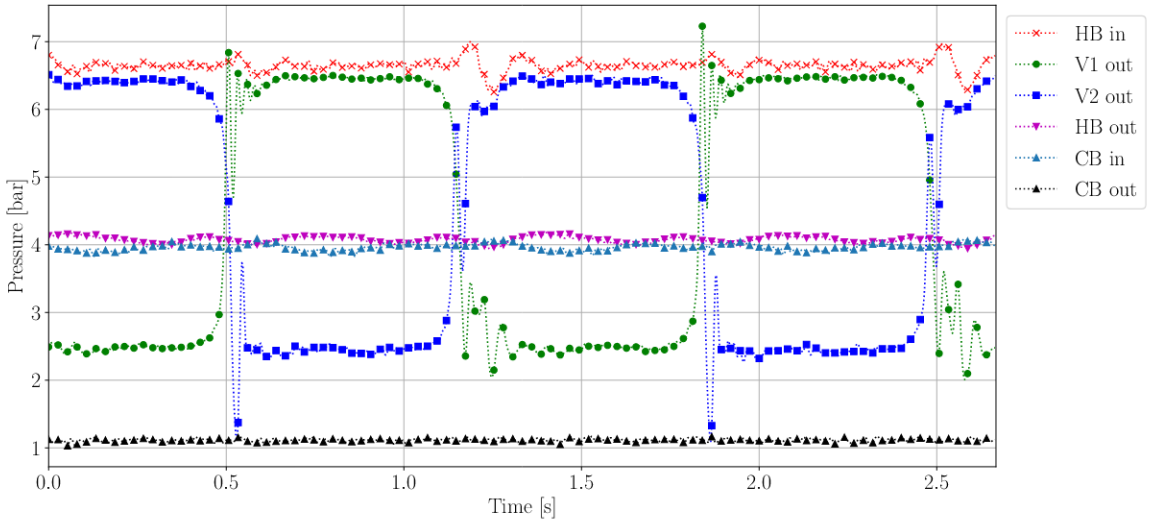
(c)

Figure 5.10 – Evaluation of the effect of the frequency for a fixed mass flow rate of 525 kg h^{-1} and blow fraction of 25%. The figures depict a frequency of (a) 0.75 Hz, (b) 1 Hz, and (c) 1.5 Hz.

frequency of 0.75 Hz for two distinct blow fraction values are displayed in Fig. 5.11.



(a)



(b)

Figure 5.11 – Evaluation of the effect of the blow fraction for a fixed frequency of 0.75 Hz and mass flow rate of 700 kg h^{-1}. The figures depict a mass flow rate of (a) 25% and (b) 40%.

The results displayed in Fig. 5.11 (a) and (b) demonstrate that the hydraulic profile improves with the rise in the blow fraction of the oscillatory flow. This result is due to the reduced period without flow in the regenerator beds in the higher blow fraction cases, as the fluid flow aids in attenuating the pressure variations. This can be especially noticeable during the closing periods of the valves.

Upon investigation of the performance of the HMS under different operating conditions, the proposed arrangement, consisting of a combination of Asco SC8210-112/220V-NC solenoid valves and check valves, was deemed adequate for the operation of the system.

5.2 Magnetic Refrigeration Unit

After the standalone evaluation of the performance of specific metrics across subsystems, the system-level performance of the MRU generations is assessed. As previously discussed, three generations of the prototype were assembled and experimentally characterized. An advanced performance evaluation, according to the metrics presented in section 4.4, is conducted for the first version, *i.e.*, the best-performing version of the prototype.

5.2.1 Performance Evolution of the System

Each iteration of the MRU underwent evaluation under specific conditions tailored to its geometric modifications in the AMR, MC, and HMS. These alterations impact operational limitations and optimal parameter ranges, as discussed earlier in this chapter. Table 5.2 presents a summary that describes the operational test conditions for each version of the MRU. As previously discussed, the operating frequency of the first MRU version was limited to 0.6 Hz due to rotor cogging. The second version, due to its continuous arrangement of regenerator beds, and the third, due to the dummy regenerators, were able to operate at higher frequencies, which were limited by the performance of the system. The mass flow rate limitations were dictated by the performance of the system and the maximum pressure at the fluid line. The blow fraction limitation was determined by the performance stability of the solenoid valves. Lastly, the temperature on the hot-side chamber was limited by the maximum temperature on the multilayer arrangement.

Table 5.2 – Operation conditions of the tests for each version of the prototype.

Parameter	version 1	version 2	version 3
f [Hz]	0.6	0.5, 0.7, 0.9, 1.1, 1.3	0.5, 1
$\dot{m}_{\mathrm{f}}$ [kg h^{-1}]	[600, 1600]	[1000, 2250]	[400, 800]
$F_{\%}$ [%]	30	35	35, 40
$\overline{T}_{\mathrm{H}}$ [°C]	35	32	18

Figure 5.12 illustrates the cooling capacity achieved by the three versions of the prototype, as given by Eq. (4.10), represented as a function of the mass flow rate and the AMR temperature span in Figs. 5.12 (a) and (b), respectively. As shown, the second version of the prototype achieved the highest cooling capacities, followed by the first and then the third. This ranking is expected due to the significantly higher mass of MCM in versions 1 and 2, with the second version also benefiting from higher mass flow rates and magnetic flux densities. Generally, cooling capacity increases with higher mass flow rates up to a maximum, though this trend is not always true. The distinct clusters observed for each version and mass flow rate primarily stem from variations in the temperature span in version 1 and frequency in versions 2 and 3. Regarding the temperature span of the AMR, Fig. 5.12 (b)

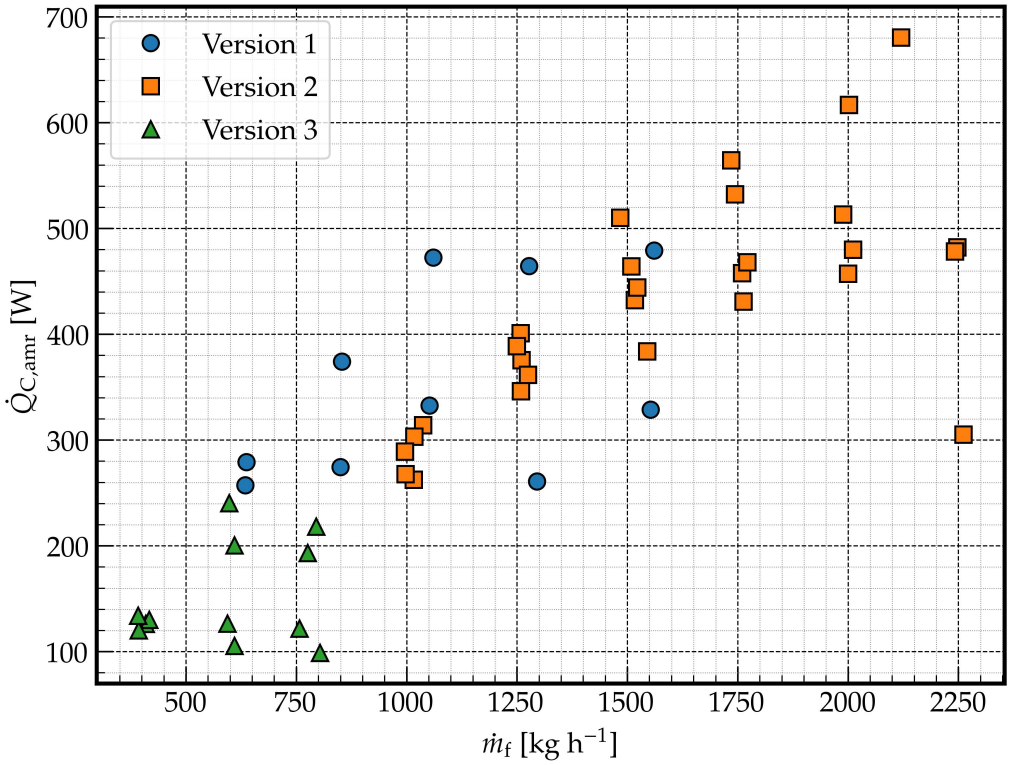
shows a different trend, where version 1 achieved the best results. Despite versions 1 and 2 having similar total MCM mass, version 1 features nearly double the mass per AMR, resulting in a larger heat transfer area and enhancing the heat exchange effectiveness of the porous medium, enabling the system to operate over a wider temperature span, which is particularly beneficial under high mass flow rate conditions.

For a deeper insight into one of the most critical irreversibilities in refrigerators, the temperature spans of the MRU are presented in Fig. 5.13. Figure 5.13(a) shows the temperature span of the AMR plotted against the mass flow rate. Each MRU version exhibits distinct clusters, highlighting variations in operational parameters. The temperature span of the AMR is influenced not only by its internal parameters, such as frequency and mass flow rate, but also by external factors, including the effectiveness of the HExs and heat losses through the calorimeter walls. All of these factors collectively impact the efficiency and performance of the MR system.

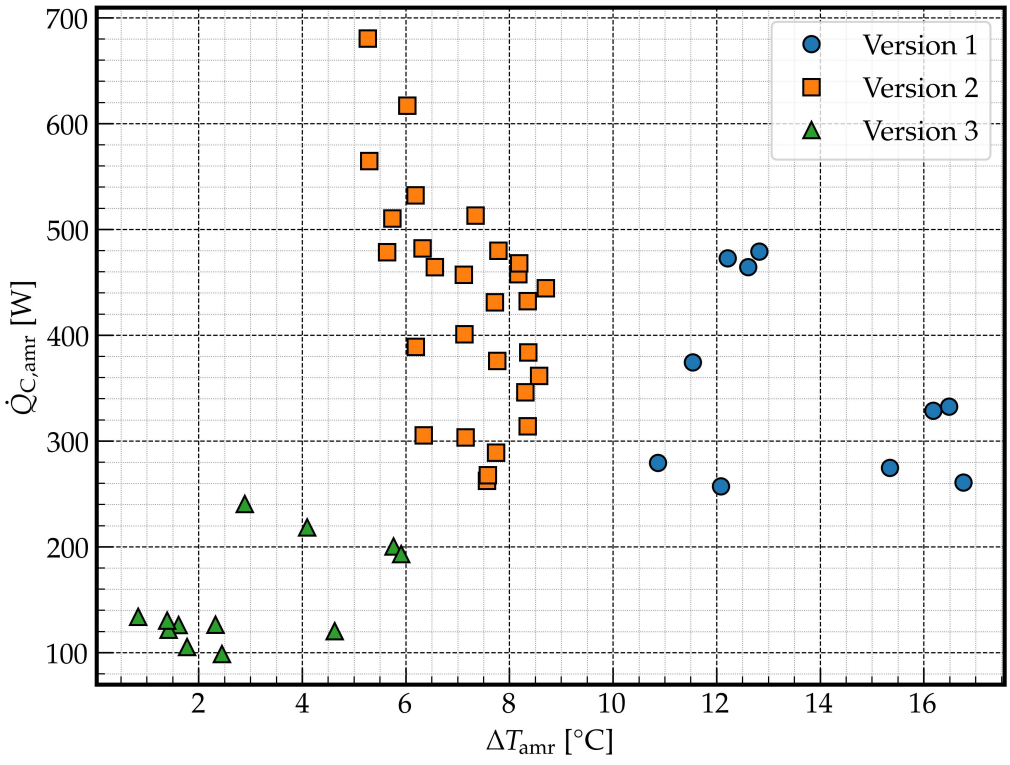
To provide a comprehensive evaluation, Fig. 5.13(b) illustrates the relationship between the temperature spans of the AMR and the system. The former is always higher than the latter, reflecting the necessary temperature difference for heat transfer between the working fluid and heat reservoirs. The MRU stands out as one of the few prototypes in the literature where these irreversibilities can be quantitatively assessed. This temperature difference is influenced by factors such as the mass flow rate through the heat exchangers and the cooling capacity of the system.

It is interesting to note that some of the experiments in version 3 achieved a system temperature span below 0°C. Although not achievable in actual systems, this was feasible within the experimental setup of the calorimeter. In such instances, even though the AMR temperature span is slightly above 0°C, the cooling capacity generated was insufficient to offset the heat dissipation from components in the cold chamber of the calorimeter, particularly the CHEx fan. Consequently, the system effectively heated the ambient environment. This thermal loss is crucial for practical applications of the MRU. To allow comparability with other MR prototypes in the literature, where such losses are not considered, a cooling capacity calculated using Eq. (4.10) is used. This approach helps standardize performance metrics across different experimental setups and allows meaningful comparisons in the research and development of MR technologies.

The energy efficiency of the system is assessed by the COP, depicted in Fig. 5.14. Figures 5.14 (a) and (b) illustrate the COP as a function of the mass flow rate from the perspectives of the AMR and the system, respectively. These figures highlight the trade-off between increased cooling power and increased power consumption, particularly in fluid pumping. From the AMR perspective, COP generally peaks at lower mass flow rates. Conversely, from the perspective of the system, optimal COP tends to occur at moderate mass flow rates. This



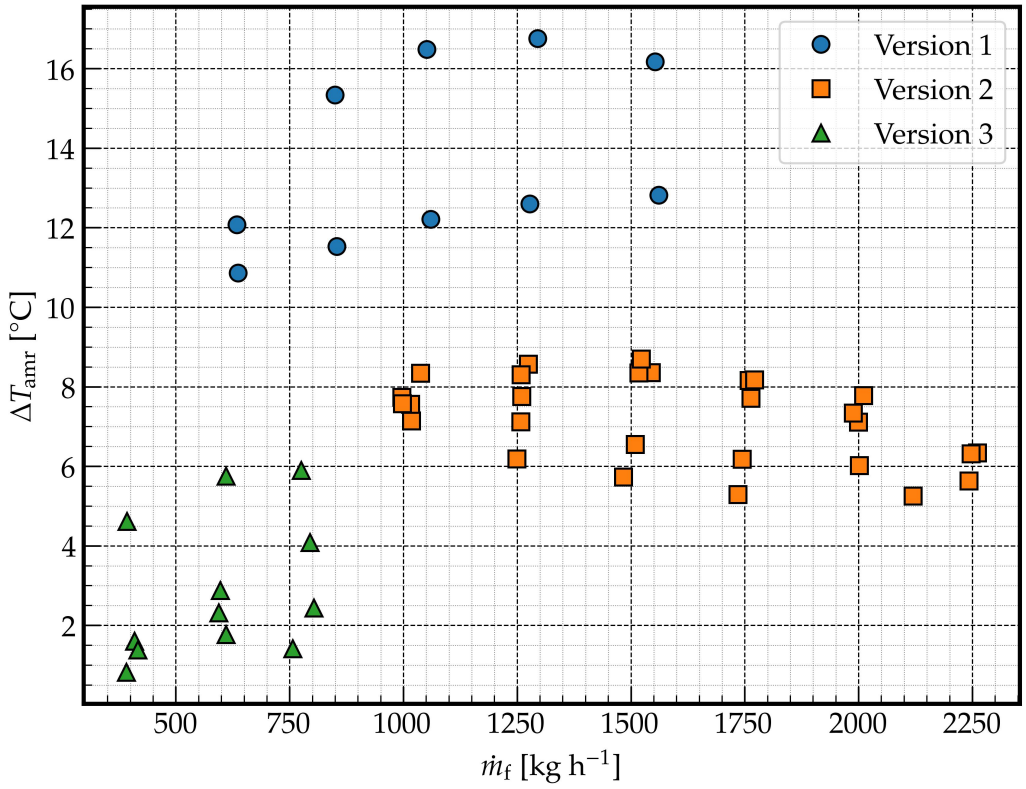
(a)



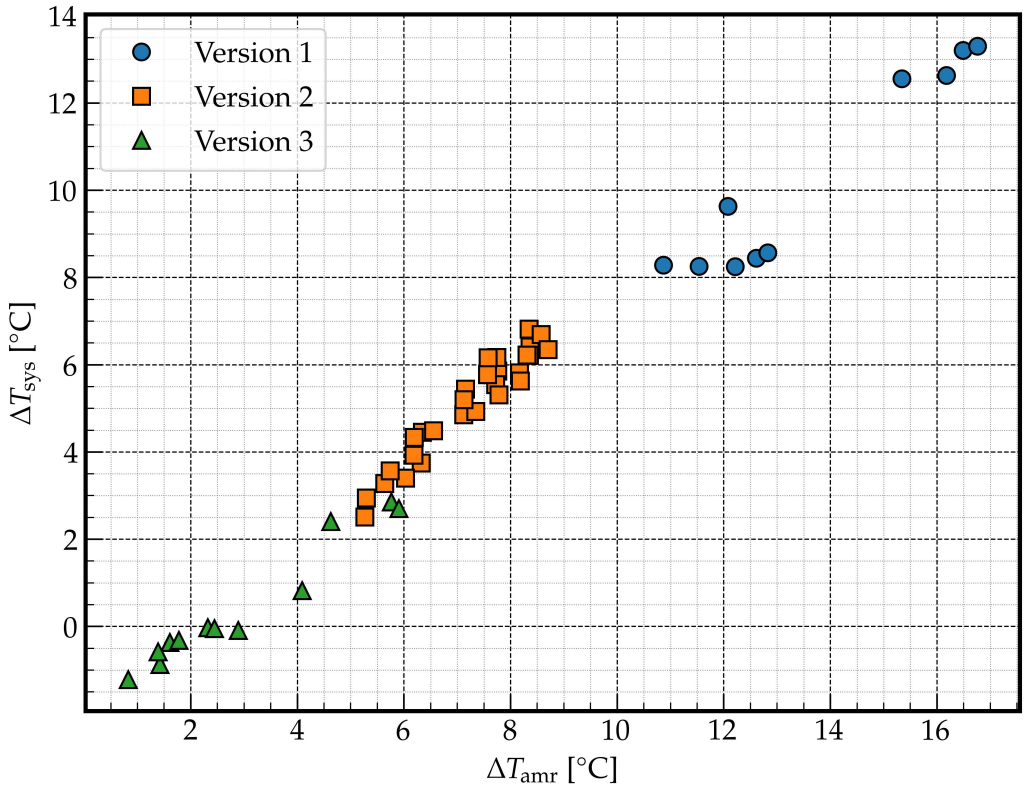
(b)

Figure 5.12 – Evaluation of the cooling capacity for each version of the MRU as a function of (a) mass flow rate and (b) AMR temperature difference.

difference reflects the comprehensive energy balance within the entire MRU setup, including losses and inefficiencies in the HEx. Among the three versions of the prototype, the first demonstrates the highest COP, followed by the second and then the third. This ranking cor-



(a)



(b)

Figure 5.13 – Evaluation of the AMR temperature spans of the system, displaying the correlation between (a) the mass flow rate, and (b) system temperature span.

relates with improvements made in subsequent versions of the AMR configuration, magnetic flux densities, and operational parameters. In particular, because external irreversibilities

are accounted for in the performance calculations, there is a discernible decrease in COP, underscoring the impact of practical operational constraints on efficiency. These findings emphasize the ongoing optimization efforts and trade-offs involved in developing practical MR systems that balance between maximizing cooling capacity and minimizing energy consumption for effective performance.

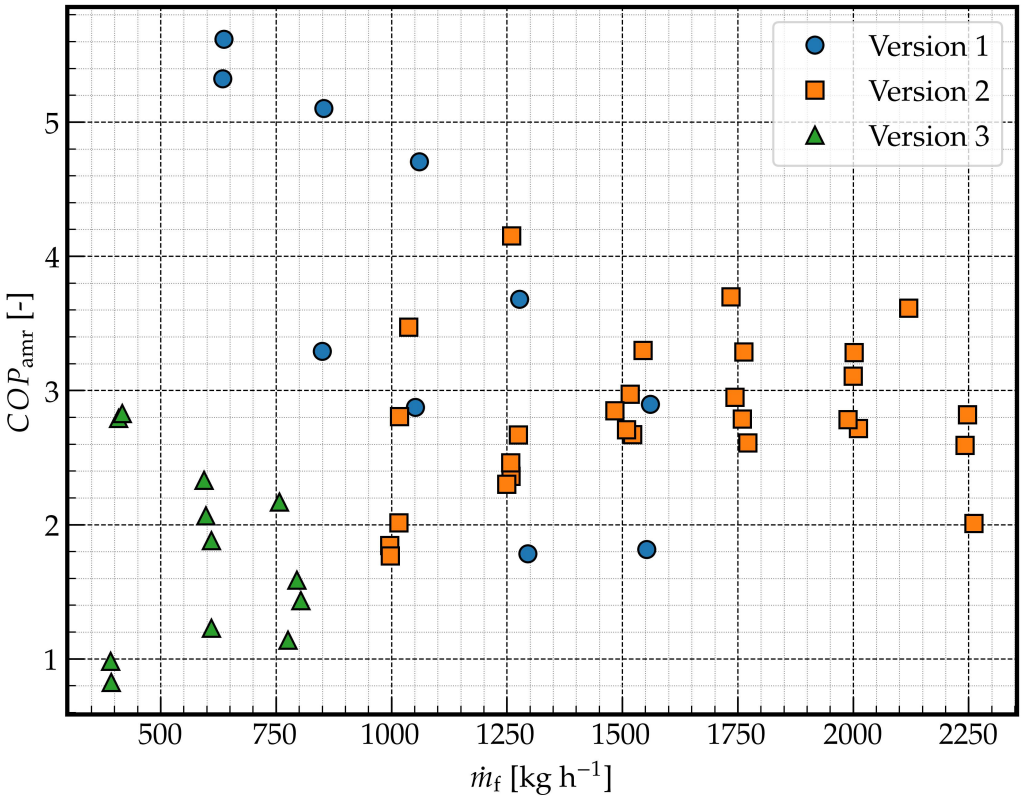
Finally, the performance comparison of the AMR and the system is also analyzed through the second law efficiency, presented in Figs. 5.15(a) and (b), respectively. Once again, the first version of the MRU achieves the highest efficiency, followed by the second and third versions. The difference between versions becomes more pronounced as the second-law efficiency accounts for the temperature span. There is a notable disparity between the efficiencies of the AMR and the system, highlighting the importance of accounting for external irreversibilities in the design of the MR system. This discrepancy reflects the real-world challenges of optimizing efficiency across all operational parameters, including the effectiveness of HEx, component coupling, and irreversibilities in auxiliary subsystems.

A summary of selected experiments and their performance metrics is presented in Tab. 5.3. Based on the results presented in this section and summarized in Tab. 5.3, the first version of the MRU is considered the best. Although the second version achieved higher cooling capacities, the first version excelled in achieving higher temperature spans and better performance, which are critical for practical applications. It is essential to acknowledge that part of this performance difference can be attributed to the degradation of MCM over time, which not only reduces its effectiveness but also shifts the Curie temperature of the materials. However, accurately quantifying this effect is challenging, and excluding all potentially degraded alloys would hinder the advancement and development of new versions of the prototype.

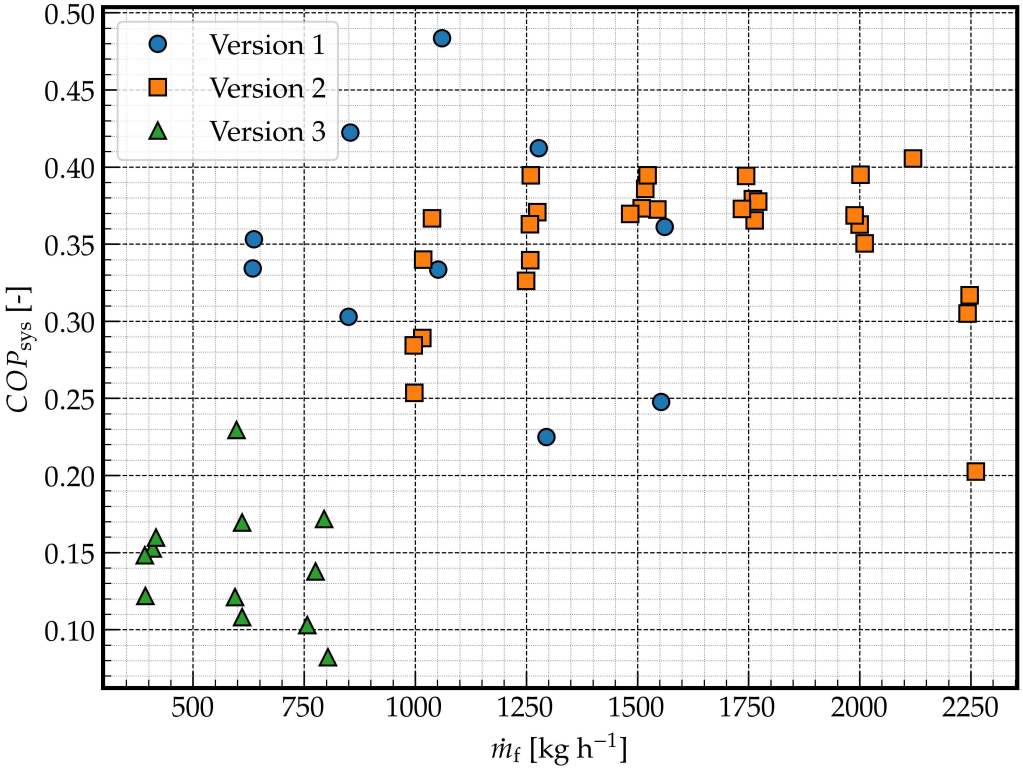
Table 5.3 – Overview of the optimal performance conditions observed across the three prototype versions.

Metric	**version 1**	**version 2**	**version 3**
$\dot{Q}_{\mathrm{C}}$ [W] (ΔT_{amr} [ºC])	480 (12.8)	680 (5.2)	240 (2.9)
ΔT_{amr} [ºC] ($\dot{Q}_{\mathrm{C}}$ [W])	16.7 (260)	8.7 (450)	5.9 (193)
ΔT_{sys} [ºC] ($\dot{Q}_{\mathrm{C}}$ [W])	12.6 (260)	6.8 (320)	2.9 (200)
COP_{amr} [-]	5.6	4.2	2.8
COP_{sys} [-]	0.48	0.41	0.23
η_{amr} [%]	22.0	10.8	2.46
η_{sys} [%]	1.49	0.84	0.16

A comparison of the performance of the three versions of the MRU with other prototypes reported in the literature is presented in Fig. 5.16. Despite the many challenges encountered in developing and operating the prototype, compared with selected benchmarks from other prototypes in the literature, the MRU demonstrates some of the most promising



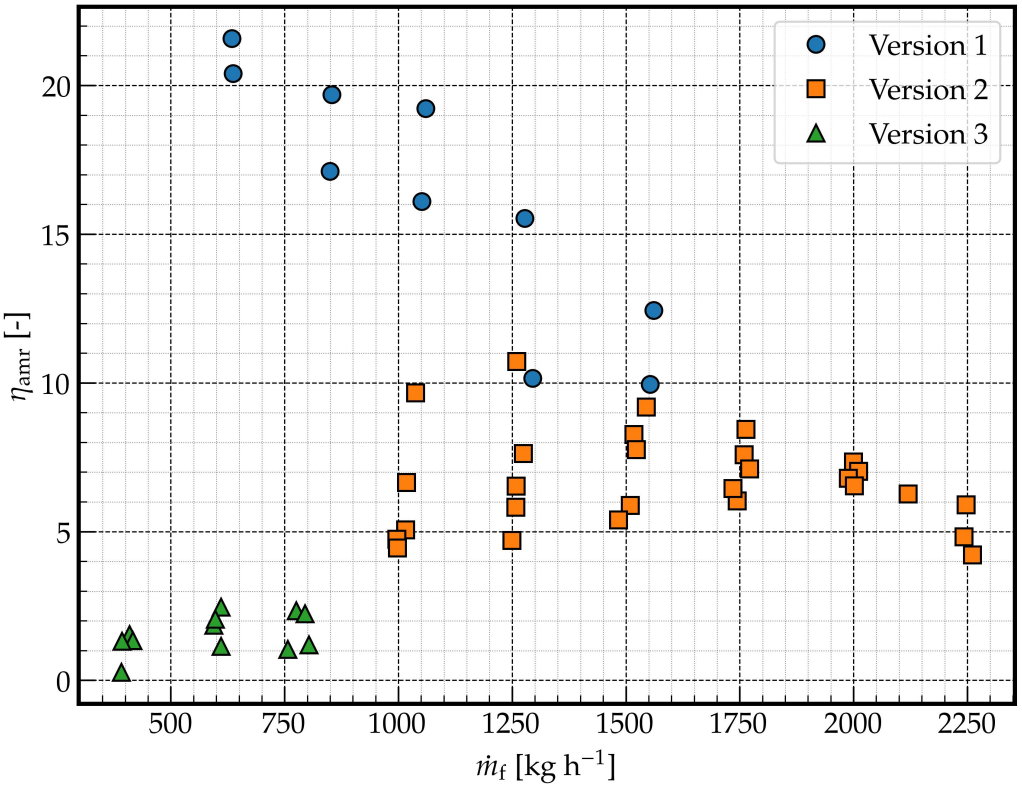
(a)



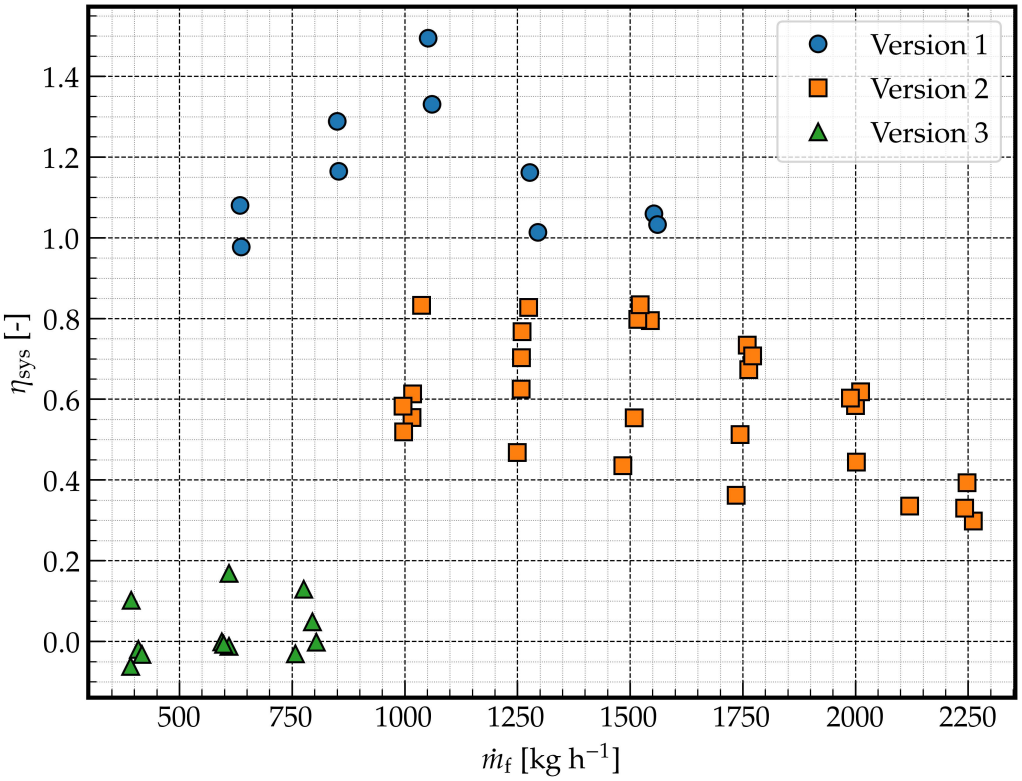
(b)

Figure 5.14 – Evaluation of the COP of the (a) AMR and (b) system, for each version of the MRU as a function of the mass flow rate.

results reported to date. This is particularly noteworthy given its ability to achieve significant cooling capacity across useful temperature spans. Furthermore, the MRU stands out among



(a)



(b)

Figure 5.15 – Evaluation of the second-law efficiency (a) of the AMR and (b) of the system, for each version of the MRU as a function of the mass flow rate.

prototypes by operating with actual heat exchangers, thereby validating its technology in a practical, relevant environment. These achievements highlight the iterative and evolving nature of MR research, which continually strives to optimize performance while addressing

real-world challenges and operational constraints.

5.2.2 Advanced Thermodynamic Evaluation

An advanced performance evaluation was conducted in the first version of the MRU, which is considered the one that achieved the best results. To investigate the performance of the system, the mean mass flow rate per regenerator was varied from 300 to 700 kg h^{-1}. Additionally, the blow fraction of the AMR was set at around 30%.

The temperature spans from the AMR and system points of view, as per Eqs. (4.1) and (4.2), respectively, are illustrated in Fig.5.17. It is noteworthy that the system temperature span exhibits a constant behavior, as anticipated, due to the fixed temperatures of the cold and hot heat reservoirs at approximately 27°C and 35°C, respectively, in compliance with air conditioning standards (ISO-5151, 2017; Inmetro, 2011; Inmetro, 2012; Inmetro, 2013). In contrast, from the AMR perspective, the temperature span increases with the mass flow rate. This behavior can be attributed to both the increase in cooling capacity observed for mass flow rates up to 600 kg h^{-1} and the decrease in the effectiveness of the HEx as the mass flow rate increases.

Figure 5.17 highlights the existence of a gap between the temperature spans of the system and the AMR, which is expected due to irreversibilities in the HEx. Many magnetic refrigerator prototypes overlook this effect by not using actual heat exchangers at the thermal reservoirs, which is somewhat problematic, since achieving larger temperature spans is one of the major challenges in MR. Conventional vapor compression refrigerators typically operate with significant temperature differences in the HEx, often spanning dozens of degrees Celsius. In contrast, as shown in Fig. 5.17, the magnetic prototype under evaluation was designed to operate with a temperature difference of approximately 1.5 to 2.5°C in each HEx. This design choice was made because it is more advantageous to oversize the HEx than the AMR, as presented in Chapter 3. Hence, the irreversibilities arising from the HEx significantly impact the performance of MR systems and must be carefully considered during their design and optimization.

The system torque breakdown, according to Eq. (4.3), is presented in Fig. 5.18 as a function of the mass flow rate. It is important to note that the parasitic and transmission torque shares were obtained from separate experiments and are considered constant across varying mass flow rates.

The torque increase observed in Fig. 5.18 is due to an increase in the magnetization of the MCM resulting from the rise in mass flow rate. Although this contribution eventually becomes the largest, one should recognize that the remaining torque shares also play a significant role, contributing between 31% and 46% of the total torque.

Considering mechanical design aspects, the transmission system has been intention-

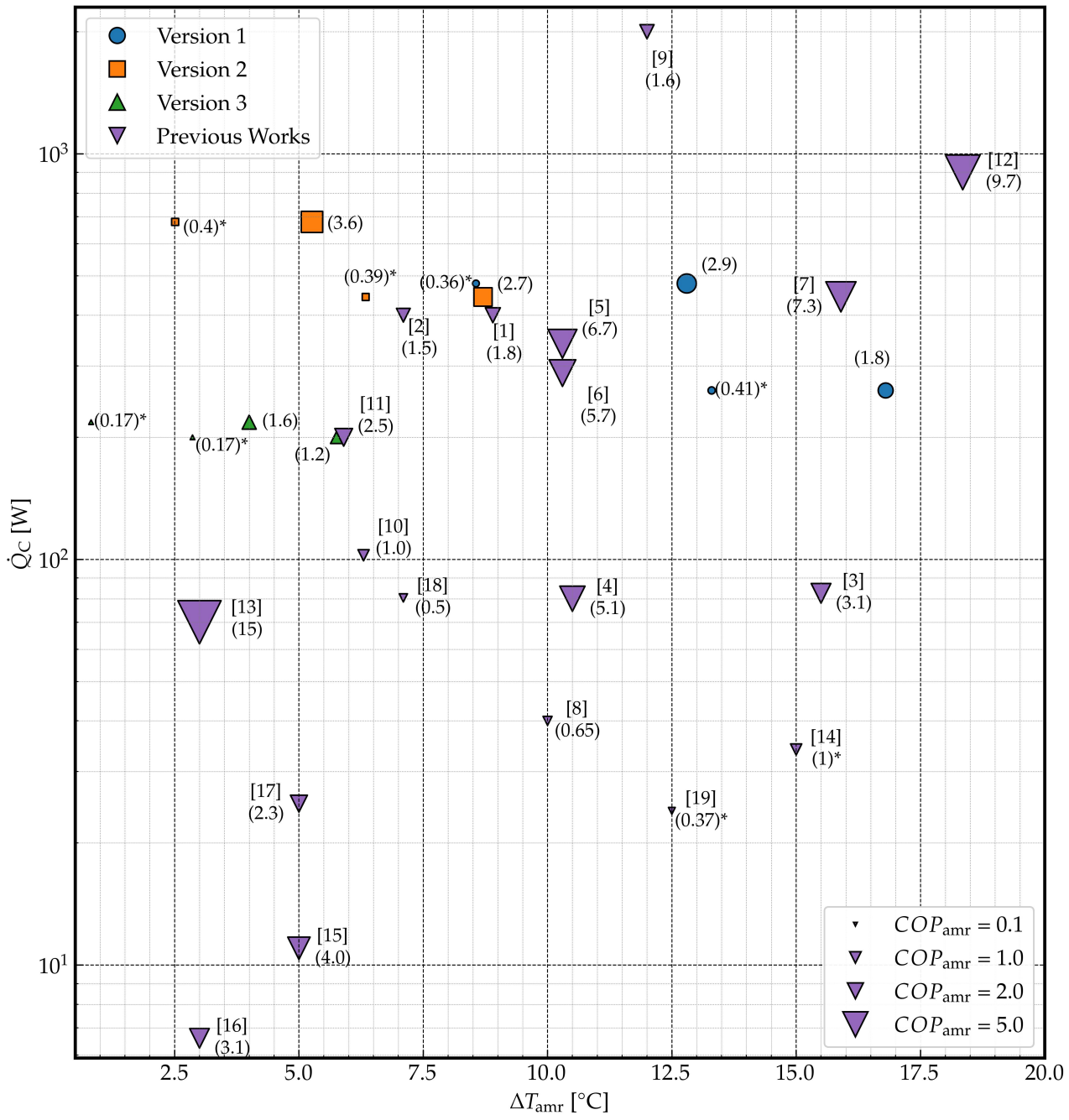


Figure 5.16 – Comparison between the performance of the three versions of the MRU and selected prototypes presented in the literature. References in the Figure are according to [1]: Engelbrecht *et al.* (2012), [2]: Lozano *et al.* (2013), [3]: Eriksen *et al.* (2015), [4]: Fortkamp *et al.* (2018), [5]: Dall'Olio *et al.* (2021), [6]: Masche *et al.* (2021), [7]: Masche *et al.* (2022), [8]: Tura & Rowe (2011), [9]: Jacobs *et al.* (2014), [10]: Huang *et al.* (2019), [11]: Aprea *et al.* (2016), [12]: Lionte *et al.* (2020), [13]: Hai *et al.* (2024), [14]: Liang *et al.* (2025), [15]: Trevizoli *et al.* (2016b),[16]: Trevizoli *et al.* (2017), [17]: Nakashima *et al.* (2018), [18]: Lozano *et al.* (2016), [19]: Nakashima *et al.* (2021). The values of the coefficient of performance from an AMR standpoint are presented in parentheses. * Represents prototypes where ΔT_{sys} and COP_{sys} are depicted.

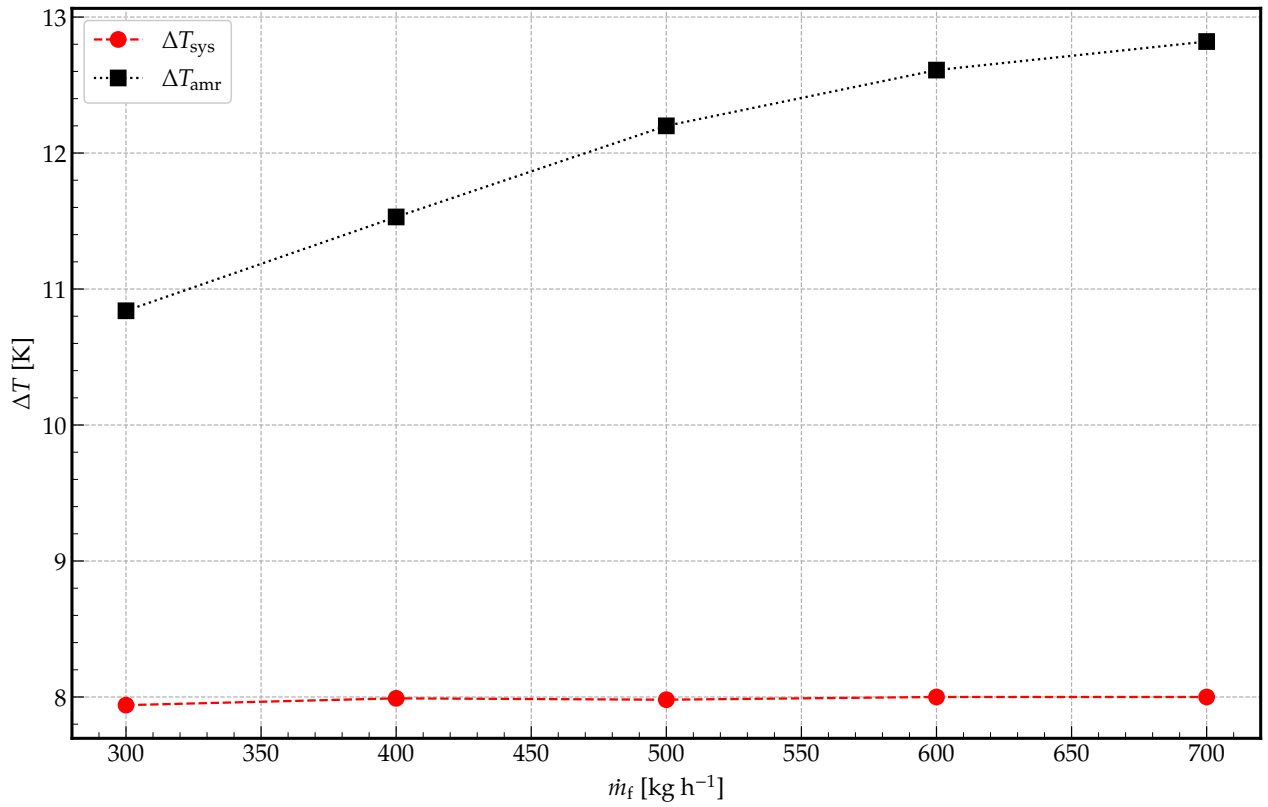


Figure 5.17 – Comparison between the temperature span from the AMR and system points of view.

ally oversized to ensure safe operation at higher frequencies, thereby increasing the required torque. An opportunity for improvement lies in replacing oversized mechanical transmission elements with smaller ones, thereby optimizing torque requirements without compromising safety.

Furthermore, as the system was expected to operate at higher frequencies, the torque demand is projected to increase considerably compared with the values obtained from the current tests, which were conducted at 0.6 Hz. Therefore, addressing this potential increase in torque is essential to maintain system efficiency and performance.

Regarding the stator lamination strategy, it has proven successful, as the parasitic torque remains below 0.2 N m, accounting for only 2.8% to 4.1% of the total torque. This demonstrates the efficiency of the chosen stator design in minimizing unwanted torque losses and improving overall system performance.

The breakdown of the shares accounting for the total pressure drop in the system, as per Eq. (4.4), is depicted in Fig. 5.19. Shares related to the internal pumping of the HEx are not shown in the figure due to their low magnitude, which is below 0.12 bar for the HHEx and 0.09 bar for the CHEx. This demonstrates the success of the multi-circuit strategy employed to minimize excessive hydraulic resistance within the tubes of both HEx. The pressure drop for the AMRs accounts for two beds, as illustrated in the hydraulic circuit of the prototype presented in Fig. 4.11.

As expected, Fig. 5.19 demonstrates that all pressure drop shares increase with

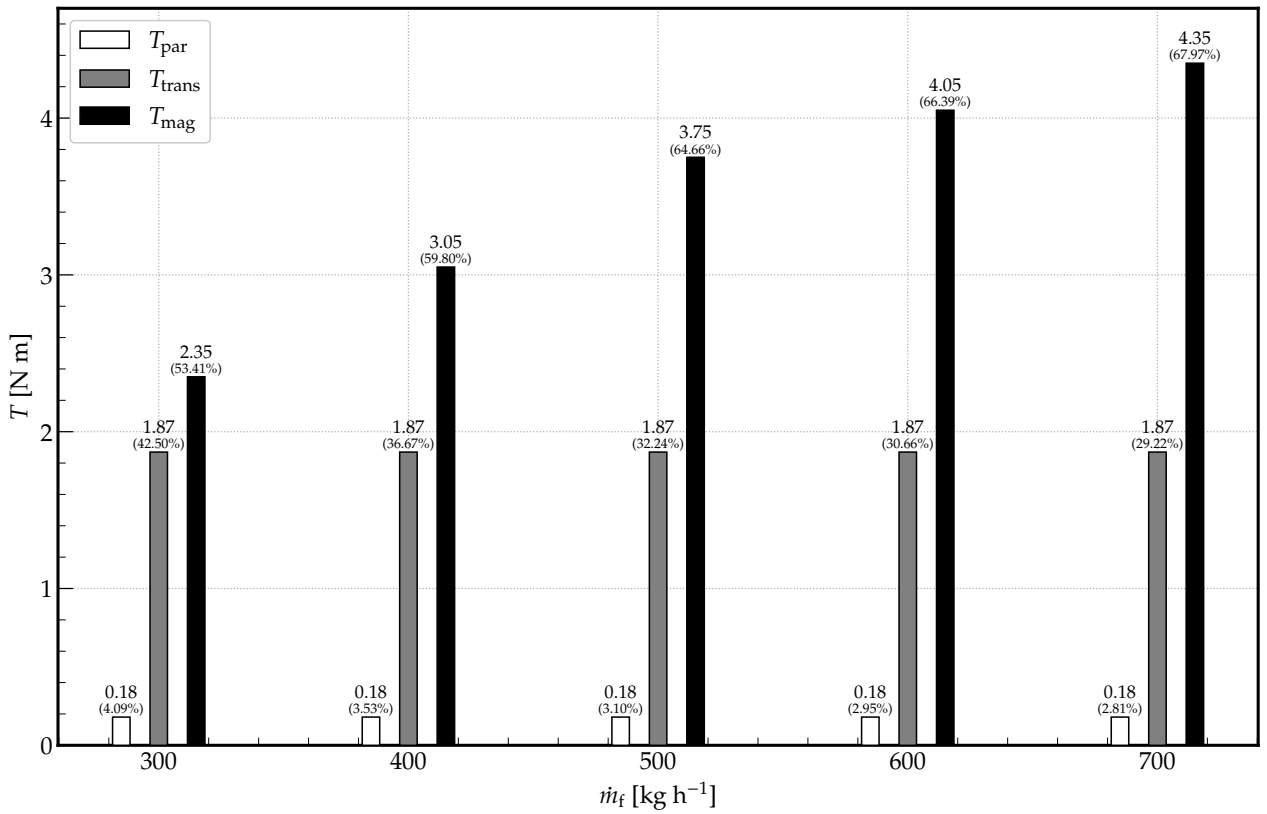


Figure 5.18 – Breakdown of the contributions of the torque in the system.

increasing mass flow rate. Notably, the hydraulic resistance of the porous medium in the AMR contributes most to the total pressure drop of the system, accounting for approximately 54% to 59%. The contributions of the other hydraulic auxiliary components and tubing are minor but still significant, accounting for more than 40% of the total pressure drop. This finding is critical since the operation of the AMR is based on a complex hydraulic arrangement, with a casing housing the porous medium featuring two ends: one hot and one cold, each equipped with channels to facilitate the inlet and outlet of fluid streams, which were not considered in the modelling of the system presented in Chapter 3. Additionally, the casing has limited volume to efficiently distribute the fluid, as a loss of volume in voids can significantly affect the performance of the AMR (Trevizoli *et al.*, 2018). Understanding the distribution of pressure drop throughout the system is essential for optimizing hydraulic design and ensuring efficient operation of the MR prototype. Addressing hydraulic resistance in the porous medium of the AMR and carefully designing the casing can lead to substantial improvements in the overall performance of the system.

The following analysis focuses on the resulting power consumption associated with the torque and pressure drop data. It is essential to note that the power consumption analysis is based on measurements from power transducers and accounts for the irreversibilities of the motor and pump. The breakdown of the power consumption associated with the mechanical transmission of the rotor, according to Eq. (4.6), is shown in Fig. 5.20.

The trends observed in Fig. 5.20 are consistent with those encountered in Fig. 5.18.

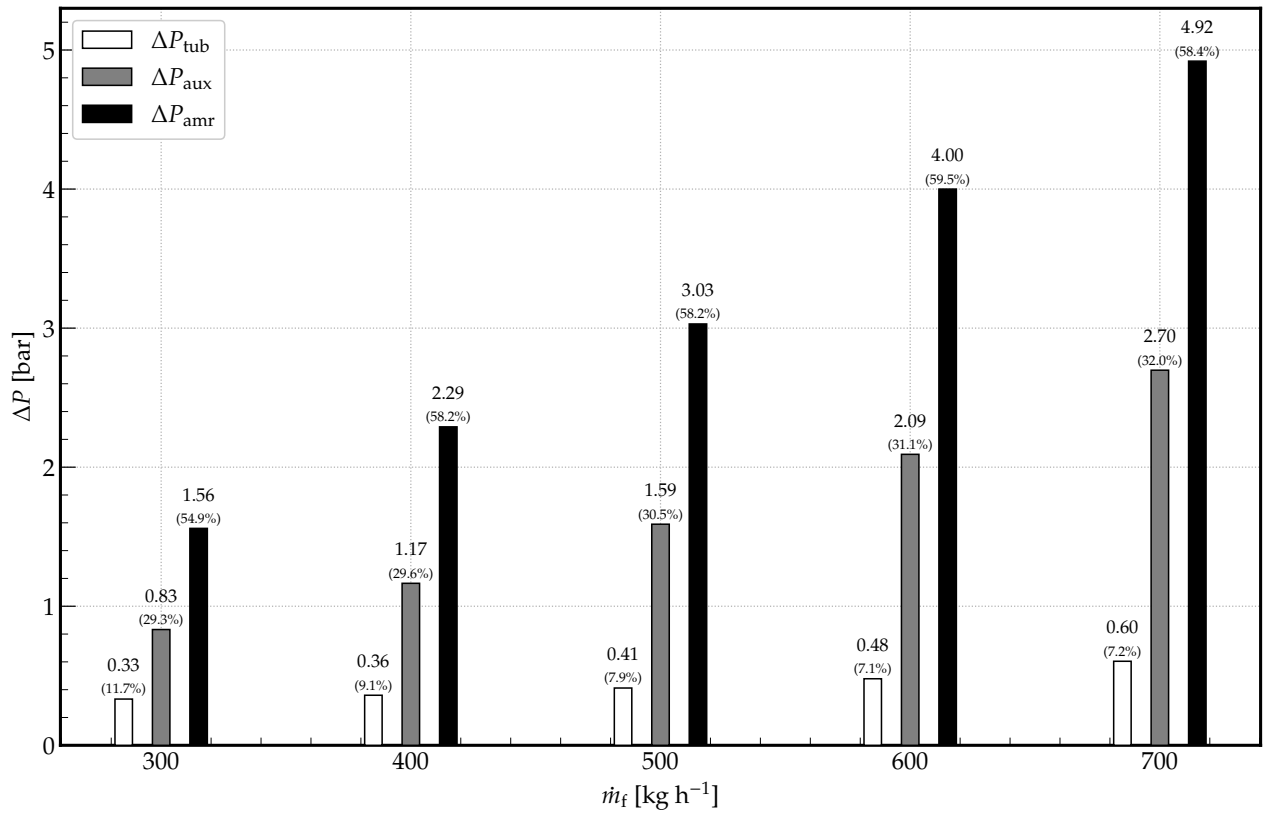


Figure 5.19 – Breakdown of the contributions of the pressure drop in the system.

Both parasitic and mechanical transmission power consumption are independent of the mass flow rate, whereas the magnetization share increases with it. What stands out most in Fig. 5.20 is the large share attributed to the inherent irreversibilities of the motor, as between 47% and 57% of the power consumption for mechanical transmission is lost in the operation of the system. While it is possible to achieve higher efficiency through the design of a motor tailored to a specific operating point, it is not anticipated that commercially available alternatives will bring about significant, game-changing improvements in system performance. Therefore, since most performance evaluations of magnetic refrigerators in the literature account only for magnetization power consumption, the final power consumption associated with the mechanical transmission system can increase by more than 300% when all power consumption shares are considered.

Similarly, the breakdown of power consumption associated with fluid pumping through the system components, as given by Eq. (4.7), is shown in Fig. 5.21. Once again, it is worth noting that contributions from HHEx and CHEx are omitted in the plot due to their low magnitudes.

Once again, the large magnitude of the loss inherent to the pump operation is evident in Fig. 5.21. This is even more noticeable than the motor loss, as the pump operates in a broader range of operating conditions. At lower mass flow rates, it operates in highly inefficient regions where more than 80% of the power consumption of the system is due to pump losses. As the mass flow rate rises, this value reaches a minimum of 55% at 700 kg

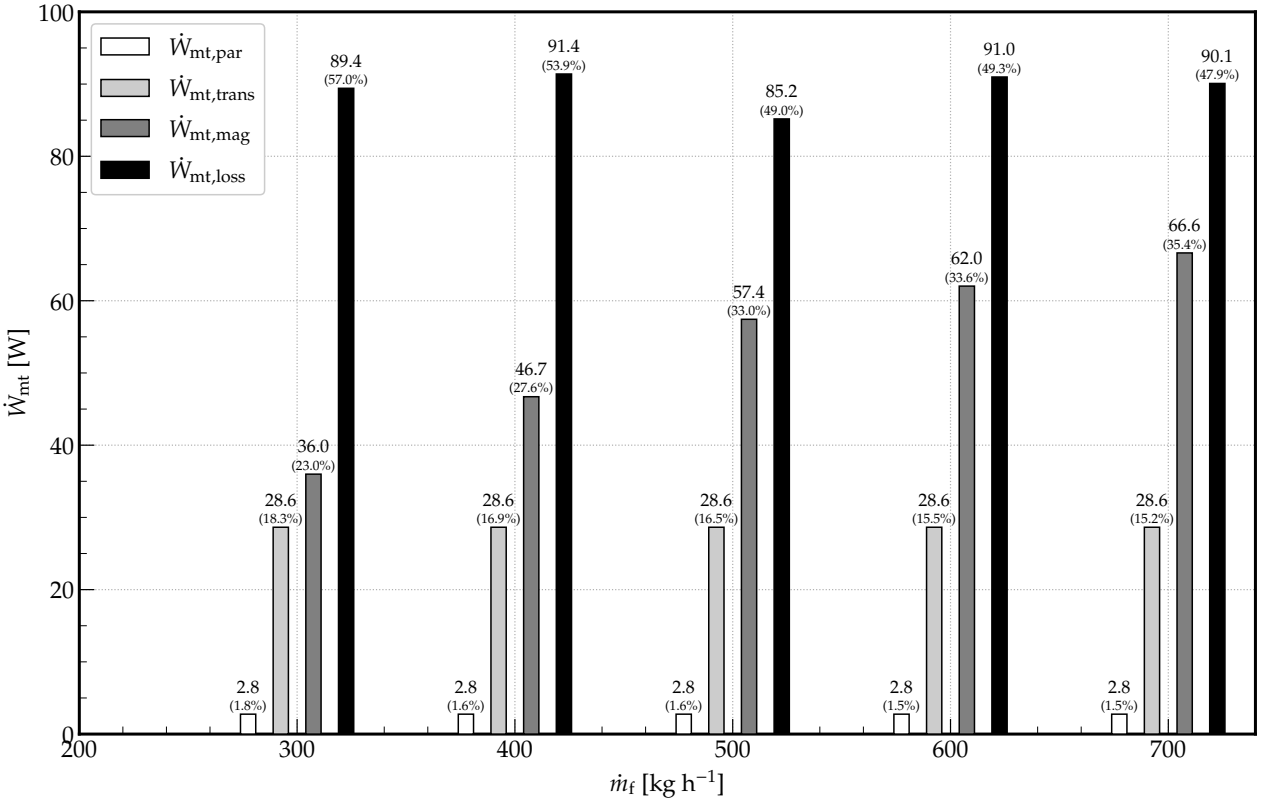


Figure 5.20 – Breakdown of the contributions of the mechanical transmission power in the system.

h^{-1}, which is still relatively high. If the system had operated at even higher mass flow rates, it is expected that the pump efficiency would have improved. However, that would entail higher overall pumping power, and as will be demonstrated later in this manuscript, it would not increase the cooling capacity. It is worth noting that properly designed, commercially available pumps can significantly enhance system performance (de SÁ *et al.*, 2023). However, when only the pressure drop share in the AMR beds is taken into account, as most MR studies assume, a considerable increase in pumping power consumption should be expected in a real system application. The minimum increase encountered in the present study is 300%, although it is significantly influenced by pump over-sizing.

Finally, Fig.5.22 illustrates the breakdown of the total system power consumption according to Eq.(4.8). It is important to note that the power consumption contributions of HHEX and CHEX include their respective fans, making them significant enough to be presented alongside the other shares. However, the power consumption of the electrovales is not displayed. The power consumption associated with pumping fluid through the AMR and magnetizing the MCM, as per Eq. (4.9), is presented independently in the pumping and mechanical transmission shares, respectively.

Figure 5.22 demonstrates that for all the mass flow rates evaluated, the leading share of power consumption was always associated with fluid pumping. Moreover, as the mass flow rate increases, the share of this contribution increases as well. Although the contribution from mechanical transmission also increases with the mass flow rate, this increase is almost

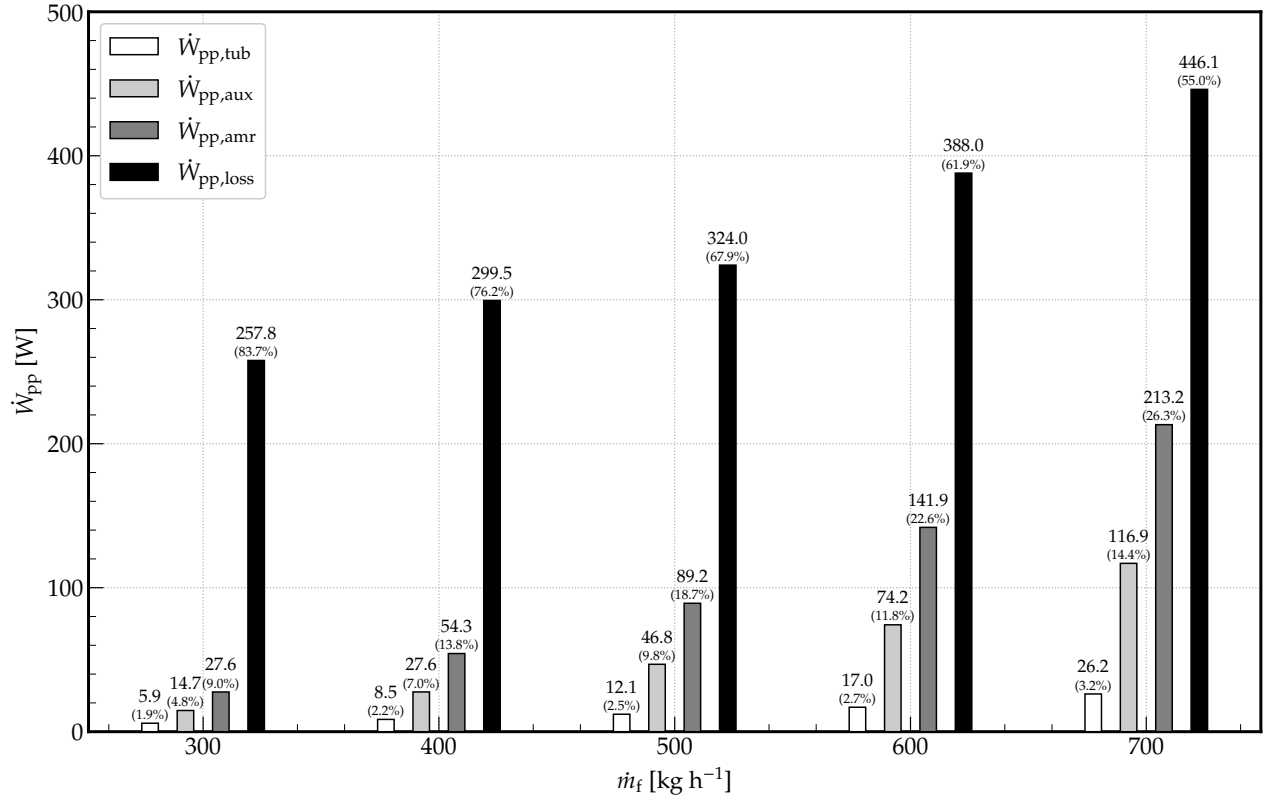


Figure 5.21 – Breakdown of the contributions of the pumping power in the system.

negligible, as the variation between the maximum and minimum values is around 30 W. In contrast, the same difference for fluid pumping exceeds 500 W. The power consumption values for the HHEx and CHEx remain relatively constant during operation, as they are mainly determined by the fan, which is kept fixed across all tests. The HHEx consumes more power since it is larger than the CHEx.

It is also clear from Fig. 5.22 that the AMR power consumption shares represent a low percentage of the total power consumption, especially at lower mass flow rates. Up to a mass flow rate of 500 kg h^{-1}, the combined power required to magnetize the MCM and pump the fluid through the AMR did not exceed that consumed by the HHEx. Hence, from both the component and system standpoints, it is clear that the performance of the MR system is severely affected by external and parasitic irreversibilities associated with the components. That finding is fundamental to the design and optimization of MR systems, as these losses were underestimated or even neglected during the design stage, as presented in Chapter 3.

After assessing the contribution to the total power consumption of the system, the next step is to evaluate the cooling capacity of the prototype, according to Eq. (4.10)- (4.12). The corresponding cooling capacities calculated by the AMR and the calorimeter energy balances are presented in Fig. 5.23.

Figure 5.23 demonstrates that for the three perspectives evaluated, an optimal mass flow rate exists that maximizes the cooling capacity, identified as 600 kg h^{-1}. This phenomenon is commonly observed in the operation of AMRs and magnetic refrigerators. It

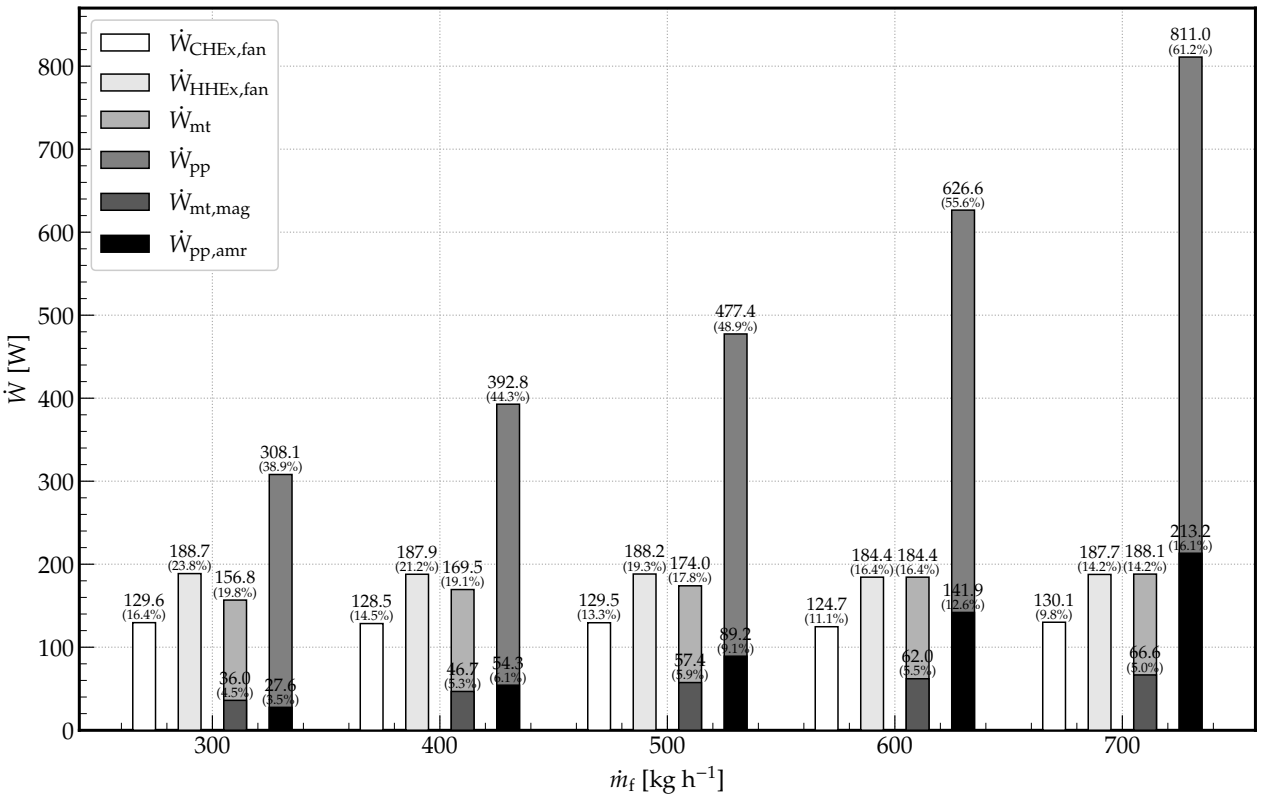


Figure 5.22 – Breakdown of the contributions to the overall power consumption in the system.

is primarily attributed to the trade-off between the increased mass of working fluid being displaced and the simultaneous loss in heat exchanger effectiveness, along with increased viscous dissipation as the mass flow rate rises. While the former factor enhances cooling capacity, the latter two exert a detrimental effect, thus defining an optimal mass flow rate. Additionally, the impact of the mass flow rate on axial conduction, dispersion, heat loss to the environment, flow maldistribution, and heat exchanger effectiveness is acknowledged. Still, it is considered to have a lesser effect on the cooling capacity of the prototype.

Key aspects of the practical application of MR are determined by comparing the three different cooling capacities. Most magnetic refrigerators measure cooling capacity solely from an AMR perspective, yielding the highest numerical values across all evaluated conditions. However, when considering the heat exchangers, including their internal irreversibilities and the heat transport to and from the AMR, a substantial reduction in cooling capacity is observed, as reflected by the system-level values. These losses are attributed to a combination of factors: fluid mixing, flow maldistribution, and heat dissipation in tubing and hydraulic components. Furthermore, the energy balance described by Eq. (4.11) is less affected by measurement uncertainties, such as those associated with thermocouples, compared to the balance described by Eq. (4.10).

Furthermore, the power dissipated by the fan results in a significant additional loss of cooling capacity. To mitigate this, conventional vapor-compression refrigeration systems often prefer HEx that operate without fans, a common feature in low-capacity appliances

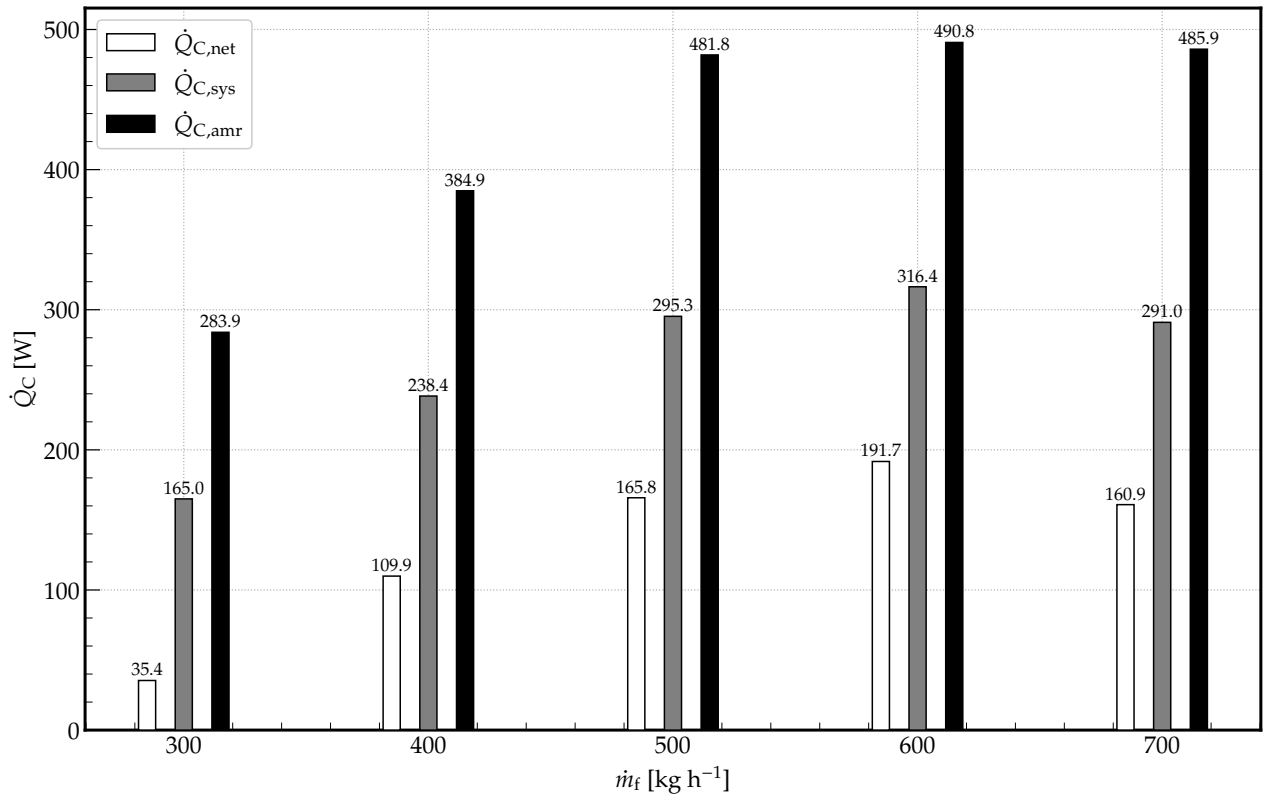


Figure 5.23 – Assessment of the cooling capacity of the system through different standpoints.

(Nakashima *et al.*, 2021). Nevertheless, for systems requiring high cooling capacity, the use of fans to enhance heat transfer and airflow through the heat exchangers is indispensable. In the context of magnetocaloric refrigeration, this issue is especially critical due to three main factors outlined below.

The first is related to the limitation of $\Delta T_{\mathrm{C,amr}}$ due to the magnitude of the MCE. To achieve substantial cooling capacities, large mass flow rates are necessary as dictated by Eq. (4.10). Unlike magnetic refrigerators, conventional vapor compression systems utilize the vaporization enthalpy of the liquid refrigerant, which results in a refrigerating effect several times greater, allowing operation at much lower mass flow rates. Consequently, the reduced mass flow rates in one of the HEx streams are less penalizing on the HEx, enabling the use of smaller components, including fans.

The second factor concerns the phase-change characteristics of the HEx used in vapor-compression refrigeration systems. These characteristics not only facilitate high heat transfer rate coefficients but also result in nearly isothermal heat transfer within one of the fluid streams. From an effectiveness standpoint, this is equivalent to operating with an infinite heat capacity rate for the streams, considered the most efficient mode of operation for a HEx (Kays & London, 1984).

Lastly, due to the low magnitude of the MCE, enhancing the temperature range attainable through MR remains a challenge. As depicted in Fig. 5.17, magnetocaloric systems are expected to operate with temperature differences significantly lower than those used

in vapor compression refrigeration. To counterbalance this, it is necessary to employ heat exchangers with greater heat transfer capacity between streams. Specifically, this requires larger components designed to handle higher mass flow rates and, consequently, necessitates more powerful fans.

Therefore, the heat dissipation by fans is a crucial aspect in the practical application of magnetocaloric refrigerators, an aspect that has been largely overlooked in the literature. Given that omitting a fan is not a viable option, the combined design of AMR and HEx is regarded as the principal strategy to reduce this loss (Peixer *et al.*, 2022).

Having presented the breakdown of power consumption and cooling capacity, the performance of the system is then evaluated. Initially, COP is examined from various perspectives, as defined by Equations (4.13) - (4.16), with the results depicted in Figure 5.24.

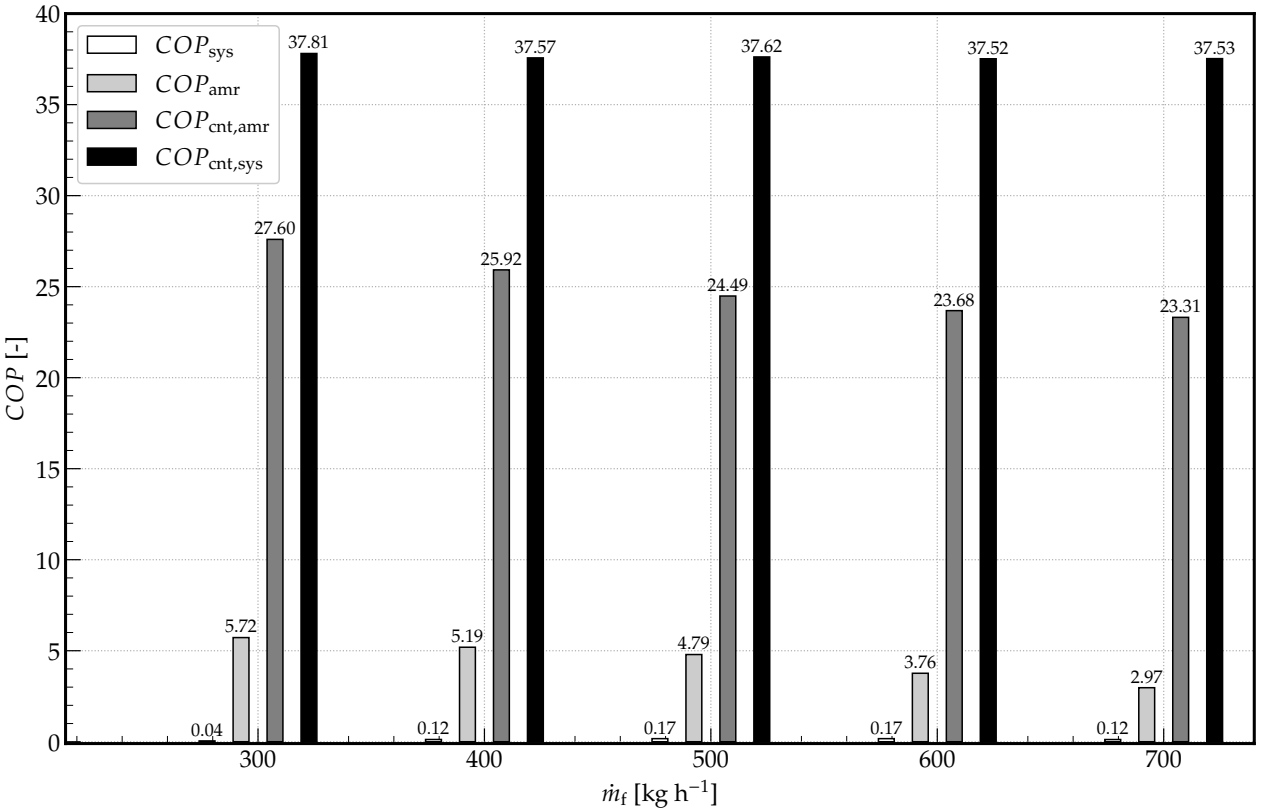


Figure 5.24 – Assessment of the coefficient of performance of the system through different standpoints.

In Fig. 5.24, it is noteworthy that the values of the COP for a Carnot cycle from both the AMR and system perspectives are solely dependent on the temperatures, as specified by Eq. (4.15) and Eq. (4.16). Therefore, $COP_{\mathrm{cnt,sys}}$ remains relatively constant, with minor variations attributed to fluctuations in the measured outdoor and indoor temperatures, which were maintained at approximately 35°C and 27°C, respectively. Conversely, $COP_{\mathrm{cnt,amr}}$ decreases in conjunction with an increase in the mass flow rate, due to the corresponding rise in the temperature span of the AMR, as depicted in Fig. 5.17. When comparing the two parameters, it is evident that the COP of the Carnot cycle is significantly higher when

assessed from the system perspective. Although this is an expected and apparent outcome, it is essential to emphasize that such a comparison can only be quantified with the inclusion of heat exchangers in the system, which is uncommon in MR designs.

Similarly, the COP values for the AMR also exhibit a maximum at the lowest mass flow rate tested and steadily decrease as this operational parameter increases. This trend is mainly a consequence of the trade-off between the impact of a rise in mass flow rate on the pumping power and the cooling capacity, as presented in Figs. 5.21 and 5.23, respectively. Conversely, this same trade-off dictates the behavior of the COP of the system. It results in an optimal point at a mass flow rate of 500 kg h^{-1}, which can be attributed to the relatively lower contribution of pumping power from a systemic perspective. When comparing the COP values from these two viewpoints, there is a clear indication of significant performance deterioration when the focus shifts from the AMR to the entire system. This outcome arises not only from the increase in power consumption and losses in the auxiliary components but also from a reduction in cooling capacity, as demonstrated in Fig. 5.24.

Lastly, a second-law efficiency analysis is conducted to understand the system losses further. Figure 5.25 presents the second law efficiencies of the system, as determined by Eqs. (4.17)- (4.20).

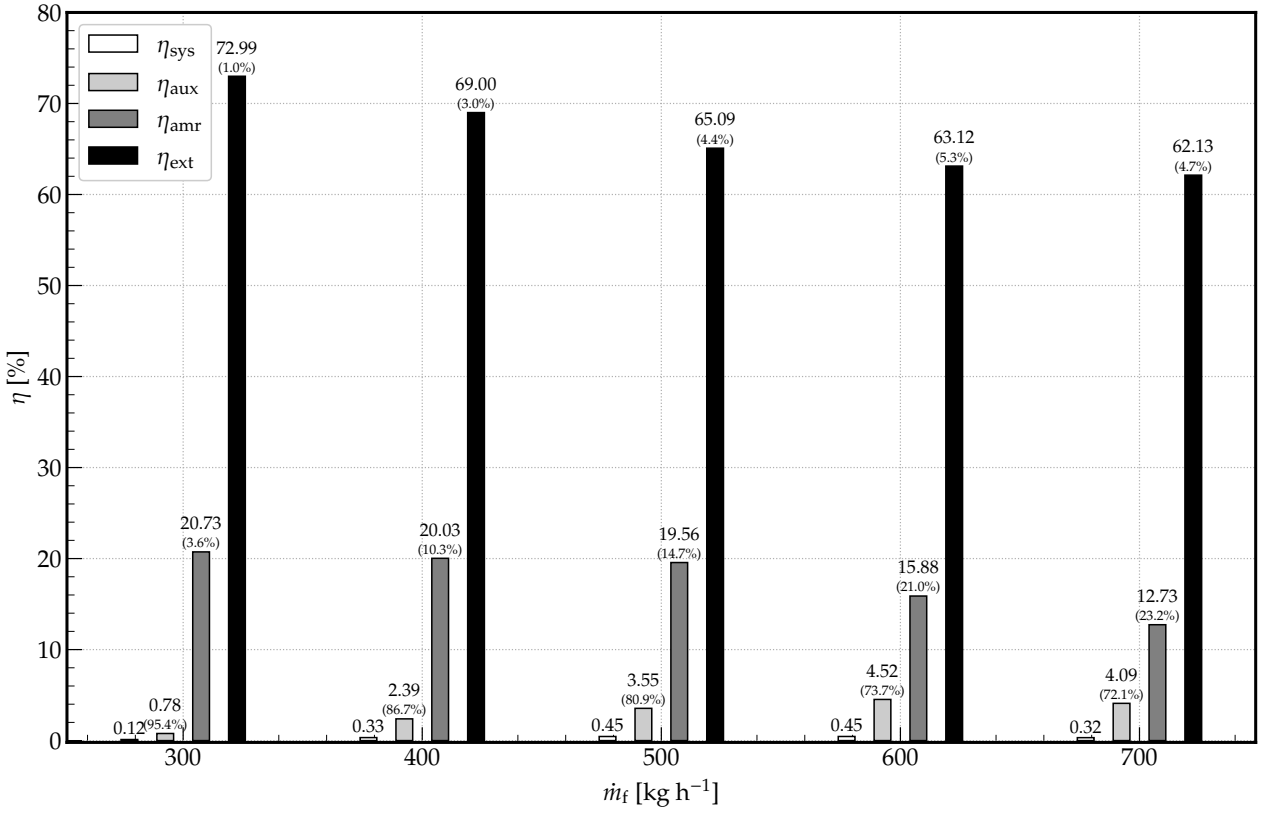


Figure 5.25 – Assessment of the second law efficiency of the system through different standpoints.

Figure 5.25 allows for a more detailed investigation of the irreversibilities within the MRU. Initially, from an external standpoint, *i.e.* the perspective of the heat exchanger, the second law efficiency attains high values, ranging from 62.13% to 72.99%. This efficiency is

notable even compared to conventional vapor-compression systems (de SÁ *et al.*, 2023). It is critical to acknowledge, however, that these high efficiencies are primarily due to the inherent operational constraints of magnetocaloric refrigeration technology, which limit the refrigerant loop of the system from operating across large temperature spans. As the temperature span and mass flow rate of the AMR are increased, there is a corresponding decrease in external second law efficiency, as depicted in Fig. 5.25.

From the perspective of the AMR, the second-law efficiency remains high, ranging from 12.73% to 20.73%, despite decreasing with increasing mass flow rate. This metric is particularly relevant for benchmarking against other MR systems since it excludes external irreversibilities of auxiliary components and disregards the disparities between the system and the temperature span specific to the AMR. When taking into account the irreversibilities of auxiliary components, as quantified by η_{aux}, the system incurs additional losses. These losses manifest as increased power consumption and diminished cooling capacity.

Evaluating the contribution of each determined share to the second law efficiency of the systems yields interesting insights. At the lowest mass flow rate, the irreversibilities attributable to the auxiliary systems account for over 95% of the total irreversibilities of the system. With an increase in mass flow rate, their contribution diminishes to at least 72%. Conversely, the external second-law efficiency is consistently lower, ranging from 1% to 4.7%. Meanwhile, the irreversibilities associated with the AMR, which has been the primary focus of most MR research, vary from 3.6% to nearly 23.2%. This analysis reaffirms that the predominant share of irreversibilities originates from components external to the AMR.

5.3 Outline of the Chapter

This chapter presented the experimental evaluation of the MRU, starting with the individual characterization of its key components, including the MC, MCM, AMR, and HMS. The overall performance of the three prototype generations was then analyzed and compared using various performance metrics, highlighting the improvements achieved across iterations. Finally, a detailed thermodynamic assessment of the prototype demonstrated the most favorable operating conditions for air conditioning applications, providing insights into its efficiency and practical potential.

Chapter 6

APPLICATION OF ARTIFICIAL INTELLIGENCE IN MAGNETIC REFRIGERATION

In this chapter, the application of AI techniques in MR is explored through steady-state and dynamic modeling approaches. Unlike what was previously developed in Chapter 3, the modeling of steady-state performance relies on experimental results rather than numerical simulations. For that, an extensive data collection process was conducted, gathering data from the most important MR prototypes reported in the literature. Following that, the development of a transient model of the performance of the MRU is presented, offering more profound insight into the transient response and performance of MR systems under varying operational conditions. Lastly, an uncertainty analysis of the effect of uncertainties in the Curie temperature on AMR performance is conducted using an ANN-enhanced Monte Carlo analysis. These AI-enhanced models aim to improve the accuracy and optimization of prediction in the design and operation of such systems.

6.1 Steady-State Model

In Chapter 3, the capabilities of ML and DL for modeling AMR and MR systems were preliminarily explored. Despite its success, it is worth noting that the models were trained on numerical data, which may be valid but is not ideal, as numerical models tend to deviate from the actual performance of the systems. Therefore, this section aims to explore ML performance on experimental MR data.

6.1.1 Problem Formulation

In MR, AI models have been used to model material properties (Maiorino *et al.*, 2019) and components (Aprea *et al.*, 2018; Maiorino *et al.*, 2022). However, previous attempts to apply ANN for the modeling of MR systems relied on either numerical data or experimental data from a single prototype. For that, this work seeks to advance the application of AI in MR by collecting data on the main room-temperature prototypes reported in the literature and applying ANNs to predict their performance over their operational ranges. The problem to be tackled, according to Eq. (2.8) is given by:

$$\dot{Q}_{\mathrm{C}} = \mathcal{F}(x) \tag{6.1}$$

6.1.2 Data Collection and Preparation

The data collection process involved gathering data from the main prototypes reported in the literature and from internal, unpublished data available at Polo. A summary of the data is presented in Tab 6.1.

Table 6.1 – Summary of the data collected from the main MR prototypes reported in the literature.

Test source	B [T]	AMR beds	Geometry	MCM	N_l	Mass of MCM [g]	Samples
Trevizoli *et al.* (2016b)	1.69	1	Spheres	Gd	1	195.5	111
Lozano *et al.* (2016)	1	16	Spheres	Gd	1	1700	51
Capovilla *et al.* (2016)	1	16	Spheres	Gd	1	1700	15
Trevizoli *et al.* (2017)	1.69	1	Spheres	Gd	1	86.4	110
			Pins			85.3	107
			Plates			83.8	66
Nakashima *et al.* (2018)	1.69	1	Spheres	Gd	1	194.8	75
Vieira *et al.* (2021)	1.69	1	Particles	CV-H	3	75	18
Teza *et al.* (2024)	1.69	1	Particles	CV-HS	10	232	90
Internal Data	1.69	1	Particles	CV-HS	5	224	36
Nakashima *et al.* (2021)	0.98	8	Spheres	Gd	3	2250	15
Internal Data	1.69	1	MCR	CV-HS	4	81	109
Peixer *et al.* (2023)	1.15	8	Particles	Hybrid	11	10360	10
Peixer *et al.* (2024)	1.47	16	Particles	Hybrid	11	11600	29
Peixer *et al.* (2026)	1.47	4	Particles	Hybrid	3	3275	12
Aprea *et al.* (2014)	1.25	8	Spheres	Gd	1	1200	25
Aprea *et al.* (2016)	1.25	8	Spheres	Gd	1	1200	10
Aprea *et al.* (2016)	1.25	8	Spheres	Gd	1	1200	76
Tušek *et al.* (2014)	1.15	1	Plates	Gd	1	176	10
				La	2	144	9
					4		9
					7		9
Tura & Rowe (2011)	1.47	2	Spheres	Gd	1	110	31
Arnold *et al.* (2014)	1.54	2	Spheres	Gd	1	650	14
Huang *et al.* (2019)	0.875	7	Spheres	Gd	1	1180	16
Engelbrecht *et al.* (2012)	1.24	24	Spheres	Gd	1	2800	31
Lozano *et al.* (2013)	1.24	24	Spheres	Gd	1	2800	20
Lozano *et al.* (2014)	1.24	24	Spheres	Gd	1	2800	29
Eriksen *et al.* (2015)	1.13	11	Spheres	Gd	4	1700	5
Fortkamp *et al.* (2018)	1.34	11	Spheres	Gd	4	1700	27
Masche *et al.* (2021)	1.44	13	Particles	CV-HS	10	3406	26
Masche *et al.* (2022)	1.44	13	Spheres	Gd	1	3830	55
Jacobs *et al.* (2014)	1.44	12	Particles	La	6	1520	48
Hai *et al.* (2024)	1.23	8	Spheres	Gd	1	1350	26

The data collected from the prototypes consist of the following sets:

- **Numerical Input Data:** Width (W_{AMR}) and Height (H_{AMR}) or Diameter (D_{AMR}) and Length (L_{AMR}) of the regenerator bed, operating frequency (f), liquid mass flow rate ($\dot{m}_{\mathrm{f}}$), minimum and maximum magnetic flux densities (B_{min} and B_{max}), hot reservoir temperature (T_{H}), cold reservoir temperature (T_{C}), blow fraction ($F_{\%}$), number of regenerator beds (N_{AMR}), particle diameter (d_{p}), porosity of the porous medium (ε), Number of MCM layers (N_{Curie}), Curie temperature of the multilayer arrangement ($\overline{T}_{\mathrm{curie}}$) and Composition of the Multilater arrangement ($\overline{X}_{\mathrm{Curie}}$);

- **Categorical Input Data**: Shape of the AMR (S^*_{AMR}): Prismatic or Circular; Magnetic profile (B^*_{prof}): Instantaneous or Sinusoidal; Geometry of the MCM (G^*_{MCM}): Plates, Pins, Spheres, Particles, and Microchannels; MCM composition (M^*_{MCM}): Gadolinium alloys (Gd), Calorivac-H (CV-H), Calorivac-HS (CV-HS), Lanthanum alloys (La), mixed Gadolinium and Calorivac-HS (Gd/CV-HS);

- **Output parameter**: cooling capacity ($\dot{Q}_{\mathrm{C}}$);

Several remarks and assumptions must be made about the data collection. The data samples for the present prototype are the ones collected by Peixer *et al.* (2023) (first version), Peixer *et al.* (2024) (second version), and Peixer *et al.* (2026) (third version). It is worth mentioning that most of the information presented in Tab. 6.1 has been collected from articles provided by the authors of the work, much of which was presented in plots or involved the calculation of parameters. Hence, minor deviations are expected. Despite that, it is assumed that the dataset does not include any outliers, duplicates, missing values, or noise, and therefore, no techniques are employed to address them.

Only two AMR shapes were considered: circular (Trevizoli *et al.*, 2016b) and prismatic ones, such as sectors of hollow cylinders (Eriksen *et al.*, 2015; Lozano *et al.*, 2016; Nakashima *et al.*, 2021; Peixer *et al.*, 2023) or tapered prisms (Dall'Olio *et al.*, 2021), which were characterized by a mean equivalent width and length. In addition, the values of the composition of $\overline{T}_{\mathrm{curie}}$, $\overline{X}_{\mathrm{Curie}}$, and MCM are combined into 100-element arrays, where each element characterizes the MCM and CUrie temperature of the element. Magnetic profiles are considered instantaneous when both low- and high-field plateaus can be identified (Insinga *et al.*, 2016; Fortkamp *et al.*, 2023), and sinusoidal when they are not easily identifiable, which is seen mainly in Halbach array magnetic circuits (Arnold *et al.*, 2014; Trevizoli *et al.*, 2015).

Moreover, classification by MCM type was based on the main characteristics of the materials. The test considered to operate with Gd covers both cases: a single Gd layer, as in Trevizoli *et al.* (2016b), or a multilayer of Gd and Gd-Y alloys, as in Nakashima *et al.* (2021). The test classified into Calorivac-H (CV-H) and Calorivac-HS (CV-HS) are the ones that operate with the La(Fe,Mn,Si)$_{13}$H$_{\mathrm{z}}$ alloys commercialized by Vacuumschmelze GmbH & Co. The distinction between them is that CV-H is an epoxy-bonded porous medium, whereas

CV-HS is not. Multilayer regenerators with mixed Gd and CV-HS are considered only those developed Peixer *et al.* (2023), Peixer *et al.* (2024), and Peixer *et al.* (2026). Lastly, CV-H and CV-HS geometries were not considered spheres because they resemble elongated cylinders, which exhibit different thermo-hydraulic behavior than spheres (Vieira *et al.*, 2021).

Categorical data are encoded using one-hot encoding. In doing so, each categorical feature is transformed into N_{enc} new binary features, where N_{enc} is the number of distinct categories in the original feature. Hence, the features: (1) Shape of the AMR, (2) Magnetic profile, (3) Geometry of the MCM, and (4) MCM composition are transformed into 2, 2, 5, and 5 new features, respectively. The data is also standardized with a z-score method. The dataset split follows a 64%, 16%, and 20% rule for training, validation, and test sets, respectively. Given the imbalance in the sample sizes across the different tests, a weighting technique was employed so that data from each experiment had the same influence on the training.

For model development, the height and width of prismatic regenerators, as well as the diameter of cylindrical regenerators, are replaced by the hydraulic diameter (D_{H}) and the aspect ratio (A_{R}), which can be calculated as follows:

$$D_{\text{h}} = \frac{2HW}{H+W} \tag{6.2}$$

$$A_{\text{R}} = \frac{H}{W} \tag{6.3}$$

and for cylindrical regenerators, the hydraulic diameter has the same value as its diameter, and the aspect ratio has a numeric value of 1.

6.1.2.1 Exploratory Data Analysis

A brief exploratory data analysis was performed to better understand the dataset used and its influence on model development. As presented in Tab. 6.1, 1304 data samples have been collected either through internal availability or literature review. It is important to note that the number of samples per experiment, or test bench, varies significantly, as expected given the wide variation in experiments conducted and the resulting data reported. An understanding of the wide range of input and output parameters is fundamental to developing a model that covers the entire design space, as is the model proposed in the present study.

Although there is a wide range of component configurations and couplings, there are roughly two clusters of experimental apparatus. One is made of Halbach-array magnetic circuits with sinusoidal magnetic profiles, up to two circular regenerator beds, and a single-layered MCM weighing less than 700 g. These are the prototypes developed at the Federal University of Santa Catarina, Brazil (Trevizoli *et al.*, 2016b) and the University of Victoria, Canada (Tura & Rowe, 2011). The second cluster consists of bigger prototypes, usually with

more than two prismatic multilayered AMR beds and instantaneous magnetic profiles, and more than 1000 g of MCM. It should be noted that there are some discrepancies between the proposed clusters, with the main outlier in the classification being the prototype developed by Tušek *et al.* (2014).

In terms of the magnetic flux density, the largest magnitudes were achieved by the Halbach-array magnetic circuits. However, that benefit is offset by the magnetic profile during the low-field plateau, which cannot maintain a value close to 0 T and is detrimental to AMR performance. For instantaneous cases, the magnetic flux density ranged from 0.875 to 1.44 T. Regarding MCM, roughly 60% of the experiments were conducted with spherical Gd. That is mainly attributed to the availability of the material during the first half of the last decade. Economic and supply restrictions on raw materials have promoted the development of novel alloys, particularly Calorivac alloys.

To better understand the dataset, the distributions of operating conditions (namely, mass flow rate, frequency, and temperature span) and the output variable (cooling capacity) will be presented as histograms. The histogram of the system mass flow rate distribution in the dataset is shown in Fig. 6.1.

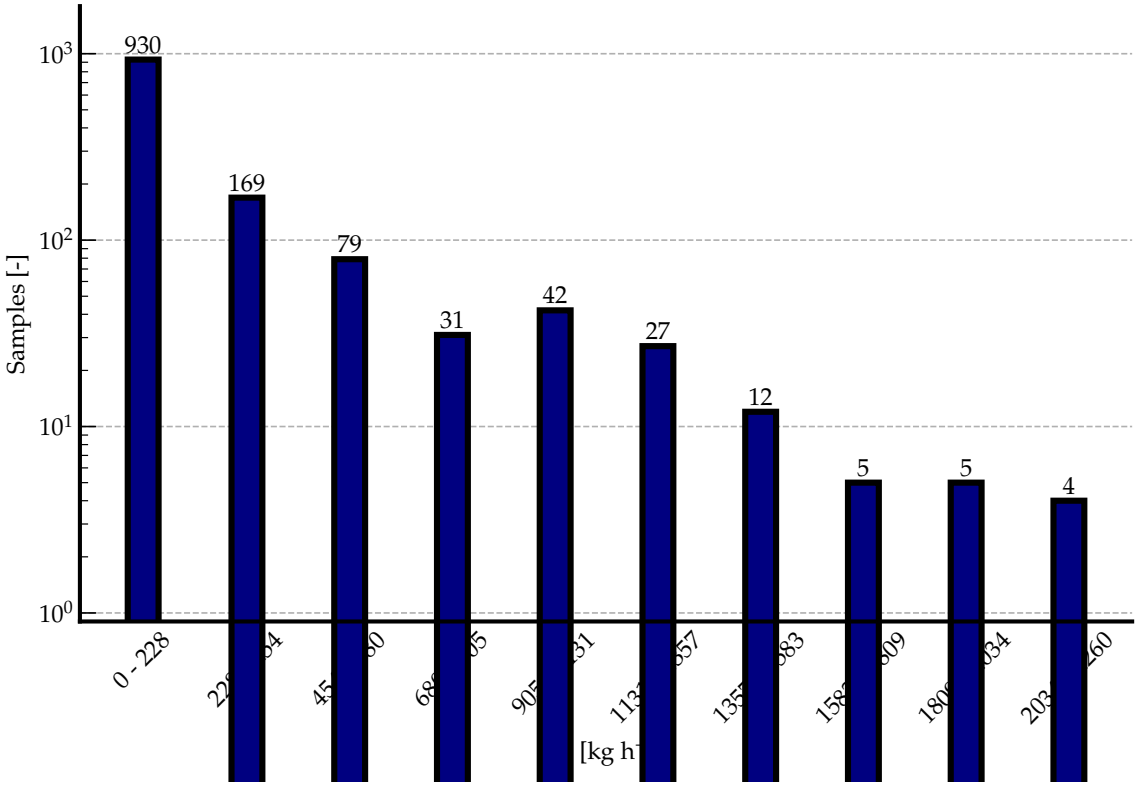


Figure 6.1 – Distribution of the mass flow rate of the system in the dataset.

Figure 6.1 shows that the largest share of the collected experiments operates with mass flow rates below 230 kg h^{-1}, and only a few tests have operated with more than 1000 kg h^{-1}. That is one of the most critical parameters in the design of magnetic refrigerators, as it influences phenomena such as the displaced fluid volume, solid-fluid heat transfer, and

viscous dissipation. In general, magnetic refrigerators must operate with high mass flow rates, especially compared to mechanical vapor compression systems, due to the magnitude of the magnetocaloric effect. From an engineering perspective, this poses a significant challenge, as pumps must be sized appropriately and typically account for the largest share of the power consumption of the system (SÁ *et al.*, 2023a), as presented in Chapter 5.

The histogram of the frequency distribution of the system in the dataset is presented in Fig. 6.2. Once again, most experiments were conducted at low frequencies, below 1 Hz. That is also a characteristic of MR, given the weight of the components, usually the magnetic circuit, and the inertia of the oscillatory fluid flow. Few magnetocaloric prototypes were able to operate at frequencies higher than 2.5 Hz, which is also considerably lower than the 50-60 Hz at which vapor compression systems usually operate. That is one of the main factors explaining the greater weight and mass of magnetocaloric refrigerators compared to conventional ones.

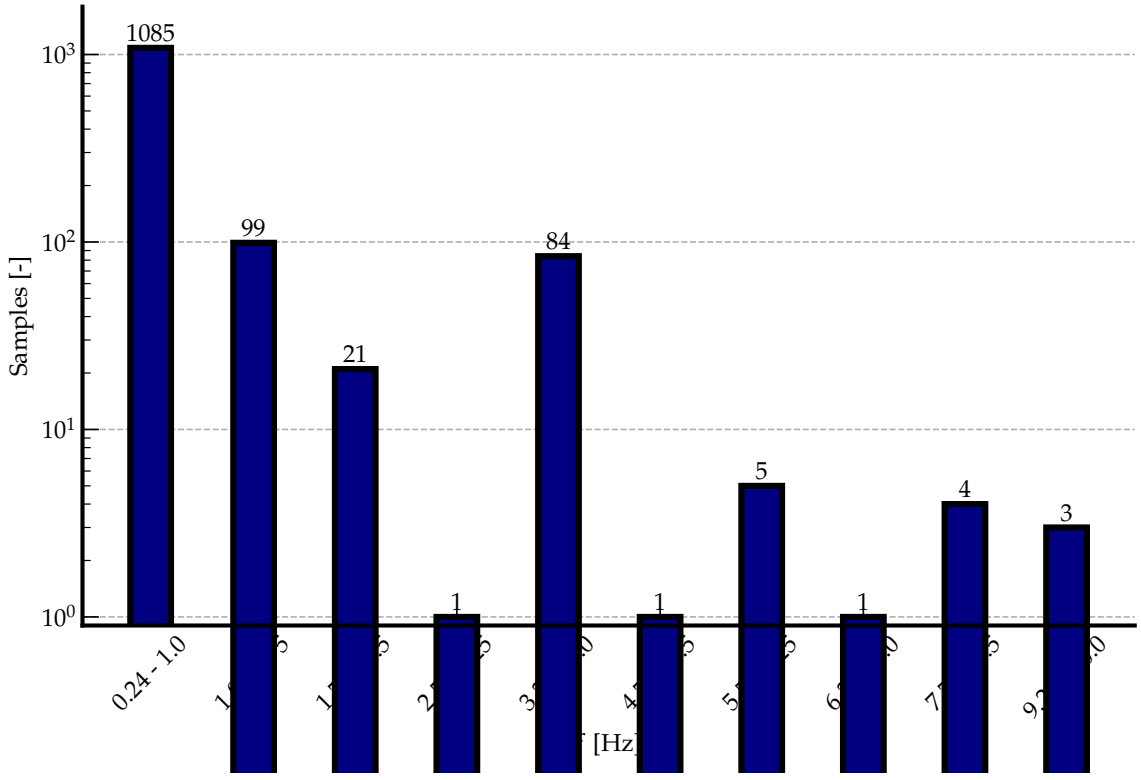


Figure 6.2 – Distribution of the operating frequency of the system in the dataset.

The following parameter to be evaluated is the temperature span of the system, as presented in Fig. 6.3. It is important to note that most experiments were conducted to characterize performance across different temperature ranges or to validate numerical models. For that, a design space that might be unfeasible from an application standpoint, such as a zero-span operation, has been extensively explored in the literature and is reflected in numerous experiments with low-temperature spans. However, from an application perspective, it is clear that magnetic refrigerators face a significant challenge in achieving temperature spans that align with the practical operation of refrigeration systems. Only a few tests exceeded

25 K in the temperature range, even without accounting for the irreversibilities of the HEx. Once again, vapor compression systems operate over much wider temperature spans, and achieving similar conditions might be the most significant challenge currently faced by MR systems.

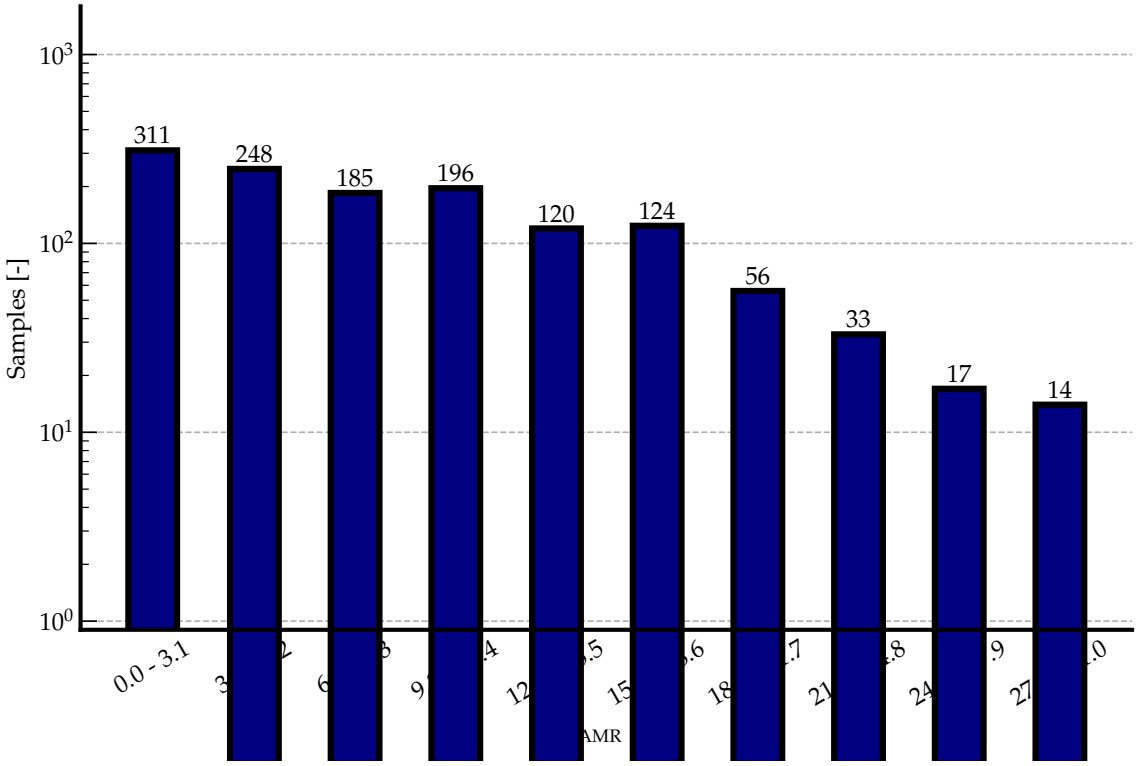


Figure 6.3 – Distribution of the temperature span in the dataset.

A standard metric for MR evaluation is the utilization factor (φ), which can be calculated according to Eq. 6.4. The parameter has considerable physical significance, as it represents the ratio of the thermal mass of the fluid displaced per blow to the thermal mass of the solid matrix. Not only does it represent a fundamental parameter for heat transfer in the porous medium (Nellis & Klein, 2009), but it also serves as a nondimensional parameter, allowing the comparison of prototypes with different scales. The frequency histogram of the utilization factor is shown in Fig. 6.4.

$$\varphi = \frac{\dot{m}_{\mathrm{f}} c_{\mathrm{f}}}{m_{\mathrm{mcm}} f c_{\mathrm{s}} F_{\%}} \tag{6.4}$$

where the specific heat for the solid is considered as 350 and 500 J kg^{-1} K^{-1} for the Gd (Trevizoli *et al.*, 2016b) and La-alloys (Masche *et al.*, 2021), respectively.

Figure 6.4 demonstrates that most prototypes operate at utilization factors below 1, mainly due to the trade-off that the parameter characterizes. There is a compromise between an increase in the mass of displaced fluid and a reduction in the effectiveness of the porous medium as utilization increases. Usually, optimal points occur at intermediate utilization values, between 0.3 and 0.8, which is why most prototypes operate in this design space.

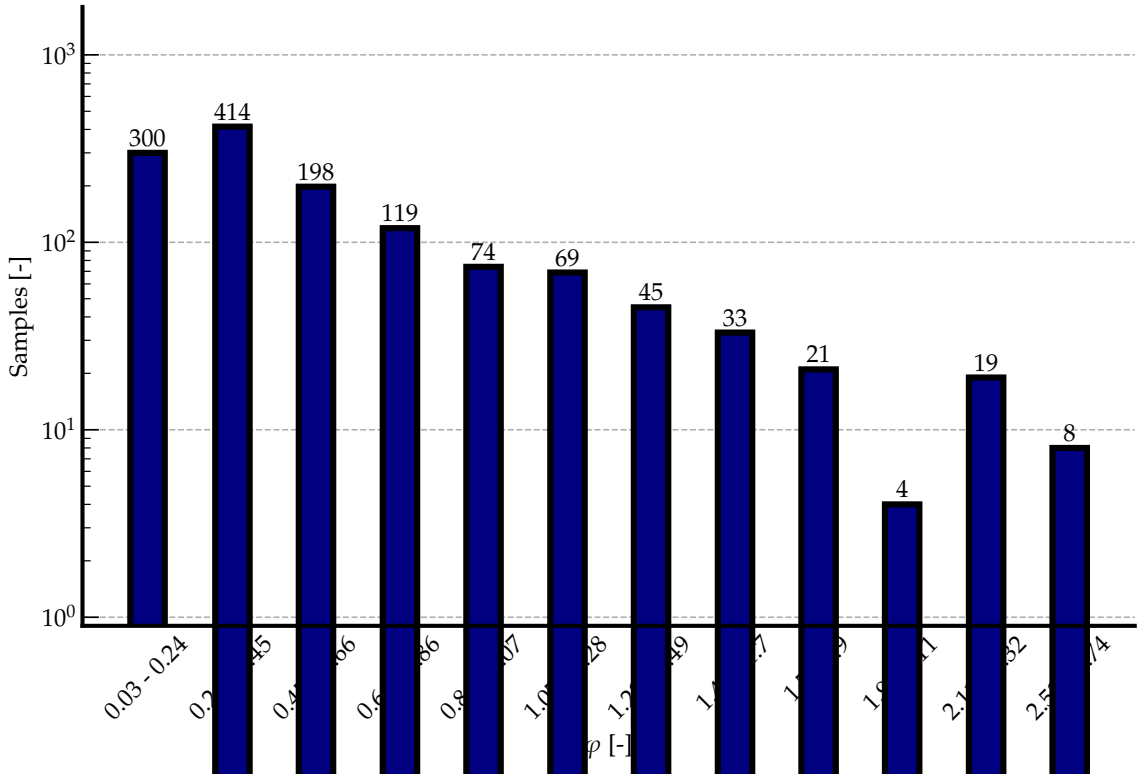


Figure 6.4 – Distribution of the utilization factor of the system in the dataset.

Lastly, the cooling capacity is the final metric to be evaluated. The histogram of the distribution of the cooling capacity achieved in the experiments is presented in Fig. 6.5. Once again, as with the temperature span, many experiments were conducted to characterize the performance or validate numerical models, resulting in cooling capacities that may not be of practical significance, especially in no-load tests. As observed in Fig. 6.5, most of the experiments achieved less than 100 W of cooling capacity and very few of them exceeded 500 W. Moreover, most of the prototypes developed and experiments carried out are unable to meet the simultaneous demands for cooling capacity and temperature span that refrigeration applications require.

To better understand the dataset, the correlation matrix of the Pearson correlation coefficient (Eq. (6.5)) between some numerical input features and the output parameter is presented in Fig. 6.6.

$$r_{\mathrm{xy}} = \frac{\mathrm{cov}(x,y)}{\sigma_x \sigma_y} = \frac{\sum_{i=1}^{n}(x_i - \bar{x})(y_i - \bar{y})}{\sqrt{\sum_{i=1}^{n}(x_i - \bar{x})^2}\sqrt{\sum_{i=1}^{n}(y_i - \bar{y})^2}} \tag{6.5}$$

The correlation matrix shows the correlation between each pair of parameters using their correlation coefficient: values closer to 1 or -1 indicate a more substantial positive or negative linear correlation, respectively, while values closer to 0 indicate no linear correlation. Despite its linear character, several interesting observations about the data set can be drawn from the matrix evaluation.

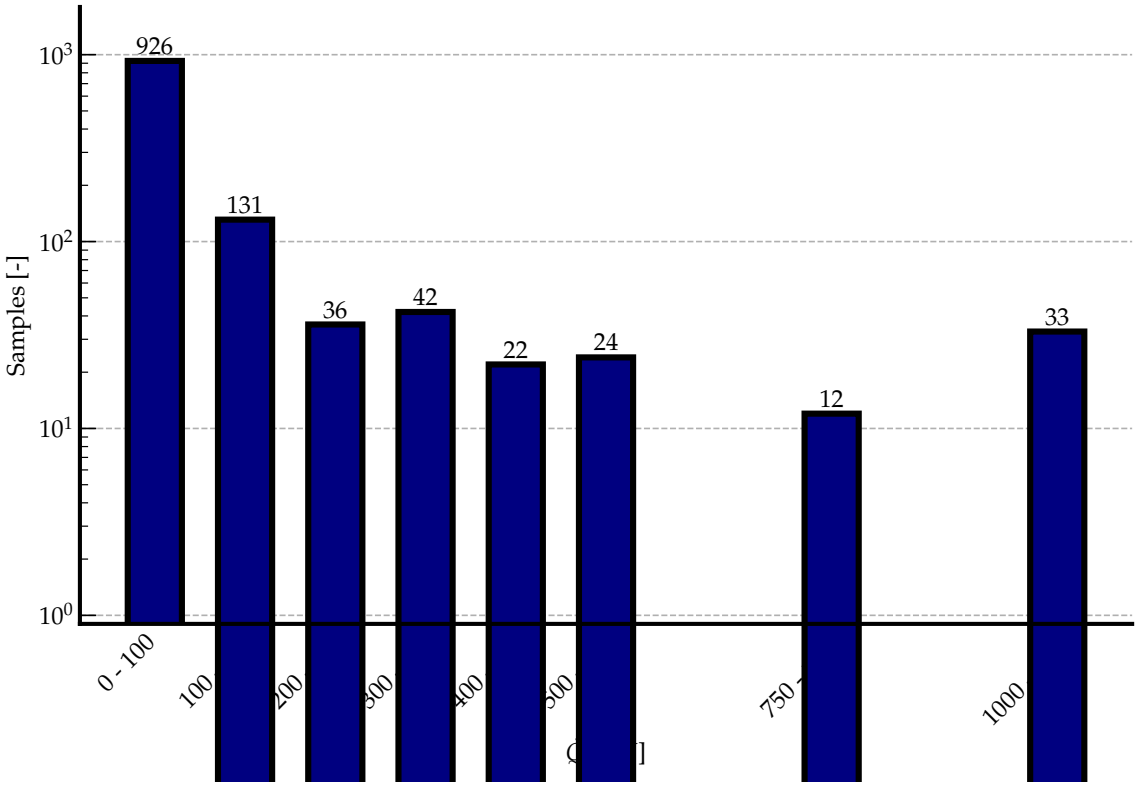


Figure 6.5 – Distribution of the cooling capacity of the system in the dataset.

For instance, the mass flow rate shows positive, high correlation coefficients (above 0.5) with the hydraulic diameter, the number of AMRs, and the cooling capacity. Those were expected, as the high number of beds and large flow area allow for higher mass flow rates and, consequently, higher cooling capacities. In addition, a correlation between design variables can be seen, such as between the blow fraction and the number of AMR beds. The variables exhibit a strong negative correlation, as the blow fraction is expected to decrease as the number of AMR beds increases, providing proper coupling between the hydraulic and magnetic profiles. Similar conclusions can also be drawn when comparing the frequency and mass flow rate, the number of AMR beds and cooling capacity, and the blow fraction and mass flow rate.

Moreover, the maximum magnetic flux density presents some insightful correlations. It is negatively correlated with the aspect ratio, which can be explained by the greater influence of regenerator height on the magnetized volume. Still, it is positively correlated with length, which seems counterintuitive. More remarkably, it has a weak negative correlation with the cooling capacity. Those two can be explained as the highest magnetic flow rates are achieved with the Halbach-array MC, which is usually employed for small-scale test benches. Hence, the simple linear correlation between the variables often provides misleading insights. For that, the correlation matrix presents a powerful tool for exploratory analysis and a better understanding of the dataset. However, the use of more complex models should better capture the complex relations involved in MR system operation.

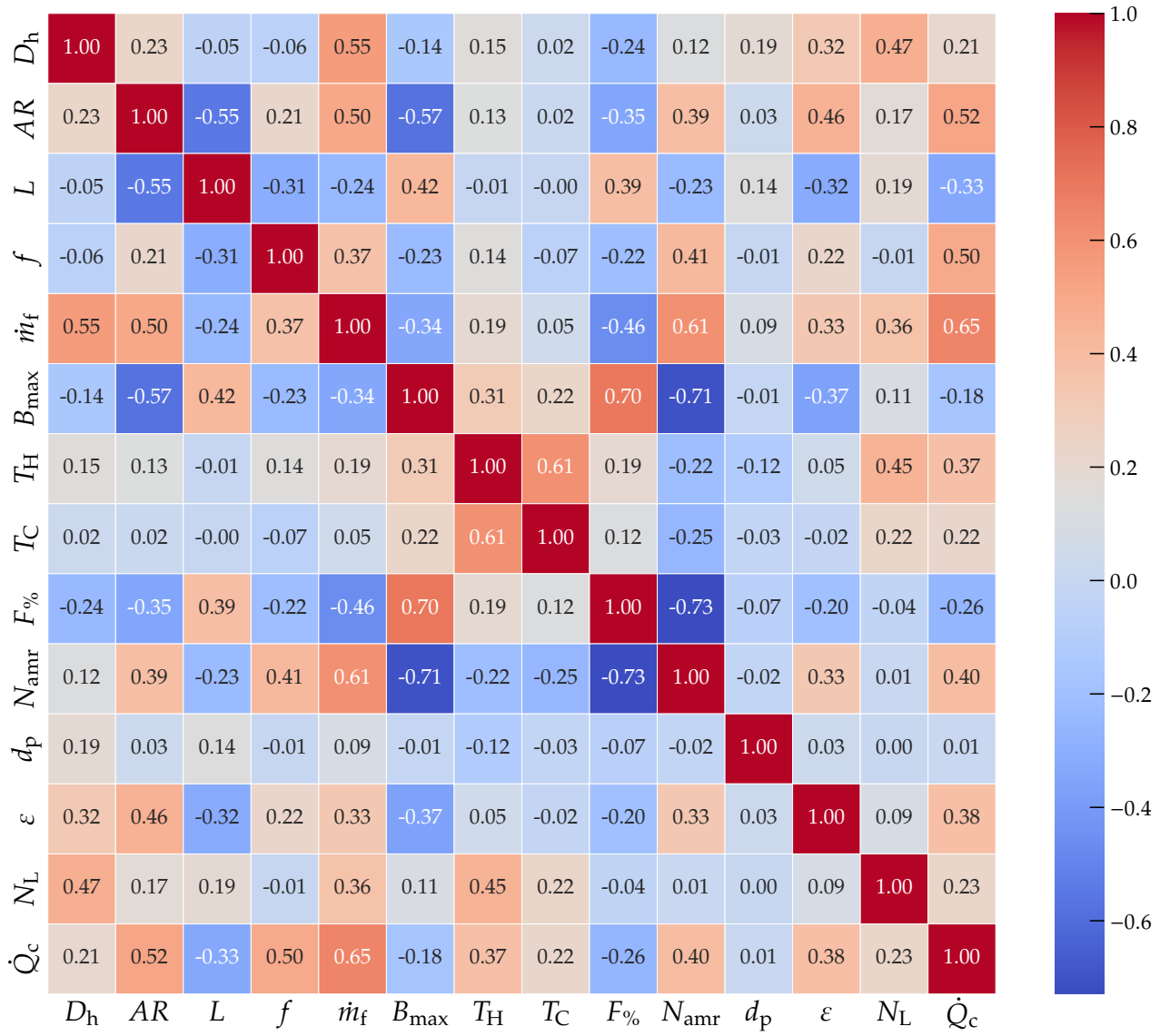


Figure 6.6 – Correlation Matrix of selected numeric parameters of the dataset.

6.1.3 Model Selection

Given the data transformation, feature engineering, and one-hot encoding of categorical variables, the ML to be developed has the form of:

$$\dot{Q}_C = \mathcal{F}\Big(D_h, A_R, L, f, \dot{m}_f, B_{max}, T_H, T_C, F_\%, N_{AMR}, d_p, \varepsilon, N_l, \overline{T}_{curie}, \overline{X}_{curie}, S^*_{AMR}, B^*_{prof}, G^*_{MCM}, M^*_{MCM}\Big) \tag{6.6}$$

where the superscript * indicates categorical variables and the overline indicates vectors.

A strategy should be adopted to handle the vector variables in Eq. (6.6). It consists of neglecting both $\overline{T}_{Curie}$ and $\overline{X}_{Curie}$ and considering only the number of layers, which is already embedded in the N_l feature. In addition, two new features are created: the lowest (T_{low}) and highest (T_{high}) Curie temperature of the AMR (Nakashima *et al.*, 2022b). By doing so, the first

model ($\mathcal{F}_1$) to be determined in this work model has 29 input parameters and is given by:

$$\dot{Q}_{\mathrm{C}} = \mathcal{F}_1\Big(D_{\mathrm{h}}, A_{\mathrm{R}}, L, f, \dot{m}_{\mathrm{f}}, B_{\max}, T_{\mathrm{H}}, T_{\mathrm{C}}, F_{\%}, N_{\mathrm{AMR}}, d_{\mathrm{p}}, \varepsilon, N_{\mathrm{l}}, T_{\mathrm{low}}, T_{\mathrm{high}}, S^*_{\mathrm{AMR}}, B^*_{\mathrm{prof}}, G^*_{\mathrm{MCM}}, M^*_{\mathrm{MCM}}\Big) \tag{6.7}$$

ANNs were selected given their prowess in regression tasks presented in Chapter 3. They were implemented with the Keras framework (Chollet *et al.*, 2015) and TensorFlow back-end (Abadi *et al.*, 2015). Given the complexity of magnetocaloric systems, embedding physics with features will be evaluated as a strategy to improve model performance.

6.1.3.1 Physics-Guided Neural Network

ANNs can be improved by embedding physical knowledge into their architecture, thereby improving performance and reducing training time and computational cost (Raissi *et al.*, 2019). To do that, it is proposed to perform feature engineering based on prior knowledge from previous work. That is referred to as Physics-Guided, even though the feature engineering process carried out does not occur by numerical means, as proposed by Daw *et al.* (2021), but by closure relations, as suggested by Montanez-Barrera *et al.* (2022) and by Chandra *et al.* (2024). Based on the previous experience, nine features are generated for model development.

The nondimensional magnetic field (Π_{B}) encodes the information about the high and low values of the magnetic flux density applied on the AMR beds, and is given by Eq. (6.8).

$$\Pi_{\mathrm{B}} = \frac{B_{\mathrm{high}}}{B_{\mathrm{high}} - B_{\mathrm{low}}} \tag{6.8}$$

Furthermore, to account for demagnetization loss, the demagnetization factor (N_{D}) is used as an input feature and calculated according to the methodology proposed by (Coey, 2010).

$$N_{\mathrm{D}} = N_{\mathrm{D,geo}} + (1 - \varepsilon)\left(N_{\mathrm{D,csg}} - N_{\mathrm{D,geo}}\right) \tag{6.9}$$

where $N_{\mathrm{D,csg}}$ is calculated according to the methods proposed by Aharoni (1998) for prismatic casings and by Sato & Ishii (1989) for cylindrical, and $N_{\mathrm{D,geo}}$ is estimated according to the methods proposed by Trevizoli *et al.* (2017) for spheres, plates and pins; by Vieira *et al.* (2021) for particles and by Faria (2022) for microchannels.

To account for the temperature span, a non-dimensional parameter given by Eq. (6.10) is used.

$$\Pi_{\mathrm{T}} = \frac{T_{\mathrm{C}}}{T_{\mathrm{H}} - T_{\mathrm{C}}} \tag{6.10}$$

To characterize the temperature range of the multilayer arrangement, a non-dimensional feature given by Eq. (6.11) is used.

$$\Pi_{\mathrm{Tc}} = \frac{T_{\mathrm{low}}}{T_{\mathrm{high}} - T_{\mathrm{low}}} \tag{6.11}$$

where T_{high} and T_{low} are the highest and lowest temperatures of the multilayer arrangement.

The Reynolds number (Re), is a widely used metric to calculate fluid flow, including AMR. The metric is also used as an input feature. It can be computed using Eq. (6.12), where the characteristic diameters for each geometry are calculated according to the conventions adopted by Trevizoli *et al.* (2017) for spheres, plates, and pins; Vieira *et al.* (2021) for particles and Faria (2022) for microchannels.

$$Re = \frac{v_{\text{s}} \rho_{\text{f}} d_{\text{h}}}{\mu_{\text{f}}} \tag{6.12}$$

In addition, the friction factor (f_{D}) characterizes the pressure drop. It is proportional to the viscous dissipation in the AMR. It is used as an input feature, given the availability of correlations and closure parameters to compute the pressure drop analytically (Irmay, 1958). The friction factor can be calculated by Eq. (6.13)

$$f_{\text{D}} = \frac{\Delta P}{L} \frac{\varepsilon^3}{(1-\varepsilon)} \frac{d}{\rho_{\text{f}} v_{\text{s}}} = a + (1-\varepsilon) \frac{b}{Re} \tag{6.13}$$

where the values of a and b are calculated according to the proposed ones by Trevizoli *et al.* (2017) for spheres, pins and plates, Vieira *et al.* (2021) for particles and Faria (2022) for microchannels. Corrections to the porosity are applied to tests where epoxy is used to bond the material particles (Vieira *et al.*, 2021).

To characterize heat transfer on the AMR, three parameters are employed. The first is the utilization factors, given by Eq. (6.4). Additionally, the number of transfer units (NTU) is used for steady-state operation, and the Fourier number (Fo) is used for transient operation. The features can be calculated according to Eq. (6.14) and Eq. (6.15), respectively.

$$NTU = Nu \frac{k_{\text{f}}}{d_{\text{h}}} \frac{A_{\text{HT}}}{\dot{m}_{\text{f}} c_{\text{f}}} \tag{6.14}$$

$$Fo = \frac{k_{\text{s}}}{\rho_{\text{s}} c_{\text{s}} f d_{\text{h}}^2} \tag{6.15}$$

where the convective heat transfer coefficient of the AMR is calculated via the Nusselt number with correlations according to the proposed ones by Trevizoli *et al.* (2017) for spheres, pins, and plates; Vieira *et al.* (2021) for particles; and Faria (2022) for microchannels.

Therefore, the Physics-Guided input features are given by the following group of dimensionless parameters:

$$x_{\text{Phy}} = [\Pi_{\text{B}}, N_{\text{D}}, \Pi_{\text{T}}, \Pi_{\text{Tc}}, \varphi, Re, f_{\text{D}}, NTU, Fo] \tag{6.16}$$

and the original features are divided into general features, x_{Gen}, and multilayer features, x_{ML}, given by:

$$x_{\text{Gen}} = [D_{\text{h}}, A_{\text{R}}, L, f, \dot{m}_{\text{f}}, B_{\max}, T_{\text{H}}, T_{\text{C}}, F_{\%}, d_{\text{p}}, \varepsilon, N_{\text{AMR}}, T_{\text{low}}, T_{\text{high}}, S^*_{\text{AMR}}, B^*_{\text{prof}}, G^*_{\text{MCM}}] \tag{6.17}$$

$$x_{\mathrm{ML}} = [N_{\mathrm{l}}, M^{*}_{\mathrm{MCM}}] \tag{6.18}$$

Three scenarios arise when incorporating the Physics-Guided features into the model. The first corresponds to the original configuration, given by Eq. (6.7), where the prediction is based solely on the general and multilayer features, and is given:

$$\dot{Q}_{\mathrm{C}} = \mathcal{F}_1(x_{\mathrm{Gen}}, x_{\mathrm{ML}}) \tag{6.19}$$

In the second scenario, the model uses only the Physics-Guided features, along with the multilayer ones, and is given as follows:

$$\dot{Q}_{\mathrm{C}} = \mathcal{F}_2(x_{\mathrm{Phy}}, x_{\mathrm{ML}}) \tag{6.20}$$

Finally, the third scenario combines all available inputs: general features, Physics-Guided features, and multilayer features, and is given by:

$$\dot{Q}_{\mathrm{C}} = \mathcal{F}_3(x_{\mathrm{Gen}}, x_{\mathrm{Phy}}, x_{\mathrm{ML}}) \tag{6.21}$$

Hence, the general architecture of the ANN used in this model is presented in Fig. 6.7. The input data for the model are x_{Gen} and x_{ML}, as previously described. Physics embedding into the ANN is carried out via the data transformation according to x_{Phy}. The input data for the models, which can comprise x_{Gen} and x_{ML}, as per Eq. (6.19); x_{Phy} and x_{ML}, as per Eq. (6.20); or x_{Gen}, x_{ML} and x_{Phy}, as per Eq. (6.21), go through a series of four dense layers (three hidden layers and one output layer) connected in a Multilayer Perceptron architecture. The dense blocks are composed of dense and activation function layers. Both input and output data are normalized according to the standardization method (z-score normalization).

6.1.4 Model Training and Optimization

The performance of the present ANN was further enhanced by hyperparameter optimization. The Hyperband Algorithm (Li *et al.*, 2018) was used to tune the hyperparameters. The Adam optimizer (Kingma, 2014) was used, with the learning rate (α) and batch size (BS) as hyperparameters.

The optimized hyperparameters in the first layer are the number of neurons ($\mathcal{N}_1$), the activation function (Ω_1), the l2-regularization coefficient (λ_1); on the second are the number of neurons ($\mathcal{N}_2$), the activation function (Ω_2), the l2-regularization coefficient (λ_2); and on the third are the number of neurons ($\mathcal{N}_3$), the activation function (Ω_3) and the l2-regularization coefficient (λ_3). The fourth dense block has a single neuron, representing the single objective of the AI model (cooling capacity), without regularization and with the SeLU as activation function. A summary of the optimized hyperparameters is presented in Table 6.2.

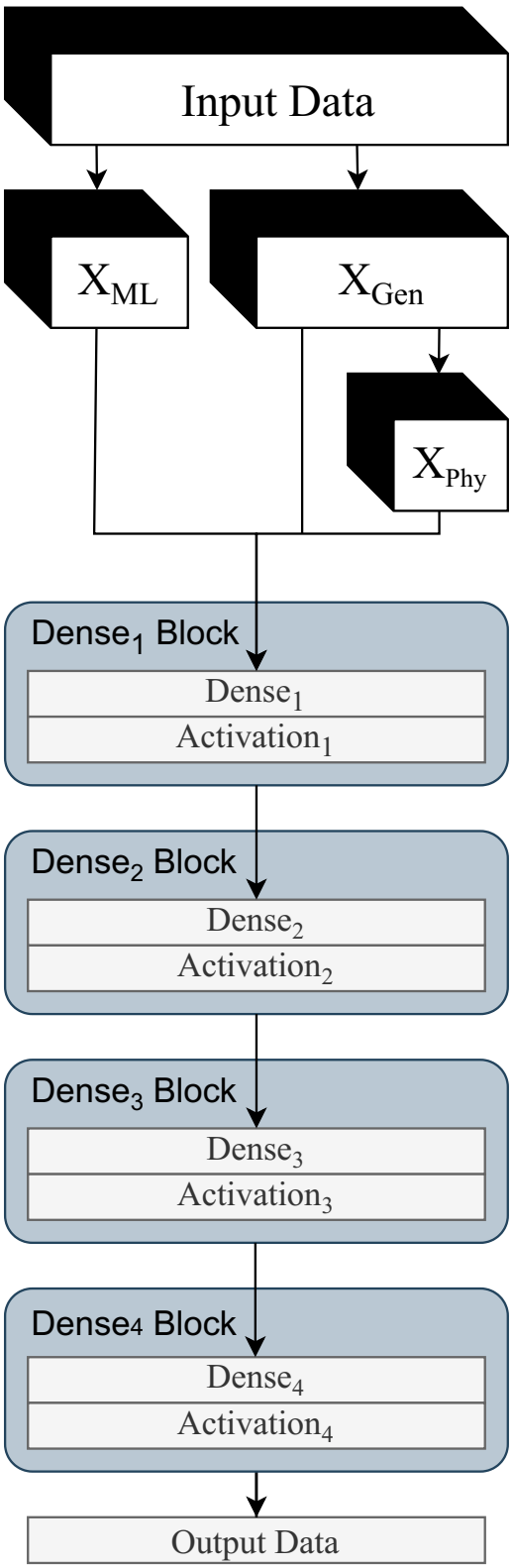


Figure 6.7 – General Representation of the Architecture of the ANN.

Hyperparameter optimization was run for 300 epochs. After that, the model with the lowest validation loss is trained for an additional 300 epochs. That was done due to limitations in computational capacity and to optimize the performance of the model. To ensure that the training process does not overfit and converges to the best possible model,

Table 6.2 – Summary of the Hyperparameters optimized in the ANN

Block	Parameter	Value range
Dense$_1$	$N_{\text{neu},1}$	[30, 35, 40, 45]
	Ω_1	[SeLU, Swish, GeLU]
	λ_1	[0, 10^{-8}, 10^{-4}]
Dense$_2$	$N_{\text{neo},2}$	[20, 25, 30]
	Ω_2	[SeLU, Swish, GeLU]
	λ_2	[0, 10^{-8}, 10^{-4}]
Dense$_3$	$N_{\text{neu},3}$	[3, 6, 9]
	Ω_3	[SeLU, Swish, GeLU]
	λ_3	[0, 10^{-8}, 10^{-4}]
Optimizer	α	[0.05, 0.01, 0.005, 0.001]
	BS	[16, 32, 48]

the early stopping technique was employed.

6.1.5 Model Evaluation

To evaluate the effect of data transformation and physics embedding on the model performance, a standard ANN architecture was selected, and the three models, given by Eq.(6.19)-(6.21), were trained. At this stage, hyperparameter optimization was not performed to ensure the use of the same ANN across all models, thereby facilitating a proper comparison of results across the different strategies. A summary of the hyperparameters implemented to evaluate the Physics-Guided ANN strategy, chosen from the range presented in Table 6.2, is shown in Table 6.3.

Table 6.3 – Summary of the Hyperparameters for the evaluation of the Physics-Guided ANN

Block	Parameter	Value range
Dense$_1$	$N_{\text{neo},1}$	35
	Ω_1	SeLU
	λ_1	10^{-8}
Dense$_2$	$N_{\text{neo},2}$	25
	Ω_2	SeLU
	λ_2	10^{-8}
Dense$_3$	$N_{\text{neo},3}$	6
	Ω_3	SeLU
	λ_3	010^{-8}
Optimizer	α	0.01
	BS	32

The training was carried out for 300 epochs, and a patience of 100 epochs for the early stopping technique. A 5-fold cross-validation method was used to better evaluate the effect of the physics embedding on each model and to reduce the influence of the dataset

split. The Xavier initialization (Kumar, 2017) was used for all of the models. The loss function used to train the model is the MSE.

The results in terms of the average loss function in the five validation sets of the 5-fold cross-validation for the three models, together with the number of input parameters for each of them, are presented in Table 6.4, to enable evaluating the effect of imposing physics as a feature engineering process on the ANN.

Table 6.4 – Results of the physics embedding on the performance of the model

Model Inputs	Inputs Size	$\overline{MSE}$
$[x_{\text{Gen}}, x_{\text{ML}}]$	29	0.0139 ± 0.0030
$[x_{\text{Phy}}, x_{\text{ML}}]$	15	0.0293 ± 0.0265
$[x_{\text{Gen}}, x_{\text{Phy}}, x_{\text{ML}}]$	38	0.0107 ± 0.0051

First, it is clear that simply replacing the original input parameters x_{Gen} with x_{Phy} is not sufficient to improve the performance. The new physics-generated features did not represent the underlying phenomena as well as the original ones. However, when the original features are combined with those generated by physics, performance improves, with the mean MSE reduced by 23%. The additional features enable the model to capture the complexities of the operation better, thereby improving performance.

Given the performance improvement obtained by incorporating physics into the input parameters, a more robust model is developed using the hyperparameter optimization described in the previous section for the model given by Eq. (6.21). Model performance is evaluated using both numerical metrics and visualizations. In addition to MSE, the MAE and the R^2 are also used to assess the performance of the model.

The resulting hyperparameters optimized with the methodology described previously in this manuscript are presented in Table 6.5

Table 6.5 – Optimal Hyperparameters for the Physics-Guided ANN

Block	**Parameter**	**Value range**
Dense$_1$	$\mathcal{N}_1$	40
	Ω_1	GeLU
	λ_1	0
Dense$_2$	$\mathcal{N}_2$	25
	Ω_2	Selu
	λ_2	10^{-8}
Dense$_3$	$\mathcal{N}_3$	9
	Ω_3	Swish
	λ_3	0
Optimizer	α	0.01
	BS	48

The performance metrics achieved by the ANN are presented in Table 6.6, where R^2, MAE, and MSE are presented for the training, validation, and test sets. To allow a better physical interpretation of the results, MSE and MAE are calculated using the original cooling capacities rather than the standardized ones.

Table 6.6 – Performance metrics of the AI Models

	R^2	MAE	MSE
Train	0.9981	6.3581	169.4926
Validation	0.9954	12.6381	646.3195
Test	0.9873	13.5539	857.3313

The results presented in Table 6.6 show that the models performed considerably well across all datasets. All models achieved R^2 values greater than 0.99 in the training and validation sets, and above 0.98 in the test set. This is further supported by the low MAE values, which indicate minimal deviation between the predictions and the actual results.

To better evaluate their accuracy, a visual representation of their performance is provided to complement the metrics presented in Table 6.13. A comparison of the experimental results with the complete predictions for the training, validation, and test sets is shown in Fig. 6.8. Two black dashed lines representing deviations of $\pm$ 10% and one red dotted line representing the ground truth are also shown in the plot.

Figure 6.8 shows that most of the predicted points using the model fall within a deviation $\pm$ 5% from the experimental results. However, some points exhibit higher percentage deviations, which is expected. Despite this, the results are considered promising, as the models successfully predict the experimental cooling capacity across most design regions, even at high frequencies and temperature spans where numerical models typically struggle to capture the behavior (Trevizoli *et al.*, 2016b). It is also worth noting that, depending on the application, evaluating absolute deviations can be more instructive than evaluating percentage deviations. For that, the comparison for the cooling capacity per AMR ($\dot{Q}_{\mathrm{C,amr}}$), taken as the cooling capacity of the system divided by the number of AMRs is shown for two different regions: AMRs operating below 50 W in Fig. 6.9, above 50 W in Fig. 6.10.

In the lower-capacity region, absolute deviations are more meaningful than percentage deviations, as relative errors can be misleading when target values are small. In such cases, even modest absolute deviations may be acceptable depending on the design requirements and tolerances of the application. This is particularly relevant when the focus is on the precision control of small-scale systems or modular units, where design decisions rely more directly on absolute performance thresholds. Therefore, Fig. 6.9 is presented with $\pm$ 7 W deviation bars, being 98.70%, 95.81% and 95.15% of the data points in the training, validation, and test sets, respectively, contained within that margin.

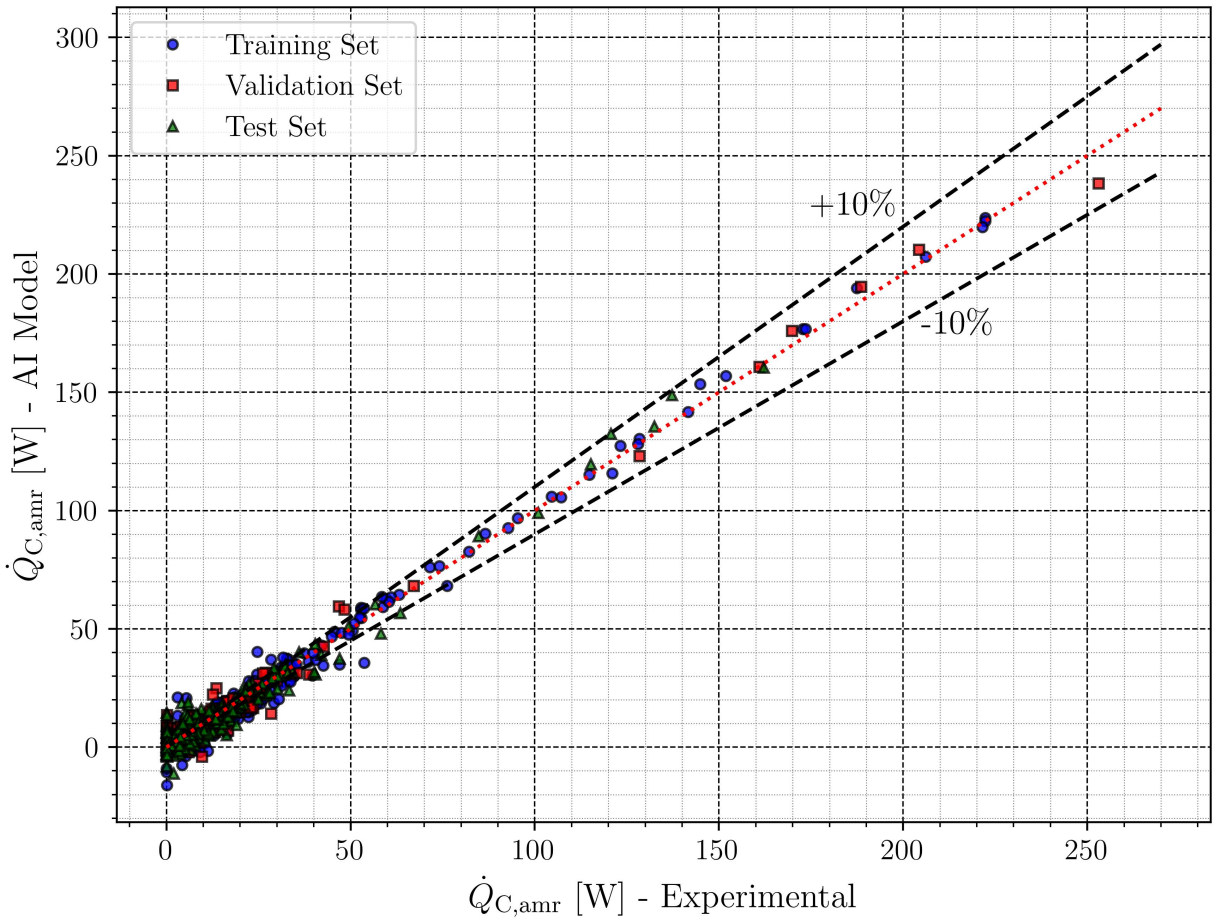


Figure 6.8 – Comparison between the experimental results for the cooling capacity and predictions by the ANN for the training, validation, and test sets. Black Dashed lines represent ± 10% deviations. The red dotted line represents the ground truth.

In contrast, for higher-capacity systems, percentage-based deviations are a more appropriate metric. In this context, maintaining low relative errors ensures reliable system-level predictions across a broader range of operating conditions. For system design and optimization, relative error is a valuable metric for providing consistent performance predictions across a wide range of operating points, helping identify trade-offs and guide parameter tuning. By accounting for absolute deviations in high-capacity AMRs and relative deviations in lower-capacity ones, the analysis provides a more comprehensive assessment of model reliability across cooling capacities, supporting more informed engineering decisions. To illustrate this, Fig. 6.9 includes ±10% deviation bands, within which 89.47%, 100%, and 90% of the training, validation, and test results are contained, respectively.

Lastly, to further evaluate the performance of the model, a histogram of the absolute deviations between the experimental and predicted cooling capacities is presented in Fig. 6.11 for all data sets.

Once again, the results depicted in Figs. 6.11 demonstrate the ability of the model to predict the cooling capacity of magnetic refrigeration systems. The predictions are within a 40 W deviation for approximately 97%, 90%, and 90% of the cases in the training, validation,

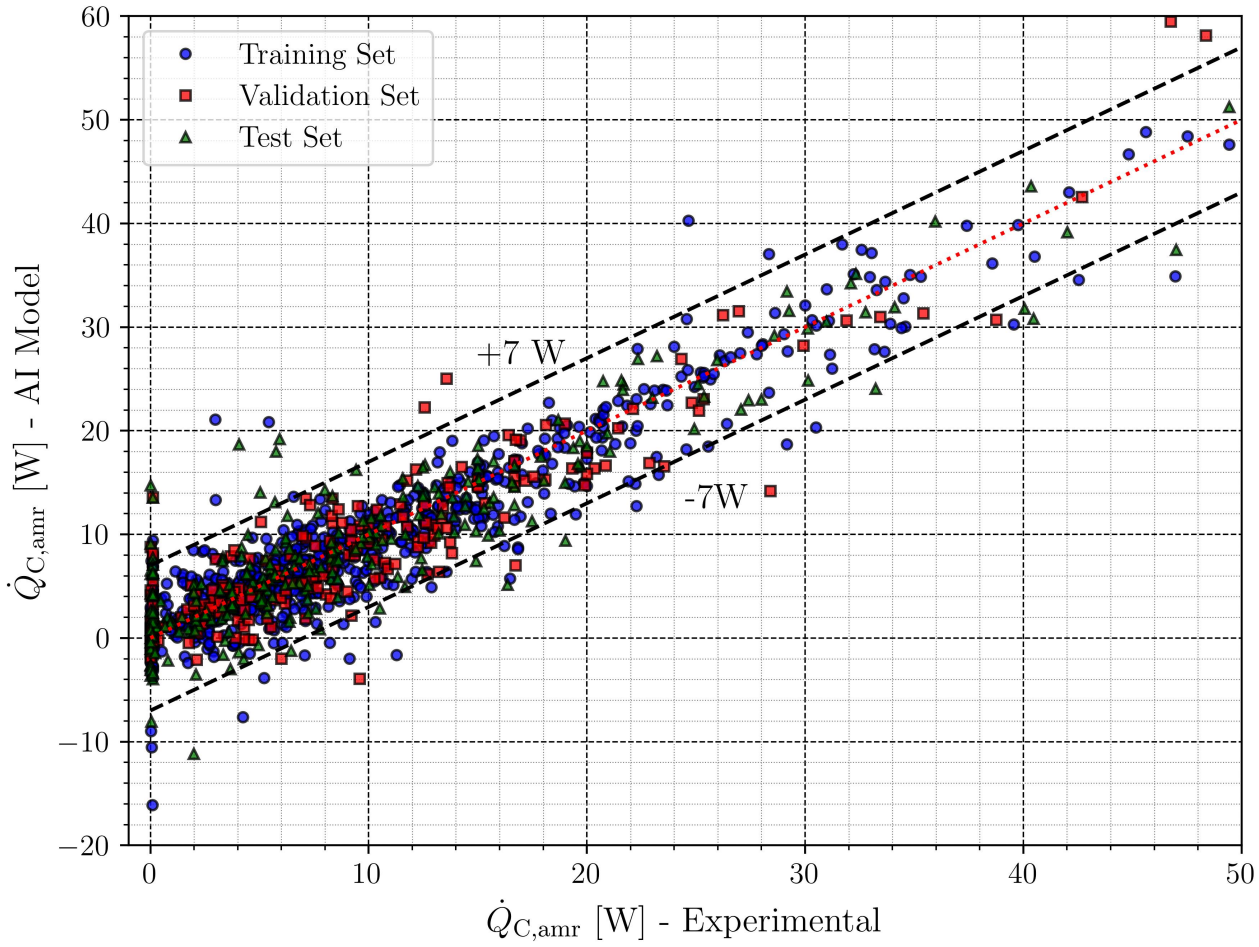


Figure 6.9 – Comparison between the experimental results for the AMR cooling capacity below 50 W and predictions by the ANN for the training, validation, and test sets. Black Dashed lines represent ± 7 W deviations. The red dotted line represents the ground truth.

and test sets, respectively.

These findings demonstrate robustness and generalization, especially given the complexity and the broad range of operating conditions in the dataset. Nevertheless, caution is required when applying this model beyond the specific conditions presented here. Despite its strong performance in this section, the model was ultimately deemed inadequate for the application discussed later in the chapter. This aligns with a well-known principle in machine learning: it is often easier to develop a model tailored to a specific task than to create one that generalizes across multiple distinct scenarios. For this reason, more specialized models are introduced in the following sections, designed explicitly for the application of interest.

Several improvements could further enhance model performance. First, additional experimental details would be highly beneficial. Important loss mechanisms, such as void volume effects and environmental heat gains, had to be omitted because they were not reported in the available literature, limiting the quality of the input features. Second, the encoding of the multilayer arrangement could be refined. Convolutional neural networks (CNNs) offer an efficient way to represent sequential or structured spatial information without incurring excessive computational cost. Third, expanding the design space would likely improve the

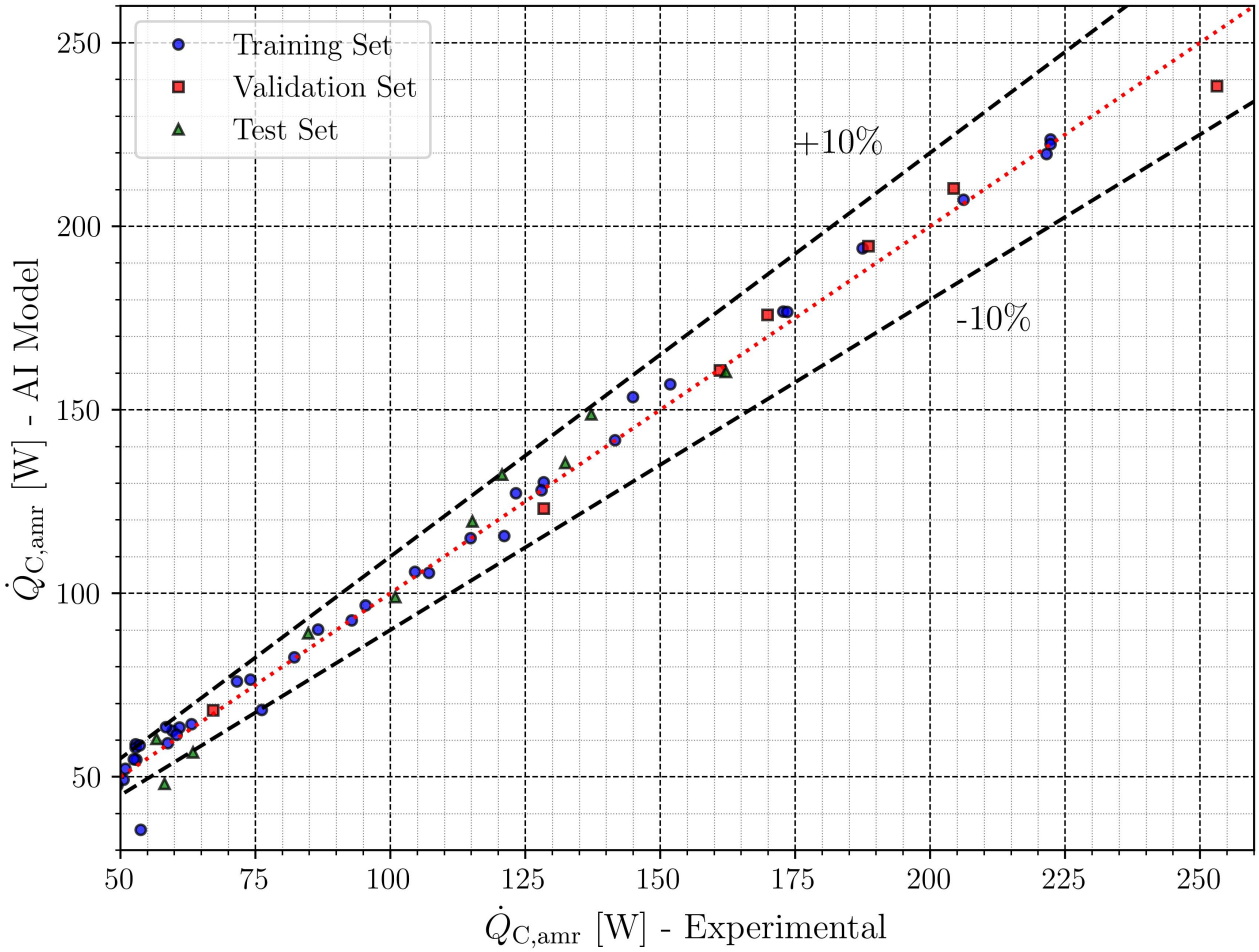


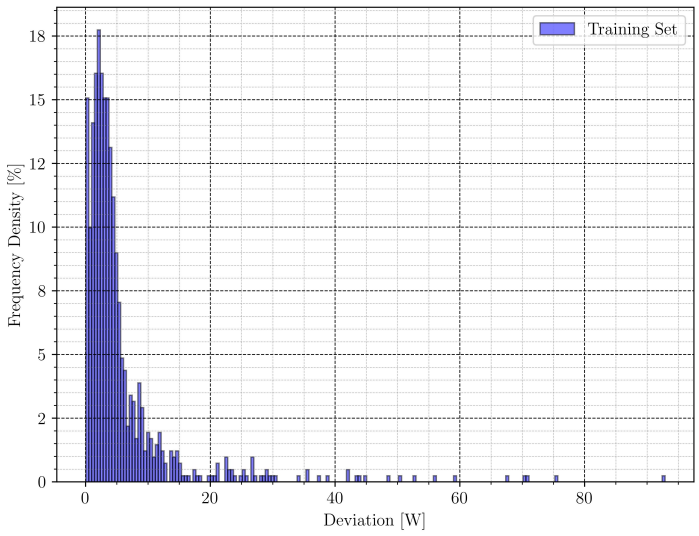
Figure 6.10 – Comparison between the experimental results for the AMR cooling capacity above 50 W and predictions by the ANN for the training, validation, and test sets. Black Dashed lines represent ± 10% deviations. The red dotted line represents the ground truth.

learning of the model for more diverse configurations, though this would require developing and testing new magnetocaloric prototypes. Finally, to improve generalization, introducing Gaussian noise to both inputs and outputs is recommended to account for measurement uncertainties. A grouped sampling strategy—where training, validation, and test subsets are created at the prototype level rather than randomly—may also prevent data leakage and lead to more realistic performance assessments.

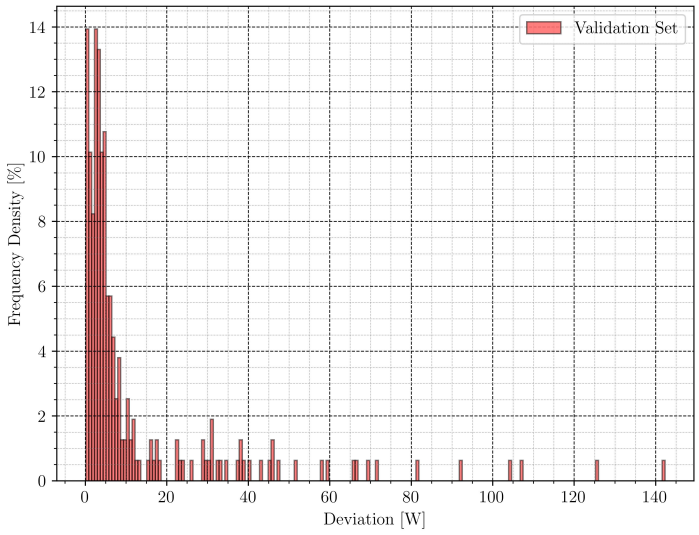
Despite the limitations of the available data, the model captured the behavior of all prototypes across a broad range of operating conditions and design parameters. This demonstrates its ability to learn the underlying thermodynamic patterns governing magnetic refrigeration performance, even when confronted with heterogeneous datasets and incomplete experimental information.

6.2 Transient Model

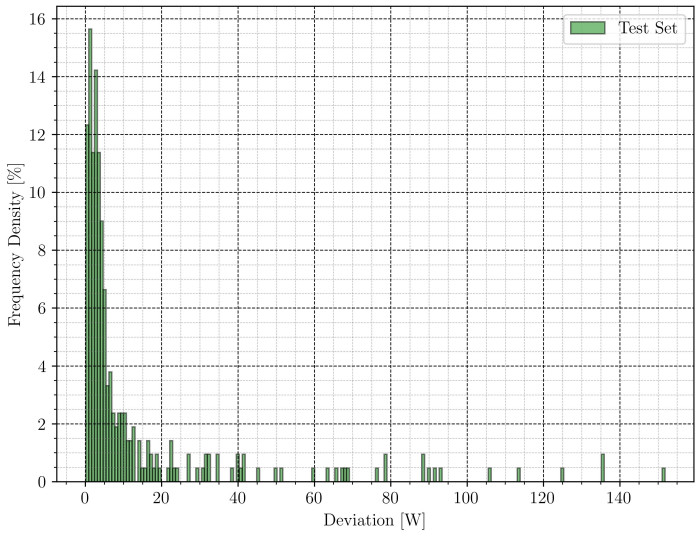
The transient, or dynamic, model captures the time-dependent behavior of MR systems, offering a more comprehensive understanding of their performance under varying



(a)



(b)



(c)

Figure 6.11 – Histogram between the deviations between the model and the experimental data for the (a) training, (b) validation, and (c) test sets.

operational conditions. Unlike steady-state models, which assume constant conditions, the dynamic model accounts for changes over time, such as temperature fluctuations, material responses, and cycling effects. This section describes the development of an AI-based dynamic model for the MRU.

6.2.1 Problem Formulation

Despite its critical role in determining the energy consumption of refrigerators (Hermes & Melo, 2008), transient modeling remains relatively unexplored in magnetic refrigerators (Calomeno *et al.*, 2022; Nakashima *et al.*, 2022b; Hoffmann *et al.*, 2024), mainly due to the computational costs involved in numerical methodologies (Nielsen *et al.*, 2011; Vieira *et al.*, 2021).

To address this challenge, a transient model of the operational behavior of the MRU is proposed. To achieve high accuracy and low computational cost, an ML-based approach was chosen. Although these techniques have recently gained increasing attention, they have been used successfully for years in dynamic system modeling, previously been used to simulate the start operation of gas turbines (Asgari *et al.*, 2016), predicting the useful life of bearings (Rai & Upadhyay, 2017), predicting solar radiation (Boussaada *et al.*, 2018), analyzing the behavior of phase change materials (Urresti *et al.*, 2019), controlling biomass gasification processes (Elmaz & Yücel, 2020), and forecasting the temperature of data centers (Asgari *et al.*, 2021).

In this framework, the output variables are the hot-blow temperature at the AMR outlet ($T_{\mathrm{HB,out}}$) and the overall system power consumption ($\dot{W}_{\mathrm{sys}}$). Several considerations drive the choice of the hot-blow temperature at the AMR outlet. Primarily because it embodies the main objective of a refrigeration system: reducing the ambient temperature. In addition, this temperature is chosen over the cold reservoir temperature because it represents the lowest temperature within the system, serves as a benchmark for comparing different MR prototypes, and offers faster response. Predicting this output ensures the system functions as per the application requirements and enables the use of sophisticated control strategies to shorten cooling time. In contrast, the overall power consumption is chosen because it indicates the energy cost associated with the generated cooling capacity. Predicting the future behavior of this variable is beneficial, as it helps minimize it during the system design phase and through approaches such as predictive control of the model.

In addition, two prediction horizons, short and long, will be evaluated. The short-horizon model focuses on 1-step-ahead predictions, using actual experimental values as input to assess the deviation without recurrence, thereby avoiding the influence of model-generated predictions. The long-horizon model, on the other hand, is designed to predict 90 steps ahead, covering a 15-minute forecast period. This horizon is used not only to evaluate

the effect of recurrence on model accuracy but also to provide a suitable timeframe for system performance predictions aimed at optimization tasks, such as minimizing power consumption. Five actuation signals were designated as input variables for the experiments: the frequency (f), power supplied to the pump ($\dot{W}_{\mathrm{pp}}$), fluid flow fraction ($F_{\%}$), and power supplied to the CHEx fan ($\dot{W}_{\mathrm{HHEx,fan}}$), and HHEx fan ($\dot{W}_{\mathrm{CHEx,fan}}$). In addition, the hot reservoir temperature was included as a measured disturbance, as it can significantly affect system performance. Hence, the problem to be tackled is given by the development of two models, which are given by:

$$T_{\mathrm{HB,out}} = \mathcal{F}(t, f, \dot{W}_{\mathrm{pp}}, F_{\%}, \dot{W}_{\mathrm{HHEx,fan}}, \dot{W}_{\mathrm{CHEx,fan}}) \tag{6.22}$$

$$\dot{W}_{\mathrm{sys}} = \mathcal{F}(t, f, \dot{W}_{\mathrm{pp}}, F_{\%}, \dot{W}_{\mathrm{HHEx,fan}}, \dot{W}_{\mathrm{CHEx,fan}}) \tag{6.23}$$

6.2.2 Data Collection and Preparation

In designing the excitation signals, careful consideration was given to the amplitude of each input variable to ensure effective system operation. The second version of the MRU was used to collect the data points for the experiment. The specific constraints and ranges set for each input variable are as follows:

1. Frequency: The minimum value was set at 0.1 Hz to avoid negatively affecting the cooling capacity of the system. In comparison, the maximum was limited to 1 Hz to prevent potential instabilities in the operation of the solenoid valves.

2. Fluid flow fraction: The minimum value was established at 20% to maintain sufficient cooling capacity, and the maximum at 40% to prevent fluid recirculation between the AMR beds.

3. Pumping power: The lower limit was set at 30% of the nominal power to ensure the minimum flow rate required for proper system operation. The upper limit was capped at 73% to avoid system pressures exceeding 8 bar.

4. Power supplied to the HHEx and CHEx fans: The minimum and maximum values for these fan actuation signals were defined as 0% and 100% of nominal power, respectively, as there are no specific operating constraints on the fans.

In determining the distribution of test points, various methods are available, including random, D-optimal, and Latin Hypercube (LHC) sampling techniques, as described in (Deflorian & Zaglauer, 2011). For this specific study, the LHC strategy was selected and used. As demonstrated in Figs. 6.12 and 6.13, this approach provides a systematic and effective way to distribute test points across the parameter space, ensuring a well-structured, representative set of data for the experiments.

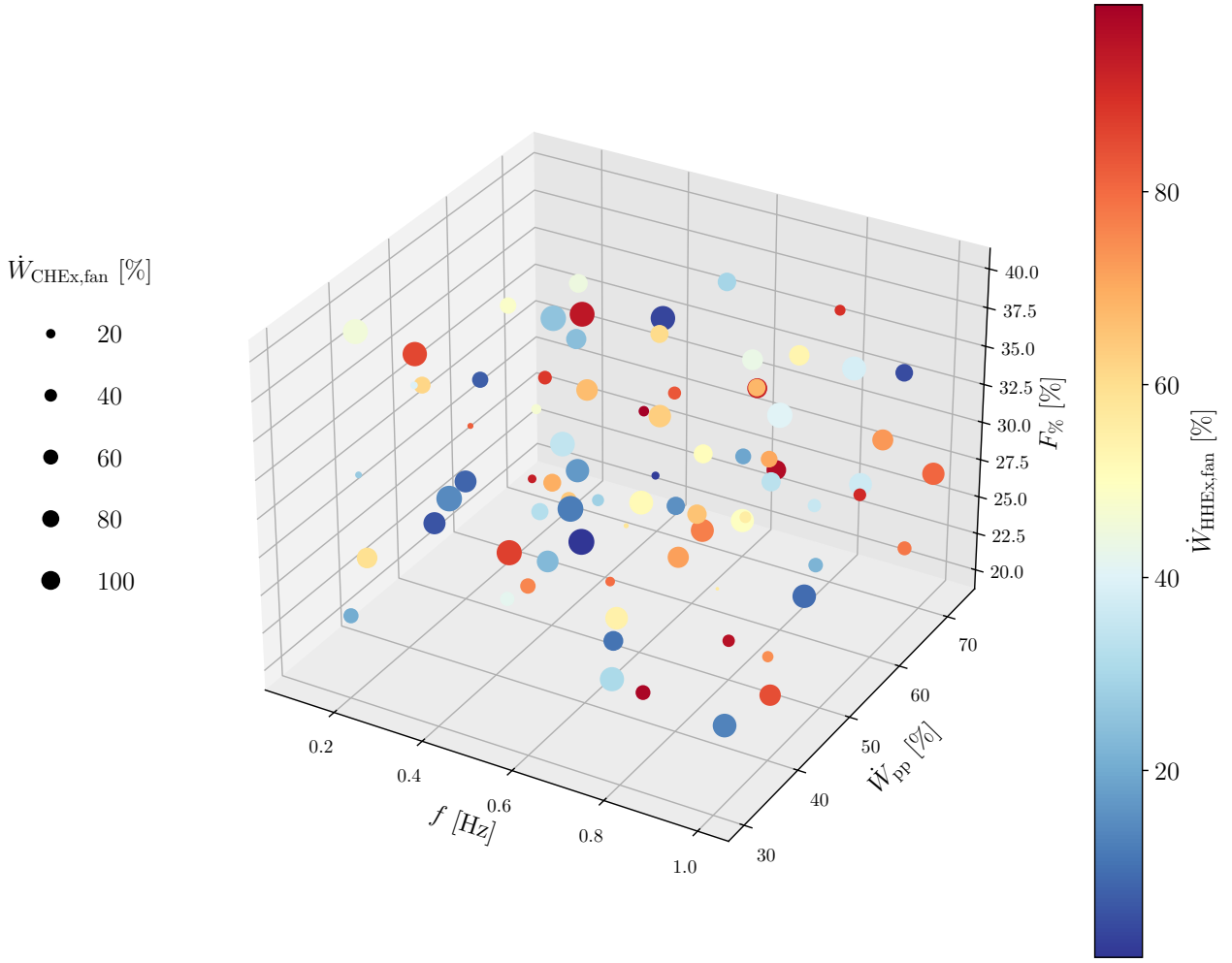


Figure 6.12 – Distribution of the five excitation signals generated by the LHC sampling strategy.

To establish the excitation hold time, the period between two consecutive tests, the time constant (*i.e.*, the time taken for the hot-end temperature during the hot blow to reach 63.2% of its steady-state value after a step input is applied) was measured during an operation when the system was off and the temperatures were at thermal equilibrium and the specific parameters were set: frequency at 0.5 Hz, pumping power at 44%, fluid flow fraction at 35%, and power supplied to the HHEx and CHEx fans at 100%. These settings represent the operating point at which the system is expected to function. The calculated time constant, denoted Φ, was determined to be 600 s. Subsequently, the hold time for each test was defined within the range of Φ to 1.5Φ, with specific values chosen using a random algorithm (Doyle *et al.*, 2002). To maintain a manageable test duration, the total number of points in the experiment was set to 80, ensuring the test would not exceed 20 hours. This careful selection of hold times allows for comprehensive data collection while managing overall testing time.

In the next step of the identification process, the shape of the excitation sequence for the parameter was designed. In this case, an adaptation of the amplitude modulated pseudo-random binary approach was employed (Shelembe & Barendse, 2021), as depicted

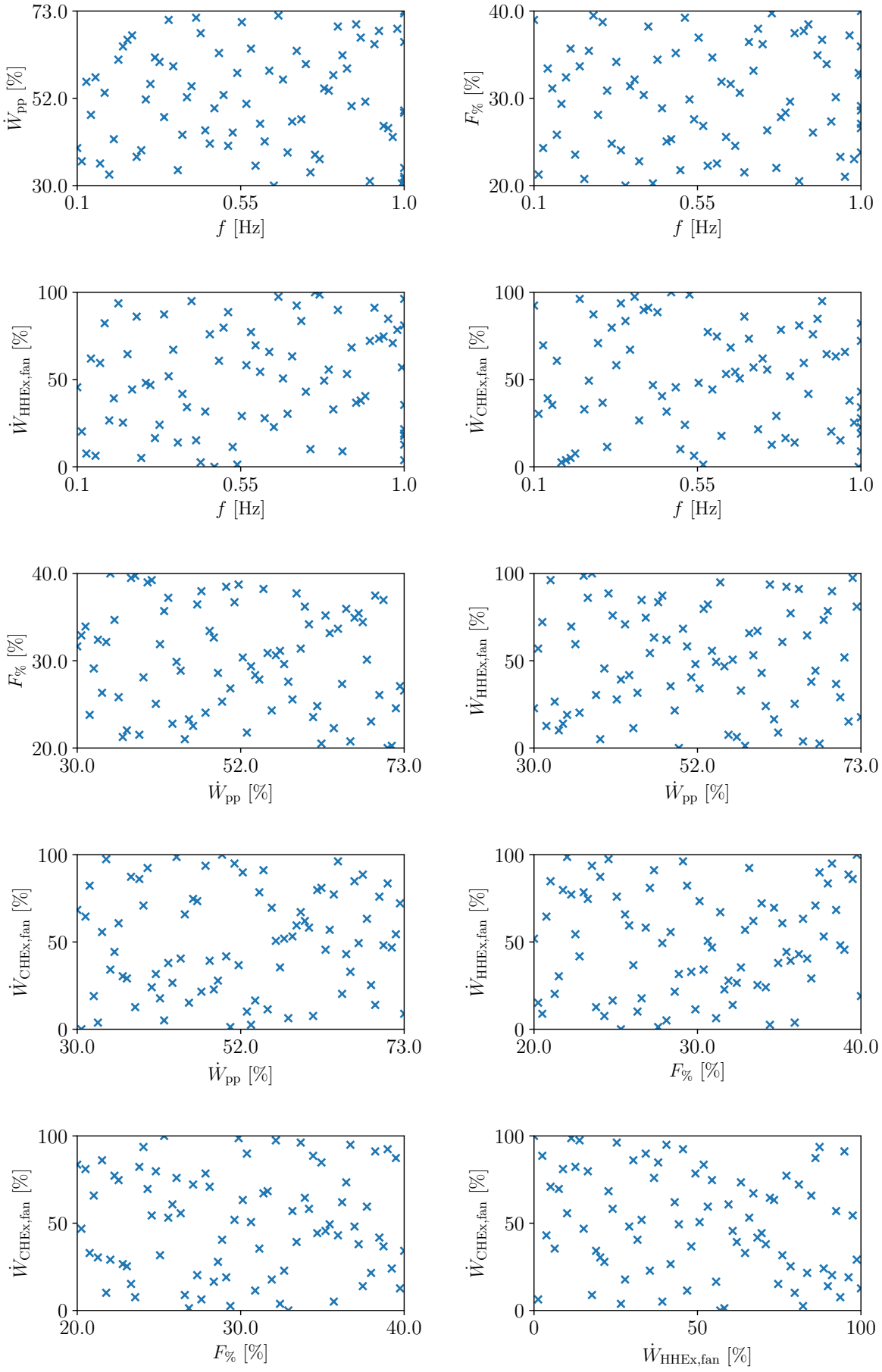


Figure 6.13 – Projections of the LHC excitation signals considering different pairs of variables.

in Fig. 6.14. This choice is informed by the understanding that low frequencies primarily govern the thermal process under examination.

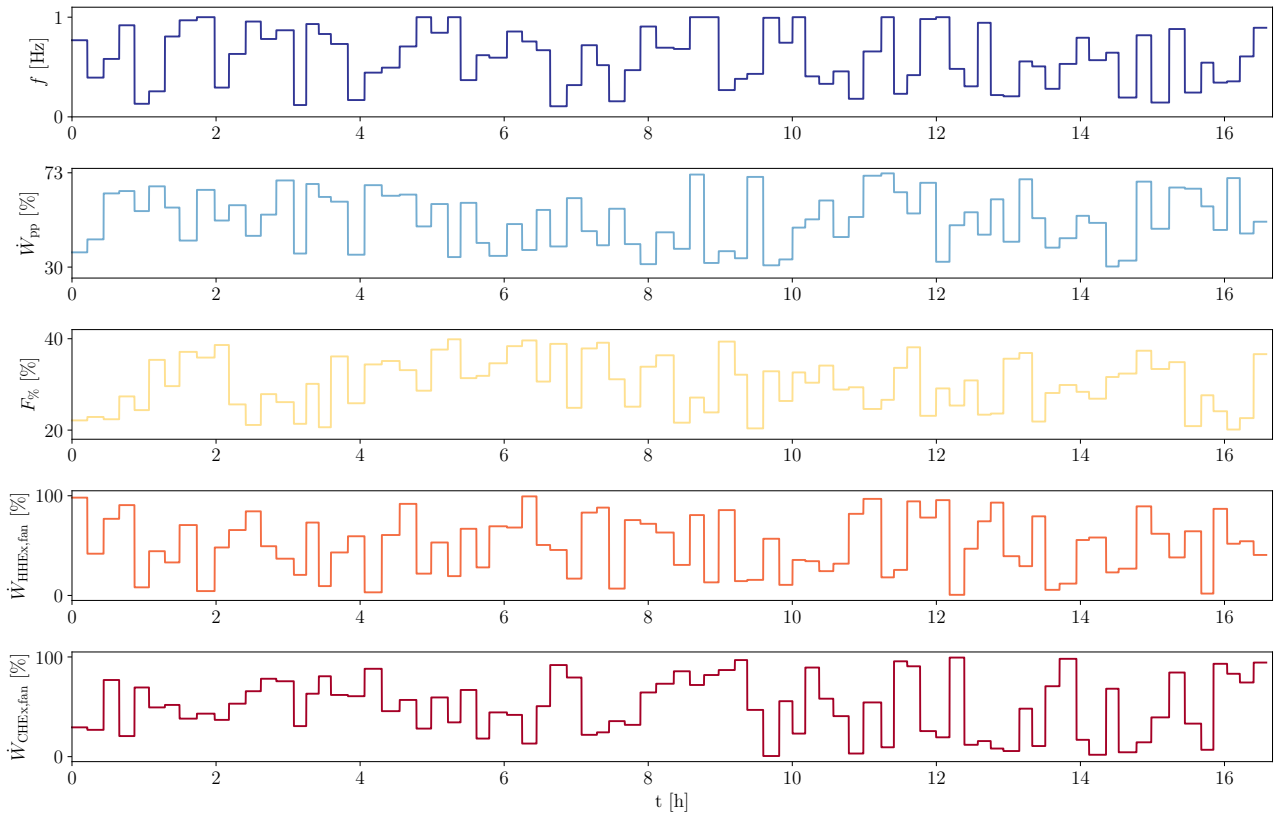


Figure 6.14 – Amplitudes of the excitation signals according to the pseudo-random binary approach.

It is assumed that the dataset lacks outliers, duplicates, and missing values, so no techniques have been adopted to address these issues. To mitigate noise in the data, a moving-average method has been implemented. Despite data being collected every second, the average over each 10-second interval is used as the time step to minimize the impact of noise on system measurements. As the dataset contains no categorical features, encoding is unnecessary. Data standardization is performed using the z-score method. The dataset is divided into 64%, 16%, and 20% for training, validation, and test sets, respectively.

6.2.3 Model Selection

The selected model for representing the system dynamics is a nonlinear autoregressive with exogenous input (NARX) ANN, an RNN with high capability to represent dynamic non-linear behaviors (Haykin, 2009). The NARX structure shown in Fig. 6.15 comprises several components, including time delay lines with sizes m for inputs and n for outputs. These delay lines enable the network to use past values from both inputs ($x(t-m+1)$) and outputs ($y(t-n+1)$) to make predictions ($\hat{y}$). Additionally, there is a recurrence mechanism that allows the return of predicted outputs. The core of the NARX structure is an MLP.

The implementation of ANNs was carried out in Python using the SysIdentPy library (LACERDA Jr. *et al.*, 2020). Mathematically, the NARX model in the so-called parallel mode,

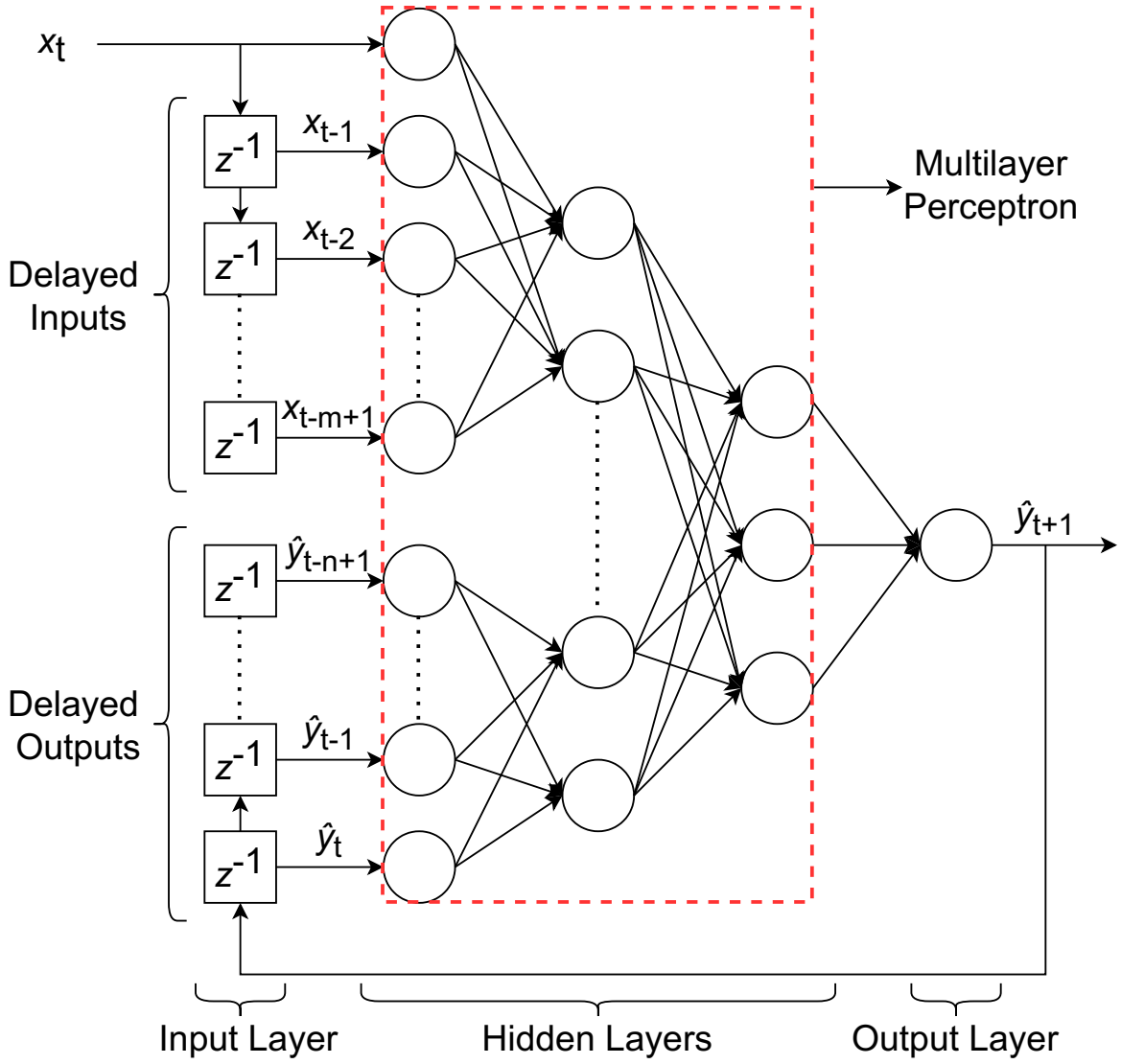


Figure 6.15 – NARX ANN comprised with m delayed inputs and n delayed outputs. z^{-1} represents a unit time delay.

when estimated outputs are fed back to the regressor, can be represented by Haykin (2009):

$$\hat{y}(t+1) = \mathcal{F}\left[\hat{y}(t), \ldots, \hat{y}\left(t-n+1\right); x(t), x(t-1), \ldots, x\left(t-m+1\right)\right] \tag{6.24}$$

6.2.4 Model Training and Optimization

Model training was performed using the Adam optimizer (Kingma, 2014). The Tanh function was used as an activation function in the hidden-layer neurons. The batch size and the number of training epochs were kept constant at 2000 and 350, respectively. The loss function used for training was the MSE.

Hyperparameter optimization was performed using a random search algorithm (Bergstra & Bengio, 2012). The optimized hyperparameters were the learning rate, α, number of hidden layers, N_{lay}, number of neurons in the hidden layers, $\mathcal{N}$, and the input, l_{x} and the output lags, l_{y}, were optimized according to the search space presented in Table 6.7. A

total of 5000 different models were trained using the training set. The model selected as the best among the 5000 cases evaluated was the one with the lowest MSE in the 90-step-ahead prediction horizon when applied to the validation set (Yu & Zhu, 2020).

Table 6.7 – Hyperparameter space for the random search.

Feature	Search space
α	0.5, 0.1, 0.05, 0.01, 0.001, 0.0001
N_{lay}	1 or 2
$\mathcal{N}_1$	20, 16, 12, 8, 4
$\mathcal{N}_2$	15, 12, 9, 6, 3
l_{x}	1 or 2
l_{y}	1 or 2

6.2.5 Model Evaluation

To enhance the predictive efficacy of the models, a hyperparameter optimization was performed via a random search over the design space outlined in Table 6.7. The resultant hyperparameters, dictating the behavior of the models tailored explicitly for predicting $T_{\text{HB,out}}$ and $\dot{W}_{\text{sys}}$, are shown in Table 6.8.

Table 6.8 – Hyperparameters of the final NARX ANN for the predictions of temperature and power consumption.

Hyperparameter	$T_{\text{HB,out}}$	$\dot{W}_{\text{sys}}$
Learning rate	0.05	0.001
Hidden layers	2	2
Neurons on the first layer	8	16
Neurons on the second layer	6	6
Input lags	1	1
Output lags	1	1

The selection of the optimal model relied on reaching the minimum MSE encountered in the 90-step ahead prediction for the validation set. This criterion was chosen to identify a model capable of accurately predicting the system long-term behavior. Notably, considerable variance emerged across the results, highlighting the sensitivity of machine learning models to hyperparameter choices.

To evaluate performance, the experimental temperature and power consumption profiles will be compared with the 1- and 90-step-ahead predictions of the models. The comparative analysis of the experimental data for the hot-end temperature during the hot blow against predicted values for both 1- and 90-step ahead is depicted in Figs. 6.16, 6.17, and 6.18 for the training, validation, and test sets, respectively. The findings reveal that the trained models successfully captured the intricate nonlinear phenomena inherent in the transient

operation of MR systems, as evidenced by the good agreement across all three datasets, especially in the test set. As anticipated, variations arise when assessing short- versus long-term predictions. Notably, the 1-step-ahead predictions exhibit a more favorable alignment with the ground truth (i.e., the experimental data) than the 90-step-ahead predictions, despite the model hyperparameter optimization targeting the latter. This discrepancy is attributed to the autoregressive nature of the NARX ANN, where outputs from one timestep serve as inputs for the next, leading to an expected accumulation of errors as the prediction horizon extends, as observed in this case. Nevertheless, the approach of employing a long-term metric for model selection has demonstrated effectiveness, affirming the aptitude of the model for predicting such scenarios.

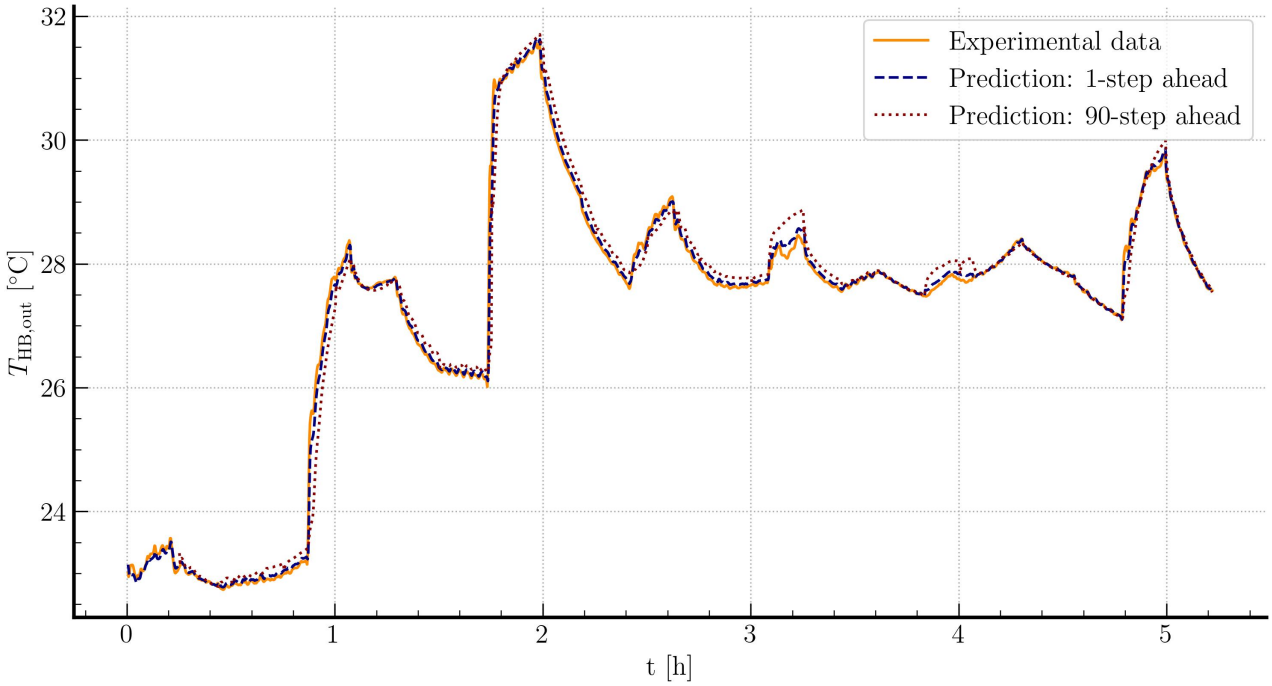


Figure 6.16 – Comparison between the experimental temperature and predictions of the model for 1- and 90-step ahead in the training set.

To enhance the visual representation of the model performance, the deviation between predictions and experimental data, denoted as $\Delta T_{\mathrm{HB,out}}$ in °C, is illustrated in Figs. 6.19, 6.20, and 6.21 for the training, validation and test sets, respectively. Upon visualizing the histogram, the pronounced superiority of the 1-step-ahead model over its 90-step-ahead counterparts becomes more apparent, with the bandwidth of deviations consistently narrower for the former across all three datasets. Additionally, the maximum deviations stand out, but it is essential to note, however, that instances of such high deviations are infrequent, occurring mainly during transitions between excitation signals. In general, the majority of data samples exhibit deviations within ±0.3°C, a notable achievement given the complexity of the phenomena and the extensive range of operating conditions considered.

Following this, the comparison between the experimental data for overall power

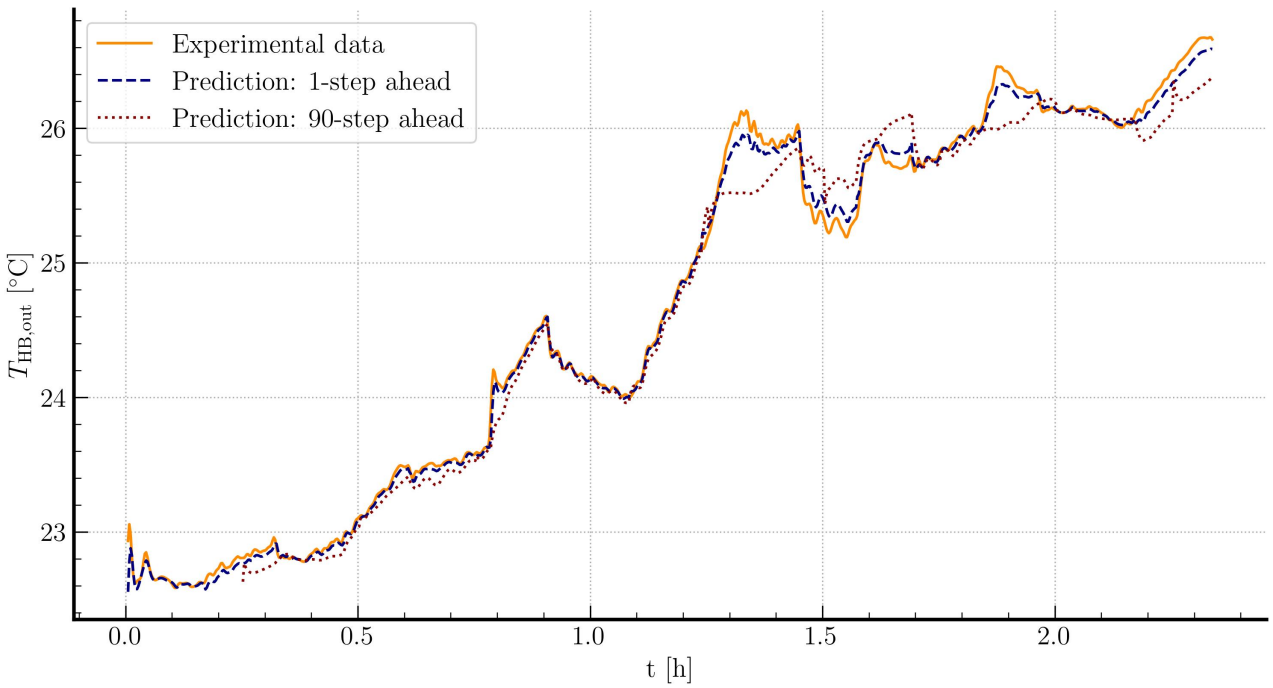


Figure 6.17 – Comparison between the experimental temperature and predictions of the model for 1- and 90-step ahead in the validation set.

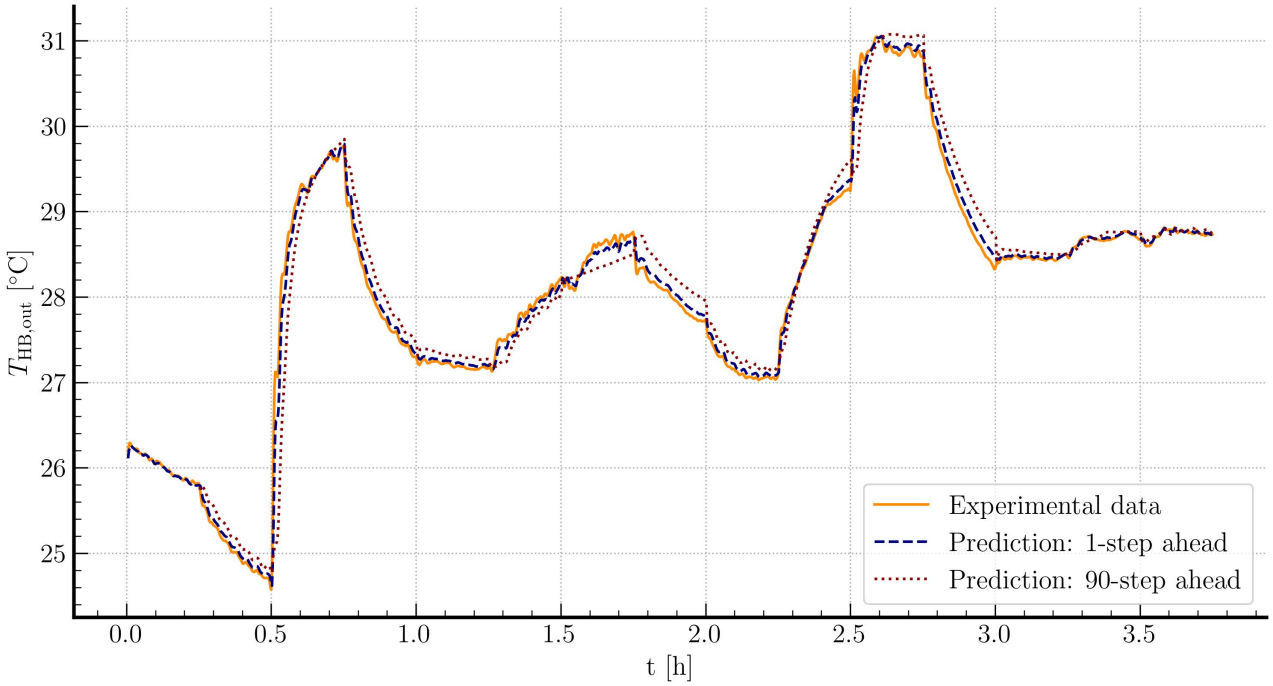


Figure 6.18 – Comparison between the experimental temperature and predictions of the model for 1- and 90-step ahead in the test set.

consumption and the corresponding predicted values for both 1- and 90-step ahead is illustrated in Figs. 6.22, 6.23, and 6.24 for the training, validation, and test sets, respectively.. The results demonstrate that the behavior of the models trained on power consumption mirrors the trends observed in those trained on temperature. Despite the inherently noisy nature of power consumption data, stemming from both the measured signal and the measurement instruments, the 1-step-ahead model consistently outperforms its 90-step counterpart, aligning

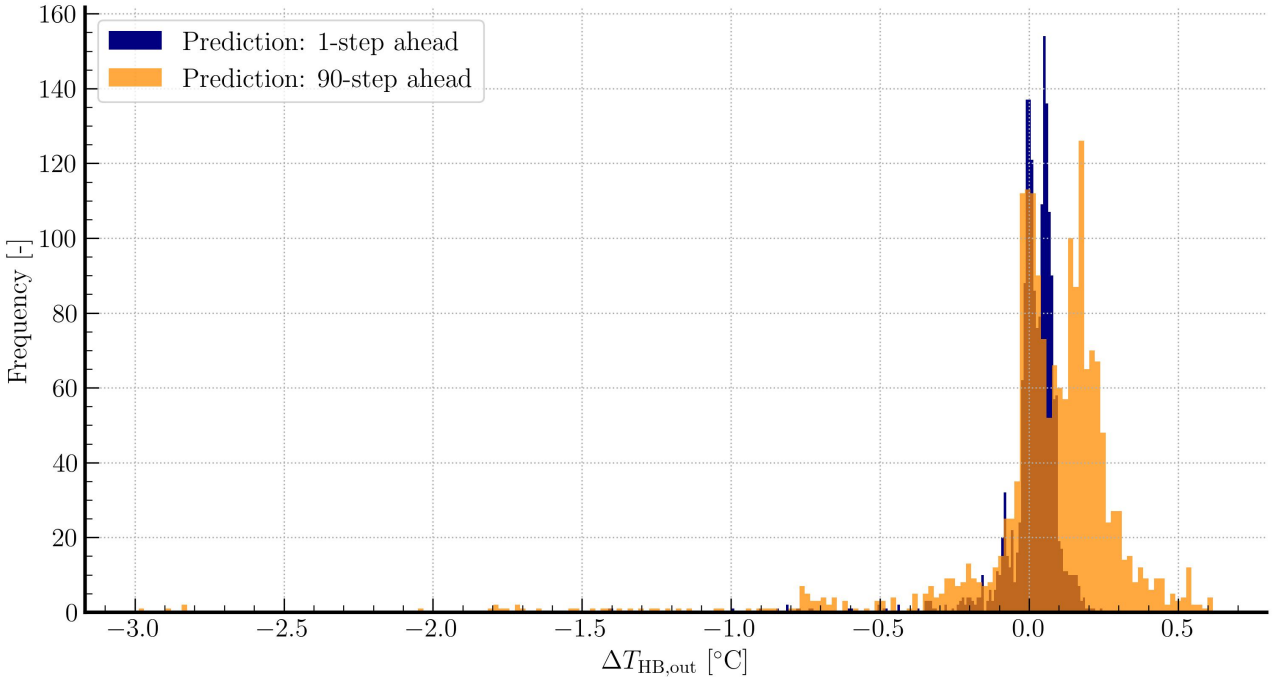


Figure 6.19 – Histogram of the deviation between the experimental temperature and predictions of the model for 1- and 90-step ahead in the training set.

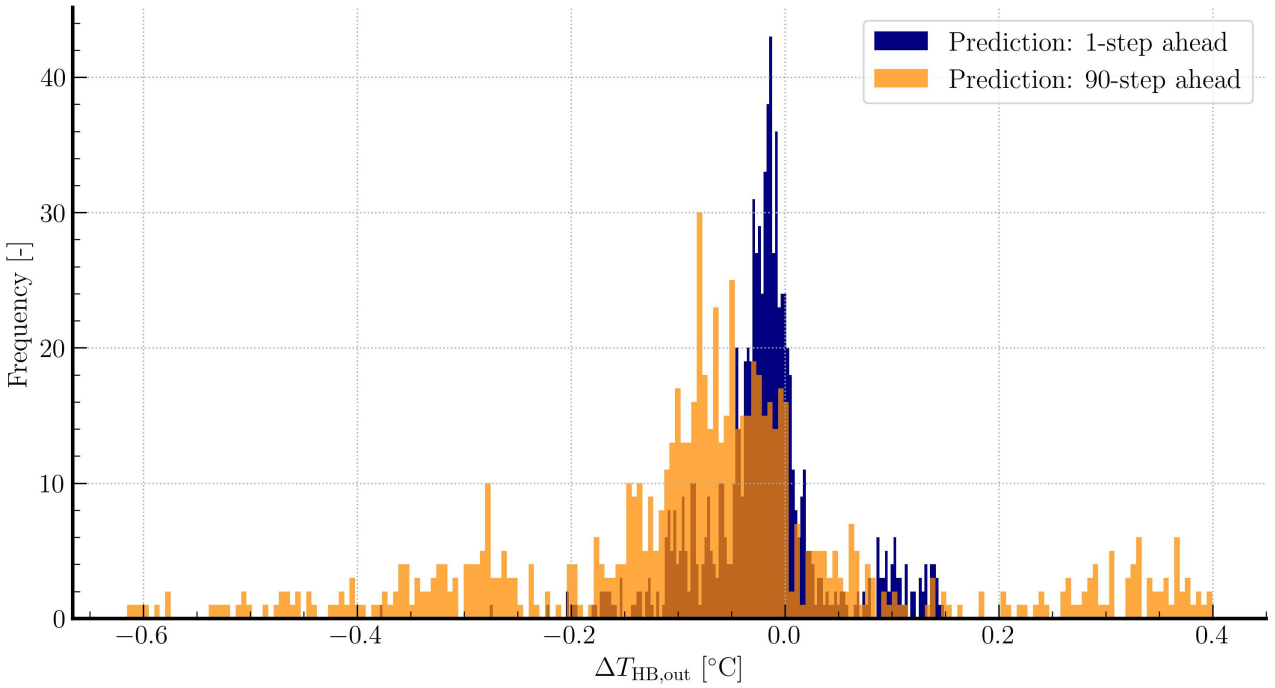


Figure 6.20 – Histogram of the deviation between the experimental temperature and predictions of the model for 1- and 90-step ahead in the validation set.

with the autoregressive nature of the NARX. Notably, through hyperparameter optimization for 90-step-ahead prediction, the models effectively preserve a significant portion of their accuracy, preventing a surge in deviations.

The magnitude of the disparities between ground truth and predictions is also dependent on the operating conditions, with instances where the model excels and deviations are minimal. However, long-term predictions did not capture the noisy behavior of the data,

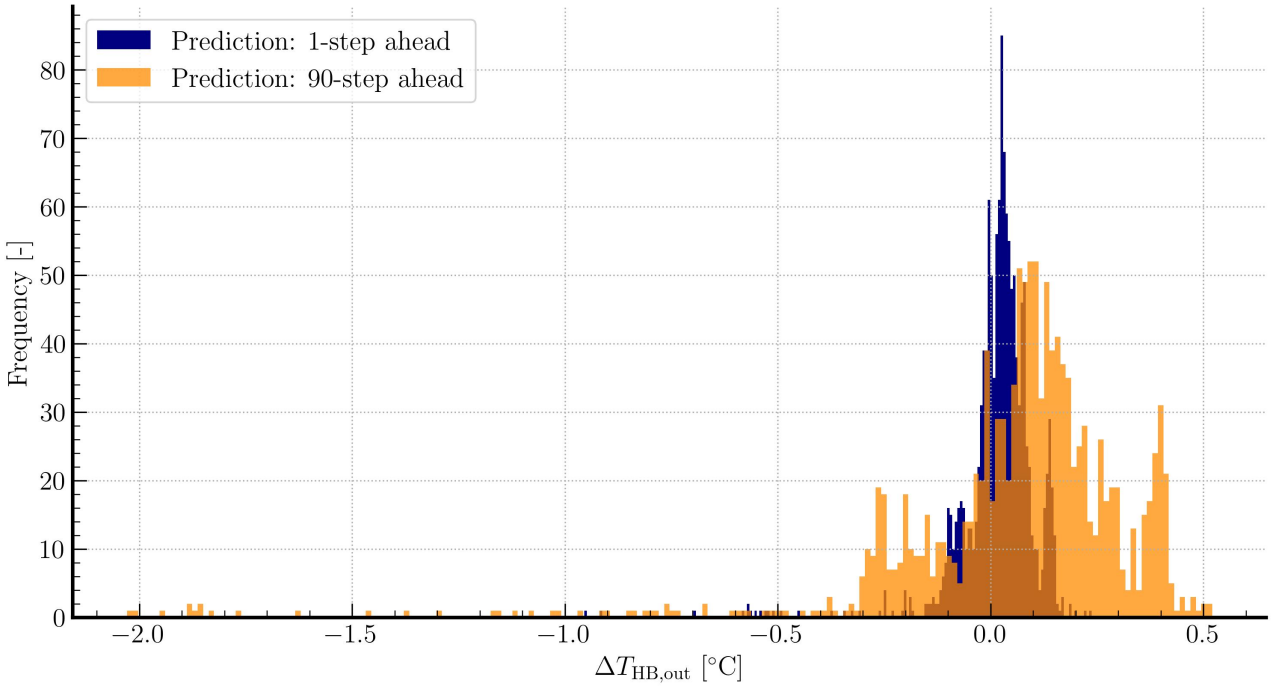


Figure 6.21 – Histogram of the deviation between the experimental temperature and predictions of the model for 1- and 90-step ahead in the test set.

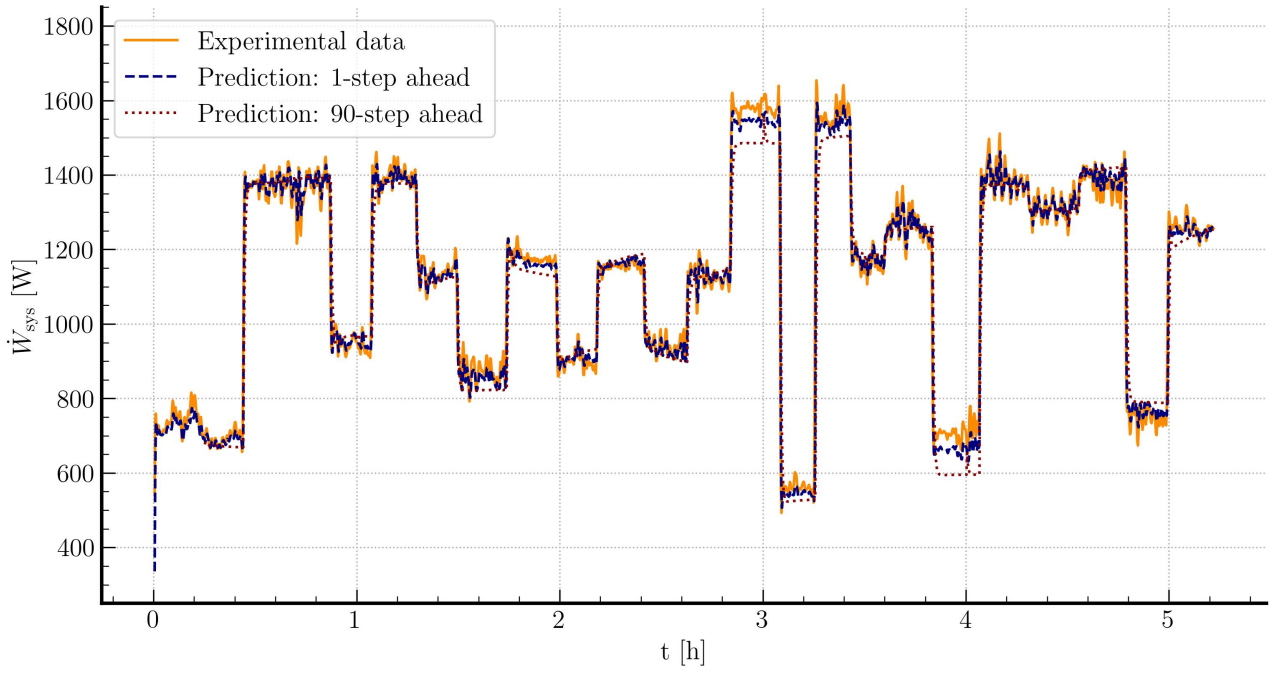


Figure 6.22 – Comparison between the experimental temperature and predictions of the model for 1- and 90-step ahead in the training set.

damping it as the forecast window increased. The behavior of the data is mainly due to measurement noise, which the model is not intended to capture. The 1-step-ahead prediction can reproduce part of it, given the small horizon and the update of the input parameters for the previous instants.

To allow a more illustrative representation, the deviation between predictions and experimental data, denoted as $\Delta\dot{W}_{\mathrm{sys}}$ in percentage values, is depicted in Figs. 6.25, 6.26, and 6.27

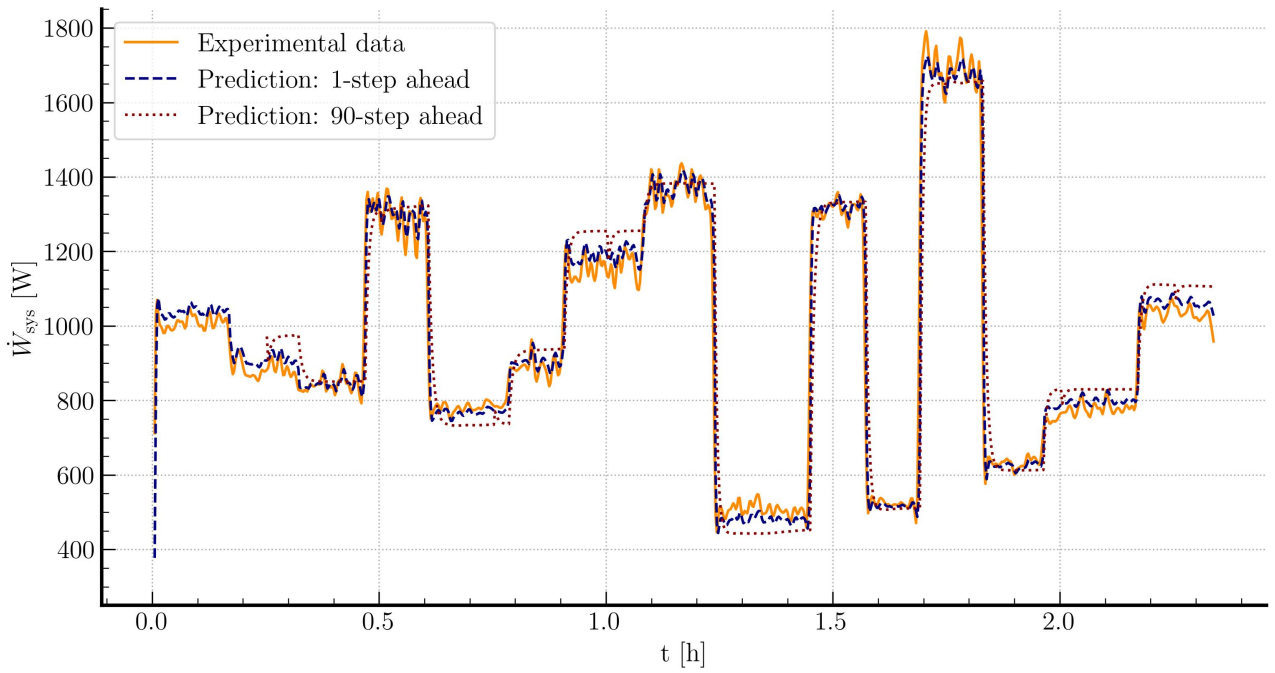


Figure 6.23 – Comparison between the experimental temperature and predictions of the model for 1- and 90-step ahead in the validation set.

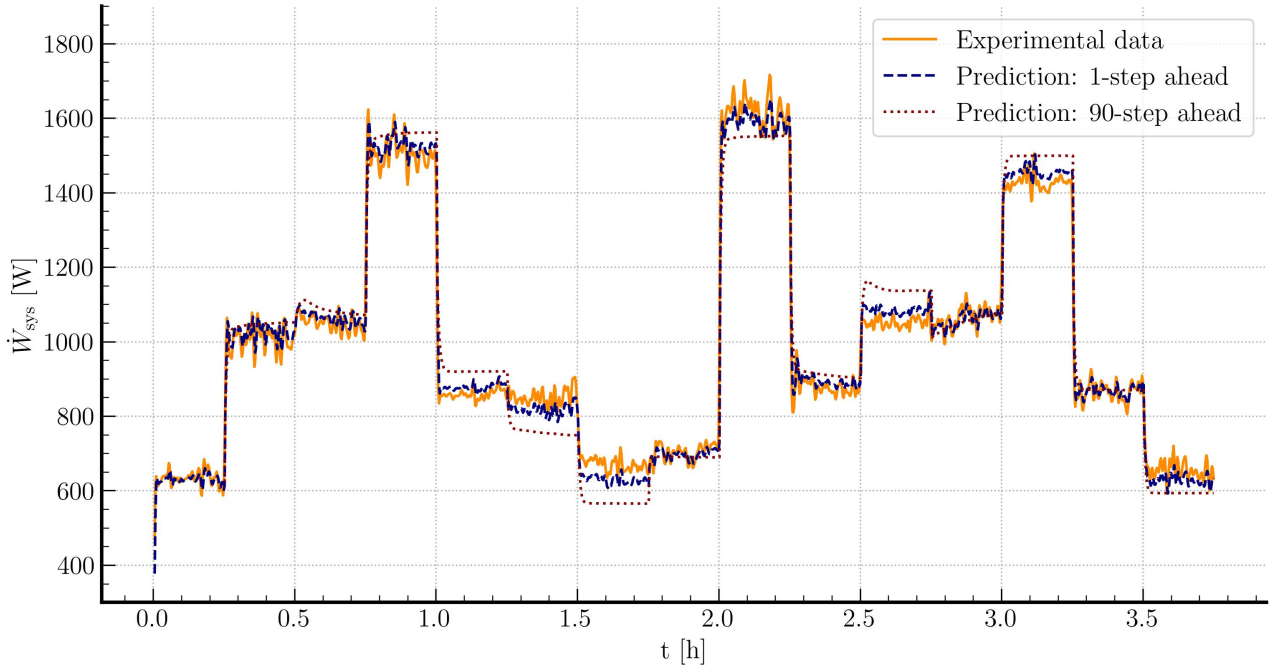


Figure 6.24 – Comparison between the experimental temperature and predictions of the model for 1- and 90-step ahead in the test set.

for the training, validation and test sets, respectively.

Once again, the evident superiority of the 1-step ahead models over their 90-step ahead counterparts is highlighted in the visual representation of the histograms in Figs. 6.25-6.27. Deviations exceeding 20% are exceptional and are typically associated with abrupt transitions between operating states. The majority of deviations across all datasets are confined to $\pm 10\%$.

While visual assessments of model performance are valuable, their subjectivity

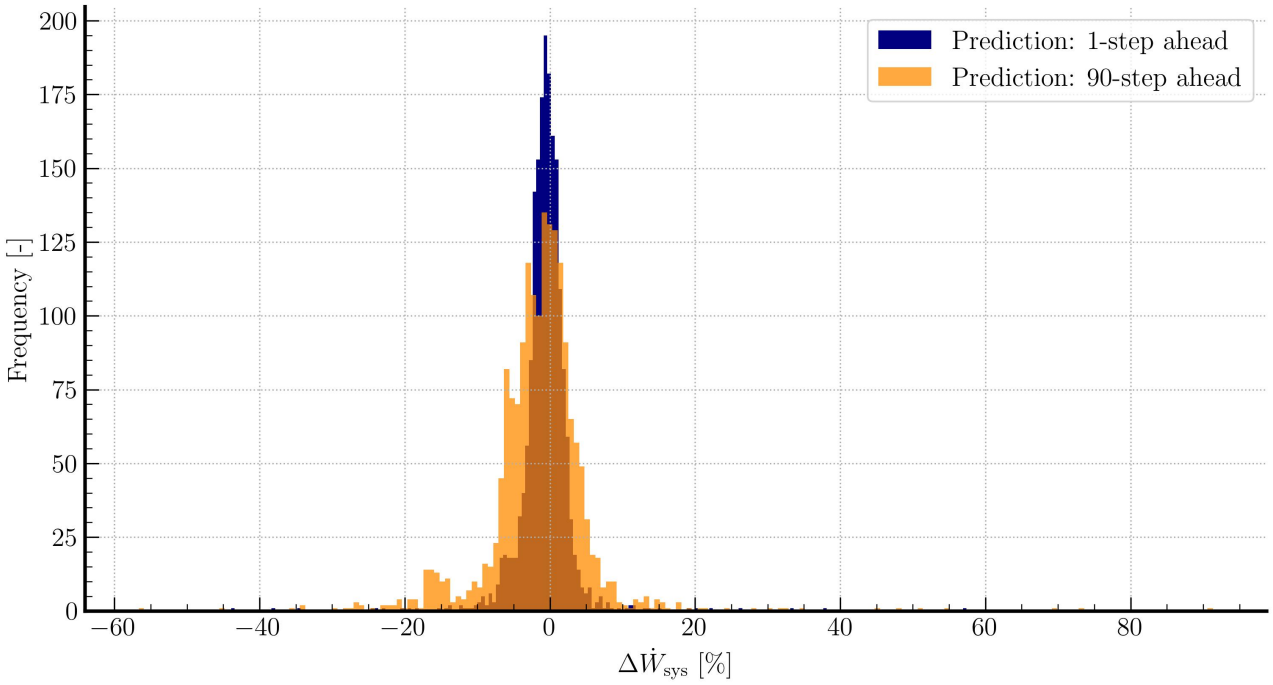


Figure 6.25 – Histogram of the deviation between the experimental temperature and predictions of the model for 1- and 90-step ahead in the training set.

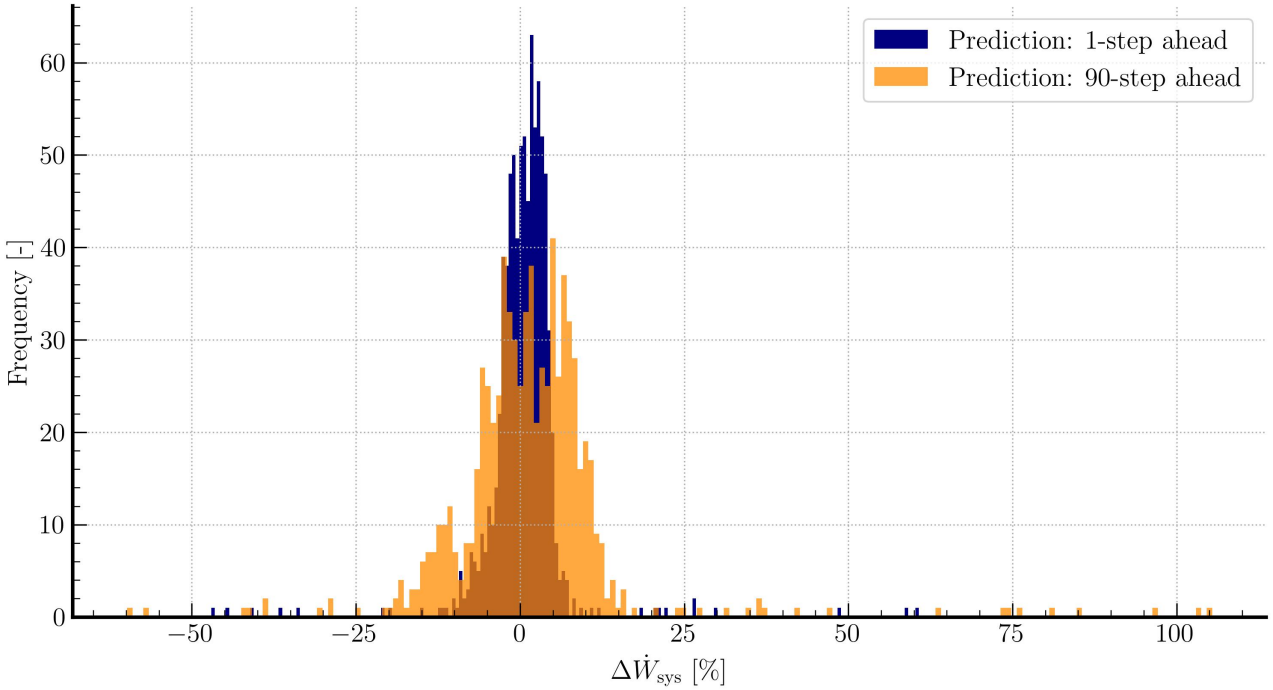


Figure 6.26 – Histogram of the deviation between the experimental temperature and predictions of the model for 1- and 90-step ahead in the validation set.

highlights the importance of employing quantitative tools for a comprehensive evaluation. To complement this assessment, R^2 and root mean squared error ($RMSE$) will be used to characterize the models developed for the hot-end temperature during the hot blow and for overall power consumption across each dataset, for both short- and long-term predictions. The obtained results are presented in Table 6.9 for all datasets. It is worth noting that the performance of the training and test sets is expected to be superior, as those datasets were

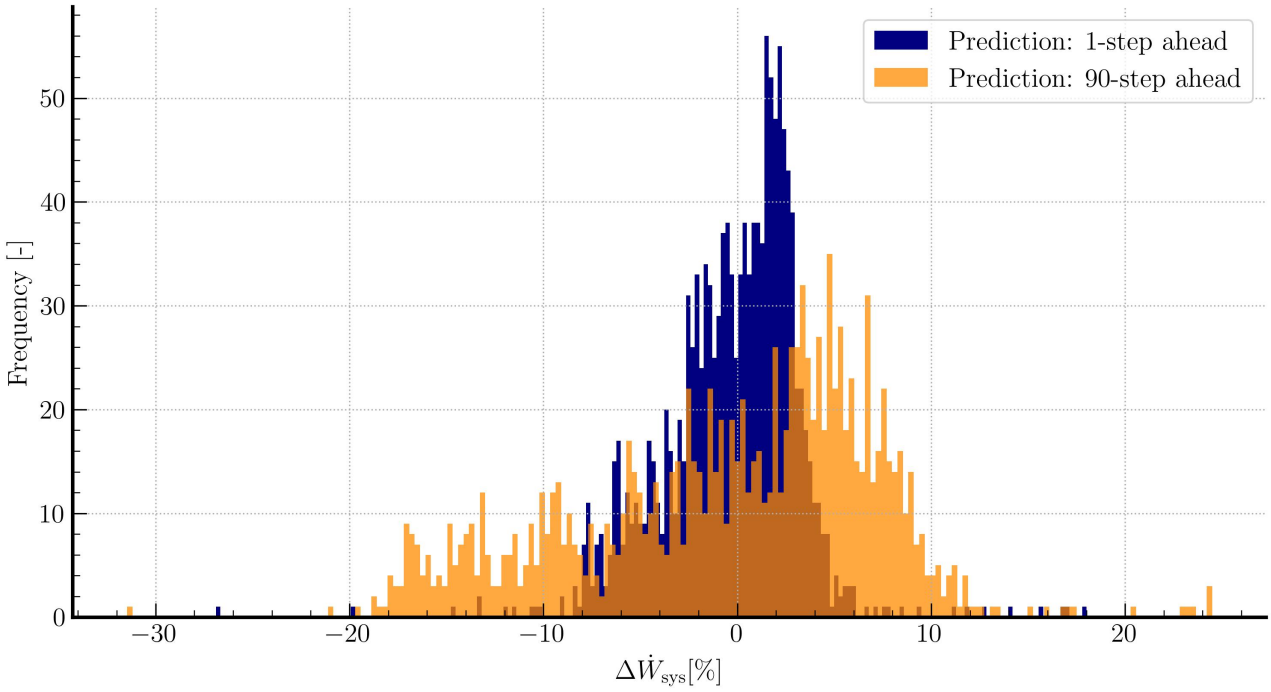


Figure 6.27 – Histogram of the deviation between the experimental temperature and predictions of the model for 1- and 90-step ahead in the test set.

used to train the model.

Table 6.9 – Performance metrics of the models for the evaluated datasets

Metric	**Dataset**	**Training**		**Validation**		**Test**	
	Steps Ahead	1	90	1	90	1	90
$\mathbf{R^2}$	$T_{HB,out}$ [-]	0.998	0.988	0.998	0.980	0.995	0.955
	$\dot{W}_{sys}$ [-]	0.978	0.923	0.967	0.881	0.988	0.949
RMSE	$T_{HB,out}$ [°C]	0.012	0.096	0.004	0.038	0.009	0.091
	$\dot{W}_{sys}$ [W]	39.05	76.06	55.77	108.96	33.17	70.38

The results align with several conclusions drawn from the evaluation of Figs. 6.16-6.27. Notably, the results for temperature showed superior agreement compared to those for the power consumption, attributed to the slower dynamics and smoother behavior of the former, in contrast to the latter. That is even more noticeable for the 90-step-ahead prediction, where deviations in the models have a more severe influence on rapid dynamic variables, such as power consumption, than on those with slower dynamics, such as temperature. Across all scenarios, the R^2 values consistently favored 1-step-ahead forecasting over the 90-step-ahead situation. However, a discernible trend in the results across datasets is not readily apparent from the evaluation of the R^2 score alone. Nevertheless, the majority of cases yielded R^2 values exceeding 0.97, indicating an exceptional level of agreement, with only one case registering a value below 0.9. Moreover, regarding the RMSE, it is clear that the short-term predictions perform better than the long-term ones, achieving values roughly 10 and 2 times higher for temperature and power consumption, respectively.

Overall, these results confirm that the models reproduced the underlying dynamics across a broad range of conditions, even when challenged with long-horizon forecasts. Despite the increased difficulty associated with predicting rapid-response variables such as power consumption, the models maintained high accuracy, with most cases achieving R^2 values above 0.97 and only moderate degradation in $RMSE$ for extended horizons. This level of performance indicates that the models not only generalize well across datasets but also capture the essential temporal behavior needed for decision-making frameworks. In particular, the demonstrated ability to track both slow and fast dynamics suggests strong potential for integration into predictive control strategies, where accurate multi-step-ahead forecasts are critical for anticipating system evolution, optimizing performance, and ensuring reliable real-time operation.

6.3 Uncertainty Analysis of the Curie Temperature of Magnetocaloric Materials

Among many challenges, including the cost and performance of the systems, MCM performance and reliability remain among the most challenging to overcome for the commercialization of MR. Not only does the small magnitude of the magnetocaloric effect (Gottschall *et al.*, 2019) affect the performance, size, and cost of the system, but as the technology matures, other critical issues arise, such as the chemical and mechanical stability of the materials (Döring *et al.*, 2024a).

Among them, one fundamental trait for the quality assurance of large-scale production of the system is the uncertainty involved in its design. For magnetocaloric systems, one critical aspect is the uncertainty in the Curie temperature of the MCM, which has been explored in a few works in the literature. Despite its seemly low magnitude, which according to MCM suppliers is between 1.5°C and 2.0°C, that effect is propagated by the use of multilayer strategies (Aprea *et al.*, 2011; Bez *et al.*, 2020; Yuan *et al.*, 2022) in AMR, especially in FOPT MCMs that rely on a large number of layers (Lei *et al.*, 2015; Zhang *et al.*, 2017; Navickaitė *et al.*, 2018). In this section, the effect of uncertainties in the Curie Temperatures of MCM is explored through an ANN-powered Monte Carlo Analysis.

6.3.1 Problem Formulation

Consider a multilayer AMR composed of N layers, according to Fig. 6.28, and focus on three layers, namely layers *i-1*, *i*, and *i+1*. For each layer, the Curie temperature was determined to be coupled with the solid temperature profile and to maximize the MCE on the AMR. However, for each *i*-th layer, a deviation σ_{i} from the original values resulting from the manufacturing process occurs. Figure 6.29 schematically shows the deviation between the original (solid lines) and the actual (dashed lines) adiabatic temperature changes achieved by

the multilayer arrangement. It is worth noting that the values on the curve are for illustrative purposes only and do not reflect the actual properties achieved by the MCM or an AMR multilayer.

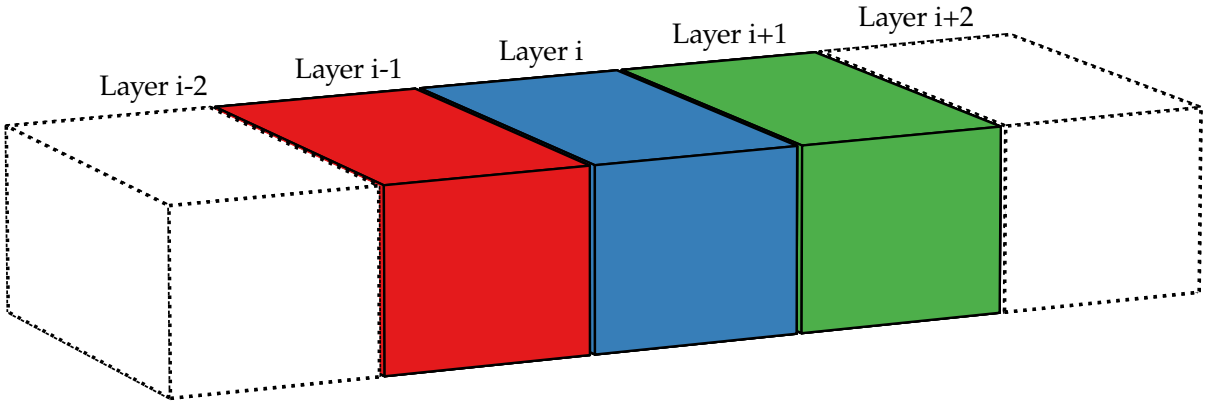


Figure 6.28 – Schematic representation of a multilayer AMR.

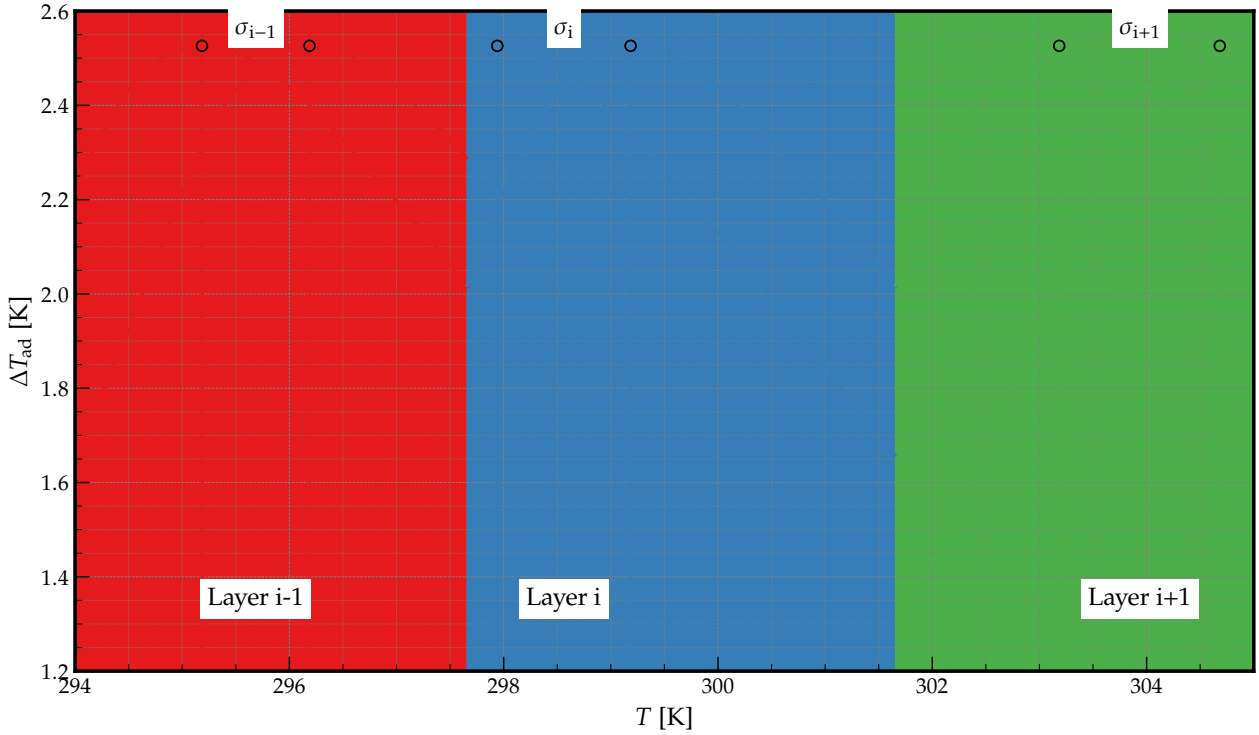


Figure 6.29 – Schematic representation of the Curie temperature deviation. Solid lines represent the original curves and dashed lines represent the ones achieved by the manufacturing process.

Figure 6.29, illustratively shows that deviation from the Curie temperature will result in a potential decoupling between the temperature profile of the solid and the multilayer arrangement. As the Curie temperature of the multilayer AMR is generally optimized (Bez *et al.*, 2020), it is expected that any deviations will reduce the performance. In one of the few studies to evaluate that effect, Lei *et al.* (2015) conducted numerical simulations of 2000 cases

to assess the impact of variations in Curie temperature on the cooling capacity of AMRs. For a 15-layer FOPT AMR with 2°C layer spacing, a deviation of 0.6°C resulted in the loss of at least 16.6% of cooling capacity. However, the number of cases evaluated can be considered low for Monte Carlo analysis (Sudret *et al.*, 2017), as the computational costs of numerical simulations hinder the prediction of a large number of cases.

That limitation becomes critical as the number of AMR layers increases and the design space grows exponentially, rendering conventional optimization approaches increasingly impractical. Furthermore, uncertainty quantification via Monte Carlo simulations remains computationally prohibitive, as each simulation can take minutes to hours to complete (Sudret *et al.*, 2017). To address these challenges, recent efforts have turned to machine learning-based surrogate models (Sudret *et al.*, 2017; Pham *et al.*, 2022; Shahane *et al.*, 2022; Wang *et al.*, 2022). These models make use of the efficiency and predictive capabilities of machine learning to accelerate Monte Carlo simulations, allowing a statistically rigorous assessment of uncertainty.

Addressing the gap in the impact of Curie temperature variability on AMR performance, Tomc *et al.* (2025) investigated its effect on the cooling capacity of second-order phase transition (SOPT) AMRs through Monte Carlo simulations. Using Radial Basis Function ANNs, they efficiently simulated a large number of cases and quantified the influence of thermal fluctuations on AMR performance.

Hence, the objective of this study was to advance on the work developed by Tomc *et al.* (2025), and to evaluate the effect of uncertainty on the Curie temperature of FOPT multilayer AMR. For that, the general expression of the model being developed according to Eq. (2.8), can be expressed as follows:

$$\dot{Q}_{\mathrm{c}} = \mathcal{F}(\overline{T}_{\mathrm{Curie}}) \tag{6.25}$$

6.3.2 Data Collection and Preparation

The data collection process in this study was carried out using results from experimentally validated numerical models. This approach enabled the generation of sufficiently large datasets to represent the design space of interest. The numerical model used to produce these results was developed by Trevizoli *et al.* (2016a) and Vieira *et al.* (2021), both of which have been previously validated in different scenarios (Trevizoli *et al.*, 2016a; Trevizoli *et al.*, 2017; Vieira *et al.*, 2023; Teza *et al.*, 2024).

To perform the numerical simulation, a set of input parameters must be specified. The most critical among them include the particle diameter (d_{p}), and porosity (ε) of the porous medium; the operating frequency (f), and mass flow rate ($\dot{m}_{\mathrm{f}}$); the height (H_{AMR}), width (W_{AMR}), and length (L_{AMR}), of the AMR bed; the magnetic flux density (B_{AMR}) applied over the AMR bed; the temperatures at the hot (T_{HE}) and cold (T_{CE}) ends of the AMR; and

the number of layers in the multilayer arrangement (N_l) and of AMR beds (N_AMR). Since this study focuses on evaluating the impact of uncertainty on Curie temperature on AMR performance, a base case was selected in which these parameters were fixed to isolate the effect under investigation. The selected case is based on the parameters of the MRU. A summary of these values is provided in Tab. 6.10.

Table 6.10 – Fixed parameters of the numerical simulation

Parameter	Value
d_p [mm]	0.65
ε [%]	48
f [Hz]	1
$\dot{m}_\mathrm{f}$ [kg h^{-1}]	800
H_AMR [mm]	45
W_AMR [mm]	57
L_AMR [mm]	120
B_AMR [T]	1.17
T_HE [°C]	38
T_CE [°C]	20
N_AMR [-]	16

The porous medium in the AMRs consists of packed beds of La(FeMnSi)$_{13}$H$_\mathrm{z}$ particles, commercialized as *Calorivac-HS2* by Vacuumschmelze GmbH & Co, which are shaped as elongated cylinders (Vieira *et al.*, 2021). In this study, three multilayer arrangements are considered to evaluate the effect of the number of layers in the AMR: 5, 10, and 15 layers. For each case, the Curie temperature in the extreme layers was set to 17°C at the cold end and 35°C at the hot end to improve system performance (Vieira *et al.*, 2021). The Curie temperatures of the intermediate layers were determined by linear interpolation based on the total number of layers in each case. Each of the three configurations receives, as input, the fixed parameters summarized in Tab. 6.10, along with the multilayer arrangement represented as a vector of Curie temperatures ($\overline{T}_\mathrm{Curie}$).

To assess the impact of the uncertainty of the Curie temperature on the performance of the system, a random perturbation was applied to each layer of the arrangement for each simulation, following a uniform distribution with an amplitude of $\pm$3°C. After the simulation, the key performance metric analyzed is the cooling capacity. Consequently, the dataset consists of pairs of perturbed Curie temperatures and their corresponding cooling capacities.

A total of 35,508, 153,429, and 162,635 numerical simulations were performed for cases with 5, 10, and 15 layers, respectively. The final number of simulations was determined using a general rule to increase the number of samples with the number of layers, while accounting for hardware limitations in model development. Following standard machine

learning practices, the dataset was divided into three subsets: training, validation, and test, with proportions of 64%, 16%, and 20%, respectively (Joseph, 2022). The number of samples for each dataset used in the model development is presented in Tab. 6.11.

Table 6.11 – Dataset samples for each case.

Dataset	Case		
	5 layers	**10 layers**	**15 layers**
Training	22724	98194	104086
Validation	5682	24549	26022
Test	7102	30686	32527
Total	35508	153429	162635

6.3.3 Model Selection

Once again, ANNs were selected for their effectiveness in regression tasks, their flexibility, and their prior success in modeling AMRs. In the current study, the evaluated cases involve ANNs composed of two layers of neurons. However, the number of neurons in each layer varies in different cases, leading to different ANN architectures. The ANNs were implemented using the Keras framework (Chollet *et al.*, 2015) with the TensorFlow back-end (Abadi *et al.*, 2015). All layers used the Exponential Linear Unit (ELU) activation function, He normal initialization (Datta, 2020), and the MAE loss function.

6.3.4 Model Training and Optimization

The Adam optimizer (Kingma, 2014) was employed to train the ANNs, with a learning rate of 0.05, a batch size of 500 samples, and a total of 10000 epochs. A learning rate scheduler (Lewkowycz, 2021) was used to improve training performance. This technique decayed the learning rate by a factor of 0.99 every 10 epochs, starting after the 200th epoch.

In addition, L2-regularization and early stopping were applied to prevent overfitting. For the latter, a patience value of 1,000 epochs was set based on the validation set loss. To ensure that the best model parameters were retained, the model was restored to the weights that yielded the lowest validation loss. The ANN architecture was determined by manual evaluation of various configurations, with the results assessed using the loss function on the test set. The final architecture, including the number of neurons for each of the three evaluated cases, is presented in Table 6.12.

6.3.5 Model Evaluation

The comparison between the numerical results and the AI predictions of the cooling capacity for the cases with 5, 10, and 15 layers is presented in Fig. 6.30(a)-(c). Each figure presents the results for the training, validation, and test sets, along with $\pm 5\%$ and $\pm 10\%$

Table 6.12 – Number of Neurons in the ANN.

Hidden Layer	Case		
	5 layers	10 layers	15 layers
First	50	100	150
Second	20	30	40

deviation bars. In addition, the results for the test set of numerical performance metrics, namely R^2, MSE, and MAE, are presented in Tab. 6.13.

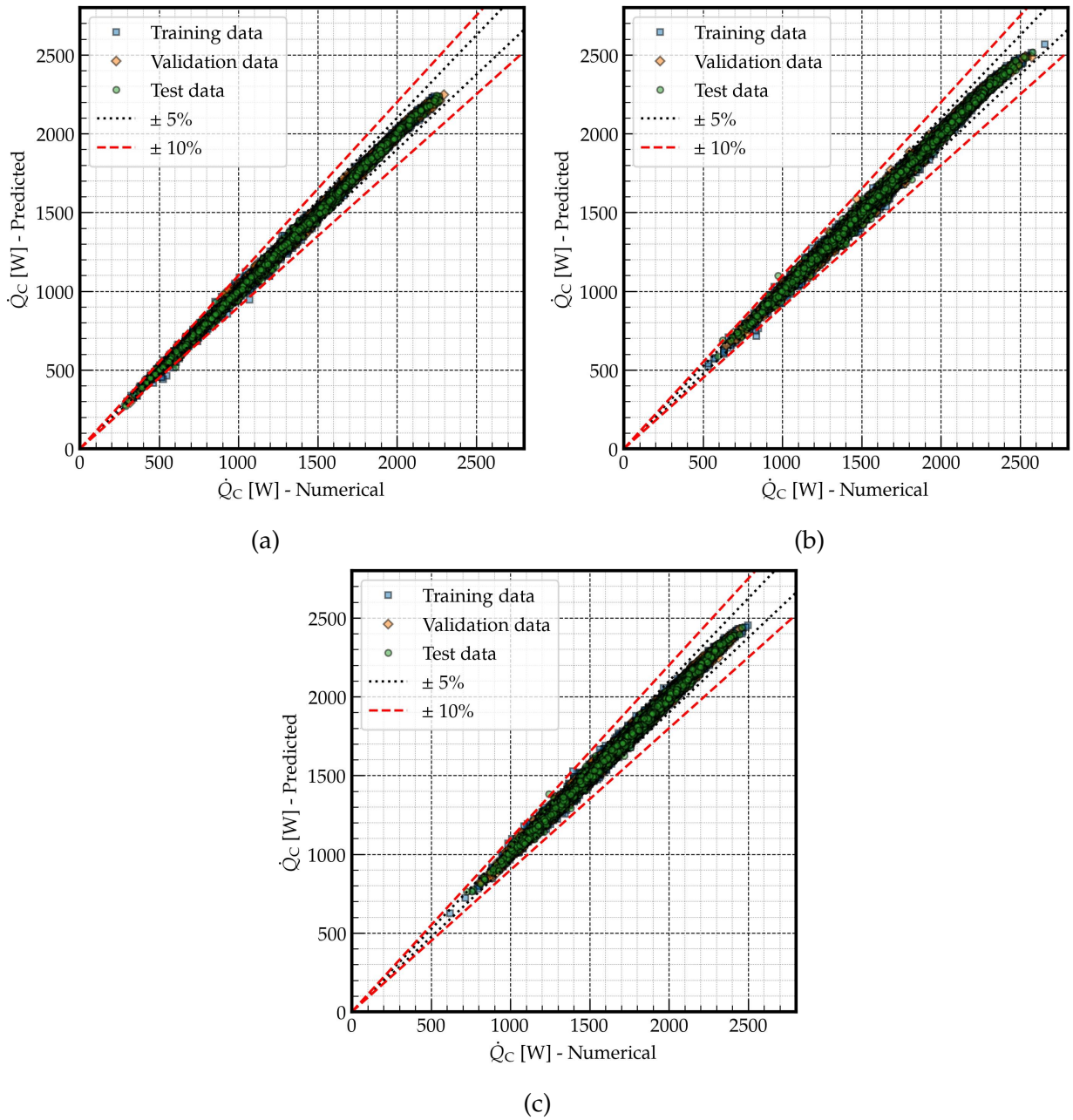


Figure 6.30 – Comparison between the cooling capacity calculated by the numerical model and predicted by the ANN for the AMR with (a) 5, (b) 10, and (c) 15 layers.

It is clear from both Fig. 6.30 and Tab. 6.13 that the developed ANNs excel at capturing the complex relations in the multilayer AMR and can predict the performance with high accuracy. It is essential to note the high effect under evaluation, as the deviation applied to

Table 6.13 – Performance metrics of the models for the AMRs with 5, 10, and 15 layers.

Metric	Case		
	5 layers	**10 layers**	**15 layers**
R^2	0.999	0.997	0.995
MSE	144.21	153.63	203.01
MAE	8.79	9.29	11.00

Curie temperatures led to cooling capacities around 20% of their original values, that is, a five-fold reduction. Not only does the significant variability in the output parameter pose a considerable challenge for modeling, but the results from all three ANNs also demonstrate their ability to capture complex phenomena.

Despite the few outliers presented in Fig. 6.30, most of the data samples in all test sets were predicted within a deviation of $\pm$5%. That visual conclusion is corroborated by the values attained by the performance metrics, since the mean values of the deviations between the AI model and the numerical simulations, as measured by MAE, are of the order of 10 W. In addition, the high values of the coefficients of determination, all exceeding 0.995, corroborate the good agreement between the models.

The performance of the three ANN models was similar, even though the complexity of the phenomena to be modeled increased with the number of layers in the AMR. That is expected, as, according to Tab. 6.12, the number of neurons per layer is higher for ANNs with more layers, that is, a higher number of inputs to the model. Hence, the greater number of neurons, and consequently the greater number of coefficients to be trained, results in more complex models, which are better suited for training more complicated systems.

6.3.6 Model Application

The uncertainty analysis in the present study is conducted via Monte Carlo simulation. That is done by selecting a standard case and then evaluating how the variability in the input parameters, in this case the Curie temperature, affects the variability of the output metrics, in this case the cooling capacity, by simulating a large number of cases, according to Eqs. (2.54) and (2.55). Since the objective is to provide a system-level overview of the influence of uncertainty on the Curie temperature, some strategies were proposed for generating the dataset and analyzing the results. These propositions reflect on the decisions that would be made when designing the prototype.

The number of cases must be large enough to achieve statistical significance and to be representative of the actual distribution. In the present case, that number was set at 10,000,000 simulations, determined by the point at which increasing the number of simulations did not yield a significant change in the results. It is worth mentioning that running such a large number of numerical simulations would be expected to take months or years, while it could

be done in a matter of hours with the ANNs.

Before Monte Carlo simulations, the Curie temperature arrangement was optimized. The objective was to determine, before the multilayer arrangement, which provided the highest cooling capacity, and this was not guaranteed to be the linear approximation used to run the numerical results. From a system perspective, that would be the expected procedure, as the proper optimization of the multilayer arrangement is fundamental to the performance of magnetic refrigeration systems. That optimization, in itself, is a challenging task with numerical models (Bez *et al.*, 2020), given the high dimensionality of the design space. However, using ANNs makes this feasible. By doing this optimization, it is ensured that the best possible case is that of the original multilayer arrangement configuration, that is, the one without disturbances or uncertainties. In addition, the maximum deviation allowed between the Curie temperature of the material in the i-th layer and the original Curie temperature of that layer is set to ± 3°C.

Hence, the optimization problem is defined by Eq. (6.26). The differential evolution algorithm (Storn & Price, 1997) implemented in the Scipy library (Virtanen *et al.*, 2020) was used. The remaining input parameters continue to be the same as in Tab. 6.10.

$$\mathbf{P} = \begin{cases} \text{Minimize} & -\dot{Q}_{\mathrm{c}}(\overline{T}_{\mathrm{Curie}}) \\ \text{subjected to} & |T_{\mathrm{Curie,i}} - T^{*}_{\mathrm{Curie,i}}| - 3 \leq 0 \end{cases} \tag{6.26}$$

After determining the standard case, Monte Carlo simulations can be performed. The method followed a similar approach to that used in numerical simulations, in which disturbances are applied to each layer of the multilayer arrangement. The main difference lies in the distribution used in this step. Instead of a uniform distribution, as was done in the data collection phase, a truncated normal distribution is used. That was done since this is the assumption for the distribution provided by the MCM suppliers, with the standard deviation being the metric to be evaluated. The present analysis considered the effect of the standard deviation with magnitudes of 0.1, 0.5, 1.0, 1.5, 2.0, 2.5, and 3.0°C, being the current deviations provided by the suppliers between 1.5 and 2°C.

In addition, a truncation was applied to the distribution, assuming that if a material is manufactured beyond a determined threshold, it is no longer strategic to employ it in the system, as it would severely deteriorate its performance. As in the previous case, this threshold was set at ± 3°C based on the authors' prior experience in the design and assembly of multilayer AMR.

Lastly, after generating the disturbed multilayer arrangement, a final preprocessing step is performed, ordering the disturbed layers in ascending order. That is proposed because, especially when high standard deviations and a large number of layers are evaluated, it is possible for disturbances between two adjacent layers to cause their Curie temperatures to overlap. Although this is possible under the assumptions of this study, from a practical

perspective, the designers would reorder the arrangement to ensure it followed a continuous ascending order from the cold to the hot ends of the AMR. For that, the same procedure is carried out in the present analysis.

After that, the Uncertainty Analysis can be carried out. A summary of the methods used in the present study, encompassing data collection with a numerical model, ANN development, and Monte Carlo Uncertainty Analysis, is presented in Fig. 6.31.

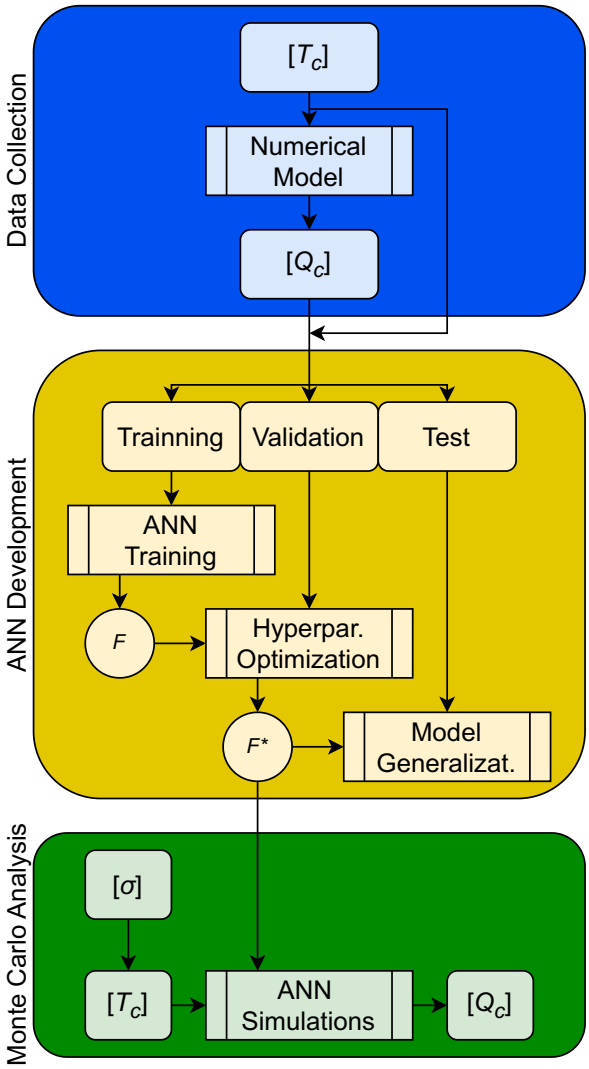
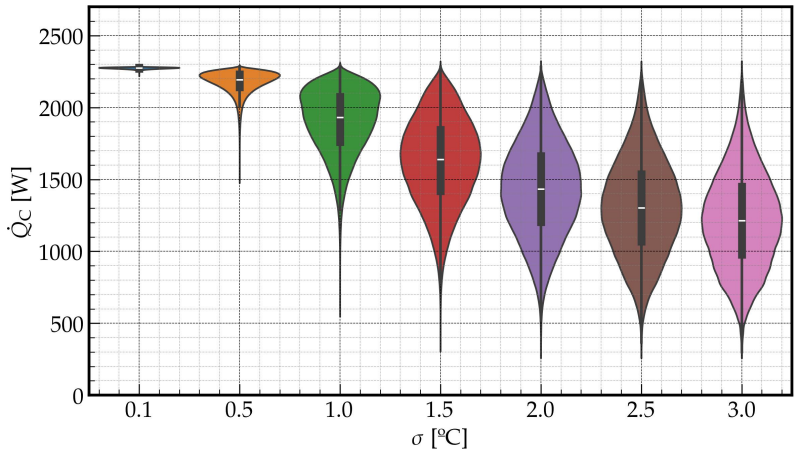


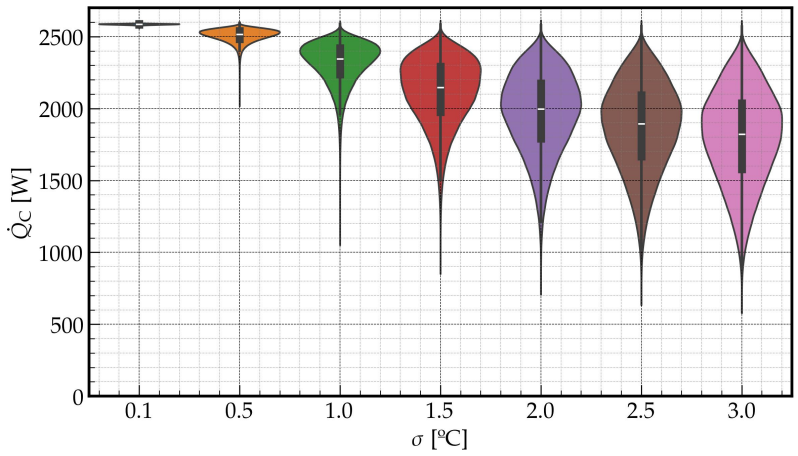
Figure 6.31 – Schematic representation of the proposed method.

6.3.6.1 Monte Carlo Uncertainty Analysis

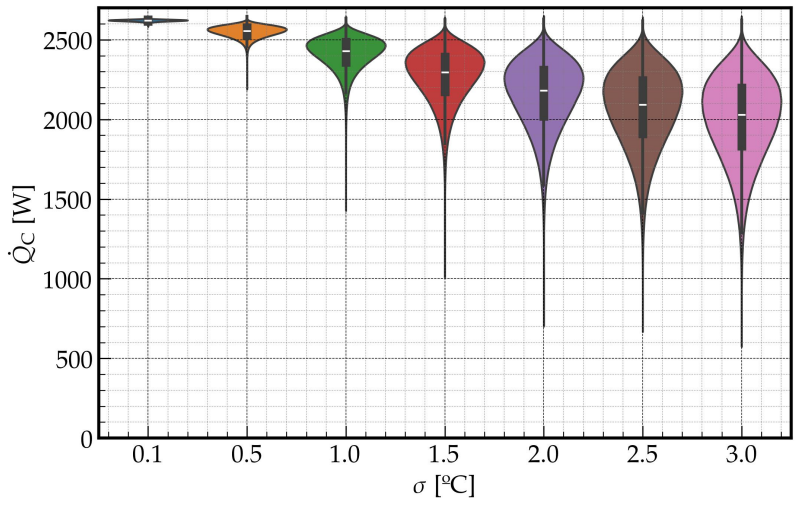
The uncertainty analysis was carried out by evaluating the effect of seven distinct standard deviations, namely 0.1, 0.5, 1.0, 1.5, 2.0, 2.5, and 3.0°C. For each of them, 10,000,000 simulations were performed with the ANN presented in the previous section. The results are displayed in the form of violin plots and presented in Fig. 6.32(a)-(c) for the cases with 5, 10, and 15 layers, respectively.



(a)



(b)



(c)

Figure 6.32 – Effect of the uncertainty of the Curie Temperature on the performance of an AMR with (a) 5, (b) 10, and (c) 15 layers.

The results presented in Fig. 6.32 presented the expected trends for the phenomenon under evaluation. First, as the standard deviation increases, both the median values achieved by the components and the deviation of the achieved values increase. Furthermore, since uncertainties in the Curie temperature are considered, none of the cases exceed the cooling capacity of the original case, validating the hypothesis of optimality and demonstrating that

the effect is only detrimental to component performance. Moreover, as the standard deviation increases, the likelihood that the components operate close to this optimal configuration decreases.

In addition, as the number of layers of the system increases, the effect of uncertainty becomes less severe. Two different motives can explain that. First, as expected, the AMR cooling capacity increases along with the number of layers, especially when comparing the maximum cooling capacity of the case with five layers with that of the cases with 10 and 15 layers, which are very similar given the diminishing returns for increasing the number of layers in an AMR (Lei *et al.*, 2015). Also, there is the effect of reordering the multilayer arrangement, which is more pronounced in cases with 15 layers than in those with 10 or 5 layers, and can help mitigate the effects of uncertainties.

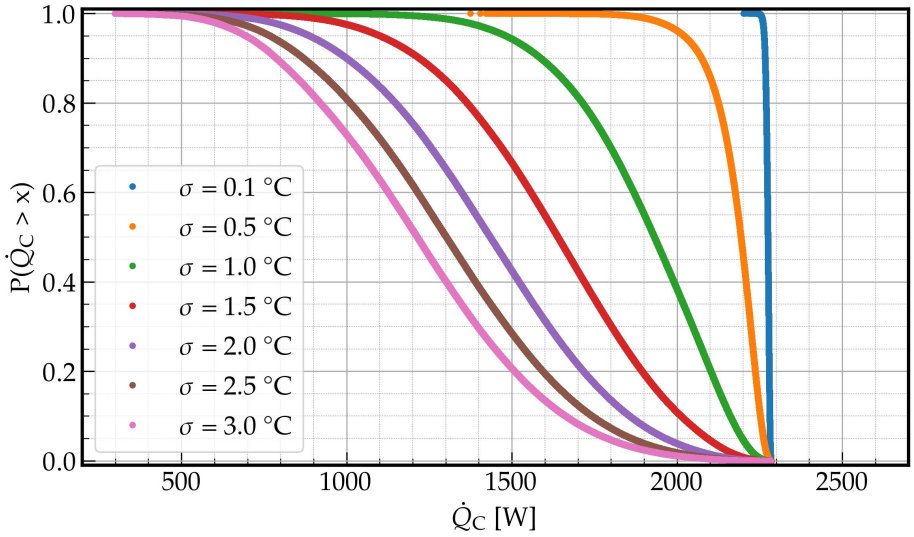
Despite the novelty of the qualitative results discussed so far, they are all within the expected margins and, at specific points, obvious. The interesting and alarming effect stems from the magnitude of the uncertainty in the Curie temperature influence on the cooling capacity. To better assess this, the complementary cumulative distribution function (CCDF) is shown in Figs. 6.33 (a)-(c) for cases with 5, 10, and 15 layers. The CCDF is the probability that a random variable exceeds a given threshold; in this case, the cooling capacity. It is defined mathematically as the complement of the cumulative distribution function, meaning it describes the tail distribution of a probability distribution. In the present case, Fig. 6.33 represents the probability that the system will achieve a determined cooling capacity for a given uncertainty level, in the form of the standard deviation.

The same results shown in Figs. 6.32 can be found in Figs. 6.33. As expected, performance deteriorates as the standard deviation increases. None of the cases achieves cooling capacities higher than the original case, and the AMRs with more layers are less susceptible to uncertainties in the Curie temperatures.

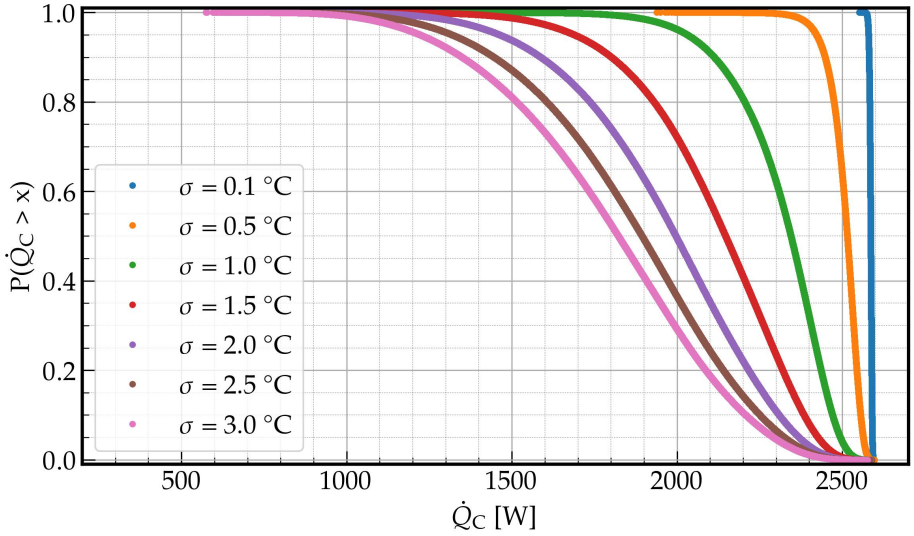
Despite that, the CCDF representation makes it easier to draw quantitative conclusions. For example, the inclinations indicate the rate at which a given cooling capacity is achieved under a given minimum threshold. By evaluating the figures, it becomes clear that as the standard deviation of the Curie temperature increases, the probability that the AMR achieves specific cooling capacities rapidly decreases.

For example, consider a magnetocaloric system being designed, with a 95% confidence level for the cooling capacity. For that case, Fig. 6.34 shows the cooling capacity which is attained for that degree of confidence as a function of the standard deviation of the system, the equivalent of drawing a horizontal line in Figs. 6.33 at the 0.95 value on the y-axis.

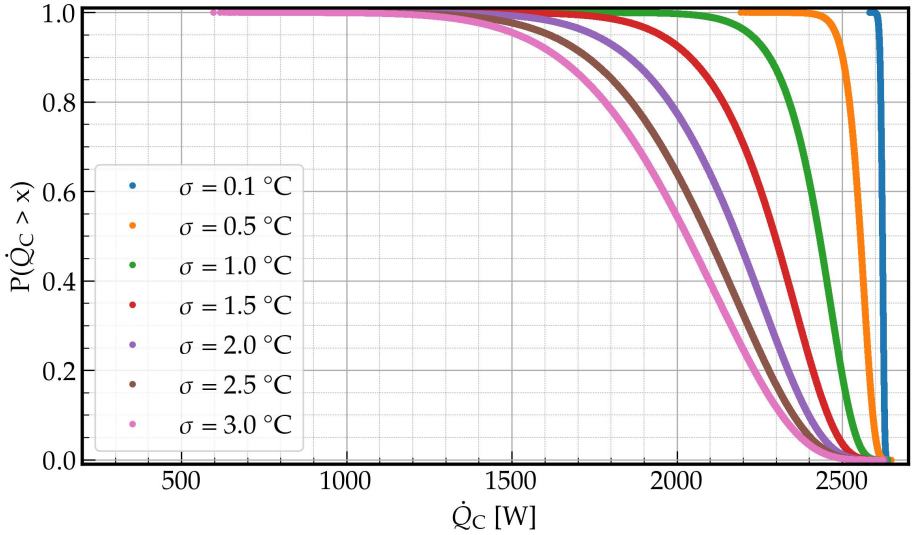
Once again, Fig. 6.34 shows that the detrimental effect increases as the standard deviation increases and the number of layers decreases. From a design perspective, the primary strategy is to oversize the magnetocaloric system to offset the reduction in cooling



(a)



(b)



(c)

Figure 6.33 – Cumulative Distribution Function for the AMR with (a) 5, (b) 10, and (c) 15 layers.

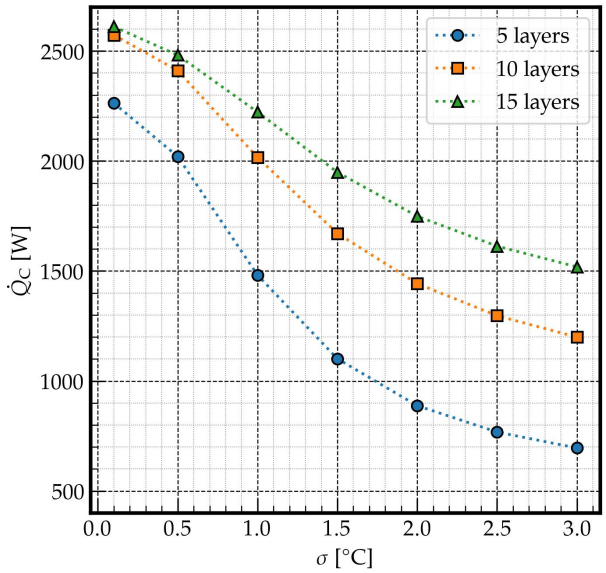


Figure 6.34 – Cooling capacity achieved with a 95% confidence for an AMR with 5, 10, and 15 layers.

capacity. Given current margins provided by MCM suppliers, that is, a standard deviation from 1.5-2°C, and a plausible number of AMR layers, which is considered between 10 and 15, the cooling capacity of the system should be designed to operate from 30% to 80% above its desired value. For a magnetic refrigeration system, this is usually done by increasing the magnetic circuit or the AMR, the two most expensive components of the system (Bjørk *et al.*, 2016). When commissioning a prototype, oversizing might not be a viable alternative for the design team to ensure the system operates under the desired conditions. In addition, from a system design standpoint, increasing the number of layers appears to be a viable alternative to reduce the effects of uncertainty in the Curie temperature. However, it should be noted that even though increasing the number of layers in an AMR is theoretically beneficial, in practical terms, other losses and complexities, such as the challenge of assembling homogeneous AMR beds and properly separating the layers, which are not considered in numerical analysis, must be taken into account by the design team.

Lastly, to evaluate the effect on the certainty of the desired threshold certainty, Figs. 6.35 show the achieved cooling capacities for the certainty of 90%, 95%, and 99% for the AMR composed of 5, 10, and 15 layers. As expected, the detrimental effect increases as the level of certainty required by the application increases.

In this study, two application scenarios are discussed. As a rule of thumb, it is expected that, for prototypes, a certainty of 90-95% is desired to guarantee a performance threshold without entailing an expensive, oversized system. In such scenarios, system designs with cooling capacities exceeding 80% of their target values can be achieved, depending on the uncertainty conditions.

Also, for large-scale production of magnetocaloric systems, thresholds of certainty above 99% are expected, as quality-control standards will require strict performance from

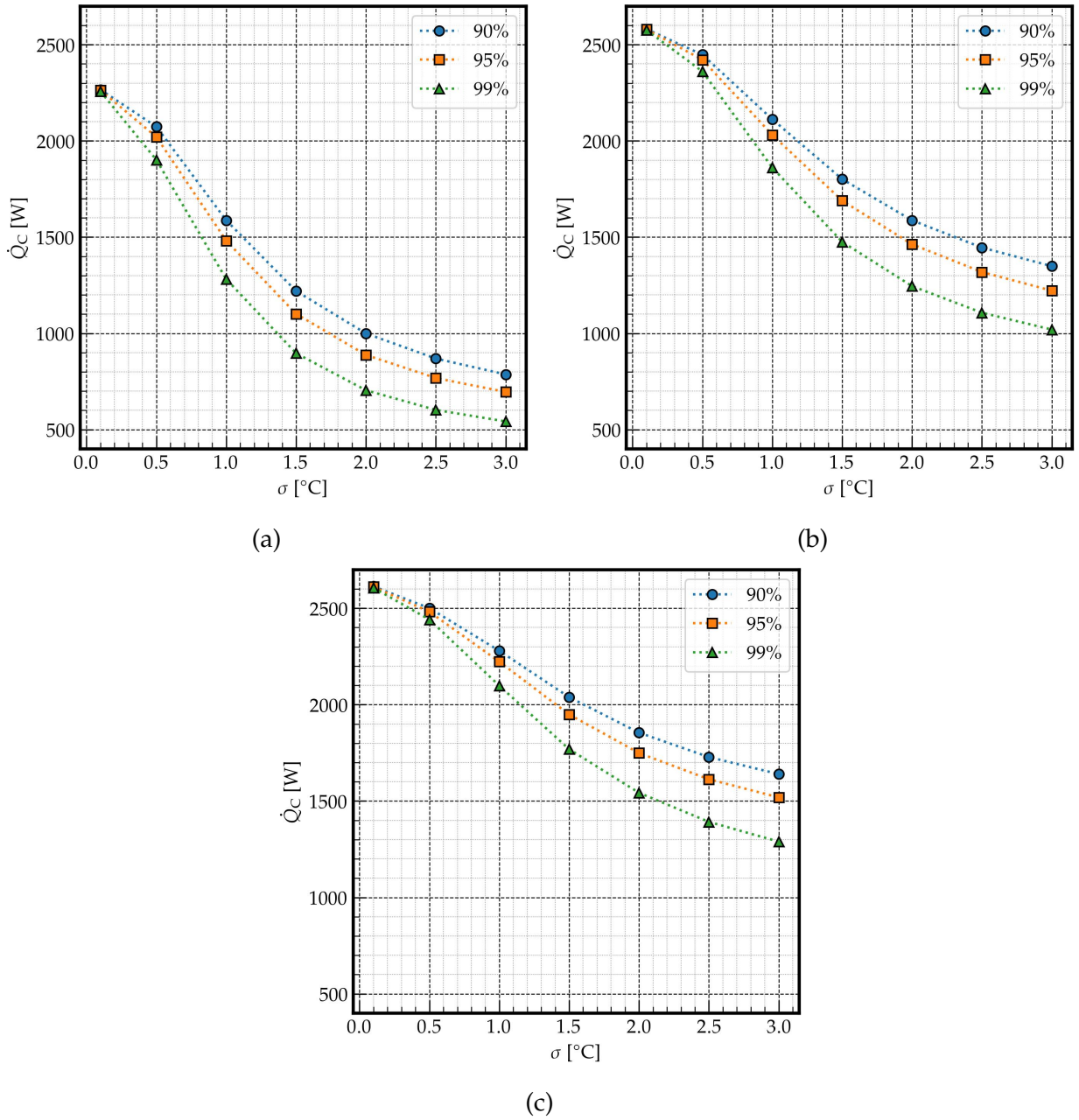


Figure 6.35 – Effect of the certainty level on the achieved performance of the AMR operating with (a) 5, (b) 10, and (c) 15 layers.

all commercialized systems. Oversizing the already expensive magnetocaloric refrigeration systems does not represent a viable alternative.

Hence, under the current levels of Curie temperature uncertainty, large-scale production of MCM-based AMRs would require significant oversizing or improved material consistency to ensure reliable performance. The ideal solution would be to reduce the uncertainty in the Curie temperature of the materials. For that, it is fundamental that the development of materials and manufacturing processes focus not only on the magnitude of the magnetocaloric effect but also on the result in functional materials to be applied in systems (Döring *et al.*, 2024b).

6.4 Outline of the Chapter

In this chapter, the application of artificial intelligence techniques to magnetic refrigeration is explored through both steady-state and dynamic modeling. The steady-state model was developed using a dataset collected from the most relevant MR prototypes reported in the literature. This model demonstrated excellent predictive performance and can be effectively used to design and optimize MR systems, enabling designers to evaluate system behavior without extensive experimental testing. However, a fundamental aspect of machine learning models is that their applicability is often limited to the type of data on which they were trained. For instance, the steady-state model, while accurate for design purposes, would not be adequate for tasks such as sensitivity analysis, highlighting a common shortcoming of ML strategies.

The chapter then presents the development of a dynamic model of the magnetic refrigeration unit. This model also achieved strong predictive performance and provides detailed insight into the transient response of MR systems under varying operational conditions. Beyond predictive accuracy, the dynamic model can be applied for model predictive control, allowing real-time optimization and control strategy development to improve system efficiency and reliability. Importantly, this demonstrates that more complex or purpose-specific models are often required to extend the applicability of AI techniques in MR.

Finally, an uncertainty analysis was carried out to assess the impact of variations in the Curie temperature on system performance. An AI-enhanced Monte Carlo approach highlighted that uncertainties in the Curie temperature pose a critical challenge for manufacturers, hindering consistent and efficient operation. This illustrates how AI-driven tools can support both performance evaluation and risk assessment, but also emphasizes that overcoming limitations in model generalization requires developing more sophisticated models and collecting new datasets tailored to specific applications.

Together, these AI-enhanced strategies have demonstrated their potential to advance the design, control, and reliability of magnetic refrigeration technologies. At the same time, they reveal the inherent challenges of ML approaches, particularly the need for purpose-specific datasets and model adaptations, which can be mitigated by developing more complex, flexible models capable of broader applications in MR research and engineering.

Chapter 7

APPLICATION OF ARTIFICIAL INTELLIGENCE IN ENGINEERING SYSTEMS

In the previous chapters, different ML models were applied to enhance the performance of the MRU. In this chapter, these techniques are extended to broader engineering applications. The emphasis is placed on problems within the energy transition and oil and gas domains. Machine learning is employed as surrogate modeling for optimization of Hydrogen liquefaction systems and for sensitivity and uncertainty analysis of thermostructural effects in oil and gas Wells, as previously demonstrated for the MR system. Additionally, ML-based strategies for anomaly detection in offshore oil wells are investigated.

7.1 Applications in Energy Transition

The global transition from fossil fuels to renewable energy has been a key focus of international climate agreements, including the 2005 Kyoto Protocol and the 2015 Paris Agreement, which aim to limit greenhouse gas emissions and the global temperature rise to 2°C (Peschka, 1992; Aziz, 2021; Lau *et al.*, 2012; Horowitz, 2016). Achieving a low-carbon energy system is essential for sustainable development (Katila *et al.*, 2019), yet it faces challenges in balancing supply and demand, particularly with respect to energy storage.

Hydrogen has emerged as a promising energy vector due to its unique properties (Aziz, 2021), with renewed political and economic interest driving technological advances that are expected to reduce production and storage costs by up to 30% by 2030 (IEA, 2019). International commitments, such as COP26, emphasize the goal of global low-carbon Hydrogen availability by 2030 (Arora & Mishra, 2021), highlighting its strategic role, especially for high-emission nations, while positioning Brazil to lead in green Hydrogen development. However, widespread Hydrogen adoption is constrained by high costs across its value chain, from primary resources and production to storage, transport, and use (Ghafri *et al.*, 2022), requiring further technological progress for complete industrial decarbonization (Korberg *et al.*, 2023). The high gravimetric energy density (118.8 MJ/kg) and low volumetric energy density (9.8 kJ/L) of Hydrogen (Juangsa *et al.*, 2018) present storage and transport challenges. Physical methods like liquefaction and ammonia storage are the most promising for large-scale applications (Moradi & Groth, 2019; Wijayanta *et al.*, 2019; Yang *et al.*, 2022). Current liquefaction technologies consume 11.9–15 kWh/kg-H_2, significantly above the theoretical minimum of 2.7 kWh/kg-H_2 at 25 bar (Wilhelmsen *et al.*, 2018), mainly due to the precooling

stage, which accounts for up to 70% of power consumption (Nandi & Sarangi, 1993). In this context, the following section presents an optimization of the precooling stage of Hydrogen liquefaction, following the strategy employed for the optimization of the MRU, *i.e.*, using an ANN as a surrogate model for an optimization carried out with genetic algorithms.

It is worth highlighting that the methodologies presented in Chapter 6 have also been employed in other decarbonization and energy transition applications, such as for the optimization of thermoelectric generators (Andrew *et al.*, 2024), materials discovery (Castro-Anaya *et al.*, 2025), Organic Rankine Cycles (Bordignon *et al.*, 2025) and hydrogen fuel cells; and also for the evaluation the effect of contaminants in the thermophysical properties of fluid mixtures for Carbon Capture, Utilization and Storage via ANN-powered Monte Carlo uncertainty analysis

7.1.1 Optimization of Hydrogen Liquefaction Systems

Among conventional Hydrogen liquefaction cycles, the Claude cycle stands out due to its higher efficiency (Aziz, 2021). In this cycle, Hydrogen is first compressed and passed through a sequence of heat exchangers. Expansion turbines are then integrated between specific heat-exchange stages: a fraction of the Hydrogen stream is expanded through these turbines, which not only cool the main stream but also recover useful work. In addition, the Claude cycle operates at lower pressures than the Linde cycle, reducing mechanical stress on system components (Nandi & Sarangi, 1993). For these reasons, all existing large-scale Hydrogen liquefaction plants are based on the precooled Claude cycle, which has undergone only incremental technological improvements over the last five decades (Krasae-In *et al.*, 2010). An illustrative schematic of the Claude process is presented in Fig. 7.1, highlighting the use of expansion turbines ($\dot{W}$) and the associated heat rejection ($\dot{Q}$).

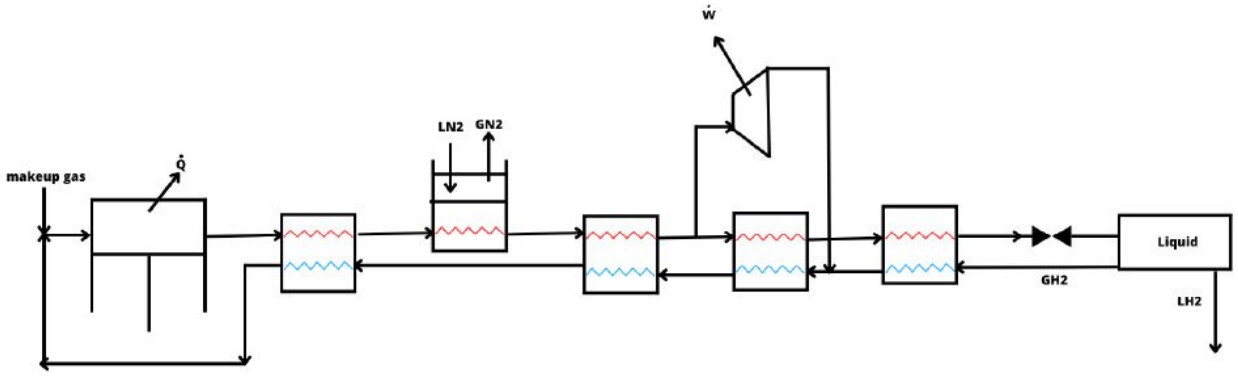


Figure 7.1 – Schematic representation of the Claude cycle. LN2 stands for liquid nitrogen, GN2 stands for gaseous nitrogen, LH2 stands for liquid Hydrogen, GH2 stands for gaseous Hydrogen, $\dot{Q}$ stands for the heat dissipated by the compressor, and $\dot{W}$ stands for the turbine power. Adapted from (Bordignon *et al.*, 2023).

Precooling is a fundamental stage in Hydrogen liquefaction. Although liquid nitrogen precooling has traditionally been the standard approach due to the low temperatures it can

achieve, the associated power consumption is significant, motivating research into alternative refrigerants and mixed-fluid cycles. In this study, the precooling subsystem is assumed to operate according to a simplified Linde cycle, in which no expansion turbines are used to generate work or cool the return stream. A schematic representation of this precooling configuration is shown in Fig. 7.2.

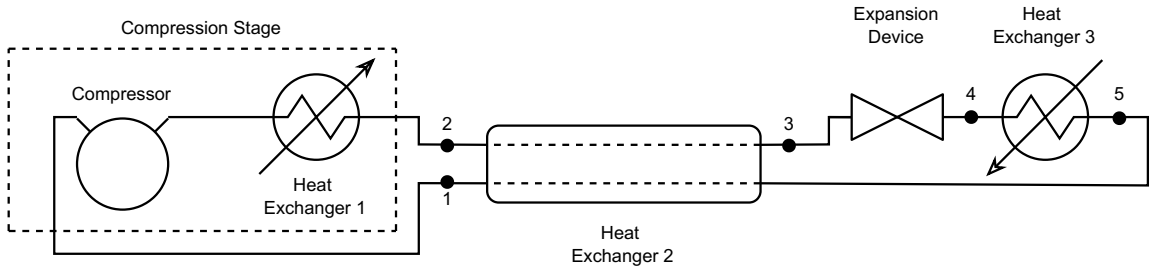


Figure 7.2 – Simplified schematic diagram of the precooling cycle.

The precooling cycle considered in this work comprises five main components. Although more advanced configurations employing additional equipment (such as expansion turbines) can achieve higher performance, a simplified architecture is adopted here to isolate the effects of fluid composition and operating conditions on system performance.

The compression stage consists of a compressor followed by Heat Exchanger 1, where the refrigerant is compressed and subsequently cooled, reducing overall energy consumption. Five compression stages are considered in this study, and an isentropic efficiency of 75% is assumed for the compressor. The inlet (state 1) and outlet (state 2) temperatures of each compression stage are fixed at 300 K. After compression, the working fluid passes through Heat Exchanger 2, where it is cooled by the low-pressure stream returning to the compressor (state 5). The stream then undergoes a Joule–Thomson expansion (state 3), resulting in an additional temperature drop (state 4). Finally, the fluid enters Heat Exchanger 3, where it precools the Hydrogen stream associated with the liquefaction cycle. The outlet state of Heat Exchanger 3 (state 5) is assumed to be saturated vapor.

7.1.1.1 Problem definition

The main parameters of interest in the precooling cycle are the power consumption by the five compressor stages, $\dot{W}_{\mathrm{comp}}$, the temperature after the Joule-Thomson expansion, T_{jt}, and the heat absorbed from the Hydrogen stream in heat exchanger 3, $\dot{Q}$. From the point of view of the Hydrogen liquefaction system, the precooling system should achieve the lowest possible temperature after the Joule-Thomson expansion, consume the lowest possible power, and maximize heat absorption. Since the precooling cycle is being optimized independently of the liquefaction cycle itself, the values of the heat absorption $\dot{Q}$ cannot be determined, as they will be a consequence of the overall performance of the Hydrogen liquefaction system.

To overcome that, the power consumption by the precooling stage is approximated by the following expression:

$$\dot{W}_{\text{comp}} = \dot{m}_{\text{f}}\left(h_2 - h_1\right) = \dot{Q}\frac{(h_2 - h_1)}{(h_5 - h_4)} = \dot{Q}\left(\frac{w}{q}\right) = \dot{Q}\left(\frac{1}{COP}\right) \tag{7.1}$$

where $\dot{m}_{\text{f}}$ represents the mass flow rate required for the system to operate to absorb heat at a rate $\dot{Q}$ from the Hydrogen stream, and h represents the enthalpy of the mixture along the stream. Hence, to minimize the power consumption and partially account for mass flow rate variations, the optimization routine seeks to maximize its coefficient of performance (COP). Hence, the problem consists in developing mapping functions for the temperature after the Joule-Thompson expansion, and COP, which is done by separate functions for the specific power,w, and specific heat absorption q, given by:

$$T_{\text{jt}} = \mathcal{F}_1(x) \tag{7.2}$$

$$w = \mathcal{F}_2(x) \tag{7.3}$$

$$q = \mathcal{F}_3(x) \tag{7.4}$$

according to the framework given by Eq. (2.8).

7.1.1.2 Data Collection and Preprocessing

To train the ML models, simulations of the precooling system were run in Aspen Hysys. A total of 11056 cases were simulated, with the input parameter values adjusted to meet the constraints of the optimization problem. The design parameters considered are the fluid composition (X) and the precooling cycle operating pressure (p_{pc}). For the composition of the mixture, five elements are considered methane (CH_4), ethane (C_2H_6), propane (C_3H_8), carbon dioxide (CO_2), and nitrogen (N_2) according to work previously developed in the literature (Chen *et al.*, 2024; Tamarona *et al.*, 2024). The operating pressure range is 20-500 bar, and the maximum allowed temperature after the Joule-Thomson expansion is 200 K.

Hence, Eqs. (7.2) - (7.4), can be updated as:

$$T_{\text{jt}} = \mathcal{F}_1(X_{\text{CH4}}, X_{\text{C2H6}}, X_{\text{C3H8}}, X_{\text{CO2}}, X_{\text{N2}}, p_{\text{pc}}) \tag{7.5}$$

$$w = \mathcal{F}_2(X_{\text{CH4}}, X_{\text{C2H6}}, X_{\text{C3H8}}, X_{\text{CO2}}, X_{\text{N2}}, p_{\text{pc}}) \tag{7.6}$$

$$q = \mathcal{F}_3(X_{\text{CH4}}, X_{\text{C2H6}}, X_{\text{C3H8}}, X_{\text{CO2}}, X_{\text{N2}}, p_{\text{pc}}) \tag{7.7}$$

7.1.1.3 Model Selection. Training and Optimization

ANNs were used to model the system and implemented in TensorFlow (Developers, 2022). The architecture consisted of two hidden layers with 250 and 25 neurons, respectively,

and the Scaled Exponential Linear Unit (SELU) activation function was applied in all layers. To mitigate overfitting, L2 regularization was applied throughout the network with a coefficient of 10^{-6} (Cortes *et al.*, 2012), and early stopping was adopted with the validation loss as the stopping criterion (Prechelt, 2002). The network was trained with the Adam optimizer (Kingma, 2014), and the mean squared error was used as the loss function. Hyperparameter optimization was performed manually through iterative adjustments to network size and training settings.

7.1.1.4 Model Evaluation

The comparison between the numerical reference values and the ANN predictions for the three key performance indicators is shown in Fig. 7.3. Additionally, Table 7.1 summarizes the values of R^2 and the MSE obtained for all three models.

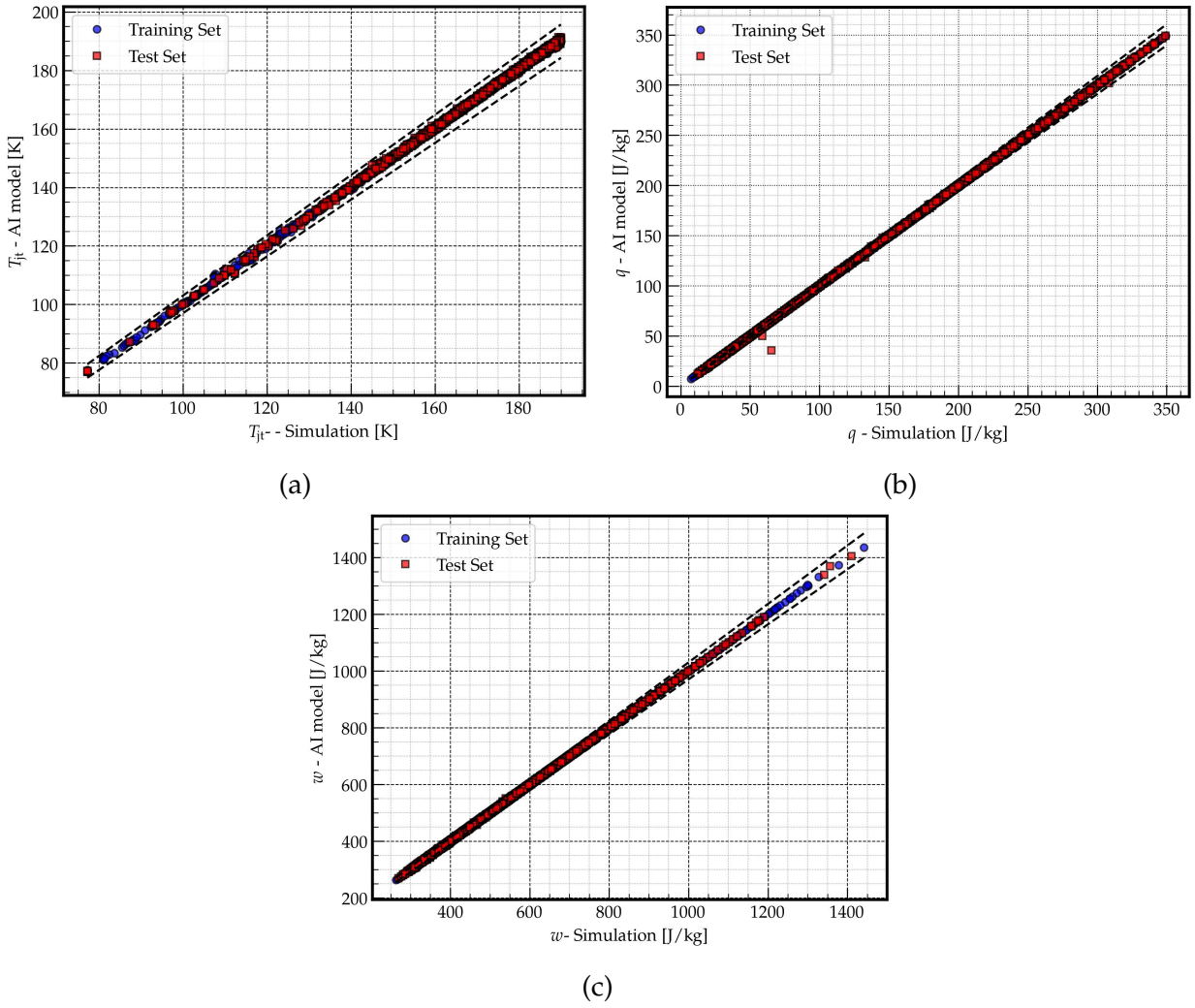


Figure 7.3 – Comparison between the numerical and ANN prediction for (a) temperature after the Joule-Thomson expansion, (b) specific heat absorption, (c) specific power.

The results demonstrate that all models achieved excellent predictive capabilities, with R^2 values effectively equal to 1.0 for the specific power, specific heat absorption, and temperature after the Joule-Thomson expansion. The absolute value of the MSE remains

Table 7.1 – R^2 and MSE of the test set for each variable.

Variable	R^2	**MSE**
T_{jt}	0.9984	0.3414
w	0.9999	0.8497
q	0.9999	0.5595

small, confirming that the ANN accurately captures the underlying nonlinear relationships of the process. From a practical standpoint, the ANN models reduced prediction time from several seconds (for a single thermodynamic evaluation using the numerical process model) to a few microseconds while maintaining high accuracy. This speed-up enables the direct embedding of the surrogate models into the multi-objective optimization routine.

7.1.1.5 Model Application

Once the surrogate models were validated, they were embedded into a multi-objective optimization framework to identify optimal fluid compositions and operating conditions for the precooling stage of hydrogen liquefaction. As previously determined, the goal was to maximize system performance (by increasing COP) and to enable lower expansion temperatures. These two objectives are inherently conflicting and cannot be optimized simultaneously. Hence, a Multi-Objective Optimization formulation was adopted. The optimization problem can be formally written as:

$$P = \begin{cases} \text{minimize} & [-\frac{q(\mathbf{x})}{w(\mathbf{x})}, T_{\mathrm{jt}}(\mathbf{x})] \\ \text{subject to} & \sum_{i=0}^{4} x_i - 1 = 0 \\ & T_{\mathrm{jt}}(\mathbf{x}) - 200 = 0 \end{cases} \tag{7.8}$$

where $\mathbf{x}$ represents the design parameters of the problem and is defined as:

$$\mathbf{x} = [X_{\mathrm{CH4}}, X_{\mathrm{C2H6}}, X_{\mathrm{C3H8}}, X_{\mathrm{CO2}}, X_{\mathrm{N2}}, p_{\mathrm{pc}}] \tag{7.9}$$

The problem was solved using the NSGA-II algorithm (Deb *et al.*, 2002), implemented through the *pymoo* Python package (Blank & Deb, 2020). The initial population contained 250 individuals, and 2000 new individuals were generated per generation. The crossover and mutation probabilities were set to 0.90 and 0.20, respectively. Convergence was defined as a variation below 0.01 in the objective function over 500 generations.

The resulting Pareto front is shown in Fig. 7.4. As expected, there is a clear trade-off between achieving a lower temperature after the Joule-Thomson expansion and improving COP. Mixtures that reach the lowest temperatures require substantially higher power consumption, thereby directly reducing COP. Conversely, mixtures that provide higher COP tend to operate at higher temperatures after expansion. From a system perspective, this trade-off is fundamental because precooling power accounts for a large share of total liquefaction

energy consumption. Nevertheless, the Pareto solutions presented here constitute the best achievable combinations of mixture composition and operating pressure for the assumed cycle configuration. Importantly, these results show that the COP obtained with optimized mixtures can significantly exceed that of pure nitrogen precooling (approximately 0.05), highlighting the potential for substantial efficiency gains in industrial liquefaction systems.

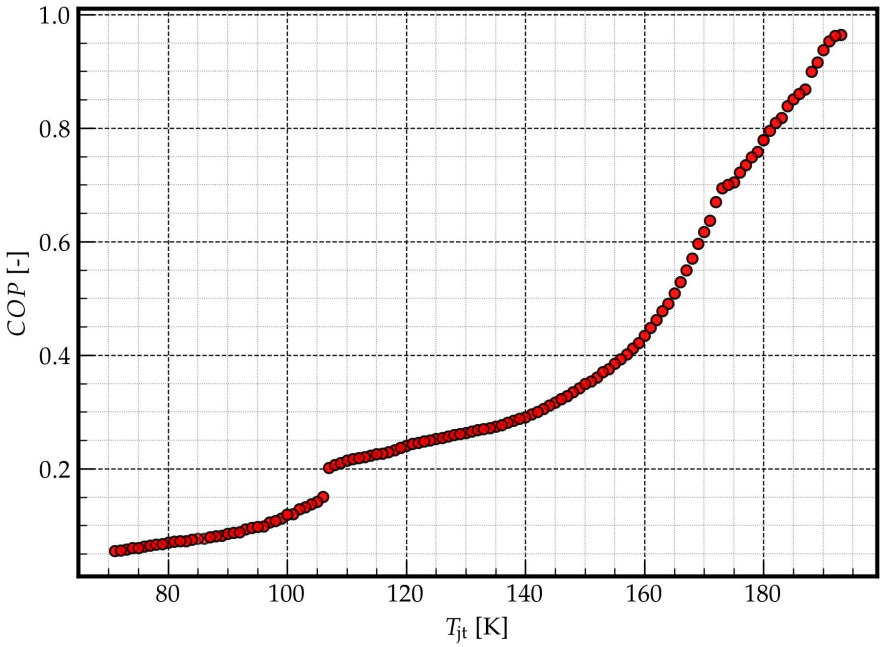


Figure 7.4 – Pareto front of the optimization problem.

To gain further insight into these results, Fig. 7.5 presents the composition of each mixture along the Pareto front. The results show a strong temperature-dependent trend: mixtures with lower temperatures tend to be dominated by nitrogen, whose low boiling point enables deeper precooling. As higher temperatures are allowed, the contribution of other species increases, particularly those with higher boiling points. This behavior is consistent with physical expectations: the mixture composition shifts to match the optimal boiling-line "shape" to the required temperature glide across the heat exchangers.

Finally, Fig. 7.6 shows the optimal high-side pressure for each solution on the Pareto front. In general, operating pressure decreases as temperature increases after the Joule-Thomson expansion (and, equivalently, as COP increases). This trend is primarily driven by the strong influence of pressure on compressor power consumption; however, the relationship is nonlinear due to the dependence of mixture thermodynamic properties on composition. This reinforces that process performance emerges from the coupled interaction between fluid formulation and operating conditions, and cannot be reliably optimized using physical intuition alone, further motivating the role of surrogate models and data-driven optimization.

The results demonstrate that surrogate models based on ANNs can be effectively integrated with multi-objective evolutionary optimization to explore and improve the perfor-

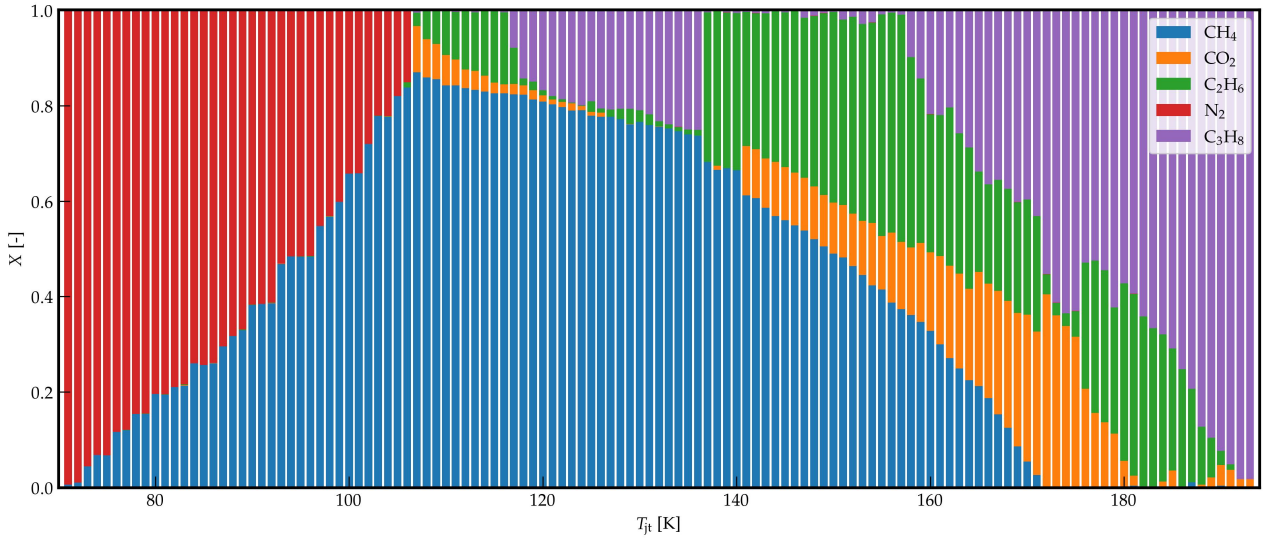


Figure 7.5 – Composition of each one of the mixtures that make up the Pareto front.

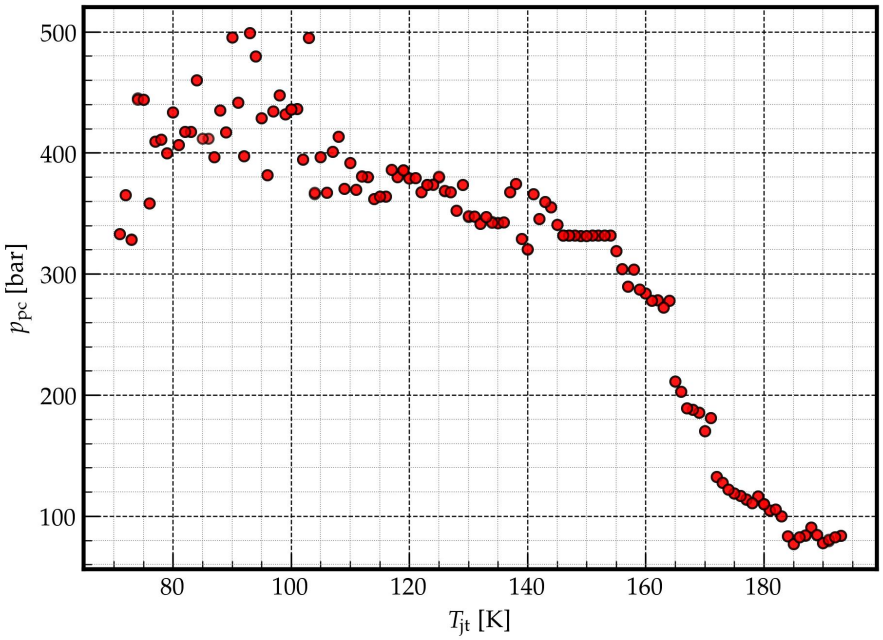


Figure 7.6 – Pressure of each one of the precooling systems that make up the Pareto front.

mance of hydrogen liquefaction precooling cycles. The data-driven approach enabled the identification of fluid mixtures and operating pressures that outperform conventional pure-nitrogen precooling, revealing tangible opportunities for efficiency gains. More importantly, the methodology provides a scalable framework: as additional fluids, architectures, or constraints are considered, the optimization can be rapidly repeated at negligible computational cost. This highlights the role of AI as an enabling technology for next-generation hydrogen infrastructure, where rapid design space exploration and system-level co-optimization are essential to accelerate progress toward cost-effective, low-carbon liquefaction solutions. As a recommendation for future work, it is suggested to evaluate more advanced cycle architectures, such as the Claude cycle, and couple the precooling stage with a model for an actual liquefaction cycle.

7.1.2 Uncertainty Analysis for Carbon Capture, Storage and Utilization Applications

Carbon Capture, Utilization and Storage (CCUS) has emerged as one of the most relevant technological pathways to achieve deep decarbonization across energy-intensive industries (IEA, 2020). While renewable energy penetration is steadily increasing, hard-to-abate sectors, such as cement, steel, refining, and petrochemicals continue to rely on fossil fuels. For these industries, CCUS represents one of the few viable near-term solutions to reduce large, concentrated sources of CO_2 emissions and meet the mitigation targets established by the Paris Agreement (Bui *et al.*, 2018). As highlighted by the International Energy Agency, achieving net-zero by mid-century requires capturing and storing more than 1.6 $GtCO_2$ annually by 2030, followed by rapid scale-up through 2050 (IEA, 2021).

A major challenge in CCUS deployment, however, lies in ensuring the safe, reliable, and economically feasible transport and storage of captured CO_2. After capture, CO_2 is typically conditioned, compressed, and transported through pipelines to geological formations, often deep saline aquifers or depleted oil and gas reservoirs, where it is injected for long-term sequestration (Bui *et al.*, 2018). Throughout this chain, the presence of contaminants such as N_2, CH_4, and CO can significantly affect thermophysical properties, corrosion rates, phase behavior, and operational safety margins (Wetenhall *et al.*, 2014; Li *et al.*, 2015). Even relatively small impurities can shift the phase envelope of CO_2-rich mixtures, change the cricondenbar and cricondentherm, modify pipeline pressure-drop characteristics, and increase the risk of two-phase flow, hydrate formation, or localized corrosion (Wang *et al.*, 2011; Peletiri *et al.*, 2017).

Accurately predicting these effects requires detailed thermodynamic modeling and high-fidelity equations of state, which are computationally expensive when explored across wide ranges of mixture compositions and operating conditions. This becomes particularly challenging in scenarios involving uncertainty quantification, sensitivity studies, or the analysis of extreme impurity levels, tasks that may require evaluating millions of thermodynamic states, and therefore benefit from surrogate models with fast evaluation speed. Moreover, as CCUS infrastructure scales up, real-time monitoring and anomaly detection in CO_2 transportation networks will become increasingly important to ensure safety and early detection of leaks or abnormal behaviors.

In this context, the same AI methodologies applied to the Magnetic Refrigeration Unit are highly relevant for CCUS. Machine learning surrogate models can replace computationally intensive thermodynamic evaluations, enabling fast prediction of mixture properties. Likewise, Monte Carlo–based uncertainty analysis, powered by ANNs, can be used to assess how measurement errors, contaminant variability, or sensor noise propagate through CCUS systems. This section therefore extends the AI-based framework to problems in CO_2 transport

and sequestration, focusing on the influence of contaminants on thermophysical properties, phase stability, and pipeline operating envelopes. The goal is to show how surrogate modeling and uncertainty quantification enable safer and more efficient CCUS operations, supporting the design and deployment of large-scale decarbonization infrastructure.

7.1.2.1 Problem Definition

In this study, the property of interest is the cricondenbar, p_{cri}, the maximum pressure at which liquid and vapor phases can coexist. This parameter is fundamental for the safe and efficient design of CO_2 transport pipelines, as it determines the upper pressure limit of the two–phase envelope and directly influences operating constraints. Although the methodology is developed here for the cricondenbar, the same framework can be extended to any other thermophysical property of interest, such as density, speed of sound, enthalpy, or phase boundary temperatures. Hence, the mapping function according to Eq. (2.8), is given by:

$$p_{\text{cri}} = \mathcal{F}(x) \tag{7.10}$$

7.1.2.2 Data Collection and Preprocessing

Defining the design space requires specifying the allowable concentration ranges of the major contaminants present in CO_2 streams. For CCUS pipeline operation, these ranges must be broad enough to encompass expected field conditions, including variability in capture technologies, upstream processing steps, and supplier specifications for CO_2 purity. Likewise, the contaminant limits must reflect realistic operational constraints, typically imposed by corrosion considerations, process equipment compatibility, and commercially feasible mixture preparation. The contaminants evaluated and their concentration ranges adopted in this study are listed in Table 7.2. These values reflect typical allowable levels for CO_2 streams intended for transport and storage, considering both industrial practice and published guidelines.

Table 7.2 – Admissible concentration range for the components of the mixtures.

Component	Concentration (mol)
CO_2	$\geq 96,0\%$
H_2	$\leq 0{,}75\%$
N_2	$\leq 4,0\%$
Ar	$\leq 4,0\%$
CH_4	$\leq 4,0\%$
CO	$\leq 0{,}1\%$
C_2H_6	$\leq 4,0\%$

By establishing this design space, the subsequent steps consist in generating thermodynamic data through numerical simulations and developing a mapping function:

$$p_{\text{cri}} = \mathcal{F}(X_{\text{CO}_2}, X_{\text{H}_2}, X_{\text{N}_2}, X_{\text{Ar}}, X_{\text{CH}_4}, X_{\text{CO}}, X_{\text{C}_2\text{H}_6}) \tag{7.11}$$

To construct the model for predicting the cricondenbar of CO_2-rich mixtures, a dataset was generated with a total of 946 790 simulation runs were performed using the E-PPR78 Equation of State (Xu *et al.*, 2017). Each simulation corresponded to a combination of mixture composition, sampled across the design space defined in Table 7.2.

7.1.2.3 Model Selection, Training and Optimization

In this task, an ANN was adopted to model the influence of mixture composition on the cricondenbar. After preliminary tests with different model sizes, a network with five hidden layers containing 1024, 512, 256, 128, and 16 neurons, respectively, was selected as the chosen configuration. All hidden layers used the GELU activation function, To ensure robust training, all weights were initialized using the He-normal initializer. To improve generalization and prevent overfitting, several complementary training strategies were applied. L2-regularization (with a coefficient of 10^{-5}) was incorporated into all dense layers. Early stopping was implemented with a patience of 80 epochs and the model weights were restored to the best-performing checkpoint. In addition, a polynomial learning-rate decay schedule was employed to ensure stable optimization.

The model was trained using the Adam optimizer, with MSE as the loss function. The training procedure used a mini-batch size of 512. The dataset, composed of the 946 790 E-PPR78 simulations, was randomly partitioned into training (64%), validation (16%), and testing (20%) sets. Training was performed for a maximum of 700 epochs, although convergence was typically achieved earlier due to the learning-rate scheduling and early-stopping mechanisms.

7.1.2.4 Model Evaluation

Figure 7.7 presents a parity plot comparing the cricondenbar values predicted by the ANN with the reference values calculated using the E-PPR78 Equation of State. The model shows excellent agreement across the entire range of pressures, with both the training and test datasets tightly clustered around the 1:1 line. Most points fall well within the ±1% deviation band, illustrated by the dashed lines, indicating strong consistency and minimal systematic bias. Only a small number of samples show deviations slightly above this tolerance, which is expected given the sharp nonlinearity of the phase boundary near critical regions. The coefficient of determination obtained for the test set is 0.993, confirming that the ANN successfully captures the dominant thermodynamic trends governing the cricondenbar.

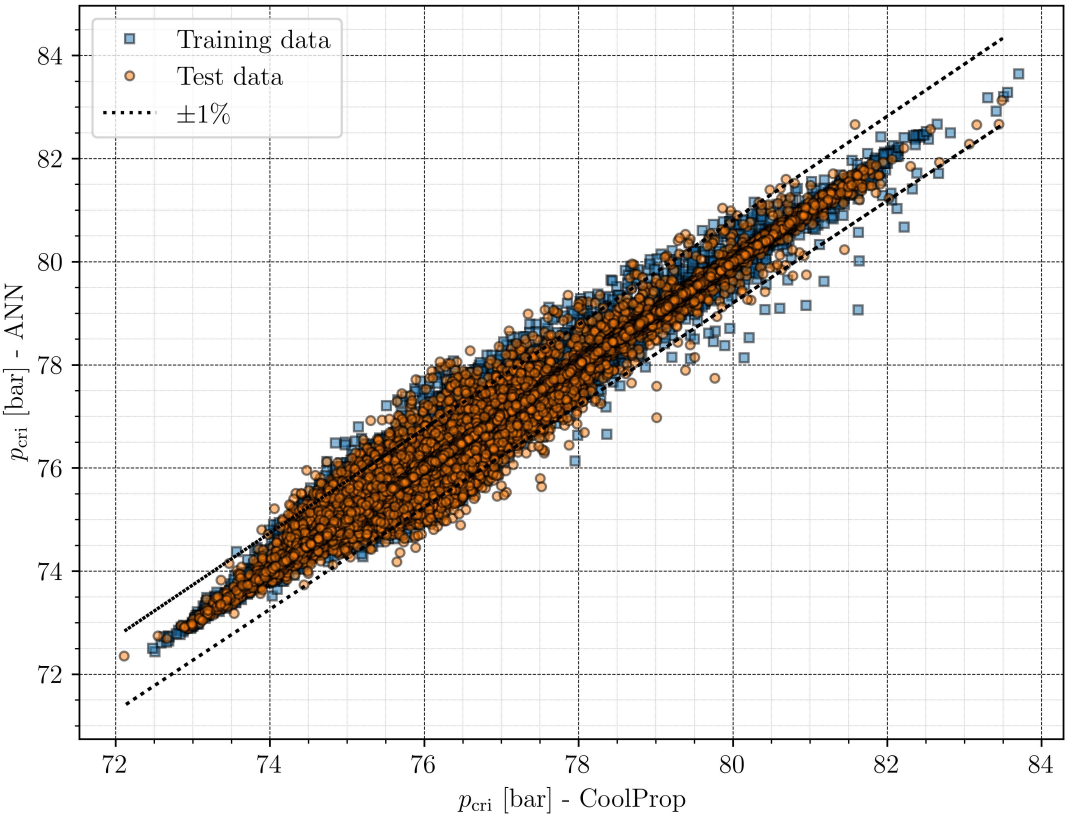


Figure 7.7 – Comparison between the predictions of the ANN and the simulations with the E-PPR78.

From a practical standpoint, the surrogate model reproduces with high fidelity the results of the high-fidelity E-PPR78 calculations while enabling fast evaluations, making it suitable for large-scale uncertainty analysis and Monte Carlo sampling required in CCUS system design. An additional advantage of the ANN surrogate is that it predicts the cricondenbar directly as a single forward evaluation. In contrast, the E-PPR78 model requires solving a full vapor–liquid equilibrium calculation and subsequently identifying the maximum coexistence pressure, a procedure that is computationally intensive and significantly slower. This direct-prediction capability, combined with fast evaluation times, makes the ANN particularly suitable for large-scale uncertainty quantification, Monte Carlo simulations, and rapid parametric exploration in CCUS system design.

7.1.2.5 Model Application

A Monte Carlo–based uncertainty analysis was conducted to quantify how variations in mixture composition propagate through the surrogate model and influence the predicted cricondenbar. For each uncertain parameter, the sampling strategy was selected to reflect both the physical constraints of CCUS mixtures and the typical variability expected during pipeline operation. When assessing the influence of individual contaminants, each component was sampled from a uniform distribution bounded by its admissible concentration range (Table 7.2). Because these limits arise from industrial specifications rather than statistical

estimates, uniform sampling is the appropriate choice, ensuring equal probability across the entire permitted interval of each impurity.

In contrast, for the global analysis, in which all mixture components were perturbed concurrently, a more advanced sampling methodology was required. A hybrid algorithm was therefore developed to ensure that the Monte Carlo set contained not only random feasible mixtures, but also representative extreme cases that capture the full complexity of multicomponent phase behavior. The hybrid sampler consists of two parts. First, a unified mixture generator produced compositions consistent with those expected in transportation scenarios and spans binary, ternary, quaternary, quinary, and senary mixtures with physically meaningful correlations between impurity levels. Also, the explicit extreme-impurity cases, in which each contaminant is assigned its maximum allowed fraction, ensuring that the Monte Carlo distribution includes the limiting operational scenarios that strongly influence the phase envelope. This hybrid strategy guarantees that the sampling space is both realistic and sufficiently broad to capture the worst-case thermodynamic interactions between CO_2 and its impurities.

For the individual scenario 100,000 cases were generated, wheres for the global scenario 10,000,000 ANN evaluations were performed. Figure 7.8 shows the distribution of the resulting cricondenbar values for uncertainties applied individually to each contaminant and for the full-mixture case. The violin plots illustrate the probability density under each perturbation scenario.

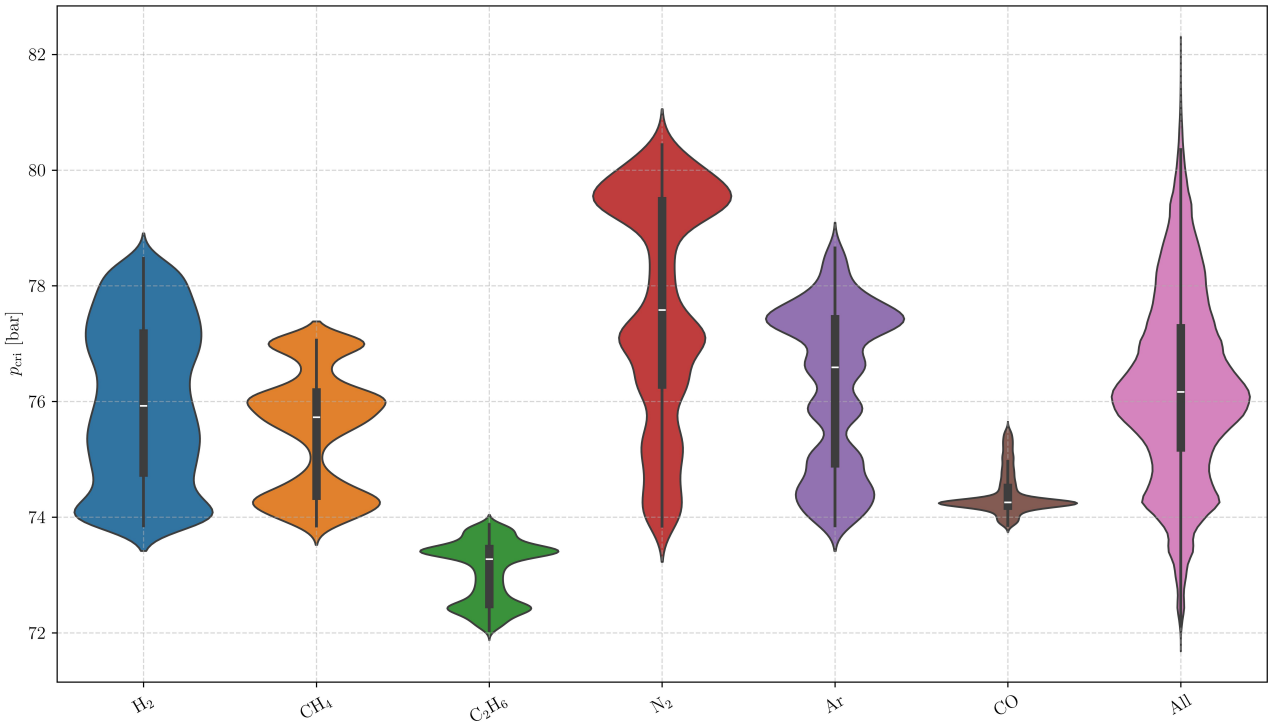


Figure 7.8 – Effect of the contaminants on the cricondenbar.

Nitrogen exhibits the largest spread, followed by Argon, Hydrogen and Methane. In

contrast, Ethane and Carbon Monoxide produce significantly narrower distributions, indicating weaker sensitivity within their admissible ranges. Especially in the case of hydrogen, even small quantities are usually associated with considerable influences on the thermophysical properties of CO_2-rich mixtures (Luna-Ortiz *et al.*, 2021).

The "All" case, which reflects simultaneous uncertainty in all impurities using the hybrid sampling scheme, displays the widest distribution. This is expected: when multiple impurities vary together, the nonlinear interactions between binary and higher-order mixture effects broaden the possible values of the cricondenbar. Importantly, the shape of this distribution confirms that the hybrid sampling successfully captures both typical operating conditions and rare but operationally relevant extreme compositions. Overall, the Monte Carlo results show that, within the expected uncertainty ranges of CO_2 stream compositions, the corresponding variation in cricondenbar remains statistically well-behaved. The ANN surrogate enables these large-scale uncertainty quantification to be executed efficiently, making it a practical tool for assessing safety margins and operating envelopes in CCUS pipeline design.

In addition, the fast-computing function given by Eq. (7.11), can also be employed to determined the composition of critical mixtures, *i.e.*, the ones that result in the largest variation of cricondenbar. To solve the following optimization problem is proposed. Given a fixed CO_2 fraction c, the goal is to determine the composition $x = (c, X_{\mathrm{H_2}}, X_{\mathrm{N_2}}, X_{\mathrm{Ar}}, X_{\mathrm{CH_4}}, X_{\mathrm{CO}}, X_{\mathrm{C_2H_6}})$ that maximizes the absolute change in cricondenbar:

$$\begin{aligned} \max_{\mathbf{x}} \quad & |p_{\mathrm{cri}}(\mathbf{x})| \\ \text{subject to} \quad & \sum_{i=1}^{6} x_i = 1 - c, \\ & 0 \le x_i \le \max_i \quad \forall i = 1, \ldots, 6 \end{aligned} \tag{7.12}$$

where $\max_i$ denotes the maximum allowable fraction for each contaminant based on the operational specifications.

Equation (7.12) is solved using a genetic algorithm, following the same strategy adopted in the previous optimization tasks. This approach is particularly suitable because of the nonlinear nature of the objective function, as well as the relatively small computational cost of evaluating p_{cri}. The resulting compositions are presented in Fig 7.9.

The trends in Fig. 7.9 reveal clear patterns in how each contaminant contributes to the maximization of the cricondenbar. Nitrogen consistently appears as the dominant component in the optimal mixtures, which is expected since it strongly increases the cricondenbar of the mixtures. Hydrogen also remains close to its allowable upper bound for most CO_2 purities. Despite its low critical temperature, has a very high critical pressure, making it particularly effective at shifting the phase boundary of the mixture. The lighter hydrocarbons, such as CH_4 and C_2H_6, together with Ar and CO, play a secondary but still relevant role.

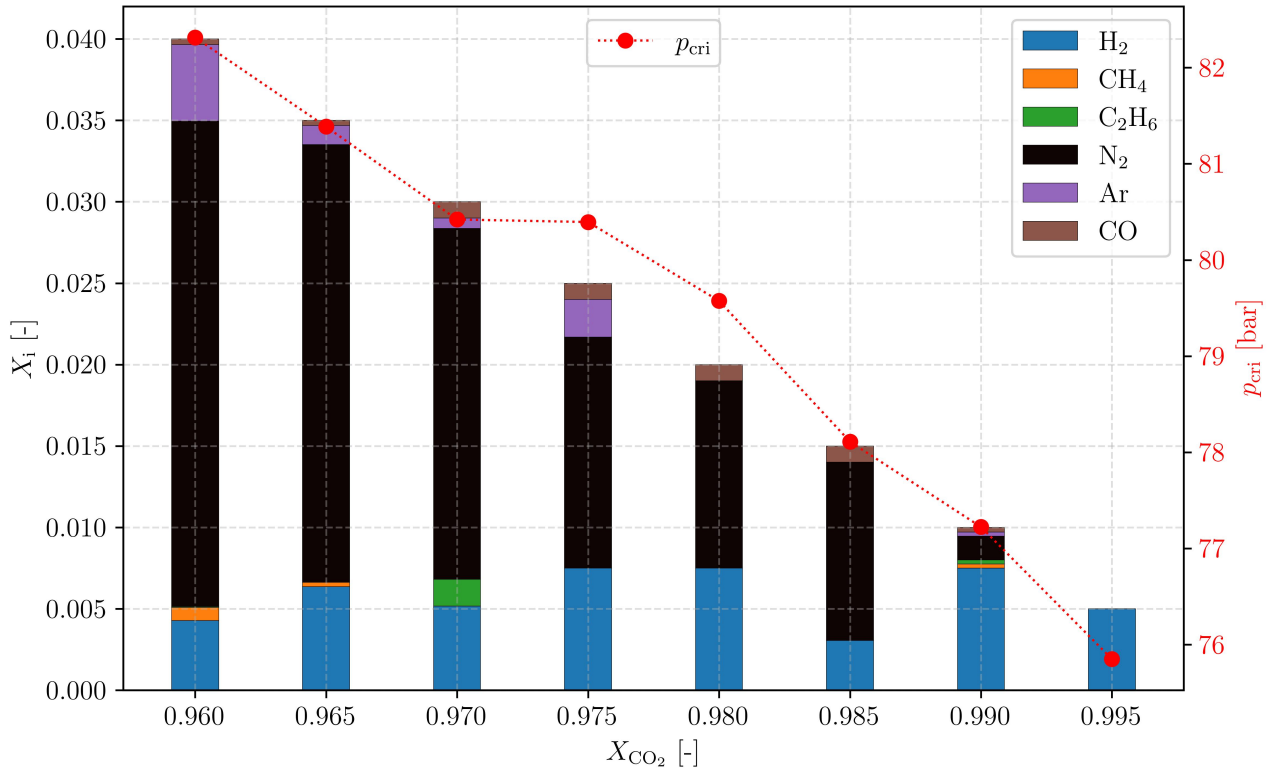


Figure 7.9 – Compositions that result in the largest cricondenbar.

Their contribution becomes more noticeable at intermediate CO_2 fractions, where different contaminants can combine nonlinearly to produce stronger deviations in the cricondenbar. As the CO_2 fraction approaches unity, the total contaminant content becomes very small, and the optimization naturally favors the species that exert the strongest influence, primarily H_2 and N_2.

The results demonstrate that ANNs can be successfully integrated with high-fidelity thermodynamic simulators to provide fast and accurate predictions of key phase-equilibrium properties in CCUS applications. By replacing the computationally intensive VLE calculations required by the E-PPR78 Equation of State, the surrogate model enables large-scale uncertainty quantification and efficient exploration of multicomponent composition effects—capabilities that are essential for designing safe and robust CO_2 transport systems. The direct prediction of the cricondenbar, combined with microsecond evaluation times, highlights the suitability of ANNs as enabling tools for next-generation CCUS process evaluation.

As a recommendation for future work, it would be valuable to extend the analysis to additional high-accuracy equations of state, particularly GERG-2008 (Kunz & Wagner, 2012) and the more recent CG-2021 (Neumann *et al.*, 2023), both of which offer improved representations of multicomponent CO_2 mixtures and may further refine predictions for critical envelope properties.

7.2 Application in Oil and Gas Systems

Petroleum remains a cornerstone of modern society, supporting global economic activity, industrial production, and critical infrastructure in transportation, manufacturing, power generation, and petrochemical supply chains (Shi *et al.*, 2021; Elanchezhiyan *et al.*, 2016; Florescu *et al.*, 2019). Even under aggressive decarbonization scenarios, oil demand is projected to remain significant in the medium- to long-term, driven mainly by hard-to-electrify sectors such as aviation, maritime transport, long-haul freight, and chemical feedstock production (IEA, 2024). For this reason, the energy transition is expected to occur not through the abrupt elimination of fossil fuels but through a progressive reduction of their carbon intensity. Accordingly, both academia and industry must continue to develop technologies that minimize the environmental footprint of oil production, processing, and consumption (Liu *et al.*, 2020; IEA, 2023). Improving safety and operational efficiency is a key part of this effort, as undesirable events (such as well blowouts, equipment degradation, pipeline failures, and fugitive emissions) can lead to catastrophic safety consequences, severe environmental damage, and significant economic losses (Chang *et al.*, 2014; Mahmood *et al.*, 2023). Detecting such events before they propagate is therefore essential for the sustainable, responsible, and economically viable operation of mature and emerging oil assets.

In this context, data-driven anomaly detection and prevention become a critical enabling capability. Modern offshore and onshore production systems generate large volumes of high-frequency operational data that AI models can use to identify abnormal behavior early, enabling corrective actions before failures escalate into major incidents. In this section, the previously developed uncertainty analysis framework for the MR system is adapted to assess the influence of design parameters on the thermo-structural behavior of petroleum wells. This analysis is further complemented by a sensitivity study using an ANN-based Sobol method. Subsequently, the scope of ML is expanded to identify anomalies in well operational data, demonstrating the potential of AI-driven approaches for improved integrity management in Oil and Gas systems. It is also worth noting that, beyond the examples presented here, the techniques developed in this thesis have already been applied in other domains of the oil industry, including the optimization of drilling operations.

7.2.1 Sensitivity and Uncertainty Analysis of Thermostructural Phenomena in Oil Wells

Among the many anomalies encountered in well integrity management, Annular Pressure Buildup (APB) is among the most relevant thermomechanical risks. APB arises from temperature-induced expansion or contraction of trapped annular fluids, which can generate pressure levels that exceed design limits and lead to casing deformation, loss of zonal isolation, environmental contamination, and significant economic losses (Bellarby,

2009; Dong & Chen, 2017; Zhang *et al.*, 2019; Junior *et al.*, 2019). Traditional thermostructural models have contributed valuable insights to the understanding of APB; however, these approaches typically rely on deterministic inputs and therefore neglect the inherent uncertainties associated with subsurface formations, fluid properties, and operational boundary conditions (RAMEY Jr, 1962; Ferreira *et al.*, 2017; Veiga *et al.*, 2022; Martins *et al.*, 2022). Recent studies have highlighted the importance of incorporating uncertainty quantification and sensitivity analysis. Still, critical parameters such as wellhead boundary conditions, fluid thermophysical properties, and well geometry remain insufficiently addressed (Pai *et al.*, 2020; Alves *et al.*, 2022; Filho *et al.*, 2024). In addition, high-fidelity simulations required for Monte Carlo-based uncertainty propagation or global sensitivity studies are computationally expensive (Sudret *et al.*, 2017).

To overcome these limitations, this section applies the ANN-powered Monte Carlo framework, previously developed for the magnetic refrigeration analysis, to quantify the impact of uncertainties in key input parameters on thermostructural phenomena in oil wells, with a particular focus on APB.

7.2.1.1 Problem definition

APB is fundamentally a thermomechanical response problem. For a given well configuration, variations in temperature along the borehole can induce fluid expansion or contraction within trapped annuli, generating pressure increases that may exceed casing design limits. In operational practice, a key performance indicator for APB risk assessment is the maximum pressure differential between two adjacent annuli at a given depth, denoted here as ΔP_{AB} (Martins *et al.*, 2022). This differential is directly related to the mechanical loading applied to the tubular system and, therefore, provides a suitable scalar metric to characterize the severity of APB.

The objective of the present ML model is to act as a surrogate to rapidly predict this differential pressure, given a set of input design and operating parameters. Formally, and according to Eq. (2.8), the surrogate model seeks to approximate the mapping:

$$\Delta P_{\mathrm{AB}} = \mathcal{F}(x) \tag{7.13}$$

7.2.1.2 Data Collection and Preprocessing

The wellbore analyzed in this study corresponds to a configuration previously modeled by Ferreira *et al.* (2017) and later refined by Veiga *et al.* (2022). It is located in the Campos Basin, one of Brazil's most significant offshore oil-producing regions. A detailed schematic of the well geometry, along with a lithological profile of the surrounding formation, is provided

in Fig. 7.10, as adapted from Veiga *et al.* (2022). This figure serves as a visual reference to understand the structural context and subsurface layering relevant to the present analysis.

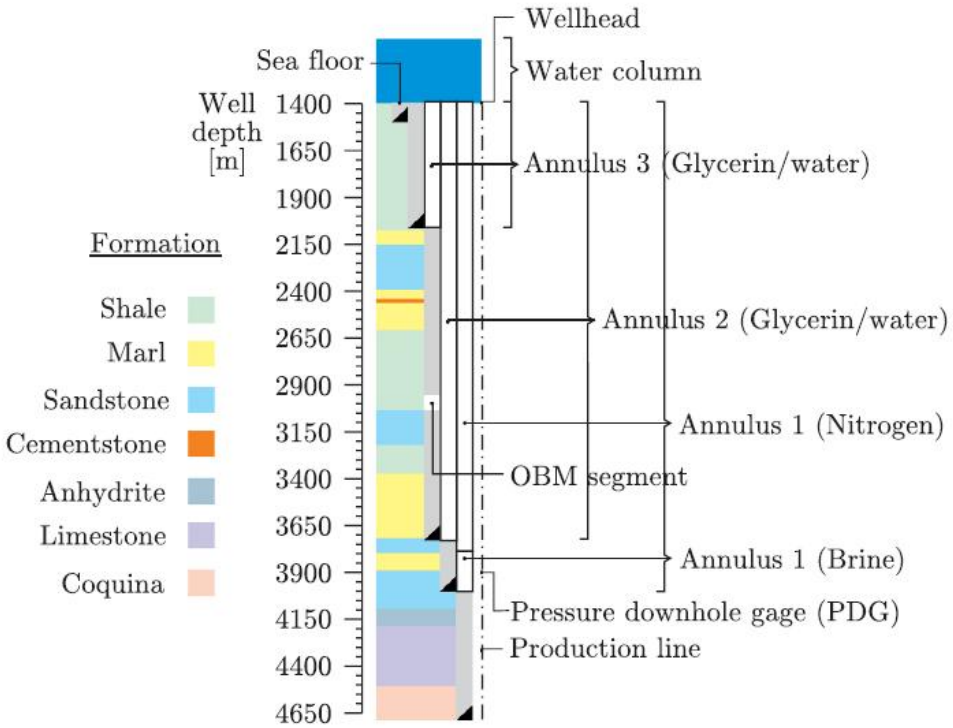


Figure 7.10 – Schematic representation of the well geometry and lithology (Veiga *et al.*, 2022).

The well contains three annular spaces, each filled with distinct fluid compositions representative of realistic field conditions. Annulus 1 is occupied by a two-phase fluid system consisting of nitrogen gas and a 27/73 weight percentage mixture of salt and water brine. Annuli 2 and 3, located in the intermediate and outer regions of the well, are filled with oil-based drilling mud. For this study, these muds are modeled as a simplified 50/50 weight percentage mixture of water and glycerin, providing a reasonable approximation of their thermophysical properties while facilitating numerical implementation (Veiga *et al.*, 2022). The production fluid is composed of a 24-component mixture (N_2, CO_2, C_1-C_3, iC_4, iC_5, nC_4-nC_{19}, nC_{20+}). The advanced Peng-Robinson equation of state described the PVT behavior of the production fluid (Peng & Robinson, 1976), with the gas-oil ratio, API density, and watercut used as input parameters, along with the composition. The properties were evaluated from interpolation of previously generated property tables with data from the Multiflash software (Veiga *et al.*, 2022).

The wellbore is discretized into depth intervals within which the diameter remains constant. Tables 7.3 and 7.4 summarize the geometric configuration adopted in the present analysis. These parameters define the annular volumes and therefore directly influence the thermodynamic response of the trapped fluids and, consequently, the APB magnitude. The geometric parameters considered in this study correspond to the inner diameters of the tubular strings (denoted as D_i) and the hole sizes (denoted as H_i).

Table 7.3 – Geometric characteristics of the tubular diameters.

Section	Start Depth [m]	End Depth [m]	Diameter [in]
D_1	1412	1437	30
D_2	1437	1472	30
D_3	1412	1437	20
D_4	1437	2040	20
D_5	1412	3729	13.375
D_6	1412	4072	10.75
D_7	4072	4165	10.75
D_8	4040	4693	7
D_9	1412	4040	6.625

Table 7.4 – Geometric characteristics of the hole sizes.

Section	Start Depth [m]	End Depth [m]	Diameter [in]
H_1	1412	1472	36
H_2	1472	2040	26
H_3	2040	2060	16
H_4	2060	2955	16
H_5	2955	3050	16
H_6	3050	3729	16
H_7	3729	3825	14.75
H_8	3825	3831	14.75
H_9	3831	4040	14.75
H_{10}	4040	4165	14.75
H_{11}	4165	4693	8.5

To simulate the behavior of hydrocarbons within the fluid strings, the governing equations of momentum and energy conservation were numerically solved (Ferreira *et al.*, 2017; Veiga *et al.*, 2022). Given the characteristics of the problem, a pseudo-steady-state was assumed, along with the hypotheses of one-dimensional vertical flow, a non-deviated well, and local thermodynamic equilibrium. The momentum and energy balance are given, respectively, by:

$$\frac{\mathrm{d}p}{\mathrm{d}z} = \left.\frac{\mathrm{d}p}{\mathrm{d}z}\right|_{fr} + \rho g + \left.\frac{\mathrm{d}p}{\mathrm{d}z}\right|_{acc} \tag{7.14}$$

$$\frac{\mathrm{d}h}{\mathrm{d}z} = \frac{q'}{\dot{m}} + g - v_m \frac{\mathrm{d}v_m}{\mathrm{d}z} \tag{7.15}$$

where p is the pressure, z is the downward direction, ρ is the density of the mixture, g is the gravitational acceleration, h is the specific enthalpy of the mixture, q' is the heat transfer per unit length and v_m the average velocity of the mixture. The subscripts fr and acc represent the friction and acceleration components of the pressure drop.

Radial heat transfer from wellbore fluids to surrounding annular spaces was modeled using a network of thermal resistances, under the assumptions of steady-state, unidirectional

heat flow and a time-dependent boundary condition represented by a time function. The system, composed of a series of thermal resistances, can be calculated as follows:

$$\frac{T_f - T_{wb}}{q'} = \sum_{i=1}^{N-1} R'_i \tag{7.16}$$

where T_{f} is the bulk temperature of the production fluid, T_{wb} the temperature at the interface between the well and the rock formation, and R'_{i} the thermal resistances per unit length of the i-th node.

The thermal resistance associated with he forced convection in the production tube is calculated by:

$$R'_{\mathrm{conv}} = \frac{1}{\hbar P} \tag{7.17}$$

where $\hbar$ is the convective heat transfer coefficient and P is the perimeter. The remaining thermal resistances can be either due to pure conduction or by a combination of natural convection and radiation, and resistances are calculated respectively as follows:

$$R'_{\mathrm{cond}} = \frac{\ln\left(r_{\mathrm{i}+1}/r_{\mathrm{i}}\right)}{2\pi k} \tag{7.18}$$

$$R'_{\mathrm{ann}} = \left(\frac{1}{R'_{\mathrm{nat}}} + \frac{1}{R'_{\mathrm{rad}}}\right)^{-1} \tag{7.19}$$

The annular thermostructural model was constructed by solving the hydrostatic pressure distribution along the depth of the well, along with the conservation of mass, while the structural behavior of the casing system was evaluated using the analytical formulation developed by (Halal & Mitchell, 1994), which accounts for thermomechanical stresses and pressure-induced deformations. Together, these components form the foundation of the integrated numerical model, PySafe (Ferreira *et al.*, 2017; Veiga *et al.*, 2022). PySafe has undergone experimental validation using real field data, including in situ temperature and pressure measurements, thereby providing a high level of confidence in its predictive capabilities. The model has been extensively documented in previous studies, particularly by Ferreira *et al.* (2017) and Veiga *et al.* (2022), to which the reader is referred for a more detailed and comprehensive discussion of the modeling framework and associated assumptions.

Three distinct sources of uncertainty were evaluated with respect to their contribution to the variability of APB predictions: (i) wellhead boundary conditions; (ii) fluid thermophysical properties; and (iii) well geometry. These categories were intentionally analyzed independently for two main reasons. First, each group corresponds to a physically different mechanism. Second, a single surrogate model that propagates all uncertainties simultaneously would require a significant number of high-fidelity simulations, which increase exponentially with the dimensionality of the input space. Thus, three surrogate models were developed (one per uncertainty class), each trained and evaluated separately.

For the boundary-condition scenario, uncertainty was applied to three operational variables measured at the wellhead: temperature, pressure, and mass flow rate. The surrogate model was trained using a dataset generated from 65,536 numerical simulations. Perturbations of ± 2 K, $\pm 10\%$, and $\pm 10\%$ were independently applied to temperature, pressure, and mass flow rate, respectively, using Saltelli's sampling strategy (Saltelli *et al.*, 2004), enabling the model to learn the response of APB to realistic operating variability. The corresponding mapping function is:

$$\Delta P_{\mathrm{AB}} = \mathcal{F}_1(T, p, \dot{m}_{\mathrm{f}}) \tag{7.20}$$

To illustrate Saltelli's sampling strategy, Fig. 7.11 presents scatter plots of the input and output parameters used to train the ANN. Each subplot displays the deviation of a particular variable from its nominal value in all 65,536 simulation samples. The uniform, uncorrelated distribution of points across the sampled domain highlights the robustness of the sampling technique, ensuring comprehensive coverage of the input space for accurate, generalizable ANN training.

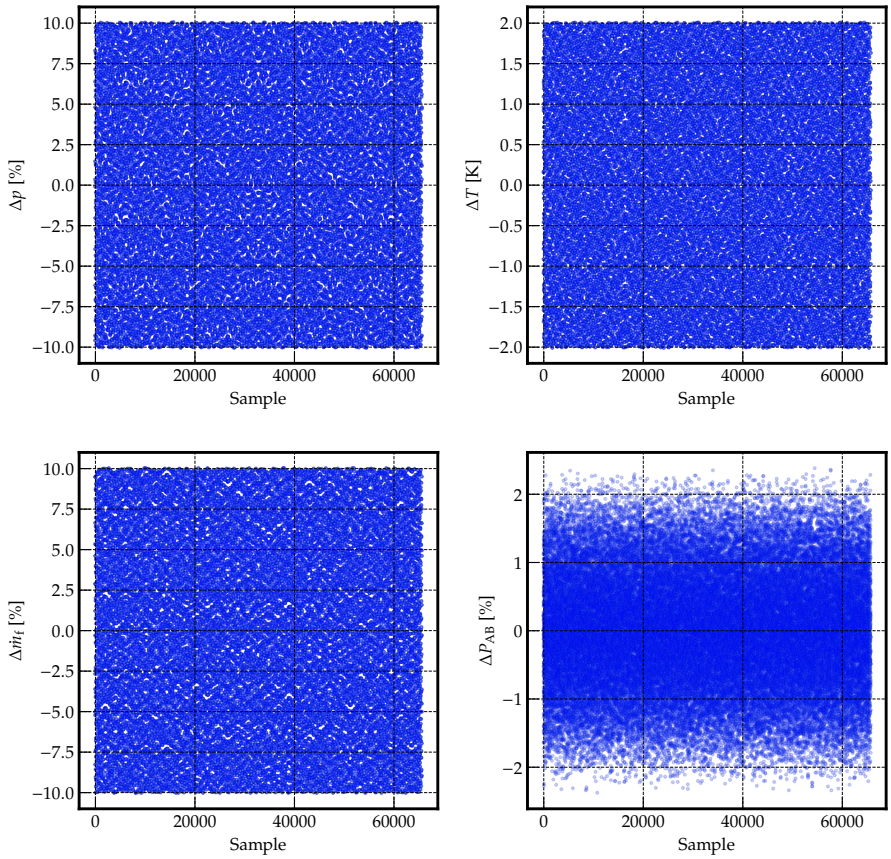


Figure 7.11 – Input variables and output parameters of the Simulation

In the second scenario, the uncertainties in the thermophysical properties of drilling mud, nitrogen, brine, and production oil were propagated. The following properties were considered: thermal conductivity (k), density (ρ), thermal expansivity (β), viscosity (μ), and specific heat at constant pressure (c_{p}). For production oil, enthalpy (h) was also included because of its significant contribution to thermal storage. Literature-derived uncertainties and

the more conservative values adopted in this analysis are listed in Table 7.5. The uncertainty in thermal expansivity was assumed to be equal to that in density.

Table 7.5 – Uncertainty ranges adopted for each fluid property.

Fluid	Property	Uncertainty (Reference)	Uncertainty (This Analysis)	Reference
Drilling Mud	ρ_{m}	2%	5%	Volk & Kähler (2018)
	μ_{m}	10%	15%	Gonzalez *et al.* (2011)
	k_{m}	5%	20%	Lotfi *et al.* (2021)
	$c_{\mathrm{p},m}$	4%	5%	Righetti *et al.* (1998)
Nitrogen	ρ_{N}	0.3%	2%	Span *et al.* (2000)
	μ_{N}	2%	5%	(Lemmon & Jacobsen, 2004)
	k_{N}	5%	10%	(Lemmon & Jacobsen, 2004)
	$c_{\mathrm{p},N}$	2%	5%	Span *et al.* (2000)
Brine	ρ_{b}	0.64%	2%	Zamora *et al.* (2013)
	μ_{b}	0.5%	2%	Kestin & Shankland (1984)
	k_{b}	0.5%	2%	Ramires *et al.* (1994)
	$c_{\mathrm{p},b}$	3%	5%	Chen (1982)
Production Fluid	ρ_{o}	5%	10%	Jr (1991)
	μ_{o}	16%	20%	Lohrenz *et al.* (1964)
	k_{o}	12%	15%	Guo *et al.* (2001)
	$c_{\mathrm{p},o}$	5%	10%	Waples & Waples (2004)
	h_{o}	5%	10%	Waples & Waples (2004)

The surrogate model was trained using a dataset generated from 204,801 numerical simulations, using Saltelli's sampling strategy (Saltelli *et al.*, 2004), that approximates:

$$\Delta P_{\mathrm{AB}} = \mathcal{F}_2\left(\rho_{\mathrm{m}}, \mu_{\mathrm{m}}, k_{\mathrm{m}}, c_{\mathrm{p},m}, \beta_{\mathrm{m}}, \rho_{\mathrm{N}}, \mu_{\mathrm{N}}, k_{\mathrm{N}}, c_{\mathrm{p},N}, \beta_{\mathrm{N}}, \rho_{\mathrm{b}}, \mu_{\mathrm{b}}, k_{\mathrm{b}}, c_{\mathrm{p},b}, \beta_{\mathrm{b}}, \rho_{\mathrm{o}}, \mu_{\mathrm{o}}, k_{\mathrm{o}}, c_{\mathrm{p},o}, \beta_{\mathrm{o}}, h_{\mathrm{o}}\right) \tag{7.21}$$

Finally, uncertainties in the geometric parameters were evaluated. All tubular diameters (D_i) and hole sizes (H_i) listed in Tables 7.3 and 7.4 were included as independent uncertain inputs. A total of 86,017 high-fidelity simulations were generated using Saltelli sampling (Saltelli *et al.*, 2004), applying a uniform $\pm 4\%$ deviation to each dimensional variable, consistent with typical manufacturing tolerances. The geometric surrogate model, therefore, approximates:

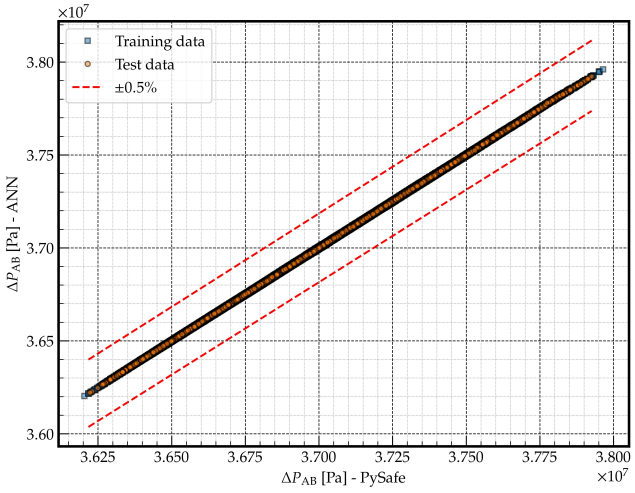
$$\Delta P_{\mathrm{AB}} = \mathcal{F}_3\left(D_1, D_2, D_3, D_4, D_5, D_6, D_7, D_8, D_9, H_1, H_2, H_3, H_4, H_5, H_6, H_7, H_8, H_9, H_{10}, H_{11}\right) \tag{7.22}$$

7.2.1.3 Model Selection Training and Optimization

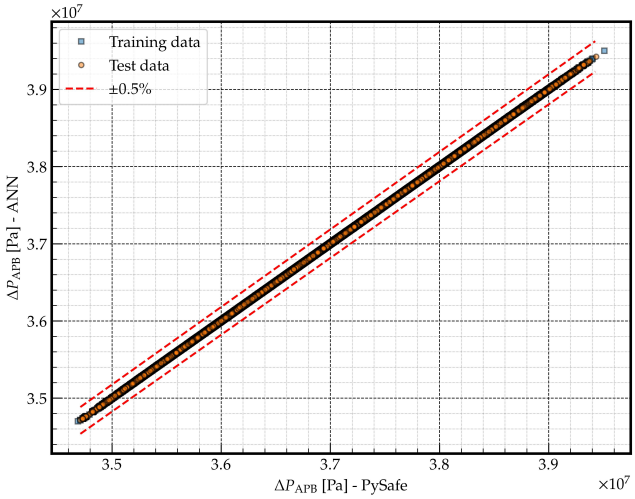
ANNs were once again employed as the surrogate model. The architecture of the ANN that models the boundary conditions comprises one hidden layer with 20 neurons; whereas the architecture used to model the influence of the thermophysical inputs and the geometric parameters comprises two hidden layers with 50 and 5 neurons, respectively. To improve generalization and avoid overfitting, a combination of training optimization strategies was implemented, including L2-regularization, batch normalization, early stopping, and learning rate scheduling (Brunton & Kutz, 2022). The model was trained using the Adam optimizer (Kingma, 2014), with MSE as the loss function and ELU as the activation function. A maximum of 1000 training epochs was specified to ensure convergence without excessive training time. In all cases, the dataset was partitioned into a training set (64%), a validation set (16%), and a test set (20%).

7.2.1.4 Model Evaluation

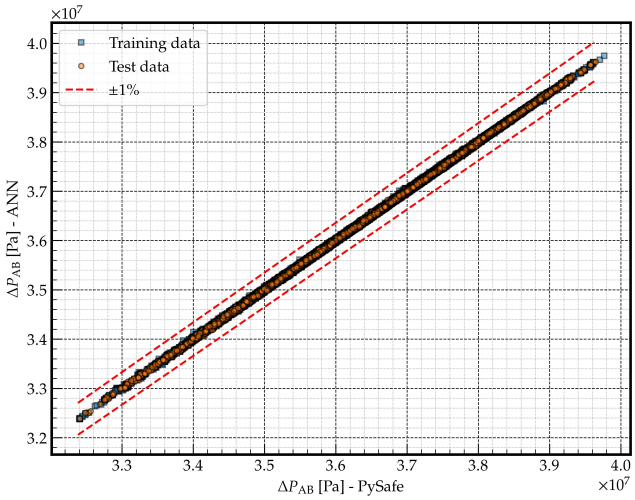
Figure 7.12 shows the comparison between the predicted values of the maximum pressure difference obtained from the trained ANN and the reference values calculated using the numerical simulation model (PySafe), for the models given by Eqs. (7.20)-(7.22). The results are plotted for both the training and test data sets, where the validation sets are included in the training sets. Error bars are also presented in the plots. Comparison of the agreement between the results of both models demonstrates the ANN ability to capture the complex interactions between the operational boundary conditions and the thermostructural phenomena at the well. Furthermore, the coefficient of determination on the test set exceeds 0.999, indicating the outstanding performance. Although the dataset is composed of numerically simulated data with homogeneous, stable inputs, characterized by low noise and no missing values, the precision remains notably high, reflecting the robustness and suitability of the approach for the modeled system.



(a)



(b)



(c)

Figure 7.12 – Comparison between the numerical and ANN prediction evaluating (a) well head boundary conditions, (b) fluid thermophysical properties of the fluids, (c) well geometry.

7.2.1.5 Model Application

To quantify the impact of uncertainties in the model input parameters, two complementary approaches were employed: sensitivity analysis and uncertainty analysis. Both methods require a large number of model evaluations, which were made computationally feasible by using ANNs as surrogate models.

The sensitivity analysis was conducted using the Sobol method, given by Eqs. (2.51)–(2.53). Three distinct cases were investigated: (i) operational boundary conditions at the wellhead; (ii) thermophysical properties of the fluids; and (iii) geometric parameters of the well. For each case, the following numbers of samples were generated with the trained ANNs: 262,144 for the boundary conditions, 3,276,800 for the thermophysical properties, and 2,752,512 for the geometric parameters. The resulting total Sobol indices are presented in Figs. 7.13–7.15. The confidence interval associated with each variable is shown as an error bar at the top of each bar.

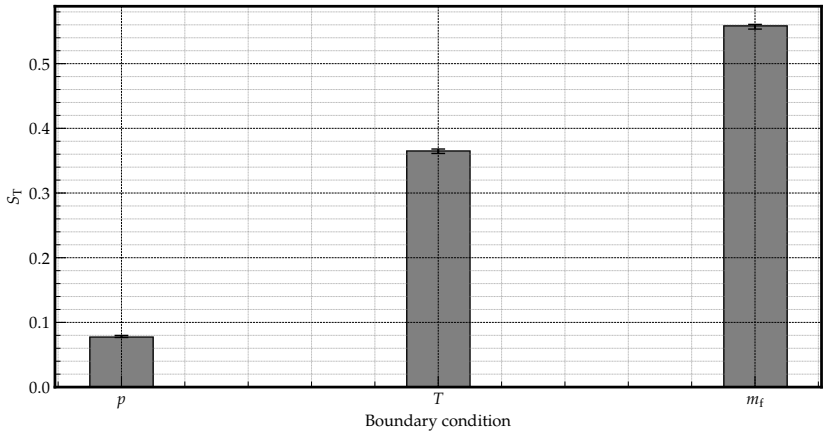


Figure 7.13 – Total Sobol coefficients for the operational boundary conditions.

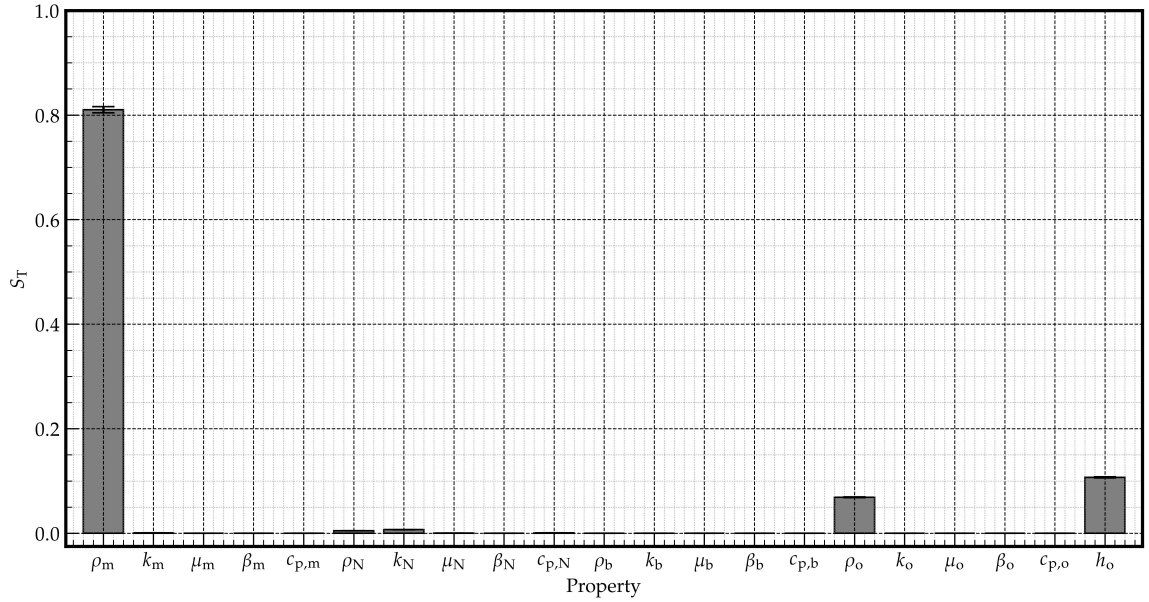


Figure 7.14 – Total Sobol coefficients for the thermophysical properties of the fluids.

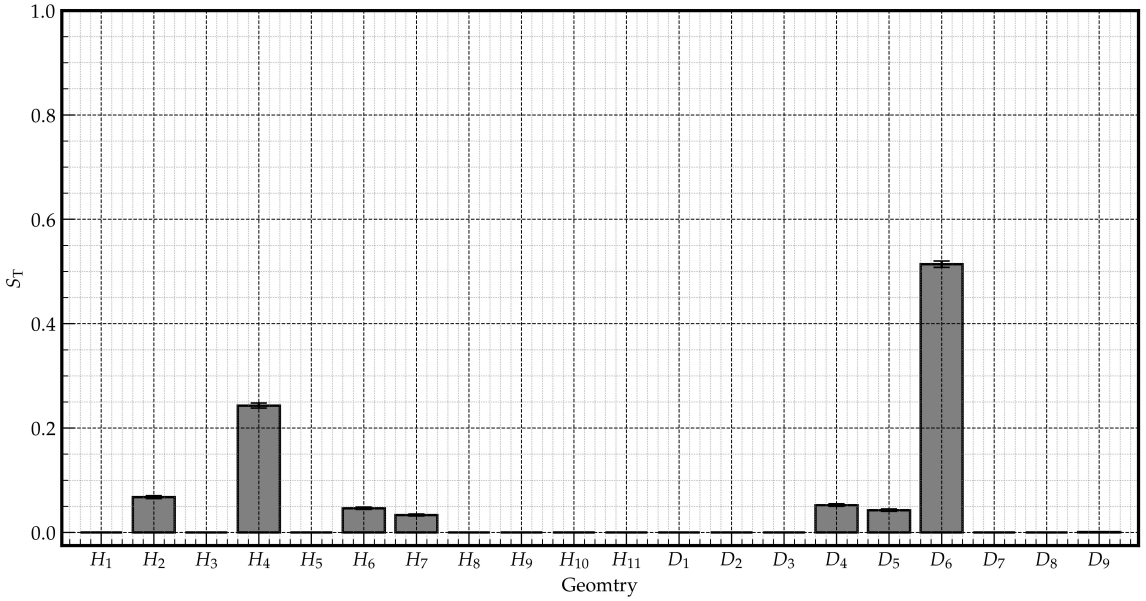


Figure 7.15 – Total Sobol coefficients for the geometric parameters of the well.

The results indicate that, within each parameter group, a small subset of specific variables dominates the model output variability. Among the boundary conditions, the mass flow rate is the most influential parameter, accounting for more than 50% of the output variance, followed by temperature. In contrast, pressure has the smallest (but still non-negligible) impact. As expected from the definition of Sobol total indices, the sum of all coefficients in each case equals 1, reflecting the complete allocation of output variance among the inputs.

In contrast, the remaining two cases are strongly driven by a single or a pair of variables. For the thermophysical properties case, the mud density, ρ_{m}, is responsible for approximately 80% of the output variance. This occurs because, even with relatively small uncertainty, density directly affects the pressure and therefore substantially influences the system behavior. For the geometric parameters case, D_6 and H_4 are the dominant contributors to the variance, which is consistent with their comparatively larger lengths (see Tables 7.3 and 7.4). Finally, the narrow confidence intervals obtained for all variables demonstrate the high statistical reliability of the estimates, which was only possible due to the large number of samples evaluated using the ANN-based surrogate models.

While the sensitivity analysis is extremely valuable for identifying which variables contribute most to the variance of the output, it does not quantify the magnitude of these effects. In other words, the Sobol indices provide a ranking of the relative importance of the inputs. Still, they do not indicate how much the predicted maximum pressure difference will change when each parameter varies within its plausible uncertainty interval. Therefore, sensitivity analysis must be complemented by an uncertainty analysis that explicitly evaluates the propagation of parameter uncertainties through the model. In this work, this was achieved through a Monte Carlo approach powered by ANN surrogate models previously developed

for uncertainty quantification in magnetic refrigeration systems.

In the Monte Carlo evaluation, all uncertain parameters were sampled from uniform distributions, with standard deviations defined as the maximum deviation used in the sampling stage divided by 1.96, such that 95% of the samples fall within the prescribed uncertainty bounds of each variable. For each case study, the influence of individual parameters was first evaluated independently. In addition, aggregated analyses were performed: in the fluid case, all properties of a given fluid were perturbed simultaneously, and in the geometry case, either all tube diameters or all hole sizes were varied as groups. Finally, a global scenario was also assessed, in which all uncertain parameters were perturbed concurrently. For each configuration, 10,000,000 ANN predictions were computed. The objective was to quantify how uncertainties in the inputs propagate through the system and affect the maximum pressure difference between the annuli.

Figure 7.16 presents the resulting distribution of the maximum pressure difference under uncertainty in the boundary conditions, shown as a violin plot. The distribution is narrow and nearly symmetric, with most values lying between 97% and 103% of the nominal prediction (defined as the median value at nominal inputs). This indicates that, under the assumed uncertainty levels in the surface boundary conditions, the corresponding variations in maximum pressure difference at a given well depth are modest and statistically well–behaved. The descending order of influence remains consistent with the sensitivity analysis: mass flow rate, temperature, and pressure.

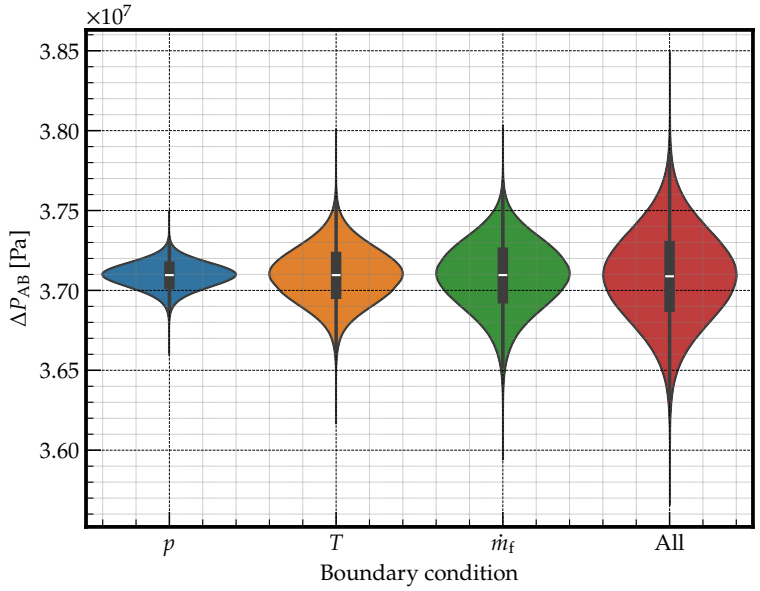


Figure 7.16 – Distribution of maximum pressure difference at a given well depth under uncertain boundary conditions using Monte Carlo simulations.

Figure 7.17 shows the effect of uncertainty in the thermophysical properties of each fluid considered. Here, all properties of each fluid are perturbed simultaneously. The spread in maximum pressure difference at a given well depth is substantially larger than in the

boundary–condition case, reaching approximately $\pm 12\%$ relative to the nominal value. The most significant contributions originate from the mud properties, followed by those of the production oil. Nitrogen and brine contribute only marginally to the variance.

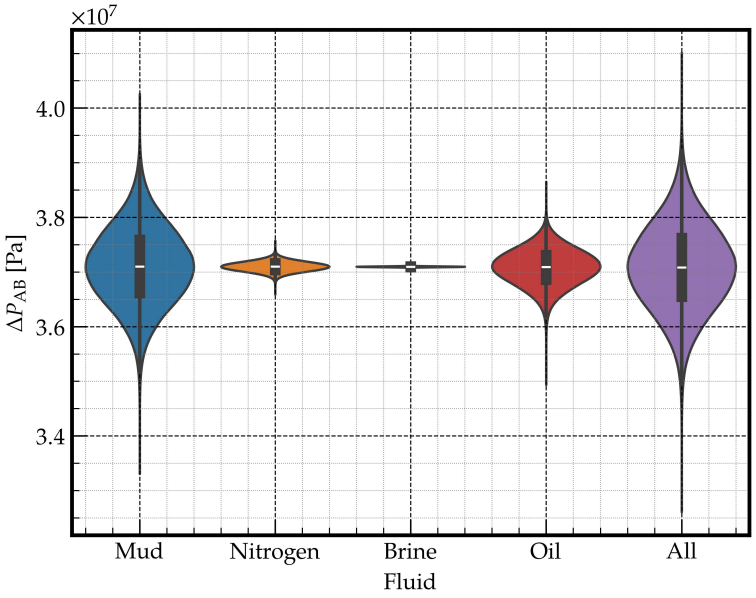


Figure 7.17 – Distribution of maximum pressure difference at a given well depth under uncertain boundary conditions using Monte Carlo simulations.

A more detailed view of the individual property contributions is shown in Fig. 7.18. In agreement with the sensitivity analysis, the mud density is the single most influential property, followed by the density and enthalpy of the production oil. All other fluid properties have minor contributions. Additionally, the density and thermal conductivity of nitrogen and the brine density show the most significant relative effects within their respective fluids. However, these effects remain small compared to those of mud and oil.

Finally, Fig. 7.20 presents the variability in maximum pressure difference at a given well depth across uncertainties associated with hole size (H), outer diameter (D), and the combined case. Uncertainties in D produce a slightly greater dispersion of outcomes than those in H. When both parameters are perturbed simultaneously, the variability increases further, revealing the additive nature of the uncertainty propagation. In this combined scenario, deviations exceeding 75% and even 110% of the nominal values are observed.

In accordance with the results presented in Fig. 7.15, the tube diameters with the most significant influence on maximum pressure difference at a given well depth are D_6, D_5 and D_4. While the sensitivity analysis (Fig. 7.15) provides a ranking of the relative influence of each diameter, the uncertainty analysis (Fig. 7.20b) quantifies the magnitude of this effect. In this case, the combined uncertainty in the tube outer diameters results in deviations of 76%-107% of the nominal value, which is operationally significant. Figure 7.20a extends this assessment by examining the effect of hole sizes on maximum pressure difference at a given well depth. These distributions are narrower than those from the diameters, indicating that

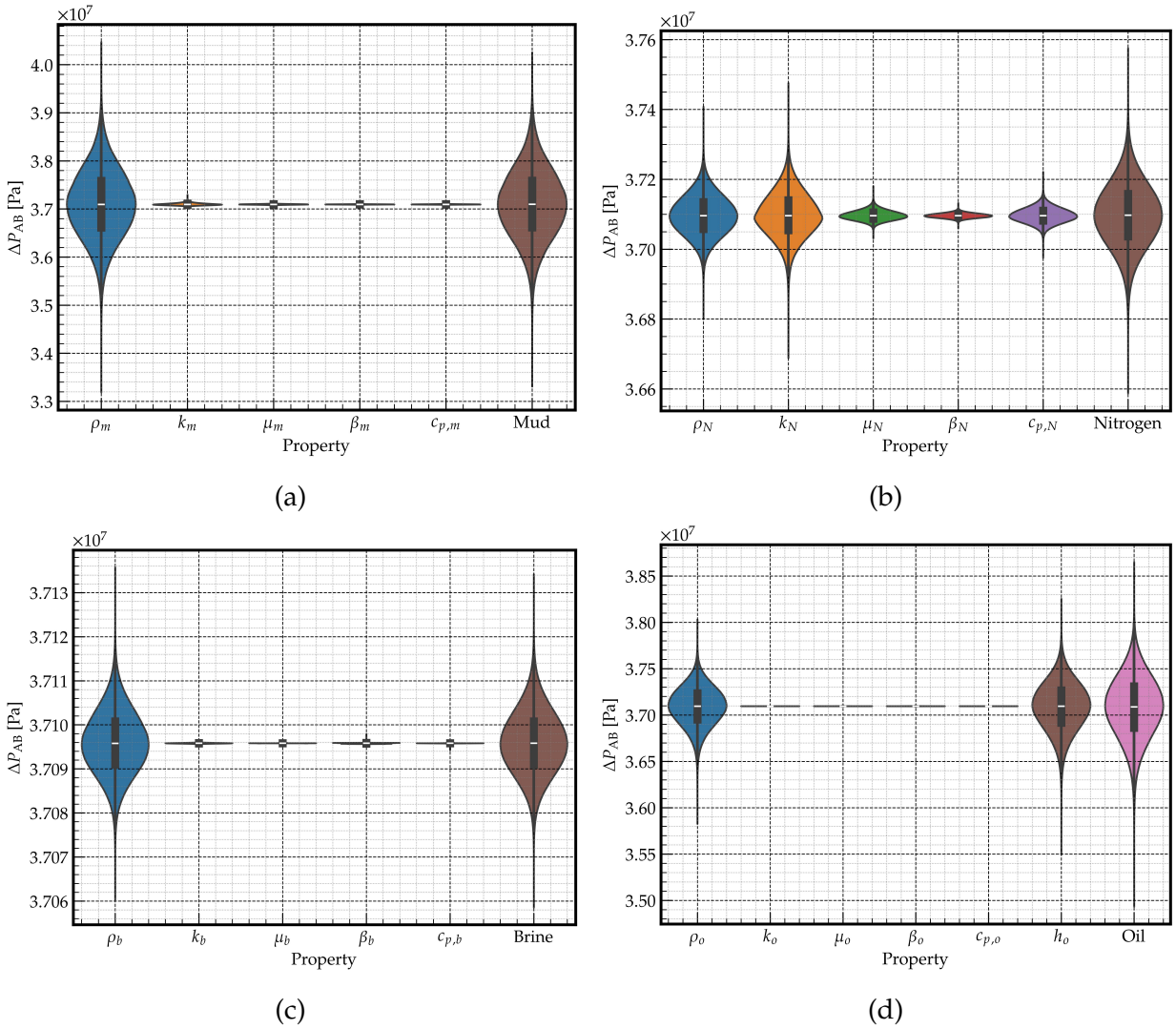


Figure 7.18 – Distribution of maximum pressure difference at a given well depth under different sources of uncertainty using Monte Carlo simulations: (a) mud, (b) nitrogen, (c) brine, and (d) production oil.

the maximum pressure difference at a given well depth is less sensitive to variations in hole size than in outer diameter. Among the tested hole sizes, H_4 exhibits the highest influence, corroborating the sensitivity analysis. In contrast to the tube-diameter case, which shows more skewed behaviour, the hole–size scenario is more symmetric, with deviations between 90% and 107% of the nominal value.

In summary, the uncertainty analysis reveals that although surface operating conditions introduce only minor variability in the system, the propagation of uncertainties in the thermophysical properties of the fluids and the geometric dimensions can lead to substantially larger deviations in the predicted maximum pressure difference at a given well depth. These findings reinforce the importance of precise characterization of mud density, production oil properties, and the well geometry, particularly the outer diameters of the tubes. Moreover, the results demonstrate the decisive advantage of using ANN surrogate models, which enable the large number of Monte Carlo evaluations needed to quantify uncertainty propagation rigorously. Ultimately, the combined use of sensitivity and uncertainty analysis

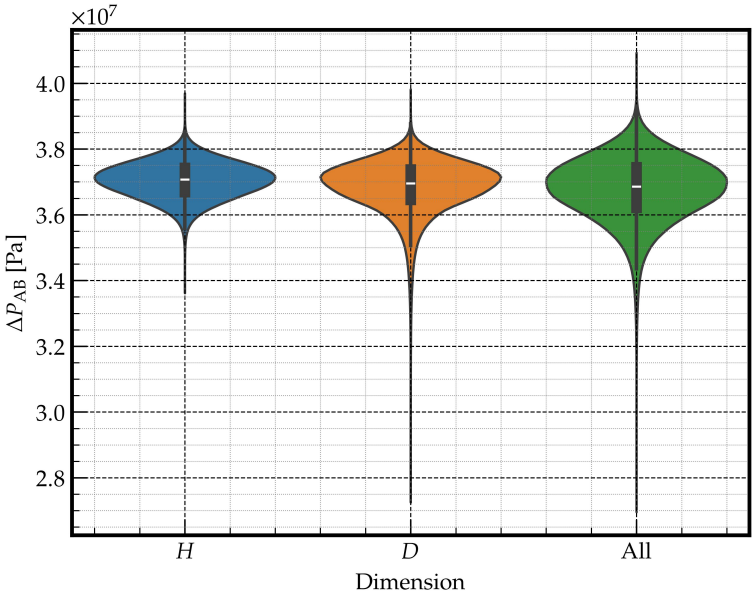
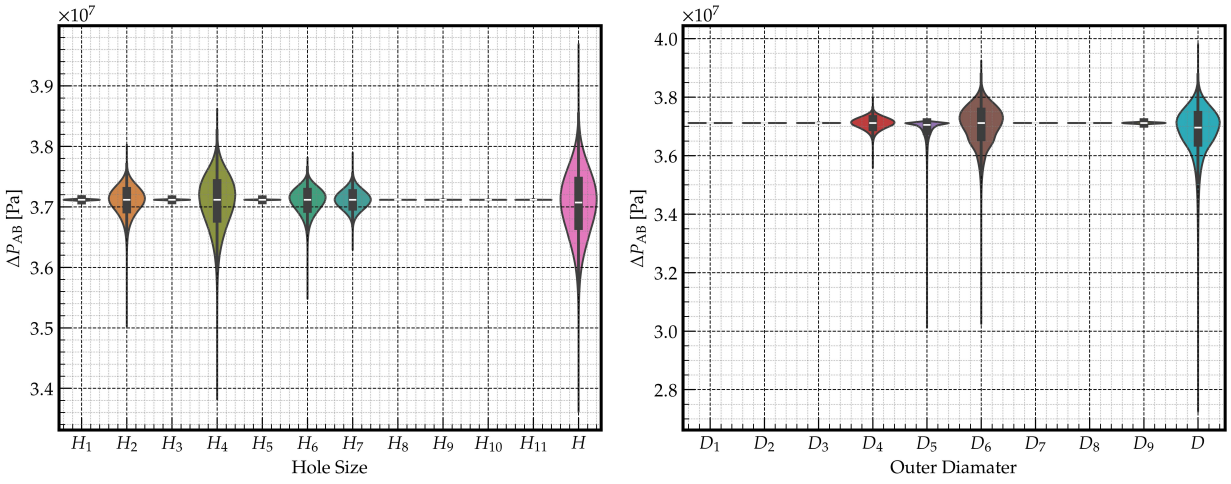


Figure 7.19 – Distribution of maximum pressure difference at a given well depth under uncertain boundary conditions using Monte Carlo simulations.



(a) (b)

Figure 7.20 – Distribution of maximum pressure difference at a given well depth under geometric parameter uncertainty using Monte Carlo simulations: (a) hole size and (b) outer diameter.

provides a comprehensive view of the system robustness and identifies which parameters must be prioritized to reduce risk in field operations.

7.2.2 Anomaly Detection in Offshore Oil Wells

To mitigate the risks associated with exploration and production, the oil and gas industry has increasingly turned to Abnormal Event Management (AEM), where machine learning plays a central role in detecting anomalies from operational data, enabling predictive maintenance, improved safety, and optimized resource utilization (Ha, 2022; Lin *et al.*, 2022; Canizo *et al.*, 2019; Xue *et al.*, 2021). Petrobras contributed to this effort by publishing the 3W dataset, the first publicly available and realistic dataset of rare, undesirable events in oil wells, comprising multivariate time-series of pressure and temperature data linked to operational

anomalies (Vargas *et al.*, 2019). Since its release, several studies have evaluated machine learning and deep learning approaches, with results highlighting the effectiveness of methods such as decision trees, Local Outlier Factor (LOF), Isolation Forest (IF), One-Class Support Vector Machine (OCSVM), and autoencoder-based architectures (Turan & Jäschke, 2021; Júnior *et al.*, 2020; Nascimento *et al.*, 2021; Machado *et al.*, 2022; FERNANDES Jr *et al.*, 2024). While LOF and LSTM autoencoders have demonstrated superior performance in anomaly detection, many promising deep learning models remain underexplored, particularly for rare event prediction in time series data (Niu *et al.*, 2020). Building on this, the present study proposes the evaluation of ML models on the 3W dataset, using their ability to capture temporal dependencies in sequential data, and benchmarking their performance against previously reported models to advance anomaly detection and abnormal event management in oil wells.

7.2.2.1 Problem Definition

The anomaly detection task investigated in this work is grounded in the 3W dataset published by Petrobras, which contains multivariate time series of pressure and temperature measurements recorded at different points along the well, along with labels indicating rare abnormal events. Let $\mathbf{x}(t) \in \mathbb{R}^d$ denote the vector of d sensor measurements at time t. Given a temporal window of length L, we define:

$$\mathbf{X}_t = \Big[\mathbf{x}(t), \mathbf{x}(t-1), \ldots, \mathbf{x}(t-L+1)\Big] \in \mathbb{R}^{L \times d}. \tag{7.23}$$

The objective of anomaly detection is to estimate a function

$$\mathcal{F} : \mathbb{R}^{L \times d} \to \mathbb{R} \tag{7.24}$$

that assigns an anomaly score $s(\mathbf{X}_t) = f(\mathbf{X}_t)$, such that normal operational behavior yields low scores, while abnormal behavior yields high scores. A binary decision is obtained by thresholding:

$$y(t) = \begin{cases} 0, & \text{if } \mathcal{F}(\mathbf{X}_t) < \tau \\ 1, & \text{if } \mathcal{F}(\mathbf{X}_t) \geq \tau \end{cases} \tag{7.25}$$

where τ is a decision threshold determined from training data.

7.2.2.2 Data Collection and Preprocessing

An oil well is a subsurface formation equipped with mechanical, pneumatic, hydraulic systems, and sensing devices, enabling the extraction of petroleum and natural gas from the reservoir to the surface (Guo, 2011). Naturally flowing wells are distinguished by their ability to produce hydrocarbons at commercially viable rates solely through reservoir

energy, without external energy injection. Figure 7.21 illustrates a typical offshore installation (Vargas *et al.*, 2019). In this configuration, hydrocarbons flow from the reservoir through the production tubing and then to the topside platform via the production line. For this study, key equipment includes the permanent downhole gauge (PDG), temperature and pressure transducer (TPT), downhole safety valve (DHSV), and production choke (PCK), whose locations are indicated in Fig. 7.21.

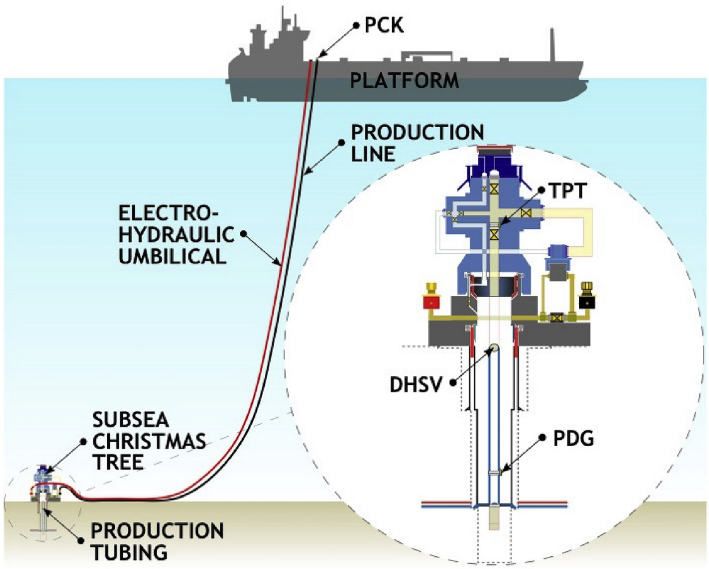


Figure 7.21 – Schematic representation of a naturally flowing offshore well (Vargas *et al.*, 2019).

Modern integrity management strategies rely on anomaly detection models to improve well operability and prevent failures. These models analyze multivariate measurements, such as temperature and pressure, at critical points (PDG, TPT, PCK, gas lift system), and classify operating conditions as normal, transient, or abnormal. The main variables adopted in this study are:

- P_{PDG} — pressure in PDG
- P_{TPT} — pressure at TPT
- T_{TPT} — temperature at TPT
- P_{PCK} — pressure upstream of the PCK
- T_{PCK} — temperature downstream of the PCK
- P_{GL} — pressure downstream of the gas lift
- T_{GL} — temperature below the gas lift
- Q_{GL} — gas lift flow rate
- Label — classification as (1) normal, (2) transient, or (3) anomalous operation

The 3W dataset is the first publicly available, realistic dataset containing rare, undesirable events in oil wells (Vargas *et al.*, 2019). It consists of multivariate time series that relate flow, pressure, and temperature signals to abnormal operating conditions. A total of 1984 instances are available, including experimental measurements from 21 wells, and additional numerically simulated or hand–crafted cases to reduce class imbalance.

The 3W dataset includes eight types of anomalies: (1) Abrupt increase of basic sediment and water, (2) Spurious DHSV closure, (3) Severe slugging, (4) Flow instability, (5) Rapid productivity loss, (6) Quick restriction in PCK, (7) Scaling in PCK, and (8) Hydrate formation in the production line. A detailed description of each event type is available in Vargas *et al.* (2019). A summary of the number of instances per class is shown in Table 7.6.

Table 7.6 – Summary of event types and their number of instances in the 3W dataset.

Class	Real	Simulated	Hand-drawn	Total
0	597	0	0	597
1	5	114	10	129
2	22	16	0	38
3	32	74	0	106
4	344	0	0	344
5	12	439	0	451
6	6	215	0	221
7	4	0	10	14
8	3	81	0	84

The dataset comprises 1984 instances, of which 597 are normal and 1397 are anomalous. Two relevant challenges are missing and frozen variables. Missing variables occur 4947 times out of 15872 (31.17% of the dataset). Frozen variables (constant for a time interval) occur 1535 times (9.67%). Strategies to handle both issues are discussed later in this work. To illustrate the temporal behavior, Fig. 7.22 shows an anomalous instance of a spurious DHSV closure. The three phases (normal, transient, anomaly) are clearly distinguishable. Frozen variables are observable for P_{PDG} and P_{GL}, which remain constant over part of the record.

To help interpret the relationship between variables and anomaly types, an adapted correlation matrix is shown in Fig. 7.23. In this representation, each column contains the Pearson correlation between an input variable and each anomaly class, resulting in a non–symmetric matrix. White cells indicate frozen variables. Significant correlations vary across event types. This reinforces the need to retain all variables to build robust anomaly detection models.

This work evaluates the second benchmark introduced in (Vargas *et al.*, 2019). First, all transient and anomalous states are relabeled as positive, and all normal states as negative. Then, the following rules are applied:

- **Rule 1**: Only real anomalous events with an initial normal period of at least 20 minutes

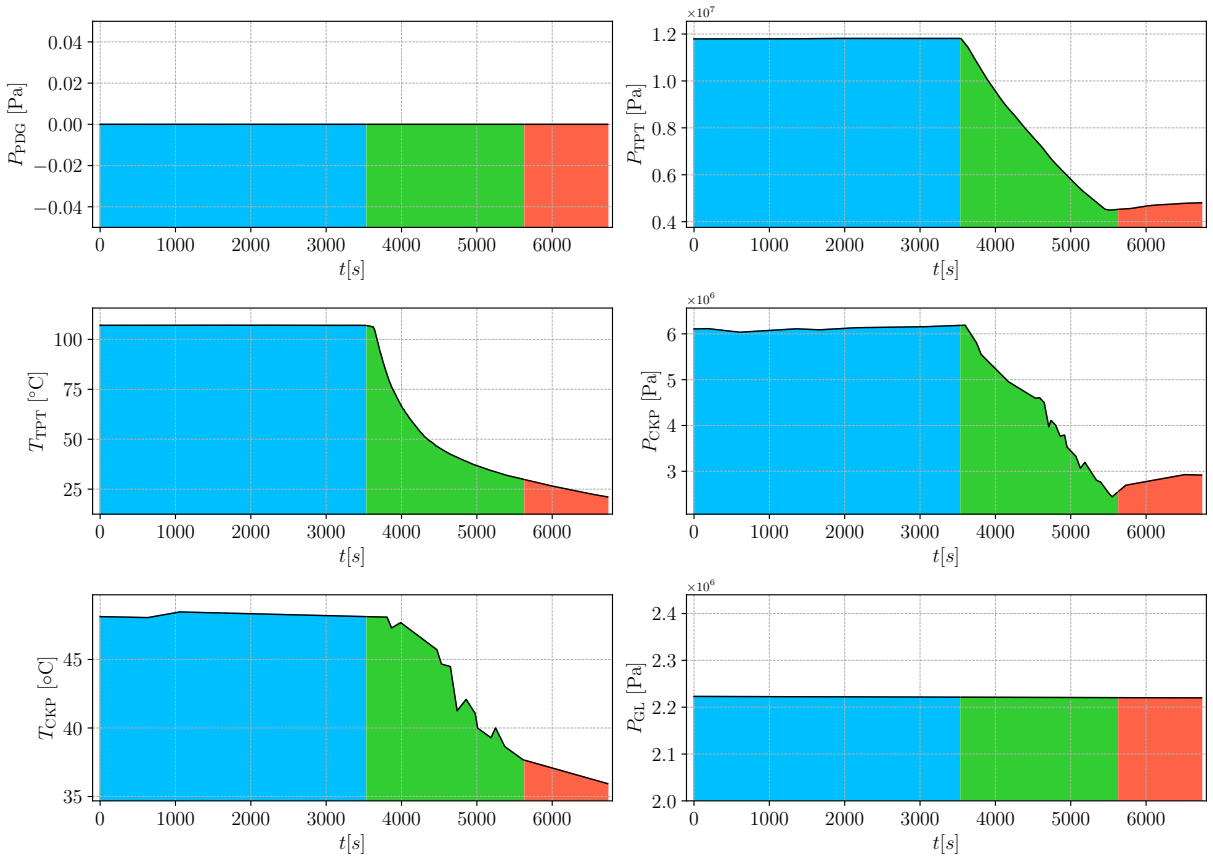


Figure 7.22 – Temporal evolution of selected variables during a spurious DHSV closure. Blue: normal; green: transient; red: anomalous state.

are considered (classes 1, 2, 5, 6, 7, and 8).

- **Rule 2**: The number of training rounds equals the number of training instances. In each round, both training and testing samples are extracted from the same instance. A portion of the negative samples is used for training, and the remainder for testing. All positive samples are used exclusively for testing. The test set is balanced across classes.

- **Rule 3**: Precision, recall, and F1 score are computed for each round.

To finish the data preprocessing, following the rule adopted by FERNANDES Jr *et al.* (2024), each instance is segmented into 180-observation windows. Samples with more than 10% missing values are discarded. Finally, standardization is applied: each variable is normalized using the mean and standard deviation computed from the training set only.

7.2.2.3 Model Selection, Training and Optimization

In the domain of anomaly detection, the choice of model is critical for reliably identifying deviations or irregular patterns within multivariate time series. Among the available techniques, recurrent neural network architectures, particularly Long Short–Term Memory (LSTM) autoencoders, have shown strong potential for modeling sequential operational data.

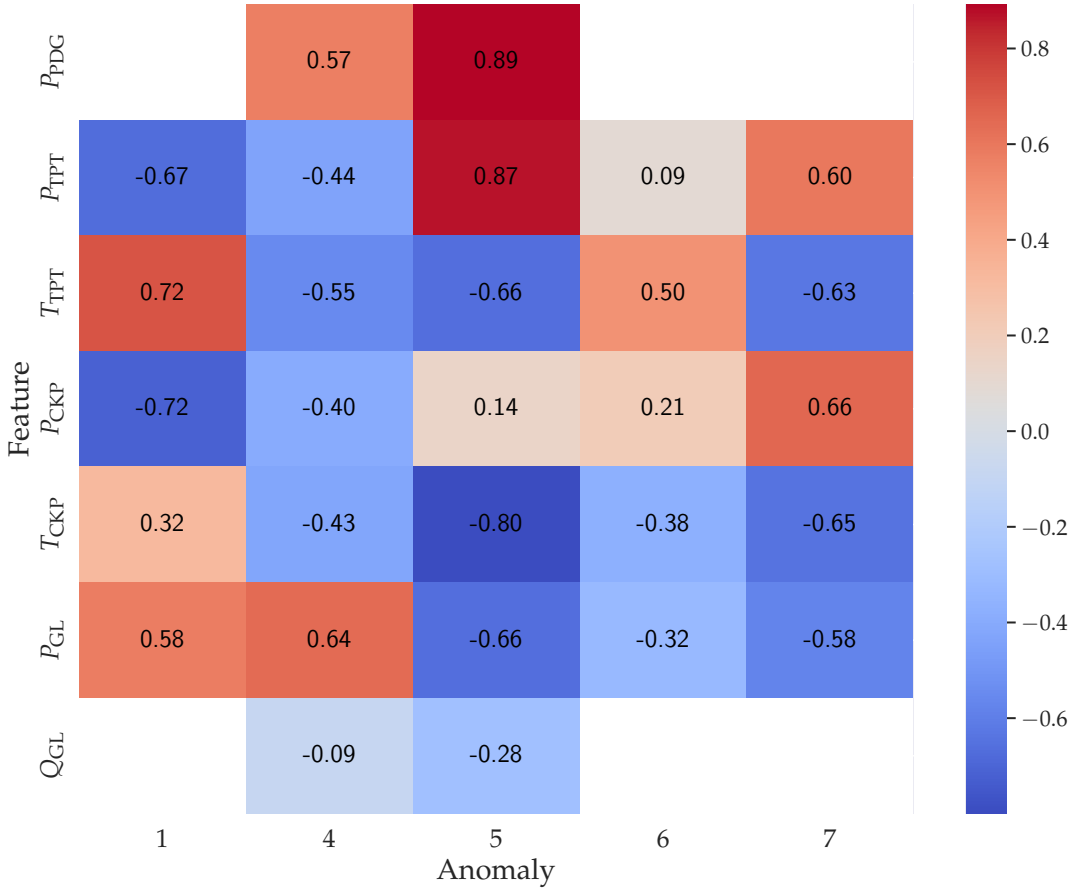


Figure 7.23 – Correlation matrix between input variables and anomaly classes.

An LSTM autoencoder consists of an encoder network that compresses the input sequence into a compact latent representation, and a decoder network that reconstructs the original signal from this representation. During training, only data corresponding to normal operating periods is used. The model is optimized to minimize the reconstruction error between its outputs and the original input sequence. Hence, according to the framework present by Eqs. (7.24) and (7.25) the mapping $\mathcal{F}$ is instantiated as the reconstruction error:

$$\mathcal{F}(\mathbf{X}_t) = \|\mathbf{X}_t - \hat{\mathbf{X}}_t\|, \tag{7.26}$$

where $\hat{\mathbf{X}}_t$ is the reconstructed sequence. Since the model is trained primarily on normal sequences extracted from 3W, high reconstruction error indicates that the current pattern is unlikely to correspond to nominal well operation, thus signaling a potential abnormal event. In doing so, the LSTM autoencoder learns the temporal dependencies and intrinsic dynamics that characterize normal well operation.

Once trained, the reconstruction error becomes a meaningful indicator of abnormality. Sequences that conform to normal operational behavior tend to be accurately reconstructed, yielding low reconstruction error. Conversely, sequences that diverge from the learned normal patterns, such as those produced during transient or anomalous events, result in significantly higher reconstruction errors. Thus, the reconstruction error acts as an implicit anomaly score.

This framework aligns with the benchmarking procedure proposed for the 3W dataset: the model is trained exclusively on periods labeled as normal, and its ability to distinguish positive (transient + anomalous) from negative (normal) samples is assessed based on the classification performance obtained by thresholding the reconstruction error (or functions derived therefrom). This approach is especially suitable for the 3W dataset, which is characterized by strong nonlinearity, temporal dependencies, class imbalance, missing values, and frozen variables, challenges that conventional static models struggle to capture.

The autoencoder architecture adopted in this work uses a symmetric LSTM. The encoder consists of two stacked LSTM layers with 32 and 16 units, respectively, while the decoder mirrors this configuration with 16 and 32 units. All recurrent layers use the hyperbolic tangent activation function. To mitigate overfitting, early stopping was employed and L_2 regularization was applied to all recurrent units, with a regularization coefficient of 0.01. The model was trained using the Adam optimizer (Kingma, 2014).

7.2.2.4 Model Evaluation

The performance of the proposed model on the test set was evaluated using the metrics defined in Eqs. (2.24)–(2.27). Figure 7.24 presents the confusion matrix, comparing the predicted labels to the ground truth for normal and anomalous operating conditions. The corresponding performance metrics obtained in the test set are reported in Table 7.7.

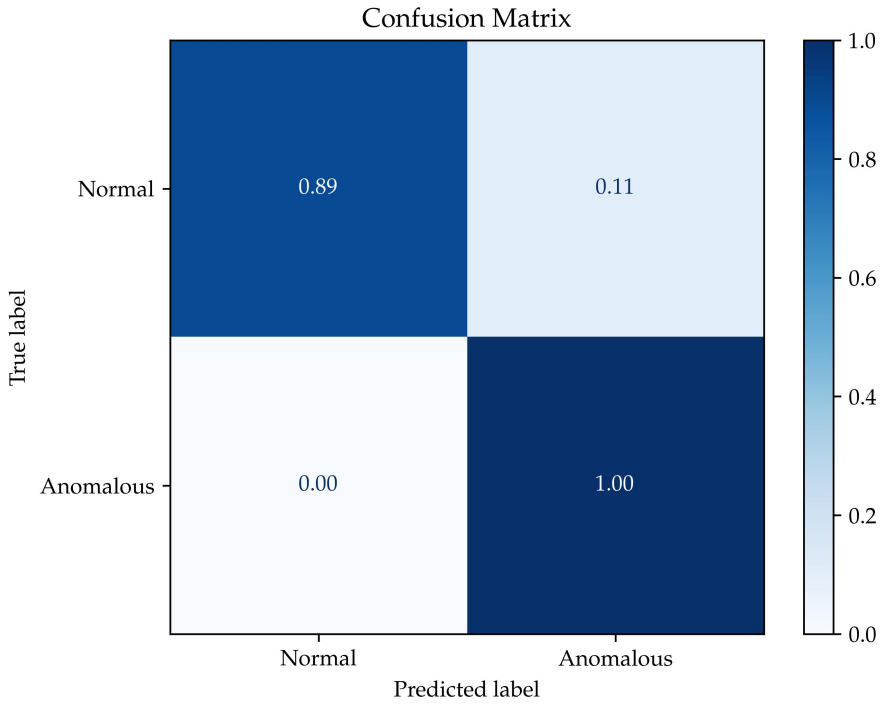


Figure 7.24 – Confusion matrix of the developed model on the test set.

As shown in Fig. 7.24 and Table 7.7, the model achieves an accuracy of approximately 94%, consistent with results reported in the literature for the 3W dataset. A more detailed

Table 7.7 – Performance metrics of the model on the test set.

Metric	Value
Accuracy	0.945
Precision	0.890
Recall	1.000
F1-Score	0.941

inspection shows that the model achieves a very high recall, meaning that almost all abnormal events are correctly identified. This implies that a higher number of false positives is tolerated, but missed anomalies are minimized. From an industrial safety perspective, this trade-off is desirable: although additional false alarms may lead to increased operator intervention, failing to detect an anomaly in real operation can result in severe equipment damage, production downtime, or catastrophic events.

In summary, the developed LSTM autoencoder demonstrated high reliability in identifying abnormal operating conditions in oil wells, particularly in recall, a critical requirement for safety–critical environments. By using the temporal dynamics contained in the 3W dataset, the model successfully captured subtle deviations from nominal behavior and translated them into meaningful anomaly scores. Although the approach still yields a non-negligible number of false positives, this trade-off is acceptable given the operational risks of missed detections. These results reinforce the suitability of deep learning methods for abnormal event management in oil production systems and highlight the potential of advanced sequence modelling techniques to improve further early warning capabilities and risk mitigation in industrial assets.

7.3 Outline of the Chapter

This chapter is structured into three main parts. First, ML-based surrogate modelling and multi-objective optimization are applied to energy-transition systems, namely hydrogen liquefaction cycles, using the same methodology previously employed in this thesis for magnetic refrigeration systems. Second, these surrogate modelling strategies are extended to oil and gas applications for large–scale sensitivity and uncertainty analysis of thermo–structural behavior in offshore wells. Finally, ML-based anomaly detection methods are applied to operational well data for abnormal event management. Throughout this chapter, a key principle is emphasized: in general, machine learning delivers the most significant impact when models and underlying datasets are designed, curated, and tailored to the specific physics and operational environment of interest. Although the applications explored here focus on energy transition and oil and gas systems, the methods demonstrated are general and directly transferable to a wide range of complex engineering problems requiring fast predictions, optimization, and decision support.

Chapter 8

FINAL REMARKS

This thesis is part of a project focused on the development and optimization of a magnetocaloric refrigeration system designed for air-conditioning applications, with a cooling capacity of 9,000 BTU/h between 22°C and 35°C. The primary goal of this work was to optimize, commission, and operationalize the system, followed by a comprehensive thermodynamic experimental evaluation of its performance. In addition, this study explored the application of artificial intelligence techniques to enhance system performance, reduce energy consumption, and optimize its overall operation. The artificial intelligence methods employed include machine learning models for both steady-state and transient behavior prediction, as well as uncertainty and sensitivity analysis for magnetocaloric materials and other system components.

The modeling of the magnetic refrigeration system was approached by developing artificial intelligence-based models for the active magnetic regenerator and the magnetic circuit, alongside analytical models for the heat exchangers and hydraulic management system. These models were integrated into a system-level simulation to minimize power consumption and cost while maximizing cooling capacity and efficiency. The optimization problem was addressed using the Non-dominated Sorting Genetic Algorithm II, which highlighted key trade-offs, particularly in magnetic flux density and mass flow rate. The final design was selected from the Pareto front using a weighted global criterion. One of the main contributions of this thesis is the exploration of machine learning as a means to reduce the time required for system design and optimization. Surrogate models based on artificial neural networks were developed for components of the magnetic refrigeration system. These models enabled a more efficient exploration of the design space and facilitated multi-objective optimization. By replacing computationally expensive simulations with high-speed predictions, the integration of surrogate models into genetic algorithms demonstrated that machine learning can significantly accelerate the identification of high-performance configurations that would otherwise be computationally prohibitive to explore.

This work also provides a detailed description of the design parameters for each component of the magnetic refrigeration unit, including the active magnetic regenerator, magnetic circuit, heat exchangers, and hydraulic management system. Information on the instrumentation and the calibrated calorimeter used for the system characterization is also included. The thesis describes the experimental evaluation of three generations of prototype configurations, focusing on the challenges faced and the rationale behind the design decisions.

A thorough thermodynamic analysis was conducted to identify the primary sources of irreversibilities and performance losses within the system and its components.

An advanced experimental evaluation of the magnetic refrigeration unit was conducted. The magnetic refrigeration unit was operated in accordance with international standards. Initial characterization was performed on the individual components of the system, including the magnetic circuit, magnetocaloric materials, active magnetic regenerators, and the hydraulic management system, to determine the operational limits of each component. The evaluation of the three generations of prototypes provided insights into the real-world behavior of these components and highlighted the main contributors to energy consumption and performance degradation. Through this experimental process, the fundamental thermodynamic challenges preventing magnetic refrigeration systems from achieving commercial viability were identified. Despite not meeting the originally designed specifications, mainly due to insufficient mass of magnetocaloric materials and uncertainties in the Curie temperatures, the magnetic refrigeration unit still demonstrated some of the highest cooling capacities and temperature spans ever reported for magnetic refrigeration systems. It is also one of the few prototypes worldwide capable of refrigerating a cold room.

As part of the operationalization of the system, artificial intelligence and machine learning techniques were applied to optimize its performance further. The first approach involved developing a general model to predict the performance of room-temperature magnetic refrigeration systems. A comprehensive review of available data from both literature and the laboratory was conducted, and the integration of physics-based principles into the artificial neural network models was explored. The model showed good agreement with experimental data, although care should be taken when applying or extrapolating its predictions. Strategies to improve model generalization, such as introducing Gaussian noise to input and output parameters and stratifying datasets by prototype, are recommended for exploration. In general, applications found that machine learning models are more effective when tailored to specific applications rather than generalized ones.

Two additional specific applications of artificial intelligence were developed within the context of this thesis. The first involved creating a transient model to predict the dynamic performance of the magnetic refrigeration unit. A curated dataset of experimental transient responses was used to train a specialized artificial neural network architecture capable of handling transient behavior. The results demonstrated that the model accurately predicted both short- and long-term performance in terms of temperature and power consumption and could be used to optimize the system through techniques such as model-predictive control.

The second application focused on evaluating the impact of uncertainties in the Curie Temperature on the performance of magnetic refrigeration systems. A dataset of numerical simulations for active magnetic regenerators composed of five, ten, and fifteen layers was

generated and used to train artificial neural networks. These models were subsequently applied to perform a Monte Carlo analysis. The results highlighted the significant challenge posed by material uncertainties in the development and widespread adoption of magnetic refrigeration. Although over-sizing components may help mitigate these uncertainties, reducing manufacturing process variability remains the most promising approach to addressing this issue.

This thesis also contributes to the broader application of machine learning-based frameworks. The optimization methodologies developed for magnetic refrigeration were successfully applied to energy transition technologies, particularly the precooling stage of hydrogen liquefaction cycles. By optimizing multi-component refrigerants with surrogate models, performance improvements were achieved beyond those attainable with conventional pure nitrogen precooling systems. These methods are now being employed in other applications, including the modeling and optimization of organic Rankine cycles, hydrogen fuel cells, and uncertainty analysis for carbon capture, utilization, and storage systems, specifically examining the effects of contaminants on the thermophysical properties of high-CO_2 mixtures.

Furthermore, these techniques were adapted for use in oil production systems. Surrogate models were applied to propagate uncertainties and quantify the impact of boundary conditions at the well head, the thermophysical properties of the fluids, and the geometric dimensions of the well on the thermostructural behavior in offshore wells, as captured by the annular pressure-build phenomena. Moreover, machine learning-based anomaly detection methods were used to analyze the three-way dataset for early detection of abnormal behavior in naturally flowing wells. The results demonstrated the reliability and industrial feasibility of these methods for real-world applications.

Taken together, these findings demonstrate that artificial intelligence is not just a supporting tool but an enabling technology with the potential to reshape how engineering systems are modeled, designed, optimized, and validated across sectors such as energy, manufacturing, and natural resource extraction.

8.1 Future Work

Although the present thesis demonstrated the feasibility and value of integrating Artificial Intelligence, experimentation, and thermodynamics for the development and assessment of magnetic refrigeration and related thermal systems, several promising research directions remain open and merit further investigation.

- To evaluate the performance of the magnetic refrigeration system with a fully optimized refrigerant load, including filling the prototype with the precise amount of refrigerant,

and assessing its impact on system efficiency and cooling capacity. This evaluation will also help determine the operational limits and performance ceiling of the system.

- To investigate novel magnetocaloric materials to enhance the performance and efficiency of the magnetic refrigeration system. This research could focus on improving the magnetic entropy change, Curie temperature, and mechanical and chemical stability, all of which are crucial for increasing the overall system efficiency and reducing energy consumption.

- To optimize the design of the mechanical transmission, structural components and hydraulic management system to operate optimally close to the performance of the prototype. This includes assessing the power consumption, flow characteristics, and mechanical losses within the system. The focus will be on minimizing energy losses, optimizing component efficiency, and ensuring stable operation under varying load conditions. Detailed analysis and experimental validation of the hydraulic management system pressure and flow characteristics, as well as mechanical efficiency improvements in the transmission system, will lead to a more efficient and reliable operation of the refrigeration unit.

- To redesign the coupling and auxiliary systems based on the learning from prior generations of prototypes. This includes refining the coupling between the magnetic regenerator and the motor, improving the efficiency of the auxiliary components such as pumps and fans, and addressing any identified weaknesses in the system design. Based on previous prototype evaluations, design modifications can be implemented to address issues like mechanical vibrations, component wear, and system efficiency. This would ensure that the system is not only more robust but also capable of operating at optimal performance over extended periods.

- To collect more experimental data, and include techniques such as group sampling and Gaussian noise to improve the robustness and generalization of the physics-guided artificial neural networks. These techniques can enhance the ability of the model to predict performance across a broader range of operating conditions, ensuring that the machine learning models remain effective even when faced with new, unseen data. Group sampling can better represent the variability in input parameters, while Gaussian noise can improve model generalization by preventing overfitting, leading to more reliable predictions and optimized system designs.

- To implement the dynamic artificial neural network in a predictive control system. This would involve integrating the neural network-based model into the control architecture of the system to enable real-time decision-making. The predictive control system can dynamically adjust operational parameters, optimizing system performance while

accounting for both transient and long-term behavior. This approach would lead to a more responsive and energy-efficient system, improving its ability to maintain desired cooling capacities and energy consumption levels under varying operating conditions.

- To evaluate the coupling between first and second-order magnetocaloric materials to reduce the effect of uncertainties on the Curie temperatures. This study could explore how different layers of magnetocaloric materials interact with respect to their thermodynamic properties and how to minimize uncertainty in Curie temperatures across the material stack. By improving the coupling and performance of these materials, the system can achieve more consistent thermal and magnetic behavior, thereby enhancing stability and reducing performance degradation caused by material variability. This approach would also help mitigate the impact of manufacturing-process uncertainties on the overall system performance.

- To continue exploring the use of machine learning and artificial intelligence in other thermophysical processes, components, and systems. Machine learning techniques can be applied further to enhance the performance and efficiency of components and systems. These methods could be used to develop advanced models for heat transfer optimization, fluid dynamics, and energy consumption reduction in other thermophysical systems.

- To explore the application of magnetic refrigeration in other niche areas, such as hydrogen liquefaction and vaccine storage. The potential for magnetocaloric refrigeration to contribute to hydrogen liquefaction processes lies in its ability to provide efficient, energy-saving cooling at cryogenic temperatures, a key requirement for hydrogen storage and transport. Additionally, in vaccine storage, especially for temperature-sensitive vaccines, magnetic refrigeration systems could provide an environmentally friendly alternative to conventional refrigeration methods, without the use of harmful refrigerants.

8.2 Closing Remarks

In conclusion, this thesis has advanced magnetocaloric refrigeration technology by developing an integrated design and optimization methodology that combines artificial intelligence, experimental validation, and thermodynamic analysis. The successful application of machine learning for surrogate modeling and multi-objective optimization has demonstrated its potential to reduce design and optimization time while improving system performance. Additionally, the experimental evaluation of the magnetic refrigeration unit provided invaluable insights into the real-world challenges and opportunities for further development.

Throughout this work, the potential of magnetocaloric refrigeration to revolutionize cooling technologies by providing an energy-efficient and environmentally friendly alternative to conventional systems was explored. By integrating artificial intelligence techniques into the design and operation of the system, this research has opened up new avenues for performance optimization, fault detection, and predictive maintenance, providing a strong foundation for future advancements in this field. Although the current work represents a significant step forward, several key areas remain for further exploration. Future research will need to address optimizing refrigerant load, exploring novel magnetocaloric materials, and refining system components to improve efficiency and scalability further. Furthermore, expanding the application of magnetic refrigeration systems to other industries, such as hydrogen liquefaction and vaccine storage, offers exciting opportunities to broaden the impact of this technology.

As we look toward the future, it is clear that integrating artificial intelligence with energy-efficient technologies such as magnetocaloric refrigeration will play a pivotal role in the transition to more sustainable systems. The findings and methodologies presented in this thesis demonstrate some of the potential for continued innovation, not only in refrigeration but also in a variety of thermophysical applications that can benefit from these advancements. The path forward holds immense promise for both the development of more efficient systems and the eventual widespread adoption of these technologies in critical sectors worldwide.

BIBLIOGRAPHY

ABADI, M.; AGARWAL, A.; BARHAM, P.; BREVDO, E.; CHEN, Z.; CITRO, C.; CORRADO, G. S.; DAVIS, A.; DEAN, J.; DEVIN, M.; GHEMAWAT, S.; GOODFELLOW, I.; HARP, A.; IRVING, G.; ISARD, M.; JIA, Y.; JOZEFOWICZ, R.; KAISER, L.; KUDLUR, M.; LEVENBERG, J.; MANé, D.; MONGA, R.; MOORE, S.; MURRAY, D.; OLAH, C.; SCHUSTER, M.; SHLENS, J.; STEINER, B.; SUTSKEVER, I.; TALWAR, K.; TUCKER, P.; VANHOUCKE, V.; VASUDEVAN, V.; VIéGAS, F.; VINYALS, O.; WARDEN, P.; WATTENBERG, M.; WICKE, M.; YU, Y.; ZHENG, X. *TensorFlow: Large-Scale Machine Learning on Heterogeneous Systems*. 2015. Software available from tensorflow.org.

ABAS, N.; KALAIR, A. R.; KHAN, N.; HAIDER, A.; SALEEM, Z.; SALEEM, M. S. Natural and synthetic refrigerants, global warming: A review. *Renewable and Sustainable Energy Reviews*, v. 90, p. 557 – 569, 2018.

ABNEY, S. Bootstrapping. In: *Proceedings of the 40th annual meeting of the Association for Computational Linguistics*. [S.l.: s.n.], 2002. p. 360–367.

ABNT/NBR-15372. *Resfriadores de ar para refrigeração - Métodos de ensaio*. [S.l.], 2006.

AHARONI, A. Demagnetizing factors for rectangular ferromagnetic prisms. *Journal of Applied Physics*, v. 83, p. 3432–3434, 1998.

ALI, P. J. M.; FARAJ, R. H.; KOYA, E.; ALI, P. J. M.; FARAJ, R. H. Data normalization and standardization: a technical report. *Mach Learn Tech Rep*, v. 1, n. 1, p. 1–6, 2014.

ALIBRAHIM, H.; LUDWIG, S. A. Hyperparameter optimization: Comparing genetic algorithm against grid search and bayesian optimization. In: IEEE. *2021 IEEE Congress on Evolutionary Computation (CEC)*. [S.l.], 2021. p. 1551–1559.

ALLISON, P. D. Missing data. *The SAGE handbook of quantitative methods in psychology*, Thousand Oaks, CA, p. 72–89, 2009.

ALVES, E. B. D. M.; CZUBINSKI, F. F.; LUCA, L. G. M. D.; JR, J. R. B. Investigation on the effects of thermophysical properties of drilling fluids on the simulation of thermally driven apb. In: *ENCIT 2022*. [S.l.: s.n.], 2022.

ANDREW, R. M. H.; SINGH, B. S. B.; REMELI, M. F.; PEIXER, G. F.; SINGH, W. K. R. Ai-enhanced generative design for efficient heat exchangers in thermoelectric generators: revolutionizing waste heat recovery in thermoelectricity/andrew robert martin hughes...[et al.]. *Journal of Mechanical Engineering (JMechE)*, UiTM Press, v. 13, n. 1, p. 235–255, 2024.

APICELLA, A.; DONNARUMMA, F.; ISGRÒ, F.; PREVETE, R. A survey on modern trainable activation functions. *Neural Networks*, Elsevier, v. 138, p. 14–32, 2021.

APREA, C.; CARDILLO, G.; GRECO, A.; MAIORINO, A.; MASSELLI, C. A rotary permanent magnet magnetic refrigerator based on amr cycle. *Applied Thermal Engineering*, v. 101, p. 699–703, 2016. ISSN 1359-4311.

APREA, C.; GRECO, A.; MAIORINO, A. A numerical analysis of an active magnetic regenerative refrigerant system with a multi-layer regenerator. *Energy conversion and management*, Elsevier, v. 52, n. 1, p. 97–107, 2011.

APREA, C.; GRECO, A.; MAIORINO, A. An application of the artificial neural network to optimise the energy performances of a magnetic refrigerator. *International Journal of Refrigeration*, v. 82, p. 238–251, 2017.

APREA, C.; GRECO, A.; MAIORINO, A.; MASTRULLO, R.; TURA, A. Initial experimental results from a rotary permanent magnet magnetic refrigerator. *International Journal of Refrigeration*, v. 43, p. 111–122, 2014. ISSN 0140-7007.

APREA, C.; GRECO, A.; MAIORINO, A.; MASSELLI, C. The energy performances of a rotary permanent magnet magnetic refrigerator. *International Journal of Refrigeration*, v. 61, p. 1–11, 2016. ISSN 0140-7007.

APREA, C.; GRECO, A.; MAIORINO, A.; MASSELLI, C. Energy performances and numerical investigation of solid-state magnetocaloric materials used as refrigerant in an active magnetic regenerator. *Thermal Science and Engineering Progress*, v. 6, p. 370 – 379, 2018.

ARNOLD, D.; TURA, A.; RUEBSAAT-TROTT, A.; ROWE, A. Design improvements of a permanent magnet active magnetic refrigerator. *International Journal of Refrigeration*, v. 37, p. 99 – 105, 2014.

ARORA, J. *Introduction to Optimum Design*. Cambridge, Massachusetts: Elsevier Science, 2004.

ARORA, N. K.; MISHRA, I. *COP26: more challenges than achievements*. [S.l.]: Springer, 2021. 585–588 p.

ASGARI, H.; CHEN, X.; MORINI, M.; PINELLI, M.; SAINUDIIN, R.; SPINA, P. R.; VENTURINI, M. NARX models for simulation of the start-up operation of a single-shaft gas turbine. *Applied Thermal Engineering*, v. 93, p. 368–376, 2016. ISSN 1359-4311.

ASGARI, S.; MIRHOSEININEJAD, S.; MOAZAMIGOODARZI, H.; GUPTA, R.; ZHENG, R.; PURI, I. K. A gray-box model for real-time transient temperature predictions in data centers. *Applied Thermal Engineering*, v. 185, p. 116319, 2021. ISSN 1359-4311.

ASSEN, M. van; MUSCOGIURI, E.; TESSARIN, G.; CECCO, C. N. D. Artificial intelligence: A century-old story. In: *Artificial Intelligence in Cardiothoracic Imaging*. [S.l.]: Springer, 2022. p. 3–13.

AULI, M.; GALLEY, M.; QUIRK, C.; ZWEIG, G. Joint language and translation modeling with recurrent neural networks. In: *Proc. of EMNLP*. [S.l.: s.n.], 2013.

AZIZ, M. Liquid hydrogen: A review on liquefaction, storage, transportation, and safety. *Energies*, MDPI, v. 14, p. 5917, 9 2021. ISSN 1996-1073.

BAHL, C.; ENGELBRECHT, K.; BJØRK, R.; ERIKSEN, D.; SMITH, A.; NIELSEN, K.; PRYDS, N. Design concepts for a continuously rotating active magnetic regenerator. *International Journal of Refrigeration*, v. 34, p. 1792 – 1796, 2011.

BAHL, C.; ENGELBRECHT, K.; ERIKSEN, D.; LOZANO, J.; BJØRK, R.; GEYTI, J.; NIELSEN, K.; SMITH, A.; PRYDS, N. Development and experimental results from a 1 kw prototype AMR. *International Journal of Refrigeration*, v. 37, p. 78 – 83, 2014.

BAHL, C.; PETERSEN, T.; PRYDS, N.; SMITH, A. A versatile magnetic refrigeration test device. *The Review of scientific instruments*, v. 79, 2008.

BAHL, C. R. H.; NIELSEN, K. K. The effect of demagnetization on the magnetocaloric properties of gadolinium. *Journal of Applied Physics*, American Institute of Physics, v. 105, p. 1 – 5, 2009.

BANK, D.; KOENIGSTEIN, N.; GIRYES, R. Autoencoders. *Machine learning for data science handbook: data mining and knowledge discovery handbook*, Springer, p. 353–374, 2023.

BANSAL, P.; VINEYARD, E.; ABDELAZIZ, O. Status of not-in-kind refrigeration technologies for household space conditioning, water heating and food refrigeration. *International Journal of Sustainable Built Environment*, v. 1, p. 85 – 101, 2012.

J. A. Barclay & W. A. Steyert. *Active Magnetic Regenerator*. 1982. US Patent No. 4332135.

BELL, I. H.; WRONSKI, J.; QUOILIN, S.; LEMORT, V. Pure and pseudo-pure fluid thermophysical property evaluation and the open-source thermophysical property library coolprop. *Industrial & Engineering Chemistry Research*, v. 53, p. 2498–2508, 2014.

BELLARBY, J. *Well completion design*. [S.l.]: Elsevier, 2009.

BENKE, D.; FRIES, M.; SPECHT, M.; WORTMANN, J.; PABST, M.; GOTTSCHALL, T.; RADULOV, I.; SKOKOV, K.; BEVAN, A. I.; PROSPERI, D.; TUDOR, C. O.; AFIUNY, P.; ZAKOTNIK, M.; GUTFLEISCH, O. Magnetic refrigeration with recycled permanent magnets and free rare-earth magnetocaloric La–Fe–Si. *Energy Technology*, v. 8, n. 7, 2020.

BERGSTRA, J.; BENGIO, Y. Random search for hyper-parameter optimization. *Journal of Machine Learning Research*, v. 13, n. 2, p. 281–305, 2012.

BERRAR, D. *et al. Cross-validation.* 2019.

BEZ, H. N. *Magnetocaloric materials and first order phase transitions*. Phd Thesis (PhD Thesis) — Technical University of Denmark, 2016.

BEZ, H. N.; NAKASHIMA, A. T. D.; LANG, G. B.; LIMA, B. S. de; MACHADO, A. J. S.; LOZANO, J. A.; BARBOSA Jr., J. R. Performance assessment and layer fraction optimization of Gd-Y multilayer regenerators for near room-temperature magnetic cooling. *International Journal of Air-Conditioning and Refrigeration*,, v. 28, p. 2050027, 2020.

BIKMUKHAMETOV, T.; JÄSCHKE, J. Combining machine learning and process engineering physics towards enhanced accuracy and explainability of data-driven models. *Computers & Chemical Engineering*, Elsevier, v. 138, p. 106834, 2020.

BINGHAM, G.; MACKE, W.; MIIKKULAINEN, R. Evolutionary optimization of deep learning activation functions. In: . [S.l.: s.n.], 2020. p. 289–296.

BJORCK, J.; GOMES, C. P.; SELMAN, B. Understanding batch normalization. *CoRR*, abs/1806.02375, 2018.

BJØRK, R.; BAHL, C.; NIELSEN, K. The lifetime cost of a magnetic refrigerator. *International Journal of Refrigeration*, Elsevier, v. 63, p. 48–62, 2016.

BJØRK, R.; BAHL, C.; SMITH, A.; CHRISTENSEN, D.; PRYDS, N. An optimized magnet for magnetic refrigeration. *Journal of Magnetism and Magnetic Materials*, v. 322, p. 3324 – 3328, 2010.

BJØRK, R.; BAHL, C.; SMITH, A.; PRYDS, N. Review and comparison of magnet designs for magnetic refrigeration. *arXiv e-prints*, p. arXiv–1409, 2014.

BLANK, J.; DEB, K. Pymoo: Multi-objective optimization in python. *Ieee access*, IEEE, v. 8, p. 89497–89509, 2020.

BOCANEGRA, J. A.; SCARPA, F.; FANGHELLA, P.; MARCHITTO, A.; TAGLIAFICO, L. A. Optimization and development of a new rotary magnetic refrigerator. *Clean Technologies and Environmental Policy*, Springer, p. 1–14, 2024.

BOLES, M.; CENGEL, D. Y. A. *Thermodynamics: An Engineering Approach*. New York ,USA: McGraw-Hill Education, 2014.

BORDIGNON, J. C.; DIAS, T. Z.; SGANZERLA, Y. F.; PEIXER, G. F.; LOZANO, J. A.; BARBOSA Jr., J. R. Hydrogen liquefaction, a review of the ongoing methods and a critical analysis of the current studies. In: *COBEM 2023 - 27th International Congress of Mechanical Engineering*. Florianópolis: [s.n.], 2023.

BORDIGNON, J. C.; PEIXER, G. F.; LOZANO, J. A.; BARBOSA Jr., J. R. Integrated thermoeconomic optimization of organic rankine cycles via artificial neural networks and multi-objective genetic algorithms. In: *COBEM 2025 - 28th International Congress of Mechanical Engineering*. Curitiba: [s.n.], 2025.

BOUSSAADA, Z.; CUREA, O.; REMACI, A.; CAMBLONG, H.; BELLAAJ, N. M. A nonlinear autoregressive exogenous (NARX) neural network model for the prediction of the daily direct solar radiation. *Energies*, v. 11, n. 3, p. 620, 2018. ISSN 1996-1073.

BRANKE, J.; DEB, K.; MIETTINEN, K.; SŁOWIUNDEFINEDSKI, R. *Multiobjective Optimization: Interactive and Evolutionary Approaches*. Berlin, Heidelberg: Springer-Verlag, 2008.

BREIMAN, L. Random forests. *Machine learning*, Springer, v. 45, p. 5–32, 2001.

BROWN, T. B.; MANN, B.; RYDER, N.; SUBBIAH, M.; KAPLAN, J.; DHARIWAL, P.; NEELAKANTAN, A.; SHYAM, P.; SASTRY, G.; ASKELL, A.; AGARWAL, S.; HERBERT-VOSS, A.; KRUEGER, G.; HENIGHAN, T.; CHILD, R.; RAMESH, A.; ZIEGLER, D. M.; WU, J.; WINTER, C.; HESSE, C.; CHEN, M.; SIGLER, E.; LITWIN, M.; GRAY, S.; CHESS, B.; CLARK, J.; BERNER, C.; MCCANDLISH, S.; RADFORD, A.; SUTSKEVER, I.; AMODEI, D. Language models are few-shot learners. *CoRR*, abs/2005.14165, 2020.

BRUNTON, S. L.; KUTZ, J. N. *Data-driven science and engineering: Machine learning, dynamical systems, and control*. [S.l.]: Cambridge University Press, 2022.

BRüCK, E. Developments in magnetocaloric refrigeration. *Journal of Physics D: Applied Physics*, v. 38, p. R381, 2005.

BRüCK, E.; TEGUS, O.; THANH, D. C.; TRUNG, N. T.; BUSCHOW, K. A review on Mn based materials for magnetic refrigeration: Structure and properties. *International Journal of Refrigeration*, v. 31, p. 763 – 770, 2008.

BUI, M.; ADJIMAN, C. S.; BARDOW, A.; ANTHONY, E. J.; BOSTON, A.; BROWN, S.; FENNELL, P. S.; FUSS, S.; GALINDO, A.; HACKETT, L. A. *et al.* Carbon capture and storage (ccs): the way forward. *Energy & Environmental Science*, Royal Society of Chemistry, v. 11, n. 5, p. 1062–1176, 2018.

BURDYNY, T.; ARNOLD, D. S.; ROWE, A. AMR thermodynamics: Semi-analytic modeling. *Cryogenics*, v. 62, p. 177 – 184, 2014.

CACUCI, D. G.; IONESCU-BUJOR, M. A comparative review of sensitivity and uncertainty analysis of large-scale systems—ii: statistical methods. *Nuclear science and engineering*, Taylor & Francis, v. 147, n. 3, p. 204–217, 2004.

CAKRA, Y. E.; TRISEDYA, B. D. Stock price prediction using linear regression based on sentiment analysis. In: IEEE. *2015 international conference on advanced computer science and information systems (ICACSIS)*. [S.l.], 2015. p. 147–154.

CALOMENO, R. S.; DUTRA, S. L.; de Sá, N. M.; PEIXER, G. F.; LOZANO, J. A.; BARBOSA Jr., J. R. Temperature pull-down of a retrofitted wine refrigerator cabinet cooled by a caloric system emulator. *Anais da Academia Brasileira de Ciências*, SciELO Brasil, v. 94, p. e20201510, 2022.

CANIZO, M.; TRIGUERO, I.; CONDE, A.; ONIEVA, E. Multi-head CNN–RNN for multi-time series anomaly detection: an industrial case study. *Neurocomputing*, v. 363, p. 246–260, 2019.

CAPOVILLA, M. S.; LOZANO, J. A.; TREVIZOLI, P. V.; BARBOSA Jr., J. R. Performance evaluation of a magnetic refrigeration system. *Science and Technology for the Built Environment*, Taylor & Francis, v. 22, n. 5, p. 534–543, 2016.

CASTRO-ANAYA, L. E.; MARESE, E.; LOZANO, J. A.; PEIXER, G. F.; JR, J. R. B.; GONZALEZ, S. Y. G. Machine learning methodologies applied to magnetocaloric perovskites discovery. *Journal of Chemical Information and Modeling*, ACS Publications, 2025.

CATTELAN, L. F.; PEIXER, G. F.; LUZ, M. V. D.; BARBOSA Jr., J. R.; LOZANO, J. A. Design of magnetic circuits for magnetocaloric refrigeration via topology optimization. *IEEE Transactions on Magnetics*, IEEE, 2024.

CERUTTI, M. A.; PEIXER, G. F.; LOZANO, J. A.; BARBOSA Jr., J. R. Evaluation of machine learning models to predict the thermal performance of active magnetic regenerators. In: *ENCIT: 19th Brazilian Congress of Thermal Sciences and Engineering*. Bento Gonçalves: [s.n.], 2022.

CERUTTI, M. A.; PEIXER, G. F.; LOZANO, J. A.; BARBOSA Jr., J. R. AiMR: Artificial intelligence for active magnetic regenerators. Brazilian Patent No. BR 10 2024 01263-0. Instituto Nacional de Propriedade Industrial. Registered on 18/04/2024. 2024.

CHANDRA, A.; BAKARJI, J.; TARTAKOVSKY, D. M. Role of physics in physics-informed machine learning. *Journal of Machine Learning for Modeling and Computing*, Begel House Inc., v. 5, n. 1, 2024.

CHANDRA, A.; KAPOOR, T.; DANIELS, B.; CURTI, M.; TIELS, K.; TARTAKOVSKY, D. M.; LOMONOVA, E. A. Generalizable models of magnetic hysteresis via physics-aware recurrent neural networks. *Computer Physics Communications*, Elsevier, p. 109650, 2025.

CHANG, C.-W.; DINH, N. T. Classification of machine learning frameworks for data-driven thermal fluid models. *International Journal of Thermal Sciences*, Elsevier BV, v. 135, p. 559–579, Jan. 2019. ISSN 1290-0729.

CHANG, H. S.; FU, M. C.; HU, J.; MARCUS, S. I. Google DeepMind's AlphaGo: operations research's unheralded role in the path-breaking achievement. *Or/Ms Today*, Institute for Operations Research and the Management Sciences, v. 43, n. 5, p. 24–30, 2016.

CHANG, S. E.; STONE, J.; DEMES, K.; PISCITELLI, M. Consequences of oil spills: a review and framework for informing planning. *Ecology and Society*, JSTOR, v. 19, n. 2, 2014.

CHATTERJEE, J.; DETHLEFS, N. Scientometric review of artificial intelligence for operations & maintenance of wind turbines: The past, present and future. *Renewable and Sustainable Energy Reviews*, Elsevier, v. 144, p. 111051, 2021.

CHAUHAN, R.; GHANSHALA, K. K.; JOSHI, R. Convolutional neural network (CNN) for image detection and recognition. In: IEEE. *2018 first international conference on secure cyber computing and communication (ICSCCC)*. [S.l.], 2018. p. 278–282.

Jeremy Chell & Carl Zimm. *Permanent Magnet Assembly*. 2006. US Patent No. 7148777 B2.

CHEN, C. T. A. Specific heat capacities of aqueous sodium chloride solutions at high pressures. *Journal of Chemical and Engineering Data*, ACS Publications, v. 27, n. 3, p. 356–358, 1982.

CHEN, S.; SHEN, Y.; QIU, C.; TAO, X.; WAN, A.; ZHANG, Z.; GAN, Z. Multi-objective optimization of a hydrogen liquefaction process coupled with mixed refrigerant cycle and steam methane reforming. *International Journal of Hydrogen Energy*, Elsevier, v. 58, p. 797–805, 2024.

CHEN, T. XGBoost: extreme gradient boosting. *R package version 0.4-2*, v. 1, n. 4, 2015.

CHOLLET, F. *et al. Keras*. [S.l.]: GitHub, 2015.

CHUNG, J.; GULCEHRE, C.; CHO, K.; BENGIO, Y. Empirical evaluation of gated recurrent neural networks on sequence modeling. *arXiv preprint arXiv:1412.3555*, 2014.

CHURCHILL, S. W. Friction-factor equation spans all fluid-flow regimes. *Chemical Engineering (New York)*, v. 84, p. 91–92, 1977.

COEY, J. M. *Magnetism and magnetic materials*. [S.l.]: Cambridge university press, 2010.

CORTES, C.; MOHRI, M.; ROSTAMIZADEH, A. L2 regularization for learning kernels. *arXiv preprint arXiv:1205.2653*, 2012.

DALL'OLIO, S.; MASCHE, M.; LIANG, J.; INSINGA, A.; ERIKSEN, D.; BJøRK, R.; NIELSEN, K.; BARCZA, A.; VIEYRA, H.; BEEK, N. V.; BEZ, H. N.; ENGELBRECHT, K.; BAHL, C. Novel design of a high efficiency multi-bed active magnetic regenerator heat pump. *International Journal of Refrigeration*, v. 132, p. 243–254, 2021. ISSN 0140-7007.

DATTA, L. A survey on activation functions and their relation with xavier and he normal initialization. *arXiv preprint arXiv:2004.06632*, 2020.

DAW, A.; KARPATNE, A.; WATKINS, W.; READ, J.; KUMAR, V. *Physics-guided Neural Networks (PGNN): An Application in Lake Temperature Modeling*. 2021.

de SÁ, N. M.; NAKASHIMA, A. T. D.; LOZANO, J. A.; JR., J. R. B. Thermodynamic comparison of magnetocaloric and vapor compression wine coolers. *International Journal of Refrigeration*, v. 156, p. 29–39, 2023.

DEB, K.; PRATAP, A.; AGARWAL, S.; MEYARIVAN, T. A fast and elitist multiobjective genetic algorithm: Nsga-ii. *IEEE transactions on evolutionary computation*, IEEE, v. 6, n. 2, p. 182–197, 2002.

DEFLORIAN, M.; ZAGLAUER, S. Design of Experiments for nonlinear dynamic system identification. In: *Proceedings in Eighteenth International Federation of Automatic Control World Congress (IFAC'11)*. Milan, Italy: [s.n.], 2011. p. 226–231.

DEVASENAN, M.; MADHAVAN, S. Thermal intelligence: exploring AI's role in optimizing thermal systems–a review. *Interactions*, Springer, v. 245, n. 1, p. 282, 2024.

DEVELOPERS, T. Tensorflow. *Zenodo*, 2022.

DEVLIN, J. Bert: Pre-training of deep bidirectional transformers for language understanding. *arXiv preprint arXiv:1810.04805*, 2018.

DOMANSKI, P. A.; DIDION, D. A. *Computer Modeling of the Vapor Compression Cycle with Constant Flow Area Expansion Device*. Washington, USA, 1983.

DONG, G.; CHEN, P. A review of the evaluation methods and control technologies for trapped annular pressure in deepwater oil and gas wells. *Journal of Natural Gas Science and Engineering*, Elsevier, v. 37, p. 85–105, 2017.

DONG, Y.; COLEMAN, M.; MILLER, S. A. Greenhouse gas emissions from air conditioning and refrigeration service expansion in developing countries. *Annual Review of Environment and Resources*, Annual Reviews, v. 46, n. 1, p. 59–83, 2021.

DOYLE, F. J.; PEARSON, R. K.; OGUNNAIKE, B. A. *Identification and control using Volterra models*. [S.l.]: Springer, 2002. 314 p.

DUBEY, S. R.; SINGH, S. K.; CHAUDHURI, B. B. Activation functions in deep learning: A comprehensive survey and benchmark. *Neurocomputing*, Elsevier, v. 503, p. 92–108, 2022.

DöRING, A.; REIF, D. D.; ROSA, M. A.; PEIXER, G. F.; MACCARI, F.; SKOKOV, K.; GUTFLEISCH, O.; WENDHAUSEN, P. A. P.; LOZANO, J. A.; BARBOSA Jr., J. R.; TEIXEIRA, C. S. Long-time aging of La(Fe,Si,Mn)$_{13}$HZ microparticles using different fluids for magnetic refrigeration systems. In: *INTERMAG 2024 - IEEE International Magnetics Conference*. Rio de Janeiro: [s.n.], 2024.

DöRING, A. M.; REIF, D. D. de A. C.; ROSA, M. A.; PEIXER, G. F.; MACCARI, F.; SKOKOV, K.; GUTFLEISCH, O.; WENDHAUSEN, P. A. P.; LOZANO, J. A.; BARBOSA Jr., J. R.; Teixeira, C. S. Long-time aging of La(Fe,Si,Mn)$_{13}$H$_z$ microparticles using different fluids for magnetic refrigeration systems. *Journal of Magnetism and Magnetic Materials*, v. 591, p. 171721, 2024.

ELANCHEZHIYAN, S.; PRABHU, S. M.; MEENAKSHI, S. Treatment of emulsified oil using biopolymer assisted materials. *Polymer Composites*, v. 39, 2016.

ELMAZ, F.; YüCEL, O. Data-driven identification and model predictive control of biomass gasification process for maximum energy production. *Energy*, v. 195, p. 117037, 2020. ISSN 0360-5442.

ELMRABIT, N.; ZHOU, F.; LI, F.; ZHOU, H. Evaluation of machine learning algorithms for anomaly detection. In: IEEE. *2020 international conference on cyber security and protection of digital services (cyber security)*. [S.l.], 2020. p. 1–8.

ELSHEIKH, A. H. Applications of machine learning in friction stir welding: Prediction of joint properties, real-time control and tool failure diagnosis. *Engineering Applications of Artificial Intelligence*, Elsevier, v. 121, p. 105961, 2023.

ENGELBRECHT, K. *A Numerical Model of an Active Magnetic Regenerator Refrigerator with Experimental Validation*. Phd Thesis (PhD Thesis) — University of Wisconsin-Madison, 2008.

ENGELBRECHT, K.; ERIKSEN, D.; BAHL, C.; BJØRK, R.; GEYTI, J.; LOZANO, J.; NIELSEN, K.; SAXILD, F.; SMITH, A.; PRYDS, N. Experimental results for a novel rotary active magnetic regenerator. *International Journal of Refrigeration*, v. 35, p. 1498 – 1505, 2012.

ERGUN, S. Fluid flow through packed collumn. *Chemical Engineering Progress*, v. 48, p. 89 – 94, 1952.

ERIKSEN, D.; ENGELBRECHT, K.; BAHL, C.; BJØRK, R.; NIELSEN, K.; INSINGA, A.; PRYDS, N. Design and experimental tests of a rotary active magnetic regenerator prototype. *International Journal of Refrigeration*, v. 58, p. 14 – 21, 2015.

ESDU. *Design and Performance Evaluation of Heat Exchangers: The Effectiveness NTU Method, Parts 1–5*. London, UK: ESDU International plc, 1998.

FARIA, P. V.; VIEIRA, B. P.; TEZA, H. F.; HOFFMANN, G.; PEIXER, G. F.; NAKASHIMA, A. T. D.; LOZANO, J. A.; BARBOSA Jr., J. R. Thermal-hydraulic characterization of a triangular micro channel regenerator via the single-blow method. In: *ENCIT: 19th Brazilian Congress of Thermal Sciences and Engineering*. Bento Gonçalves: [s.n.], 2022.

FARIA, P. V. de. Caracterização termo-hidráulica e magnética de regeneradores magnético ativos em ligas de La-Fe-Si com geometria de microcanais triangulares. Master's thesis, Universidade Federal de Santa Catarina, Florianópolis, Brazil. 2022.

FERNANDES Jr, W.; KOMATI, K. S.; GAZOLLI, K. Assis de S. Anomaly detection in oil-producing wells: a comparative study of one-class classifiers in a multivariate time series dataset. *Journal of Petroleum Exploration and Production Technology*, Springer, v. 14, n. 1, p. 343–363, 2024.

FERREIRA, M. V.; HAFEMANN, T. E.; JR, J. R. B.; SILVA, A. K. da; HASAN, R. A numerical study on the thermal behavior of wellbores. *SPE Production & Operations*, SPE, v. 32, n. 04, p. 564–574, 2017.

FEURER, M.; HUTTER, F. Hyperparameter optimization. *Automated machine learning: Methods, systems, challenges*, Springer International Publishing, p. 3–33, 2019.

FILHO, L. E. da S.; SILVA, T. B. da; FERNANDES, C. N. de A.; LIRA, W. W. M.; SANTOS, J. P. L.; SOUZA, C. O. de; SILVA, E. C. C. M. da. Sa of thermal phenomena in apb in oil wells. In: *Ibero-Latin American Congress on Computational Methods in Engineering (CILAMCE)*. [S.l.: s.n.], 2024.

FISCHER, L.; EHRLINGER, L.; GEIST, V.; RAMLER, R.; SOBIEZKY, F.; ZELLINGER, W.; BRUNNER, D.; KUMAR, M.; MOSER, B. AI system engineering—key challenges and lessons learned. *Machine Learning and Knowledge Extraction*, MDPI, v. 3, n. 1, p. 56–83, 2020.

FLORESCU, M. S.; CEPTUREANU, E. G.; CRUCERU, A. F.; CEPTUREANU, S. I. Sustainable supply chain management strategy influence on supply chain management functions in the oil and gas distribution industry. *Energies*, v. 12, p. 1632, 2019.

FONSECA, C.; FLEMING, P. Genetic algorithms for multiobjective optimization: Formulation discussion and generalization. *the fifth International conference on Genetic Algorithms*, v. 93, 02 1999.

FONSECA, C. M.; Fleming, P. J. Multiobjective optimization and multiple constraint handling with evolutionary algorithms. ii. application example. *IEEE Transactions on Systems, Man, and Cybernetics - Part A: Systems and Humans*, v. 28, n. 1, p. 38–47, 1998.

FORTKAMP, F.; ALVES, E. B. D. M.; VIEIRA, B. P.; PEIXER, G. F.; PEREIRA, M. A.; VEIGA, A. P.; VICENTE, A. S. M.; BARBOSA Jr., J. R. Wellboreprops: um pacote computacional para cálculo de propriedades de fluidos de poços. In: *ENAHPE: Encontro Nacional de Construção de Poços de Petróleo e Gás*. Matinhos: [s.n.], 2023.

FORTKAMP, F.; ERIKSEN, D.; ENGELBRECHT, K.; BAHL, C.; LOZANO, J.; BARBOSA Jr., J. R. Experimental investigation of different fluid flow profiles in a rotary multi-bed active magnetic regenerator device. *International Journal of Refrigeration*, v. 91, p. 46 – 54, 2018.

FORTKAMP, F. P.; LANG, G. B.; LOZANO, J. A.; BARBOSA Jr., J. R. Design trade-offs for an active magnetic regenerator device. *Applied Thermal Engineering*, v. 165, 2020.

FORTKAMP, F. P.; LANG, G. B.; LOZANO, J. A.; BARBOSA Jr., J. R. Numerical analysis of the influence of magnetic field waveforms on the performance of active magnetic regenerators. *Journal of the Brazilian Society of Mechanical Sciences and Engineering*, Springer Berlin Heidelberg, v. 42, n. 7, p. 378, 2020. ISSN 18063691.

FORTKAMP, F. P.; NAKASHIMA, A. T.; dos SANTOS, V. M.; LOZANO, J. A.; BARBOSA, J. R. Computationally-efficient optimization of the remanence angles of permanent magnet circuits for magnetic refrigeration. *Journal of Magnetism and Magnetic Materials*, v. 569, p. 170429, 2023. ISSN 0304-8853.

FOX, R.; MCDONALD, A.; PRITCHARD, P. *Introdução à mecânica dos fluidos*. [S.l.]: LTC, 2014.

FRANCESCHI, L.; DONINI, M.; FRASCONI, P.; PONTIL, M. Forward and reverse gradient-based hyperparameter optimization. In: PMLR. *International Conference on Machine Learning*. [S.l.], 2017. p. 1165–1173.

FRANCO, V. Magnetocaloric characterization of materials. In: ____. *Magnetic Measurement Techniques for Materials Characterization*. Cham: Springer International Publishing, 2021. p. 697–726. ISBN 978-3-030-70443-8.

FRERKING, M. JPL technology readiness level assessment guideline. *IEEE Aerospace Conference Proceedings*, 2016.

GAUß, R.; HOMM, G.; GUTFLEISCH, O. The resource basis of magnetic refrigeration. *Journal of Industrial Ecology*, v. 21, p. 1291–1300, 2017.

GHAFRI, S. Z. A.; MUNRO, S.; CARDELLA, U.; FUNKE, T.; NOTARDONATO, W.; TRUSLER, J. M.; LEACHMAN, J.; SPAN, R.; KAMIYA, S.; PEARCE, G. *et al.* Hydrogen liquefaction: a review of the fundamental physics, engineering practice and future opportunities. *Energy & environmental science*, Royal Society of Chemistry, v. 15, n. 7, p. 2690–2731, 2022.

GHAHRAMANI, Z. Unsupervised learning. In: *Summer school on machine learning*. [S.l.]: Springer, 2003. p. 72–112.

GLOROT, X.; BENGIO, Y. Understanding the difficulty of training deep feedforward neural networks. In: JMLR WORKSHOP AND CONFERENCE PROCEEDINGS. *Proceedings of the thirteenth international conference on artificial intelligence and statistics*. [S.l.], 2010. p. 249–256.

GNIELINSKI, V. New Equations for Heat and Mass Transfer in Turbulent Pipe and Channel Flow. *International Chemical Engineering*, 1976.

GOKHALE, G.; CLAESSENS, B.; DEVELDER, C. Physics informed neural networks for control oriented thermal modeling of buildings. *Applied Energy*, v. 314, p. 118852, 2022. ISSN 0306-2619.

GOLDSTEIN, E. B.; COCO, G. *Machine learning components in deterministic models: hybrid synergy in the age of data*. [S.l.]: Frontiers Media SA, 2015. 33 p.

GONG, S. A collaborative filtering recommendation algorithm based on user clustering and item clustering. *J. Softw.*, Citeseer, v. 5, n. 7, p. 745–752, 2010.

GONZALEZ, J. A. T.; LONGINOTTI, M. P.; CORTI, H. R. The viscosity of glycerol- water mixtures including the supercooled region. *Journal of Chemical & Engineering Data*, ACS Publications, v. 56, n. 4, p. 1397–1406, 2011.

GOSNEY, W. *Principles of Refrigeration*. Cambridge, United Kingdom: Cambridge University Press, 1982.

GOTTSCHALL, T.; SKOKOV, K. P.; FRIES, M.; TAUBEL, A.; RADULOV, I.; SCHEIBEL, F.; BENKE, D.; RIEGG, S.; GUTFLEISCH, O. Making a cool choice: the materials library of magnetic refrigeration. *Advanced Energy Materials*, Wiley Online Library, v. 9, n. 34, p. 1901322, 2019.

GRAVES, A.; GRAVES, A. Long short-term memory. *Supervised sequence labelling with recurrent neural networks*, Springer, p. 37–45, 2012.

GRECO, A.; APREA, C.; MAIORINO, A.; MASSELLI, C. A review of the state of the art of solid-state caloric cooling processes at room-temperature before 2019. *International Journal of Refrigeration*, v. 106, p. 66–88, 2019. ISSN 0140-7007.

GUIÑÓN, J. L.; ORTEGA, E.; GARCÍA-ANTÓN, J.; PÉREZ-HERRANZ, V. Moving average and savitzki-golay smoothing filters using mathcad. *Papers ICEE*, v. 2007, p. 1–4, 2007.

GUO, B. *Petroleum production engineering, a computer-assisted approach*. [S.l.]: Elsevier, 2011.

GUO, X.-Q.; SUN, C.-Y.; RONG, S.-X.; CHEN, G.-J.; GUO, T.-M. Equation of state analog correlations for the viscosity and thermal conductivity of hydrocarbons and reservoir fluids. *Journal of Petroleum Science and Engineering*, Elsevier, v. 30, n. 1, p. 15–27, 2001.

GUTFLEISCH, O.; WILLARD, M. A.; BRÜCK, E.; CHEN, C. H.; SANKAR, S. G.; LIU, J. P. *Magnetic materials and devices for the 21st century: Stronger, lighter, and more energy efficient*. 2011.

HA, T. M. Two-phase defect detection using clustering and classification methods. *REV Journal on Electronics and Communications*, v. 12, 2022.

HAI, P.; SHEN, J.; LI, Z.; LI, K.; DAI, W. Development and experimental analysis of a multi-bed active magnetic regenerator. *International Journal of Refrigeration*, Elsevier, v. 162, p. 169–178, 2024.

HALAL, A.; MITCHELL, R. Casing design for trapped apb. *SPE Drilling & Completion*, OnePetro, v. 9, n. 02, p. 107–114, 1994.

HAYKIN, S. *Neural Networks and Learning Machines*. [S.l.]: Pearson, 2009.

HEATH, E. A. Amendment to the montreal protocol on substances that deplete the ozone layer (kigali amendment). *International Legal Materials*, Cambridge University Press, v. 56, n. 1, p. 193–205, 2017.

HERMES, C. J.; MELO, C. A first-principles simulation model for the start-up and cycling transients of household refrigerators. *International Journal of Refrigeration*, v. 31, n. 8, p. 1341–1357, 2008. ISSN 0140-7007.

HEWAMALAGE, H.; BERGMEIR, C.; BANDARA, K. Recurrent neural networks for time series forecasting: Current status and future directions. *International Journal of Forecasting*, Elsevier, v. 37, n. 1, p. 388–427, 2021.

HITTINGER, M.; CHAUDRON, J.-B.; ELOUAD, L.; MULLER, C.; HAEGEL, P.; VASILE, C. Impact of the integration work on the performance measurements of the magnetocaloric cooling system and its target refrigerated cabinet. In: *Seventh IIF-IIR International Conference on Magnetic Refrigeration at Room Temperature, THERMAG VII*. Torino, Italy: [s.n.], 2016.

HOFFMANN, G.; NAKASHIMA, A. T.; PEIXER, G. F.; LOZANO, J. A.; FLESCH, R. C. C.; BARBOSA Jr., J. R. Cabinet temperature control logic in a magnetic refrigerator. In: *Nineth IIR International Conference on Caloric Cooling and Applications of Caloric Materials, THERMAG IX*. Maryland, United States: [s.n.], 2021.

HOFFMANN, G.; NAKASHIMA, A. T.; PEIXER, G. F.; LOZANO, J. A.; BARBOSA Jr., J. R.; FLESCH, R. C. Static and dynamic modeling and identification of a magnetic refrigerator. *International Journal of Refrigeration*, Elsevier, v. 158, p. 303–312, 2024.

HORN, J.; NAFPLIOTIS, N.; GOLDBERG, D. A niched pareto genetic algorithm for multi-objective optimization. In: . [S.l.: s.n.], 1994. v. 1, p. 82 – 87 vol.1. ISBN 0-7803-1899-4.

HOROWITZ, C. A. Paris agreement. *International Legal Materials*, v. 55, n. 4, p. 740–755, 2016.

HSU, F.-h. Ibm's deep blue chess grandmaster chips. *IEEE micro*, IEEE, v. 19, n. 2, p. 70–81, 1999.

HUANG, B.; LAI, J.; ZENG, D.; ZHENG, Z.; HARRISON, B.; OORT, A.; van DIJK, N.; BRüCK, E. Development of an experimental rotary magnetic refrigerator prototype. *International Journal of Refrigeration*, v. 104, p. 42–50, 2019. ISSN 0140-7007.

IEA. *The Future of Cooling*. [S.l.], 2018.

IEA. *The Future of Hydrogen*. 2019.

IEA. *CCUS in Clean Energy Transitions*. [S.l.], 2020.

IEA. *Net Zero by 2050*. [S.l.], 2021.

IEA. *Tracking Clean Energy Progress 2023*. [S.l.], 2023.

IEA. *Oil 2024*. [S.l.], 2024.

IIR. *IIR Informatory Note highlights global air conditioning's CO2 emissions and energy impact*. [S.l.], 2024.

IIR. *The Role of Refrigeration in the Global Economy 3rd edition, 60th IIR Technical Brief on Refrigeration Technologies.*. 35th Informatory Note on Refrigeration Technologies. International Institute of Refrigeration. Technical Report. Paris, France, 2025.

ILYAS, I. F.; CHU, X. *Data cleaning*. [S.l.]: Morgan & Claypool, 2019.

INCROPERA, F. P.; DEWITT, D. P.; BERGMAN, T. L.; LAVINE, A. S. *Fundamentals of Heat and Mass Transfer 6th Edition*. Hoboken, USA: John Wiley and Sons, 2007.

INMETRO. *Portaria n.º 007 - Requisitos de avaliação da conformidade para condicionadores de ar.* [S.l.], 2011.

INMETRO. *Portaria n.º 643 - Requisitos de avaliação da conformidade para condicionadores de ar.* [S.l.], 2012.

INMETRO. *Portaria n.º 410 - Requisitos de avaliação da conformidade para condicionadores de ar.* [S.l.], 2013.

INSINGA, A. R.; BJøRK, R.; SMITH, A.; BAHL, C. R. H. Optimally segmented permanent magnet structures. *IEEE Transactions on Magnetics*, v. 52, n. 12, p. 1–6, 2016.

IOFFE, S.; SZEGEDY, C. Batch normalization: Accelerating deep network training by reducing internal covariate shift. *CoRR*, abs/1502.03167, 2015.

IOFFE, S.; SZEGEDY, C. *Batch Normalization: Accelerating Deep Network Training by Reducing Internal Covariate Shift*. [S.l.]: arXiv, 2015.

IONESCU-BUJOR, M.; CACUCI, D. G. A comparative review of sensitivity and uncertainty analysis of large-scale systems—i: Deterministic methods. *Nuclear science and engineering*, Taylor & Francis, v. 147, n. 3, p. 189–203, 2004.

IOOSS, B.; LEMAÎTRE, P. A review on global sensitivity analysis methods. *Uncertainty management in simulation-optimization of complex systems: algorithms and applications*, Springer, p. 101–122, 2015.

IRMAY, S. On the theoretical derivation of Darcy and Forchheimer formulas. *Transactions American Geophysical Union*, v. 39, p. 702–707, 1958.

ISO-5151. *Non-ducted air conditioners and heat pumps - Testing and rating for performance*. [S.l.], 2017.

IZANLOO, M.; ASLANI, A.; ZAHEDI, R. Development of a machine learning assessment method for renewable energy investment decision making. *Applied Energy*, v. 327, p. 120096, 2022. ISSN 0306-2619.

JABBAR, H.; KHAN, R. Z. Methods to avoid over-fitting and under-fitting in supervised machine learning (comparative study). *Computer Science, Communication and Instrumentation Devices*, Res. Publ Singapore, v. 70, n. 10.3850, p. 978–981, 2015.

JACOB, B.; KLIGYS, S.; CHEN, B.; ZHU, M.; TANG, M.; HOWARD, A. G.; ADAM, H.; KALENICHENKO, D. Quantization and training of neural networks for efficient integer-arithmetic-only inference. *CoRR*, abs/1712.05877, 2017.

JACOBS, S.; AURINGER, J.; BOEDER, A.; CHELL, J.; KOMOROWSKI, L.; LEONARD, J.; RUSSEK, S.; ZIMM, C. The performance of a large-scale rotary magnetic refrigerator. *International Journal of Refrigeration*, v. 37, p. 84–91, 2014.

JADHAV, A.; PRAMOD, D.; RAMANATHAN, K. Comparison of performance of data imputation methods for numeric dataset. *Applied Artificial Intelligence*, Taylor & Francis, v. 33, n. 10, p. 913–933, 2019.

JAMBOL, D. D.; SOFOLUWE, O. O.; UKATO, A.; OCHULOR, O. J. Transforming equipment management in oil and gas with ai-driven predictive maintenance. *Computer Science & IT Research Journal*, v. 5, n. 5, p. 1090–1112, 2024.

JAMEI, M.; SAID, Z. Recent advances in the prediction of thermophysical properties of nanofluids using artificial intelligence. *Hybrid Nanofluids*, Elsevier, p. 203–232, 2022.

JARADAT, Y.; MASOUD, M.; JANNOUD, I.; MANASRAH, A.; ALIA, M. A tutorial on singular value decomposition with applications on image compression and dimensionality reduction. In: IEEE. *2021 international conference on information technology (ICIT)*. [S.l.], 2021. p. 769–772.

JIA, X.; WILLARD, J.; KARPATNE, A.; READ, J. S.; ZWART, J. A.; STEINBACH, M.; KUMAR, V. Physics-guided machine learning for scientific discovery: An application in simulating lake temperature profiles. *ACM/IMS Transactions on Data Science*, ACM New York, NY, v. 2, n. 3, p. 1–26, 2021.

JOHANSSON, E.; DOWLA, F.; GOODMAN, D. Backpropagation learning for multilayer feed-forward neural networks using the conjugate gradient method. *International Journal of Neural Systems*, v. 02, 11 2011.

JOSEPH, V. R. Optimal ratio for data splitting. *Statistical Analysis and Data Mining: The ASA Data Science Journal*, Wiley Online Library, v. 15, n. 4, p. 531–538, 2022.

JR, W. M. Reservoir-fluid property correlations—state of the art. *SPE Reservoir Engineering*, SPE, v. 6, n. 02, p. 266–272, 1991.

JUANGSA, F. B.; PRANANTO, L. A.; MUFRODI, Z.; BUDIMAN, A.; ODA, T.; AZIZ, M. Highly energy-efficient combination of dehydrogenation of methylcyclohexane and hydrogen-based power generation. *Applied energy*, Elsevier, v. 226, p. 31–38, 2018.

JUNIOR, N. M.; AGOSTINI, C. E.; SANTOS, C. M. D.; ROMAN, R. S.; SCHNITZLER, E.; MAGALHÃES, M. D.; FERREIRA, M. V. D.; SOUZA, C. O. D. Structural analysis of thermal behavior on cooling trapped annular pressure in water and gas injection wells. In: OTC. *Offshore Technology Conference Brasil*. [S.l.], 2019. p. D031S032R005.

JÚNIOR, W. F.; VARGAS, R. E. V.; KOMATI, K. S.; GAZOLLI, K. A. de S. Detecçao de anomalias em poços produtores de petróleo usando aprendizado de máquina. In: *Congresso Brasileiro de Automática-CBA*. [S.l.: s.n.], 2020. v. 2, n. 1.

KAELBLING, L. P.; LITTMAN, M. L.; MOORE, A. W. Reinforcement learning: A survey. *Journal of artificial intelligence research*, v. 4, p. 237–285, 1996.

KAKAC, S.; LIU, H. *Heat Exchanhers: selection, rating and thermal design*. New York, USA: CRC Press, 2002.

KAMRAN, M. S.; AHMAD, H. O.; WANG, H. S. Review on the developments of active magnetic regenerator refrigerators – evaluated by performance. *Renewable and Sustainable Energy Reviews*, v. 133, p. 110247, 2020.

KANG, M.; KWON, B. Deep learning of forced convection heat transfer. *Journal of Heat Transfer*, American Society of Mechanical Engineers, v. 144, n. 2, p. 021801, 2022.

KANSAL, T.; BAHUGUNA, S.; SINGH, V.; CHOUDHURY, T. Customer segmentation using k-means clustering. In: IEEE. *2018 international conference on computational techniques, electronics and mechanical systems (CTEMS)*. [S.l.], 2018. p. 135–139.

KARNIADAKIS, G. E.; KEVREKIDIS, I. G.; LU, L.; PERDIKARIS, P.; WANG, S.; YANG, L. Physics-informed machine learning. *Nature Reviews Physics*, v. 3, n. 6, p. 422–440, Jun. 2021. ISSN 2522-5820.

KATILA, P.; COLFER, C. J. P.; JONG, W. D.; GALLOWAY, G.; PACHECO, P.; WINKEL, G. *Sustainable development goals*. [S.l.]: Cambridge University Press, 2019.

KAUR, S. Noise types and various removal techniques. *International Journal of Advanced Research in Electronics and Communication Engineering (IJARECE)*, Citeseer, v. 4, n. 2, p. 226–230, 2015.

KAYS, W. M.; LONDON, A. L. *Compact Heat Exchangers*. New York, USA: McGraw-Hill, 1984.

KESTIN, J.; SHANKLAND, I. R. Viscosity of aqueous nacl solutions in the temperature range 25–200 c and in the pressure range 0.1–30 mpa. *International Journal of Thermophysics*, Springer, v. 5, n. 3, p. 241–263, 1984.

KETKAR, N.; KETKAR, N. Stochastic gradient descent. *Deep learning with Python: A hands-on introduction*, Springer, p. 113–132, 2017.

KHIRIRAT, S.; FEYZMAHDAVIAN, H. R.; JOHANSSON, M. Mini-batch gradient descent: Faster convergence under data sparsity. In: IEEE. *2017 IEEE 56th Annual Conference on Decision and Control (CDC)*. [S.l.], 2017. p. 2880–2887.

KIM, B.-W. Data preprocessing methods-strategies and best practices: Investigating strategies and best practices for preprocessing data, including cleaning, transformation, and feature engineering. *Australian Journal of Machine Learning Research & Applications*, v. 4, n. 1, p. 208–214, 2024.

KIM, D.; AZAD, M. M.; KHALID, S.; KIM, H. S. Data-driven surrogate modeling for global sensitivity analysis and the design optimization of medical waste shredding systems. *Alexandria Engineering Journal*, Elsevier, v. 82, p. 69–81, 2023.

KINGMA, D. P. Adam: A method for stochastic optimization. *arXiv preprint arXiv:1412.6980*, 2014.

KINGSFORD, C.; SALZBERG, S. L. What are decision trees? *Nature biotechnology*, Nature Publishing Group US New York, v. 26, n. 9, p. 1011–1013, 2008.

KITANOVSKI, A. Energy Applications of Magnetocaloric Materials. *Advanced Energy Materials*, v. 10, n. 10, p. 1903741, 2020.

KITANOVSKI, A.; PLAZNIK, U.; TOMC, U.; POREDOš, A. Present and future caloric refrigeration and heat-pump technologies. *International Journal of Refrigeration*, v. 57, p. 288 – 298, 2015.

KITANOVSKI, A.; PLAZNIK, U.; TUšEK, J.; POREDOš, A. New thermodynamic cycles for magnetic refrigeration. *International Journal of Refrigeration*, v. 37, p. 28 – 35, 2014.

KITANOVSKI, A.; TUSEK, J.; TOMC, U.; PLAZNIK, U.; OZBOLT, M.; POREDOS, A. *Magnetocaloric Energy Conversion: From Theory to Applications*. [S.l.]: Springer International Publishing, 2015.

KLINAR, K.; LAW, J. Y.; FRANCO, V.; MOYA, X.; KITANOVSKI, A. Perspectives and energy applications of magnetocaloric, pyromagnetic, electrocaloric, and pyroelectric materials. *Advanced Energy Materials*, Wiley Online Library, p. 2401739, 2024.

KLINAR, K.; TOMC, U.; JELENC, B.; NOSAN, S.; KITANOVSKI, A. New frontiers in magnetic refrigeration with high oscillation energy-efficient electromagnets. *Applied energy*, Elsevier, v. 236, p. 1062–1077, 2019.

KORBERG, A. D.; THELLUFSEN, J. Z.; SKOV, I. R.; CHANG, M.; PAARDEKOOPER, S.; LUND, H.; MATHIESEN, B. V. On the feasibility of direct hydrogen utilisation in a fossil-free europe. *International Journal of Hydrogen Energy*, v. 48, p. 2877–2891, 1 2023. ISSN 03603199.

KRASAE-IN, S.; STANG, J. H.; NEKSA, P. Development of large-scale hydrogen liquefaction processes from 1898 to 2009. *International journal of hydrogen energy*, Elsevier, v. 35, n. 10, p. 4524–4533, 2010.

KRIZHEVSKY, A.; SUTSKEVER, I.; HINTON, G. E. Imagenet classification with deep convolutional neural networks. *Advances in neural information processing systems*, v. 25, 2012.

KUEHN, T.; RAMSEY, J.; THRELKELD, J. *Thermal Environmental Engineering*. New Jersey, USA: Prentice Hall, 1998.

KUMAR, S.; DATTA, S.; SINGH, V.; SINGH, S. K.; SHARMA, R. Opportunities and challenges in data-centric ai. *IEEE Access*, v. 12, p. 33173–33189, 2024.

KUMAR, S. K. On weight initialization in deep neural networks. *arXiv preprint arXiv:1704.08863*, 2017.

KUNZ, O.; WAGNER, W. The gerg-2008 wide-range equation of state for natural gases and other mixtures: An expansion of gerg-2004. *Journal of chemical & engineering data*, ACS Publications, v. 57, n. 11, p. 3032–3091, 2012.

LACERDA Jr., W. R.; ANDRADE, L. P. C. da; OLIVEIRA, S. C. P.; MARTINS, S. A. M. Sysidentpy: A Python package for system identification using NARMAX models. *Journal of Open Source Software*, The Open Journal, v. 5, n. 54, p. 2384, 2020.

LAU, L. C.; LEE, K. T.; MOHAMED, A. R. Global warming mitigation and renewable energy policy development from the kyoto protocol to the copenhagen accord—a comment. *Renewable and Sustainable Energy Reviews*, Elsevier, v. 16, n. 7, p. 5280–5284, 2012.

LECUN, Y.; BOTTOU, L.; ORR, G. B.; MÜLLER, K.-R. Efficient backprop. In: *Neural networks: Tricks of the trade*. [S.l.]: Springer, 2002. p. 9–50.

LEI, G.; PENGYU, W.; YARU, G.; MOHAN, D.; HAO, P.; JIAOHONG, H.; PEIYU, J.; CUILAN, L.; YINGDE, Z.; JUAN, C. *et al.* Performance study of a double-regenerator room temperature magnetic refrigerator with 26° c temperature span. *International Journal of Refrigeration*, Elsevier, v. 148, p. 143–151, 2023.

LEI, T.; NAVICKAITĖ, K.; ENGELBRECHT, K.; BARCZA, A.; VIEYRA, H.; NIELSEN, K. K.; BAHL, C. R. Passive characterization and active testing of epoxy bonded regenerators for room temperature magnetic refrigeration. *Applied Thermal Engineering*, Elsevier, v. 128, p. 10–19, 2018.

LEI, T.; NIELSEN, K. K.; ENGELBRECHT, K.; BAHL, C. R. H.; BEZ, H. N.; VEJE, C. Sensitivity study of multi-layer active magnetic regenerators using first order magnetocaloric material La(Fe,Mn,Si)$_{13}$H$_y$. *Journal of Applied Physics*, v. 118, p. 014903, 2015.

LEMMON, E. W.; JACOBSEN, R. T. Viscosity and thermal conductivity equations for nitrogen, oxygen, argon, and air. *International journal of thermophysics*, Springer, v. 25, n. 1, p. 21–69, 2004.

LEWKOWYCZ, A. How to decay your learning rate. *arXiv preprint arXiv:2103.12682*, 2021.

LI, H.; WILHELMSEN, Ø.; YAN, J. Properties of co 2 mixtures and impacts on carbon capture and storage. *Handbook of clean energy systems*, Wiley Online Library, p. 1–17, 2015.

LI, L.; JAMIESON, K.; DESALVO, G.; ROSTAMIZADEH, A.; TALWALKAR, A. Hyperband: A novel bandit-based approach to hyperparameter optimization. *Journal of Machine Learning Research*, v. 18, n. 185, p. 1–52, 2018.

LI, Z.; ARORA, S. An exponential learning rate schedule for deep learning. *arXiv preprint arXiv:1910.07454*, 2019.

LI, Z.; LIU, F.; YANG, W.; PENG, S.; ZHOU, J. A survey of convolutional neural networks: analysis, applications, and prospects. *IEEE transactions on neural networks and learning systems*, IEEE, v. 33, n. 12, p. 6999–7019, 2021.

LIANG, J.; ENGELBRECHT, K.; NIELSEN, K. K.; LOEWE, K.; VIEYRA, H.; BARCZA, A.; BAHL, C. R. Performance assessment of a triangular microchannel active magnetic regenerator. *Applied Thermal Engineering*, Elsevier, v. 186, p. 116519, 2021.

LIANG, J.; NIELSEN, K. K.; ENGELBRECHT, K.; BAHL, C. R. Heat transfer figures of merit for mapping passive regenerator performance to active regenerator cooling power. *Applied Thermal Engineering*, Elsevier, v. 181, p. 115993, 2020.

LIANG, J.; PICKETT, J.; HERMANN, S.; SITTIG, T.; REICHERT, T.; LEHMANN, M.; STÖTZER, J.; ZWICK, J.-P.; GREIFENSTEIN, M.; STRAUCH, M. *et al.* Polaris: From laboratory prototypes to market-ready sustainable magnetic beverage coolers. *SSRN 5396814*, 2025.

LIANG, W.; TADESSE, G. A.; HO, D.; FEI-FEI, L.; ZAHARIA, M.; ZHANG, C.; ZOU, J. Advances, challenges and opportunities in creating data for trustworthy ai. *Nature Machine Intelligence*, Nature Publishing Group UK London, v. 4, n. 8, p. 669–677, 2022.

LIASHCHYNSKYI, P.; LIASHCHYNSKYI, P. Grid search, random search, genetic algorithm: a big comparison for nas. *arXiv preprint arXiv:1912.06059*, 2019.

LIN, L.; CHEN, Z.; WANG, Y.; JIANG, L. Improving anomaly detection in iot-based solar energy system using smote-pso and svm model. *Machine Learning and Artificial Intelligence*, 2022.

LIONTE, S.; RISSER, M.; MULLER, C. A 15kw magnetocaloric proof-of-concept unit: Initial development and first experimental results. *International Journal of Refrigeration*, v. 122, 09 2020.

LIU, Y.; LI, S.; LIU, Y. Machine learning-driven multiobjective optimization: an opportunity of microfluidic platforms applied in cancer research. *Cells*, MDPI, v. 11, n. 5, p. 905, 2022.

LIU, Y.; LU, S.; YAN, X.; GAO, S.; CUI, X.; CUI, Z. Life cycle assessment of petroleum refining process: A case study in china. *Journal of Cleaner Production*, Elsevier, v. 256, p. 120422, 2020.

LOHRENZ, J.; BRAY, B. G.; CLARK, C. R. Calculating viscosities of reservoir fluids from their compositions. *Journal of Petroleum Technology*, SPE, v. 16, n. 10, p. 1171–1176, 1964.

LOTFI, M.; HEYD, R.; BAKAK, A.; HADAOUI, A.; KOUMINA, A. Experimental measurements on the thermal conductivity of glycerol-based nanofluids with different thermal contrasts. *Journal of Nanomaterials*, Wiley Online Library, v. 2021, n. 1, p. 3190877, 2021.

LOUCKS, D. P.; BEEK, E. V.; LOUCKS, D. P.; BEEK, E. van. System sensitivity and uncertainty analysis. *Water Resource Systems Planning and Management: An Introduction to Methods, Models, and Applications*, Springer, p. 331–374, 2017.

LOZANO, J.; ENGELBRECHT, K.; BAHL, C.; NIELSEN, K.; ERIKSEN, D.; OLSEN, U.; BARBOSA Jr., J. R.; SMITH, A.; PRATA, A.; PRYDS, N. Performance analysis of a rotary active magnetic refrigerator. *Applied Energy*, v. 111, p. 669 – 680, 2013.

LOZANO, J.; ENGELBRECHT, K.; BAHL, C. R.; NIELSEN, K. K.; JR, J. B.; PRATA, A.; PRYDS, N. Experimental and numerical results of a high frequency rotating active magnetic refrigerator. *International Journal of Refrigeration*, v. 37, p. 92–98, 2014.

LOZANO, J. A.; CAPOVILLA, M. S.; TREVIZOLI, P. V.; ENGELBRECHT, K.; BAHL, C. R.; BARBOSA Jr., J. R. Development of a novel rotary magnetic refrigerator. *International Journal of Refrigeration*, v. 68, p. 187 – 197, 2016.

LOZANO, J. A.; PEIXER, G. F.; LORENZONI, A. M.; HOFFMANN, G.; SILVA, M. C. R.; DUTRA, S. L.; RIBEIRO, M. C.; dos Santos, D.; ROSáRIO, G. M.; CATTELAN, L. F.; TEZA, H. F.; PAGNAN, E.; FORTKAMP, F. P.; VIEIRA, B. P.; NAKASHIMA, A. T. D.; BARBOSA Jr., J. R. Magnetocaloric unit. Brazilian Patent No. BR 10 2021 023316. Instituto Nacional de Propriedade Industrial. 2021.

LU, C.-J. Sales forecasting of computer products based on variable selection scheme and support vector regression. *Neurocomputing*, Elsevier, v. 128, p. 491–499, 2014.

LU, D.; WENG, Q. A survey of image classification methods and techniques for improving classification performance. *International journal of Remote sensing*, Taylor & Francis, v. 28, n. 5, p. 823–870, 2007.

LUNA-ORTIZ, E.; SZKLARCZYK-MARSHALL, K.; WINTER, M.; MCALLISTER-FOGNINI, E. Impact of hydrogen as impurity in the physical and transport properties of co2 streams in ccs/ccus transport systems: A technical discussion. In: *Proceedings of the 15th Greenhouse Gas Control Technologies Conference*. [S.l.: s.n.], 2021. p. 15–18.

MAATEN, L. V. D.; POSTMA, E. O.; HERIK, H. J. V. D. *et al.* Dimensionality reduction: A comparative review. *Journal of Machine Learning Research*, v. 10, n. 66-71, p. 13, 2009.

MACDONALD, I.; STRACHAN, P. Practical application of uncertainty analysis. *Energy and Buildings*, Elsevier, v. 33, n. 3, p. 219–227, 2001.

MACHADO, A. P. F.; VARGAS, R. E. V.; CIARELLI, P. M.; MUNARO, C. J. Improving performance of one-class classifiers applied to anomaly detection in oil wells. *Journal of Petroleum Science and Engineering*, Elsevier, v. 218, p. 110983, 2022.

MAHMOOD, Y.; AFRIN, T.; HUANG, Y.; YODO, N. Sustainable development for oil and gas infrastructure from risk, reliability, and resilience perspectives. *Sustainability*, MDPI, v. 15, n. 6, p. 4953, 2023.

MAHMOUD, S. A.; BAMAKHRAMAH, A.; AL-TUNAIJI, S. A. Low-noise low-pass filter for ecg portable detection systems with digitally programmable range. *Circuits, Systems, and Signal Processing*, Springer, v. 32, p. 2029–2045, 2013.

MAIORINO, A.; Del Duca, M. G.; APREA, C. ART.I.CO. (ARTificial Intelligence for COoling): An innovative method for optimizing the control of refrigeration systems based on artificial neural networks. *Applied Energy*, v. 306, p. 118072, 2022. ISSN 0306-2619.

MAIORINO, A.; DUCA, M. D.; TOMC, U.; TUšEK, J.; KITANOVSKI, A.; APREA, C. A numerical modelling of a multi-layer LaFeCoSi active magnetic regenerator by using artificial neural networks. *Applied Thermal Engineering*, v. 197, p. 117375, 07 2021.

MAIORINO, A.; DUCA, M. G. D.; TUŠEK, J.; TOMC, U.; KITANOVSKI, A.; APREA, C. Evaluating magnetocaloric effect in magnetocaloric materials: a novel approach based on indirect measurements using artificial neural networks. *Energies*, MDPI, v. 12, n. 10, p. 1871, 2019.

MANSOOR, R.; JAYASINGHE, N. D.; MUSLAM, M. M. A. A comprehensive review on email spam classification using machine learning algorithms. In: IEEE. *2021 International Conference on Information Networking (ICOIN)*. [S.l.], 2021. p. 327–332.

MARLER, R.; ARORA, J. Survey of multi-objective optimization methods for engineering. *Structural and Multidisciplinary Optimization*, v. 26, p. 369–395, 2004.

MARTINS, I. O.; SILVA, A. K. da; SILVA, E. C.; HASAN, A. R.; JR, J. R. B. Predicting the annular pressure behavior during water injection in offshore wells with a transient, multiphysics model. *Journal of Petroleum Science and Engineering*, Elsevier, v. 218, p. 110992, 2022.

MASCHE, M.; LIANG, J.; DALL'OLIO, S.; ENGELBRECHT, K.; BAHL, C. R. H. Performance analysis of a high-efficiency multi-bed active magnetic regenerator device. *Applied Thermal Engineering*, v. 199, p. 117569, 2021. ISSN 1359-4311.

MASCHE, M.; LIANG, J.; ENGELBRECHT, K.; BAHL, C. Performance assessment of a rotary active magnetic regenerator prototype using gadolinium. *Applied Thermal Engineering*, v. 204, p. 117947, 2022. ISSN 1359-4311.

MCCULLOCH, W. S.; PITTS, W. A logical calculus of the ideas immanent in nervous activity. *The bulletin of mathematical biophysics*, Springer, v. 5, n. 4, p. 115–133, 1943.

MEDSKER, L. R.; JAIN, L. *et al.* Recurrent neural networks. *Design and Applications*, v. 5, n. 64-67, p. 2, 2001.

MIAO, Y.; GOWAYYED, M.; METZE, F. Eesen: End-to-end speech recognition using deep rnn models and wfst-based decoding. In: IEEE. *2015 IEEE workshop on automatic speech recognition and understanding (ASRU)*. [S.l.], 2015. p. 167–174.

MITCHELL, T. M.; MITCHELL, T. M. *Machine learning*. [S.l.]: McGraw-hill New York, 1997.

MOHANRAJ, M.; JAYARAJ, S.; MURALEEDHARAN, C. Applications of artificial neural networks for refrigeration, air-conditioning and heat pump systems—a review. *Renewable and Sustainable Energy Reviews*, v. 16, n. 2, p. 1340–1358, 2012. ISSN 1364-0321.

MONFARED, B.; FURBERG, R.; PALM, B. Magnetic vs. vapor-compression household refrigerators: A preliminary comparative life cycle assessment. *International Journal of Refrigeration*, v. 42, p. 69 – 76, 2014.

MONTANEZ-BARRERA, J. A.; BARROSO-MALDONADO, J. M.; BEDOYA-SANTACRUZ, A. F.; MOTA-BABILONI, A. Correlated-informed neural networks: a new machine learning framework to predict pressure drop in micro-channels. Jan. 2022.

MOORE, R.; DENERO, J. L1 and l2 regularization for multiclass hinge loss models. In: *Symposium on machine learning in speech and language processing*. [S.l.: s.n.], 2011.

MORADI, R.; GROTH, K. M. Hydrogen storage and delivery: Review of the state of the art technologies and risk and reliability analysis. *International Journal of Hydrogen Energy*, Elsevier, v. 44, n. 23, p. 12254–12269, 2019.

MÜHLENBEIN, H. Limitations of multi-layer perceptron networks-steps towards genetic neural networks. *Parallel Computing*, Elsevier, v. 14, n. 3, p. 249–260, 1990.

MÜNZ, G.; LI, S.; CARLE, G. Traffic anomaly detection using k-means clustering. In: *Gi/itg workshop mmbnet*. [S.l.: s.n.], 2007. v. 7, n. 9.

NAGELKERKE, N. J. *et al.* A note on a general definition of the coefficient of determination. *biometrika*, Oxford University Press, v. 78, n. 3, p. 691–692, 1991.

NAKASHIMA, A. T.; DUTRA, S. L.; TREVIZOLI, P. V.; BARBOSA Jr., J. R. Influence of the flow rate waveform and mass imbalance on the performance of active magnetic regenerators. part i: Experimental analysis. *International Journal of Refrigeration*, v. 93, p. 236 – 248, 2018.

NAKASHIMA, A. T.; FORTKAMP, F. P.; de SÁ, N. M.; dos SANTOS, V. M.; HOFFMANN, G.; PEIXER, G. F.; DUTRA, S. L.; RIBEIRO, M. C.; LOZANO, J. A.; BARBOSA Jr., J. R. A magnetic wine cooler prototype. *International Journal of Refrigeration*, v. 122, p. 110–121, 2021. ISSN 0140-7007.

NAKASHIMA, A. T. D.; DUTRA, S. L.; HOFFMANN, G.; LOZANO, J. A.; BARBOSA Jr., J. R. Performance assessment of solenoid valves as flow distributors for an active magnetic regenerator. In: *8th International Conference on Caloric Cooling, THERMAG VIII*. Darmstadt, Germany: [s.n.], 2018.

NAKASHIMA, A. T. D.; PAGNAN, E.; Sá, N. M.; LORENZONI, A. M.; LUZ, G. M.; HOFFMANN, G.; PEIXER, G. F.; LOZANO, J. A.; BARBOSA Jr., J. R. Magnetic refrigeration technology assessment: Design of a magnetic wine cooler. In: *ENCIT: 19th Brazilian Congress of Thermal Sciences and Engineering*. Bento Gonçalves: [s.n.], 2022.

NAKASHIMA, A. T. D.; PEIXER, G. F.; LOZANO, J. A.; BARBOSA Jr., J. R. A lumped-element magnetic refrigerator model. *Applied Thermal Engineering*, v. 204, p. 117918, 2022. ISSN 1359-4311.

NAKASHIMA, A. T. D.; Sá, N. M. D.; SANTOS, V. M. A. D.; HOFFMANN, G.; LOZANO, J. A.; BARBOSA Jr., J. R. Performance assessment of a magnetic wine cooler prototype. In: *Nineth IIR International Conference on Caloric Cooling and Applications of Caloric Materials, THERMAG IX*. Maryland, United States: [s.n.], 2021.

NANDI, T. K.; SARANGI, S. Performance and optimization of hydrogen liquefaction cycles. *Int. J. Hydrogen Energy*, v. 18, p. 131–139, 1993.

NASCIMENTO, R. S. F. do; BARBOSA Jr., B. H. G.; VARGAS, R. E. V.; SANTOS, I. H. F. dos. Detecçao de anomalias em poços de petróleo surgentes com stacked autoencoders. In: *Simpósio Brasileiro de Automação Inteligente-SBAI*. [S.l.: s.n.], 2021. v. 1, n. 1.

NAVICKAITĖ, K.; BEZ, H. N.; LEI, T.; BARCZA, A.; VIEYRA, H.; BAHL, C. R.; ENGELBRECHT, K. Experimental and numerical comparison of multi-layered la (fe, si, mn) 13hy active magnetic regenerators. *International Journal of Refrigeration*, Elsevier, v. 86, p. 322–330, 2018.

NELLIS, G.; KLEIN, S. *Heat Transfer*. Cambridge, United Kingdom: Cambridge University Press, 2009.

NEUMANN, T.; HERRIG, S.; BELL, I. H.; BECKMÜLLER, R.; LEMMON, E. W.; THOL, M.; SPAN, R. Eos-cg-2021: A mixture model for the calculation of thermodynamic properties of ccs mixtures. *International Journal of Thermophysics*, Springer, v. 44, n. 12, p. 178, 2023.

NGO, Q.-H.; NGUYEN, B. L.; VU, T. V.; ZHANG, J.; NGO, T. Physics-informed graphical neural network for power system state estimation. *Applied Energy*, v. 358, p. 122602, 2024. ISSN 0306-2619.

NIELSEN, K.; BAHL, C. R. H.; SMITH, A. Constraints on the adiabatic temperature change in magnetocaloric materials. *Physical Review B*, v. 81, 2010.

NIELSEN, K.; TUSEK, J.; ENGELBRECHT, K.; SCHOPFER, S.; KITANOVSKI, A.; BAHL, C.; SMITH, A.; PRYDS, N.; POREDOS, A. Review on numerical modeling of active magnetic regenerators for room temperature applications. *International Journal of Refrigeration*, Elsevier BV, v. 34, n. 3, p. 603–616, 2011.

NIKNIA, I.; CAMPBELL, O.; CHRISTIAANSE, T.; GOVINDAPPA, P.; TEYBER, R.; TREVIZOLI, P.; ROWE, A. Impacts of configuration losses on active magnetic regenerator device performance. *Applied Thermal Engineering*, Elsevier, v. 106, p. 601–612, 2016.

NIU, Z.; YU, K.; WU, X. Lstm-based vae-gan for time-series anomaly detection. *Sensors*, MDPI, v. 20, n. 13, p. 3738, 2020.

OLABI, A.; ABDELGHAFAR, A. A.; MAGHRABIE, H. M.; SAYED, E. T.; REZK, H.; RADI, M. A.; OBAIDEEN, K.; ABDELKAREEM, M. A. Application of artificial intelligence for prediction, optimization, and control of thermal energy storage systems. *Thermal Science and Engineering Progress*, Elsevier, v. 39, p. 101730, 2023.

OLIVEIRA, M. S.; PEIXER, G. F.; FORCELLINI, F. A.; BARBOSA Jr., J. R.; LOZANO, J. A. Innovation level in set-based design: an integrated approach with chosen-to-fit and custom-to-fit solutions. *Journal of Engineering Design*, Taylor and Francis, v. 33, n. 12, p. 990–1015, 2022.

OLIVEIRA, M. S. D.; LOZANO, J. A.; JR, J. B.; FORCELLINI, F. A. The toyota kata approach for lean product development. In: *Transdisciplinary Engineering Methods for Social Innovation of Industry 4.0*. [S.l.]: IOS Press, 2018. p. 361–370.

OLIVEIRA, M. S. D.; PEIXER, G. F.; FORCELLINI, F. A.; BARBOSA Jr., J. R.; CADENA, J. A. L. Model-based trade-off curves to support the set-based concurrent engineering of highly innovative projects. *Concurrent Engineering*, v. 31, n. 3-4, p. 89–100, 2023.

OLIVEIRA, M. S. de; PEIXER, G. F.; ROSA, M. A.; FORCELLINI, F. A.; JR, J. R. B.; CADENA, J. A. L. Value deployment in set-based design: Design space propagation to integrate manufacturing in the narrowing-down process. *Systems Engineering*, Wiley Online Library, v. 28, n. 2, p. 175–189, 2025.

OSTERTAGOVÁ, E. Modelling using polynomial regression. *Procedia engineering*, Elsevier, v. 48, p. 500–506, 2012.

PAGNAN, E.; CATTELAN, L. F.; PEIXER, G. F.; LORENZONI, A. M.; HOFFMANN, G.; SILVA, M. C. R.; NAKASHIMA, A. T. D.; LOZANO, J. A.; BARBOSA Jr., J. R. Enhancing the frequency of magnetic refrigerators using dummy regenerators. In: *ENCIT: 19th Brazilian Congress of Thermal Sciences and Engineering*. Bento Gonçalves: [s.n.], 2022.

PAI, R.; GUPTA, A.; SATHUVALLI, U. B.; SURYANARAYANA, P.; AFFES, S.; OKOROAFOR, J.; NWAMARA, N. Validation of transient annular pressure build-up apb model predictions with field measurements in an offshore well and characterization of uncertainty bounds. In: SPE. *SPE/IADC Drilling Conference and Exhibition*. [S.l.], 2020. p. D091S011R003.

PANIAGUA-TINEO, A.; SALCEDO-SANZ, S.; CASANOVA-MATEO, C.; ORTIZ-GARCÍA, E.; CONY, M.; HERNÁNDEZ-MARTÍN, E. Prediction of daily maximum temperature using a support vector regression algorithm. *Renewable Energy*, Elsevier, v. 36, n. 11, p. 3054–3060, 2011.

PATEL, A. R.; RAMAIYA, K. K.; BHATIA, C. V.; SHAH, H. N.; BHAVSAR, S. N. Artificial intelligence: Prospect in mechanical engineering field—a review. *Data Science and Intelligent Applications: Proceedings of ICDSIA 2020*, Springer, p. 267–282, 2021.

PECHARSKY, V. K.; GSCHNEIDNER JR., K. A. Magnetocaloric effect and magnetic refrigeration. *Journal of Magnetism and Magnetic Materials*, v. 200, p. 44 – 56, 1999.

PEDREGOSA, F.; VAROQUAUX, G.; GRAMFORT, A.; MICHEL, V.; THIRION, B.; GRISEL, O.; BLONDEL, M.; PRETTENHOFER, P.; WEISS, R.; DUBOURG, V.; VANDERPLAS, J.; PASSOS, A.; COURNAPEAU, D.; BRUCHER, M.; PERROT, M.; DUCHESNAY, E. Scikit-learn: Machine learning in Python. *Journal of Machine Learning Research*, v. 12, p. 2825–2830, 2011.

PEIXER, G.; LOZANO, J.; BARBOSA Jr., J. Performance evaluation of amrs using different casings. *Book of Abstracts for the Danish Days on Caloric Materials and Devices*, 2017.

PEIXER, G.; LOZANO, J. A.; BARBOSA Jr., J. R. Performance evaluation of AMRs using different casings. In: *Book of Abstracts for the Danish Days on Caloric Materials and Devices*. Roskilde, Denmark: [s.n.], 2017.

PEIXER, G. F. Thermodynamic design of a magnetic cooling system for air-conditioning applications. Master's thesis, Universidade Federal de Santa Catarina, Florianópolis, Brazil. 2020.

PEIXER, G. F.; DUTRA, S. L.; CALOMENO, R. S.; SÁ, N. M. de; LANG, G. B.; LOZANO, J. A.; BARBOSA Jr., J. R. Influence of heat exchanger design on the thermal performance of a domestic wine cooler driven by a magnetic refrigeration system. *Anais da Academia Brasileira de Ciências*,, 2022.

PEIXER, G. F.; LORENZONI, A. M.; AZEREDO, Y. C.; SILVA, P. M.; SILVA, M. C.; HOFFMANN, G.; dos Santos, D.; DUTRA, S. L.; do Rosário, G. M.; TEZA, H. F.; PAGNAN, E.; SUCARIA, R. S.; CATTELAN, L. F.; REIF, D. D.; HSUAN, C. T.; DöRING, A. M.; FARIA, P.; VIEIRA, B. P.; FORTKAMP, F. P.; de Olivera, M. S.; NAKASHIMA, A. T.; FORCELLINI, F. A.; FLESCH, R. C.; TEIXEIRA, C. S.; LOZANO, J. A.; BARBOSA, J. R. Thermodynamic assessment of a large-scale magnetic air conditioning prototype. *International Journal of Refrigeration*, 2024. ISSN 0140-7007.

PEIXER, G. F.; LORENZONI, A. M.; AZEREDO, Y. C.; SILVA, P. M.; SILVA, M. C.; HOFFMANN, G.; SANTOS, D. dos; DUTRA, S. L.; ROSÁRIO, G. M. do; TEZA, H. F.; PAGNAN, E.; SUCARIA, R. S.; CATTELAN, L. F.; REIF, D. D.; HSUAN, C. T.; ROSA, M. A.; DÖRING, A. M.; FARIA, P.; VIEIRA, B. P.; FORTKAMP, F. P.; OLIVEIRA, M. S. de; NAKASHIMA, A. T.; FORCELLINI, F. A.; WENDHAUSEN, P. A. P.; FLESCH, R. C.; TEIXEIRA, C. S.; LOZANO, J. A.; JR., J. R. B. Evaluation of the thermodynamic performance evolution of three generations of a large-scale magnetic refrigerator. In preparation. 2026.

PEIXER, G. F.; NAKASHIMA, A. T.; LOZANO, J. A.; JR, J. R. B. System-level multi-objective optimization of a magnetic air conditioner through coupling of artificial neural networks and genetic algorithms. *Applied Thermal Engineering*, Elsevier, v. 227, p. 120368, 2023.

PEIXER, G. F.; NAKASHIMA, A. T. D.; LOZANO, J. A.; BARBOSA Jr., J. R. Optsys: Optimization of thermal systems. Brazilian Patent No. BR 10 2024 01274-5. Instituto Nacional de Propriedade Industrial. Registered on 19/04/2024. 2024.

PEIXER, G. F.; SILVA, M. C.; LORENZONI, A.; HOFFMANN, G.; dos SANTOS, D.; do Rosário, G. M.; PAGNAN, E.; TEZA, H. F.; SILVA, P. M.; DUTRA, S. L.; RIBEIRO, M. C.; ROSA, M. A.; DöRING, A.; VIEIRA, B. P.; NAKASHIMA, A. T.; WENDHAUSEN, P. A.; TEIXEIRA, C. S.; LOZANO, J. A.; BARBOSA Jr., J. R. A magnetocaloric air-conditioning system prototype. *International Journal of Refrigeration*, v. 151, p. 1–13, 2023. ISSN 0140-7007.

PEIXER, G. F.; SILVA, M. C. R.; LORENZONI, A. M.; HOFFMANN, G.; SANTOS, D.; DUTRA, S. L.; TEZA, H. F.; PAGNAN, E.; VIEIRA, B. P.; NAKASHIMA, A. T. D.; LOZANO, J. A.; BARBOSA Jr., J. R. Evaluating the performance of a trl-6 magnetic air conditioner prototype. In: *19th International Refrigeration and Air Conditioning Conference at Purdue*. Purdue, Estados Unidos: [s.n.], 2022.

PELETIRI, S. P.; RAHMANIAN, N.; MUJTABA, I. M. Effects of impurities on co2 pipeline performance. *Chem Eng Trans*, v. 57, n. 6, 2017.

PENG, D.-Y.; ROBINSON, D. B. A new two-constant equation of state. *Industrial & Engineering Chemistry Fundamentals*, ACS Publications, v. 15, n. 1, p. 59–64, 1976.

PÉREZ-GOMARIZ, M.; LÓPEZ-GÓMEZ, A.; CERDÁN-CARTAGENA, F. Artificial neural networks as artificial intelligence technique for energy saving in refrigeration systems—a review. *Clean Technologies*, MDPI, v. 5, n. 1, p. 116–136, 2023.

PESCHKA, W. *Liquid Hydrogen*. [S.l.]: Springer Vienna, 1992. ISBN 978-3-7091-9128-6.

PHAM, T.; HOANG, T. V.; TRAN, X.; FETNI, S.; DUCHÊNE, L.; TRAN, H.; HABRAKEN, A. Characterization, propagation, and sensitivity analysis of uncertainties in the directed energy deposition process using a deep learning-based surrogate model. *Probabilistic Engineering Mechanics*, Elsevier, v. 69, p. 103297, 2022.

PLASCENCIA, G.; DÍAZ-DAMACILLO, L.; ROBLES-AGUDO, M. On the estimation of the friction factor: A review of recent approaches. *SN Applied Sciences*, Springer, v. 2, n. 2, p. 163, 2020.

POPESCU, M.-C.; BALAS, V. E.; PERESCU-POPESCU, L.; MASTORAKIS, N. Multilayer perceptron and neural networks. *WSEAS Transactions on Circuits and Systems*, World Scientific and Engineering Academy and Society (WSEAS) Stevens Point . . . , v. 8, n. 7, p. 579–588, 2009.

PRATELLA, D.; SAADI, S. A.-E.-M.; BANNWARTH, S.; PAQUIS-FLUCKINGER, V.; BOTTINI, S. A survey of autoencoder algorithms to pave the diagnosis of rare diseases. *International journal of molecular sciences*, MDPI, v. 22, n. 19, p. 10891, 2021.

PRECHELT, L. Early stopping-but when? In: *Neural Networks: Tricks of the trade*. [S.l.]: Springer, 2002. p. 55–69.

PRESS, W. H.; TEUKOLSKY, S. A.; VETTERLING, W. T.; FLANNERY, B. P. *Numerical Recipes 3rd Edition: The Art of Scientific Computing*. 3. ed. USA: Cambridge University Press, 2007.

QIAN, N. On the momentum term in gradient descent learning algorithms. *Neural networks*, Elsevier, v. 12, n. 1, p. 145–151, 1999.

QIAN, S.; NASUTA, D.; RHOADS, A.; WANG, Y.; GENG, Y.; HWANG, Y.; RADERMACHER, R.; TAKEUCHI, I. Not-in-kind cooling technologies: A quantitative comparison of refrigerants and system performance. *International Journal of Refrigeration*, v. 62, p. 177 – 192, 2016.

QU, Q.; MA, Z.; CLAUSEN, A.; JØRGENSEN, B. N. A comprehensive review of machine learning in multi-objective optimization. In: IEEE. *2021 IEEE 4th International Conference on Big Data and Artificial Intelligence (BDAI)*. [S.l.], 2021. p. 7–14.

RAI, A.; UPADHYAY, S. The use of MD-CUMSUM and NARX neural network for anticipating the remaining useful life of bearings. *Measurement*, v. 111, p. 397–410, 2017. ISSN 0263-2241.

RAISSI, M.; PERDIKARIS, P.; KARNIADAKIS, G. Physics-informed neural networks: A deep learning framework for solving forward and inverse problems involving nonlinear partial differential equations. *Journal of Computational Physics*, v. 378, p. 686–707, 2019. ISSN 0021-9991.

RAMEY Jr, H. J. Wellbore heat transmission. *Journal of petroleum Technology*, SPE, v. 14, n. 04, p. 427–435, 1962.

RAMIRES, M. L.; CASTRO, C. A. Nieto de; FARELEIRA, J. M.; WAKEHAM, W. A. Thermal conductivity of aqueous sodium chloride solutions. *Journal of Chemical and Engineering Data*, ACS Publications, v. 39, n. 1, p. 186–190, 1994.

RASAMOELINA, A. D.; ADJAILIA, F.; SINČÁK, P. A review of activation function for artificial neural network. In: IEEE. *2020 IEEE 18th World Symposium on Applied Machine Intelligence and Informatics (SAMI)*. [S.l.], 2020. p. 281–286.

RAZAVI, S.; JAKEMAN, A.; SALTELLI, A.; PRIEUR, C.; IOOSS, B.; BORGONOVO, E.; PLISCHKE, E.; PIANO, S. L.; IWANAGA, T.; BECKER, W. *et al.* The future of sensitivity analysis: an essential discipline for systems modeling and policy support. *Environmental Modelling & Software*, Elsevier, v. 137, p. 104954, 2021.

RIBEIRO, G. B. *Análise de sistemas de condicionamento de ar com capacidade variável considerando o efeito da mistura óleo-refrigerante*. Phd Thesis (PhD Thesis) — Graduate Program in Mechanical Engineering, Federal University of Santa Catarina, Florianópolis, Brasil, 2015.

RIGHETTI, M.; SALVETTI, G.; TOMBARI, E. Heat capacity of glycerol from 298 to 383 k. *Thermochimica acta*, Elsevier, v. 316, n. 2, p. 193–195, 1998.

ROJAS, R.; ROJAS, R. The backpropagation algorithm. *Neural networks: a systematic introduction*, Springer, p. 149–182, 1996.

ROKACH, L.; MAIMON, O. Decision trees. *Data mining and knowledge discovery handbook*, Springer, p. 165–192, 2005.

ROSENBLATT, F. The perceptron: A probabilistic model for information storage and organization (1958). 2021.

RUDER, S. An overview of gradient descent optimization algorithms. *arXiv preprint arXiv:1609.04747*, 2016.

SALTELLI, A.; TARANTOLA, S.; CAMPOLONGO, F.; RATTO, M. *et al. SA in practice: a guide to assessing scientific models*. [S.l.: s.n.], 2004.

SANTOS, D.; DUTRA, S. L.; RIBEIRO, M.; LORENZONI, A. M.; ROSáRIO, G. M.; SILVA, M. C. R.; HOFFMANN, G.; PEIXER, G. F.; LOZANO, J. A.; BARBOSA Jr., J. R. Designing a hydraulic management system for a large-scale magnetic refrigerator. In: *9th IIR International Conference on Caloric Cooling and Applications of Caloric Materials (THERMAG IX), 2021*. Maryland: [s.n.], 2021.

SANTOS, D.; DUTRA, S. L.; ROSáRIO, G. M.; SILVA, M. C. R.; RIBEIRO, M.; LORENZONI, A. M.; PEIXER, G. F.; LOZANO, J. A.; BARBOSA Jr., J. R. Design and experimental validation of a management system for a large magnetic refrigerator. In: ABCM. *18th Brazilian Congress of Thermal Sciences and Engineering*. Porto Alegre, 2020.

SANTOS, D. dos; SILVA, M. C. Régio e; HOFFMANN, G.; LORENZONI, A.; PEIXER, G. F.; LOZANO, J.; BARBOSA Jr., J. Experimental evaluation of the fluid flow management system of a magnetic air conditioner. In: *Proceedings of the 26th International Congress of Mechanical Engineering*. [S.l.: s.n.], 2021.

SATO, M.; ISHII, Y. Simple and approximate expressions of demagnetizing factors of uniformly magnetized rectangular rod and cylinder. *Journal of Applied Physics*, American Institute of Physics, v. 66, n. 2, p. 983–985, 1989.

SCHAFFER, J. Multiple objective optimization with vector evaluated genetic algorithms. In: . [S.l.: s.n.], 1985. p. 93–100.

SCHMIDT, T. E. La production calorifique des surfaces munies d'ailettes. *Bulletin de l'Institut International du Froid, Annexe G-5*, 1945.

SCHOLBECK, C. A.; MOOSBAUER, J.; CASALICCHIO, G.; GUPTA, H.; BISCHL, B.; HEUMANN, C. *Position Paper: Bridging the Gap Between Machine Learning and Sensitivity Analysis*. 2024.

SCHRYEN, G. Parallel computational optimization in operations research: A new integrative framework, literature review and research directions. *European Journal of Operational Research*, Elsevier, v. 287, n. 1, p. 1–18, 2020.

SCHWEIDTMANN, A.; MITSOS, A. Global deterministic optimization with artificial neural networks embedded. *Journal of Optimization Theory and Applications*, v. 180, 03 2019.

SHAH, R. K.; SEKULIC, D. P. *Fundamentals of Heat Exchanger Design*. [S.l.]: Wiley, 2003.

SHAHANE, S.; GULERYUZ, E.; ABUEIDDA, D. W.; LEE, A.; LIU, J.; YU, X.; CHIU, R.; KORIC, S.; ALURU, N. R.; FERREIRA, P. M. Surrogate neural network model for sensitivity analysis and uncertainty quantification of the mechanical behavior in the optical lens-barrel assembly. *Computers & Structures*, Elsevier, v. 270, p. 106843, 2022.

SHELEMBE, L.; BARENDSE, P. An amplitude-modulated pseudo-random binary sequence approach to broadband impedance spectroscopy for photovoltaic module system identification. In: *2021 IEEE Energy Conversion Congress and Exposition (ECCE)*. [S.l.: s.n.], 2021. p. 443–450.

SHEN, B. G.; SUN, J. R.; HU, F. X.; ZHANG, H. W.; CHENG, Z. H. Recent progress in exploring magnetocaloric materials. *Advanced Materials*, v. 21, p. 4545–4564, 2009.

SHEYBANI, E. Dimensionality reduction and noise removal in wireless sensor networks. In: IEEE. *2011 4th IFIP International Conference on New Technologies, Mobility and Security*. [S.l.], 2011. p. 1–5.

SHI, P.; JIANG, Q.; SHI, C.; XI, J.; TAO, G.; ZHANG, S.; ZHANG, Z.; LIU, B.; GAO, X.; WU, Q. Oil well detection via large-scale and high-resolution remote sensing images based on improved yolo v4. *Remote Sensing*, v. 13, p. 3243, 2021.

SILVA, M. C. R.; ROSáRIO, G. S.; DUTRA, S. L.; CAPOVILLA, M.; LIMA, R.; LORENZONI, A.; dos SANTOS, D.; HOFFMANN, G.; PEIXER, G. F.; LOZANO, J. A.; BARBOSA Jr., J. R. Development and characterization of a calibrated calorimeter to evaluate air conditioning systems. In: *Proceedings of the 26th ABCM International Congress of Mechanical Engineering*. Florianópolis, Brazil: [s.n.], 2021.

SILVA, P. M.; PEIXER, G. F.; LOZANO, J. A.; BARBOSA Jr., J. R. Deepmag: Dynamics of magnetic refrigerators via deep learning. Brazilian Patent No. BR 10 2024 01278-8. Instituto Nacional de Propriedade Industrial. Registered on 19/04/2024. 2024.

SMITH, A.; BAHL, C. R.; BJØRK, R.; ENGELBRECHT, K.; NIELSEN, K. K.; PRYDS, N. Materials challenges for high performance magnetocaloric refrigeration devices. *Advanced Energy Materials*, v. 2, p. 1288–1318, 2012.

SMITH, L. N. *A disciplined approach to neural network hyper-parameters: Part 1 – learning rate, batch size, momentum, and weight decay*. [S.l.]: arXiv, 2018.

SOLOMATINE, D. P.; OSTFELD, A. Data-driven modelling: some past experiences and new approaches. *Journal of Hydroinformatics*, v. 10, n. 1, p. 3–22, 01 2008. ISSN 1464-7141.

SPAN, R.; LEMMON, E. W.; JACOBSEN, R. T.; WAGNER, W.; YOKOZEKI, A. A reference equation of state for the thermodynamic properties of nitrogen for temperatures from 63.151 to 1000 k and pressures to 2200 mpa. *Journal of physical and chemical reference data*, American Institute of Physics for the National Institute of Standards and ..., v. 29, n. 6, p. 1361–1433, 2000.

SRINIVAS, N.; DEB, K. Muiltiobjective optimization using nondominated sorting in genetic algorithms. *Evolutionary Computation*, v. 2, n. 3, p. 221–248, 1994.

SRIVASTAVA, N.; HINTON, G.; KRIZHEVSKY, A.; SUTSKEVER, I.; SALAKHUTDINOV, R. Dropout: a simple way to prevent neural networks from overfitting. *The journal of machine learning research*, JMLR. org, v. 15, n. 1, p. 1929–1958, 2014.

STORN, R.; PRICE, K. Differential evolution–a simple and efficient heuristic for global optimization over continuous spaces. *Journal of global optimization*, Springer, v. 11, p. 341–359, 1997.

SU, X.; YAN, X.; TSAI, C.-L. Linear regression. *Wiley Interdisciplinary Reviews: Computational Statistics*, Wiley Online Library, v. 4, n. 3, p. 275–294, 2012.

SUDRET, B.; MARELLI, S.; WIART, J. Surrogate models for uncertainty quantification: An overview. In: IEEE. *2017 11th European conference on antennas and propagation (EUCAP)*. [S.l.], 2017. p. 793–797.

SUTHAHARAN, S.; SUTHAHARAN, S. Support vector machine. *Machine learning models and algorithms for big data classification: thinking with examples for effective learning*, Springer, p. 207–235, 2016.

SÁ, N. M.; NAKASHIMA, A. T.; LOZANO, J. A.; BARBOSA Jr., J. R. Thermodynamic comparison of magnetocaloric and vapor compression wine coolers. *International Journal of Refrigeration*, v. 156, p. 29–39, 2023a. ISSN 0140-7007.

Sá, N. M.; LUZ, G. M.; NAKASHIMA, A. T. D.; PAGNAN, E.; LORENZONI, A. M.; PEIXER, G. F.; LOZANO, J. A.; BARBOSA Jr., J. R. Performance prediction of a novel compact magnetocaloric wine cooler. In: *COBEM 2023 - 27th International Congress of Mechanical Engineering*. Florianópolis: [s.n.], 2023.

TAMARONA, P. B.; PECNIK, R.; RAMDIN, M. Viability assessment of large-scale claude cycle hydrogen liquefaction: A study on technical and economic perspective. *International Journal of Hydrogen Energy*, Elsevier, v. 77, p. 383–396, 2024.

TAYLOR, M. What is sensitivity analysis. *Consortium YHE: University of York*, p. 1–8, 2009.

TEYBER, R.; TREVIZOLI, P.; CHRISTIAANSE, T.; GOVINDAPPA, P.; NIKNIA, I.; ROWE, A. Permanent magnet design for magnetic heat pumps using total cost minimization. *Journal of Magnetism and Magnetic Materials*, Elsevier, v. 442, p. 87–96, 2017.

TEYBER, R.; TREVIZOLI, P.; NIKNIA, I.; CHRISTIAANSE, T.; GOVINDAPPA, P.; ROWE, A. Experimental performance investigation of an active magnetic regenerator subject to different fluid flow waveforms. *International Journal of Refrigeration*, v. 74, p. 38–46, 2017.

TEZA, H. F.; VIEIRA, B. P.; de Faria, P. V.; HOFFMANN, G.; LOZANO, J. A.; BARBOSA, J. R. Experimental assessment of a multilayered packed-sphere La-Fe-Si active magnetic regenerator. *International Journal of Refrigeration*, 2024. ISSN 0140-7007.

TEZA, H. F.; VIEIRA, B. P.; Sá, N. M. de; NAKASHIMA, A. T. D.; PEIXER, G. F.; HOFFMANN, G.; LOZANO, J. A.; BARBOSA Jr., J. R. Characterization of the thermo-hydraulic performance of a la(fe,mn,si)$_{13}$hy regenerator. In: *26th International Congress of Mechanical Engineering*. Florianópolis: [s.n.], 2021.

TISHIN, A. M.; SPICHKIN, Y. I. *The magnetocaloric effect and its application*. [S.l.]: Institute of Physics Publishing, 2003.

TOMC, U.; NOSAN, S.; KLINAR, K.; KITANOVSKI, A. Towards powerful magnetocaloric devices with static electro-permanent magnets. *Journal of advanced research*, Elsevier, v. 45, p. 157–181, 2023.

TOMC, U.; PEIXER, G. F.; BAHL, C. R.; NIELSEN, K. K.; LOZANO, J. A.; BARBOSA, J. R.; KITANOVSKI, A. Influence of layering and curie temperature uncertainty on the performance of multilayer active magnetic regenerators. *Advanced Functional Materials*, Wiley Online Library, p. e24282, 2025.

TOUVRON, H.; LAVRIL, T.; IZACARD, G.; MARTINET, X.; LACHAUX, M.-A.; LACROIX, T.; ROZIèRE, B.; GOYAL, N.; HAMBRO, E.; AZHAR, F.; RODRIGUEZ, A.; JOULIN, A.; GRAVE, E.; LAMPLE, G. *LLaMA: Open and Efficient Foundation Language Models*. 2023.

TRAHAN, C.; LOVELAND, M.; DENT, S. Quantum physics-informed neural networks. *Entropy*, MDPI, v. 26, n. 8, p. 649, 2024.

TREVIZOLI, P.; PEIXER, G.; NAKASHIMA, A.; CAPOVILLA, M.; LOZANO, J.; BARBOSA Jr., J. R. Influence of inlet flow maldistribution and carryover losses on the performance of thermal regenerators. *Applied Thermal Engineering*, v. 133, p. 472 – 482, 2018.

TREVIZOLI, P. V. *Development of thermal regenerators for magnetic applications*. Phd Thesis (PhD Thesis) — Federal Univeristy of Santa Catarina, 2015.

TREVIZOLI, P. V.; BARBOSA Jr., J. R.; FERREIRA, R. T. Experimental evaluation of a Gd-based linear reciprocating active magnetic regenerator test apparatus. *International Journal of Refrigeration*, v. 34, p. 1518 – 1526, 2011.

TREVIZOLI, P. V.; BARBOSA Jr., J. R.; OLIVEIRA, P. A.; CANESIN, F. C.; FERREIRA, R. T. Assessment of demagnetization phenomena in the performance of an active magnetic regenerator. *International Journal of Refrigeration*, v. 35, p. 1043 – 1054, 2012.

TREVIZOLI, P. V.; CHRISTIAANSE, T. V.; GOVINDAPPA, P.; NIKNIA, I.; TEYBER, R.; BARBOSA Jr., J. R.; ROWE, A. Magnetic heat pumps: An overview of design principles and challenges. *Science and Technology for the Built Environment*, v. 22, p. 507–519, 2016.

TREVIZOLI, P. V.; LOZANO, J. A.; PEIXER, G. F.; BARBOSA Jr., J. R. Design of nested halbach cylinder arrays for magnetic refrigeration applications. *Journal of Magnetism and Magnetic Materials*, Elsevier, v. 395, p. 109–122, 2015.

TREVIZOLI, P. V.; NAKASHIMA, A. T.; BARBOSA Jr., J. R. Performance evaluation of an active magnetic regenerator for cooling applications – part II: Mathematical modeling and thermal losses. *International Journal of Refrigeration*, v. 72, p. 206–217, 2016. ISSN 0140-7007.

TREVIZOLI, P. V.; NAKASHIMA, A. T.; PEIXER, G. F.; BARBOSA Jr., J. R. Performance evaluation of an active magnetic regenerator for cooling applications – part I: Experimental analysis and thermodynamic performance. *International Journal of Refrigeration*, v. 72, p. 192–205, 2016. ISSN 0140-7007.

TREVIZOLI, P. V.; NAKASHIMA, A. T.; PEIXER, G. F.; BARBOSA Jr., J. R. Performance assessment of different porous matrix geometries for active magnetic regenerators. *Applied Energy*, v. 187, p. 847 – 861, 2017.

TREVIZOLI, P. V.; PEIXER, G. F.; BARBOSA Jr., J. R. Thermal–hydraulic evaluation of oscillating-flow regenerators using water: Experimental analysis of packed beds of spheres. *International Journal of Heat and Mass Transfer*, v. 99, p. 918 – 930, 2016.

TSCHORA, L.; PIERRE, E.; PLANTEVIT, M.; ROBARDET, C. Electricity price forecasting on the day-ahead market using machine learning. *Applied Energy*, v. 313, p. 118752, 2022. ISSN 0306-2619.

TURA, A.; ROWE, A. Permanent magnet magnetic refrigerator design and experimental characterization. *International Journal of Refrigeration*, v. 34, p. 628 – 639, 2011.

TURAN, E. M.; JäSCHKE, J. Classification of undesirable events in oil well operation. In: *2021 23rd International Conference on Process Control (PC)*. [S.l.: s.n.], 2021. p. 157–162.

TUŠEK, J.; KITANOVSKI, A.; TOMC, U.; FAVERO, C.; POREDOŠ, A. Experimental comparison of multi-layered la–fe–co–si and single-layered gd active magnetic regenerators for use in a room-temperature magnetic refrigerator. *International journal of refrigeration*, Elsevier, v. 37, p. 117–126, 2014.

TUšEK, J.; KITANOVSKI, A.; POREDOš, A. Geometrical optimization of packed-bed and parallel-plate active magnetic regenerators. *International Journal of Refrigeration*, v. 36, p. 1456 – 1464, 2013.

TUšEK, J.; KITANOVSKI, A.; PREBIL, I.; POREDOš, A. Dynamic operation of an active magnetic regenerator(AMR): Numerical optimization of a packed-bed AMR. *International Journal of Refrigeration*, v. 34, p. 1507 – 1517, 2011.

TUšEK, J.; ZUPAN, S.; ŠARLAH, A.; PREBIL, I.; POREDOš, A. Development of a rotary magnetic refrigerator. *International Journal of Refrigeration*, v. 33, n. 2, p. 294–300, 2010. ISSN 0140-7007.

URRESTI, A.; CAMPOS-CELADOR, A.; SALA, J. Dynamic neural networks to analyze the behavior of phase change materials embedded in building envelopes. *Applied Thermal Engineering*, v. 158, p. 113783, 2019. ISSN 1359-4311.

VARGAS, R. E. V.; MUNARO, C. J.; CIARELLI, P. M.; MEDEIROS, A. G.; AMARAL, B. G. do; BARRIONUEVO, D. C.; ARAúJO, J. C. D. de; RIBEIRO, J. L.; MAGALHãES, L. P. A realistic and public dataset with rare undesirable real events in oil wells. *Journal of Petroleum Science and Engineering*, v. 181, p. 106223, 2019. ISSN 0920-4105.

VASWANI, A. Attention is all you need. *Advances in Neural Information Processing Systems*, 2017.

VEIGA, A. P. da; MARTINS, I. O.; BARCELOS, J. G.; FERREIRA, M. V. D.; ALVES, E. B.; SILVA, A. K. da; HASAN, A. R.; JR, J. R. B. Predicting thermal expansion pressure buildup in a deepwater oil well with an annulus partially filled with nitrogen. *Journal of Petroleum Science and Engineering*, Elsevier, v. 208, p. 109275, 2022.

VIEIRA, B. P. Modeling and optimization of active magnetic regenerators using La-Fe-Si based alloys. Master's thesis, Universidade Federal de Santa Catarina, Florianópolis, Brazil. 2020.

VIEIRA, B. P.; BEZ, H. N.; dos Santos, D.; LOZANO, J. A.; BARBOSA Jr., J. R. Interrelationship between flow profiles and the magnetic waveform and their influence on the performance of first-order active magnetic regenerators. *Applied Thermal Engineering*, v. 219, p. 119581, 2023. ISSN 1359-4311.

VIEIRA, B. P.; BEZ, H. N.; KUEPFERLING, M.; ROSA, M. A.; SCHAFER, D.; Plá Cid, C. C.; VIEYRA, H. A.; BASSO, V.; LOZANO, J. A.; BARBOSA Jr., J. R. Magnetocaloric properties of spheroidal La(Fe,Si,Mn)$_{13}$H$_{y}$ granules and their performance in epoxy-bonded active magnetic regenerators. *Applied Thermal Engineering*, v. 183, p. 116185, 2021.

VINCENT, A. M.; JIDESH, P. An improved hyperparameter optimization framework for automl systems using evolutionary algorithms. *Scientific Reports*, Nature Publishing Group UK London, v. 13, n. 1, p. 4737, 2023.

VIRTANEN, P.; GOMMERS, R.; OLIPHANT, T. E.; HABERLAND, M.; REDDY, T.; COURNAPEAU, D.; BUROVSKI, E.; PETERSON, P.; WECKESSER, W.; BRIGHT, J. *et al.* Scipy 1.0: fundamental algorithms for scientific computing in python. *Nature methods*, Nature Publishing Group US New York, v. 17, n. 3, p. 261–272, 2020.

VOLK, A.; KÄHLER, C. J. Density model for aqueous glycerol solutions. *Experiments in Fluids*, Springer, v. 59, n. 5, p. 75, 2018.

WANG, C.; QIANG, X.; XU, M.; WU, T. Recent advances in surrogate modeling methods for uncertainty quantification and propagation. *Symmetry*, MDPI, v. 14, n. 6, p. 1219, 2022.

WANG, C.-C.; CHI, K.-Y.; CHANG, C.-J. Heat transfer and friction characteristics of plain fin-and-tube heat exchangers, part II: Correlation. *International Journal of Heat and Mass Transfer*, v. 43, p. 2693 – 2700, 2000.

WANG, C.-C.; LIN, Y.-T.; LEE, C.-J.; CHANG, Y.-J. Investigation of wavy fin-and-tube heat exchangers: A contribution to databank. *Experimental Heat Transfer*, Taylor and Francis, v. 12, p. 73–89, 1999.

WANG, J.; RYAN, D.; ANTHONY, E. J.; WILDGUST, N.; AIKEN, T. Effects of impurities on co2 transport, injection and storage. *Energy Procedia*, Elsevier, v. 4, p. 3071–3078, 2011.

WANG, Q.; MA, Y.; ZHAO, K.; TIAN, Y. A comprehensive survey of loss functions in machine learning. *Annals of Data Science*, Springer, p. 1–26, 2020.

WAPLES, D. W.; WAPLES, J. S. A review and evaluation of specific heat capacities of rocks, minerals, and subsurface fluids. part 1: Minerals and nonporous rocks. *Natural resources research*, Springer, v. 13, n. 2, p. 97–122, 2004.

WATANABE, K.; TOMITA, Y.; ISHIBASHI, K.; IOKI, M.; SHIRASAKA, S. Framework for problem definition–a joint method of design thinking and systems thinking. In: WILEY ONLINE LIBRARY. *INCOSE International Symposium*. [S.l.], 2017. v. 27, n. 1, p. 57–71.

WETENHALL, B.; AGHAJANI, H.; CHALMERS, H.; BENSON, S.; FERRARI, M.; LI, J.; RACE, J.; SINGH, P.; DAVISON, J. Impact of co2 impurity on co2 compression, liquefaction and transportation. *Energy Procedia*, Elsevier, v. 63, p. 2764–2778, 2014.

WIJAYANTA, A. T.; ODA, T.; PURNOMO, C. W.; KASHIWAGI, T.; AZIZ, M. Liquid hydrogen, methylcyclohexane, and ammonia as potential hydrogen storage: Comparison review. *International Journal of Hydrogen Energy*, Elsevier, v. 44, n. 29, p. 15026–15044, 2019.

WILHELMSEN, Ø.; BERSTAD, D.; AASEN, A.; NEKSÅ, P.; SKAUGEN, G. Reducing the exergy destruction in the cryogenic heat exchangers of hydrogen liquefaction processes. *International Journal of Hydrogen Energy*, Elsevier, v. 43, n. 10, p. 5033–5047, 2018.

WU, J. Introduction to convolutional neural networks. *National Key Lab for Novel Software Technology. Nanjing University. China*, v. 5, n. 23, p. 495, 2017.

WU, J.; CHEN, X.-Y.; ZHANG, H.; XIONG, L.-D.; LEI, H.; DENG, S.-H. Hyperparameter optimization for machine learning models based on bayesian optimization. *Journal of Electronic Science and Technology*, Elsevier, v. 17, n. 1, p. 26–40, 2019.

WYLIE, E.; STREETER, V. *Fluid transients*. [S.l.]: FEB Press, 1983.

XU, R.; WUNSCH, D. *Clustering*. [S.l.]: John Wiley & Sons, 2008.

XU, X.; LASALA, S.; PRIVAT, R.; JAUBERT, J.-N. E-ppr78: A proper cubic eos for modelling fluids involved in the design and operation of carbon dioxide capture and storage (ccs) processes. *International Journal of Greenhouse Gas Control*, Elsevier, v. 56, p. 126–154, 2017.

XUE, Q.; LI, G.; ZHANG, H.; SHEN, S.; CHEN, Z.; LIU, Y. Fault diagnosis and abnormality detection of lithium-ion battery packs based on statistical distribution. *Journal of Power Sources*, v. 482, p. 228964, 2021.

YAN, J.; ZHANG, B.; LIU, N.; YAN, S.; CHENG, Q.; FAN, W.; YANG, Q.; XI, W.; CHEN, Z. Effective and efficient dimensionality reduction for large-scale and streaming data preprocessing. *IEEE transactions on Knowledge and Data Engineering*, IEEE, v. 18, n. 3, p. 320–333, 2006.

YANG, K.-T. Role of artificial intelligence (ai) in thermal science and engineering. In: *Heat Transfer Summer Conference*. [S.l.: s.n.], 2007. v. 42762, p. 871–883.

YANG, L.; SHAMI, A. On hyperparameter optimization of machine learning algorithms: Theory and practice. *Neurocomputing*, Elsevier, v. 415, p. 295–316, 2020.

YANG, Y.; TONG, L.; YIN, S.; LIU, Y.; WANG, L.; QIU, Y.; DING, Y. Status and challenges of applications and industry chain technologies of hydrogen in the context of carbon neutrality. *Journal of Cleaner Production*, Elsevier, v. 376, p. 134347, 2022.

YAO, Y.; ROSASCO, L.; CAPONNETTO, A. On early stopping in gradient descent learning. *Constructive Approximation*, Springer, v. 26, n. 2, p. 289–315, 2007.

YOUSEFZADEH, R.; CAO, X. To what extent should we trust ai models when they extrapolate? *arXiv preprint arXiv:2201.11260*, 2022.

YU, B.; LIU, M.; EGOLF, P. W.; KITANOVSKI, A. A review of magnetic refrigerator and heat pump prototypes built before the year 2010. *International Journal of Refrigeration*, v. 33, p. 1029 – 1060, 2010.

YU, T.; ZHU, H. *Hyper-Parameter Optimization: A Review of Algorithms and Applications*. 2020.

YUAN, L.; QIAN, S.; YU, J. Numerical study on the multi-layered magnetocaloric regenerators. *Applied Thermal Engineering*, Elsevier, v. 204, p. 118001, 2022.

ZAHEER, R.; SHAZIYA, H. A study of the optimization algorithms in deep learning. In: IEEE. *2019 third international conference on inventive systems and control (ICISC)*. [S.l.], 2019. p. 536–539.

ZAMORA, M.; ROY, S.; SLATER, K.; TRONCOSO, J. Study on the volumetric behavior of base oils, brines, and drilling fluids under extreme temperatures and pressures. *SPE Drilling & Completion*, OnePetro, v. 28, n. 03, p. 278–288, 2013.

ZHA, D.; BHAT, Z. P.; LAI, K.-H.; YANG, F.; HU, X. Data-centric ai: Perspectives and challenges. In: SIAM. *Proceedings of the 2023 SIAM International Conference on Data Mining (SDM)*. [S.l.], 2023. p. 945–948.

ZHANG, B.; GUAN, Z.; LU, N.; HASAN, A. R.; WANG, Q.; XU, B. Trapped annular pressure caused by thermal expansion in oil and gas wells: A review of prediction approaches, risk assessment and mitigation strategies. *Journal of Petroleum Science and Engineering*, Elsevier, v. 172, p. 70–82, 2019.

ZHANG, J. Modern monte carlo methods for efficient uncertainty quantification and propagation: A survey. *Wiley Interdisciplinary Reviews: Computational Statistics*, Wiley Online Library, v. 13, n. 5, p. e1539, 2021.

ZHANG, M.; ABDELAZIZ, O.; MOMEN, A. M.; ABU-HEIBA, A. A numerical analysis of a magnetocaloric refrigerator with a 16-layer regenerator. *Scientific Reports*, Nature Publishing Group UK London, v. 7, n. 1, p. 13962, 2017.

ZHANG, X.; LIU, C.-A. Model averaging prediction by k-fold cross-validation. *Journal of Econometrics*, Elsevier, v. 235, n. 1, p. 280–301, 2023.

ZHANG, Y.; WU, J.; ZHANG, H. Performance analysis of a cascade room temperature magnetic refrigerator for improving temperature span. *International Journal of Refrigeration*, Elsevier, v. 143, p. 68–77, 2022.

ZHANG, Z. Missing data imputation: focusing on single imputation. *Annals of translational medicine*, AME Publications, v. 4, n. 1, 2016.

ZHU, X. J. Semi-supervised learning literature survey. University of Wisconsin-Madison Department of Computer Sciences, 2005.

ZIMM, C.; BOEDER, A.; CHELL, J.; STERNBERG, A.; FUJITA, A.; FUJIEDA, S.; FUKAMICHI, K. Design and performance of a permanent-magnet rotary refrigerator. *International Journal of Refrigeration*, v. 29, p. 1302 – 1306, 2006.

ZITZLER, E.; DEB, K.; THIELE, L. Comparison of multiobjective evolutionary algorithms: Empirical results. *Evolutionary Computation*, MIT Press, Cambridge, MA, USA, v. 8, n. 2, p. 173–195, 2000.

LIST OF PUBLICATIONS

Papers Published in Peer-Reviewed Journals

1. **PEIXER, G. F.**; LORENZONI, A. M.; FARIA, P. V.; REIF, D. D. de; NAKASHIMA, A. T. D.; TEIXEIRA, C. S.; LOZANO, J. A.; BARBOSA Jr., J. R. From concept to operation: design strategies, experimental evaluation, and engineering challenges across three generations of a magnetocaloric air conditioner. *AIP Advances*, 2026. *Accepted for publication*.

2. **PEIXER, G. F.**; LORENZONI, A. M.; AZEREDO, Y. C.; SILVA, P. M.; SILVA, M. C.; HOFFMANN, G.; SANTOS, D. dos; DUTRA, S. L.; ROSÁRIO, G. M. do; TEZA, H. F.; PAGNAN, E.; *et al.* Energy and efficiency breakdown analysis of a large-scale magnetic refrigerator. *Applied Thermal Engineering*, v. 280, p. 128157, 2025.

3. **PEIXER, G. F.**; TOMC, U.; KITANOVSKY, A.; LOZANO, J. A.; BARBOSA Jr., J. R. AI-driven Monte Carlo uncertainty analysis of Curie temperature effects on active magnetic regenerator performance. *International Journal of Refrigeration*, 2025.

4. TOMC, U.; **PEIXER, G. F.**; BAHL, C.; NIELSEN, K.; LOZANO, J. A.; BARBOSA Jr., J. R.; KITANOVSKY, A. Influence of layering and Curie temperature uncertainty on the performance of multilayer active magnetic regenerators. *Advanced Functional Materials*, 2025.

5. REIF, D. D. de; DÖRING, A. M.; ANDRE, F. M.; POFFO, C. M.; **PEIXER, G. F.**; LOZANO, J. A.; BARBOSA Jr., J. R.; TEIXEIRA, C. S. Influence of the magnetic state in the thermo-structural properties of commercially available $La(Fe,Si,Mn)_{13}Hz$ microparticles applied in magnetic refrigeration prototypes. *IEEE Transactions on Magnetics*, 2025.

6. CASTTRO-ANAYA, L. E.; MARESE, E.; **PEIXER, G. F.**; LOZANO, J. A.; BARBOSA Jr., J. R.; GONZÁLEZ, S. Y. G. Machine learning methodologies applied to magnetocaloric perovskites discovery. *Journal of Chemical Information and Modeling*, v. 65, n. 4, p. 1812–1825, 2025.

7. **PEIXER, G. F.**; LORENZONI, A. M.; AZEREDO, Y. C.; SILVA, P. M.; SILVA, M. C.; HOFFMANN, G.; SANTOS, D. dos; DUTRA, S. L.; ROSÁRIO, G. M. do; TEZA, H. F.; PAGNAN, E.; *et al.* Thermodynamic assessment of a large-scale magnetic air conditioning prototype. *International Journal of Refrigeration*, 2024.

8. DÖRING, A. M.; REIF, D. D. de; ROSA, M. A.; **PEIXER, G. F.**; MACCARI, F.; SKOKOV, K.; GUTFLEISCH, O.; *et al.* Long-time aging of La(Fe,Si,Mn)$_{13}$Hz microparticles using different fluids for magnetic refrigeration systems. *Journal of Magnetism and Magnetic Materials*, v. 591, p. 171721, 2024.

9. HOFFMANN, G.; NAKASHIMA, A. T.; **PEIXER, G. F.**; LOZANO, J. A.; BARBOSA Jr., J. R.; FLESCH, R. C. Static and dynamic modeling and identification of a magnetic refrigerator. *International Journal of Refrigeration*, v. 158, p. 303–312, 2024.

10. CATTELAN, L. F.; **PEIXER, G. F.**; LUZ, M. V. D.; BARBOSA Jr., J. R.; LOZANO, J. A. Design of magnetic circuits for magnetocaloric refrigeration via topology optimization. *IEEE Transactions on Magnetics*, 2024.

11. SILVA, P. M.; **PEIXER, G. F.**; LORENZONI, A. M.; AZEREDO, Y.; FLESCH, R. C.; LOZANO, J. A.; BARBOSA Jr., J. R. Predicting the dynamic behavior of a magnetocaloric cooling prototype via artificial neural networks. *Applied Thermal Engineering*, v. 248, p. 123060, 2024.

12. OLIVEIRA, M. S. de; **PEIXER, G. F.**; ROSA, M. A. A.; FORCELLINI, F. A.; BARBOSA Jr., J. R.; LOZANO, J. A. Value deployment in set-based design: a design space propagation perspective to integrate manufacturing in the narrowing-down process. *Systems Engineering*, v. 28, n. 2, p. 175–189, 2024.

13. HUGHES, A. R. M.; SINGH, B. S. B.; REMELI, M. F.; **PEIXER, G. F.**; SINGH, W. K. R. AI-enhanced generative design for efficient heat exchangers in thermoelectric generators: revolutionizing waste heat recovery in thermoelectricity. *Journal of Mechanical Engineering*, v. 13, p. 235–255, 2024.

14. **PEIXER, G. F.**; SILVA, M. C.; LORENZONI, A.; HOFFMANN, G.; SANTOS, D. dos; ROSÁRIO, G. M. do; TEZA, H. F.; PAGNAN, E.; SILVA, P. M.; DUTRA, S. L.; *et al.* A magnetocaloric air-conditioning system prototype. *International Journal of Refrigeration*, v. 151, p. 1–13, 2023.

15. **PEIXER, G. F.**; NAKASHIMA, A. T. D.; LOZANO, J. A.; BARBOSA Jr., J. R. System-level multiobjective optimization of a magnetic air conditioner through coupling of artificial neural networks and genetic algorithms. *Applied Thermal Engineering*, v. 227, p. 120368, 2023.

16. OLIVEIRA, M. S. de; **PEIXER, G. F.**; FORCELLINI, F. A.; BARBOSA Jr., J. R.; LOZANO, J. A. Model-based trade-off curves to support the set-based concurrent engineering of highly innovative projects. *Concurrent Engineering*, 2023.

17. **PEIXER, G. F.**; DUTRA, S. L.; CALOMENO, R. S.; SÁ, N. M. de; LANG, G. B.; LOZANO, J. A.; *et al.* Influence of heat exchanger design on the thermal performance of a domestic wine cooler driven by a magnetic refrigeration system. *Anais da Academia Brasileira de Ciências*, v. 94, 2022.

18. CALOMENO, R. S.; DUTRA, S. L.; SÁ, N. M. de; **PEIXER, G. F.**; LOZANO, J. A.; BARBOSA Jr., J. R. Temperature pull-down of a retrofitted wine refrigerator cabinet cooled by a caloric system emulator. *Anais da Academia Brasileira de Ciências*, v. 94, n. 4, p. e20201510, 2022.

19. NAKASHIMA, A. T. D.; **PEIXER, G. F.**; LOZANO, J. A.; BARBOSA Jr., J. R. A lumped-element magnetic refrigerator model. *Applied Thermal Engineering*, v. 204, p. 117918, 2022.

20. OLIVEIRA, M. S. de; **PEIXER, G. F.**; FORCELLINI, F. A.; BARBOSA Jr., J. R.; LOZANO, J. A. Innovation level in set-based design: an integrated approach with chosen-to-fit and custom-to-fit solutions. *Journal of Engineering Design*, v. 33, n. 12, p. 990–1015, 2022.

21. NAKASHIMA, A. T.; FORTKAMP, F. P.; SÁ, N. M. de; SANTOS, V. M. dos; HOFFMANN, G.; **PEIXER, G. F.**; *et al.* A magnetic wine cooler prototype. *International Journal of Refrigeration*, v. 122, p. 110–121, 2021.

Papers Published or Presented in Conference Proceedings

1. **PEIXER, G. F.**; LORENZONI, A. M.; SUCARIA, R.; FARIA, P. V.; NAKASHIMA, A. T. D.; TEIXEIRA, C. S.; LOZANO, J. A.; BARBOSA Jr., J. R. Experimental evaluation and performance optimization of a large-scale magnetic refrigeration prototype for air conditioning systems. In: 15th REHVA HVAC World Congress – CLIMA, 2025, Milan, Italy.

2. **PEIXER, G. F.**; LORENZONI, A. M.; AZEREDO, Y.; SILVA, P. M.; SUCARIA, R.; FARIA, P. V.; VIEIRA, B. P.; NAKASHIMA, A. T. D.; TEIXEIRA, C. S.; LOZANO, J. A.; BARBOSA Jr., J. R. Assessment of thermodynamic progression in the performance of a large-scale magnetic refrigeration system. In: Workshop on I-Caloric Effects (WiCE), 2025, online.

3. **PEIXER, G. F.**; SGANZERLA, Y. F.; CASAGRANDE, J. B.; TOMC, U.; KITANOVSKY, A.; LOZANO, J. A.; BARBOSA Jr., J. R. AI-driven multiobjective optimization of hydrogen liquefaction precooling systems. In: European PhD Hydrogen Conference, 2025, Trieste, Italy.

4. **PEIXER, G. F.**; ALVES, E. B. M.; BARBOSA Jr., J. R.; LOZANO, J. A. Assessment of the effect of geometric uncertainty on thermostructural responses in oil wells using artificial neural networks. In: National Meeting on Construction of Oil and Gas Wells (ENAHPE), 2025, Campina Grande, Brazil.

5. VIEIRA, A. L. L.; **PEIXER, G. F.**; LOZANO, J. A. Estudo de tecnologias para a liquefação de hidrogênio: modelagem, simulação e otimização. In: National Meeting on Construction of Oil and Gas Wells (ENAHPE), 2025, São Carlos, Brazil.

6. SCHMOCKEL, K. C.; **PEIXER, G. F.**; LOZANO, J. A.; BARBOSA Jr., J. R. Development and evaluation of anomaly detection in oil wells via LSTM-autoencoders. In: Workshop on the 3W Dataset (3W), 2025, online.

7. **PEIXER, G. F.**; SGANZERLA, Y. F.; CASAGRANDE, J. B.; CARNEIRO, M. V. P.; BARBOSA Jr., J. R.; LOZANO, J. A. AI-driven multiobjective optimization of hydrogen liquefaction precooling systems. In: Brazilian Congress of Hydrogen, 2025, Brasília, Brazil.

8. VICENTE, A. S. M.; CARNEIRO, M. V. P.; FARIA, P. V.; **PEIXER, G. F.**; BARBOSA Jr., J. R.; LOZANO, J. A. Análise de desempenho térmico de sistemas de resfriamento em FCEVs por meio do método efetividade–NUT TV 3. In: Brazilian Congress of Hydrogen, 2025, Brasília, Brazil.

9. DIAS, T. Z.; FARIA, P. V.; CARNEIRO, M. V. P.; **PEIXER, G. F.**; BARBOSA Jr., J. R.; LOZANO, J. A. Visualização em alta velocidade da formação de bolhas de hidrogênio em eletrodos planos: efeitos da densidade de corrente na eletrólise alcalina. In: Brazilian Congress of Hydrogen, 2025, Brasília, Brazil.

10. DIAS, T. Z.; FARIA, P. V.; CARNEIRO, M. V. P.; **PEIXER, G. F.**; BARBOSA Jr., J. R.; LOZANO, J. A. Caracterização experimental de um eletrolisador do tipo PEM de 500 W: avaliação estática para produção de hidrogênio. In: Brazilian Congress of Hydrogen, 2025, Brasília, Brazil.

11. FARIA, P. V.; REMLINGER, E.; CARNEIRO, M. V. P.; **PEIXER, G. F.**; BOENG, J.; OLIVEIRA Jr., A. A.; BARBOSA Jr., J. R.; LOZANO, J. A. Caracterização experimental de uma célula a combustível do tipo PEM de 100 W: avaliação estática e dinâmica para aplicações em transporte. In: Brazilian Congress of Hydrogen, 2025, Brasília, Brazil.

12. CARNEIRO, M. V. P.; FARIA, P. V.; **PEIXER, G. F.**; BARBOSA Jr., J. R.; LOZANO, J. A. Comparação experimental entre resfriamento por spray e microcanais como estratégias compactas de gerenciamento térmico. In: Brazilian Congress of Hydrogen, 2025, Brasília, Brazil.

13. CASAGRANDE, J. B.; **PEIXER, G. F.**; LOZANO, J. A.; BARBOSA Jr., J. R. Multiobjective optimization of reheated Organic Rankine Cycle in depleted oil well using artificial neural networks and evolutionary algorithms. In: 28th ABCM International Congress of Mechanical Engineering, 2025, Curitiba, Brazil.

14. SCHMOCKEL, K. C.; **PEIXER, G. F.**; LOZANO, J. A.; BARBOSA Jr., J. R. Anomaly detection in oil-producing wells using LSTM autoencoder. In: 28th ABCM International Congress of Mechanical Engineering, 2025, Curitiba, Brazil.

15. **PEIXER, G. F.**; ALVES, E. B. D. M.; FERREIRA, J. C. A.; FORTKAMP, F.; LOZANO, J. A.; BARBOSA Jr., J. R. AI-driven sensitivity and uncertainty analysis of thermostructural effects in offshore oil wells. In: 28th ABCM International Congress of Mechanical Engineering, 2025, Curitiba, Brazil.

16. LUZ, G. M.; NAKASHIMA, A. T. D.; **PEIXER, G. F.**; BARBOSA Jr., J. R.; LOZANO, J. A. Development of a thermal systems modeling software for energy research applications. In: 28th ABCM International Congress of Mechanical Engineering, 2025, Curitiba, Brazil.

17. VICENTE, A. S. M.; CARNEIRO, M. V. P.; FARIA, P. V.; **PEIXER, G. F.**; LOZANO, J. A. Heat transfer analysis of radiator and fuel cell stack in FCEVs under variable operating conditions. In: 28th ABCM International Congress of Mechanical Engineering, 2025, Curitiba, Brazil.

18. FARIA, P. V.; DIAS, T. Z.; CARNEIRO, M. V. P.; **PEIXER, G. F.**; LOZANO, J. A. Hydrogen evolution in planar electrodes: current density effects and high-speed visualization. In: 28th ABCM International Congress of Mechanical Engineering, 2025, Curitiba, Brazil.

19. FARIA, P. V.; REMLINGER, E.; CARNEIRO, M. V. P.; **PEIXER, G. F.**; BOENG, J.; OLIVEIRA Jr., A. A.; LOZANO, J. A. Steady-state and dynamic analysis of a 350 W proton exchange membrane fuel cell: experimental insights for model validation. In: 28th ABCM International Congress of Mechanical Engineering, 2025, Curitiba, Brazil.

20. **PEIXER, G. F.**; NAKASHIMA, A. T. D.; SÁ, N. M. de; AZEREDO, Y.; LORENZONI, A. M.; LUZ, G.; SUCARIA, R.; *et al.* Performance evaluation of TRL-6 magnetic refrigeration prototypes. In: IEEE International Magnetics Conference (INTERMAG), 2024, Rio de Janeiro, Brazil.

21. DÖRING, A.; REIF, D. D.; ROSA, M. A.; **PEIXER, G. F.**; MACCARI, F.; SKOKOV, K.; GUTFLEISCH, O.; *et al.* Long-time aging of La(Fe,Si,Mn)$_{13}$Hz microparticles using different fluids for magnetic refrigeration systems. In: IEEE International Magnetics Conference (INTERMAG), 2024, Rio de Janeiro, Brazil.

22. SGANZERLA, Y. F.; CASAGRANDE, J. B.; **PEIXER, G. F.**; LOZANO, J. A.; BARBOSA Jr., J. R. Optimization of precooling cycles for hydrogen liquefaction systems by machine-learning-enhanced genetic algorithms. In: 20th Brazilian Congress of Thermal Sciences and Engineering, 2024, Foz do Iguaçu, Brazil.

23. **PEIXER, G. F.**; LORENZONI, A. M.; AZEREDO, Y.; SILVA, P. M.; SUCARIA, R.; FARIA, P. V.; VIEIRA, B. P.; *et al.* Thermodynamic evaluation of the evolution of the performance of a large-scale magnetic refrigeration system. In: 20th Brazilian Congress of Thermal Sciences and Engineering, 2024, Foz do Iguaçu, Brazil.

24. DIAS, T. Z.; FARIA, P. V.; CARNEIRO, M. V. P.; FERREIRA, J. C. A.; **PEIXER, G. F.**; LOZANO, J. A.; BARBOSA Jr., J. R. Sensitivity analysis of electrochemical modeling parameters on PEMFC polarization curve/efficiency. In: 20th Brazilian Congress of Thermal Sciences and Engineering, 2024, Foz do Iguaçu, Brazil.

25. VILLAMIL, R. H.; MAY, J. S.; FALLGATER, R. H.; VARGAS, R.; NAKASHIMA, A. T. D.; **PEIXER, G. F.**; LOZANO, J. A.; BARBOSA Jr., J. R. Assessment of deep learning techniques for anomaly detection in offshore oil wells. In: 20th Brazilian Congress of Thermal Sciences and Engineering, 2024, Foz do Iguaçu, Brazil.

26. **PEIXER, G. F.**; CASAGRANDE, J. B.; SGANZERLA, Y. F.; LOZANO, J. A.; BARBOSA Jr., J. R. Comparative analysis of commercial and emerging hydrogen liquefaction technologies. In: Petrobras Workshop on Low-Carbon Hydrogen, 2024, Rio de Janeiro, Brazil.

27. **PEIXER, G. F.**; VILLAMIL, R. H.; MAY, J. S.; FALLGATER, R. H.; VARGAS, R.; NAKASHIMA, A. T. D.; LOZANO, J. A.; BARBOSA Jr., J. R. Evaluation of anomaly detection in oil wells via LSTM-autoencoders. In: Workshop on the 3W Dataset (3W), 2024, online.

28. **PEIXER, G. F.**; CASAGRANDE, J. B.; DIAS, T. Z.; SGANZERLA, Y. F.; LOZANO, J. A.; BARBOSA Jr., J. R. Avaliação de tecnologias inovadoras para a liquefação de hidrogênio. In: 3rd Brazilian Congress of Hydrogen, 2023, Maricá, Brazil.

29. FERREIRA, J. C.; FARIA, P. V.; **PEIXER, G. F.**; GONZÁLEZ, S. Y.; OLIVEIRA, A. M. Jr.; LOZANO, J. A.; BARBOSA Jr., J. R. Modelagem computacional do resfriamento direto com mudança de fase em células combustíveis de troca de prótons. In: 3rd Brazilian Congress of Hydrogen, 2023, Maricá, Brazil.

30. **PEIXER, G. F.**; CASAGRANDE, J. B.; DIAS, T. Z.; SGANZERLA, Y. F.; LOZANO, J. A.; BARBOSA Jr., J. R. Performance assessment of commercial and innovative technologies for hydrogen liquefaction. In: Energy Transition Research and Innovation (ETRI), 2023, São Paulo, Brazil.

31. LOZANO, J. A.; **PEIXER, G. F.**; NAKASHIMA, A. T.; VIEIRA, B. P.; SÁ, N. M. de; FARIA, P. V.; *et al.* Oportunidades e desafios na refrigeração magnetocalórica. In: 18th Brazilian Congress of Refrigeration, Air Conditioning, Ventilation, Heating and Air Treatment, 2023, São Paulo, Brazil.

32. **PEIXER, G. F.**; CASAGRANDE, J. B.; DIAS, T. Z.; SGANZERLA, Y. F.; LOZANO, J. A.; BARBOSA Jr., J. R. Comparison of conventional and emerging technologies for hydrogen liquefaction. In: 26th International Congress of Refrigeration, 2023, Paris, France.

33. **PEIXER, G. F.**; LORENZONI, A. M.; AZEREDO, Y.; SILVA, P. M.; SILVA, M. C. R.; HOFFMANN, G.; *et al.* Thermodynamic performance evaluation of a magnetocaloric air conditioner prototype. In: 26th International Congress of Refrigeration, 2023, Paris, France.

34. SÁ, N. M. de; LUZ, G. M.; NAKASHIMA, A. T. D.; PAGNAN, E.; LORENZONI, A. M.; **PEIXER, G. F.**; *et al.* Polomag project: designing a compact magnetocaloric wine cooler. In: 26th International Congress of Refrigeration, 2023, Paris, France.

35. DIAS, T. Z.; CASAGRANDE, J. B.; SGANZERLA, Y. F.; **PEIXER, G. F.**; LOZANO, J. A.; BARBOSA Jr., J. R. An overview and a comparative analysis of the main technologies for hydrogen storage. In: 27th International Congress of Mechanical Engineering, 2023, Florianópolis, Brazil.

36. CASAGRANDE, J. B.; DIAS, T. Z.; SGANZERLA, Y. F.; **PEIXER, G. F.**; LOZANO, J. A.; BARBOSA Jr., J. R. Hydrogen liquefaction: a review of the ongoing methods and a critical analysis of the current studies. In: 27th International Congress of Mechanical Engineering, 2023, Florianópolis, Brazil.

37. SILVA, P. M.; AZEREDO, Y.; LORENZONI, A. M.; **PEIXER, G. F.**; FLESCH, R. C. C.; LOZANO, J. A.; BARBOSA Jr., J. R. Modeling the dynamic operation of a magnetic refrigerator via recurrent neural networks. In: 27th International Congress of Mechanical Engineering, 2023, Florianópolis, Brazil.

38. SUCARIA, R.; LORENZONI, A. M.; AZEREDO, Y.; NAKASHIMA, A. T. D.; **PEIXER, G. F.**; LOZANO, J. A.; BARBOSA Jr., J. R. Optimization of a magnetocaloric air conditioner prototype. In: 27th International Congress of Mechanical Engineering, 2023, Florianópolis, Brazil.

39. FARIA, P. V.; FERREIRA, J. C. A.; **PEIXER, G. F.**; LOZANO, J. A.; BARBOSA Jr., J. R. A critical review of thermal management of proton-exchange membrane fuel cells. In: 27th International Congress of Mechanical Engineering, 2023, Florianópolis, Brazil.

40. SÁ, N. M. de; LUZ, G. M.; NAKASHIMA, A. T. D.; PAGNAN, E.; LORENZONI, A. M.; **PEIXER, G. F.**; LOZANO, J. A.; BARBOSA Jr., J. R. Performance prediction of a novel compact magnetocaloric wine cooler. In: 27th International Congress of Mechanical Engineering, 2023, Florianópolis, Brazil.

41. **PEIXER, G. F.**; NAKASHIMA, A. T. D.; SÁ, N. M.; AZEREDO, Y.; LORENZONI, A. M.; LUZ, G.; SUCARIA, R.; *et al.* Performance evaluation of TRL-6 magnetic refrigeration

prototypes. In: IEEE International Magnetics Conference (INTERMAG), 2023, Rio de Janeiro, Brazil.

42. **PEIXER, G. F.**; SILVA, M. C. R.; LORENZONI, A. M.; HOFFMANN, G.; SANTOS, D.; DUTRA, S. L.; *et al.* Evaluating the performance of a TRL-6 magnetic air conditioner prototype. In: 19th International Refrigeration and Air Conditioning Conference at Purdue, 2022, West Lafayette, United States.

43. CERUTTI, M. A.; **PEIXER, G. F.**; LOZANO, J. A.; BARBOSA Jr., J. R. Evaluation of machine learning models to predict the thermal performance of active magnetic regenerators. In: 19th Brazilian Congress of Thermal Sciences and Engineering, 2022, Bento Gonçalves, Brazil.

44. FARIA, P. V.; VIEIRA, B. P.; TEZA, H. F.; HOFFMANN, G.; **PEIXER, G. F.**; NAKASHIMA, A. T. D.; *et al.* Thermal-hydraulic characterization of a triangular micro channel regenerator via the single-blow method. In: 19th Brazilian Congress of Thermal Sciences and Engineering, 2022, Bento Gonçalves, Brazil.

45. NAKASHIMA, A. T. D.; PAGNAN, E.; SÁ, N. M. de; LORENZONI, A. M.; LUZ, G. M.; HOFFMANN, G.; *et al.* Magnetic refrigeration technology assessment: design of a magnetic wine cooler. In: 19th Brazilian Congress of Thermal Sciences and Engineering, 2022, Bento Gonçalves, Brazil.

46. PAGNAN, E.; CATTELAN, L. F.; **PEIXER, G. F.**; LORENZONI, A. M.; HOFFMANN, G.; SILVA, M. C. R.; *et al.* Enhancing the frequency of magnetic refrigerators using dummy regenerators. In: 19th Brazilian Congress of Thermal Sciences and Engineering, 2022, Bento Gonçalves, Brazil.

47. CERUTTI, M. A.; **PEIXER, G. F.**; LOZANO, J. A.; BARBOSA Jr., J. R. Evaluation of machine learning models to predict the thermal performance of active magnetic regenerators. In: Workshop Brasileiro em Efeitos I-Calóricos (WBEIC), 2022, online.

48. **PEIXER, G. F.**; VIEIRA, B. P.; FORTKAMP, F.; BEZ, H. N.; CATTELAN, L. F.; TEZA, H. F.; *et al.* Integrated design of a large-scale magnetic refrigerator. In: 9th IIR International Conference on Caloric Cooling and Applications of Caloric Materials, 2021, Maryland, United States.

49. FORTKAMP, F.; CATTELAN, L. F.; **PEIXER, G. F.**; LOZANO, J. A.; BARBOSA Jr., J. R. Using machine learning to design a large-scale magnetic circuit. In: 9th IIR International Conference on Caloric Cooling and Applications of Caloric Materials, 2021, Maryland, United States.

50. HOFFMANN, G.; NAKASHIMA, A. T. D.; **PEIXER, G. F.**; LOZANO, J. A.; FLESCH, R. C.; BARBOSA Jr., J. R. Cabinet temperature control logic in a magnetic refrigerator. In: 9th IIR International Conference on Caloric Cooling and Applications of Caloric Materials, 2021, Maryland, United States.

51. SANTOS, D. dos; DUTRA, S. L.; RIBEIRO, M.; LORENZONI, A. M.; ROSÁRIO, G. M. do; SILVA, M. C.; *et al.* Designing a hydraulic management system for a large-scale magnetic refrigerator. In: 9th IIR International Conference on Caloric Cooling and Applications of Caloric Materials, 2021, Maryland, United States.

52. NAKASHIMA, A. T. D.; **PEIXER, G. F.**; LOZANO, J. A.; BARBOSA Jr., J. R. An AMR lumped model for magnetic refrigerator system simulation. In: 9th IIR International Conference on Caloric Cooling and Applications of Caloric Materials, 2021, Maryland, United States.

53. PAGNAN, E.; **PEIXER, G. F.**; TEZA, H. F.; VIEIRA, B.; LOZANO, J. A.; BARBOSA Jr., J. Influence of the heat transfer fluid on the performance of an active magnetic regenerator: a sensitivity analysis. In: 26th International Congress of Mechanical Engineering, 2021, Florianópolis, Brazil.

54. SANTOS, D. dos; SILVA, M. C. Régio e; HOFFMANN, G.; LORENZONI, A.; **PEIXER, G. F.**; LOZANO, J. A.; BARBOSA Jr., J. Experimental evaluation of the fluid flow management system of a magnetic air conditioner. In: 26th International Congress of Mechanical Engineering, 2021, Florianópolis, Brazil.

55. SILVA, M. C. Régio e; ROSÁRIO, G. M. do; DUTRA, S. L.; CAPOVILLA, M.; LIMA, R. V. de; LORENZONI, A.; *et al.* Development and characterization of a calibrated calorimeter to evaluate air conditioning systems. In: 26th International Congress of Mechanical Engineering, 2021, Florianópolis, Brazil.

56. TEZA, H. F.; VIEIRA, B. P.; SÁ, N. M. de; NAKASHIMA, A. T. D.; **PEIXER, G. F.**; HOFFMANN, G.; *et al.* Characterization of the thermo-hydraulic performance of a $La(Fe,Mn,Si)_{13}Hy$ regenerator. In: 26th International Congress of Mechanical Engineering, 2021, Florianópolis, Brazil.

Papers Submitted for Publication or in Preparation

1. **PEIXER, G. F.**; LORENZONI, A.; FARIA, P. V.; NAKASHIMA, A.; TEIXEIRA, C. S.; BARBOSA, J. R.; LOZANO, J. A. Design and Experimental Evaluation of a Pilot-Scale Magnetocaloric Air Conditioner. *Abstract accepted in the International Heat Conference 2026*.

2. VARGAS, R.; MELO Jr., A.; MUNARO, C.; LIMA, C.; LIMA Jr., E.; BARROCAS, F.; VAREJÃO, F.; **PEIXER, G. F.**; MELO, I.; OLIVEIRA, N.; BARBOSA Jr., J. R.; LOZANO, J. A.; ARAUJO, J.; CARNEIRO, J.; LOPES, L.; GOUVEIA, L.; FERNANDES, M.; SCRAMINGNON, M.; CIARELLI, P.; BRANCO, R.; *et al.* 3W Dataset 2.0.0: a realistic and public dataset with rare undesirable real events in oil wells. *Submitted for publication in Nature Scientific Data*.

3. TOMC, U.; **PEIXER, G. F.**; BAHL, C. R. H.; NIELSEN, K. K.; LOZANO, J. A.; BARBOSA Jr., J. R.; KITANOVSKI, A. Evaluation of Curie Temperature Effects in the Performance of Active Magnetic Regenerators – Part I: Second Order Phase Transition. *Abstract accepted in the XIth IIR THERMAG International Conference on Solid-State Cooling, Heating, and Energy Harvesting*.

4. **PEIXER, G. F.**; TOMC, U.; KITANOVSKI, A.; BARBOSA Jr., J. R.; LOZANO, J. A. Evaluation of Curie Temperature Effects in the Performance of Active Magnetic Regenerators – Part II: First Order Phase Transition. *Abstract accepted in the XIth IIR THERMAG International Conference on Solid-State Cooling, Heating, and Energy Harvesting*.

5. **PEIXER, G. F.**; LORENZONI, A.; FARIA, P.; REIF, D.; NAKASHIMA, A. D.; TEIXEIRA, C. S.; BARBOSA Jr., J. R.; LOZANO, J. A. Assessment of the Thermodynamic Performance Evolution of a Magnetic Air Conditioner Prototype. *Abstract accepted in the XIth IIR THERMAG International Conference on Solid-State Cooling, Heating, and Energy Harvesting*.

6. **PEIXER, G. F.**; LORENZONI, A.; NAKASHIMA, A. D.; TEIXEIRA, C. S.; BARBOSA Jr., J. R.; LOZANO, J. A. Pilot-Scale Demonstration and Perspectives of Magnetic Refrigeration Systems. *Abstract submitted for the 2026 Herrick Conferences at Purdue University*.

7. **PEIXER, G. F.**; ALVES, E. B. D. M.; BARBOSA Jr., J. R.; LOZANO, J. A. Uncertainty Evaluation of Fluid Thermophysical Properties on Thermostructural Responses of Oil Wells Using Artificial Neural Networks. *Abstract submitted for 2026 Rio Oil and Gas*.

8. **PEIXER, G. F.**; MILITÃO, L.; DA VEIGA, G. P.; DE SOUZA NETO, A. S.; CORDEIRO, A. F.; CAVALCANTI FILHO, V. O.; PAIVA, L.; BARBOSA Jr., J.; LOZANO, J. A. Assessment of the Impact of Impurities on the Thermophysical Properties of CO_2-Rich Mixtures for CCUS Applications. *Abstract submitted for 2026 Rio Oil and Gas*.

9. SCHMOCKEL, K. C.; **PEIXER, G. F.**; LOZANO, J. A.; BARBOSA Jr., J. R. Improving the performance of an LSTM-autoncoder for anomaly detection in oil wells. *Abstract submitted for 2026 Rio Oil and Gas*.

10. **PEIXER, G. F.**; LOZANO, J. A.; BARBOSA Jr., J. R. A general room-temperature magnetic refrigeration model based on physics-guided hybrid neural networks. *In preparation*.

11. **PEIXER, G. F.**; LORENZONI, A. M.; AZEREDO, Y. C.; SILVA, P. M.; SILVA, M. C.; HOFFMANN, G.; SANTOS, D. dos; DUTRA, S. L.; ROSÁRIO, G. M. do; TEZA, H. F.; PAGNAN, E.; SUCARIA, R. S.; CATTELAN, L. F.; REIF, D. D.; HSUAN, C. T.; ROSA, M. A.; DÖRING, A. M.; FARIA, P.; VIEIRA, B. P.; FORTKAMP, F. P.; OLIVEIRA, M. S. de; NAKASHIMA, A. T.; FORCELLINI, F. A.; WENDHAUSEN, P. A. P.; FLESCH, R. C.; TEIXEIRA, C. S.; LOZANO, J. A.; BARBOSA Jr., J. R. Evaluation of the thermodynamic performance evolution of three generations of a large-scale magnetic refrigerator. *In preparation*.

12. OLIVEIRA, M. S. D.; **PEIXER, G. F.**; ROSA, M. A. A.; FORCELLINI, F. A.; BARBOSA Jr., J. R.; LOZANO, J. A. TKDev: managing highly innovative projects with the Toyota Kata approach. *In preparation*.

13. BORDIGNON, J. C.; **PEIXER, G. F.**; LOZANO, J. A.; BARBOSA Jr., J. R. Integrated thermoeconomic optimization of Organic Rankine Cycles via artificial neural networks and multiobjective genetic algorithms. *In preparation*.

14. LEX, T.; **PEIXER, G. F.**; SCHWEIGLER, C.; LOZANO, J. A.; BARBOSA Jr., J. R. Techno-economic analysis of an absorption heat transformer for steam generation. *In preparation*.

15. **PEIXER, G. F.**; SCHMOCKEL, K. C.; VILLAMIL, R. H.; MAY, J. S.; FALLGATER, R. H.; VARGAS, R.; NAKASHIMA, A. T.; LOZANO, J. A.; BARBOSA Jr., J. R. Anomaly detection in offshore oil wells using an LSTM-autoencoder. *In preparation*.

Intellectual Property Registered

1. LOZANO, J. A.; **PEIXER, G. F.**; LORENZONI, A. M.; HOFFMANN, G.; SILVA, M. C. R.; DUTRA, S. L.; RIBEIRO, M. C.; SANTOS, D. dos; ROSÁRIO, G. M. do; CATTELAN, L. F.; TEZA, H. F.; PAGNAN, E.; FORTKAMP, F. P.; VIEIRA, B. P.; NAKASHIMA, A. T. D.; BARBOSA Jr., J. R. Magnetocaloric unit. Brazilian Patent No. BR 10 2021 023316, Instituto Nacional de Propriedade Industrial, 2021.

2. **PEIXER, G. F.**; CERUTTI, M. A.; LOZANO, J. A.; BARBOSA Jr., J. R. AiMR: artificial intelligence for active magnetic regenerators. Brazilian Patent No. BR 10 2024 01263-0, Instituto Nacional da Propriedade Industrial, registrado em 18/04/2024.

3. NAKASHIMA, A. T. D.; PAGNAN, E.; **PEIXER, G. F.**; LOZANO, J. A.; BARBOSA Jr., J. R. Magsim. Brazilian Patent No. BR 10 2024 01273-7, Instituto Nacional da Propriedade Industrial, registrado em 19/04/2024.

4. **PEIXER, G. F.**; NAKASHIMA, A. T. D.; LOZANO, J. A.; BARBOSA Jr., J. R. OptSys: optimization of thermal systems. Brazilian Patent No. BR 10 2024 01274-5, Instituto Nacional da Propriedade Industrial, registrado em 19/04/2024.

5. **PEIXER, G. F.**; SILVA, P. M.; LOZANO, J. A.; BARBOSA Jr., J. R. DeepMag: dynamics of magnetic refrigerators via deep learning. Brazilian Patent No. BR 10 2024 01278-8, Instituto Nacional da Propriedade Industrial, registrado em 19/04/2024.

Awards and Grants

1. 2025 - CNPq SWE (Doutorado Sanduíche no Exterior), Stanford University (Stanford, USA).
2. 2025 — Finalist, Best Student Presentation Award, 70th Annual Conference on Magnetism and Magnetic Materials (West Palm Beach, USA).
3. 2025 — Winner, ROP Challenge — X ENAHPE, ESSS O&G (Campina Grande, BRA).
4. 2025 — First Prize, 7th Belt and Road International Energy and Power Business Market Simulation Competition (Shanghai, CHI).
5. 2025 — Grand Prize Winner, SUEP CUP Belt and Road International Contest (Shanghai, CHI).
6. 2025 — Erasmus+ Internship, University of Ljubljana (Ljubljana, SLO).
7. 2024 — Finalist, BRICS 7th Young Innovator Prize 2024, Brazilian Academy of Sciences (SOchi, RUS).
8. 2024 — First Place at the Falling Walls Lab Brazil (Recife, BRA) and Finalist of the Falling Walls Lab (Berlin, GER), German Centre for Science and Innovation.
9. 2024 — Finalist, Pesquisadores Destaque 2024, Brazil Conference at Harvard and MIT.
10. 2023 — Metalinox Cogne do Hidrogênio Destaque Tecnológico — melhor trabalho apresentado, 3rd Brazilian Congress of Hydrogen (Maricá, BRA).
11. 2021 — Best Pre-Recorded Presentation, 9th IIR International Conference on Caloric Cooling and Applications of Caloric Materials (Maryland, USA).

Appendix A

NUMERICAL METHODS

In this Appendix, a brief introduction and explanation of the numerical methods implemented in the present dissertation are presented, with a focus on optimization and regression methods.

A.1 Nondominated Sorting Genetic Algorithm II (NSGA-II)

The majority of real-world and engineering problems involve the simultaneous optimization of multiple, competing objectives, which are referred to as Multi-Objective Optimization (MOO) problems. In contrast to Single-Objective Optimization (SOO) problems, which have a single optimal solution, MOO yields a set of optimal solutions, known as Pareto-optimal solutions. For many years, the strategy to solve such problems was to turn the objectives of the problem into constraints or to convert the MOO into an SOO by defining a utility function and combining all the objectives into a single objective (FONSECA & Fleming, 1999; Horn *et al.*, 1994). This last method can be used to find the Pareto-optimal set by altering the utility function and repeatedly solving the SOO, which is computationally costly.

To overcome that, Schaffer (1985) proposed the application of a Genetic Algorithm to an MOO, which he called the Vector Evaluated Genetic Algorithm. Besides their desirable properties to find solutions even for functions with multiple peaks, noises and discontinuities, which were already proven to outperform gradient-based methods in some applications, VEGA had a potential advantage over other optimization techniques which made it very attractive for MOO problems: rather than maintaining a single best solution, it kept a set of possible solutions, called a population, which could search for many nondominated solutions simultaneously. Ever since, several algorithms based on this technique have been proposed, such as the Multiple Objective Genetic Algorithm (FONSECA & Fleming, 1999), the Nondominated Sorting Genetic Algorithm (NSGA) (Srinivas & Deb, 1994), and the Niched Pareto Genetic Algorithm (Horn *et al.*, 1994).

The optimization algorithm utilized in the present is denominated Nondominated Sorting Genetic Algorithm II (NSGA-II) (Deb *et al.*, 2002). This algorithm is an improved version of the NSGA (Srinivas & Deb, 1994), which was focused on enhancing its performance based on three main issues: (i) high computational complexity of nondominated sorting, (ii) lack of elitism (Zitzler *et al.*, 2000), and (iii) need for the specification of a sharing parameter (Fonseca & Fleming, 1998). To overcome those issues, Deb *et al.* (2002) proposed modifications

that included a fast nondominated sorting procedure, an elitist-preservation approach, and a parameterless niching operator. A schematic diagram of the NSGA-II method is shown in Fig. A.1.

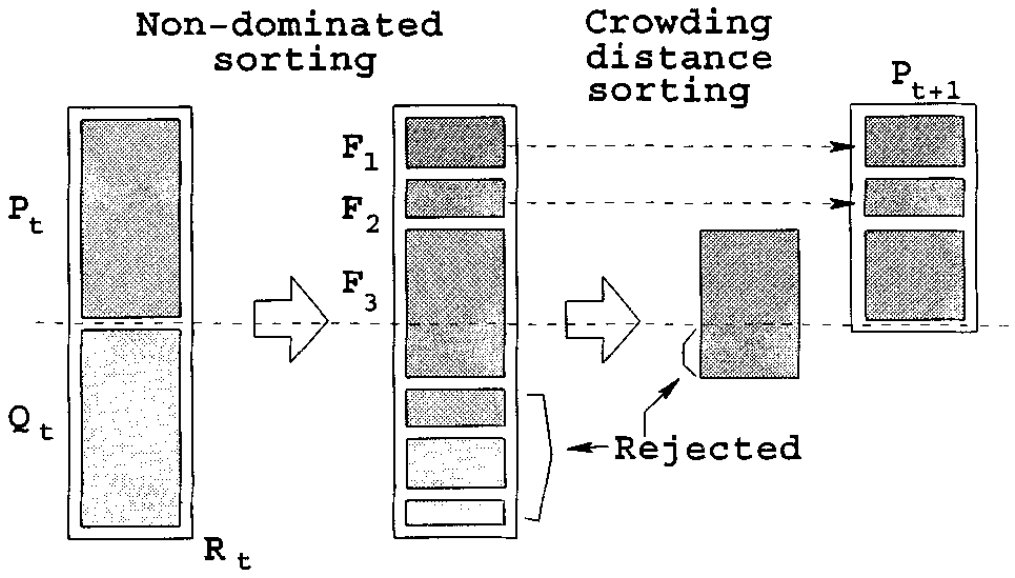


Figure A.1 – Schematic diagram of the procedure performed by the NSGA-II algorithm. Adapted from Deb *et al.* (2002)

The algorithm starts by creating a random population P_{t} of size M, predefined by the user. For each one of the M solutions, a fitness rank is assigned based on its objective function non-domination level. Therefore, the solutions are classified into K non-dominant sets F_{i}, with F_1 the highest-ranking set and F_{K} the lowest. Beyond the rank, a set of dominated solutions is assigned for each one of the evaluated ones, and by the use of this information and gradual removal of nondominated levels, the computational cost to rank all of the solutions is substantially reduced when compared to NSGA (Srinivas & Deb, 1994).

After that, an offspring population Q_{t} of size N is created by tournament selection, crossover, and mutation. Every child in q_{t} will have two parents, who are chosen by tournament selection. That technique consists of randomly selecting two individuals from P_{t} and comparing their fitness ranking and crowding distance; the one with the better rank (Parent 1) will be allowed to reproduce with another individual (Parent 2), generated by another tournament selection. Given two individuals, an offspring is produced by a technique called crossover, which combines the genes (design parameters) of each parent. In addition to random mutation, a predefined percentage can occur when the value assigned to a gene is randomly modified. By that, the offspring population Q_{t} is created and combined with the parent population P_{t}, making the population R_{t}.

The population R_t is then sorted according to non-dominance. Since all previous and current members of the population are included, elitism is ensured. As R_t has a size of $M+ N$, N of its members must be rejected and not utilized in further generations. The individuals who will be dismissed are those with the lowest fitness rank. Therefore, the new parent population P_{t+1} will be composed of the first non-dominated solution sets, up to the point where the population size is below the value of M, which is represented by the sets F_1, F_2 and F_3 in Fig. A.1. To choose exactly M individuals in P_{t+1}, the solutions of the last set are classified according to a crowding distance parameter, which is schematically represented in Fig. A.2.

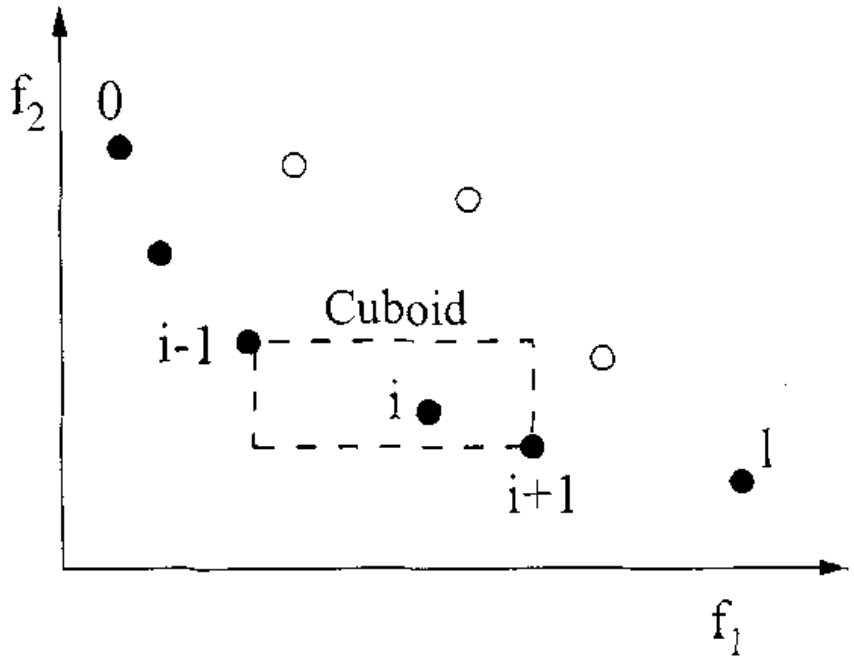


Figure A.2 – Schematic representation of the crowding-distance calculation. Filled circles represent the solutions of the same nondominated front. Adapted from Deb *et al.* (2002)

The crowding distance provides an estimate of the density of solutions surrounding a given individual in the population, and solutions located in less crowded regions are preferred by the algorithm and selected to compose P_{t+1}. Beyond this population reduction, the crowding distance is also used in the tournament selection step when parents of the same rank are selected. Therefore, diversity among the nondominated solutions is introduced without requiring additional niching parameters. Hence, the three most significant issues of NSGA have been addressed and solved by the modifications proposed by NSGA-II.

Given the new population P_{t+1}, the loop starts over by creating an offspring population Q_{t+1} by tournament selection, crossover, and mutation, and following the steps previously described. The algorithm can run until a termination criterion is reached, which may involve reaching a specified number of generations, attaining a maximum increment in the genes (design parameters), or attaining a maximum increment in the objective functions.

Appendix B

MATHEMATICAL MODEL OF THE HEAT EXCHANGERS

This Appendix presents a detailed description of the geometric and thermal-hydraulic model used to evaluate the HEx, along with the adopted solution methodology. Firstly, some basic definitions regarding the geometry of the multi-circuit tube-fin HEx are given. Next, the relations used to calculate the heat transfer rate through the tubes, as well as the heat transfer rates and pressure drop for both internal and external fluid flows, are presented. Lastly, the detailing of the ε-NTU method is presented.

B.1 Design and Modeling of the Heat Exchanger

A schematic representation of HEx and its main geometric parameters is presented in Fig. B.1. Due to its favorable thermal-hydraulic performance and compactness, a corrugated fin on a staggered tube array HEx configuration was selected for heat exchange between the refrigeration system and the cold and hot reservoirs.

Given the characteristics of the application, particularly high mass flow rates and large heat transfer areas, an elevated pressure drop and consumption of power are expected to pump the liquid inside the tubes of the HEx. To overcome that, a multi-circuit configuration (Kakac & Liu, 2002) was used in the design of this component. Using this design strategy, instead of going through all the tubes of the HEx, the fluid flow is divided by a separator at the entrance, and each stream flows through an associated set of tubes, forming a circuit. Later, the fluid stream is brought together by a collector and then moves forward through the device.

Those sets of tubes were separated in the longitudinal direction, as presented in Fig.B.1 by the double lines. This way, the fluid from the AMRs is divided among the circuits, reducing pressure drop in the component and power consumption to pump the liquid in the HEx.

To model this arrangement of HEx, a strategy based on the tube-by-tube technique (Domanski & Didion, 1983) was utilized. This technique consists of splitting each tube of the HEx, evaluating it as a control volume, and applying an energy balance over it. The same methodology was used, treating each circuit as a control volume and allowing it to be modeled separately as an individual HEx.

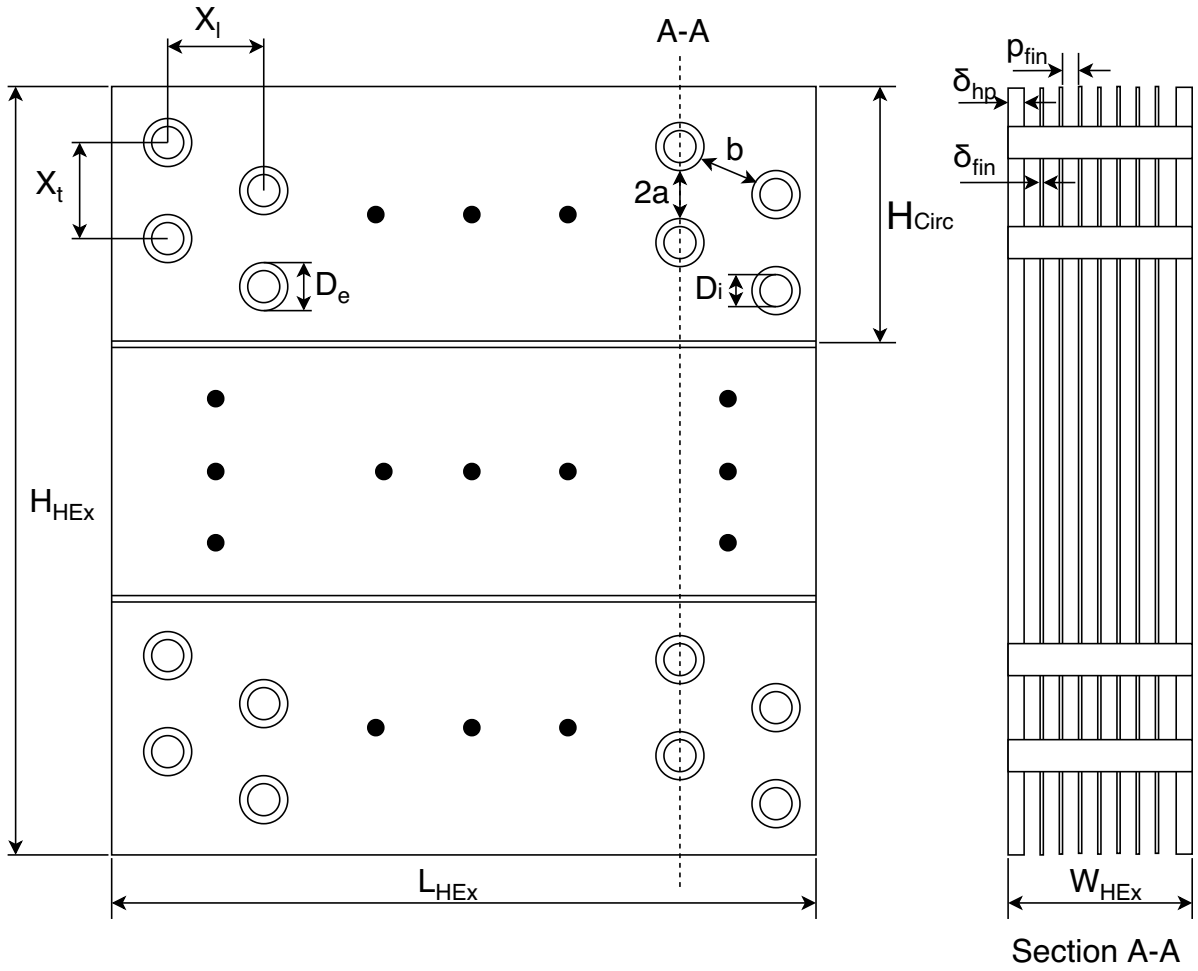


Figure B.1 – Schematic representation of a multi-circuit tube-fin HEx and its main geometric parameters. The figure presents the side view (left) and the front view (right).

As discussed throughout this Appendix, the heat transfer and fluid flow associated with the internal flow in a circuit are treated independently of the entire HEx. On the other hand, the fluid flow and heat transfer rate associated with the external flow are calculated for the entire HEx and later assigned to each circuit by dividing the thermal resistance and airflow rate. For that, it is assumed that the air mass flow rate is distributed uniformly over the external area of the HEX, regardless of circuit or fan positioning (Domanski & Didion, 1983), and that the HEX core thermal-hydraulic characteristics, namely the friction factor and Colburn factor, are independent of the HEX envelope dimensions.

The overall internal and external pumping power, as well as the heat transfer rates, will be given by the sum of the parcels of these parameters for each circuit of the HEx.

B.2 Basic Geometric Definitions

The envelope of the HEx can be characterized by three dimensions: its length, height, and width. The length of the HEx L_{HEx}, which is the dimension parallel to the airflow

direction, can be calculated by:

$$L_{\mathrm{HEx}} = N_{\mathrm{l}} X_{\mathrm{l}} \tag{B.1}$$

where N_{l} is the longitudinal number of tube rows and X_{l} the tube pitch, in that same direction.

The height of the HEx H_{HEx}, the directions perpendicular to both the air and liquid streams, can be calculated by:

$$H_{\mathrm{HEx}} = \frac{N_{\mathrm{t}} X_{\mathrm{t}}}{2} \tag{B.2}$$

where N_{t} is the transversal number of tube rows of the HEx and X_{t} the transversal tube pitch.

The height of a circuit of the HEx H_{circ}, is calculated by:

$$H_{\mathrm{circ}} = \frac{N_{\mathrm{t,circ}} X_{\mathrm{t}}}{2} \tag{B.3}$$

where $N_{\mathrm{t,circ}}$ is the quantity of tube rows of each circuit of the HEx in the transversal direction.

A relation between the transversal number of tube rows of the HEx and the circuit is given by:

$$N_{\mathrm{t}} = N_{\mathrm{circ}} N_{\mathrm{t,circ}} \tag{B.4}$$

where N_{circ} is the total number of circuits on the HExs.

The total number of tubes of a single circuit of the HEx $N_{\mathrm{T,circ}}$, can be calculated by:

$$N_{\mathrm{T,circ}} = \frac{N_{\mathrm{l}} N_{\mathrm{t,circ}}}{2} \tag{B.5}$$

The total number of tubes of all circuits of the HEx N_{T} is given by:

$$N_{\mathrm{T}} = \frac{N_{\mathrm{l}} N_{\mathrm{t}}}{2} \tag{B.6}$$

Through the arrangement of the equations presented previously, some relations involving the number of circuits can be defined by:

$$N_{\mathrm{circ}} = \frac{H_{\mathrm{HEx}}}{H_{\mathrm{circ}}} = \frac{N_{\mathrm{T}}}{N_{\mathrm{T,circ}}} \tag{B.7}$$

Lastly, the fin density of the HEx β_{HEx}, is defined as:

$$\beta_{\mathrm{HEx}} = \frac{1}{p_{\mathrm{fin}}} \tag{B.8}$$

where p_{fin} represents the fin pitch of the HEx.

The number of fins in the HExs N_{fin}, can be calculated by:

$$N_{\mathrm{fin}} = \beta_{\mathrm{HEx}} W_{\mathrm{HEx}} \tag{B.9}$$

where W_{HEx} is the length of the HEx, the second dimension parallel to the liquid stream, and the final one to characterize the envelope of the HEx.

B.3 Thermal-Hydraulic Model

The HEx model has been separated into three sub-models that represent the thermal and hydraulic/aerodynamic phenomena occurring on these components: the tubes, internal convection, and external convection.

B.3.1 Conduction Through the Tubes

The heat transfer through the tube walls in the HEx is assumed to be purely due to heat conduction. To calculate that, thermal contact resistances are assumed to be negligible, and the tube thermal conductivity is assumed to be constant. Hence, the conduction thermal resistance in the tubes, R_{T}, is given by (Incropera *et al.*, 2007):

$$R_{\mathrm{T}} = \frac{ln\left(\frac{D_{\mathrm{o}}}{D_{\mathrm{i}}}\right)}{2\pi L_{\mathrm{T}} k_{\mathrm{T}}} \tag{B.10}$$

where D_{o} and D_{i} are the external and internal tube diameters, respectively and k_{T} the thermal conductivity of the tube, which is made of copper, and has a value of 402 W m^{-1} K^{-1} (Boles & Cengel, 2014). L_{T} stands for the equivalent tube length and can be calculated by:

$$L_{\mathrm{T}} = W_{\mathrm{HEx}} N_{\mathrm{T,circ}} \tag{B.11}$$

B.3.2 Internal Convection

As previously explained, the fluid flow and heat transfer associated with the internal flow of the HEx are evaluated independently for each circuit. Assuming the hydraulic resistance to be the same for all the circuits, the mass flow rate of liquid inside each circuit of the HEx $\dot{m}_{\mathrm{circ,l}}$ can be calculated by:

$$\dot{m}_{\mathrm{circ,l}} = \frac{\dot{m}_{\mathrm{HEx,l}}}{N_{\mathrm{circ}}} \tag{B.12}$$

where $\dot{m}_{\mathrm{HEx,l}}$ is the total mass flow rate of liquid inside the tubes of the heat exchangers, which corresponds to the sum of the mass flow rate of fluid leaving all the regenerators operating simultaneously at the same blow.

The mass flux of liquid inside the tubes of one of the circuits of the HExs, G_{i}, can be calculated by:

$$G_{\mathrm{i}} = \frac{4\dot{m}_{\mathrm{circ,l}}}{\pi D_{\mathrm{i}}^2} \tag{B.13}$$

The Reynolds number associated with the fluid flow inside the tubes of each circuit Re_{i}, is given by:

$$Re_{\mathrm{i}} = \frac{G_{\mathrm{i}} D_{\mathrm{i}}}{\mu_{\mathrm{l}}} \tag{B.14}$$

where μ_{l} is the dynamic viscosity of the fluid inside the HEx.

To evaluate the pressure drop, the Fanning friction factor, f_{i}, is calculated by the correlation given by (Churchill, 1977):

$$\frac{f_{\mathrm{i}}}{2} = \left[\left(\frac{8}{Re_{\mathrm{i}}}\right)^{12} + (\mathrm{A}+\mathrm{B})^{-3/2}\right]^{1/12} \tag{B.15}$$

where the coefficients A and B can be calculated by Eq. (B.16) and Eq. (B.17), respectively.

$$A = \left[2.457 \ln\left(\frac{1}{(7/Re_{\mathrm{i}})^{0.9} + 0.27\,(e/D_{\mathrm{i}})}\right)\right]^{16} \tag{B.16}$$

$$\mathrm{B} = \left(\frac{37530}{\mathrm{Re_i}}\right)^{16} \tag{B.17}$$

where the constant e represents the surface roughness and has a value of 0.00015 cm for a copper drawn tubing (Wylie & Streeter, 1983). The correlation is valid for all fluid flow regimes.

The pressure drop of the fluid flow inside the tubes of HEx, $\Delta P_{\mathrm{HEx,i}}$, can be calculated by the expression given by (Shah & Sekulic, 2003).

$$\Delta P_{\mathrm{HEx,i}} = \frac{G_{\mathrm{i}}^2}{2\rho_{\mathrm{l}}^{\mathrm{in}}}\left[2\left(\frac{\rho_{\mathrm{l}}^{\mathrm{in}}}{\rho_{\mathrm{l}}^{\mathrm{out}}} - 1\right) + f_{\mathrm{i}}\frac{4L_{\mathrm{T}}}{D_{\mathrm{i}}}\frac{\rho_{\mathrm{l}}^{\mathrm{in}}}{\overline{\rho_{\mathrm{l}}}} + 4f_{\mathrm{i}}N_{\mathrm{bend}}K_{\mathrm{bend}}\right] \tag{B.18}$$

where $\rho_{\mathrm{l}}^{\mathrm{in}}$ and $\rho_{\mathrm{l}}^{\mathrm{out}}$ are the densities of the fluid inside the tubes at the inlet and outlet of the HEx, N_{bend} is the number of 180° return bends in the HEx and K_{bend} the equivalent dimensionless length of these bends, which is considered to be equal as 50 (Kakac & Liu, 2002). The first term of Eq. (B.18) represents the pressure variation caused by the acceleration of the fluid flow, while the second one represents the drop generated by core friction, and the last one the loss in the 180° return bends of the HExs.

The parameter $\overline{\rho_{\mathrm{l}}}$ can be calculated by and Eq. (B.19).

$$\overline{\rho_{\mathrm{l}}} = \left[\frac{1}{2}\left(\frac{1}{\rho_{\mathrm{f,i}}} + \frac{1}{\rho_{\mathrm{f,o}}}\right)\right]^{-1} \tag{B.19}$$

Since the density variation at the inlet and outlet of the HEx is not considered to be substantial, given the small temperature difference between these two points, the density of the fluid inside the HEx is deemed to be constant and equal to the one at the inlet of the HEx. Hence, the pressure drop calculation can be simplified and is presented in Eq. (B.20).

$$\Delta P_{\mathrm{HEx,i}} = \frac{2f_{\mathrm{i}}G_{\mathrm{i}}^2}{\rho_{\mathrm{f}}^{\mathrm{in}}}\left[\frac{L_{\mathrm{T}}}{D_{\mathrm{i}}} + N_{\mathrm{bend}}K_{\mathrm{bend}}\right] \tag{B.20}$$

The power consumption associated with the internal pumping at each HEx, $\dot{W}_{\mathrm{HEX,Pump}}$, can be calculated by:

$$\dot{W}_{\mathrm{HEx,pump}} = N_{\mathrm{circ}}\left(\frac{\dot{m}_{\mathrm{circ,l}}\Delta P_{\mathrm{HEx,i}}}{\rho_{\mathrm{l}}^{\mathrm{in}}\eta_{\mathrm{pump}}}\right) \tag{B.21}$$

where the term inside the parentheses represents the power consumption for the internal pumping power of one circuit and η_{pump} is the efficiency of the pump and considered to be equal to 70%.

The convective heat transfer coefficient of the internal fluid flow is calculated through the Nusselt number, Nu_{i}. This parameter can be calculated by the correlation developed by Gnielinski (1976) and given by:

$$Nu_{\text{i}} = \frac{(f_{\text{i}}/2)\,(Re_{\text{i}} - 10^3)\,Pr_{\text{l}}}{1 + 12.7\sqrt{f_{\text{i}}/2}\left(Pr_{\text{l}}^{2/3} - 1\right)} \tag{B.22}$$

where Pr_{l} is the Prandtl number for the fluid inside the tubes. The correlation is valid for $0.5 \leq Pr_{\text{l}} \leq 2000$ and $3000 \leq Re_{\text{i}} \leq 5000000$.

The convective heat transfer coefficient of the flow inside the tubes h_{i} is given by:

$$\hbar_{\text{i}} = \frac{Nu_{\text{i}} k_{\text{l}}}{D_{\text{i}}} \tag{B.23}$$

where k_{l} is the thermal conductivity of the fluid.

The heat transfer surface area of the internal part of the tubes of the HExs, $A_{\text{s,i}}$, can be calculated by:

$$A_{\text{s,i}} = \pi D_{\text{i}} L_{\text{T}} \tag{B.24}$$

Through the calculation developed so far, the thermal resistance of the flow inside the tubes in the HEx, R_{l}, can be calculated as:

$$R_{\text{l}} = \frac{1}{\hbar_{\text{i}} A_{\text{s,i}}} \tag{B.25}$$

B.3.3 External Convection

Whereas the internal flow heat transfer and hydraulic analyses were carried out for each circuit separately, the external flow is evaluated for the whole HEX. This strategy is adopted due to the coupling between the pressure and mass flow rate of the HEx and the fan. It is based on the assumptions of airflow rate homogeneity and independence of the thermal-hydraulic characteristics from the envelope dimensions, provided they meet the correlation restrictions.

The geometric and thermal-hydraulic characteristics of the external flow will be defined, among other parameters, by some geometric features of the corrugated fins. To better illustrate these characteristics, some of them are displayed in Fig. B.2 (Shah & Sekulic, 2003).

At the external side of the HEx, forced airflow is generated by a fan, and the surface area is composed of fractions corresponding to the tubes, the header plates, and the extended surface. The primary surface area, $A_{\text{p,o}}$, corresponds to the sum of the areas of the tubes and

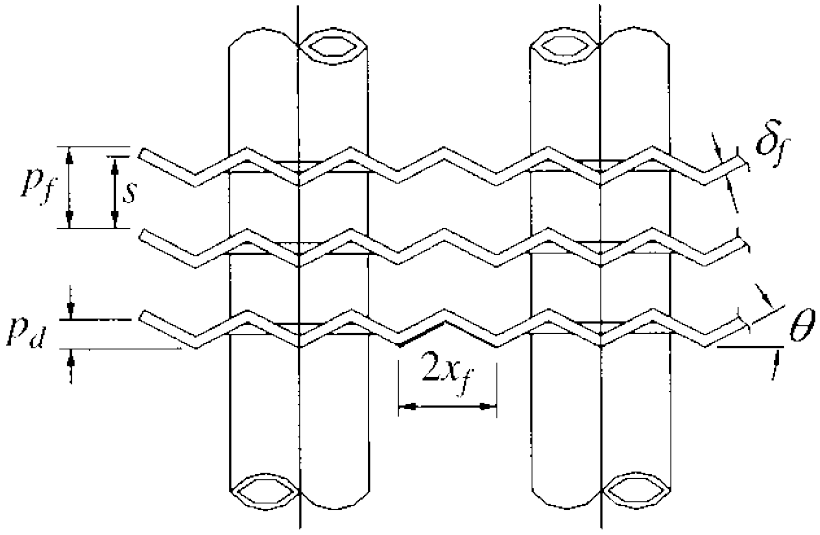


Figure B.2 – Schematic diagram of the corrugated fin on a tube array and its main geometric parameters. Adapted from Shah & Sekulic (2003)

the header plates, minus the area that is blocked by the fins. This parameter can be calculated by:

$$A_{\mathrm{p,o}} = \pi D_{\mathrm{o}} \left[\left(W_{\mathrm{HEx}} - \frac{\delta_{\mathrm{fin}}}{cos(\theta_{\mathrm{fin}})} \beta_{\mathrm{HEx}} W_{\mathrm{HEx}} \right) N_{\mathrm{T}} + 2 \left(L_{\mathrm{HEx}} H_{\mathrm{HEx}} - \frac{\pi D_{\mathrm{o}}^2 N_{\mathrm{T}}}{4} \right) \right] \tag{B.26}$$

where δ_{fin} corresponds to the thickness of the fins. By the relations defined by Eq. (B.7), Eq. (B.26) can be rearranged into:

$$A_{\mathrm{p,o}} = N_{\mathrm{circ}} \left[\pi D_{\mathrm{o}} \left(W_{\mathrm{HEx}} - \frac{\delta_{\mathrm{fin}}}{cos(\theta_{\mathrm{fin}})} \beta_{\mathrm{HEx}} W_{\mathrm{HEx}} \right) N_{\mathrm{T,circ}} + 2 \left(L_{\mathrm{HEx}} H_{\mathrm{circ}} - \frac{\pi D_{\mathrm{o}}^2 N_{\mathrm{T,circ}}}{4} \right) \right] \tag{B.27}$$

the value of θ_{fin} can be calculated by:

$$\theta_{\mathrm{fin}} = atan \left(\frac{p_{\mathrm{d}}}{x_{\mathrm{fin}}} \right) \tag{B.28}$$

where x_{fin} and p_{d} correspond to the projected fin pattern length for one-half wavelength and depth.

The secondary surface area, $A_{\mathrm{f,o}}$, is composed of the areas associated with the lateral and the leading and trailing edges of the fins. This parameter can be calculated by:

$$A_{\mathrm{f,o}} = 2\beta_{\mathrm{HEx}} W_{\mathrm{HEx}} \left[\frac{L_{\mathrm{HEx}} H_{\mathrm{HEx}}}{\cos(\theta_{\mathrm{fin}})} - \frac{\pi D_{\mathrm{o}}^2 N_{\mathrm{T}}}{4} \right] + \frac{2 H_{\mathrm{HEx}} \delta_{\mathrm{fin}} \beta_{\mathrm{HEx}} W_{\mathrm{HEx}}}{\cos(\theta_{\mathrm{fin}})} \tag{B.29}$$

Analogously, by using the relations defined in Eq. (B.7), Eq. (B.29) can be rearranged into:

$$A_{\mathrm{f,o}} = N_{\mathrm{circ}} \left\{ 2\beta_{\mathrm{HEx}} W_{\mathrm{HEx}} \left[\frac{L_{\mathrm{HEx}} H_{\mathrm{circ}}}{\cos(\theta_{\mathrm{fin}})} - \frac{\pi D_{\mathrm{o}}^2 N_{\mathrm{T,circ}}}{4} \right] + \frac{2 H_{\mathrm{circ}} \delta_{\mathrm{fin}} \beta_{\mathrm{HEx}} W_{\mathrm{HEx}}}{\cos(\theta_{\mathrm{fin}})} \right\} \tag{B.30}$$

The total surface area, $A_{\mathrm{s,o}}$, is given by the sum of the primary and secondary surface areas and can be calculated by:

$$A_{\mathrm{s,o}} = A_{\mathrm{p,o}} + A_{\mathrm{f,o}} \tag{B.31}$$

As can be evaluated by Eq. (B.27), Eq. (B.30) and Eq. (B.31), the total surface area scales linearly with the number of circuits of the HEx.

The outside surface area of the tube rows, without fins, $A_{\mathrm{T,o}}$, can be calculated by:

$$A_{\mathrm{T,o}} = \pi D_{\mathrm{o}} L_{\mathrm{T}} \tag{B.32}$$

For a staggered HEx configuration, the minimum free-flow area can occur either at the front row (2a) or through the diagonal (b), as presented in Fig. B.3. To evaluate that, both dimensions are calculated by Eq. (B.33) and Eq. (B.34), respectively (Shah & Sekulic, 2003).

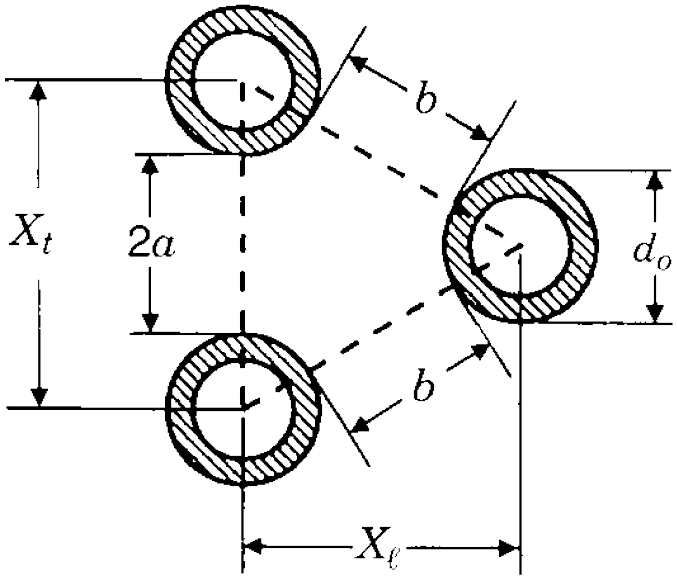


Figure B.3 – Schematic representation of a unit cell of a staggered tube arrangement and the parameters used to define the minimum free-flow area. Adapted from Shah & Sekulic (2003)

$$2a = (X_{\mathrm{t}} - D_{\mathrm{o}}) - (X_{\mathrm{t}} - D_{\mathrm{o}}) \frac{\delta_{\mathrm{fin}}}{cos(\theta_{\mathrm{fin}})} \beta_{\mathrm{HEx}} \tag{B.33}$$

$$b = \sqrt{\left[\left(\frac{X_{\mathrm{t}}}{2}\right)^2 + X_{\mathrm{l}}^2\right]} - D_{\mathrm{o}} - (X_{\mathrm{t}} - D_{\mathrm{o}}) \frac{\delta_{\mathrm{fin}}}{cos(\theta_{\mathrm{fin}})} \beta_{\mathrm{HEx}} \tag{B.34}$$

Hence, a parameter c is defined based on the dimension that represents the minimum free-flow path and given by:

$$c = \begin{cases} 2a, & 2b > 2a \\ 2b, & 2a > 2b \end{cases} \tag{B.35}$$

The minimum free-flow path of the external flow, $A_{\mathrm{min,o}}$, can be calculated by:

$$A_{\mathrm{min,o}} = \left[\left(\frac{H_{\mathrm{HEx}}}{X_{\mathrm{t}}} - 1\right) c + (X_{\mathrm{t}} - D_{\mathrm{o}}) - (X_{\mathrm{t}} - D_{\mathrm{o}}) \frac{\delta_{\mathrm{fin}}}{cos(\theta_{\mathrm{fin}})} \beta_{\mathrm{HEx}}\right] W_{\mathrm{HEx}} \tag{B.36}$$

Given the minimum free-flow area, the maximum flow speed, u_{max}, can be calculated by:

$$u_{\mathrm{max}} = \frac{\dot{m}_{\mathrm{a}}}{\sigma_{\mathrm{e}} \rho_{\mathrm{a}}^{\mathrm{in}} A_{fr,o}} \tag{B.37}$$

where $\dot{m}_{\mathrm{a}}$ represents the airflow rate through all of the HEx, $\rho_{\mathrm{a}}^{\mathrm{in}}$ the density of the air at the inlet of the HEx. The external frontal area,$A_{\mathrm{fr,o}}$, and the ratio of minimum free-flow area and frontal area, σ_{e}, can be calculated by:

$$A_{\mathrm{fr,o}} = W_{\mathrm{HEx}} H_{\mathrm{HEx}} \tag{B.38}$$

$$\sigma_{\mathrm{e}} = \frac{A_{\mathrm{min,o}}}{A_{\mathrm{fr,o}}} \tag{B.39}$$

Similarly to what has been done to the internal flow, the external flow pressure drop is calculated through the friction factor, f_{o}, developed by Wang *et al.* (2000) and given by Eq. (B.40).

$$f_{\mathrm{o}} = 0.05273 Re_{\mathrm{o}}^{\mathrm{c_2}} \left(\frac{p_{\mathrm{d}}}{x_{\mathrm{f}}}\right)^{\mathrm{c_3}} \left(\frac{p_{\mathrm{l}}}{X_{\mathrm{t}}}\right)^{\mathrm{c_4}} \left[\ln\left(\frac{A_{\mathrm{s,o}}}{A_{\mathrm{T,o}}}\right)\right]^{-2.726} \left(\frac{D_{\mathrm{h}}}{D_{\mathrm{c}}}\right)^{0.1325} N_{\mathrm{l}}^{0.02305} \tag{B.40}$$

the hydraulic diameter, D_{h}, and collar diameter, D_{c}, can be calculated by Eq. (B.41) and Eq. (B.42), respectively.

$$D_{\mathrm{h}} = \frac{4 A_{\mathrm{min,o}} L_{\mathrm{HEx}}}{A_{\mathrm{s,o}}} \tag{B.41}$$

$$D_{\mathrm{c}} = D_{\mathrm{o}} + 2\delta_{\mathrm{fin}} \tag{B.42}$$

coefficients c_2, c_3 and c_4 can be calculated by Eq. (B.43), Eq. (B.44) and Eq. (B.45), respectively.

$$c_2 = 0.1714 - 0.07372 \left(\frac{p_{\mathrm{l}}}{X_{\mathrm{l}}}\right)^{0.25} \left[\ln\left(\frac{A_{\mathrm{s,o}}}{A_{\mathrm{T,o}}}\right)\right] \left(\frac{p_{\mathrm{d}}}{x_{\mathrm{l}}}\right)^{-0.2} \tag{B.43}$$

$$c_3 = 0.426 \left(\frac{p_{\mathrm{l}}}{X_{\mathrm{t}}}\right)^{0.3} \ln\left(\frac{A_{\mathrm{s,o}}}{A_{\mathrm{T,o}}}\right) \tag{B.44}$$

$$c_4 = -\frac{10.2192}{\ln Re_{\mathrm{o}}} \tag{B.45}$$

where the Reynolds number associated with the external flow of the HEx, Re_{o}, is given by:

$$Re_{\mathrm{o}} = \frac{u_{\max} \rho_{\mathrm{a}}^{\mathrm{in}} D_{\mathrm{c}}}{\mu_{\mathrm{a}}} \tag{B.46}$$

where ρ_{a} represents the density and μ_{a} the dynamic viscosity of the air.

The pressure drop of the external side of the HEx, $\Delta P_{\mathrm{HEx,o}}$, can be calculated by Eq. (B.47) (Shah & Sekulic, 2003).

$$\Delta P_{\mathrm{HEx,o}} = \frac{G_{\mathrm{o}}^2}{2\rho_{\mathrm{a}}^{\mathrm{in}}} \left[f_{\mathrm{o}} \frac{A_{\mathrm{s,o}}}{A_{\mathrm{min,o}}} \frac{\rho_{\mathrm{a}}^{\mathrm{in}}}{\overline{\rho}_{\mathrm{a}}} + \left(1 + \sigma_{\mathrm{o}}^2\right) \left(\frac{\rho_{\mathrm{a}}^{\mathrm{in}}}{\rho_{\mathrm{a}}^{\mathrm{out}}} - 1\right) \right] \tag{B.47}$$

the external air mass flux, G_{o}, contraction and expansion ratio, σ_{o}, and mean air density, $\overline{\rho_{\mathrm{a}}}$ are given by Eq. (B.48), Eq. (B.49) and Eq. (B.50).

$$G_{\mathrm{o}} = u_{\max} \overline{\rho}_{\mathrm{a}} \tag{B.48}$$

$$\sigma_{\mathrm{o}} = \frac{H_{\mathrm{HEx}} W_{\mathrm{HEx}} - H_{\mathrm{HEx}} \delta_{\mathrm{fin}} \beta_{\mathrm{HEx}} W_{\mathrm{HEx}}}{H_{\mathrm{HEx}} W_{\mathrm{HEx}}} \tag{B.49}$$

$$\overline{\rho}_{\mathrm{a}} = \frac{1}{2}\left(\frac{1}{\rho_{\mathrm{a}}^{\mathrm{in}}} + \frac{1}{\rho_{\mathrm{a}}^{\mathrm{out}}}\right)^{-1} \tag{B.50}$$

The first term of Eq. (B.47) represents the pressure drop due to friction, whereas the second one represents the loss due to flow acceleration. Likewise, what has happened in the fluid flow inside the tubes of the HEx, the temperature, and therefore density, the variation of the fluid outside the HEx is small. Hence, the density is considered to be constant and equal to the value at the inlet of the HEx, the pressure drop equation can be simplified and is given by :

$$\Delta P_{\mathrm{HEx,o}} = f_{\mathrm{o}} \frac{G_{\mathrm{o}}^2}{2\rho_{\mathrm{a}}^{\mathrm{in}}} \frac{A_{\mathrm{s,o}}}{A_{\mathrm{min,o}}} \tag{B.51}$$

Given the calculation developed previously, the power consumption by the fan to pump the air through the external side of the HEx, $\dot{W}_{\mathrm{fan}}$, is given by:

$$\dot{W}_{\mathrm{fan}} = \frac{\dot{m}_{\mathrm{a}} \Delta P_{\mathrm{HEx,o}}}{\rho_{\mathrm{a}}^{\mathrm{in}} \eta_{\mathrm{fan}}} \tag{B.52}$$

where η_{fan} is the efficiency of the fan and calculated by a fit of experimental data provided by the fan supplier.

The definition of the operating point (pressure drop and mass flow rate) for the external flow of the fan-assisted tube-fin HEx is given by the coupling of the pressure drop on the HEx, given by Eq. (B.51), and the head curve of the fan, given by Eq. (C.2) in Appendix C.

The thermal modeling of the convection on the external side of the HEx is developed through the Colburn factor, j_{o}. The correlation developed by Wang *et al.* (2000) is given by:

$$j_{\mathrm{o}} = 1.7910 Re_{\mathrm{o}}^{c_1} \left(\frac{X_{\mathrm{l}}}{\delta_{\mathrm{fin}}}\right)^{-0.465} N_{\mathrm{l}}^{-0.27} \left(\frac{p_{\mathrm{l}}}{D_{\mathrm{c}}}\right)^{-1.343} \left(\frac{p_{\mathrm{d}}}{x_{\mathrm{fin}}}\right)^{0.317} \tag{B.53}$$

where the coefficient c_1 is calculated by:

$$c_1 = -0.1707 - 1.374 \left(\frac{X_{\mathrm{l}}}{\delta_{\mathrm{fin}}}\right)^{-0.493} \left(\frac{p_{\mathrm{l}}}{D_{\mathrm{c}}}\right)^{-0.886} N_{\mathrm{l}}^{-0.143} \left(\frac{p_{\mathrm{d}}}{x_{\mathrm{fin}}}\right)^{-0.0296} \tag{B.54}$$

The heat transfer convective coefficient associated with the external flow, h_{o}, can be calculated by:

$$\hbar_{\mathrm{o}} = j_{\mathrm{o}} \rho_{\mathrm{a}}^{\mathrm{in}} u_{\max} c_{\mathrm{p,a}} Pr_{\mathrm{a}}^{-2/3} \tag{B.55}$$

where $c_{\mathrm{p,a}}$ is the specific heat at constant pressure and Pr_{a} the Prandtl number, both referent to air at the inlet of the HEx.

The relations given by Eq. (B.40) and Eq. (B.53) are valid for the following ranges of parameters: $500 \leq Re_{\mathrm{o}} \leq 10000$, $3.63 \leq D_{\mathrm{h}} \leq 7.23$ mm, $13.6 \leq D_{\mathrm{c}} \leq 16.85$ mm, $31.75 \leq X_{\mathrm{t}} \leq 38.1$ mm, $27.5 \leq X_{\mathrm{l}} \leq 33$ mm, $2.98 \leq X_{\mathrm{t}} \leq 6.43$ mm, $1 \leq N_{\mathrm{l}} \leq 6$, $6.87 \leq x_{\mathrm{fin}} \leq 8.25$ mm, $12.3 \leq \theta_{\mathrm{fin}} \leq 14.7°$, p_{d} = 1.8 mm and D_{o} = 12.7 and 15.88 mm.

Since the circuit has an extended surface on its external side, it is necessary to compute the surface efficiency when developing a heat transfer analysis of the component. The extended surface efficiency, η_{o}, can be calculated by the equation (Incropera *et al.*, 2007):

$$\eta_{\mathrm{o}} = 1 - \frac{A_{f,o}}{A_{s,o}}(1 - \eta_{\mathrm{fin}}) \tag{B.56}$$

where η_{fin} is the fin efficiency. An approximation for the calculation of this parameter is proposed by Schmidt (1945) and given by:

$$\eta_{\mathrm{fin}} = \frac{\tanh\left(\kappa r_{\mathrm{i}} \xi\right)}{\kappa r_{\mathrm{i}} \xi} \tag{B.57}$$

where r_{i} is the internal radius of the tube. The expressions used to calculate both κ and ξ are given below by Eq. (B.58) and Eq. (B.59), respectively. The complete set of equations required to calculate the extended surface efficiency is given by Eq. (B.60), Eq. (B.61), and Eq. (B.62).

$$\kappa = \sqrt{\frac{2h_{\mathrm{o}}}{k_{\mathrm{fin}}\delta_{\mathrm{fin}}}} \tag{B.58}$$

$$\xi = \left(\frac{R_{\mathrm{eq}}}{r_{\mathrm{i}}} - 1\right)\left[1 + 0.35\ln\left(\frac{R_{\mathrm{eq}}}{r_{\mathrm{i}}}\right)\right] \tag{B.59}$$

$$\frac{R_{\mathrm{eq}}}{r_{\mathrm{i}}} = 1.27\frac{P_{\mathrm{m}}}{r_{\mathrm{r}}}\sqrt{\frac{P_{\mathrm{l}}}{P_{\mathrm{m}}} - 0.3} \tag{B.60}$$

$$P_{\mathrm{m}} = \frac{X_{\mathrm{l}}}{2} \tag{B.61}$$

$$P_{\mathrm{l}} = \frac{\sqrt{\left(X_{\mathrm{t}}/2\right)^2 + X_{\mathrm{l}}^2}}{2} \tag{B.62}$$

where k_{fin} is the thermal conductivity of the fin, which is made of aluminum, and has a value of 205 W m^{-1} K^{-1} (Boles & Cengel, 2014).

Having calculated the extended surface efficiency, the external heat transfer coefficient, and external total surface area, all the parameters required for the calculation of the thermal resistance associated with the airflow in one of the circuits of the HEx, R_{a}, have been obtained. To do that, a relation between the parameters calculated for the whole HEx and the thermal resistance associated with a single circuit must be developed.

Assuming that the extended surface efficiency and convective heat transfer, which were calculated for the whole HEx, are defined by the core characteristics of the HEx, they are also valid for the circuit. That same assumption can not be applied to the heat transfer area, which varies with the number of circuits according to Eq. (B.27), Eq. (B.30), and Eq. (B.31). Hence, the thermal resistance associated with the airflow in one of the circuits is given by:

$$R_{\mathrm{a}} = \frac{N_{\mathrm{circ}}}{\eta_{\mathrm{o}}\hbar_{\mathrm{o}}A_{\mathrm{s,o}}} \tag{B.63}$$

Throughout the calculations in the present section, the pumping power associated with both the internal and external fluid flows of the HEx can be calculated using Eqs. (B.21) and (B.52). The next step is to calculate the heat transfer rate associated with each HEx through the thermal resistance that was calculated and ε-NTU method.

B.4 The εNTU Method

The ε-NTU method (Kays & London, 1984) consists of calculating the actual heat transfer on a HEx by comparing it to the maximum heat transfer possible on that component. This is achieved by defining the effectiveness of the heat exchanger, which is determined as the ratio of the actual to the ideal heat transfer rate on a HEx. For that, some characteristic parameters of the HEx must be calculated, and relations for effectiveness must be developed.

In the previous section, the calculation to obtain the thermal resistances associated with internal convection, conduction through the tube, and external convection was developed. With this information, the overall thermal conductance of one of the circuits of the HEx, UA_{circ}, can be calculated through an association of thermal resistances and is given by Eq. (B.64).

$$UA_{\text{circ}} = \left(\frac{1}{R_{\text{T}}} + \frac{1}{R_{\text{l}}} + \frac{1}{R_{\text{a}}}\right)^{-1} \tag{B.64}$$

The number of transfer units associated with the circuit, NTU_{circ}, is defined by the ratio of its overall thermal conductance of the circuit and the minimum heat capacity ratio of its fluid streams, $(\dot{m}_{\text{l}} c_{\text{p}})_{\text{min}}$, which results in:

$$NTU_{\text{circ}} = \frac{UA_{\text{circ}}}{(\dot{m}_{\text{f}} c_{\text{p}})_{\text{min}}} = N_{\text{circ}} \frac{UA_{\text{circ}}}{(\dot{m}_{\text{a}} c_{\text{p,a}})} \tag{B.65}$$

Another fundamental parameter on the ε-NTU method is the heat capacity ratio, $\dot{C}^{*}_{\text{HEx}}$, which is given by the ratio between the minimum and maximum heat capacity ratios of the HEx streams. This parameter can be calculated by:

$$\dot{C}^{*}_{\text{HEx}} = \frac{(\dot{m}_{\text{f}} c_{\text{p}})_{\text{min}}}{(\dot{m}_{\text{f}} c_{\text{p}})_{\text{max}}} = \frac{(\dot{m}_{\text{a}} c_{\text{p,a}})}{N_{\text{circ}} \, (\dot{m}_{\text{circ,l}} c_{\text{p,l}})} \tag{B.66}$$

As can be observed in Eq. (B.65) and Eq. (B.66), for all the HExs evaluated on the present analysis, the stream of the circuit, or the HEx, with the minimum heat capacity is the air one (external); thus, the one with the maximum heat capacity is the liquid one (internal).

Tube-fin HEx is classified as a cross-flow type of HEx, with its effectiveness not only dependent on the parameters presented previously in this section (NTU_{circ} and $\dot{C}^{*}_{\text{HEx}}$). For the correlations applied in the current modeling (Wang *et al.*, 1999), the longitudinal number of tubes and rows must also be accounted for in the calculation of effectiveness.

Relations for the effectiveness, ε, of tube fin HExs composed of 1, 2, 3, and 4 rows are given by Eq. (B.67) - Eq. (B.70) (ESDU, 1998; Wang *et al.*, 1999). For an arrangement with more than four rows, the effectiveness can be calculated by Eq. (B.71).

$$\varepsilon = \frac{1 - \exp\left(-\dot{C}^{*}_{\text{HEx}} K\right)}{\dot{C}^{*}_{\text{HEx}}} \tag{B.67}$$

$$\varepsilon = \frac{1 - e^{-2K\dot{C}^{*}_{\text{HEx}}} \left(1 + \dot{C}^{*}_{\text{HEx}} K^{2}\right)}{\dot{C}^{*}_{\text{HEx}}} \tag{B.68}$$

$$\varepsilon = \frac{1 - e^{-3K\dot{C}^*_{\mathrm{HEx}}}\left(1 + \dot{C}^*_{\mathrm{HEx}}K^2(3-K) + 3(\dot{C}^*_{\mathrm{HEx}})^2K^4/2\right)}{\dot{C}^*_{\mathrm{HEx}}} \tag{B.69}$$

$$\varepsilon = \frac{1}{\dot{C}^*_{\mathrm{HEx}}}\left(1 - e^{-4K\dot{C}^*_{\mathrm{HEx}}}\left[1 + \dot{C}^*_{\mathrm{HEx}}K^2\left(6 - 4K + K^2\right) + 4(\dot{C}^*_{\mathrm{HEx}})^2K^4(2-K) + 8(\dot{C}^*_{\mathrm{HEx}})^3K^6/3\right]\right) \tag{B.70}$$

$$\varepsilon = 1 - \exp\left[\frac{NTU^{0.22}_{\mathrm{circ}}\left(\exp\left(-\dot{C}^*NTU^{0,78}_{\mathrm{circ}}\right) - 1\right)}{\dot{C}^*}\right] \tag{B.71}$$

the parameter K present in Eq. (B.67), Eq. (B.68), Eq. (B.69) and Eq. (B.70) can be calculated by:

$$K = 1 - \exp\left(\frac{NTU_{\mathrm{circ}}}{N_{\mathrm{l}}}\right) \tag{B.72}$$

Given the calculation of the effectiveness, the heat transfer rate by each one of the circuits can be calculated by:

$$\dot{Q}_{\mathrm{circ}} = \varepsilon_{\mathrm{circ}}\left(\dot{m}_{\mathrm{f}}c_{\mathrm{p}}\right)_{\mathrm{min}}\Delta T_{\mathrm{max}} = \dot{m}_{\mathrm{circ,l}}c_{\mathrm{p,l}}(\varepsilon C^*)_{\mathrm{circ}}\Delta T_{\mathrm{max}} \tag{B.73}$$

where the maximum temperature difference in the circuit, ΔT_{max}, is given by the difference between the inlet temperatures of the air and liquid streams.

For the CHEx, ΔT_{max} is given by the difference between the inlet temperature of the air stream, $T_{\mathrm{a,c,in}}$, and the inlet temperature of the liquid stream, $T_{\mathrm{f,c,in}}$. Therefore, the rate of heat absorbed from the cold reservoir, which is also known as cooling capacity, $\dot{Q}_c$, can be calculated by:

$$\begin{aligned}\dot{Q}_{\mathrm{CHEx}} =& \varepsilon_{\mathrm{CHEx}}\dot{m}_{\mathrm{ca}}c_{\mathrm{p,c,a}}\left(T^{\mathrm{in}}_{\mathrm{CHEX,a}} - T^{\mathrm{in}}_{\mathrm{CHEX,l}}\right)\\ =& N_{\mathrm{circ}}\dot{m}_{\mathrm{circ,l}}c_{\mathrm{p,l}}(\varepsilon C^*)_{\mathrm{CHEx}}\left(T^{\mathrm{in}}_{\mathrm{CHEX,a}} - T^{\mathrm{in}}_{\mathrm{CHEX,l}}\right)\end{aligned} \tag{B.74}$$

where $\varepsilon_{\mathrm{CHEx}}$ stands for the effectiveness of the circuits of the CHEx, $\dot{m}_{\mathrm{CHEX,a}}$ for the airflow rate on the CHEX, $T^{\mathrm{in}}_{\mathrm{CHEX,a}}$ for the inlet temperature of the air stream in the CHEx, and $T^{\mathrm{in}}_{\mathrm{CHEX,l}}$ for the inlet temperature of the liquid stream in the CHEx.

Analogously, for the HHEx, the ΔT_{max} is given by the difference between the inlet temperature of the liquid stream, $T_{\mathrm{l,h,in}}$, and the inlet temperature of the air stream, $T_{\mathrm{a,h,in}}$. By applying Eq. (B.73) in the HHEx, the heat rejection rate to the hot reservoir, $\dot{Q}_h$, can be calculated by:

$$\begin{aligned}\dot{Q}_{\mathrm{HHEx}} =& \varepsilon_{\mathrm{HEx}}\dot{m}_{\mathrm{ha}}c_{\mathrm{p,h,a}}\left(T^{\mathrm{in}}_{\mathrm{HHEx,l}} - T^{\mathrm{in}}_{\mathrm{HHEx,a}}\right)\\ =& N_{\mathrm{circ}}\dot{m}_{\mathrm{circ,l}}c_{\mathrm{p,l}}(\varepsilon C^*)_{\mathrm{HHEx}}\left(T^{\mathrm{in}}_{\mathrm{HHEX,a}} - T^{\mathrm{in}}_{\mathrm{HHEX,l}}\right)\end{aligned} \tag{B.75}$$

where $\varepsilon_{\mathrm{HHEx}}$ stands for the effectiveness of the circuits of the HHEx, $\dot{m}_{\mathrm{HHEX,a}}$ for the airflow rate on the HHEX, $T^{\mathrm{in}}_{\mathrm{HHEX,a}}$ for the inlet temperature of the air stream in the HHEx, and $T^{\mathrm{in}}_{\mathrm{HHEX,l}}$ for the inlet temperature of the liquid stream in the HHEx.

Using the geometric and thermal-hydraulic models presented in this Appendix, the relevant performance metrics for both the HHEx and CHEx can be calculated and used for system design and optimization.

Appendix C

CHARACTERISTICS OF THE FAN

In Appendix B, the mathematical models used to predict the performance of a fan-assisted herringbone wave tube-fin HEx were presented. This Appendix presents the geometric, operational, and aerodynamic characteristics of the fans coupled to the HEx, which enhance airflow through them.

C.1 Selection of the Fan

A magnetocaloric refrigeration system typically operates at higher working fluid mass flow rates than refrigerant systems in traditional vapor compression systems. Besides that, given the low magnitude of the MCE, low-temperature differences are required in the HEx, resulting in a high heat transfer area. These two requirements also generate a demand for an elevated airflow rate for the HEx to reject or absorb the required heat.

The first step in the selection process is regarding the fan type. Although tangential-type fans are usually employed in air conditioning applications similar to the one being developed in the present work, the gains in low noise and compactness they provide do not outweigh the losses in output performance and efficiency they entail for the system. Therefore, axial-type fans were selected primarily because of their high airflow rates and efficiencies (Kuehn *et al.*, 1998).

There are several trade-offs in defining the mass flow rate of air, which are dictated by the operating point, and most of the design parameters related to HEx geometric definitions and how they affect the pressure drop relation. Besides that, at the component level, one can select fans with a large blade diameter, which results in larger frontal areas and higher mass flow rates.

Another requirement for the fan concerns the power supply. The performance of a refrigeration system can be enhanced by controlling the rotational speed (Hittinger *et al.*, 2016). Hence, an AC power supply for the fan is required, and a phase-angle relay is used to maintain its rotation speed (Hoffmann *et al.*, 2021).

Given the requirements listed below, the fan model S4E350-AN19-43 from Ebm-Papst was selected due to its desirable characteristics and availability. The main characteristics of the fan are given in Tab. C.1.

At this point in the design process, it was considered an over-sizing strategy for the fan. This was done to ensure some reliability of the component; once it blows too much air

Parameter	Value
Weight	5.1 kg
Size	350 mm
Number of blades	5
Frequency	50 Hz
Type of Voltage	AC

Table C.1 – Main characteristics of the model S4E350-AN19-43 fan

into the HEx, the phase angle relay can decrease the rotating speed.

C.2 Characteristics of the Fan

The supplier of the fan provided four experimental points for the operation of the S4E350-AN19-43 at 50 Hz, where the performance of the fan was evaluated in terms of volumetric airflow rate ($\dot{V}_{\mathrm{a}}$), pressure (ΔP) and power consumption ($\dot{W}_{\mathrm{fan}}$). These results are summarized in Tab. C.2.

Parameter	$\dot{V}_{\mathrm{a}}$ [m^3/h]	ΔP_{fan} [Pa]	$\dot{W}_{\mathrm{fan}}$ [W]
Point 1	3200	0	134
Point 2	2775	30	142
Point 3	2270	60	151
Point 4	1760	80	158

Table C.2 – Operation points provided in the catalogue by the supplier for the model S4E350-AN19-43 fan

The head curve of the fan is an essential parameter for the model, since its coupling with the pressure drop relation for the external flow of the HEx will dictate the operation point of the HEx-fan set. To perform that, a non-linear least square method (Press *et al.*, 2007) was applied to fit a predefined function, generating a relation for the head curve of the fan. Given the expected results of a fan head curve (Fox *et al.*, 2014) and the experimental points distribution, a quadratic equation, given by Eq. (C.1) was used as the predefined function for the application of the fit.

$$Y = \alpha_0 + \alpha_1 X + \alpha_2 X^2 \tag{C.1}$$

By substituting the ΔP and $\dot{V}_{\mathrm{a}}$ values in Tab. (C.2) as Y and X, respectively, in Eq. (C.1), the coefficients α_0, α_1 and α_2 are obtained through the application of the fit. The resulting equation is defined as:

$$\Delta P_{\mathrm{fan}} = 86.078 + 2.550 \cdot 10^{-2} \cdot \dot{V}_{\mathrm{a}} - 1.639 \cdot 10^{-5} \cdot \dot{V}_{\mathrm{a}}^2 \tag{C.2}$$

Equation (C.2) is plotted in Fig. C.1 along with the experimental points presented in Tab.C.2, defined in the figure as Training Set. Besides that, three other points were manually

collected from the head curve figure provided by the catalog, as shown in Fig. C.4. As can be seen, excellent agreement between the training and test sets and the fitted equation is obtained.

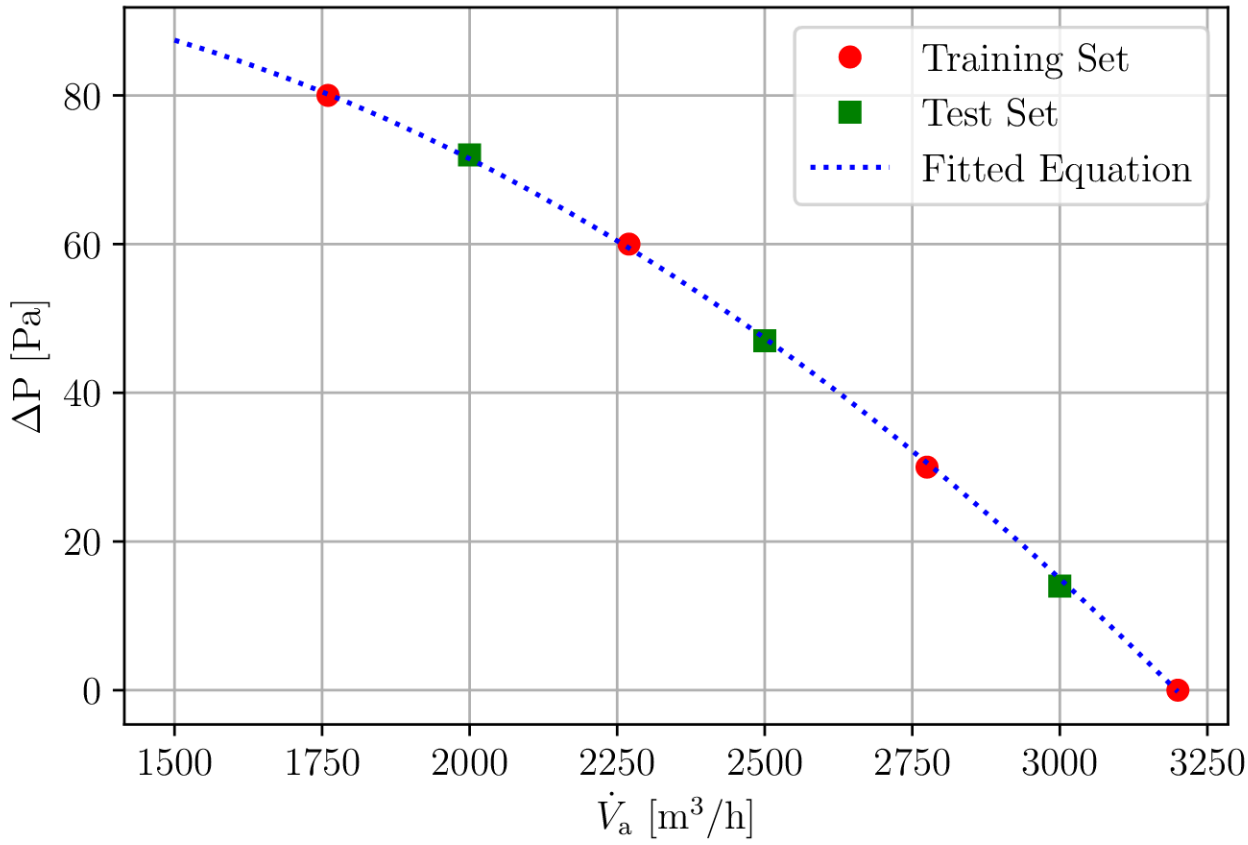


Figure C.1 – Comparison between the experimental results, training and test sets, and the fitted equation for the performance curve of the model S4E350-AN19-43 fan.

Another important parameter that is evaluated in the performance of the fan is $\dot{W}_{\text{fan}}$. As shown in Tab. C.2, this parameter depends on the operating point; therefore, a similar strategy to that adopted for the head curve is used. Firstly, the efficiency of the fan is calculated by:

$$\eta_{\text{fan}} = \frac{\Delta P_{\text{fan}} \dot{V}_a}{\dot{W}_{\text{fan}}} \tag{C.3}$$

After that, the same methodology used for fitting the ΔP data is applied, only this time the variable Y in Eq. (C.1) is defined as η_{fan}. The resulting equation is given by:

$$\eta_{\text{fan}} = -0.571 + 8.138 \cdot 10^{-4} \cdot \dot{V}_a - 1.984 \cdot 10^{-7} \cdot \dot{V}_a^2 \tag{C.4}$$

Eq. (C.4) is plotted along with the experimental points of efficiency in Fig. (C.2). Once again, an excellent agreement is obtained from the experimental data and the fitted equation. Besides that, the efficiency curve also has the expected trend (Fox *et al.*, 2014)

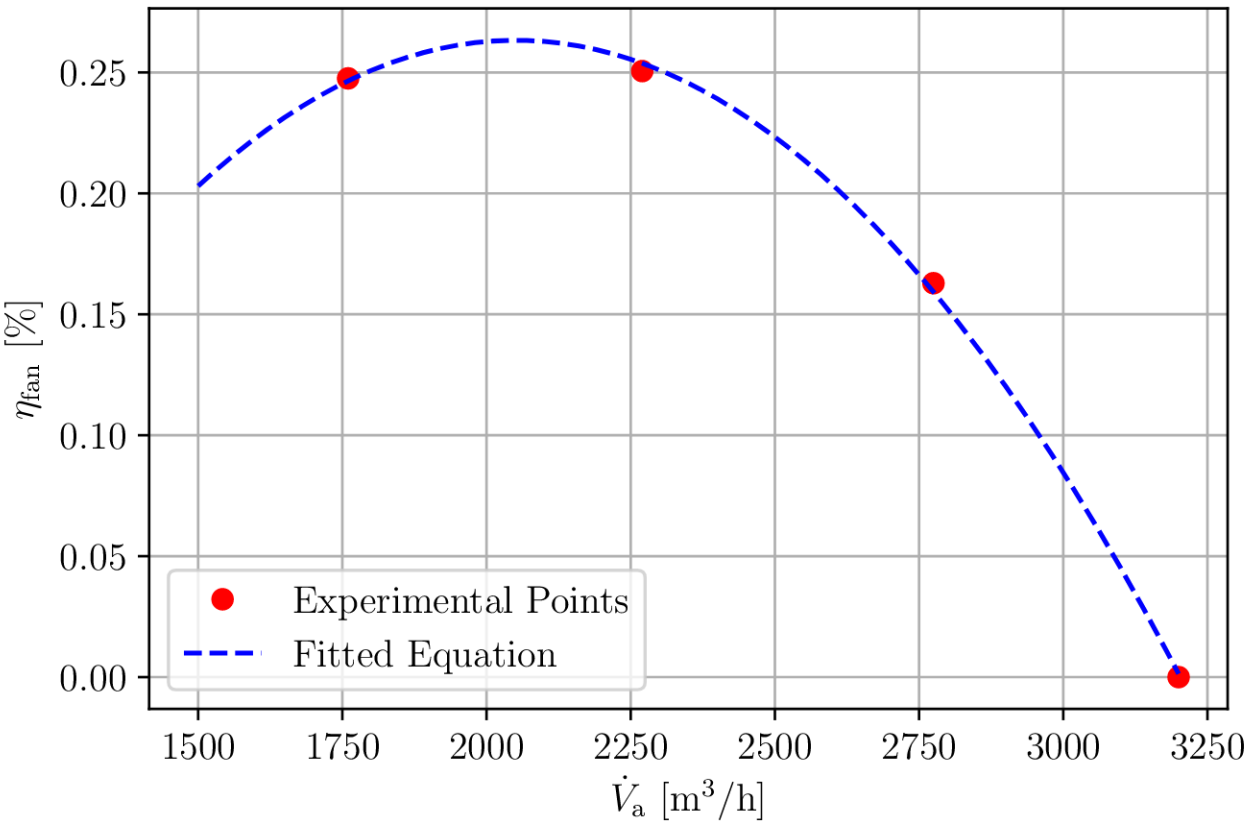


Figure C.2 – Comparison between the experimental results and the fitted equation for the efficiency curve of the model S4E350-AN19-43 fan.

C.3 Catalogue Figures

The detailed drawings for the S4E350-AN19-43 fan provided by the catalog are shown in Fig. C.3.

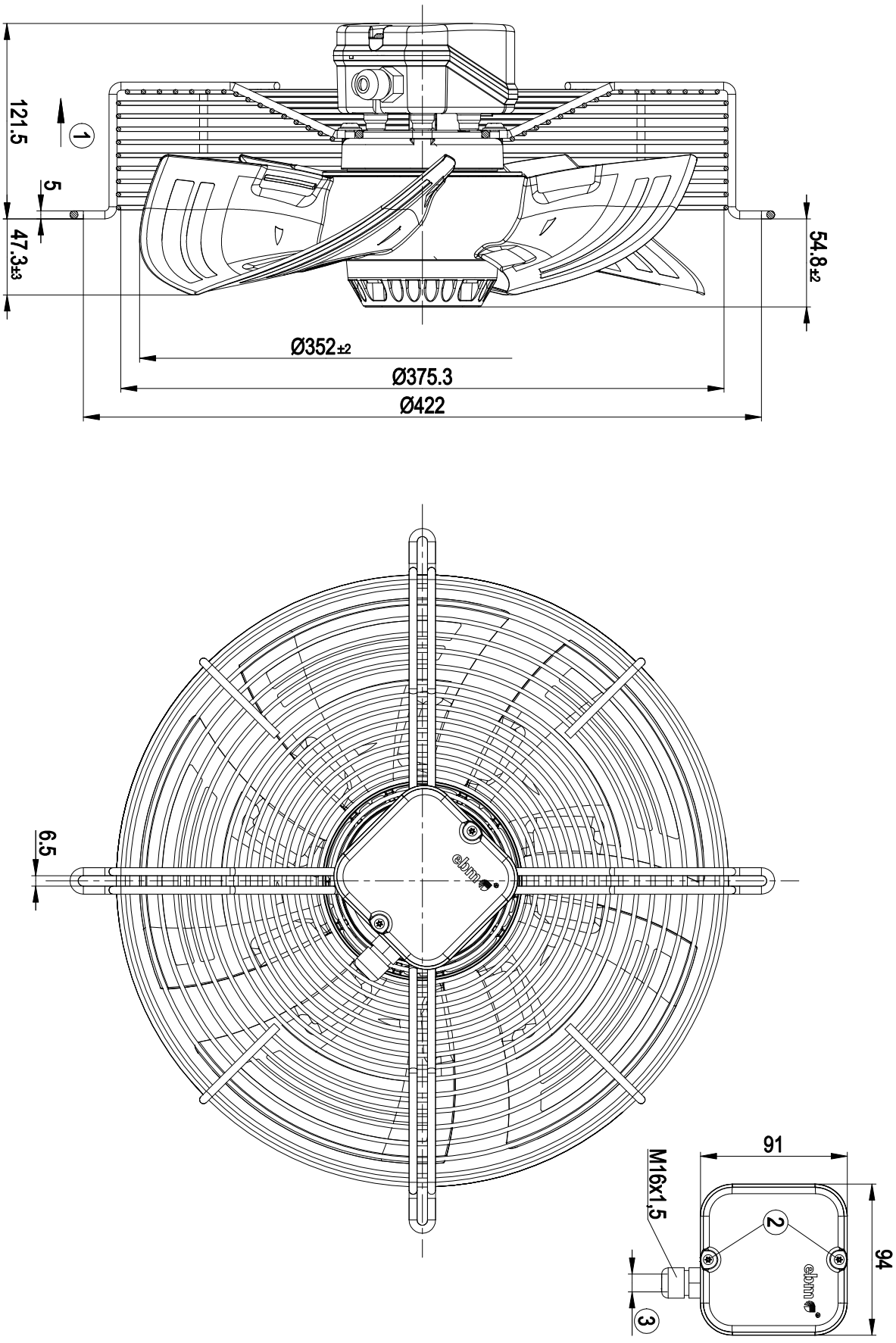


Figure C.3 – Product drawings for the model S4E350-AN19-43 fan

The performance curve for the S4E350-AN19-43 fan provided by the catalog is shown in Fig. C.4.

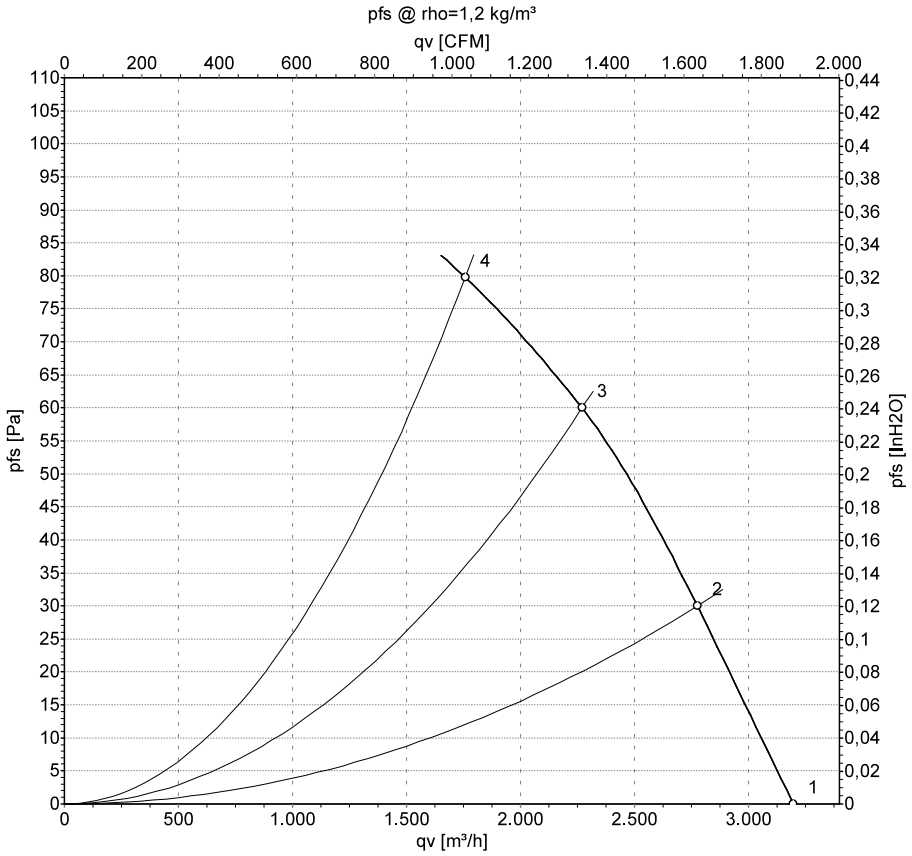


Figure C.4 – Performance curve provided by the catalogue for the S4E350-AN19-43 fan